ERCOFTAC Series

Dimokratis G.E. Grigoriadis
Bernard J. Geurts
Hans Kuerten
Jochen Fröhlich
Vincenzo Armenio *Editors*

Direct and Large-Eddy Simulation X

Springer

ERCOFTAC Series

Volume 24

Aims and Scope of the Series

ERCOFTAC (European Research Community on Flow, Turbulence and Combustion) was founded as an international association with scientific objectives in 1988. ERCOFTAC strongly promotes joint efforts of European research institutes and industries that are active in the field of flow, turbulence and combustion, in order to enhance the exchange of technical and scientific information on fundamental and applied research and design. Each year, ERCOFTAC organizes several meetings in the form of workshops, conferences and summerschools, where ERCOFTAC members and other researchers meet and exchange information.

The ERCOFTAC Series will publish the proceedings of ERCOFTAC meetings, which cover all aspects of fluid mechanics. The series will comprise proceedings of conferences and workshops, and of textbooks presenting the material taught at summerschools.

The series covers the entire domain of fluid mechanics, which includes physical modelling, computational fluid dynamics including grid generation and turbulence modelling, measuring-techniques, flow visualization as applied to industrial flows, aerodynamics, combustion, geophysical and environmental flows, hydraulics, multiphase flows, non-Newtonian flows, astrophysical flows, laminar, turbulent and transitional flows.

More information about this series at http://www.springer.com/series/5934

Dimokratis G.E. Grigoriadis
Bernard J. Geurts · Hans Kuerten
Jochen Fröhlich · Vincenzo Armenio
Editors

Direct and Large-Eddy Simulation X

Springer

Editors
Dimokratis G.E. Grigoriadis
Department of Mechanical and
Manufacturing Engineering
University of Cyprus
Nicosia
Cyprus

Bernard J. Geurts
Multiscale Modeling and Simulation
University of Twente
Enschede
The Netherlands

Hans Kuerten
Department of Mechanical Engineering
Eindhoven University of Technology
Eindhoven
The Netherlands

Jochen Fröhlich
Institute of Fluid Mechanics
Technische Universität Dresden
Dresden
Germany

Vincenzo Armenio
Dipartimento di Ingegneria e Architettura
Università di Trieste
Trieste
Italy

ISSN 1382-4309 ISSN 2215-1826 (electronic)
ERCOFTAC Series
ISBN 978-3-319-63211-7 ISBN 978-3-319-63212-4 (eBook)
https://doi.org/10.1007/978-3-319-63212-4

Library of Congress Control Number: 2017946948

Printed on acid-free paper

This Springer imprint is published by Springer Nature
The registered company is Springer International Publishing AG
The registered company address is: Gewerbestrasse 11, 6330 Cham, Switzerland

Preface

More than half a century has passed after the pioneering work on atmospheric circulation predictions by Joseph Smagorinsky who established the scientific foundations of Large Eddy Simulations. Almost thirty years later, in 1994, the first international Workshop devoted to Direct and Large Eddy Simulations, DLES1 was hosted at the University Of Surrey. The success of the first ERCOFTAC DLES1 (European Research Community On Flow, Turbulence and Combustion) initiated a series of biannual DLES events. During these years—even with the most conservative estimates—the computing power has increased by at least two orders of magnitude. This continuing progress motivated and inspired researchers to apply DNS and LES to ever more challenging flows at ever higher Reynolds numbers, including multiple physical phenomena.

The present volume contains the proceedings of the 10th ERCOFTAC Workshop on Direct and Large Eddy Simulation, DLES10, which was hosted by the Department of Mechanical and Manufacturing Engineering of the University of Cyprus, 27–29 May 2015 in Limassol, Cyprus. The main goal of the workshop was to discuss state-of-the-art DNS, LES and related techniques for the computation and modelling of turbulent and transitional flows. We hope that this volume, together with the expected advances in computational power, will motivate further developments in turbulent flow predictions and shed more light on this main problem of fluid mechanics.

The gathering at DLES10 of specialists in the field offered a unique opportunity to the participants to exchange ideas and discuss in a fruitful manner recent advances on the partial or full resolution of instantaneous turbulent flow and its statistical aspects. A total of 85 people participated from twenty different countries and three different continents, including seven invited speakers and 37 PhD students who were kindly financially supported by the European Research Community on Flow, Turbulence and Combustion, ERCOFTAC.

The broad range of featured topics for the 10th edition of DLES in Cyprus were as follows: LES fundamentals and modelling, quality of LES, numerical techniques, heat and mass transfer, biological flows, multiphase flows, industrial applications, environmental and geophysical applications as well as reacting flows and

combustion. Based on the submitted contributions, the scientific program was divided into two parallel sessions of oral presentations covering the three days of the workshop. Following the workshop schedule, the material contained in this volume is organized in nine basic thematic areas. The thematic framework of the entire workshop was established by keynote presentations delivered by the invited speakers. Following the increasing interest on the assessment of the quality and reliability of LES results, Prof. Maria Vittoria Salvetti (University of Pisa) presented counter-intuitive results for cases where increased numerical resolution could lead to the deterioration of accuracy. Assoc. Prof. Elisabetta De Angelis (University of Bologna) highlighted improvements of modelling subgrid-stresses in LES based on the energy transfer phenomena in turbulent flows. Professor Elias Balaras (The George Washington University) presented interesting numerical methodologies applied to biological flows with applications in biology, physiology, animal locomotion and bio-prosthetic devices. Dr. Ruud L.G.M. Eggels (Rolls-Royce Deutschland Ltd & Co KG) focused on the role of CFD for the design process of aero engines, spray-modelling, combustion and emissions processes. The need for further developments on modelling the mechanisms of spray break-up and soot prediction was also demonstrated. Professor Dominique Thévenin (University of Magdeburg) discussed the connection between DNS, LES and POD for a variety of transition-related applications. Three main issues were presented in detail: the efficient implementation of—reacting or not—dispersed particles or droplets in DNS, the impact of the disperse phase on the turbulence properties and transition and the possibility of quantifying transition to turbulence using a POD analysis. Professor Maarten Van Reeuwijk (Imperial College London) demonstrated the state of the art for Direct and Large Eddy Simulation of atmospheric boundary layers, with emphasis on turbulent entrainment and stratification effects. Professor Richard D. Sandberg (University of Southampton) presented challenging DNS investigations of compressible flows in realistic configurations for problems related to turbomachinery and aeroacoustics. Impressive results were presented for the significance of various noise sources in a pipe-jet configuration, the flow through a linear high-pressure turbine cascade and the sensitivity of low-pressure turbines to inflow disturbances.

The organization of DLES10 and the preparation of the present volume are the outcome of an international team effort. The local organizers would like first of all to acknowledge the support of ERCOFTAC, as the main sponsor of the event. We are also grateful for the contributions of The University of Cyprus, the J.M. Burgerscentrum (JMBC) and the Cypriot Tourism Organization. Last but not least, the organizers also gratefully acknowledge all participating scientists for providing valuable contributions and all members of the Scientific Committee of DLES10 for their efforts to complete the review process of the submitted contributions.

Nicosia, Cyprus
February 2015

Dimokratis G.E. Grigoriadis
Bernard J. Geurts
Hans Kuerten
Jochen Fröhlich
Vincenzo Armenio

Committees

Local Organizing Committee

Dimokratis G.E. Grigoriadis, University of Cyprus, Cyprus
Stavros Kassinos, University of Cyprus, Cyprus

Scientific Committee

B.J. Boersma, TU Delft, The Netherlands
D. Borello, University of Rome, Italy
M. Breuer, Helmut-Schmidt-Univ. Hamburg, Germany
L. Davidson, Chalmers University of Technology, Sweden
S. Elghobashi, University of California, Irvine, USA
R. Friedrich, TU Munich, Germany
K. Fukagata, Keio University, Japan
M. García-Villalba, Universidad Carlos III de Madrid, Spain
W.P. Jones, Imperial College, London, Great Britain
T. Kempe, TU Dresden, Germany
L. Kleiser, ETH Zurich, Switzerland
E. Lamballais, PPRIME Poitiers, France
C. Meneveau, Johns Hopkins University, USA
J. Meyers, University Leuven, The Netherlands
U. Piomelli, Queens University, Kingston, Canada
S.B. Pope, Cornell University, USA
M.-V. Salvetti, University of Pisa, Italy
S. Sarkar, University of California, San Diego, USA
W. Schröder, RWTH Aachen, Germany
J. Sesterhenn, TU Berlin, Germany
S. Sherwin, Imperial College London, Great Britain

F. Stefani, HZDR, Dresden, Germany
D. Thévenin, Universität Magdeburg, Germany
A. Tomboulides, Aristotle University of Thessaloniki, Greece
F. Toschi, TU Eindhoven, The Netherlands
M. Uhlmann, Karlsruhe Institute of Technology, Germany
L. Vervisch, Coria, Rouen, France

Contents

Part I
Keynote Papers

The Application of Combustion LES Within Industry

Ruud L.G.M. Eggels

Within this paper the combustion CFD approach which is followed within Rolls-Royce is described. Combustion CFD computations are based on the in-house code PRECISE-UNS. An overview of the applied models for turbulence, combustion and spray modelling is given, and the results for a few validation cases for which experimental data is available are presented. For the validation cases both RANS and LES computations are performed, and it is shown that RANS gives reasonable accurate results, whereas the LES results show a better agreement with the experimental results. Furthermore, LES simulations of an aero engine combustor are presented.

1 Introduction

Due to the increasing capacity of high performance computers and to improved numerical modelling capability, the application of CFD within the design process for aero engine increases continuously. The accuracy of CFD prediction has not only been improved due to more advanced modelling capabilities for spray, combustion and emissions, but also by increasing the computational domain and by the application of higher resolution meshes. Nowadays, complete combustion systems, from compressor exit to turbine entry, are included in combustion CFD computations. Consequently the flow splits between the different air streams have to be estimated. In order to be able to support and influence the design of a new combustor, turnaround times of CFD have to be in the order of a day, since many configurations should be considered. Furthermore, parameterised CAD models have been introduced to speed up design modifications and consequent numerical analyses. CFD computations to support the combustor design are currently based on RANS due to the required short turnaround time. However, the application of LES is increasing. The role of LES in the combustion design process is to verify optimised designs.

R.L.G.M. Eggels (✉)
Rolls-Royce Deutschland, Eschenweg 11, 15827 Blankenfelde-mahlow, Germany
e-mail: ruud.eggels@rolls-royce.com

D.G.E. Grigoriadis et al. (eds.), *Direct and Large-Eddy Simulation X*,
ERCOFTAC Series 24, https://doi.org/10.1007/978-3-319-63212-4_1

Within the Rolls-Royce in-house combustion CFD code PRECISE−UNS both RANS and LES turbulence models are available. Different variants of the k-epsilon turbulence model have been implemented (standard, realizable, RNG, SST-k-ω), as well as different variants of the Reynolds stress model. Additionally, different LES sub-grid stress models are available: constant Smagorinsky, WALE, Vreman and a dynamic Smagorinsky model. Mostly the sgs model from Vreman is used, as it provides a more realistic behaviour near walls. Is has to be noted that turbulence generated near walls, play a minor role in combustion simulations, since most turbulence is generated within the combustor due to shear from injector and/or dilution ports.

A Lagrangian approach to model the spray droplet transport is used. The spray model includes transport, evaporation and dispersion. The spray and flow field are two-way coupled. The spray model has been initially developed for RANS, next it has been extended to be used for unsteady flow. For LES specially boundary conditions have been developed to ensure that the droplets are introduced using an stochastic approach (for position and droplet size).

Combustion models also initially have been developed for RANS, but specific sub models for LES have been developed as well. For example, the stochastic field PDF model, initially developed at Imperial College [1], is based on the transient nature of LES. In this model, the PDF of a scalar is represented by a limited amount of stochastic fields (4–8).

2 CFD Approach

The in-house combustion CFD code PRECISE−UNS is based on a finite volume approach. Conservation equations for momentum, enthalpy, turbulence and combustion variables are solved. A pressure correction method based on the SIMPLE approach of Patankar [2] is used for the pressure. The approach of Karki and Patankar [3] is being followed for compressible flows [4].

The equations are discretized using the co-located approach for unstructured grids [5]. Several second order convection schemes have been implemented; central, gamma, minmod, weno, linear-upwind, upwind. For scalar generally TVD schemes, e.g. the gamma scheme are applied. The time discretization is also second order. All equations are solved implicit in space and time using a segregated solver.

The CFD infrastructure for unstructured grid is adapted from the opensource code Dolfyn [6]. For the domain partitioning Parmetis is used. To solve the pressure equation the parallel solver Hypre [7] or the AGMG solver [8] are applied.

For the hereafter presented results, the FGM combustion model is applied. The FGM model is based on the assumption that the flame structure is unique, so that it can be computed using freely propagation laminar flames. The flame structure is parameterised with a progress variable, which is a combination of specific mole numbers of species. As default progress variable, the sum of the specific mole number of H_2O, CO_2 and H_2 is used. Furthermore, flames are computed for a range of

mixture fractions. For turbulent combustion processes also the effect of combustion turbulence interaction has to be taken into account. Here this is done using presumed PDF's. Therefore, additional equations are solved for the variances for the progress variable and the mixture fraction. As presumed PDF's a beta function is adapted for the mixture fraction, whereas a three delta PDF is used for the progress variable. While a scaled progress variable is not unique defined for unburned conditions (and air), a transport equation for the (non-scaled) specific mole number for the progress variable is solved. On the other hand, an equation for the scaled progress variable variance is solved, to eliminate the dependence of the progress variable variance on mixture fraction gradients (without the need to add high order correction terms). NOx concentrations are not taken from the FGM tables, but a separate equation for NO is solved. The source term is split into a thermal and prompt parts, and the thermal part is split into a production term and an destruction term:

$$S_{NO} = S^{+}_{NO,thermal} - S^{-}_{NO,thermal}\phi_{NO} + S_{prompt}. \tag{1}$$

Heat loss is incorporated by computing a range of FGM tables for different enthalpy values. The latter is done by computing tables with different temperatures for the unburned mixture. For gas turbines this approach can be applied without numerical problems, since unburned temperatures are in the range of 600–1000 K, so that heat-losses in the order of 300 K can be taken into account by lowering the inlet temperature. For atmospheric conditions this would be a problem, since the thermodynamic properties and reaction rates are not defined below temperatures of 250 K. This is overcome by computing burner stabilised flames for a range of velocities.

3 Validation Strategy

To validated the CFD code, it has been tested on a range of testcases, ranging from simple well defined benchmark cases, to generic test rigs with realistic geometries and operating conditions and finally complete engine combustor systems.

As example for a benchmark case, a generic combustor from DLR (Deutsches Luft und Raumfahrtzentrum) is provided. This test case has been setup to generate validation data for CFD, with a focus on soot modelling. The test rig is presented in Fig. 1. For this case detailed measurement data for temperatures, velocities and soot distributions are available [9, 10]. Within the CFD model, the injector has been included in the computational domain. The rig has been operated at a pressure of 3bar, an air temperature of 293 K and calorimetry $\phi = 1.2$. The applied massflow rates are given in Table 1. Velocity results of RANS and LES computations are provided in Fig. 3. The velocity results of RANS and LES are similar, but locally the differences are considerable. Overall, the velocity field prediction by RANS is reasonable, but as may be expected, not as good as the LES results (Fig. 2).

The predicted temperature fields are presented in Fig. 4. It is seen that also the temperature fields of RANS and LES predictions are similar, but the difference in

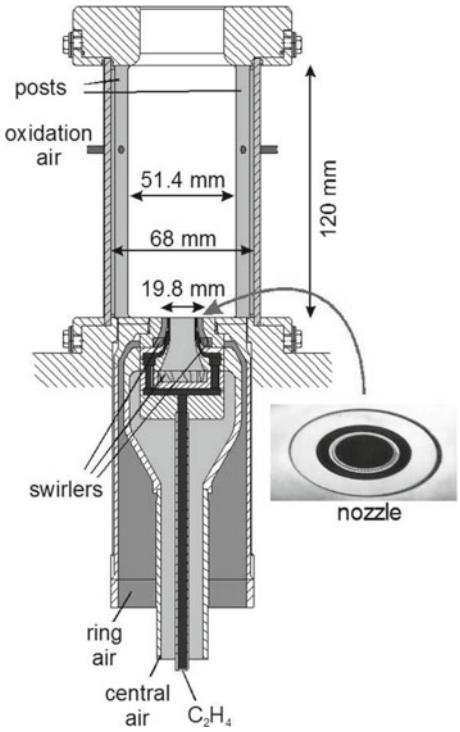

Fig. 1 Generic DLR rig set-up (courtesy of DLR)

Table 1 Boundary conditions for generic DLR combustor

Applied massflows	(gr/s)
Inner swirler	3.034
Outer swirler	7.079
Dilution jets	4.038
Fuel passage	0.82

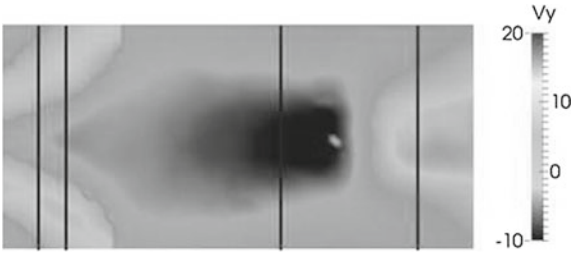

Fig. 2 Measured velocity field

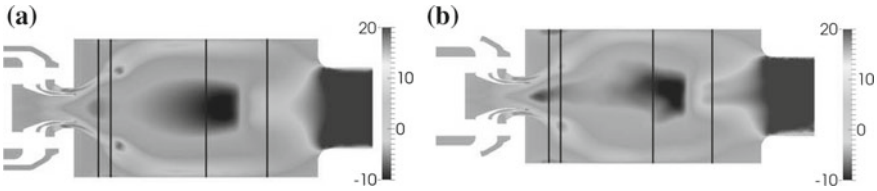

Fig. 3 **a** RANS velocity field. **b** LES velocity field

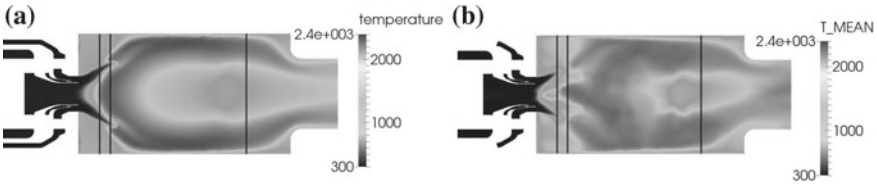

Fig. 4 **a** RANS temperature field. **b** LES temperature field

predicted temperature by RANS and LES results are larger than the differences in the predicted velocities. Especially, the stabilitation of the flame close to the injector is different. When comparing the computed temperature profiles with the measured data (Fig. 5) as function of the radial coordinate at three different axial positions, it can be seen that the LES predictions are more accurate, especially in the stabilisation area. Furthermore, in Fig. 6 the temperature and its variation on the centreline of the combustor are presented.

Experimental and predicted soot results are presented in Figs. 7 and 8. The results show that the magnitude of the soot volume fraction is not correctly predicted, whereas the shape of the soot volume fraction is better predicted by LES than by RANS; within the RANS result no soot is present on the centerline, whereas the LES and the experimental results do show soot on the centreline. Further improvement on the soot modelling is required to improve the quantitative prediction of soot.

Next an example of a generic test case is presented. Here an industrial aero lean burn injector is measured in a single sector high pressure rig facility of DLR in Cologne [11]. Velocities have been measured using PIV and the temperature field has been derived from OH*. LES computations have been performed and results are compared with the experimental data.

A sketch of the Rig and the applied injector are provided in Figs. 9 and 10. The velocities results are presented in Fig. 12. Results are presented for two different LES integration times, showing that for the pilot long integration times are required. The predicted velocity profiles agree well with the measured velocities (Fig. 11).

In Fig. 13, the predicted temperatures from the LES computations are compared with experimental temperatures derived from OH*. Note that this method is only valid at lean conditions. It can be seen that the flame shape is predicted well for both the pilot and main flame.

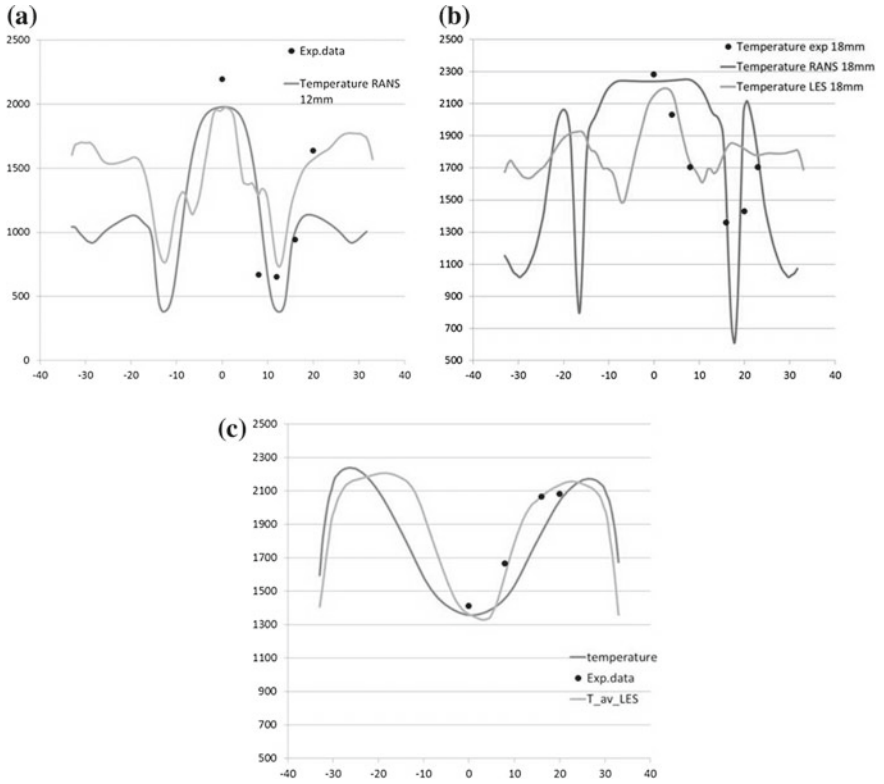

Fig. 5 **a** Radial temperature profile at 12 mm. **b** Radial temperature profile at 18 mm. **c** Radial temperature profile at 95 mm

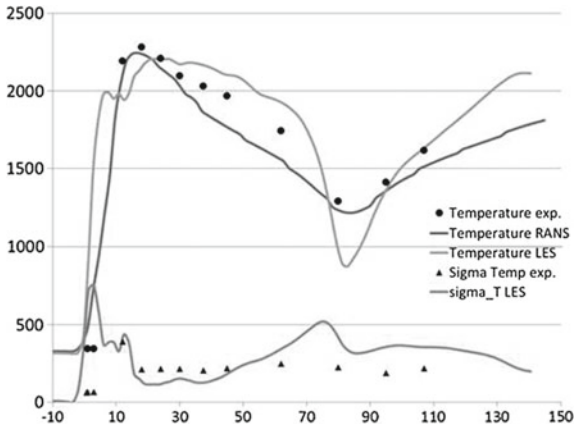

Fig. 6 Axial temperature profile

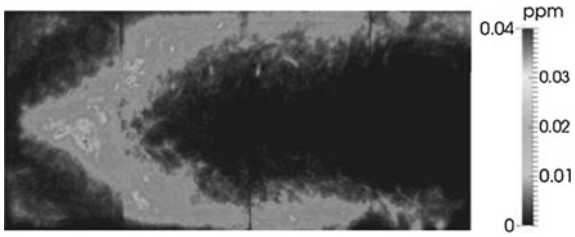

Fig. 7 Measured soot volume fraction

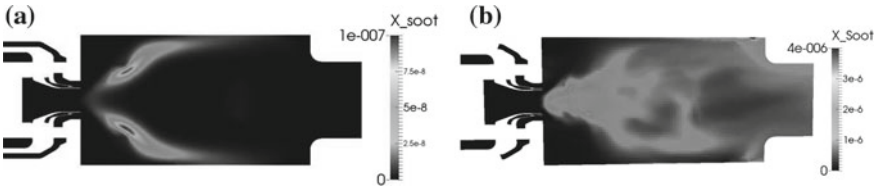

Fig. 8 **a** RANS soot volume fraction. **b** LES soot volume fraction

Fig. 9 DLR BOSS rig (courtesy of DLR)

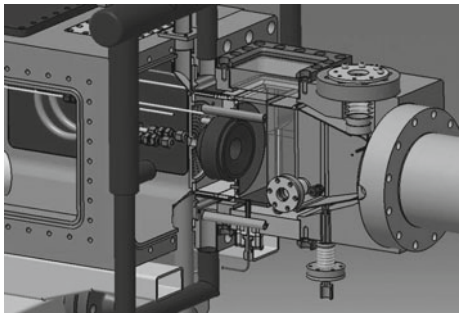

Fig. 10 Lean burn injector

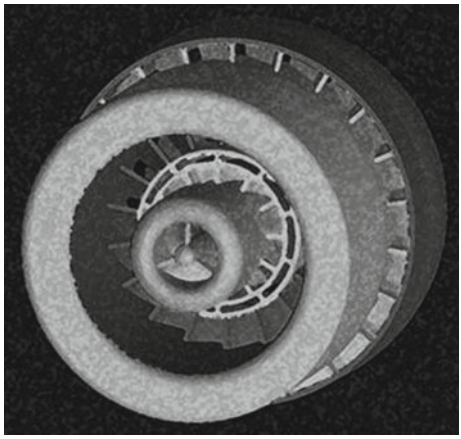

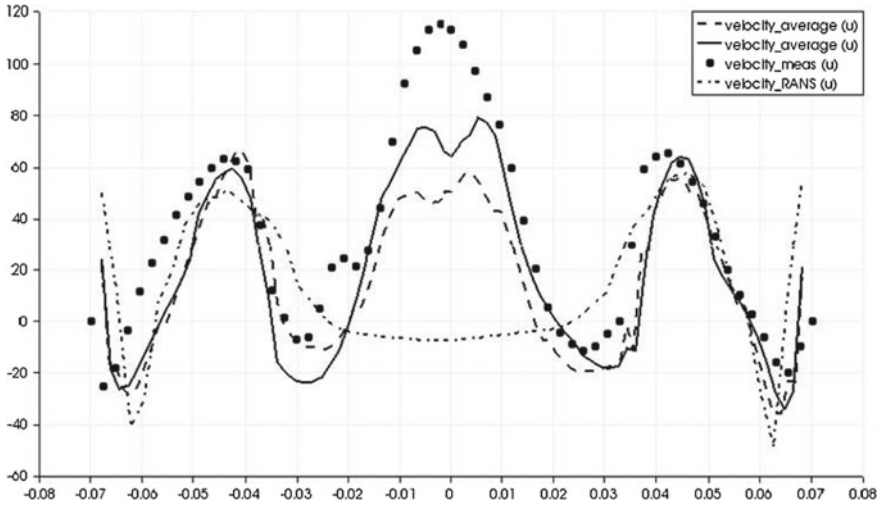

Fig. 11 Axial velocities of LES compared with measurements, at a distance of 10 mm above the burner

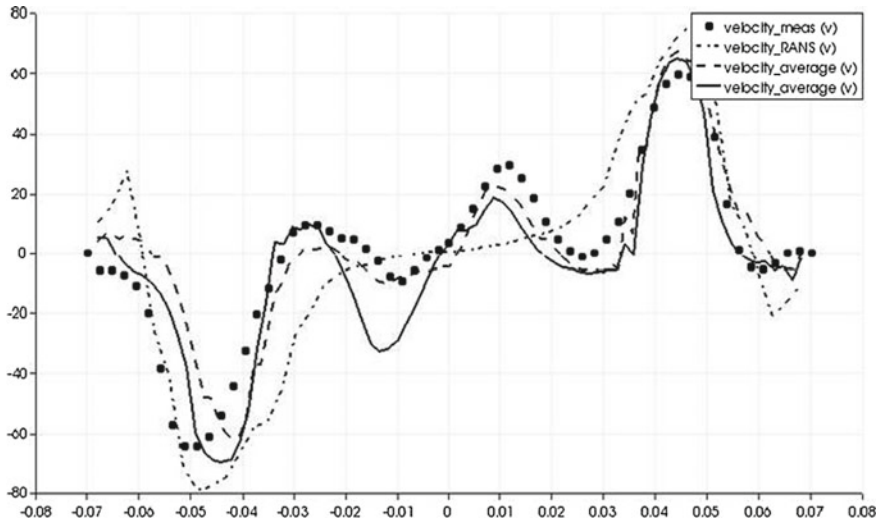

Fig. 12 Radial velocities of LES compared with measured, at a distance of 10 mm above the burner

Finally an example of a aero gas turbine combustor is presented. In Fig. 14, instantaneous velocity and temperatures of a rich burn combustor are presented. The primary zone shows a recirculation zone which stabilises the combustion process, whereas the dilution jets cause a rapid mixing to avoid stoichiometric conditions. Behind the fuel injector and at the location of the dilution jets large turbulent structures can be observed. In the downstreampart of the combustor these are dissipated to smaller scales structures.

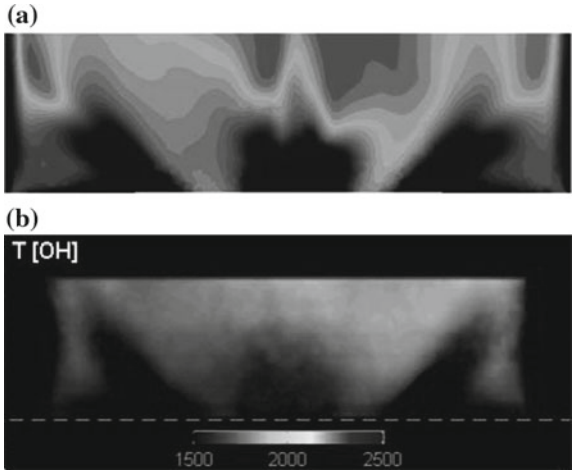

Fig. 13 **a** Predicted temperature field. **b** Measured temperature field

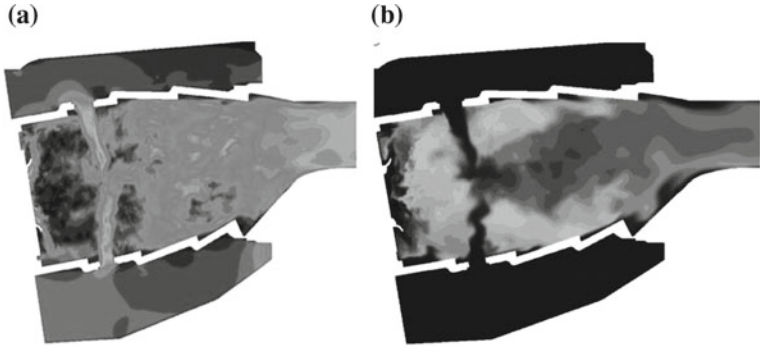

Fig. 14 **a** Predicted velocity field. **b** Predicted temperature field

Fig. 15 Comparison of predicted and measured radiation averaged temperatures

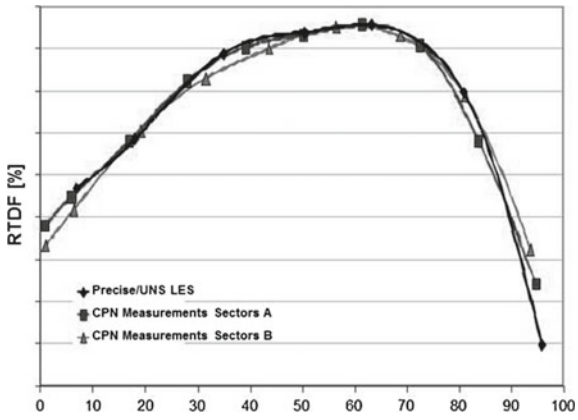

As mentioned before, for industrial combustors limited experimental data is available, generally only measurement data is available at the combustor exit, due to limited access within the combustor. Radial averaged temperature results at the exit of the combustor are presented as function of the radius in Fig. 15. The predicted temperature profile agrees very well with the measured profile.

4 Summary

The combustion CFD approach which is followed within Rolls-Royce has been presented. It has been described which modeling approaches for turbulence, combustion and turbulence−combustion interaction have been taken. Examples for different validation cases have been presented, for which the numerical results have been compared with experimental data. Finally also an example of an industrial combustor is presented.

Acknowledgements Part of the presented work and experimental data has been achieved within the 7th framework project "Fuel Injector Research for Sustainable Transport" (FIRST), funded by the European Commission under contract FP7-AAT-2010-RTD-1. Furthermore, the work has been done in cooperation of the global combustion method team: Max Staufer and Torsten Voigt (Rolls-Royce Deutschland), Marco Zedda, Chris Goddard and Simon Stow (Rolls-Royce plc, Derby, UK), M.S. Anand, Jiang Zhu and Cris Nastasa (Rolls-Royce Corporation, Indianapolis, USA).

References

1. Jones, W.P., Marquis, A.J., Prasad, V.N.: LES of a turbulent premixed swirl burning using the Eulerean stochastic field method. Combust. Flame **159**(10), 30793095 (2012)
2. Patankar, S.V.: Numerical Heat Transfer and Fluid Flow. McGraw-Hill, New York (1980)
3. Karki, K.C., Patankar, S.V.: Pressure based calculation procedure for viscous flows at all speeds in arbitrary configurations. AIAA J. **27**(9), 1167–1174 (1989)
4. Klapdor, V., Pyliouras, S., Eggels, R., Janicka, J.: Towards Simulation of combustor turbine interaction in an integrated simulation, ASME Paper GT 2010-22933. In: Proceedings of ASME Turbo Expo, Glasgow, UK (2010)
5. Ferziger, J.H., Peric, M.: Computational Methods for Fluid Dynamics, 3rd edn. Springer, Berlin (2002)
6. Stichting Dolfyn. https://www.dolfyn.net/
7. HYPRE: Users manual, Center for Applied Scientific Computing, Lawrence Livermore National Laboratory (2006)
8. Notay, Y.: Aggregation-based algebraic multigrid for convection-diffusion equations. SIAM J. Sci. Comput. **34**, A2288–A2316 (2012)
9. Geigle, K.P., Khler, M.: OLoughlin, W., Meier, W.: Investigation of soot formation in pressurized swirl flames by laser measurements of temperature, flame structures and soot concentrations. Proc. Combust. Inst. **35**(3), 3373–3380 (2014)
10. Geigle, K.P., Hadef, R., Meier, W.: Soot formation and flame characterization of an aero-engine model combustor burning ethylene at elevated pressure. J. Eng. Gas Turbines Power **136**(2), 021505 (2014)

11. Meier, U., Freitag, S., Heinze, J., Lange, L., Magens, E., Schroll, M., Willert, C., Hassa, C., Bagchi, I., Lazik, W., Whiteman, M.: Characterization of lean burn module air blast pilot injector with laser techniques. J. Eng. Gas Turbines Power **135**(12), 121508 (2013)
12. Broy, M.: Software engineering - from auxiliary to key technologies. In: Broy, M., Dener, E. (eds.) Software Pioneers, pp. 10–13. Springer, Heidelberg (2002)
13. Coupland, J., Priddin, C.H.: Modeling the flow and combustion in a production gas turbine combustor. Turbul. Shear Flow **5**, 310–323 (1987)
14. Anand, M.S., Zhu, J., Connor, C., Razdan, M.K.: Combustor flow analysis using an advanced finite-volume design system, ASME Paper 99-GT-273. In: 44th International Gas Turbine and Aerospace Congress and Exhibition, Indianapolis, Indiana, 7–10 June (1999)
15. Anand, M.S., Eggels, R., Staufer, M., Zedda, M., Zhu, J.: An advanced unstructured grid finite volume design system for gas turbine combustion analysis, ASME Paper GTINDIA 2013-3537 (2013)
16. Valino, L.: A field Monte Carlo formulation for calculating the probability density function of a single scalar in a turbulent flow. Flow Turbul. Combust. **60**, 157–172 (1998)

Reliability of Large-Eddy Simulations: Benchmarking and Uncertainty Quantification

M.V. Salvetti, M. Meldi, L. Bruno and P. Sagaut

1 Assessment of Quality and Reliability of Large-Eddy Simulations

Nowadays, large-eddy simulation (LES) is increasingly applied to complex flow configurations of interest in technological or environmental applications. In this context, the assessment of the quality and reliability of LES results has become a topic of increasing interest. For LES this task is particularly difficult, because different sources of uncertainty may have comparable effects and may interact in a nonlinear way leading to counterintuitive results. A typical example is the interaction between discretization errors and subgrid scale (SGS) modeling. The related unexpected result behaviors observed in the literature are the following: (i) for given scheme and SGS model, accuracy deteriorating with grid refinement, (ii) for given grid and SGS modeling, lower-order schemes giving better results than higher-order ones or, (iii) for given grid and numerical scheme, no model simulations giving better results than LES with SGS modeling (see e.g. [1, 2]). The strategies proposed in the literature to manage numerical errors are rather controversial. A first way of thinking is that numerical errors should be made negligible and all the burden should be on the SGS model. This can be achieved either by using high-order not-dissipative schemes, as recommended e.g. in [3, 4], or by applying explicit filtering of width significantly larger than the grid size [5, 6]. However, due to the huge computational resources

M.V. Salvetti (✉)
Dipartimento di Ingegneria Civile e Industriale, University of Pisa, Pisa, Italy
e-mail: mv.salvetti@ing.unipi.it

M. Meldi
PPRIME, CNRS-University of Poitiers-ENSMA, Poitiers, France

L. Bruno
Dipartimento di Architettura e Design, Politecnico di Torino, Turin, Italy

P. Sagaut
M2P2, Aix Marseille University, CNRS, Marseille, France

D.G.E. Grigoriadis et al. (eds.), *Direct and Large-Eddy Simulation X*,
ERCOFTAC Series 24, https://doi.org/10.1007/978-3-319-63212-4_2

required, both these strategies are unpractical for complex flows of practical interest. A completely different approach is to get rid of physically based SGS models and to use the dissipation provided by numerical schemes both for numerical stabilization and SGS modeling (see, e.g., [7, 8]). Although this latter strategy may be attractive from a practical viewpoint, since it eliminates the need of implementing a SGS model, the quality of the results strongly depend on the characteristics of the used numerical methods, which should have again a high-order of accuracy and provide a dissipation concentrated on the smallest resolved scales. Numerical schemes usually available in commercial and open-source codes may conversely lead to inaccurate results due to a too strong numerical damping (see, e.g., [9]). As a consequence, the most widely adopted practice is to use an explicit SGS model and to accept a *not-perfect* numerics. In this context, the importance of different errors and their interactions should be assessed.

Benchmarks and comparisons with reference data, either from experiments or direct numerical simulations, have classically been used in the last decades for appraising the accuracy of LES results and the suitability of numerical methods or SGS models. However, uncertainties can also derive from a lack of knowledge of the considered problem set-up, as for instance some features of the incoming flow which are difficult to be perfectly controlled and/or characterized in experiments. Another critical issue is indeed the sensitivity of LES results to the different simulation parameters. Systematic sensitivity studies are difficult to be carried out because of the large cost of each single LES simulation.

Methodologies aimed at obtaining insights in the error behavior and interaction and in the sensitivity to the parameters of the LES results have been recently proposed. One is the error-landscape approach (see, e.g., [10]) in which a full response surface of the LES error behavior is built from a systematic variation of influencing parameters, as, e.g., model constants and grid resolution. This approach provides a framework to characterize the combined effects of modeling and discretization, but at the cost of a large number of simulations, which may become unaffordable for complex cases or when a large number of parameters is involved. Another approach, which is being increasingly used in recent years in computational fluid dynamics, is Uncertainty Quantification (UQ), in which the uncertain or unknown parameters are modeled as input random variables with a given probability distribution. These uncertainties can be propagated through the computational model to statistically quantify their effect on the results. Since this propagation process implies large computational costs, especially for LES, a computationally inexpensive surrogate model is usually adopted to build continuous response surfaces in the parameter space starting from a few deterministic simulations. Different techniques exist to build these surrogate models, such as, for instance, generalized Polynomial Chaos, Stochastic Collocation or Kriging. A few specific applications of stochastic UQ approaches to LES can be found in the recent literature [11–16].

The paper is further organized as follows. In Sect. 2 a few examples of benchmarks involving LES simulations are presented, to highlight the kind of useful indications but also the limits of this approach. In Sect. 3 an example of stochastic UQ for LES, based on generalized Polynomial chaos (gPC), is given.

2 Benchmarking: A Few Examples

Benchmarks are commonly used to assess the accuracy and reliability of CFD results. Usually, there is a reference experiment or DNS and different numerical results are collected and compared against the reference data. Several benchmarks are documented in the literature also involving LES.

As an example, among the oldest ones is the benchmark on the flow around a square cylinder at Re = 22,000 (see the review in [17] and the ERCOFTAC Wiki database, http://uriah.dedi.melbourne.co.uk/). RANS and LES results were compared against reference experimental data in terms of aerodynamic loads and of mean and fluctuating velocity fields. It was concluded in [17] that all in all LES seems to give better predictions than RANS and it better captures the complex features of the flow. However, none of the LES results were found to be uniformly good and entirely satisfactory and there were large differences between the individual calculations which were not completely explained. Several possible reasons for the lack of agreement of LES results with the experiments were indicated, such as insufficient grid resolution near the side walls of the cylinder and/or in the spanwise direction, neglect of turbulence in the incoming stream, numerical diffusion and insufficient domain extent.

Benchmark results are even more difficult to be analyzed for benchmarks in which a-priori there are no reference experiments or simulations, as in the case of the BARC benchmark, dealing with the flow around a rectangular cylinder with chord-to-depth ratio equal to 5 and infinite spanwise length, recently reviewed in [18]. This configuration is of practical interest for civil and industrial structures; in spite of the simple geometry, the related flow dynamics and topology is complex, being turbulent with separation from the upstream corners and reattachment on the cylinder side and vortex shedding from the rear corners. Besides comparing experimental and numerical results, one of the goals of BARC is to assess the consistency of wind tunnel measurements carried out in different facilities and of computational results obtained through different approaches. About 20 wind tunnel tests and 50 numerical simulations were reviewed in [18]. LES simulations amount to more than 50% of the collected numerical contributions to BARC; therefore, this context gives also a good opportunity for the assessment and the validation of results obtained through LES codes. The LES contributions to BARC were specifically reviewed in [19]. For some quantities an overall very good agreement was found between the different numerical results and experimental data. An example is the mean drag coefficient, $\langle C_D \rangle$, i.e. the non-dimensionalized drag acting on the cylinder averaged in time and in the spanwise direction. Only one measurement of this quantity is available within BARC, giving $\langle C_D \rangle = 1.03$; previous experiments also indicate that the mean drag coefficient is very close to one. The predictions of the numerical contributions to BARC are summarized in Table 1. It can be seen that the ensemble average of the values given by LES simulations and that of the predictions of URANS and hybrid approaches are practically the same and very close to the experimental value. However, rather unexpectedly, it appears that the dispersion of the LES predictions is

Table 1 Mean drag coefficient: BARC numerical results

	LES	Hybrid and URANS	Selected LES
Ensemble average	1.07	1.07	0.99
Range	0.96–1.39	0.96–1.29	0.96–1.04

larger than that of URANS and hybrid URANS/LES simulations. Nonetheless, it turns out that the largest values of $\langle C_D \rangle$ were obtained in a 2D LES and in 3D LES having a too small computational domain; if these simulations are discarded, the dispersion range of LES predictions becomes smaller than that of URANS and hybrid simulations (see the last column of Table 1). Therefore, it appears that wrong choices of the computational domain dimensions in LES can lead to very bad predictions, worse than those of URANS, independently of the other numerical and modeling ingredients. This gives an example of best practice indications that can be obtained from benchmarks. On the other hand, for other quantities, such as the pressure distribution over the cylinder lateral surface or the amplitude of time oscillations of lift, the dispersion of both experimental and numerical results is so large that it would be unacceptable for engineering or design applications. As an example, Fig. 1 summarizes the ensemble statistics of standard deviation in time of the pressure coefficient on the lateral cylinder side; the range of values obtained in experiments and in LES and detached-eddy (DES) simulations is reported for different locations over the cylinder lateral side, together with the median, the 25-th and the 75-th percentile values computed among all the contributions. LES and DES give a distribution qualitatively similar to the experiments but their dispersion is larger than in experiments. Different possible reasons of the observed large dispersion were analyzed in [18], but not conclusive remarks could be drawn. It is certain that some flow features of the BARC are extremely sensitive to small uncertainties, which may be present both in wind-tunnel tests and in computations. Sources of uncertainties are different in experiments and in simulations, further complicating their comparison. Recent stochastic UQ and sensitivity studies for URANS and LES of the BARC flow can be found in [20, 21] (not shown here for the sake of brevity).

3 Uncertainty Quantification Through Generalized Polynomial Chaos

The polynomial chaos approach is a spectral decomposition of random processes in terms of an orthogonal basis. The uncertain parameters are assumed to be random variables, $\xi(\omega)$ and the output quantities, $E(\omega)$, also considered as random fields, are approximated through their Galerkin projection over a polynomial orthogonal basis: $E(\omega) = \sum_{k=0}^{\infty} a_k \xi(\omega)$. In gPC, the response surface of the output quantities in the parameter space is obtained by truncating the sum to a finite (small) number, N. The polynomial family is chosen by the user, on the basis of the (assumed) stochastic

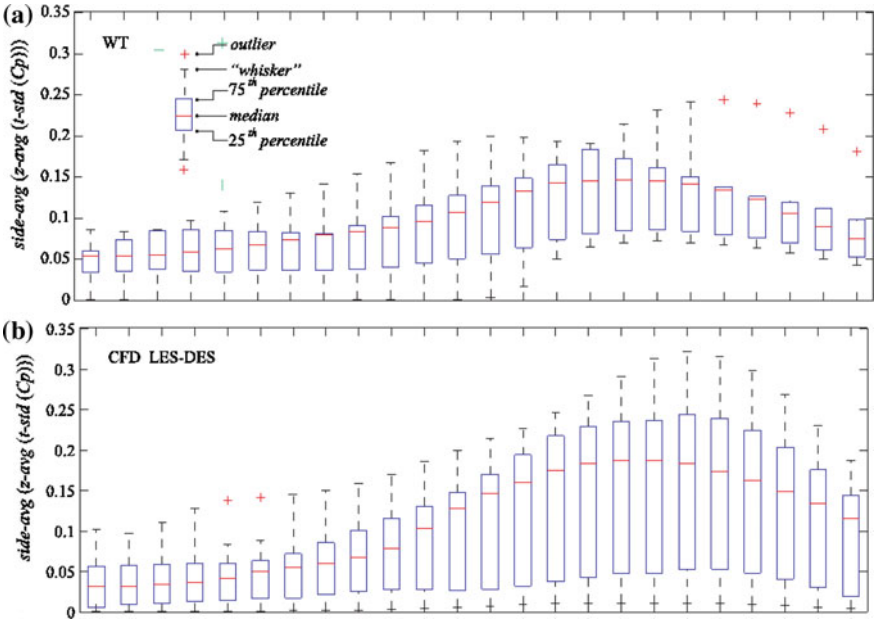

Fig. 1 Ensemble statistics of the time standard deviation of the pressure coefficient distribution over the cylinder side; **a** experiments, **b** LES and DES contributions. Taken from [18]

properties of the input parameters. This choice affects the speed of convergence of the truncated series. Each coefficient of the truncated series can be computed as follows: $a_k = \dfrac{\langle E, \phi_k \rangle}{\langle \phi_k, \phi_k \rangle}$, where $\langle \cdot, \cdot \rangle$ is a suitable scalar product. The number of points used to discretize the random variable space, which corresponds to the number of deterministic simulations to be carried out, is chosen in order to obtain converged integrals when computing the polynomial coefficients. Each deterministic simulation corresponds to a quadrature point in the parameter space.

As an example of error quantification in LES through gPC, we consider a spatially evolving mixing layer at a Reynolds number, based on the difference between the two stream velocities and on the vorticity thickness at the inlet, equal to 700. A highly-resolved LES (HRLES) was carried out by using the dynamic Smagorinsky SGS model; the results were validated against DNS and LES data in the literature and are used as a reference for the UQ of errors in LES carried out on grids having a resolution four time coarser than the HRLES one in the streamwise direction and twice coarser in the other directions and using the standard Smagorinsky SGS model. Further details on the test case and on the simulation set up can be found in [14]. The sensitivity of coarse LES results to the following parameters is investigated: the stretching ratio of the grid cells in the streamwise and lateral directions and the Smagorinsky model coefficient. Although these parameters can obviously be fixed to precise deterministic values, the lack of knowledge of their appropriate values

can be considered as an epistemic uncertainty. They are then considered as uncertain parameters and the previously described gPC approach is used for UQ. Their probability density function (PDF) is assumed here to be uniform over the considered variation range (see [14]) and, hence, Legendre polynomials are considered in the gPC expansion, which is truncated to $N = 3$; 64 coarse LES were then carried out to build the response surface in the parameter space. Uncertainty propagation on the errors for three quantities of practical interest, viz. the mean streamwise velocity, the momentum thickness and the shear stress, is investigated. The error was computed as the L_2 norm of the difference between the values of the above quantities in HRLES and those in coarse LES, for different streamwise sections, averaging over the y and z directions. A typical feature of the considered spatially evolving flow is the progressive transition from a laminar regime, highly dependent on the inlet conditions, to a fully-turbulent one. The computational domain can therefore be divided in two zones, by assuming that the fully-turbulent region starts at the location where the signature of the inlet perturbations on the flow is no more apparent, roughly at $x = 12\Lambda$, Λ being the adopted reference length, multiple of the inlet vorticity thickness. As an example of the kind of information which can be obtained from such an analysis, Fig. 2a shows the behavior of the mean stochastic error for the considered quantities of interest, at different distances from the domain inlet. It is clear that error on the mean streamwise velocity (circles) is much lower than that on the other two variables, never exceeding 1.5%. The mean errors on the momentum thickness and on the shear stress significantly vary with the distance from the domain inlet. In the inlet-dependent zone, the stochastic error decreases moving downstream. This indicates that the most critical part of this region is connected with the initial stages of transition. The opposite behavior of the error is observed in the turbulent region; this is probably due to a progressively coarsening of the streamwise resolution when moving downstream (the grid nodes are clustered near the inlet) and to the pres-

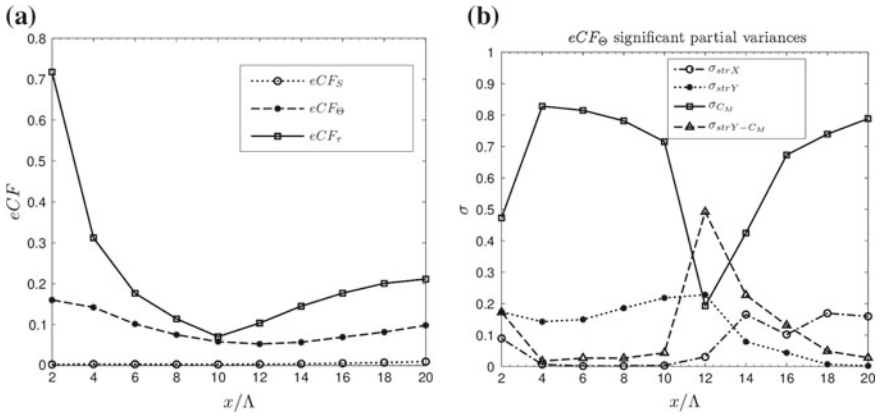

Fig. 2 **a** Mean stochastic error for different output quantities. **b** Partial variances for the error on momentum thickness. Taken from [14]

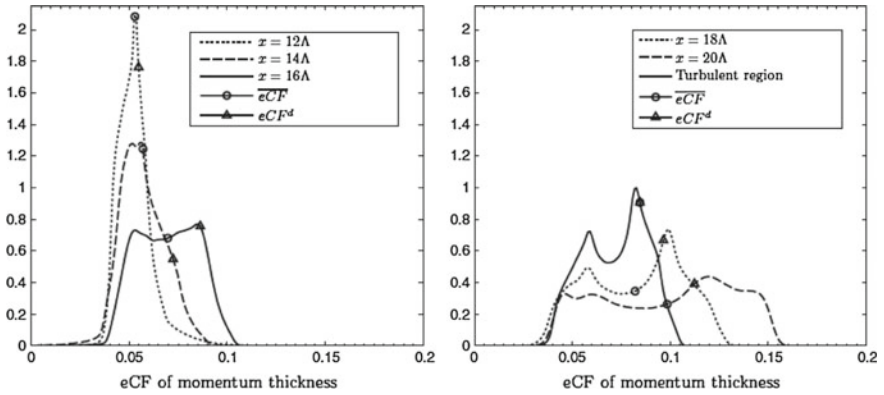

Fig. 3 PDF of the error on the momentum thickness in the inlet-dependent zone (*left panel*) and in the fully-turbulent one (*right panel*). *Open circles* mean stochastic value of the error; *triangles* error obtained in deterministic simulations carried out with average values of the input parameters. Taken from [14]

ence of progressively smaller turbulent flow scales. Partial variances, which quantify the sensitivity of the errors to the single parameters and to their interactions, can also be computed and analyzed. An example is given in Fig. 2b showing the partial variances for the error on the momentum thickness. It can be seen that the value of the Smagorinsky constant has the largest impact on the error; however, a peculiar behavior is observed near the border between the inlet-dependent and fully-turbulent zones with strong coupling between the effects of the Smagorinsky constant and of the grid stretching in the lateral direction. Further information on the error behavior can be obtained from the error PDFs, as shown for instance in Fig. 3 again for the momentum thickness. In the inlet-dependent region, a huge number of parameter combinations give error values close to the most probable one (the peak in the PDF), but the error may be significantly larger for some combinations of the parameters. Conversely, in the fully-turbulent region, the error distribution is less clustered than in the inlet-dependent zone, and, hence, the stochastic mean error value (open circles) can be significantly different from the most probable one. In both zones, both the stochastic mean and most probable error values are in turn different from the errors obtained in deterministic LES carried out with a set of average parameter values in the considered range. For a more detailed analysis we refer to [14], where an optimization of the parameters based on the built error response surface can also be found.

Summarizing, assessment of the accuracy and reliability of LES results, especially for complex applications, is still today a challenge. Benchmarks can highlight clear trends, but the reasons of observed dispersion can not always be explained, due to different uncertainty sources present both in experiments and simulations. Uncertainty quantification techniques can be useful to give hints on the error dynamics and on the reliability of LES results. However, also UQ techniques become not viable

for large numbers of uncertain parameters (the so-called 'curse of dimensionality'). A huge research effort is indeed currently made by the UQ scientific community to develop more efficient techniques to overcome this problem.

References

1. Vreman, B., Geurts, B.J., Kuerten, H.: Comparison of numerical schemes in large-eddy simulations of the temporal mixing layer. Int. J. Numer. Methods Fluids **22**, 297–311 (1996)
2. Ouvrard, H., Koobus, B., Dervieux, A., Salvetti, M.V.: Classical and variational multiscale LES of the flow around a circular cylinder on unstructured grids. Comput. Fluids **39**, 1083–1094 (2010)
3. Ghosal, S.: An analysis of numerical errors in large-eddy simulations of turbulence. J. Comput. Phys. **125**, 187–206 (1996)
4. Kravchenko, A.G., Moin, P.: On the effect of numerical errors in large eddy simulations of turbulent flows. J. Comput. Phys. **131**, 310–322 (1997)
5. Geurts, B.J., van der Bos, F.: Numerically induced high-pass dynamics in large-eddy simulation. Phys. Fluids **17**, 125103 (2005)
6. Bose, S.T., Moin, P., You, D.: Grid-independent large-eddy simulation using explicit filtering. Phys. Fluids **22**, 105103 (2010)
7. Boris, J.P., Grinstein, F.F., Oran, E.S., Kolbe, R.L.: New insights into large eddy simulation. Fluid Dyn. Res. **10**, 199–228 (1992)
8. Karamanos, G.S., Karniadakis, G.E.: A spectral vanishing viscosity method for large-eddy simulations. J. Comput. Phys. **163**, 22–50 (2000)
9. Garnier, E., Mossi, M., Sagaut, P., Comte, P., Deville, M.: A spectral vanishing viscosity method for large-eddy simulations. J. Comput. Phys. **163**, 22–50 (2000)
10. Meyers, J., Geurts, B.J., Baelmans, M.: Database analysis of errors in large-eddy simulations. Phys. Fluids **15**, 2740–2755 (2003)
11. Christophe, J., Moreau, S., Hamman, C.W., Witteveen, J.A.S., Iaccarino, G.: Uncertainty quantification for the trailing-edge noise of a controlled-diffusion airfoil. AIAA J. **53**, 42–54 (2015)
12. Carnevale, M., Montomoli, F., D'Ammaro, A., Salvadori, S., Martelli, F.: Uncertainty quantification: a stochastic method for heat transfer prediction using LES. J. Turbomach. **135**, 051021 (2013)
13. Congedo, P.M., Duprat, C., Balarac, G., Corre, C.: Numerical prediction of turbulent flows using Reynolds-averaged Navier-Stokes and large-eddy simulation with uncertain inflow conditions. Int. J. Numer. Methods Fluids **72**, 341358 (2013)
14. Meldi, M., Salvetti, M.V., Sagaut, P.: Quantification of errors in large-eddy simulations of a spatially evolving mixing layer using polynomial chaos. Phys. Fluids **24**, 035101 (2012)
15. Meldi, M., Lucor, D., Sagaut, P.: Is the Smagorinsky coefficient sensitive to uncertainty in the form of the energy spectrum? Phys. Fluids **23**, 125109 (2011)
16. Lucor, D., Meyers, J., Sagaut, P.: Sensitivity analysis of large-eddy simulations to subgrid-scale-model parametric uncertainty using polynomial chaos. J. Fluid Mech. **585**, 255–279 (2007)
17. Rodi, W.: Comparison of LES and RANS calculations of the flow around bluff bodies. J. Wind Eng. Ind. Aerodyn. **69–71**, 55–75 (1997)
18. Bruno, L., Salvetti, M.V., Ricciardelli, F.: Benchmark on the aerodynamics of a rectangular 5:1 cylinder: an overview after the first four years of activity. J. Wind Eng. Ind. Aerodyn. **126**, 87–106 (2014)
19. Salvetti, M.V., Bruno, L.: Reliability of LES simulations in the context of a benchmark on the aerodynamics of a rectangular 5:1 cylinder. In: Fröhlich, J., Kuerten, H., Geurts, B.J., Armenio, V. (eds.) Direct and Large-Eddy Simulation IX. ERCOFTAC Series, pp. 161–167. Springer, Berlin (2015)

20. Mariotti, A., Salvetti, M.V., Shoebi-Omrani, P., Witteveen, J.A.S.: Stochastic analysis of the impact of freestream conditions on the aerodynamics of a rectangular 5:1 cylinder. Comput. Fluids **136**, 170–192 (2016)
21. Mariotti, A., Siconolfi, L., Salvetti, M.V.: Stochastic sensitivity analysis of large-eddy simulation predictions of the flow around a 5:1 rectangular cylinder. Eur. J. Mech. B. Fluids **62**, 149–165 (2017)

Large-Scale Compressible-Flow Direct Numerical Simulations

R.D. Sandberg

1 Introduction

Direct numerical simulation (DNS) of turbulent flows began in the early 1970s with the study of incompressible isotropic turbulence by Orszag and Patterson [8], and compressible DNS were not conducted until the 1980s. Due to the adverse scaling of computational effort with Reynolds number, roughly as Re^3, DNS have mostly been used for computing simplified canonical flows, rather than being used as an engineering design tool. Nevertheless, for flows that could be reliably computed, DNS has provided a wealth of data, not obtainable by traditional laboratory experiments, that have helped gain insight into fundamental mechanisms in fluid mechanics or aeroacoustics. DNS data have also been heavily used for developing, validating, or improving turbulence models.

The purpose of the current contribution is to demonstrate how the relentless growth in computing resources over the last decades has enabled the use of high-fidelity DNS for investigation of compressible flows in ever more realistic configurations. In particular, it will be shown that using a compressible Navier–Stokes code developed to enable large-scale DNS on modern HPC architectures, conducting parametric sweeps at realistic Reynolds numbers using DNS have now become a reality for turbomachinery applications.

R.D. Sandberg (✉)
Faculty of Engineering and the Environment, Aerodynamics and Flight Mechanics Research Group, University of Southampton, Southampton, UK
e-mail: richard.sandberg@unimelb.edu.au

D.G.E. Grigoriadis et al. (eds.), *Direct and Large-Eddy Simulation X*,
ERCOFTAC Series 24, https://doi.org/10.1007/978-3-319-63212-4_3

2 High-Performance Computing

The tremendous increase in available computing power over the last decades has been truly staggering and is the enabler for the sophistication of computational studies that can be achieved today. The first DNS of isotropic turbulence mentioned above [8] were conducted on a room-sized CDC 7600 computer with 36 MFLOPs performance. Today's latest NVIDIA Kepler K80 GPU card, which easily fits into the palm of our hand, achieves 1,870 GFLOPs in double precision (and even much more in single precision). This is an increase by a factor of 52,000! It is noteworthy that at the same time the cost of computing has fallen dramatically. While the cost per installed GFLOPs was USD 33 Million in 1984, it was USD 0.08 in 2015. With computing power becoming so affordable, HPC has become ubiquitous and routine use of high-fidelity simulations have become feasible. However, the recent increase in computing power has been mainly due to the introduction of hybrid architectures with increased parallelism, featuring CPUs and accelerators that combine to millions of threads. These systems are characterized by limited bandwidth and communications and pose additional challenges for the software developers.

3 Compressible Navier–Stokes Solver

To exploit the enormous computing resources that are available now, purposely developed numerical codes are required for DNS. One such code is the in-house multi-block structured curvilinear compressible Navier–Stokes solver HiPSTAR (High Performance Solver for Turbulence and Aeroacoustics Research).

Reducing the memory requirement of a simulations is one of the most effective ways for increasing performance of a numerical code on bandwidth-limited systems. In HiPSTAR, this is achieved by (a) using a parallel wavenumber-optimized compact finite difference scheme [4] in the streamwise/lateral plane in conjunction with a spectral method (using the FFTW3 library) for the discretization of the span-wise direction to reduce the grid size needed for a given problem, (b) employing a state-of-the-art Runge–Kutta scheme with fourth-order accuracy using only two registers of memory, and (c) restricting the coordinate mapping to two-dimensions, resulting in a smaller number of metric terms that are two dimensional only.

To take full advantage of massively parallel HPC systems, the code was initially parallelized using hybrid OMP/MPI parallelization. More recently, the code has been ported to hybrid CPU/GPU machines using OpenACC through two Oakridge Leadership facility director's grants in conjunction with the CRAY Centre of Excellence. Additional details of the code's capabilities, thorough validation and its application to low-pressure turbine flows are given in reference [13].

Performance of the DNS code has been evaluated on different computing architectures, and results for performance studies on CPU-based CRAY XE and XC architectures were previously reported [9]. Here, results from additional testing are presented.

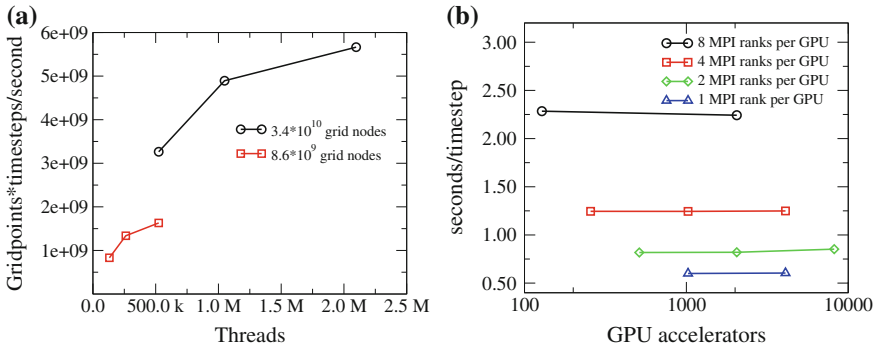

Fig. 1 **a** Strong scaling for single-block test cases of different size on *Blue* Gene/Q (MIRA). Results achieved using hyper-threading, obtained without additional physical cores; **b** Weak scaling on CRAY XK7 (TITAN). Grid points per GPU kept constant at 73,728 in all cases

Test results from the Argonne Mira BlueGene/Q system are given in Fig. 1a. These show that thread counts of over 2 million (running on 524,288 physical cores) were achievable and that the use of hyper-threading delivered some performance benefit.

The performance of the code was also evaluated on the hybrid GPU/CPU system TITAN at the Oakridge leadership facility. This system is currently being used to execute production simulations, typically using 512+ GPUs. Scaling to much greater GPU counts can be demonstrated for more challenging problems, however. Here, weak scaling is shown, i.e. the number of operations every GPU has to perform and the MPI messages every GPU has to send/receive is kept identical for increasing overall number of GPUs. This is particularly important when considering ever more challenging simulations at higher Reynolds number, which require more grid points and need to be distributed on a larger number of nodes. Figure 1b shows that if the ratio of MPI ranks to GPUs is kept constant, in addition to also keeping constant the grid size to GPU ratio, the wall clock time per time step remains constant to over 8,000 GPUs.

4 Jet Noise

Several different sources contribute to the overall sound radiation from subsonic jets and the contributions from these various sources are known to vary with the direction from the jet downstream axis, θ, and frequency, e.g. large scale structures predominantly radiate low frequency sound in the downstream direction, whereas fine-scale turbulence (shear layers, breakdown of the potential core) is mainly responsible for the high-frequency sound that is considered to be less directional [15].

DNS of turbulent flow exiting a pipe into a laminar co-flow were recently conducted [12], intended to capture all noise generation mechanisms. However, using

phased-array techniques it was found that the DNS were contaminated by high levels of internal noise, generated within the pipe, that made extraction of jet mixing noise difficult, in particular for the axisymmetric mode [16].

Therefore, a new set of DNS have been performed with several vital modifications intended to reduce the internal noise generated in the pipe. These are the explicit elimination of fluctuations in the axisymmetric mode of the turbulent inflow generation, and the use of an acoustic liner boundary condition for the inside of the pipe, which had been shown to remove acoustic fluctuations within the pipe without affecting the turbulent flow field [7].

The computational domain was discretized with 3,432 and 918 points in the axial and radial directions, respectively, and in the azimuthal direction 64 or 8 Fourier modes corresponding to 130 or 18 collocation points were used in the turbulent flow and acoustic regions, respectively, resulting in a total of 225×10^6 grid points. The dimensions of the computational domain and the spatial and temporal resolution are discussed in [12] and detailed information on the numerical set-up, in particular the acoustic liner condition is given in [11].

A total of five DNS cases were conducted at a target jet Reynolds number of 8,000, based on diameter, to study the effect of the liner and the effect of co-flow Mach number for a given jet exit Mach number. The jet Mach number was either 0.8, 0.62 or 0.45, while the co-flow Mach number was 0.1, 0.15 or 0.2. The case with jet Mach number 0.8 and coflow Mach number 0.2 (M8c2) was run with ('L') and without ('nL') liner. The changes in density and temperature were less than 15% of the wall values, with the wall set to be isothermal at the respective adiabatic temperature. All DNS were run for 150 nondimensional time units (based on diameter and bulk velocity inside the pipe) to allow the initial transients to leave the domain and then continued for at least 350 time units to achieve statistical convergence.

In Fig. 2 instantaneous contours of the streamwise density gradient are shown for the near-nozzle region (a, b) and the entire computational domain (c). The near-nozzle region illustrates qualitatively the fully developed turbulent pipe flow exiting the nozzle and rapidly developing into a jet. The inclusion of a liner boundary condition in case M8c2L does not seem to affect the flow exiting the nozzle. However, the images reveal a pronounced difference in the acoustic near field, namely higher amplitude high-frequency acoustic waves originating from $z/D \approx 1$, present only in the unlined case. Looking at the figure of the entire domain, acoustic waves can be seen emanating from the nozzle corner and from the jet core. Importantly, no interference from boundary reflections can be detected, which is particularly encouraging given the very small contour levels chosen ($\pm 2 \times 10^{-4}$). The highest intensity of noise radiation is observed at roughly $\theta = 40°$. In addition, the figure also reveals upstream radiating noise emanating from the nozzle lip.

To assess whether the new set of simulations were successful in reducing the nozzle-based noise sources, pressure PSDs for all new DNS compared with the previous DNS data at $\theta = 90°$ and at 30 nozzle diameters distance are shown in Fig. 3a for the axisymmetric mode. At this angle noise generated by fine-scale structures in the shear layers of the jet and noise associated with the nozzle should be captured. In contrast to the previous DNS with an unmodified turbulent inflow generation

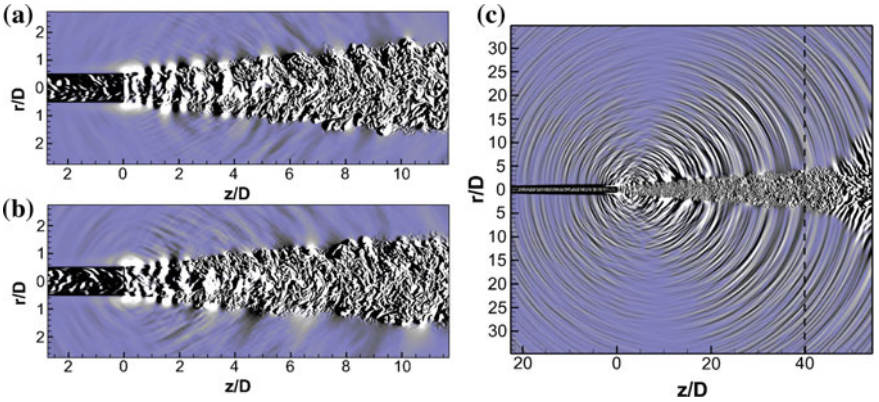

Fig. 2 Instantaneous contours of streamwise density gradient for azimuthal plane $\Theta = 0°, 180°$; near the nozzle with levels $[-1 \times 10^{-2}; 1 \times 10^{-2}]$ for case M8c2L (**a**) and M8c2nL (**b**); entire domain with levels $[-2 \times 10^{-4}; 2 \times 10^{-4}]$ for case M8c2L (**c**); *dashed line* at $z/D = 39.5$ denotes onset of zonal characteristic boundary condition [10]

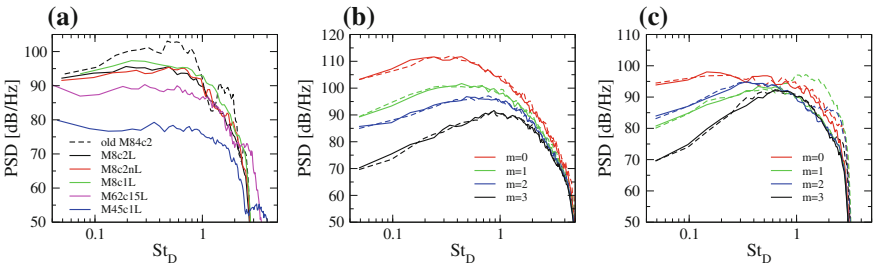

Fig. 3 Power spectral density of azimuthal modes of pressure at 30 diameters distance from the nozzle at 90° for different DNS cases (**a**), at 30° (**b**) and 60° (**c**) for cases M8c2nL *(dashed lines)* and M8c2L *(solid lines)*

technique, the spectra obtained from the new simulations do not show any dips but exhibit a broadband peak followed by a monotonic decay of energy for increasing frequencies. The spectra of cases M8c2L and M8c2nL are very similar, indicating that the removal of the cut-on peak at higher frequencies is due to the change in pipe-inflow boundary condition and not due to the inclusion of the liner. Figure 3a also reveals that the case with lower co-flow Mach number generates more noise, as expected due to the larger velocity of the jet relative to the co-flow and that the cases with lower jet Mach number (M45c1L and M62c15L) show considerably reduced far field noise levels.

The pressure PSDs were Fourier decomposed in the circumferential direction to assess the contribution of individual azimuthal modes to the overall noise. The resulting spectra for each azimuthal mode at angles 30 and 60° are shown in Fig. 3b, c. Comparing the data obtained from the lined and unlined cases M8c2nL and M8c2L at two angles, considerable differences can be observed. At the lower angle, the

shapes of the spectra for all azimuthal modes show a typical broadband behavior. The differences between the lined and unlined cases are negligible. This supports the above suggestions that the noise measured at the probe location is due to jet-mixing, which is similar for both cases due to the similarity of the turbulence field exiting the nozzle, and not contaminated by internal noise from the nozzle. At the larger angle, however, the picture changes and higher modes in the unlined case M8c2nL, most notably $m = 1$, display an increase in amplitude at frequencies above 'cut-on'. All cases conducted with an acoustic liner inside the nozzle do not exhibit this cut-on behavior of the higher azimuthal modes and are free from any dips in the axisymmetric mode. Thus, the modified inlet boundary condition and the acoustic liner are able to suppress the unwanted internal noise sources. This will allow for the DNS data to be more useful for the extraction of jet-mixing noise mechanisms.

5 Low-Pressure Turbine

To reduce weight and cost of jet engines, it is desirable to decrease the number of blades in the low-pressure turbines (LPT). Due to the resulting high loading of the individual blades and the moderate Mach and Reynolds numbers in LPTs, the blade boundary layers are prone to laminar separation. The separation bubbles and the type/location of laminar-turbulent transition of the boundary layer are known to be sensitive to upstream disturbances. In particular incoming wakes have a profound effect on laminar separation bubbles and boundary layer mechanisms. The most recent RANS approaches incorporating the latest transition models can achieve good agreement with experiments in terms of pressure coefficient and transition onset but are often unable to provide accurate results in terms of total pressure losses [3]. RANS also struggle to accurately represent the complex interactions of periodic inflow perturbations, such as incoming wakes, with the boundary layers. Therefore, there has been a large body of work on LTP flows using Large Eddy Simulation (LES) due to the improved accuracy achieved by resolving the dynamically relevant scales in the flow at a reasonable computational cost [14]. However, LES suffers from difficulties in predicting boundary layer transition and capturing the delay of laminar separation with varying inlet turbulence levels [5]. Thus a series of DNS, using a novel approach to realize a sliding mesh [2], have been conducted of linear LPT cascades to remedy the above problems and to gain better understanding of loss generation mechanisms. Most of the results have been reported recently [6, 13] and here only a short summary of key results is given.

Twelve DNS at isentropic Reynolds numbers $Re_{2is} = 60{,}000$ and 100,000, with reduced frequency $F_{red} = 0 - 1.22$ and inflow turbulence level $Tu = 0 - 4\%$ were carried out with an isentropic Mach number $M_{2is} = 0.405$. All simulations were initially run for 10 flow through times through the initial transient period, then statistics were collected over 20 wake-generating bar passing periods. For the lower Reynolds number case the number of grid points along the surface of the blade was 864 points and in the wall normal direction the spacing was nearly constant around

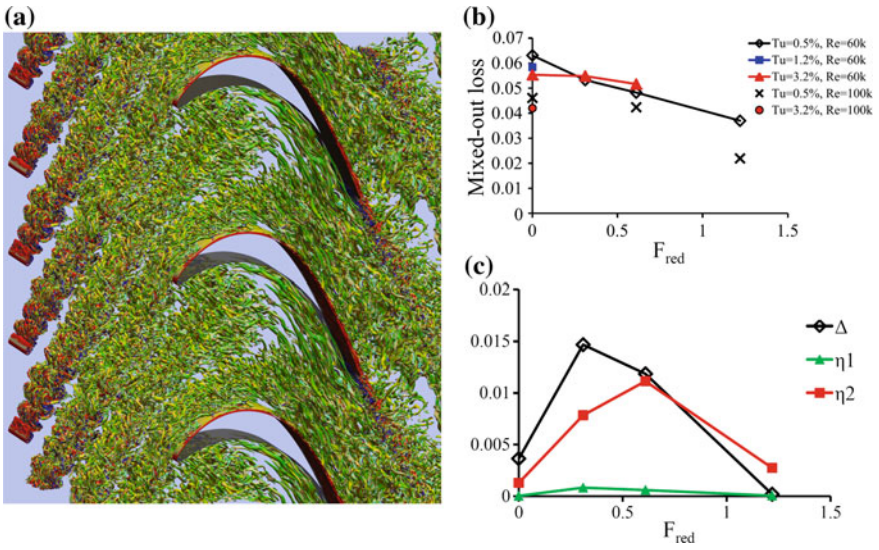

Fig. 4 **a** Instantaneous iso-surfaces of Q, coloured by spanwise vorticity obtained from DNS at $Re_{2is} = 100{,}000$; **b** stagnation pressure losses calculated from DNS and **c** deviation between stagnation pressure loss from DNS and control volume result Δ, wake mixing η_1 and wake distortion losses η_2

the blade with $\Delta y = 2.8 \times 10^{-4}$ and 336 points spanning the blade passage in the pitchwise direction. Using 32 Fourier modes in the spanwise direction, the overall number of grid points was 18.1×10^6. At $Re_{2is} = 100{,}000$, the grid comprised 1296 grid points along the blade and 526 points in the pitchwise direction, resulting in the first off-the wall point being at $\Delta y = 1.5 \times 10^{-4}$. 64 Fourier modes were used for the spanwise discretization leading to a total of 75.6×10^6 grid points. A snapshot of the instantaneous flow field at $Re_{2is} = 100{,}000$ is shown in Fig. 4a, showing how the wakes are accelerated through the blade passage, resulting in stretching of the large-scale structures.

Figure 4b shows the stagnation pressure loss as a function of reduced frequency, obtained directly from the DNS using mixed-out quantities. It is clear that for both Reynolds numbers, and for varying inflow turbulence levels, losses reduce as reduced frequency increases. Broadly speaking, this is mainly due to the upstream disturbances causing the separation bubble on the aft section of the suction side of the blade to reduce in size or vanish entirely. This explanation, however, is overly simplified and according to control volume analysis performed by Denton [1] there are several loss mechanisms that contribute to the overall loss: (1) loss due to the low base pressure acting on the trailing edge, (2) loss due to the momentum deficit loss of the boundary layer on the blade surface, and (3) blockage loss.

Using the high-fidelity DNS database, the individual terms and the overall loss can be computed according to Denton's formula. The difference between Denton's control volume analysis and the stagnation pressure loss from DNS is shown in Fig. 4c

as Δ. It can be observed that the control volume analysis works reasonably well at zero reduced frequency (no wakes) or at the highest F_{red}. It would be expected that Denton's formula is accurate at $F_{red} = 0$ as it was derived for steady flow. The fact that it also produces good results at the highest F_{red} can be explained by 'fogging' of the wakes, i.e. the wakes merge and mix upstream of the blade passage and thus the blade is not subjected to discrete wakes but rather to disturbances reminiscent of inflow turbulence.

However, for the reduced frequencies 0.31 and 0.62 a significant difference (Δ) can be seen. In an attempt to explain this increase in loss found in the DNS data, the mixing loss of the wakes upstream of the blade (constant area mixing, η_1) and the loss due to the distortion of the wakes when convecting through the passage (variable area mixing, η_2) were computed (for details, see [6]) and added to Fig. 4c. It can be seen that the constant area mixing of the wakes does not contribute significantly to overall losses but that loss caused by variable area mixing, η_2, largely accounts for the additional losses. Thus the DNS results show that the wake distortion loss can contribute 20–30% of the total loss.

Acknowledgements The author thanks Professor V. Michelassi and Drs B.J. Tester, A.P.S. Wheeler, R. Pichler and L.W. Chen for their contributions to this work. Funding for the low-pressure turbine work by General Electric is acknowledged. Computer time was provided by the UK turbulence consortium under EPSRC grant EP/L000261/1.

References

1. Denton, J.D.: Loss mechanisms in turbomachines. J. Turbomach. **115**(4), 621–656 (1993)
2. Johnstone, R., Chen, L., Sandberg, R.D.: A sliding characteristic interface condition for direct numerical simulations. Comput. Fluids **107**, 165–177 (2015)
3. Keadle, K., McQuilling, M.: Evaluation of RANS transition modeling for high lift LPT flows at low Reynolds number. In: ASME Turboexpo, GT2013-95069, ASME (2013)
4. Kim, J.W., Sandberg, R.D.: Efficient parallel computing with a compact finite difference scheme. Comput. Fluids **58**, 70–87 (2012)
5. Medic, G., Sharma, O.P.: Large-eddy simulation of flow in a low-pressure turbine cascade. In: ASME Turboexpo, GT2012-68878, ASME (2012)
6. Michelassi, V., Pichler, R., Chen, L., Sandberg, R.D.: Compressible direct numerical simulation of low-pressure turbines: part II - effect of inflow disturbances. J. Turbomach. **137**, 071005-1–071005-12 (2015)
7. Olivetti, S., Sandberg, R.D., Tester, B.J.: Direct numerical simulation of turbulent flow with an impedance condition. J. Sound Vib. **344**, 28 (2015)
8. Orszag, S.A., Patterson, G.S.J.: Numerical simulation of three-dimensional homogeneous isotropic turbulence. Phys. Rev. Lett. **28**(2), 76–79 (1972)
9. Sandberg, R.D.: Compressible-flow DNS with application to airfoil noise. Flow Turbul. Combust. pp. 1–19 (2015)
10. Sandberg, R.D., Sandham, N.D.: Nonreflecting zonal characteristic boundary condition for direct numerical simulation of aerodynamic sound. AIAA J. **44**(2), 402–405 (2006)
11. Sandberg, R.D., Tester, B.J.: DNS of turbulent jets issuing from acoustically lined pipes at different Mach numbers. In: Ninth International Symposium on Turbulence and Shear Flow Phenomena (2015)

12. Sandberg, R.D., Suponitsky, V., Sandham, N.D.: DNS of compressible pipe flow exiting into a coflow. Int. J. Heat Fluid Flow **35**, 33–44 (2012)
13. Sandberg, R.D., Pichler, R., Chen, L., Johnstone, R., Michelassi, V.: Compressible direct numerical simulation of low-pressure turbines: part I - methodology. J. Turbomach. **137**, 051011-1–051011-10 (2015)
14. Sarkar, S.: Influence of wake structure on unsteady flow in a low pressure turbine blade passage. J. Turbomach. **131**(4) (2009)
15. Tam, C., Viswanathan, K., Ahuja, K., Panda, J.: The sources of jet noise: experimental evidence. J. Fluid Mech. **615**, 253–292 (2008)
16. Tester, B.J., Sandberg, R.D.: Application of a phased array technique to DNS-generated turbulent subsonic jet data: source identification and comparison with an analytic model. AIAA Paper 2013–2235 (2013)

DNS and LES of Transitional and Two-Phase Flows

D. Thévenin

1 Introduction

Transition to turbulence, possibly followed by a relaminarization process, remains one of the most intriguing features found in many fluid flows. It is at the same time a highly relevant process for practical applications, since it will suddenly impact drag losses (along an aircraft wing), mixing properties (within a static mixer) or shear forces acting on cells (in a tubular bioreactor), to name just a few such cases. Additionally, it is still unclear how transition processes might be modified in the presence of an additional, disperse phase. Considering for instance blood [1], i.e., (with some simplification) a continuous liquid phase (plasma, mostly water) with a high loading of red blood cells ("particles"), is the tendency to undergo transition increased, decreased or unchanged, compared to a single-phase flow? Direct Numerical Simulation (DNS) is recognized as the best possible approach to investigate such questions. However, it is well-known that, due to the underlying computational requirements, DNS can only be carried out for relatively simple configurations and/or at relatively low Reynolds numbers. For other conditions, Large-Eddy Simulations (LES) constitute the logical alternative to DNS, but involve of course additional challenges concerning subgrid-scale modeling and near-wall resolution.

D. Thévenin (✉)
Laboratory of Fluid Dynamics and Technical Flows (LSS),
University of Magdeburg "Otto von Guericke", Magdeburg, Germany
e-mail: thevenin@ovgu.de

D.G.E. Grigoriadis et al. (eds.), *Direct and Large-Eddy Simulation X*,
ERCOFTAC Series 24, https://doi.org/10.1007/978-3-319-63212-4_4

2 Flow Simulations

For this project, the 3rd-generation DNS code called DINO has been used. It has been developed within the last years based on our previous experience in DNS, obtained first by the developing the compressible code PARCOMB [2, 3], followed later by the low-Mach number code π^3 [4, 5].

It has been demonstrated during the last decades that DNS can be successfully employed to investigate numerically gaseous reactive flows. Nevertheless, many issues remain, since the underlying configuration is extremely challenging. As a consequence, high-performance computers are absolutely necessary to solve this problem. When considering a second phase, for instance for reacting sprays, the complexity becomes even higher [6].

Following previous work, DINO is able to take into account detailed reaction schemes, allowing an accurate description of kinetics. Then, the computational challenge becomes even worse compared to non-reacting flows or to crude approximations like single-step chemistry. For complex fuel molecules like n-heptane or ethylene, the computational overhead induced by chemistry dominates the overall computation time. Additionally, studies involving detailed chemistry require a comparable level of accuracy for all relevant molecular transport and thermodynamic properties, like diffusion coefficients, specific heat, thermal conductivity, and viscosity.

An Immersed Boundary Method (IBM) has been implemented in DINO. In this manner, DNS of configurations with a complex geometry become possible. Finally,

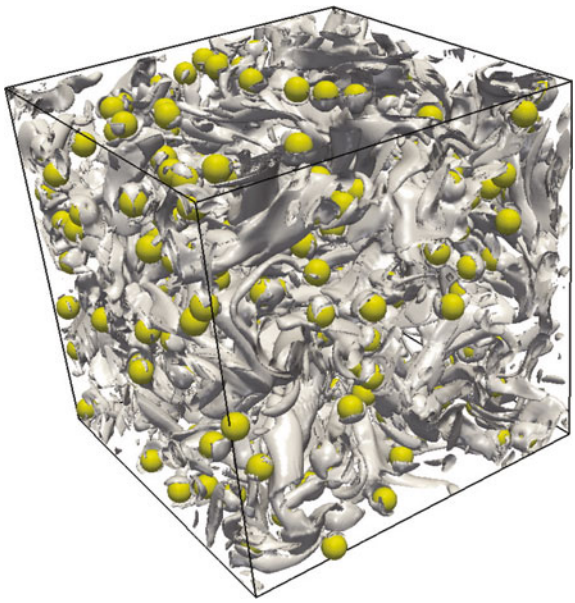

Fig. 1 Enstrophy field obtained by DINO in a particulate flow at a mass loading of 35% (fully resolved particles using IBM)

DINO has been employed for all simulations in this project. DINO solves the Navier–Stokes equations in the low-Mach number regime. It is possible to take into account the presence of a disperse phase (point particles, or particles resolved by direct-force IBM, allowing for 1-way up to 4-way coupling [7, 8]). Additionally, complex chemical schemes can be taken into account. An implicit time integration scheme is implemented to solve the usually very stiff chemistry source terms. For computing kinetic and transport properties, Cantera1.8 and Eglib3.4 have been coupled to DINO. More details on the code can be found in another chapter of this book [9]. DINO results for a heavily loaded particulate flow are shown in Fig. 1, while a turbulent flame is exemplarily shown in Fig. 2.

The wall-resolved LES simulations ($y^+ \simeq 1$) used for comparison have been systematically carried out with established software tools (OpenFOAM, Ansys-Fluent,

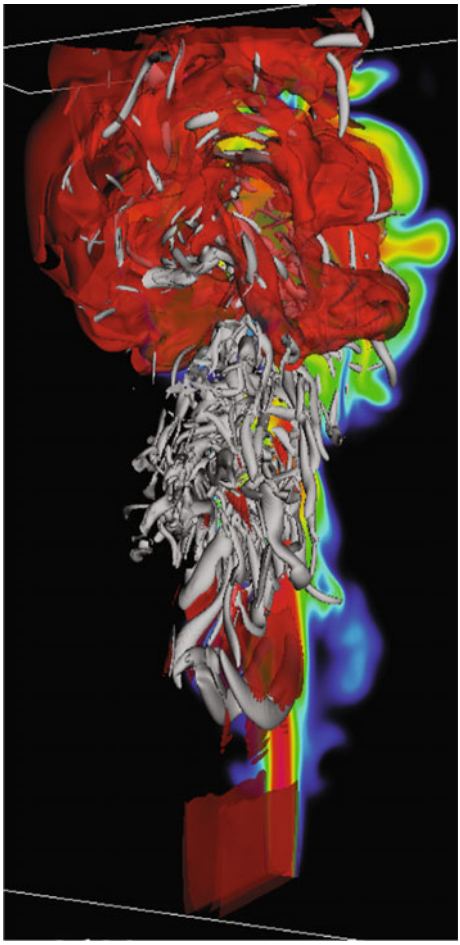

Fig. 2 Structure of a turbulent hydrogen jet flame computed with DINO using a full reaction scheme

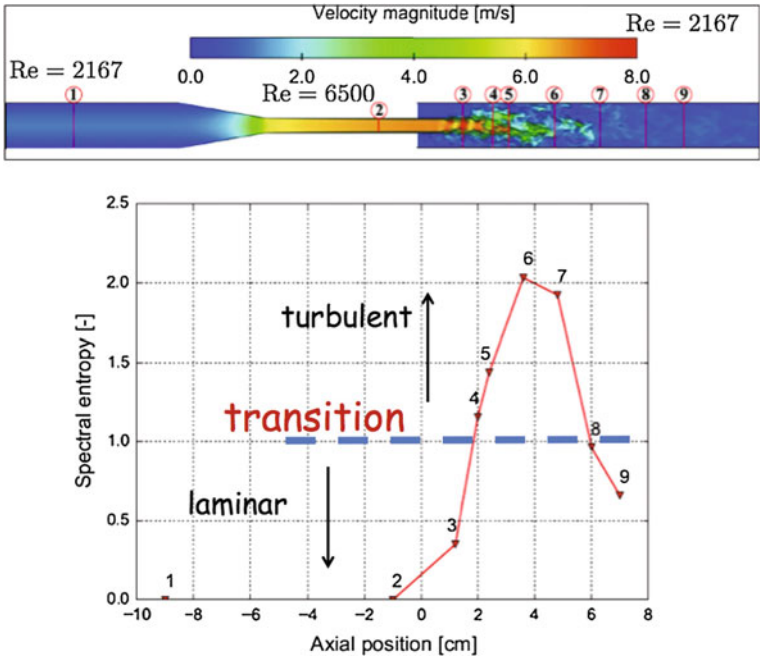

Fig. 3 Blood nozzle computed by LES used to check the validity of the criterion based on POD spectral entropy to delineate between different flow regimes (laminar, transition to turbulence followed by relaminarization)

STAR-CCM+), since they should be ultimately used for industrially-relevant applications. For the blood nozzle presented later in Fig. 3, Ansys-Fluent has been employed. All details of the computation can be found in [10].

3 Proper Orthogonal Decomposition

The software library used here for analysis and understanding of DNS and LES data is the in-house tool SIVAPOD developed and validated in previous projects to analyze both numerical and experimental data [11]. It allows for Proper Orthogonal Decomposition (POD), both as Snapshot POD (SPOD) and as Singular Value Decomposition (SVD). Those approaches, though very similar, involve subtle differences in the methodology used to handle the data. Therefore, one or the other might be more appropriate or efficient, depending on the available hardware and on the size of the problem (number of time instants, number of grid points, number of variables). In what follows, the SPOD has been employed.

The aim of the snapshot POD is to find the function ϕ maximizing the value of $\langle |(\mathbf{u}, \phi)| \rangle / \| \phi \|^2$, where $\langle \cdot \rangle$, $(\cdot, \cdot)$ and $\| \cdot \|$ are spatial average, inner product

and norm, respectively. The function ϕ spans a subspace of the original space of the snapshot $\mathbf{u}(t_k, \mathbf{x})$ such that the error of the orthogonal projection is minimized. Solving an optimization problem leads to an eigenvalue problem, where the functions ϕ are the eigenfunctions. In the snapshot POD ϕ can be described for one mode by

$$\phi(\mathbf{x}) = \sum_{k=1}^{N_s} a(t_k)\mathbf{u}(t_k, \mathbf{x}) \ , \tag{1}$$

where $a(t_k)$ is the entry k of the eigenvectors $\mathbf{A}$ of an eigenvalue problem,

$$\mathbf{CA} = \lambda \mathbf{A} \, , \tag{2}$$

$$\mathbf{A} = (a(t_1), a(t_2), ..., a(t_{N_s}))^T \, , \tag{3}$$

$$C_{ij} = \frac{\left(\mathbf{u}(t_i, \mathbf{x}), \mathbf{u}(t_j, \mathbf{x})\right)}{N_s} \ . \tag{4}$$

Solving this eigenvalue problem, Eq. (2), leads to a total of N_s eigenvalues, written λ_l, and eigenvectors, denoted $\mathbf{A}_l$ ($l \in 1, 2, 3, ..., N_s$).

The eigenvectors A_l are sorted by ordering the corresponding eigenvalues λ_l in descending order, and are then scaled as follows:

$$\sum_{k=1}^{N_s} a_i(t_k)a_j(t_k) = N_s \lambda_i \delta_{ij} \ , \tag{5}$$

where δ_{ij} is the Kronecker delta. In this way, the scaled entries, $a_l(t_k)$, represent the *temporal coefficients* for function ϕ_l, where subscripts l and k refer to the mode number and index of corresponding snapshot (or timestep), respectively. At the same time, λ_l quantifies the energy contained in mode ϕ_l, and this mode can be normalized to represent the corresponding *spatial eigenvector* (also called spatial or POD mode):

$$\phi_l(\mathbf{x}) = \frac{1}{N_s \lambda_l} \sum_{k=1}^{N_s} a_l(t_k)\mathbf{u}(t_k, \mathbf{x}) \ . \tag{6}$$

Using this approach the original signal (for us, the flow velocity) can be represented as follows, highlighting the connection between original data-set ($\mathbf{u}$), spatial mode ϕ_l and temporal coefficients a_l:

$$\mathbf{u}(t, \mathbf{x}) = \sum_{l=1}^{N_s} a_l(t)\phi_l(\mathbf{x}) \ . \tag{7}$$

In order to characterize now the intensity of the turbulence contained in the analyzed velocity field $\mathbf{u}$, the spectral entropy S_d classically used in information theory has been computed. This quantity should hopefully allow us to distinguish between

different flow regimes, from "highly disordered" (for us, turbulence), to "partially ordered" (for us, transition), or "well ordered" (for us, laminar flow). For the computation of the spectral entropy, the probability P_l of each mode is first computed, after ordering in decreasing order based on λ_l, as:

$$P_l = \frac{\lambda_l}{\sum_{j=1}^{N_s} \lambda_j} , \tag{8}$$

Then, the spectral entropy can be determined as:

$$S_d = -\sum_{l=1}^{N_s} P_l \ln P_l . \tag{9}$$

According to Eq. (3), the maximum possible value of S_d is reached when all eigenvalues are equal to each others, i.e., $P_l = 1/N_s$, and consequently $S_d = \ln(N_s)$. Physically, this means that the energy is equally distributed on all the N_s modes. The minimum value of S_d corresponds to the case where the original signal contains only one mode, the first one, meaning that the flow field is steady. Then, $S_d = 0$. Further discussions can be found in [12].

4 Results

To calibrate the approach, DNS simulations of homogeneous isotropic turbulence have been carried out with DINO. After checking the connection between POD spectral entropy and turbulence intensity by computing S_d for increasing values of the turbulent Reynolds number, as documented in Table 1, a very clear relationship can be established. There is indeed a monotonous relationship between S_d and the flow

Table 1 Computed spectral entropy S_d

Flow regime	Re_λ	Re_Λ	S_d
Quasi-laminar	1.01	1.780	0.057
	5.00	8.900	0.140
	15.2	26.80	0.470
	20.3	35.90	0.623
Transition	32.0	53.80	0.879
	40.7	71.80	1.089
	50.8	89.73	1.265
Turbulent	61.1	107.7	1.418
	81.5	143.7	1.660
	101.8	179.6	1.848

state, and specific thresholds can be associated to transition to turbulence ($S_d \approx 1$) and to fully turbulent flows ($S_d > 1.25$).

To check the generality of the developed approach, the resulting thresholds have then been employed to predict the flow state in a completely different case, a complex blood nozzle proposed as a benchmark by the Food and Drug Administration. As shown in Fig. 3, a perfect agreement is obtained compared with a user-based analysis of the flow, showing that S_d can be used to characterize in an automatic manner the state of an unsteady, three-dimensional flow.

5 Conclusions

Based on these first tests, it appears that the spectral entropy computed from the POD decomposition can be used to quantify the flow state (laminar, transitional or turbulent) in an automatic, user-independent manner. Starting from a three-dimensional, unsteady velocity field, a single scalar quantity S_d is obtained in this manner. A value of S_d around unity denotes a transitional value, while $S_d > 1.25$ characterizes full-developed turbulence, the parameter S_d increasing in a monotonic way with the turbulence intensity. Further tests will be needed in order to check that these thresholds are generally applicable.

Acknowledgements All the results discussed in this paper have been obtained in close collaboration with A. Abdelsamie, P. Arányi, P. Berg, G. Fru, G. Martello and G. Janiga from my own research group. The financial support of the DFG (Deutsche Forschungsgemeinschaft) within the Forschergruppe (Research unit) number 1447 as well as the computer resources provided by the Gauss Center for Supercomputing/Leibniz Supercomputing Center Munich under grant pro84qo are highly acknowledged.

References

1. Berg, P., Abdelsamie, A., Yu, H., Janiga, G. Thévenin, D.: Multi-phase blood flow modeling in intracranial aneurysms considering possible transition to turbulence. 8th International Symposium on Turbulence and Shear Flow Phenomena, BIOE/1–6, Poitiers (F) (2013)
2. Thévenin, D., Behrendt, F., Maas, U., Przywara, B., Warnatz, J.: Development of a parallel direct simulation code to investigate reactive flows. Comput. Fluids **25**(5), 485–496 (1996)
3. Hilbert, R., Thévenin, D.: Influence of differential diffusion on maximum flame temperature in turbulent non-premixed hydrogen/air flames. Combust. Flame **138**, 175–187 (2004)
4. Thévenin, D., Gicquel, O., de Charentenay, J., Hilbert, R., Veynante, D.: Two- versus three-dimensional direct simulations of turbulent methane flame kernels using realistic chemistry. Proc. Combust. Inst. **29**, 2031–2039 (2003)
5. Thévenin, D.: Three-dimensional direct simulations and structure of expanding turbulent methane flames. Proc. Combust. Inst. **30**, 629–637 (2005)
6. Reveillon, J., Pera, C., Bouali, Z.: Examples of the potential of DNS for the understanding of reactive multiphase flows. Int. J. Spray Combust. Dyn. **3**(1), 63–92 (2011)

7. Abdelsamie, A., Thévenin, D.: Turbulence modulation by fully resolved particles using immersed boundary methods. In: EUROMECH/ERCOFTAC Colloquium Immersed Boundary Methods, pp. 145–147. Leiden (NL) (2013)
8. Abdelsamie, A., Thévenin, D.: Modulation of isotropic turbulence by resolved and non-resolved spherical particles. In: Fröhlich, J., Kuerten, H., Geurts, B.J., Armenio, V. (eds.) Direct and Large-Eddy Simulation IX, pp. 621–629. Springer, Berlin (2015)
9. Abdelsamie, A., Thévenin, D.: Direct numerical simulation of turbulent lean premixed syngas flames at elevated pressure. In: Direct and Large-Eddy Simulation X. Springer, Berlin. (This same book)
10. Janiga, G.: Large-eddy simulation of the FDA benchmark nozzle for a Reynolds number of 6500. Comput. Biol. Med. **47**, 113–119 (2014)
11. Arányi, P., Janiga, G., Zähringer, K., Thévenin, D.: Analysis of different POD methods for PIV-measurements in complex unsteady flows. Int. J. Heat Fluid Flow **43**, 204–211 (2013)
12. Abdelsamie, A., Janiga, G., Thévenin, D.: Spectral entropy as a flow-state indicator. Int. J. Heat Fluid Flow, (2016). Submitted for publication

Direct and Large-Eddy Simulations of Biological Flows

M. Vanella, S. Wang and E. Balaras

1 Introduction

The broader area of bio-fluid dynamics includes a wide array of applications from very diverse fields. The study of animal locomotion (i.e. swimming, flying) is probably one of the areas where eddy resolving approaches such as direct numerical simulations (DNS) and large-eddy simulations (LES) can have a major impact. Flapping flight, for example, is known to be the single most successful mode of animal locomotion that is exhibited by thousands of species of birds, and millions of flying insects [1]. The fact that all powered flying creatures have flapping wings can be attributed in part to the constraint of muscle actuation, which is a biological necessity, not necessarily shared by man-made devices [2]. However, there is evidence that at small scales, flapping wings may offer some unique advantages such as better lift and thrust generation capabilities without weight penalties.

Natural systems have adopted two fundamentally different approaches to flapping wing locomotion, which is driven their the sensing and actuation capabilities: Avian flapping motions typically occur on the timescales of the rigid body motion of the animal (5 Hz), and are characterized by active deformations of the wing to generate the aerodynamic forces that are necessary for stabilization and maneuvering. This approach requires not only rich sensing capabilities, but also precise spatial and temporal resolution in their actuation systems (e.g., fast twitch muscles in the wings). As wing deformation is the dominant control mechanism, coupling between structural deformations and fluid physics play an essential role in this case. Insects, on the

M. Vanella (✉) · S. Wang (✉) · E. Balaras (✉)
The George Washington University, Washington, DC, USA
e-mail: vanella@gwu.edu

S. Wang
e-mail: wang@gwu.edu

E. Balaras
e-mail: balaras@gwu.edu

D.G.E. Grigoriadis et al. (eds.), *Direct and Large-Eddy Simulation X*,
ERCOFTAC Series 24, https://doi.org/10.1007/978-3-319-63212-4_5

other hand, are sensor rich, but actuator poor; they have control over kinematics, but do not have the musculature for fine motor control of wing deformations as seen in their avian counterparts. The primary actuation is restricted to the base of the wing hinge, which allows for subtle changes to wing kinematic patterns, which produce small changes in the aerodynamic force per wing-stroke. This type of actuation at rigid body timescales would not be sufficient for stabilization and maneuverability. To compensate for this disadvantage, actuation bandwidth is significantly increased, sometimes by several orders of magnitude. For example, the Drosophila melanogster wing-beat frequencies are on the order of 200 Hz, and its rigid body motion of the order of 20 Hz.

For bird or insect flight typical flight speeds can range from 1 to 20 m/s, while typical length scales range from 1 to 10 cm. As a result, typical forward flight Reynolds numbers are of the order of, $O[10^4]$. Such Reynolds numbers are much smaller than the ones in classical aerodynamic applications, $O[10^7]$, where viscous effects are confined in very thin attached boundary layers, and at the same time higher than the ones characterizing laminar well organized flow over the body and in the wake, ($O[10^2]$). Consequently, the above class of problems is a particularly attractive area of applications for DNS/LES because the required spatio-temporal resolution to accurately represent all significant turbulent scales is such that it brings them within reach of today's supercomputers. For example, while a resolved LES of the flow around a small aircraft would require approximately $O[10^{14}]$ points, which is beyond the reach of computers that are even orders of magnitude faster than the ones presently available, around the flapping wings of an insect or bird would require only $O[10^6$–$10^7]$ points, which is well within reach of current high-performance computers. In addition, given that the mean flow, in most cases, is three-dimensional and unsteady, classical turbulence modeling strategies will not reduce the cost dramatically. This class of problems, however, introduces new challenges: the flow is highly unsteady and involves moving and/or deforming boundaries, introducing the need for further developments in several aspects of eddy resolving techniques. In this work we will discuss such a formulation and present an example application to flapping flight.

2 Methodologies

2.1 Overview

The motion of fluid is governed by the Navier–Stokes equations for incompressible flows:

$$\frac{\partial \mathbf{u}}{\partial t} + \mathbf{u} \cdot \nabla \mathbf{u} = -\nabla p + \frac{1}{Re} \nabla^2 \mathbf{u} + \mathbf{f}, \tag{1}$$

$$\nabla \cdot \mathbf{u} = 0, \tag{2}$$

where $\mathbf{u}$ is the velocity normalized by a characteristic velocity U, and p is the pressure normalized by $\rho_f U^2$. Here, ρ_f and L are the density of the fluid and the characteristic length, respectively. The Reynolds number is, $Re = UL/\nu$, where ν is the kinematic viscosity of fluid. $\mathbf{f}$ is a forcing term to introduce the effect of a solid boundary on the fluid. For the purpose of discussion let us also consider the motion of a solid body immersed in the fluid, given by Newton's second law [3]:

$$\begin{bmatrix} \mathbf{I} & 0 \\ 0 & \mathbf{M} \end{bmatrix} \frac{d}{dt} \begin{pmatrix} \mathbf{q_1} \\ \mathbf{q_2} \end{pmatrix} = \begin{pmatrix} \mathbf{q_2} \\ \mathbf{F} \end{pmatrix}, \tag{3}$$

where $\mathbf{q_1}$ is the generalized displacement of the rigid body system, $\mathbf{q_2} = d\mathbf{q_1}/dt$ is the generalized velocity, $\mathbf{I}$ is the identity matrix, $\mathbf{M}$ is the generalized mass matrix, and $\mathbf{F}$ is the generalized forces. This above set of equations needs to be solved as a coupled system.

In DNS the governing equations are directly solved using a projection method. All spatial derivatives are approximated using second-order central differences on a staggered grid. In the case of LES a filtered version of the governing equations is adopted, where all scales smaller that the filter size (typically comparable to the grid size) are parametrized using a subgrid scale (SGS) model. The interaction of the fluid with moving boundaries is done using the formulation by Yang et al. [4], in which the fluid-structure interaction is treated as a single dynamical system using an interactive predictor-corrector process.

To avoid complications associated with moving/deforming grids an immersed boundary method (IB) is adopted. In such case, the equations governing the dynamics of the fluid are solved on a fixed Cartesian grid, and the requirement for the grid to conform to the solid body, which is defined by a set of Lagrangian points, is relaxed. A moving-least-squares (MLS) reconstruction IB method is used to couple the solutions on the Eulerian and Lagrangian grids, and compute the IB forcing term, $\mathbf{f}$, in the above equations. Details can be found in [5].

Central to the accuracy of the overall method is the computation of the hydrodynamic forces on the solid surface, which is not trivial in IB methods. For the class of IB methods considered in this study Uhlmann [6] has provided a moment balance approach to evaluate the hydrodynamic force based on the IB forcing term and the inertia force of the artificial flow within the solid body. The advantage of this approach is that the flow details outside the solid body can be ignored. This approach has been successfully used is cases of simple geometries, such as spheres or circular cylinders [6–8]. However, arbitrary shaped bodies introduce complications. Moreover, this approach cannot give the distribution of hydrodynamic forces on the solid surface, thus it is not applicable to flexible body.

Yang and Balaras [9] and Vanella and Balaras [5] proposed a linear reconstruction to compute the hydrodynamic force on the solid surface. This approach, however, requires a very fine grid near the wall. In this study the hydrodynamic force on the wall is computed using a model-based approach, which follows the ideas in [10, 11]. It takes into account the effect of surface curvature on the variation of pressure in the normal direction. The model fits the variation of pressure normal to the solid surface

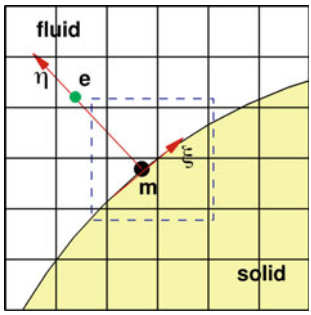

Fig. 1 Schematic of the supporting domain (*dashed line*) and local coordinate system $\xi o \eta$ for a Lagrangian point m on the solid surface. e is the external point along the normal direction at m

by a linear function, and computes the pressure and viscous stress using the external flow near the surface:

$$p|_m = p|_e - \frac{1}{2}\left(\left.\frac{\partial p}{\partial \eta}\right|_m + \left.\frac{\partial p}{\partial \eta}\right|_e\right) h, \tag{4}$$

$$\mathbf{f}_v|_m = \frac{1}{Re}\left.\frac{\partial u_\xi}{\partial \eta}\right|_e \mathbf{t} - \frac{1}{Re}\left.\frac{\partial^2 u_\xi}{\partial \eta^2}\right|_e h\mathbf{t} - \frac{1}{Re}\frac{1}{2}\left.\frac{\partial^3 u_\xi}{\partial \eta^3}\right|_e h^2\mathbf{t}, \tag{5}$$

where m is a point on the solid surface, and e is an external point along the normal direction at m, as shown in Fig. 1. $\mathbf{t}$ is the unit vector in the tangent direction at point m. Details are given in [12].

3 Results

3.1 Falling Non-circular Solid Body

To test the proposed hydrodynamic stress model a free falling elliptical cylinder is simulated. The simulation mimics the conditions in the work by Xia et al. [13], where both body-fitted mesh method is used. The elliptical cylinder has an aspect ratio of $b/a = 2$, where a and b are the minor and major axes of the ellipse, respectively. The non-dimensional computational domain is $[-2, 2] \times [-30, 10]$, where the characteristic length is b. The elliptical cylinder center starts to move vertically from $(0, 0)$ at $t = 0$ with a zero initial velocity and a initial angle $\alpha_0 = \pi/4$ with respect to the horizontal axis. The density ratio between the cylinder and fluid is $\rho_s/\rho_f = 1.1$. The gravity is $98U_t^2/b$, where U_t is the terminal velocity. The Reynolds number is $Re = U_t b/\nu = 10$. The non-slip boundary condition is used at all the boundaries. The initial velocity of the flow is zero. The grid length is $dh = a/24$. The time step is adapted to keep the CFL fixing at 0.1.

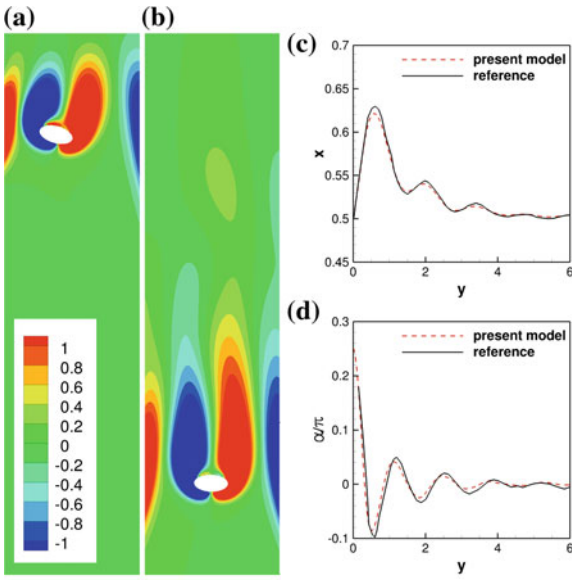

Fig. 2 The instantaneous vorticity field of the free falling elliptical cylinder, **a** $t = 2.0$, **b** $t = 10.0$, and the trajectory of the free falling elliptical cylinder, **a** x-y phase plot, **b** angle-y phase plot

The elliptical cylinder moves downward with angular oscillation. The instantaneous flow fields at two different instants are shown in Fig. 2 together with the trajectory of the center of the cylinder. The latter is in excellent agreement with the reference data, despite the fact that we use a much coarser grid, demonstrating the accuracy of the proposed model.

3.2 Free Longitudinal Flight of Musca Domestica model

In this section we will present results of free longitudinal flight for a fly model created using CAD software from digital images of a *Musca Domestica*. The model is composed of one pair of rigid wings, *RW* and *LW*, hinged to a rigid body, *RB*1, which represents the insect's head and thorax, and another body, *RB*2, representing the insect's abdomen. The latter is also articulated to *RB*1 (see Fig. 3). The coordinate transformations among the different body reference frames with respect to the inertial frame, N, are defined in terms of Euler angle sequences. For the case of longitudinal flight considered here, the lateral motion and rotations around axes in the insects symmetry plane are neglected. The wing kinematics and inertia properties are symmetric. Details on the derivation of the kinematics and Lagrangian dynamics for this system are found in [14].

The head-abdomen length of the model is $L_{TA} = 1.03b$, where b is the one wingspan (hinge to tip). The wings have a thickness of $0.025b$. A simple set of wing kinematics, representative of *Diptera* wing motion is prescribed in all simulations.

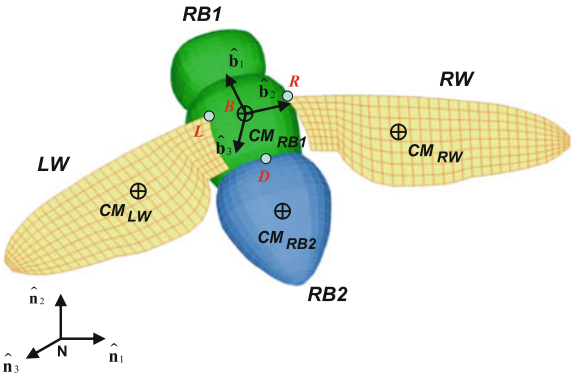

Fig. 3 Four rigid body model for the full insect. Rigid Body $RB1$, head-thorax, is represented by the tracking frame B attached to its center of mass. Rigid body $RB2$, the abdomen, is hinged to $RB1$ at point D where its respective body frame is defined. The wing bodies RW and LW are articulated to $RB1$ at points R and L respectively, where their tracking frames are defined

For the right wing, for example, we set:

$$\phi_3(t) = A_\phi sin\left(\omega_f t + \alpha\right), \quad \theta_3(t) = 0, \quad \psi_3(t) = \psi_m + A_\psi cos\left(\omega_f t\right), \tag{6}$$

where $A_\phi = \pi/4$ is the amplitude of the wing-thorax relative angle of attack, and $\alpha = \pi/6$ (advanced rotation) is the phase. The mean stroke angle is $\psi_m = -\pi/36$, and the stroke amplitude $A_\psi = 55\pi/180$. The reference velocity U_R used is the mean wing tip velocity given by $U_R = \dot{\psi}_{3mean} b$, where $\dot{\psi}_{3mean} = 2A_\psi \omega_f/\pi$. The Reynolds number is $Re = U_R b/\nu = 500$. The left wing angles were defined such that symmetric flapping occurs. The $RB1$ orientation angle on an initial prescribed kinematics simulation was set to $\theta = \pi/3$, and the stroke plane was aligned to the horizontal plane.

In order to define a suitable set of inertia properties for the four body model, we assume the regime is one of high fluid-structure coupling and $\overline{F}_{in}/\overline{D}_w \simeq 1.3$, where $\overline{F}_{in} = 2m_w x_{CR} A_\psi \omega^2/\pi$ is the mean inertia force due to the wings tangential acceleration and $\overline{D}_w$ is the mean drag force from the initial prescribed kinematics computation. The resulting necessary wing mass m_w is obtained for a density ratio $\rho_w/\rho_f \simeq 30$, which we assume constant for the model. The desired inertia properties were then obtained by numerical integration [14].

The field acceleration was set to $g = 0.01U_R^2/b$, providing a weight force lower than the mean lift force of the prescribed simulation. Thus, it is expected that the model would have an upward net motion. Also the initial conditions on the state variables were set to $x_o = 0$, $z_o = -0.5b$, $\theta_o = 90°$, $\theta_{2o} = 0$, and zero velocities. A unitary dimensionless torsion stiffness K_T was employed at the abdomen hinge, keeping the relative angle between $RB1$ and $RB2$ within a 5° amplitude. Also, an advanced mean stroke angle of, $\psi_m = 5.5\pi/180$ was used. A slight pitch up motion was found along the simulation. It is important to note that, in several flapping

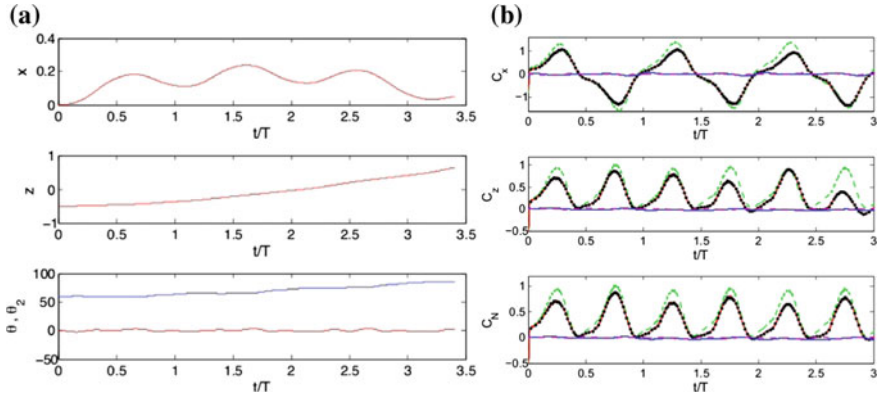

Fig. 4 **a** Variation of positions $x(t)$, $z(t)$ and angular coordinates $\theta(t)$ (*blue*), $\theta_2(t)$ (*red*) with time for the free longitudinal flight; **b** Variation of force coefficients $C_x(t)$, $C_z(t)$ and $C_N(t)$ (force normal to stroke plane) with time for the free longitudinal flight: (*blue*) *RB*1, (*dashed magenta*) *RB*2, (*red*) *RW*, and (•) *LW*. The *green curves* correspond to $C_x(t)$, $C_z(t)$ and $C_L(t)$ from the prescribed kinematics simulation

wing systems, both hovering and forward flight have been found to be dynamically unstable through linear stability analysis (i.e. [15, 16]). Therefore, it is expected that the solution will eventually diverge as the integration progresses.

In Fig. 4a the values of the state variables $x(t)$, $y(t)$, $\theta(t)$ and $\theta_2(t)$ as a function of integration time are shown. The vertical position $z(t)$ is seen to increase throughout the calculation consistent with the fact that the mean resulting vertical force is directed upwards. The horizontal coordinate of the center of mass of *RB*1 takes oscillating positive values, which diminish as the calculation progresses. This is due to the fact that the orientation angle $\theta(t)$ (and stroke plane angle) of *RB*1 increases, introducing a horizontal force component along the $-x$ direction. The oscillatory component of $x(t)$ is about $0.1b$, which is consistent to the data reported in [17] for a *Manduca Sexta* hawkmoth model with similar wing to body mass ratio. The orientation angle $\theta(t)$ increases steadily, due to moment imbalance. A lower value of ψ_m is required to reduce this effect. Also, $\theta(t)$ oscillates with a peak to peak amplitude of 4° similarly to what is reported in [17].

In Fig. 4b the time variation of force coefficients in the horizontal, x, and vertical, z, directions, and also in a direction normal to the stroke plane (lift direction for the prescribed kinematics simulation) are shown. It is seen that, due to the stroke plane rotation, C_x and C_z vary significantly as time increases. The coefficients resulting from the prescribed kinematics calculation are plotted on the same figures for comparison. All force coefficients take lower values than the fixed body calculation. This body motion effect results in lower ability of the wings to transfer momentum to the fluid. As a consequence, the flight performance of the flapping system is reduced.

The instantaneous flow fields at different simulation times are shown in Fig. 5. Here, an isocontour of the second invariant of the velocity gradient tensor, Q, colored

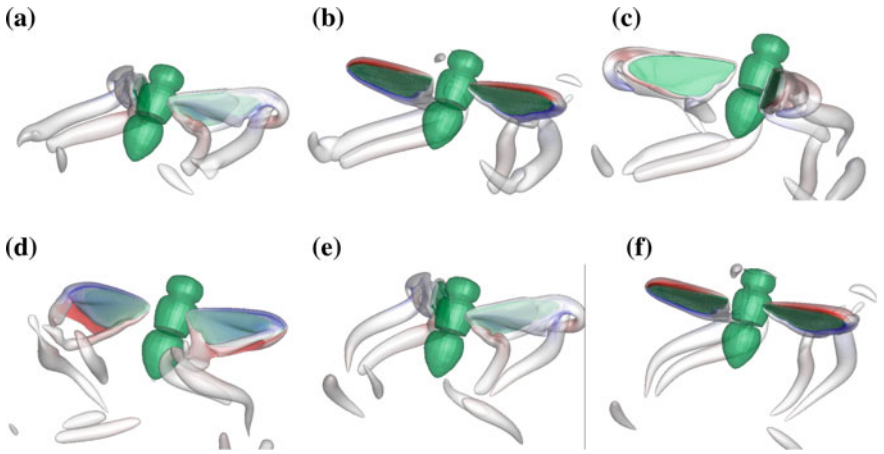

Fig. 5 Q isocontour colored by vorticity on the y direction. 40 contours of ω_y from -20 to 20 are used. **a**–**f**: $t/T = 0.75, 1, 1.25, 1.5, 1.75, 2$

by the vorticity, ω_y, shows the evolution of the large coherent structures, namely the leading edge and tip vortices. The leading edge vortices attached to each wing detach in the vicinity of the tips (see Fig. 5a, b), where the vorticity is reoriented forming the wing tip vortices. Vorticity is also shed from the regions of the wing proximal to the bodies. As a result two vortical structures are being generated on each wing as shown in Fig. 5c, d. The secondary vortices are dependent on the planform geometry of the wings used. The sequence visualized in Fig. 5 shows the vertical displacement of the model due to lift force.

References

1. Dickinson, M.H.: Solving the mystery of insect flight. Sci. Am. **284**, 48–57 (2001)
2. Spedding, G.R., Lissaman, P.B.S.: Technical aspects of microscale flight systems. J. Avian Biol. **29**, 458–468 (1998)
3. Baruh, H.: Analytical Dynamics. WCB/McGraw-Hill, Boston (1999)
4. Yang, J., Preidikman, S., Balaras, E.: A strongly coupled, embedded-boundary method for fluid? structure interactions of elastically mounted rigid bodies. J. Fluid. Struct. **24**, 167–182 (2008)
5. Vanella, M., Balaras, E.: A moving-least-squares reconstruction for embedded-boundary formulations. J. Comp. Phys. **228**, 6617–6628 (2009)
6. Uhlmann, M.: An immersed boundary method with direct forcing for the simulation of particulate flows. J. Comp. Phys. **209**, 448–476 (2005)
7. Wang, S., Zhang, X.: An immersed boundary method based on discrete stream function formulation for two-and three-dimensional incompressible flows. J. Comp. Phys. **230**, 3479–3499 (2011)
8. Kempe, T., Frhlich, J.: An improved immersed boundary method with direct forcing for the simulation of particle laden flows. J. Comp. Phys. **231**, 3663–3684 (2012)

9. Yang, J., Balaras, E.: An embedded-boundary formulation for large-eddy simulation of turbulent flows interacting with moving boundaries. J. Comp. Phys. **215**, 12–40 (2006)
10. Balaras, E., Benocci, C., Piomelli, U.: Two-layer approximate boundary conditions for large-eddy simulations. AIAA J. **34**, 1111–1119 (1996)
11. Posa, A., Balaras, E.: Model-based near-wall reconstructions for immersed-boundary methods. Theor. Comp. Fluid Dyn. **28**, 473–483 (2014)
12. Wang, S., Vanella, M., Balaras, E.: A hydrodynamic stress model for immersed boundary methods to simulate turbulence interacting with particles of arbitrary shape. J. Comput. Phys. (2016) Submitted
13. Xia, Z., Connington, K.W., Rapaka, S., Yue, P., Feng, J.J., Chen, S.: Flow patterns in the sedimentation of an elliptical particle. J. Fluid Mech. **625**, 249–272 (2009)
14. Vanella, M.: A fluid structure interaction strategy with application to low Reynolds number flapping flight. Ph.D. Thesis. Department of Mechanical Engineering, University of Maryland (2010)
15. Sun, M., Xiong, Y.: Dynamic flight stability of a hovering bumblebee. J. Exp. Biol. **208**, 447–459 (2005)
16. Taylor, G.K., Thomas, A.L.R.: Dynamic flight stability in the desert locust Schistocerca gregaria. J. Exp. Biol. **206**, 2803–2829 (2003)
17. Wu, J.H., Zhang, Y.L., Sun, M.: Hovering of model insects: simulation by coupling equations of motion with Navier–Stokes equations. J. Exp. Biol. **212**, 3313–3329 (2009)

Understanding Entrainment Processes in the Atmosphere: The Role of Numerical Simulation

Maarten van Reeuwijk and Harm J.J. Jonker

Abstract Turbulent entrainment is a process of primary importance in the atmospheric boundary layer; however despite several decades of intense study much remains to be understood. Direct Numerical Simulation (DNS) and Large-Eddy Simulation (LES) have a tremendous potential to improve the understanding of turbulent entrainment, particularly if combined with theory. We discuss a recently developed framework for turbulent jets and plumes to decompose turbulent entrainment in various physical processes, and modify it for use in a stably stratified shear driven (nocturnal) boundary layer. The decomposition shows that inner layer processes become negligible as time progresses and that the entrainment coefficient is determined by turbulence production in the outer layer only.

1 Introduction

Turbulent entrainment plays a central role in the evolution of the atmospheric boundary layer, the life cycle of clouds, katabatic winds and many other physical processes in the atmosphere [13]. Turbulent entrainment occurs on the interface of two fluid layers with differing turbulence intensity and entails the incorporation of fluid from the relatively quiescent layer into the turbulent layer. One of the canonical examples in the atmosphere is the entrainment of fluid from the free troposphere (which is relatively quiescent) into the atmospheric boundary layer (ABL), which is the turbulent fluid layer closest to the earth's surface. Turbulent entrainment will cause the ABL of thickness h to increase in time at a rate

M. van Reeuwijk (✉)
Imperial College London, London, UK
e-mail: m.vanreeuwijk@imperial.ac.uk

H.J.J. Jonker
Delft University of Technology, Delft, Netherlands
e-mail: h.j.j.jonker@tudelft.nl

D.G.E. Grigoriadis et al. (eds.), *Direct and Large-Eddy Simulation X*,
ERCOFTAC Series 24, https://doi.org/10.1007/978-3-319-63212-4_6

$$w_e = \frac{\mathrm{d}h}{\mathrm{d}t}, \tag{1}$$

where w_e is referred to as an entrainment velocity.

Restricting attention to dry conditions, the (potential) temperature θ in the ABL is relatively uniform due to the turbulent mixing and the quiescent layer overhead is warmer; a relatively sharp temperature jump of magnitude $\Delta\theta$ is present at the interface of the two layers. Turbulent entrainment will be inhibited by the temperature jump as the turbulence will need to perform work to pull the warm fluid down, causing an increase in the potential potential energy of the ABL. Introducing a typical turbulent velocity scale $\mathscr{U}$, it is thus expected that (assuming very high Reynolds and Péclet numbers)

$$E \equiv \frac{w_e}{\mathscr{U}} = f(\mathrm{Ri}), \qquad \text{where} \qquad \mathrm{Ri} = \frac{\Delta b h}{\mathscr{U}^2}. \tag{2}$$

Here, Ri is a bulk Richardson number and $\Delta b = (g/\theta_0)\Delta\theta$ is the buoyancy jump between the two layers, g is the gravitational acceleration and θ_0 is a reference temperature.

Entrainment laws are important in numerical weather prediction because three-dimensional turbulence is not resolved. For example, the UK Unified Model currently employs a horizontal resolution of 1.5 km, insufficient to resolve any of the turbulence which has scales as small as 1 mm in a typical daytime ABL. Hence, finding the appropriate function f has received significant attention over the last half century [5]. However, turbulent entrainment velocities w_e are usually very small compared to the other velocity scales (wind, turbulence) and its measurement is a formidable challenge. Consequently, experiments and observations sometimes report a factor 5 difference in the measured entrainment velocities [5].

The tremendous increase in computational power has enabled significant progress to be made in understanding entrainment via the turbulence-resolving methods of large-eddy simulation and direct numerical simulation, in the context of daytime boundary layers [7, 8, 14], nocturnal boundary layers [2, 9] and clouds [1, 4]. The turbulence community has made substantial progress in understanding entrainment from a small-scale perspective, e.g. [3, 16]. However, the understanding remains fragmented and case-specific, with an overarching theory being absent.

Recently, a framework was developed for turbulent jets and plumes which enables turbulent entrainment to be decomposed into different physical processes [15]. The framework relies on the internal consistency of the continuity, momentum and mean kinetic energy equations. For jets and plumes, it was shown that the dimensionless turbulence production is practically identical in jets and plumes, which implied that the Priestley and Ball entrainment model [6, 12, 15] is the appropriate model for jets and plumes in a neutral environment. In this contribution, this framework will be extended to a wall-bounded flow, specifically the nocturnal boundary layer discussed in [9].

2 Sheared Nocturnal Boundary Layer

Consider an idealised sheared nocturnal boundary layer with an initially linear stratification $b_0 = N^2 z$ and a uniform wall shear stress $\tau_w \equiv \rho u_*^2$ as discussed in [9, 10] and schematically shown in Fig. 1. This problem has two homogeneous directions and is mathematically described after Reynolds-averaging by

$$\frac{\partial \overline{u}}{\partial t} + \frac{\partial \overline{w'u'}}{\partial z} = \nu \frac{\partial^2 \overline{u}}{\partial z^2}, \qquad \frac{\partial \overline{b}}{\partial t} + \frac{\partial \overline{w'b'}}{\partial z} = \kappa \frac{\partial^2 \overline{b}}{\partial z^2}, \tag{3}$$

$$\left.\frac{\partial \overline{u}}{\partial z}\right|_w = \frac{u_*^2}{\nu}, \qquad \left.\frac{\partial \overline{b}}{\partial z}\right|_w = 0, \tag{4}$$

$$\overline{u}(z, t = 0) = 0, \qquad \overline{b}(z, t = 0) = N^2 z. \tag{5}$$

We performed Direct Numerical Simulation with our in-house code SPARKLE of a domain of $1024 \times 1024 \times 256$ m and a constant (eddy) viscosity $\nu = 0.046$ m^{2}s^{-1}. Further simulation details are provided in Table 1. Here, $h_* = u_*/N$ is the buoyancy length scale and $\mathrm{Re}_N = u_* h_*/\nu$ is the buoyancy Reynolds number, which were shown in [9] to be fundamental quantities for this problem.

The system (3–5) evolves in a self-similar manner and has an inner and outer layer structure (Fig. 2). The characteristic scales of the inner layer are the classical shear length scale ν/u_*, velocity scale u_* and buoyancy scale u_*^3/ν. The middle panels of

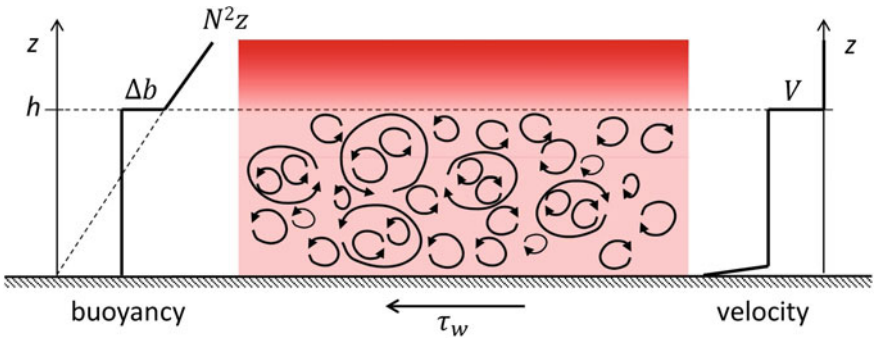

Fig. 1 Schematic of the idealised sheared nocturnal boundary layer simulation setup

Table 1 DNS cases; the domain size is $4H \times 4H \times H$ with $\mathrm{Pr} = 1$ and $\nu = 0.046$ m^2/s

Simulation	u_* [ms^{-1}]	H [m]	$N_x \times N_y \times N_z$	N^2 [s^{-2}]	h_* [m]	Re_N
1a	0.16	256	$1024 \times 1024 \times 512$	3.24×10^{-4}	8.9	31
1b	0.16	256	$1024 \times 1024 \times 512$	1.62×10^{-4}	12.6	44
1c	0.16	256	$1024 \times 1024 \times 512$	6.48×10^{-5}	19.9	69

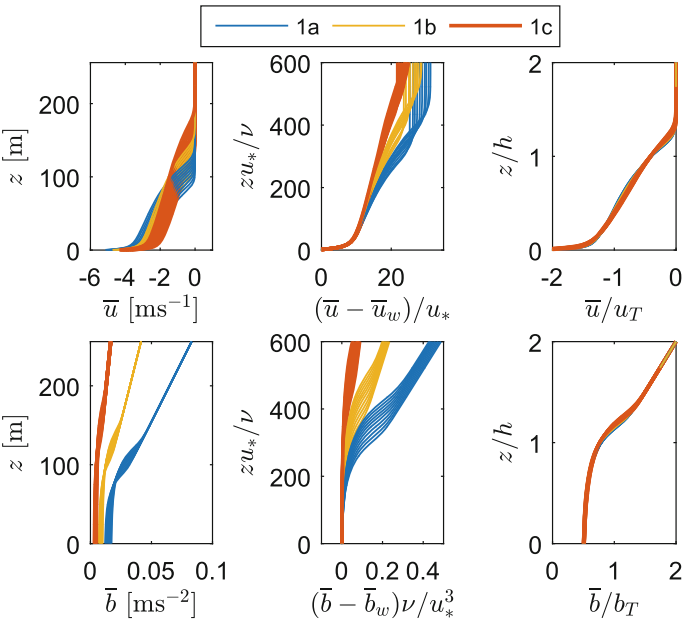

Fig. 2 Velocity and buoyancy profiles for simulations 1a–c. *Left panel* unnormalised variables. *Middle panel* normalised by inner scales. *Right panel* normalised by outer scales

Fig. 2 show a collapse of the velocity and buoyancy profiles for all three simulations for $zu_*/\nu < 150$.

The outer length and velocity scales will be denoted by h and u_T, respectively. In [9] we diagnosed h based on the location of the inflection point in $\overline{b}$ [14], but in order to decompose entrainment we will need an estimate of h based on integral quantities. We choose the scales

$$h = \frac{Q^2}{M}, \qquad u_T = -\frac{M}{Q}, \qquad b_T = N^2 h, \tag{6}$$

where the volume flux Q [L^{2}T^{-1}] and specific momentum flux M [L^{3}T^{-2}] are defined as, respectively

$$Q = \int_0^\infty \overline{u}\mathrm{d}z, \qquad M = \int_0^\infty \overline{u}^2\mathrm{d}z. \tag{7}$$

Here we note that the minus sign in the definition of u_T is present to make this quantity positive. The definition of b_T ensures that the self-similarity solution remains consistent with the stratification in the ambient. The self-similar profiles in the outer layer scales are shown in the right panels of Fig. 2. An excellent collapse can be observed, except very near the surface.

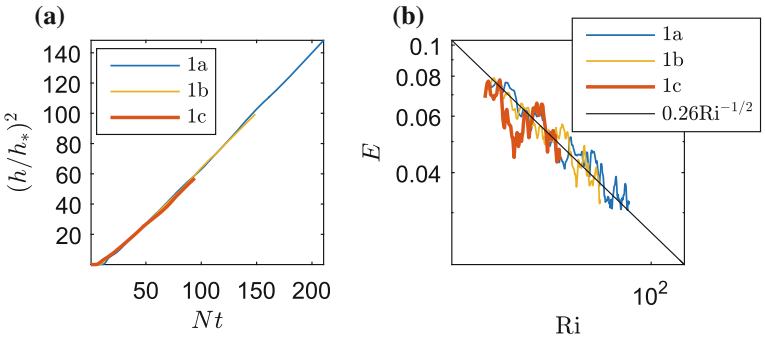

Fig. 3 **a** The layer thickness h as a function of Nt. **b** The entrainment coefficient E as a function of Ri

The dependence of $(h/h_*)^2$ on Nt is shown in the left panel of Fig. 3 for all three cases under consideration and displays almost perfect linear scaling with time, which implies that $h/h_* \sim (Nt)^{1/2}$ [9]. For the case under consideration, $\mathscr{U} = u_*$ and $\Delta b = N^2 h/2$ (Fig. 1), implying that Eq. (2) becomes

$$E = \frac{1}{u_*}\frac{\mathrm{d}h}{\mathrm{d}t}, \qquad \mathrm{Ri} = \frac{N^2 h^2}{2u_*^2}. \tag{8}$$

Noting that $\mathrm{Ri} = (h/h_*)^2/2$, it is clear that Ri will increase linearly with time. In the right panel of Fig. 3, the entrainment coefficient E is plotted as a function of $\mathrm{Ri}(t)$, together with the power law $E = 0.26\mathrm{Ri}^{-1/2}$. The proportionality constant is lower than in [9] because of the different definition of h in this paper.

3 Entrainment Decomposition

By substituting the the definition of h in Eq. (6) into the definition of E in Eq. (8) it follows that [15]

$$E = \frac{1}{u_*}\frac{\mathrm{d}}{\mathrm{d}t}\left(\frac{Q^2}{M}\right) = -\frac{2}{u_* u_T}\frac{\mathrm{d}Q}{\mathrm{d}t} - \frac{1}{u_* u_T^2}\frac{\mathrm{d}M}{\mathrm{d}t}. \tag{9}$$

This provides important information as it reveals that an explicit equation for the entrainment law can be obtained by combining the integral momentum and mean energy equations. Taking the time-derivative of Q and M results in

$$\frac{\mathrm{d}Q}{\mathrm{d}t} = -u_*^2, \qquad \frac{\mathrm{d}M}{\mathrm{d}t} = 2\int_0^\infty \overline{w'u'}\frac{\partial \overline{u}}{\partial z}\mathrm{d}z - 2\nu\int_0^\infty \left(\frac{\partial \overline{u}}{\partial z}\right)^2 \mathrm{d}z - 2\overline{u}_w u_*^2, \tag{10}$$

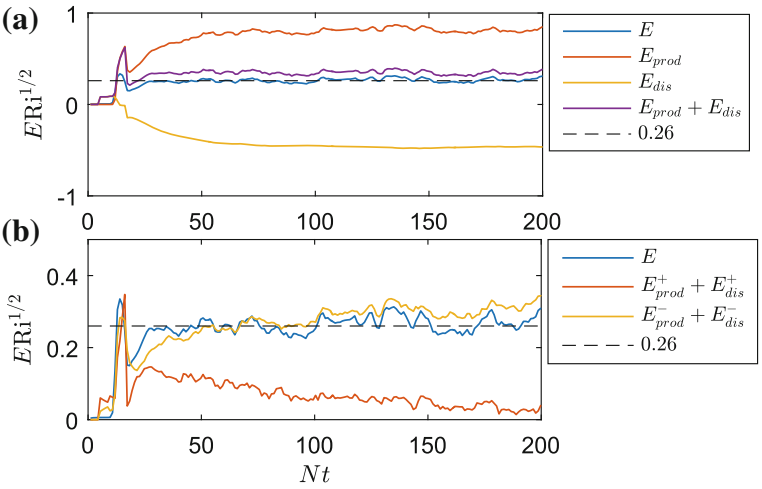

Fig. 4 Entrainment decomposition for simulation 1a: **a** in terms of E_{prod} and E_{dis} and compared with the direct definition (E); **b** in terms of inner and outer layer contributions E^+_χ and E^-_χ, respectively

where $\overline{u}_w = \overline{u}(z = 0, t)$. Substitution of Eq. (10) into Eq. (9) leads to

$$E = \underbrace{-\frac{2}{u_* u_T^2}\int_0^\infty \overline{w'u'}\frac{\partial \overline{u}}{\partial z}\mathrm{d}z}_{E_{\mathrm{prod}}} + \underbrace{\frac{2\nu}{u_* u_T^2}\int_0^\infty \left(\frac{\partial \overline{u}}{\partial z}\right)^2 \mathrm{d}z + \frac{2u_*}{u_T}\left(1 + \frac{\overline{u}_w}{u_T}\right)}_{E_{\mathrm{dis}}}. \quad (11)$$

The first term is the turbulent production contribution E_{prod}, which is the prime contributor to turbulent entrainment. The second term E_{dis} includes contributions of the dissipation rate of mean kinetic energy and friction.

The top panel of Fig. 4 shows the individual terms of the decomposition and their sum. Here, E has been corrected for the expected powerlaw-dependence on Ri, and it can indeed be observed that all quantities become constant with time, demonstrating once more the robustness of the $E \sim \mathrm{Ri}^{-1/2}$ relation. The correspondence between E calculated directly from the definition of Eq. (8) and from the decomposition (11) are within 10% of each other. Clearly, E_{prod} has a positive contribution and E_{dis} a negative contribution; E_{prod} is about a factor two larger than E.

It is useful to be able to distinguish inner layer contributions to E from outer layer contributions. To this end, we split the integrals in Eq. (11) into two parts:

$$\int_0^\infty \mathrm{d}z = \underbrace{\int_0^{h/2} \mathrm{d}z}_{\mathrm{inner}} + \underbrace{\int_{h/2}^\infty \mathrm{d}z}_{\mathrm{outer}} \quad (12)$$

and denote inner and outer layer contributions by E_χ^+ and E_χ^-, respectively; these are displayed in the bottom panel of Fig. 4. The inner layer contributions vanish over time; this because in the inner layer, production and dissipation are in equilibrium so that the difference will come from the boundary terms which reduce to zero due to the factor u_*/u_T. Hence, outer layer processes are solely responsible for the observed entrainment coefficient E (consistent with [11]). Furthermore, the outer layer term E_{dis}^- is negligible, implying that

$$E \approx E_{prod}^- = -\frac{2}{u_* u_T^2} \int_{h/2}^{\infty} \overline{w'u'} \frac{\partial \overline{u}}{\partial z} \mathrm{d}z. \tag{13}$$

This is a remarkably simple expression. Using the gradient-diffusion hypothesis $\overline{w'u'} = -\nu_T \partial \overline{u}/\partial z$, noting that $\nu_T \sim h_* u_*$ [9], and using the outer layer scaling suitable for the integral under consideration, it follows directly that

$$E \approx \frac{2}{u_* u_T^2} \int_{h/2}^{\infty} \nu_T \left(\frac{\partial \overline{u}}{\partial z} \right)^2 \mathrm{d}z \sim \frac{h_*}{h} \sim \mathrm{Ri}^{-1/2}. \tag{14}$$

4 Conclusions

Large-eddy Simulation and Direct Numerical Simulations are important numerical techniques for understanding turbulent entrainment. The availability of noise-free fully resolved data under "ideal" circumstances allows one to systematically diagnose the small but important signals that comprise turbulent entrainment. Particularly in combination with theory, DNS and LES provide a unique tool to probe deeply into what causes turbulent entrainment, often at Reynolds numbers equal or exceeding those from the canonical laboratory experiments carried out in the seventies and eighties [5] (although not in terms of their Prandtl/Schmidt number, as most experiments were carried out using salt).

In this paper, we decomposed entrainment into contributions from distinct physical processes. The method, originally developed for free-shear layers [15], was extended to wall-bounded flows which have both an inner and outer layer structure. An analysis of an idealised sheared nocturnal boundary layer revealed that the inner layer contributions provide a negligible contribution to E provided enough time has passed. In the outer layer, the dissipation is negligible, implying that the turbulent entrainment coefficient E is determined primarily by the production of turbulence kinetic energy.

Acknowledgements We would like to acknowledge the UK Turbulence consortium (grant number EP/L000261/1), an ARCHER Leadership grant for simulation time on the UK national supercomputer and an NWO/NCF (Netherlands) grant for computations on Huygens.

References

1. Abma, D., Heus, T., Mellado, J.P.: Direct numerical simulation of evaporative cooling at the lateral boundary of shallow cumulus clouds. J. Atmos. Sci. **70**, 2088–2102 (2013)
2. Ansorge, C., Mellado, J.P.: Global intermittency and collapsing turbulence in the stratified planetary boundary layer. Bound. Layer Meteorol. **153**, 89–116 (2014)
3. Da Silva, C., Westerweel, J., Hunt, J.C.R., Eames, I.: Interfacial layers between regions of different turbulence intensity. Ann. Rev. Fluid Mech. **46**, 567–590 (2014)
4. de Rooy, W.C., Bechtold, P., Frohlich, K., Hohenegger, C., Jonker, H.J.J., Mironov, D., Siebesma, A.P., Teixeira, J., Yano, J.I.: Entrainment and detrainment in cumulus convection: an overview. Q. J. R. Meteorol. Soc. **139**(670), 1–19 (2013)
5. Fernando, H.J.S.: Turbulent mixing in stratified fluids. Annu. Rev. Fluid Mech. **23**, 455–493 (1991)
6. Fox, D.G.: Forced plume in a stratified fluid. J. Geophys. Res. **75**(33), 6818–6835 (1970)
7. Garcia, J.R., Mellado, J.P.: The two-layer structure of the entrainment zone in the convective boundary layer. J. Atmos. Sci. **71**, 1935–1955 (2014)
8. Jonker, H.J.J., van Reeuwijk, M., Sullivan, P.P., Patton, E.G.: Interfacial layers in clear and cloudy atmospheric boundary layers. In: Turbulence, Heat and Mass Transfer, 7 September 2012
9. Jonker, H.J.J., van Reeuwijk, M., Sullivan, P.P., Patton, E.G.: On the scaling of shear-driven entrainment: a dns study. J. Fluid Mech. **732**, 150–165 (2013)
10. Kato, H., Phillips, O.M.: On the penetration of a turbulent layer into stratified fluid. J. Fluid Mech. **37**(04), 643–655 (1969)
11. Pollard, R.T., Rhines, P.B., Thompson, R.O.R.Y.: The deepening of the wind-mixed layer. Geophys. Fluid. Dyn. **3**, 381–404 (1973)
12. Priestley, C.H.B., Ball, F.K.: Continuous convection from an isolated source of heat. Q. J. R. Meteorol. Soc. **81**, 144–157 (1955)
13. Stull, R.B.: An Introduction To Boundary Layer Meteorology. Kluwer Academic Publishers, 1998
14. Sullivan, P.P., Moeng, C.-H., Stevens, B., Lenschow, D.H., Major, S.D.: Structure of the entrainment zone capping the convective atmospheric boundary layer. J. Atmos. Sci. **55**, 3042–3064 (1998)
15. van Reeuwijk, M., Craske, J.: Energy-consistent entrainment relation for jets and plumes. J. Fluid. Mech. **782**, 333–355 (2015)
16. Van Reeuwijk, M., Holzner, M.: The turbulence boundary of a temporal jet. J. Fluid Mech **739**, 254–275 (2014)

Part II
LES Quality

Application and Extension of a Synthetic Turbulence Inflow Generator Within a Hybrid LES–URANS Methodology

S. Schmidt and M. Breuer

1 Introduction

Since the development of many flows strongly depends on the inflow conditions, the formulation of feasible conditions at the inlet is a crucial research topic. A procedure such as the precursor simulation is able to deliver appropriate inflow conditions, but this method is limited to simple inflow geometries. A similar conclusion can be drawn for the application of periodic boundary conditions in streamwise direction circumventing the inflow challenge. The synthetic generation of spatially–developing inflow data is a proper way to take the most important characteristics of the turbulent inflow at high Reynolds numbers into account. Thus, the objective of the present study is the application of a reasonable inflow generator to describe the flow past the SD7003 airfoil [10] at $\mathrm{Re} = 6 \times 10^4$ and an angle of attack of $\alpha = 4°$ investigating the impact of the inflow turbulence intensities. As earlier investigations [7, 8] on the airfoil flow without inflow turbulence have shown, the turbulence level has a strong impact on the flow field along the airfoil and hence makes the comparison between experimental findings and numerical results difficult.

2 Hybrid LES–URANS Method

In the last years the combination of large–eddy simulations (LES) and unsteady Reynolds–averaged Navier–Stokes (URANS) predictions to hybrid models has become popular to predict complex flows with reasonable computational effort and high accuracy [1]. For wall–bounded flows the basic concept of the present hybrid LES–URANS approach [3, 7, 8] is to resolve the large unsteady vortical structures,

S. Schmidt · M. Breuer (✉)
Department of Fluid Mechanics, Helmut–Schmidt–Universität Hamburg, Hamburg, Germany
e-mail: breuer@hsu-hh.de

S. Schmidt
e-mail: schmidst@hsu-hh.de

D.G.E. Grigoriadis et al. (eds.), *Direct and Large-Eddy Simulation X*,
ERCOFTAC Series 24, https://doi.org/10.1007/978-3-319-63212-4_7

whereas URANS is performed in the near–wall region. Due to the enormous computational costs to resolve the immediate vicinity of the wall within the LES mode, the URANS formulation plays a dominant role to reduce the costs and to guarantee appropriate results. In order to take the strong anisotropy of the Reynolds stresses into account, an explicit algebraic Reynolds stress model [12] is used in the URANS domain. The non–closed terms of the URANS mode, i.e., the production, the diffusion and the dissipation term are adequately modeled (see Jaffrézic and Breuer [3] and Schmidt and Breuer [7, 8]). Owing to the description of the near–wall region by URANS, the modeling approach of the LES mode is less sophisticated since a large part of the energy spectrum in the core of the flow is resolved. Following the one–equation concept of the URANS mode, a one–equation subgrid–scale model is applied for the LES mode. The location of the interface is determined based on instantaneous flow quantities, which facilitates the automatic selection of the appropriate method (URANS or LES) based on the current flow properties. Thus, the correct switching behavior between both modes is ensured. The interface definition as well as the entire hybrid methodology was already validated for internal [3] as well as external flows including laminar–turbulent transition [7, 8].

3 Synthetic Turbulence Inflow Generator (STIG)

Several concepts were developed and the review by Tabor and Baba–Ahmadi [11] offers an overview of different synthetic methods as well as precursor simulations. Klein et al. [4] proposed a method for generating turbulent inflow data based on a digital filter which depends on statistical properties. These spatial and temporal correlations and the resulting length and time scales allow a simple adjustment on the flow situation of the particular test case. The realization of an appropriate inflow content is achieved by the multiplication of filter coefficients b_s, which describe the two–point correlations (in space) and autocorrelation (in time) of the inflow turbulence, with a series of random numbers r_m. The latter are characterized by zero mean and unity variance. The resulting synthetic velocity fluctuations written as:

$$\left(u_i'\right)_m^{syn} = \sum_{s=-N}^{N} b_s r_{m+s}, \tag{1}$$

are thus provided by a discrete linear digital non–recursive filter for a one–dimensional signal. A required three–dimensional correlation between the filter coefficients is achieved by the convolution of the three one–dimensional filter coefficients $b_{ijk} = b_i \cdot b_j \cdot b_k$. Following the definition of Klein et al. [4] the inflow correlations are described by a homogeneous formulation depending on the corresponding integral length scale L_i and the applied spacing of the grid Δx_i at the location, where the instantaneous profiles are generated. Furthermore, the integral length scales are formulated as the product of the normalized scales n_i and Δx_i. The instantaneous

velocity fluctuations are generated on a two–dimensional plane and the required information of the third dimension is defined by an integral time scale T defined as:

$$T(y) = \int_0^{t_{lim}} \frac{u'(x,y,z,t)\, u'\left(x,y,z,t+\hat{t}\right)}{u'(x,y,z,t)^2} d\hat{t} \quad \text{with:} \quad t_{lim} = 0.01. \quad (2)$$

Here $\hat{t}$ is a multiple of the recorded time step Δt of the input data source (experiment or simulation). Moreover, the cross–correlations between all three velocity components and thus the representation of a realistic inflow behavior is guaranteed due the application of the method by Lund et al. [6]. The resulting velocity fluctuations are superimposed on mean reference velocity data provided by experiments or numerical simulations.

In general, the inlet region of such configurations often provides only a grid resolution which leads to a strong damping of small flow structures. In this case, a dampened flow field reaches the airfoil after a certain development length. To overcome this problem, the fluctuations are introduced by source terms in the momentum equation, which allows a shift of the artificial turbulence generation closer to the airfoil, where a higher resolution guarantees the correct development of the flow structures. The source terms are imposed in an area which includes some grid nodes in the up– and downstream direction. The fluctuations are distributed according to a Gaussian distribution which depends on the distance from the middle of the source term area and the domain width itself. This width is defined by the integral time scale which is transformed to an integral length scale by the Taylor hypothesis.

Additional information on the modeled turbulent kinetic k_{mod} as an instantaneous Dirichlet boundary condition is required to apply the digital filter concept to the hybrid method. The issue of meaningful inflow profiles of k_{mod} based on a linear interpolation procedure is extensively discussed in Schmidt and Breuer [9].

4 Application and Results

The flow around a SD7003 airfoil [10] is performed at a Reynolds number of Re = 60,000 based on the chord length c and the free–stream velocity U_∞ and an angle of attack $\alpha = 4°$ is applied. Note that the angle of attack was considered during the generation of the mesh. The nose of the airfoil is located at the origin of a C–grid with a radius of $r/c = 7$. The wake regime is defined by the length $l/c = 4$ and the extension in the spanwise direction is prescribed with $z/c = 0.25$. A constant inflow profile $U/U_\infty = 1$ is employed at the curved inlet and the instantaneous velocity fluctuations provided by the STIG are introduced within the domain as source term at $x/c = -0.5$ as motivated before. At the outlet a convective boundary condition is applied. At the lateral edges symmetry boundary conditions and in spanwise direction periodic boundary conditions are used. A no–slip boundary condition is employed at the surface of the airfoil. In order to evaluate the performance of the hybrid simulation,

a reference LES prediction based on the dynamic SGS model of Germano/Lilly [5] was carried out to ensure the correct prediction of the transition phenomenon. The reference simulation denoted by WR–LES is performed on a fine grid with about 17.2 million CVs and the hybrid simulation on a coarse grid with about 5.8 million CVs. Both grids possess the same wall–normal resolution for the wall–nearest grid points $y_{1st}/c = 5 \times 10^{-4}$. The normalized time step $\Delta t U_c/c = 2 \times 10^{-4}$ is used for all simulations. Despite the different grids the vertical size of the STIG–plane at $x/c = -0.5$ is comparable covering the entire flow domain which impinges on the airfoil.

In the case of external flows with free–stream conditions, the integral scales and the reference velocity fluctuations depend on the turbulence intensity. In the present case the mean velocity fluctuations are based on the turbulence intensity Tu = 0.28% measured by Hain et al. [2]. With the help of a measurement of an instantaneous velocity signal in streamwise direction of the test facility (see Fig. 1), the required integral time scale T is determined using Eq. (2) (see Fig. 2).

Based on these velocity fluctuations of the experiment the resulting normalized integral time scales is $T = 0.118$. The two missing integral length scales are calculated based on the assumptions of an isotropic flow. Using the Taylor hypothesis and the free–stream velocity the normalized integral time scale is transformed to a corresponding normalized integral length scale leading to $L_y = L_z = 0.118$.

Figure 3 shows the distributions of the mean streamwise velocity U/U_∞, the total (sum of the resolved and the modeled part) turbulent kinetic energy k_{tot}/U_∞^2 and the total Reynolds shear stresses $\overline{u'v'}_{tot}/U_\infty^2$ of the WR–LES and the hybrid method. The strong impact of the application of the STIG is directly visible in the upper part of Fig. 3, where the dotted lines depict the corresponding predictions without considering an inflow turbulence intensity. An enhanced level of agreement between the experiment and the results of the simulations applying the STIG is seen compared to the predictions with a constant free–stream velocity. This increased level of turbulence leads to an increased momentum exchange. That results in a delayed

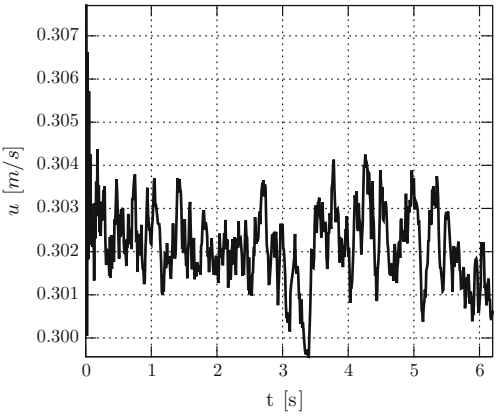

Fig. 1 Instantaneous fream–stream velocity signal of the inflow with Tu = 0.28% [2]

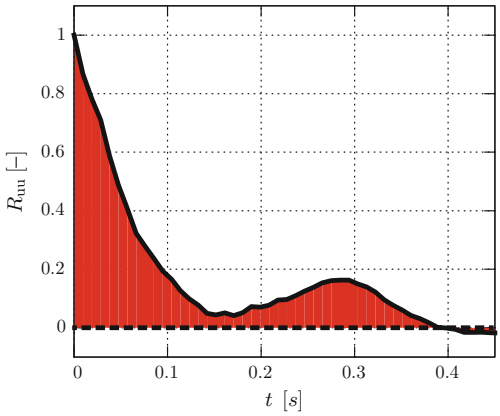

Fig. 2 Auto–correlation of the instantaneous velocity signal

separation and further downstream to an earlier transition onset and subsequently earlier reattachment point. Compared with the experimental findings, the hybrid simulation delivers a slightly better estimation of U/U_∞ than the WR–LES within the laminar separation bubble ($x/c \approx 0.3$–0.55). However, further downstream both simulations predict equivalent velocity distributions for the attached flow field.

The analysis of the second–order moments concentrates on the turbulent flow regime after the transition onset at $x/c \leq 0.45$. In contrast to the WR–LES, the profiles of the hybrid method match the distributions k_{tot}/U_∞^2 as well as $\overline{u'v'}_{tot}/U_\infty^2$ at $x/c = 0.5$ of the experiment very well. The behavior of the WR–LES indicates that the predicted transition onset is slightly delayed. Based on the determination of the transition onset by the shape factor, the predicted transition onset of the WR–LES is $x_{tra,WR-LES}/c = 0.50$, whereas the transition onset of the experiment is $x_{tra,Exp}/c = 0.46$ confirming this observation. As indicated by the smaller discrepancies between the results of the hybrid simulation and the experiment, the transition onset predicted by the hybrid simulation ($x_{tra,Hyb}/c = 0.45$) delivers the expected minor deviation compared to $x_{tra,Exp}/c$. However, further downstream at $x/c > 0.6$ the level of agreement between the experiment and both simulations is high and the influence of the delayed transition onset of the WR–LES is not notable anymore. Furthermore, similar to the observation made for the mean velocity field after the reattachment point the distributions of the second–order moments predicted by the hybrid simulation and the WR–LES are nearly equal.

5 Conclusions

In order to enable reasonable and accurate simulations of the flow past a SD7003 airfoil, realistic velocity fluctuations mimicking the oncoming turbulence are introduced within the simulation by a STIG applied as source terms. The expected behav-

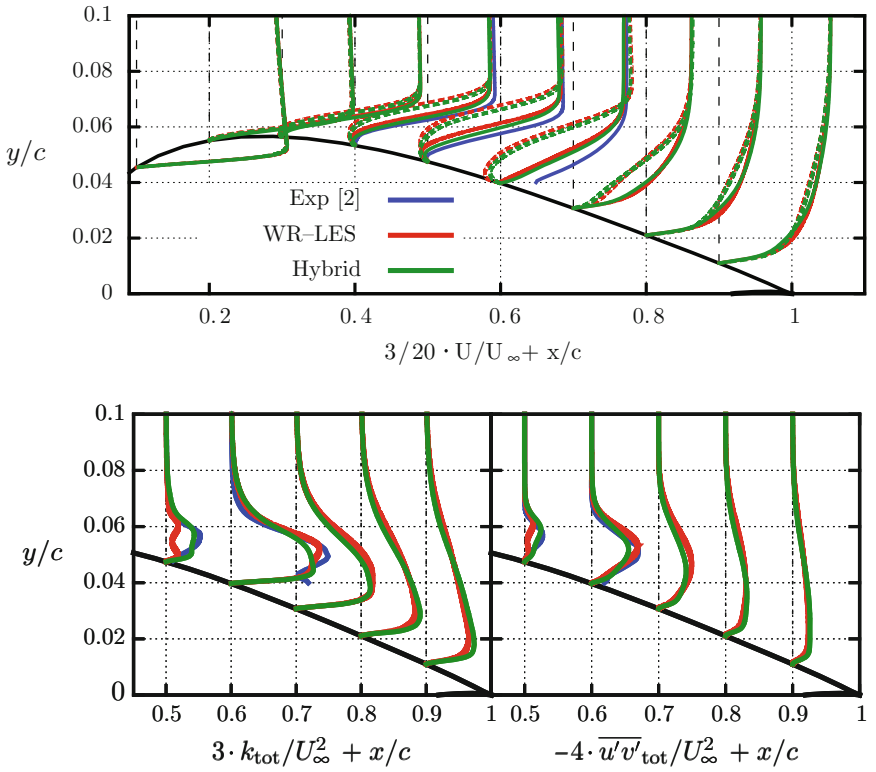

Fig. 3 Time–averaged results of the SD7003 airfoil at Re = 60,000 and $\alpha = 4°$. Distributions of U/U_∞ (*upper*), k_{tot}/U_∞^2 (*lower left*) and $\overline{u'v'}_{tot}/U_\infty^2$ (*lower right*). *Dotted lines* are the results of the simulations without turbulence intensity

ior of a smaller laminar separation bubble due to an increased momentum exchange imposed by the inflow turbulence is observed for the predictions based on the WR–LES and the hybrid method. A detailed evaluation of the flow results shows that the hybrid method applying the STIG delivers a high level of agreement with the experiments. Thus, both objectives were achieved:

(i) To prove the influence of the inflow turbulence level on the size of the laminar separation bubble and
(ii) To successfully marry the STIG and the hybrid LES–URANS method.

References

1. Fröhlich, J., von Terzi, D.: Hybrid LES/RANS methods for the simulation of turbulent flows. Prog. Aerosp. Sci. **44**, 349–377 (2008)
2. Hain, R., Kähler, C.J., Radespiel, R.: Dynamics of laminar separation bubbles at low-Reynolds number aerofoils. J. Fluid Mech. **630**, 129–153 (2009)
3. Jaffrézic, B., Breuer, M.: Application of an explicit algebraic Reynolds stress model within a hybrid LES–RANS method. J. Flow, Turb. Combus. **81**, 415–448 (2008)
4. Klein, M., Sadiki, A., Janicka, J.: A digital filter based generation of inflow data for spatially-developing direct numerical or large-eddy simulations. J. Comput. Phys. **186**, 652–665 (2003)
5. Lilly, D.K.: A Proposed modification of the Germano subgrid scale closure model. Phys. Fluids A **4**(3), 633–635 (1992)
6. Lund, T., Wu, X., Squires, D.: Generation of turbulent inflow data for spatially-developing boundary layer simulations. J. Comp. Phys. **140**, 233–258 (1998)
7. Schmidt, S., Breuer, M.: Hybrid LES-URANS methodology for the prediction of non-equilibrium wall-bounded internal and external flows. Comput. Fluids **96**, 226–252 (2014)
8. Schmidt, S., Breuer, M.: Hybrid LES–URANS methodology for wall–bounded flows, ERCOF-TAC Series, Direct and Large-Eddy Simulation IX, 9th International ERCOFTAC Workshop on Direct and Large–Eddy Simulation: DLES-9, Dresden, Germany, April 3–5, (2013)
9. Schmidt, S., Breuer, M.: Extended synthethic turbulence inflow generator within a hybrid LES–URANS methodology for the prediction of non–equilibrium wall–bounded flows. J. Flow, Turb. Combus. **95**, 669–707 (2015)
10. Selig, M. and Guglielmo, J. and Broeren, A., Giguére.: Summary of low–speed airfoil data, vol. 1, SoarTech Publications, Virginia Beach, Virginia USA, (1995)
11. Tabor, G.R., Bab-Ahmadi, M.H.: Inlet conditions for large-eddy simulation: A review. Comput. Fluids **39**, 553–567 (2010)
12. Wallin, S., Johansson, A.V.: An explicit algebraic Reynolds stress model for incompressible and compressible turbulent flows. J. Fluid Mech. **403**, 89–132 (2000)

Reliability of Wall Shear Stress Estimations in Front of a Wall-Mounted Cylinder

Wolfgang Schanderl and Michael Manhart

1 Introduction

We investigate the flow around a circular cylinder mounted on a flat plate which has attracted attention due to a number of effects. Our focus is on modeling erosion rates during scour evolution around a cylindrical bridge pier in a river bed. Current models of sediment erosion rates use the average wall shear stress acting on sediment grains. We aim at understanding how instantaneous shear stress fluctuations affect the erosion rates, how they can be used in erosion rate modeling and how instantaneous and average wall shear stresses scale with Reynolds number. To do so, the wall shear stresses around a wall-mounted cylinder have to be estimated first.

The shear stress exerted by a moving fluid on a wall can be calculated by:

$$\tau_w = \mu \frac{du}{dz}|_{z=0} \tag{1}$$

Since velocity gradients directly at the wall can hardly be measured, they are commonly deduced from velocity measurements in the near wall region at, e.g., z_0 by assuming a constant velocity gradient:

$$\tau_w = \mu \frac{u(z_0)}{z_0} \tag{2}$$

If the velocity probe is located in the viscous sublayer, where the velocity profile is linear, this approximation is accurate [7]. Nevertheless, in absence of sufficient computational resources it was not possible for a long time to resolve this viscous sublayer by numerical simulations for a wide range of flow situations at medium or high Reynolds numbers. Therefore wall shear stresses had to be modeled or Eq. (2) had to be applied beyond its range of validity.

W. Schanderl (✉) · M. Manhart
Chair of Hydromechanics, Arcisstr. 21, 80333 München, Germany
e-mail: wolfgang.schanderl@tum.de

M. Manhart
e-mail: michael.manhart@tum.de

D.G.E. Grigoriadis et al. (eds.), *Direct and Large-Eddy Simulation X*,
ERCOFTAC Series 24, https://doi.org/10.1007/978-3-319-63212-4_8

We performed a highly resolved Large Eddy Simulation LES of the flow around a wall-mounted cylinder applying a fully developed turbulent boundary layer as inflow condition with a Reynolds number $Re_D = 39,000$ based on the bulk velocity u_b and the diameter of the cylinder D. We designed a grid fine enough to estimate the wall shear stresses without applying a wall model. In this study, we compare simulated wall shear stresses to experimental results provided by literature [1].

2 Computational Setup

The LES was performed using our in-house code MGLET, which is a Cartesian finite volume code [4, 6]. It provides second order central approximations and a third order Runge-Kutta time integration as well as an algorithm for grid refinement with locally embedded grids [4]. The cylinder was represented by a second order Immersed Boundary Method [6]. The WALE model [5] is applied to model the subgrid scales.

Being aware of the strong influence of the inflow profile on the flow pattern around the cylinder [8], we applied a precursor grid to simulate a fully developed turbulent open-channel flow at a water depth of $\delta = 1.5D$ as inflow condition. To provide comparability to experimental results the sidewalls are defined as no-slip boundary conditions. Since the top wall holds a slip condition, the oncoming flow corresponds to an open-channel flow with low Froude number.

In the region of interest around the cylinder, the grid was successively refined by locally embedded grids [4] until the differences in the flow between to adjacent refinement levels were small and the flow topology did not change anymore. In total, three steps of refinement had to be performed, each reducing the grid spacing by a factor of two. Table 1 shows the resulting grid resolution around the cylinder for the corresponding level of refinement. The finest grid (grid 3) provides a grid spacing of $\Delta z^+ = 1.9$ and $\Delta x^+ = \Delta y^+ = 7.5$ in wall-normal and parallel directions, where the wall units are based on τ_0 of the undisturbed oncoming flow profile.

Table 1 The wall shear stress parameters of the applied grids

Referred to as	Level of refinement	$\Delta x/D = \Delta y/D$	$\Delta z/D$	z^+
Precursor	0	0.0305	0.008	15
Base grid	0	0.0305	0.008	15
Grid 1	1	0.0153	0.004	7.5
Grid 2	2	0.0076	0.002	3.7
Grid 3	3	0.0038	0.001	1.9

3 Flow Field

The precursor grid provides a fully developed turbulent open-channel flow as inflow boundary condition for the grid holding the cylinder. The time averaged velocity profile is shown in Fig. 1. To represent the velocity profile actually approaching the cylinder and exclude the influence of the sidewalls, the profile is averaged in spanwise direction over a width of $-1.25D < y < 1.25D$. Even though the velocity at the wall nearest grid point at about $z^+ = 7.5$ is slightly overestimated, the velocity profile follows the logarithmic law of the wall and shows a distinct wake region. The Reynolds stresses are in accordance to experimental values provided by literature [3].

The approaching fully developed turbulent boundary layer leads to a downflow in front of the cylinder, resulting in a complex turbulent flow pattern. This flow pattern contains a main vortex—see Fig. 2—rotating in clockwise direction around the spanwise axis and several secondary vortices. The main vortex leads to a backflow region

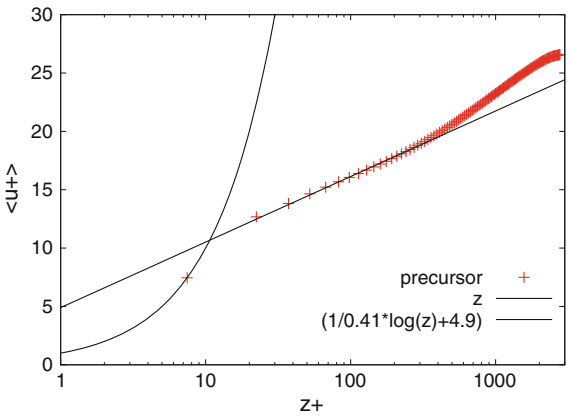

Fig. 1 Time averaged velocity profile in the precursor grid

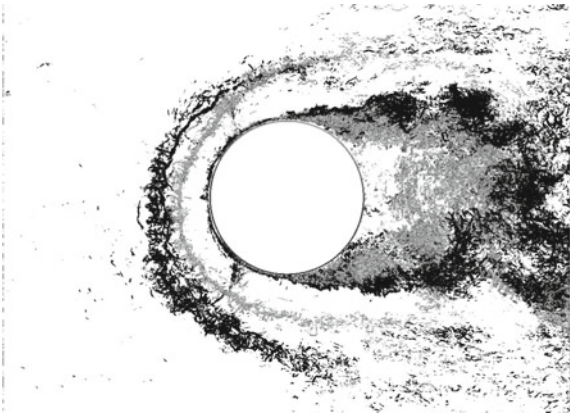

Fig. 2 Instantaneous visualization of the main vortex at two different time steps, indicated by isosurfaces of the second invariant of the velocity gradient tensor (Q-criterion) plotted for a value of Q =1,000. The two *different colours* indicate the different time steps

and a wall shear stress amplification in front of the cylinder. Due to the main flow, this vortex system wraps around the cylinder and forms the so-called horseshoe vortex system.

4 Validation of the Results

Figure 3 exemplifies the convergence of the wall shear stresses in the symmetry plane in front of the cylinder. Evaluated are values from simulations with different levels of grid refinement. While there are significant differences between the run with one level (grid 1) and the run with two levels of grid refinement (grid 2), the differences between grid 2 and grid 3 (three levels of refinement) are comparatively small. Further reducing of the grid spacing was omitted due to the enormous computational costs linked to such a refinement.

Due to these computational costs, a comparison of different SGS-models was omitted, too. Nevertheless, the grid is fine enough to guarantee the influence of the SGS-model to be small. This is demonstrated by the contribution of the SGS fluxes to the momentum balance (Fig. 4). Plotted are values in the region of the main horseshoe vortex. Compared to the resolved and viscous stresses $-\rho < u'w' >$ and $\mu \frac{\partial < u >}{\partial z}$ respectively, the modeled stresses $< \mu_t \frac{\partial u}{\partial z} >$ are small. Therefore substituting the SGS-model would lead to minor changes only.

Figure 5 compares measured wall shear stresses [1] to those obtained from our LES with three levels of grid refinement. Evaluated are profiles obtained by Eq. (2) using velocity probes at different wall distances z_0. The center of the cylinder is placed at $(x, y) = (0, 0)$; negative values indicate backflow.

The distributions in Fig. 5 can be split in three regions: In region (i) at $-0.8 < x/D$ one can identify the footprint of a strong clockwise rotating vortex; in region (ii) at $x/D < -0.8$ the simulation shows a second clockwise rotating vortex; region (iii) at

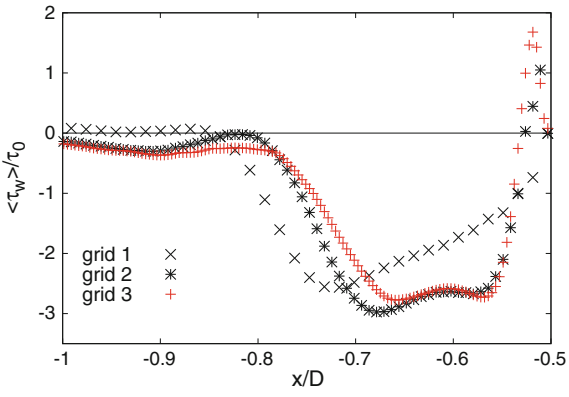

Fig. 3 Wall shear stress distribution in the symmetry plane in front of the cylinder for different levels of refinement, normalized with the wall shear stress in the undisturbed oncoming flow τ_0

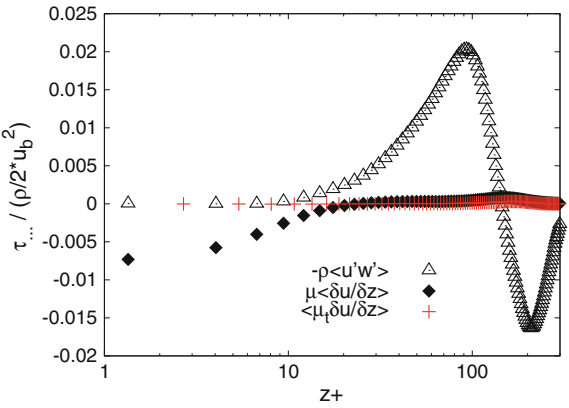

Fig. 4 Representative instants of the resolved ($-\rho < u'w' >$), the viscous ($\mu \frac{\partial < u >}{\partial z}$) and the modeled stresses ($< \mu_t \frac{\partial u}{\partial z} >$) in the symmetry plane in front of the cylinder at $x = -0.7D$

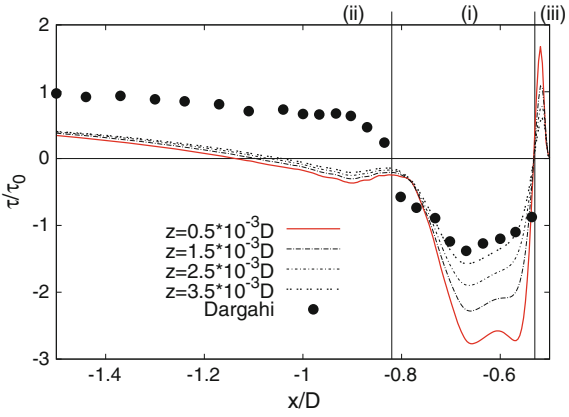

Fig. 5 Time averaged wall shear stress amplification in the symmetry plane in front of the cylinder. *Lines* represent values from the present study; *dots* mark experimental results by Dargahi [1]. The wall shear stresses are normalized by the undisturbed value in the oncoming boundary layer τ_0

$-0.55 < x/D$ represents a small anti-clockwise rotating vortex in the corner between cylinder and bottom wall. These three regions are also described by Devenport and Simpson [2], who conducted oil film visualization of the flow around a wall-mounted wing-shaped cylinder at $Re_D = 120,000$. They also observe no stagnation point between region (i) and (ii), but a minimum wall shear stress amplification only [2].

There are some major differences between our results and Dargahi's measurements [1] (Fig. 5). In region (ii), our results show a backflow region and indicate therefore the existence of a vortex. Dargahi's results do not. A reason for that discrepancy might be the measuring technique. Dargahi applied a pitot tube (Preston method) [1], which is strongly dependent on the flow direction and is hardly applicable when the instantaneous flow direction is strongly fluctuating.

Dargahi measured velocities for his wall shear stress estimation at a wall distance of $z = 3.3 \cdot 10^{-3} D$ [1]. In region (i), these values are in remarkably good accordance with presented wall shear stresses based on Eq. (2) and velocity probes at a height of

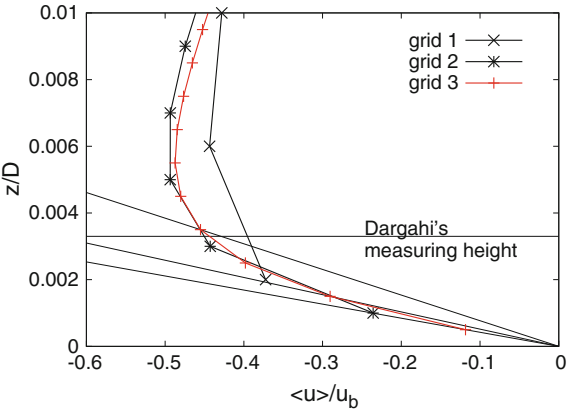

Fig. 6 Time averaged velocity profile in the symmetry plane in front of the cylinder at $x = -0.65D$. Plotted are values evaluated on different levels of grid refinement. Nevertheless, these values are all taken from the same simulation run

$z = 3.5 \cdot 10^{-3} D$. Width and shape of the peak in region (i) are matching well. The amplification factor shows a maximum difference of about 15%.

Evaluating the wall shear stress based on velocities closer to the wall results in an increase of the amplitude. In addition, the peak is slightly transformed into a double peak. Wall shear stresses measured by probes at the wall nearest grid point at $z = 0.5 \cdot 10^{-3} D$ are almost twice as large as the results evaluated at the measuring height Dargahi [1] used.

In order to elucidate the dependence of the estimated wall shear stress on the wall distance of the probe, we investigate profiles of the time averaged streamwise velocity at $x/D = -0.65$ in the symmetry plane in front of the cylinder. The wall nearest velocity probe of grid 3 in this position has a wall distance of $z = 0.5 \cdot 10^{-3} D$. This corresponds to $z^+ = 1.5$ wall units based on the local wall shear stress τ_w. Figure 6 implies, that the measuring height Dargahi [1] used is outside of the viscous sublayer. Therefore the assumption of a linear velocity distribution is not valid at this point. Assuming a constant gradient from this probe to the wall by applying Eq. (2) underestimates the velocity gradient at the wall by a factor of two - which is in accordance to Fig. 5.

5 Conclusion

We conducted a highly resolved LES of the flow around a wall-mounted cylinder. The solution converges with grid refinement and the influence of the SGS-model is small. Despite the discrepancy to Dargahi's measurements in region (ii), our results are in good agreement with experimental results [1, 2]. The velocity profiles indicate that at least the used grid resolution is necessary to estimate the wall shear stresses around a wall-mounted circular cylinder at $Re_D = 39{,}000$. Nevertheless, accurate

wall resolved measurements of the wall shear stresses in the described setup might be helpful to fully validate the presented results and to provide data in other regions around the cylinder.

References

1. Dargahi, B.: The turbulent flow field around a circular cylinder. Exp. Fluids **8**, 1–12 (1989)
2. Devenport, W.J., Simpson, R.L.: Time-dependent and time-averaged turbulence structure near the nose of a wing-body junction. J. Fluid Mech. **210**, 23–55 (1990)
3. Fernholz, H.H., Finley, P.J.: The incompressible zero-pressure-gradient turbulent boundary layer: An assessment of the data. Prog. Aerosp. Sci. **32**, 245–311 (1996)
4. Manhart, M.: A zonal grid algorithm for DNS of turbulent boundary layers. Comput. Fluids **33**, 435–461 (2004)
5. Nicoud, F., Ducros, F.: Subgrid-Scale Stress Modeling Based on the Square of the Velocity Gradient Tensor. Flow Turbul. Combust. **62**, 183–200 (1999)
6. Peller, N., Duc, A.Le, Tremblay, F., Manhart, M.: High-order stable interpolations for immersed boundary methods. Int. J. Numer. Meth Fluids **52**, 1175–1193 (2006)
7. Pope, S.B. : Turbulent Flows. Cambridge University Press (2011)
8. Schanderl, W., Manhart, M. : Large-eddy simulation of the flow around a wall-mounted circular cylinder. In: Proceedings of the 3rd IAHR Europe Congress Porto (2014)

Hydrodynamic - Acoustic Filtering of a Supersonic Under-Expanded Jet

C. Pérez Arroyo, G. Daviller, G. Puigt and C. Airiau

1 Introduction

The main noise that is perceived inside the cabin of an airplane originates in the turbofan engines and their associated exhaust jets. Due to flight conditions, a pressure difference appears at the exit of the secondary flow which engenders a series of expansion and compression waves known as shock-cells. A particular noise known as shock-cell noise is generated from the interaction of this semi-periodic system of shock-cells and the shear-layer of the jet. Shock-cell noise has a higher frequency and amplitude than the mixing noise of subsonic jets [15]. Shock-cell noise has the characteristic to radiate mainly in the upstream directions which impacts a larger area of the airplane fuselage increasing the noise for the passengers and cabin crew.

In this paper, the shock-cell noise generated by an axisymmetric under-expanded single jet is investigated using Large-Eddy Simulations (LES). The paper addresses in a first term, the code characteristics and simulation setup and procedure. The second part of the paper focuses on the application of acoustic-hydrodynamic filtering and its impact on the cross-correlation in the near-field.

C. Pérez Arroyo (✉) · G. Puigt
Centre Européen de Recherche et de Formation Avancée en Calcul Scientifique,
42 Avenue Gaspard Coriolis, 31057 Toulouse Cedex 01, France
e-mail: cparroyo@cerfacs.fr

G. Puigt
e-mail: guillaume.puigt@cerfacs.fr

G. Daviller · C. Airiau
Institut de Mcanique des Fluides de Toulouse, UMR 5502 CNRS/INPT-UPS,
Alle du Professeur Camille Soula, 31400 Toulouse, France
e-mail: guillaume.daviller@imft.fr

C. Airiau
e-mail: christophe.airiau@imft.fr

D.G.E. Grigoriadis et al. (eds.), *Direct and Large-Eddy Simulation X*,
ERCOFTAC Series 24, https://doi.org/10.1007/978-3-319-63212-4_9

2 Numerical Formulation

The compressible Navier–Stokes equations are solved using the Finite Volume multi-block structured solver ***elsA*** [4]. The spatial scheme is a 6th order compact scheme [7] extended to Finite Volumes in [6]. The compact scheme is stabilized by a 6th order compact filter [18] that is used as implicit subgrid-scale model in the present simulations. A six-step 2rd order Runge-Kutta DRP optimized scheme [3] is used for the time integration.

3 Simulation Setup and Procedure

The case of study is a supersonic under-expanded jet at perfectly expanded Mach number $M_j = 1.15$ issued from a convergent nozzle with exit diameter $D = 38.0\,\text{mm}$ and a nozzle lip thickness $t = 0.125D$. The Reynolds number based on the exit diameter is $Re = 1.2 \times 10^6$. More information about the working conditions can be found in [1].

The initial conditions for the LES are obtained with a RANS simulation using the Spalart-Allmaras turbulence model [13]. The RANS computation fully resolves the wall inside and outside the nozzle with $y^+ < 1$. In order to avoid mesh constraints, the inner part of the nozzle is removed for the LES and the RANS conservative variables are imposed at the nozzle exit plane as in [9–12, 14, 19].

The computational domain used for the LES simulation extends $40D$ in the axial direction and $7D$ in the radial direction. The mesh has 75×10^6 cells with $(1052 \times 270 \times 256)$ cells in the axial, radial and azimuthal directions respectively. The maximum expansion ratio between adjacent cells achieved in the mesh has been kept below 4% to avoid the generation of spurious noise from the numerical schemes.

The boundary conditions need to take into account that low-disspersive and low-dissipative numerical schemes are used in a aeroacoustic simulation. For this reason, non-reflective boundary conditions [2, 16] are used in the exterior inlet as well as in the lateral boundaries to avoid any reflections of the acoustic waves. In a similar fashion, the passage of the vortices through the outlet boundary are taken into account with a characteristic formulation [8]. Furthermore, sponge layers are defined around the domain to attenuate the exiting vorticity waves. Because the interior of the nozzle is not computed, no inflow forcing is applied at the exit of the nozzle to avoid parasite noise.

The simulation is run for 120 non-dimensional times ($\hat{t} = tD/C_\infty$) in order to reach statistically independent results.

4 Hydrodynamic - Acoustic Filtering

The acoustic component of a jet can be filtered from the hydrodynamic one in the near-field, where the mean velocity is zero using the methodology shown by Tinney and Jordan [17]. The original pressure signal $p(x_p, t)$ is transformed into the wavelength - frequency domain by

$$p(k_x, \omega) = \int \int p(x_p, t) W(x_p) e^{-j(k_x x_p + \omega t)} dx_p dt, \tag{1}$$

where the reference coordinate x_p is such that it is located outside the jet verifying a null mean velocity throughout the new coordinate. $W(x_p)$ is a weight function used to smooth the signal at the ends of the axis. An acoustic fluctuation generated by a noise source inside the jet will be propagated outside the jet at the ambient sound speed c_∞. However, the acoustic perturbation will be propagated at a supersonic speed $c_x^2 = c_\infty(2df + c_\infty)$ in the x_p coordinate system, where d is the perpendicular distance from the axis to the noise source and f is its frequency. The subsonic and supersonic components, i.e. the hydrodynamic and acoustic components can be recovered from the transformed signal obtained by Eq. 1 using only the ranges $p(k_x > \omega, \omega < k_x c_\infty)$ and $p(k_x < \omega, \omega > k_x c_\infty)$ respectively as:

$$p_{sub}(x_p, t) = \int p(k_x > \omega, \omega < k_x c_\infty) e^{-j(k_x x_p + \omega t)} dk_x d\omega, \tag{2}$$

$$p_{super}(x_p, t) = \int p(k_x < \omega, \omega > k_x c_\infty) e^{-j(k_x x_p + \omega t)} dk_x d\omega. \tag{3}$$

The filtering has been applied to the supersonic under-expanded jet near-field over several lines in order to obtain a two-dimensional field of the pressure perturbation. Figure 1 shows the original pressure perturbations of a snapshot where the jet is represented by the axial velocity. It can be compared with the filtered hydrodynamic and acoustic components in Fig. 1b and c respectively. The filtering allows the hydrodynamic component to be clearly visible and the acoustic component to gain in detail specially near the jet, where the hydrodynamic perturbations are more intense.

The importance of the hydrodynamic-acoustic filtering is further noted when spatio-temporal cross-correlations of the filtered pressure are carried out in the near-field. Figure 2a, b and c show the cross-correlation between one point located at $[x/D = 0, y/D = 3]$ and an array located at $y/D = 1$ with an inclination of 5°, following the expansion of the shear layer.

The shock-cell noise is found around $x/D = 4$ with a cross-correlation of 0.38. When the filtering is applied, the cross-correlation peak increases up to 0.41 and it becomes clearer downstream of the end of the potential core ($x/D > 9$). The filtering improves the cross-correlation specially downstream where the hydrodynamic components have the same general direction as the acoustic waves. Figures 3a, b and c now focus the cross-correlation on the point located at $[x/D = 15, y/D = 3]$ and the

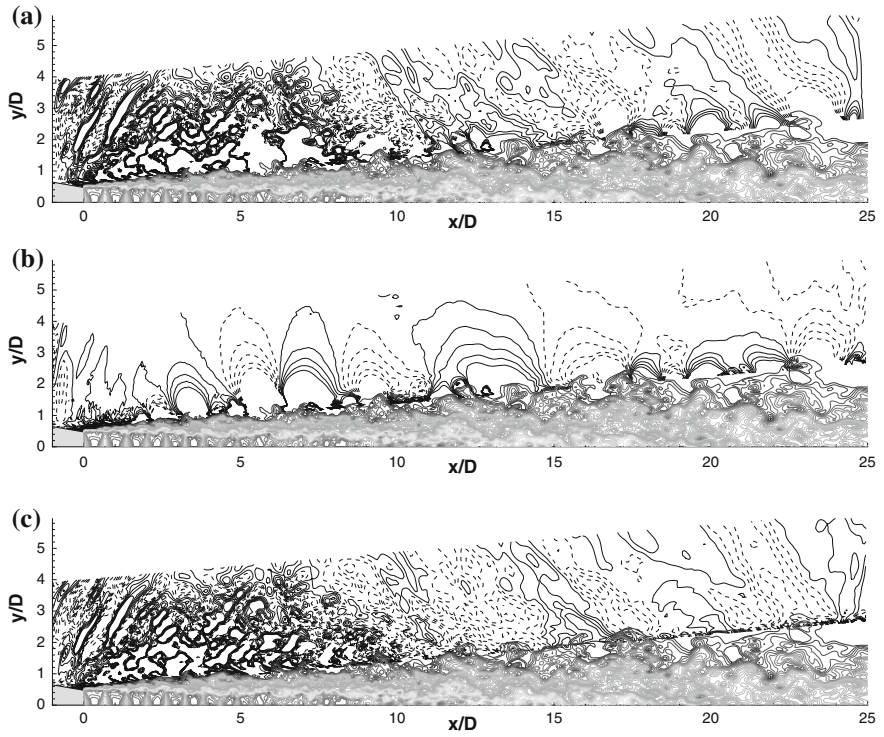

Fig. 1 **a** Pressure perturbations of the original flow, $-150\,\text{Pa} < p \leq 150\,\text{Pa}$. **b** Pressure perturbations of the subsonic (hydrodynamic) component, $-150\,\text{Pa} < p \leq 150\,\text{Pa}$. **c** Pressure perturbations of the supersonic (acoustic) component, $-150\,\text{Pa} < p \leq 150\,\text{Pa}$

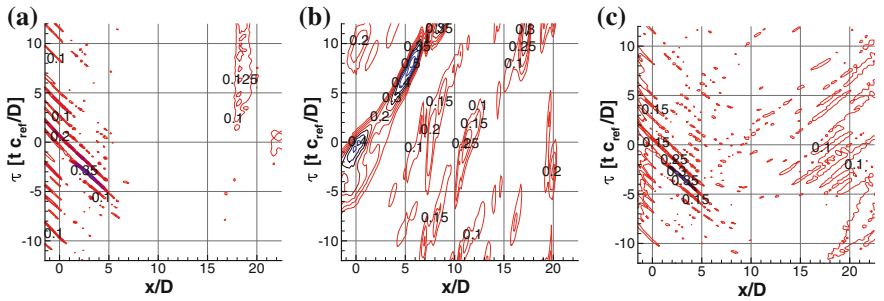

Fig. 2 **a** Spatio-temporal pressure cross-correlation of the complete original signal at $x/D = 0.0$. **b** Spatio-temporal pressure cross-correlation of the hydrodynamic component at $x/D = 0.0$. **c** Spatio-temporal pressure cross-correlation of the acoustic component at $x/D = 0.0$

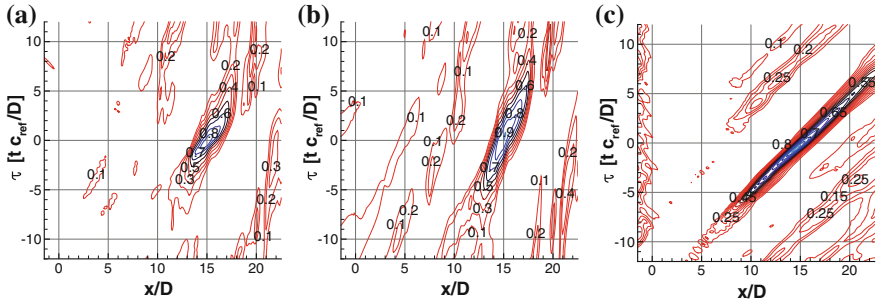

Fig. 3 **a** Spatio-temporal pressure cross-correlation of the complete original signal at $x/D = 15.0$. **b** Spatio-temporal pressure cross-correlation of the hydrodynamic component at $x/D = 15.0$. **c** Spatio-temporal pressure cross-correlation of the acoustic component at $x/D = 15.0$

above-mentioned array. At this position, the original cross-correlation shown in Fig. 3 differs completely from the acoustic component shown in Fig. 3c. The original signal is clearly dominated by the hydrodynamic component shown in Fig. 3b adopting the same shape. The mixing noise of the large turbulent structures is mostly generated at the end of the potential core and radiated at 30° [15]. The cross-correlation of the acoustic component agrees with the theory showing a high correlation up to this location, with a convective velocity at the speed of sound.

5 Conclusions

The hydrodynamic - acoustic filtering of the near-field of a supersonic under-expanded axisymmetric jet has been carried out. Post-processing techniques such as spatio-temporal cross-correlations are affected by the filtering achieving different conclusions depending on whether or not the filtering is used. The shock-cell noise and the mixing noise of the large turbulent structures have been identified in Figs. 2c and 3c respectively. This approach looks very promising to study in depth the shock-cell noise mechanism.

Acknowledgements This research project has been supported by a Marie Curie Initial Training Networks (ITN) AeroTraNet 2 of the European Community Seventh Framework Programme (FP7) under contract number PITN-GA-2012-317142 that aims to generate a ready to use model for shock-cell noise characterization. This work was performed using HPC resources from GENCI-[CCRT/CINES/IDRIS] (Grant 2015-[x20152a6074]).

References

1. André, B.: Etude expérimentale de l'effet du vol sur le bruit de choc de jets supersoniques sous-détendus. (2012)
2. Bogey, C., Bailly, C.: Three-dimensional non-reflective boundary conditions for acoustic simulations: far field formulation and validation test cases. Acta Acust. **88**, 463–471 (2002)
3. Bogey, C., Bailly, C.: A family of low dispersive and low dissipative explicit schemes for flow and noise computations. J. Comput. Phys. **194**, 194–214 (2004)
4. Cambier, L., Heib, S., Plot, S.: The Onera elsA CFD software: input from research and feedback from industry. Mech. Ind. **14**, 159–174 (2013)
5. Farassat, F., Succi, G. P.: The prediction of helicopter rotor discrete frequency noise. American Helicopter Society, Annual Forum, 38th, Anaheim, CA, May 4–7, Proceedings.(A82-40505 20-01) Washington, DC, vol.1, 497–507 (1982)
6. Fosso-Pouangué, A., Deniau, H., Sicot, F., Sagaut, P.: Curvilinear finite volume schemes using high order compact interpolation. J. Comput. Phys. **229**, 5090–5122 (2010)
7. Lele, S.: Compact finite difference schemes with spectral-like resolution. J. Comput. Phys. **103**, 16–42 (1992)
8. Poinsot, T.J., Lele, S.K.: Boundary conditions for direct simulations of compressible viscous flows. J. Comput. Phys. **101**, 104–129 (1992)
9. Schaupp, C., Sesterhenn, J., Friedrich, R.: On a method for direct numerical simulation of shear layer/compression wave interaction for aeroacoustic investigations. Comput. Fluids **37**, 463–474 (2008)
10. Schulze, J., Sesterhenn, J., Schmid, P., Bogey, C., de Cacqueray, N., Berland, J., Bailly, C.: Numerical simulation of supersonic jet noise. Num. Sim. Turbul. Flows Noise Gener. **104**, 29–46 (2009)
11. Shur, M.; Spalart, P., Strelets, M.: Noise prediction for increasingly complex jets. Part I: methods and tests. Int. J. Aeroacoust. **4**, 213–246 (2005)
12. Shur, M.L., Spalart, P.R., Strelets, M.K., Garbaruk, A.V.: Further steps in LES-based noise prediction for complex jets. AIAAP 44th AIAA aerospace sciences meeting and exhibit, Reno, Nevada, AIAA Paper 2006–485, **485** (2006)
13. Spalart, P., Allmaras, S.: A one-equation turbulence model for aerodynamic flows. AIAA Paper 92–0439, 30th Aerospace Sciences Meeting and Exhibit, Reno, Nevada (1992)
14. Suzuki, T., Lele, S.K.: Shock leakage through an unsteady vortex-laden mixing layer: application to jet screech. J. Fluid Mech. **490**, 139–167 (2003)
15. Tam, C.K.: Supersonic jet noise. Annu. Rev. Fluid Mech. **27**, 17–43 (1995)
16. Tam, C., Dong, Z.: Radiation and outflow boundary conditions for direct computation of acoustic and flow disturbances in a nonuniform mean flow. J. Comput. Phys. **4**, 175–201 (1996)
17. Tinney, C., Jordan, P.: others: The near pressure field of co-axial subsonic jets. J. Fluid Mech. **611**, 175–204 (2008)
18. Visbal, M., Gaitonde, D.: On the use of higher-order finite-difference schemes on curvilinear and deforming meshes. J. Comput. Phys. **181**, 155–185 (2002)
19. Viswanathan, K.; Shur, M.; Strelets, M., Spalart, P. R.: Numerical Prediction of Noise from Round and Beveled Nozzles. Turbulent Flow and Noise Generation, EUROMECH Colloquium Marseille, France, **467** (2005)

Large Eddy Simulation of an Asymmetric Jet in Crossflow

M. Folkersma and J. Bodart

1 Introduction

On turbine blades, film cooling is an efficient way to prevent temperature to reach the blade material melting point, downstream the combustion chamber. Protection against continuous feeding of incoming hot gases is achieved by injecting coolant at the blade surface. To study turbulent mixing occurring in the jet vicinity we focus our attention on a jet in crossflow configuration. This class of problems has been extensively studied, both experimentally and numerically and for a more complete review, the reader is referred to the work of [6]. In this study, we perform a high fidelity, large eddy simulation of an inclined jet in crossflow with compound angle. A reference experiment by [9] provides three dimensional measurements of velocity and concentration using MRV/MRC techniques [1, 5]. The computational domain includes all the geometric complexities, such as the inclination and a skew angle for the pipe inflow. Notably, the simulated pipe has a finite length and includes the junction with a plenum. The flow is thus not fully developed in the pipe, similarly to industrial systems with strong design constraints. An exhaustive validation step is proposed and because no turbulent quantities can be measured with MRV/MRC, the present results nicely complete the experimental database by providing the missing quantities. In the simulation, the major part of the turbulent scales are resolved, as attested by the negligible contribution of the subgrid-scale model which is measured *a posteriori*.

M. Folkersma · J. Bodart (✉)
Dépt. Aérodynamique Energétique et Propulsion, ISAE-SUPAERO,
Université de Toulouse, Toulouse, France
e-mail: julien.bodart@isae.fr

M. Folkersma
e-mail: mikko.folkersma@isae.fr

D.G.E. Grigoriadis et al. (eds.), *Direct and Large-Eddy Simulation X*,
ERCOFTAC Series 24, https://doi.org/10.1007/978-3-319-63212-4_10

2 Simulation Details

The configuration is characterized by a 30 degrees inclination of the jet as well as a 30 degrees skew angle leading to a fully asymmetric setup as represented in Fig. 1. Dimensionless parameters are summarized in Table 1. As previously discussed in [2], we use a unity Schmidt number to keep the Batchelor and Kolmogorov scales of the same order and minimize the effect of the subgrid scale model. Regarding the low Reynolds number of the experiment, it is doubled in the present simulation in order to allow a more comparable turbulence development. Note that the simulation uses a synthetic turbulence generation technique while the transition from laminar to turbulent state is triggered in the experiments.

We use Charles^X, a compressible solver originally developed at the Center for Turbulence Research and now co-developed in our group. In addition to the Navier Stokes equations, a passive scalar equation is solved. The computational mesh contains overall 101 million cells which are all of hexahedral type for increased accuracy. The total number of cells is divided as follows: 82, 17 and 2 million cells for

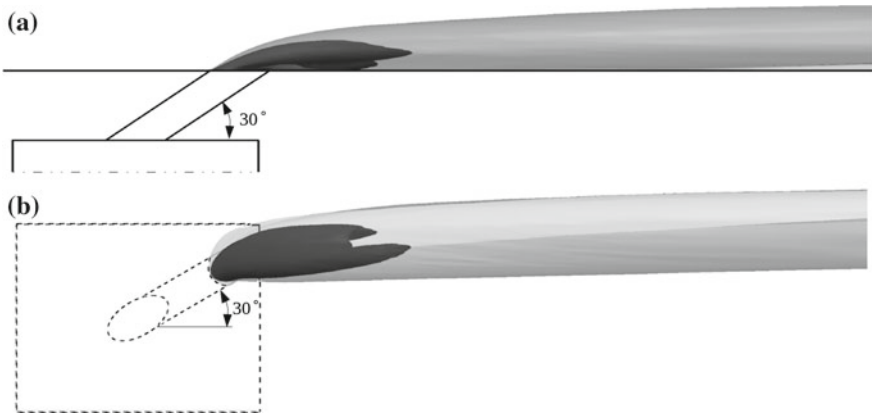

Fig. 1 Flow configuration with isocontours of mean passive scalar. (*Grey*) $\overline{C} = 0.1$ and (*black*) $\overline{C} = 0.5$. (*above*) side view, (*below*) top view

Table 1 Non-dimensional parameters of present simulation and experiments by [9]. Subscript $_j$ is jet bulk quantity inside nozzle and $_\infty$ is crossflow freestream quantity. D is jet nozzle diameter, δ_{99} is 99% thickness of boundary layer and $\mathcal{D}$ is passive scalar diffusivity

		LES	EXP
Velocity ratio (r)	U_j/U_∞	1	1
Momentum ratio (J)	$\rho_j U_j^2/\rho_\infty U_\infty^2$	1	1
Jet Reynolds number (Re_j)	$U_j D/\nu$	5800	2900
Boyndary-layer thickness	δ_{99}/D	1	1
Schmidt number(Sc)	$\nu/\mathcal{D}$	1	1500

Table 2 Characteristic cell size in various regions and first cell size in wall units

Region	$\Delta x/D$	$\Delta y/D$	$\Delta z/D$	Average			Maximum		
				$\Delta x+$	$\Delta y+$	$\Delta z+$	$\Delta x+$	$\Delta y+$	$\Delta z+$
Inflow	0.081	0.016	0.016	7.9	0.4	1.6	32.0	1.5	6.4
Jet hole	0.001	0.016	0.009	2.1	0.4	2.2	6.1	1.0	6.3
Interaction zone	0.016	0.016	0.016	3.2	0.8	3.2	6.3	1.5	6.4

respectively the channel, the cooling hole and the plenum. In the interaction region, we use about 60 cells per diameter D in every directions. The near wall turbulence structures are also well resolved as attested by the grid sizes given in Table 2. The approaching crossflow boundary layer characteristics have a significant effect to the interaction of the jet and the crossflow: a thicker incoming boundary layer means higher jet penetration [7] and higher turbulence level may enhance the mixing of the jet and the crossflow [3]. At the inlet a similar strategy as in [2] is adopted to generate a fully turbulent inflow. The main characteristic is the rather long incoming development length ($40D$) used to allow the crossflow boundary layer to develop from a synthetic to a fully physical state.

3 Results

Statistical sampling is performed after the steady state has been reached. Samples are extracted every 20 time steps and the simulation is carried for $t = 250D/U_{bulk}$. In the Fig. 2, we see the evolution of mean velocity and turbulence kinetic energy profiles in streamwise direction. Despite the absence of homogeneous directions in this configuration, a satisfactory level of statistical convergence is reached after 200 time units. Both incoming flows are compared with experiments. The channel developing boundary layer upstream the jet exit hole is compared with PIV data [4] at two locations. Figure 3 shows the mean velocity and Reynolds stress profile of the present simulation compared with experiments. Both profiles show an excellent agreement and demonstrate the validity of the synthetic turbulence generation method. Figure 4 shows the mean axial velocity at six different cut planes inside the cooling jet hole. The first cut plane (a) is at the plenum/hole interface while the last (f) is at the hole/channel interface. The very good level of agreement demonstrates the ability of the simulation to capture all the relevant features of the complex dynamic of the flow in the hole before the interaction with the crossflow, in particular the large recirculation occurring at the plenum exit.

The resulting contaminant concentration is compared at the region of jet and crossflow interaction. Figure 5 shows contours in two streamwise-normal and one wall-normal planes. The asymmetric shape of the classical counter rotating vortex

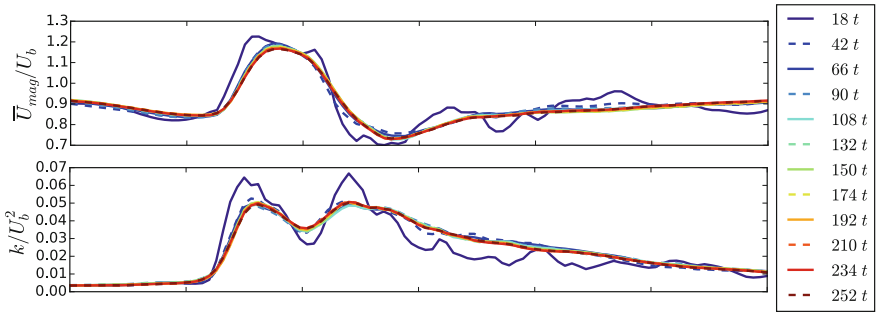

Fig. 2 Evolution of the mean velocity and turbulence kinetic energy profile in streamwise direction at $y = 0.6D$, $z = -0.6D$

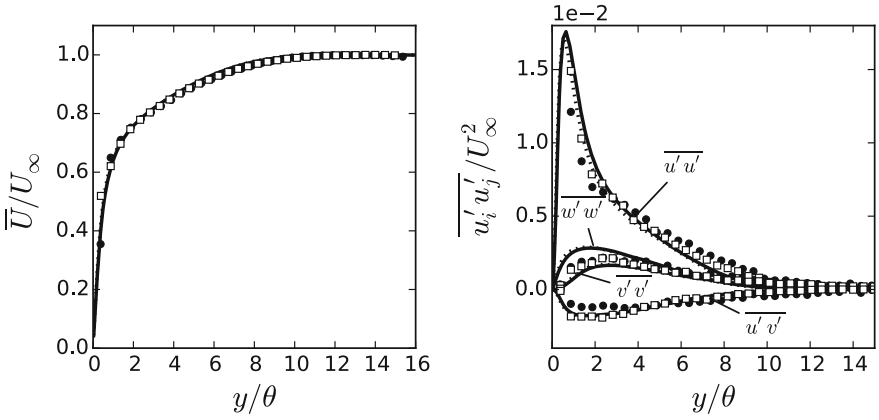

Fig. 3 Mean velocity and Reynolds stress profile at two locations upstream jet exit hole; lines: present simulation; markers: experiment by [4]; *solid line*, *circle* $x = -13.7D$; *dashed line*, *square* $x = -7.2D$

pair (CVP) is well seen on plane (b) and confirm the significant footprint of these structure on the overall mixing. It is readily seen that the right vortex is stronger, which is also highlighted by the longer leg of the contaminant concentration field in plane (c). The agreement is overall excellent and similar conclusions have been extracted from the velocity field (not shown here).

We finally propose a measure of the entrainment in the present simulation, which typically results from large scale mixing and engulfment of the crossflow fluid in the jet due to their interaction. A common way to evaluate this entrainment is to measure the volume flux flowing inside a surface delimited by a low value (i.e. $\overline{C} < 0.01$) of contaminant concentration. Results of the present configuration are compared in the Fig. 6, with the symmetric configuration studied by [2] and an axisymmetric jet. Contrary to the axisymmetric jet, the two jet in crossflow configurations are characterized by a higher entrainment at the jet exit which can be attributed to both

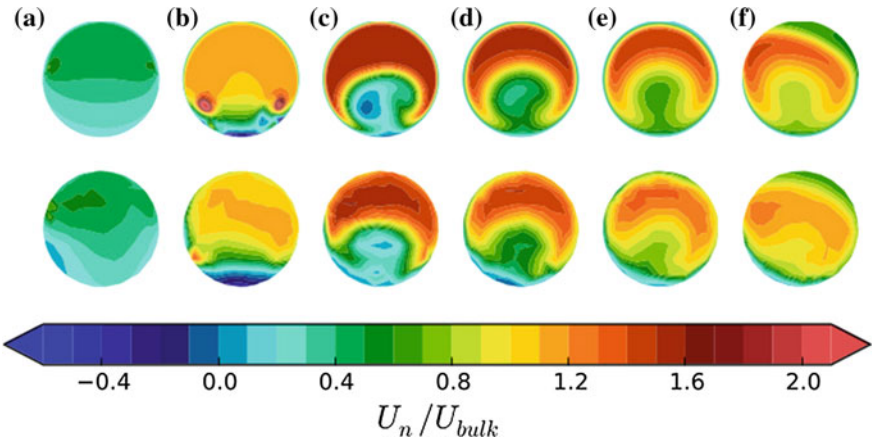

Fig. 4 Mean axial velocity inside the jet exit hole at six cut planes. (*above*) present simulation, (*below*) experiment by [9]

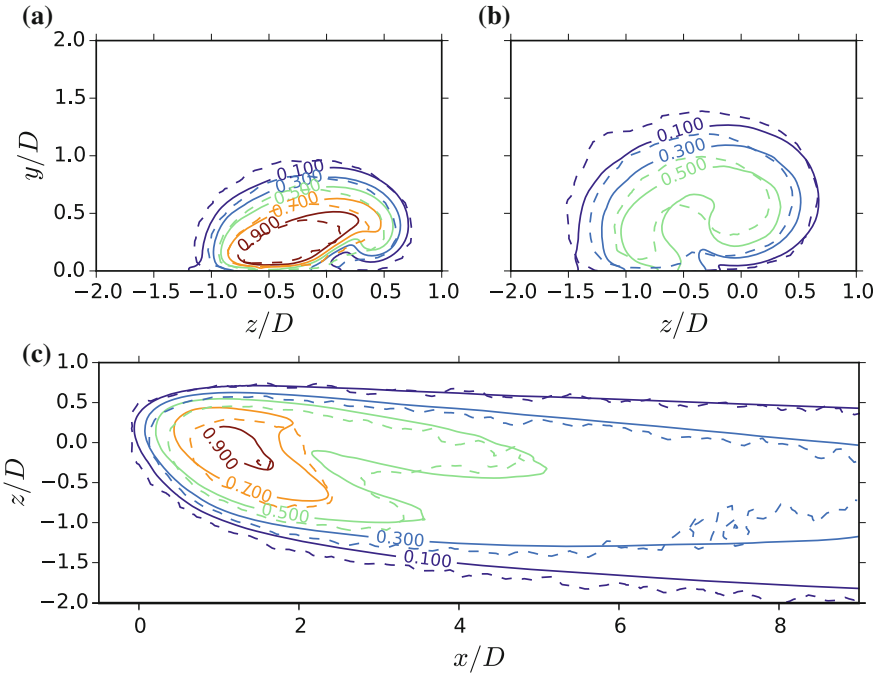

Fig. 5 Contaminant concentration; *solid* – present simulation; *dashed* – experiment by [9]; Plane **(a)** $x = D$ and **(b)** $x = 3D$ and **(c)** $y = 0.5D$

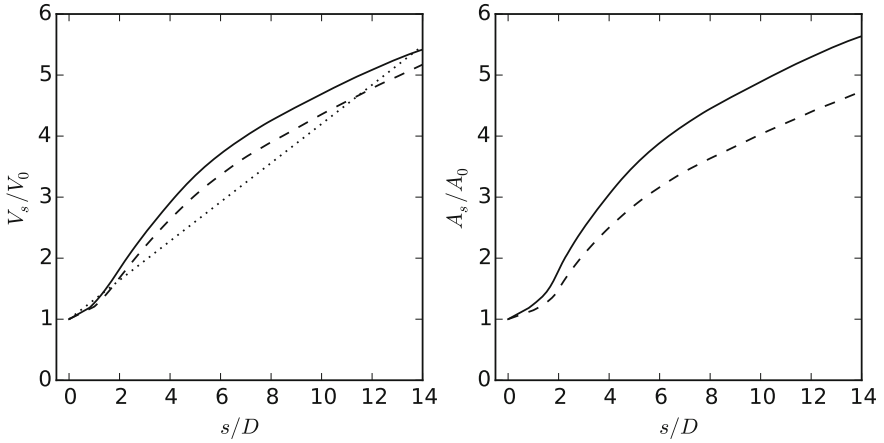

Fig. 6 Jet entrainment, with V the volume flux, and A the associated jet area along the jet: *solid* – present simulation; *dashed* – symmetric jet by [2]; *dotted* – Ricou-Spalding correlation for axisymmetric jet [8]

the counter rotating vortex pair that injects crossflow fluid in the jet but also to the intense shear layers created in the ejection zone. The highest entrainment is measured for the asymmetric jet, which is consistent with a larger interface region between the jet and the crossflow induced by the compound angle. The resulting efficiency of the shear layers to create jet entrainment may be increased. Additionally, the intensity of the CVP is much stronger in the case of the asymmetric jet, and should induce higher entrainment.

4 Conclusion

A large eddy simulation was carried to study turbulent mixing occurring in an asymmetric jet in crossflow. The chosen grid resolution shows negligible contribution of the subgrid scale model and a rather long integration time leads to a reasonable level of convergence. An excellent agreement is found with the tridimensional mean flow quantities provided by MRV/MRC techniques in the experiments carried by [9]. Preliminary analysis have been conducted to characterize the jet entrainment in this configuration. We show non negligible effect of the compound angle, which is attributed to the difference in strength of the counter rotating vortex pair.

Acknowledgements Authors are grateful for the computational resources that were provided by (i) CNRS on the BlueGene/Q system Turing, through the GENCI-IDRIS grants x20142a7178 and x20152a7178 and (ii) CALMIP on the Eos system through the p1425 allocation.

References

1. Benson, M.J., Elkins, C.J., Mobley, P.D., Alley, M.T., Eaton, J.K.: Three-dimensional concentration field measurements in a mixing layer using magnetic resonance imaging. Exp. Fluids **49**, 43–55 (2010)
2. Bodart, J., Coletti, F., Bermejo-Moreno, I., Eaton, J.K.: High-fidelity simulation of a turbulent inclined jet in a crossflow, pp. 263–275. Annual, Research Briefs (2013)
3. Bogard, D.G.: The Gas Turbine Handbook. chapter 4.2.2.1 Airfoil Film Cooling. National Energy Technology Laboratory, 2006
4. Coletti, F., Benson, M.J., Ling, J., Elkins, C.J., Eaton, J.K.: Turbulent transport in an inclined jet in crossflow. Int. J. Heat Fluid Flow **43**, 149–160 (2013)
5. Elkins, C.J., Markl, M., Pelc, N., Eaton, J.K.: 4D magnetic resonance velocimetry for mean velocity measurements in complex turbulent flows. Exp. Fluids **34**(4), 494–503 (2003)
6. Mahesh, K.: The interaction of jets with crossflow. Annu. Rev. Fluid Mech. **45**(1), 379–407 (2013)
7. Muppidi, S., Mahesh, K.: Two-dimensional model problem to explain counter-rotationg vortex pair formation in a transverse jet. Phys. of Fluids **18**(8), 2006
8. Ricou, F.P., Spalding, D.B.: Measurements of entrainment by axisymmetrical turbulent jets. J. Fluid Mech. **11**, 21–32 (1961)
9. Ryan, K., Bodart, J., Folkersma, M., Elkins, C.J., Eaton J.K.: Turbulent scalar mixing in a skewed jet in crossflow: experiments and modeling. In: TSFP9 conference, July 2015

LES in a Concentric Annular Pipe: Analysis of Mesh Sensitivity and Wall Pressure Fluctuations

S. Bhattacharjee, G. Ricciardi and S. Viazzo

1 Introduction

Annular pipe flows have varied application in the domains of nuclear reactors, heat exchangers, drilling operations in oil industry etc. The first part of the paper (Sect. 2) presents a comparison of large eddy simulations (LES) of turbulent flow in a concentric annular pipe for 5 different mesh resolutions. Results are compared with benchmark DNS data. The second part (Sect. 3) presents its interesting application of pipe flow in the nuclear field. Inside a pressurized water nuclear reactor (PWR) core, flow-induced vibrations due to spacer grids can cause damage to the structure. Understanding this behavior is a challenge. Here the effect of a 'simplified' circular spacer grid on the vortex induced vibrations of the pipe is investigated. LES was performed with the CFD code Trio_U [9] which uses a hybrid finite volume based finite element approach [1]. Simulations were carried out on the Airain and Curie supercomputers at the Computing Center for Research and Technology (CCRT), Bruyères-le-Châtel, France [2].

S. Bhattacharjee (✉) · G. Ricciardi
French Alternative Energies and Atomic Energy Commission (CEA)-Cadarache Center, DEN/DTN/STCP/LHC, 13108 St Paul lez Durance Cedex, France
e-mail: saptarshi.bhattacharjee@outlook.com

G. Ricciardi
e-mail: guillaume.ricciardi@cea.fr

S. Bhattacharjee · S. Viazzo
Laboratoire de Mécanique, Modélisation et Procédés, Propres (M2P2), UMR7340 CNRS, Aix-Marseille Université, Centrale Marseille, 13451 Marseille Cedex, France
e-mail: stephane.viazzo@univ-amu.fr

D.G.E. Grigoriadis et al. (eds.), *Direct and Large-Eddy Simulation X*,
ERCOFTAC Series 24, https://doi.org/10.1007/978-3-319-63212-4_11

2 Mesh Sensitivity Analysis for LES in a Concentric Annular Pipe

The outer and inner diameters of the pipe were 60 mm and 30 mm respectively. The radius ratio, i.e., the ratio between the inner and outer radii was 0.5. Water flowed through the pipe in axial direction. A schematic diagram is shown in Fig. 1. The hydraulic diameter, defined as $HD = 4A_{flow}/P_{wet}$, was 0.03 m where A_{flow} is the surface area of duct cross-section and P_{wet} is the wetted perimeter. The bulk velocity was 0.298 m/s. Reynolds number based on the bulk velocity and hydraulic diameter was 8900. The length of the domain was 0.24 m, i.e., 8 times hydraulic diameter.

Fully structured tetrahedral meshes were generated with Gmsh [4] and Trio_U's internal meshing tool. The grid was more refined near the boundary in radial direction to study the near-wall behavior (Fig. 2). It was uniform in axial and azimuthal directions. Five different mesh resolutions were considered. Table 1 shows the number of grid points as well as the grid resolution in wall units in each direction for each simulation. Figure 3a–f illustrate the stretching of the tetrahedral elements relative to each other.

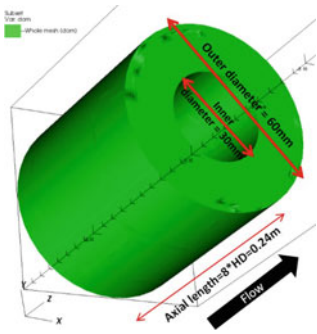

Fig. 1 Schematic diagram of the pipe

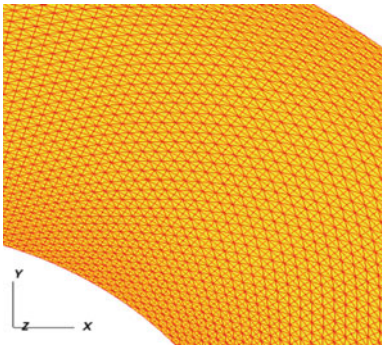

Fig. 2 Non-uniform grid spacing on the radial plane

Table 1 Grid resolution in wall units for 5 different cases

Case	Number of grid points (N_r, N_θ, N_z)	Δ_r^+	Δ_θ^+	Δ_z^+	Elements (in millions)	CPU time (in hours)
C1 (Coarse)	(25, 80, 120)	7.7	9.2	15.3	1.3	4140
C2 (Coarse)	(25, 160, 120)	8.8	5.3	17.6	2.7	9315
F1 (Fine)	(73, 160, 480)	1.3	5.1	2.4	33	74980
F2 (Fine)	(73, 320, 240)	1.3	2.7	4.9	33	111780
UF (Ultra-fine)	(73, 640, 120)	1.3	1.3	9.6	33	74980

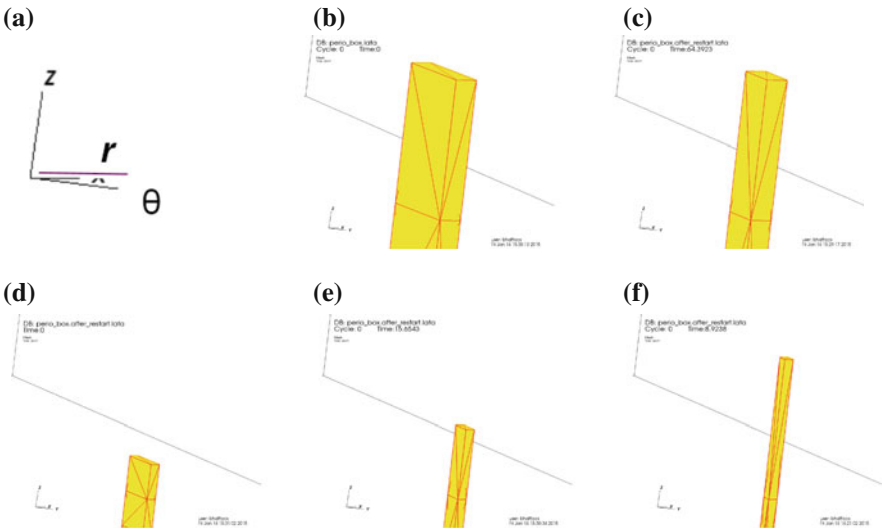

Fig. 3 **a** Axes, **b** C1 (Coarse), **c** C2 (Coarse), **d** F1 (Fine), **e** F2 (Fine), **f** UF (Ultra-fine)

Space discretization was done with the second order centered stabilized "EF_stab" scheme [6] and time discretization with the second order explicit Adams-Bashforth scheme. The wall-adaptive local eddy viscosity (WALE) model [7] was used to model the universal small scale eddies. In cases where the grid resolution near the wall is not of order 1, the Reichardt wall law [5] was used.

Due to the regular pattern of the grid, a constant velocity profile as initial condition was not sufficient to generate turbulence. So a fully developed turbulent flow field from another simulation (on a coarser mesh) was used as initial condition. Periodic boundary condition was applied axially. A momentum source term was added to maintain constant flow rate. Two point correlation coefficient between the velocity component in the streamwise (axial) direction is plotted in Fig. 4. It falls to zero at half a period suggesting that the streamwise domain length is sufficient. No-slip condition was imposed on the inner and outer walls.

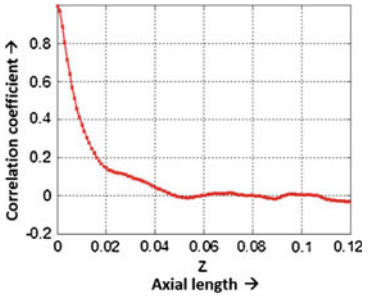

Fig. 4 Two point correlation for streamwise velocity

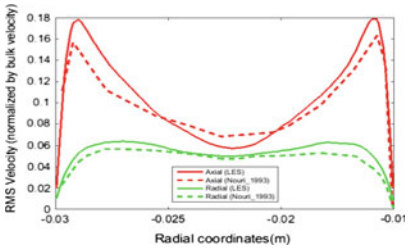

Fig. 5 Standard deviation of velocity for F2 case

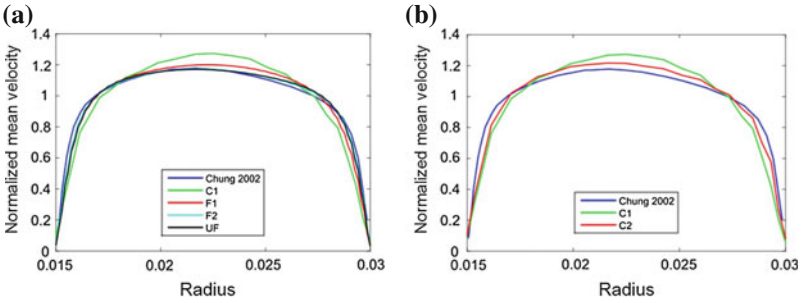

Fig. 6 **a** Comparison for fine meshes, **b** Comparison for coarse meshes

2.1 Results

The turbulent statistics were collected after the flow stabilized. The averaging was done over 25 flow traversals. For the case F2, standard deviation of radial and axial velocity was computed as shown in Fig. 5. It is in good agreement with experimental data of [8]. A comparison of mean velocity profiles for 4 different simulations in Table 1 is presented in Fig. 6a. Comparison of the coarse C1 profile with F1 shows an improvement due to the refinement in all directions. The F2 mesh was created with the same number of elements as F1 but the resolution in azimuth was doubled and

that in axial was halved. The profile for F2 agrees well with DNS of [3]. UF mesh also shows similar profile as F2. Hence one could go up to the resolution in wall units of the order of 10 in axial, 3 in azimuthal and 1.3 in radial to reproducing the benchmark result. It should be noted that the total number of elements was maintained for cases F1, F2, UF. The above sensitivity analysis shows that the mean velocity profile has a stronger dependence on azimuthal resolution compared to axial resolution for the 4 said meshes. A similar test was made with the coarse mesh. The azimuthal resolution in C1 was doubled to create C2 mesh. Again, Fig. 6b shows a significant improvement in the profile from C1 to C2.

3 Pressure Fluctuations in an Annular Pipe with a Circular Grid

A realistic PWR core has a square spacer grid. However, creation of a square grid inside an annular pipe would lead to unstructured mesh (at least in its vicinity if we implement hybrid meshing). Since the aim is to understand the physics of the problem, we implemented a circular grid instead. As a result, generation of a fully structured mesh was possible. Also the domain became symmetric. This improved the speed of simulation. In order to make it more realistic, the ratio of hydraulic diameters between the inner and outer flow areas was kept the same for both types of grids. The pipe with the circular grid is shown in Fig. 7. The length of the domain was 0.2688 m, i.e., approximately 9 hydraulic diameters.

Table 2 presents the grid resolutions in different directions. An attempt was made to keep in consideration the acceptable resolutions obtained in Sect. 2.1. However, as seen from Table 2, some compromise had to be made due to lack of computational time and resources. The domain consisted of 20.7 million tetrahedrons and simulation was carried out on 710 parallel processors. All numerical parameters were the same as in Sect. 2 except the boundary conditions at the inlet and outlet. A fully developed

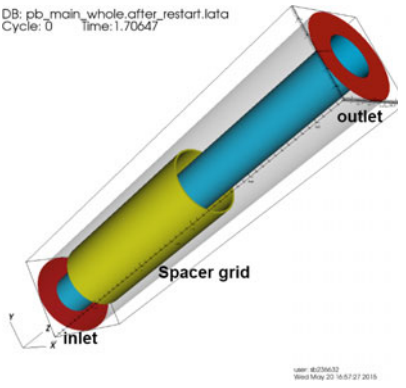

Fig. 7 Annular pipe with circular grid

Table 2 Grid resolution

Direction	Boundary	Grid resolution (in wall units)	Grid resolution (in meters)
Radial	Inner wall	3.2	0.0003
	Outer wall	2.9	0.0003
	Circular grid	3.6	0.0003
Azimuthal	Inner wall	2.8	0.00026
	Outer wall	5.4	0.00055
	Circular grid	4.8	0.0004
Axial	Inner wall	12.9	0.0012
	Outer wall	11.7	0.0012
	Circular grid	14.5	0.0012

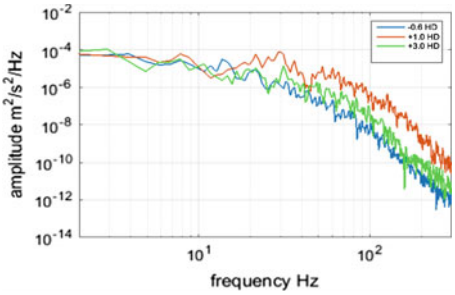

Fig. 8 PSD of instantaneous velocity

turbulent velocity field was injected at the inlet at each time step (from a simultaneous LES). A constant pressure zero was imposed at the outlet.

3.1 Results

Instantaneous velocity fluctuations were analyzed in terms of power spectral density (PSD) at 3 heights: 0.6 HD upstream, 1 HD downstream and 3 HD downstream. Figure 8 shows that the amplitude of fluctuations 1 HD downstream is a decade higher than that upstream. At 3 HD, the amplitude is reduced but still higher than that upstream. This increase in fluctuation is due to the presence of the circular spacer grid. In Fig. 9, the PSD of pressure fluctuations on the inner wall of the pipe shows that the amplitude of fluctuation is higher downstream compared to upstream. The fluctuations or amplitude of power decrease with frequency. Figure 10 shows an angular distribution of standard deviation of the pressure field on the inner wall. The deviation increases by 50% at 1 HD downstream. The symmetric distribution is due to the symmetry of the grid.

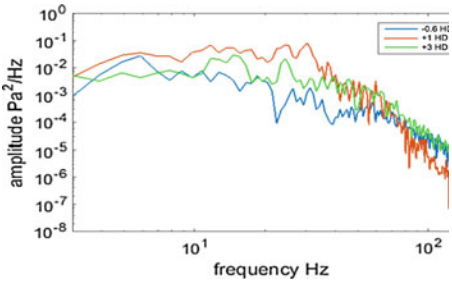

Fig. 9 PSD of pressure fluctuations on the inner wall

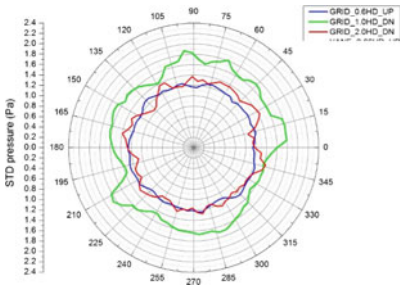

Fig. 10 Angular distribution of standard deviation of pressure on the inner wall

4 Conclusion

A mesh sensitivity analysis with structured grids was performed in an annular pipe using LES. Velocity profiles for 5 different meshes were compared with benchmark DNS, following which an acceptable grid resolution of the order of 10 (axial), 3 (azimuthal) and 1.3 (radial) in wall units was proposed. It was observed that the results are more sensitive to azimuthal resolution than axial resolution. Presence of a circular spacer grid in the pipe increased the fluctuation downstream of the grid as seen from the PSD plots of velocity and wall pressure. As future work, it would be interesting to repeat the same study with a square spacer grid. Also the grid resolutions in Table 2 could be improved to reach the one discussed in Sect. 2.1.

References

1. Bieder, U., Graffard, E.: Qualification of the CFD code Trio_U for full-scale reactor applications. Nucl. Eng. Des. **238**, 671–679 (2008)
2. CCRT-Computing Center for Research and Technology, France. http://www-hpc.cea.fr/en/complexe/tgcc-curie.htm
3. Chung, S.Y., Rhee, G.H., Sung, H.J.: Direct numerical simulation of turbulent concentric annular pipe flow Part 1: Flow field. Int. J. Heat Fluid Flow. **23**, 426–440 (2002)
4. Geuzaine, C., Remacle, J.F.: Gmsh–A three dimensional finite element mesh generator with built-in pre- and post-processing facilities. Int. J. Numer. Methods Eng. **79**, 1309–1331 (2009)
5. Hinze, J.O.: Turbulence. McGraw-Hill, New York (1959)

6. Kuzmin, D., Turek, S.: Multi dimensional FEM-TVD paradigm for convection-dominated flows. Proc. ECCOMAS, Jyvaskyla. 24–28 July, 1–19 (2004)
7. Nicoud, F., Ducros, F.: Sub-grid scale stress modeling based on the square of the velocity gradient tensor. Flow Turbul. combust. **62**, 183–200 (1999)
8. Nouri, J.M., Umur, H., Whitelaw, J.H.: Flow of Newtonian and non-Newtonian fluids in concentric and eccentric annuli. J. Fluid Mech. **253**, 617–641 (1993)
9. Trio_U-Computational Fluid Dynamics code version 1.7.0: French Alternative Energies and Atomic Energy Commission (CEA), France. http://www-trio-u.cea.fr

Uncertainty Quantification in Large-Eddy Simulations of the Flow Around a 5:1 Rectangular Cylinder

L. Siconolfi, A. Mariotti and M.V. Salvetti

1 Introduction

The Benchmark on the Aerodynamics of a Rectangular Cylinder (BARC) with chord-to-depth ratio equal to 5, sketched in Fig. 1a, was launched in 2008 with the aim of collecting a large number of flow realizations obtained both in wind tunnels and in numerical simulations. The considered flow configuration is of practical interest, e.g. in civil engineering, and, in spite of the simple geometry, the related flow dynamics and topology is complex. Indeed, the flow around the stationary elongated cylinder at the considered aspect ratio and high Reynolds numbers is turbulent with unsteady flow separation form the upstream corners and reattachment on the cylinder side. This adds to the vortex shedding from the rear corners. An example of the mean flow streamlines is shown in Fig. 1b. The results of about 70 experimental and numerical realizations of the BARC flow configuration were collected and reviewed in [2]. The dispersion of the LES contributions and their sensitivity to the simulation parameters were specifically analyzed in [6]. It was observed that some of the flow quantities, as the standard deviation of the lift coefficient or the distribution of mean and fluctuating pressure on the cylinder sides, are affected by significant dispersion, both in experiments and in simulations, including LES. The observed dispersion can be explained by the extreme sensitivities of some flow features to uncertainties which can be hardly avoided or controlled in experiments or simulations. The uncertainty sources in numerical simulations are obviously different than in experiments, but all

L. Siconolfi · A. Mariotti · M.V. Salvetti (✉)
Dipartimento di Ingegneria Civile e Industriale, Università di Pisa,
Via G. Caruso 8, 56122 Pisa, Italy
e-mail: mv.salvetti@ing.unipi.it

L. Siconolfi
e-mail: siconolfi.lorenzo@gmail.com

A. Mariotti
e-mail: alessandro.mariotti@for.unipi.it

D.G.E. Grigoriadis et al. (eds.), *Direct and Large-Eddy Simulation X*,
ERCOFTAC Series 24, https://doi.org/10.1007/978-3-319-63212-4_12

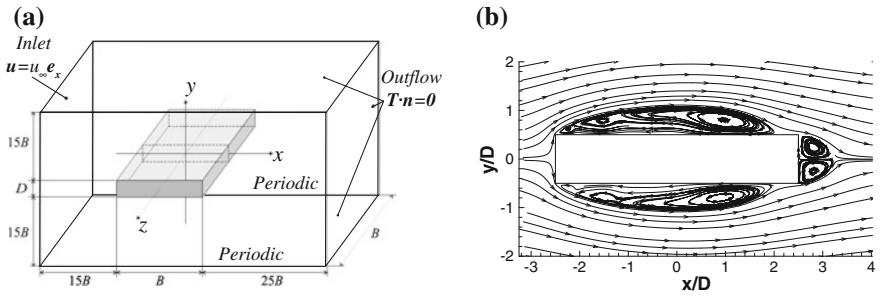

Fig. 1 **a** Sketch of the computational domain and **b** common mean flow pattern around the BARC configuration

produced a similar dispersion. More specifically, sensitivity analysis to some parameters have been carried out in the LES contribution to BARC; however, they are not conclusive and in some case controversial. For instance, in a single contribution a strong sensitivity to the grid resolution in the spanwise direction was pointed out, but the results obtained for the finest grid significantly deviated from the ensemble average of those of the experimental and numerical contributions [2].

In this context, in the present work we address the sensitivity to grid resolution and SGS modeling by using a stochastic Uncertainty Quantification (UQ) approach, as described in more detail in the following section. The basic idea is to model these computational set-up parameters as input random variables with a given probability distribution and to propagate the uncertainty through the computational model to statistically quantify the impact on the results. Continuous response surfaces in the parameter space are built from a small number of LES simulations by using the generalized Polynomial Chaos (gPC) approach (see, e.g. [4]).

2 Description of the Test Case and of the UQ Procedures

Simulations are carried out for the incompressible flow around a fixed sharp-edged rectangular cylinder with a chord-to-depth ratio, B/D, equal to 5. The angle of attack is zero. The computational domain, sketched in Fig. 1a, is such that $-15.5 \leq x/B \leq 25.5$, $-15.1 \leq y/B \leq 15.1$, where x and y denote the streamwise and transverse directions respectively, the cylinder center being located at $x = y = 0$. The spanwise domain size is equal to B. A uniform velocity profile is imposed at the inflow, while no-slip conditions are applied at the solid walls. Periodic conditions are imposed in the spanwise direction and traction-free outflow boundary conditions are used at the outflow, on the top and on the bottom of the computational domain. Finally, the Reynolds number based on the free stream velocity and on the cylinder depth, Re, is equal to 40,000. This value is in the range recommended for the BARC benchmark. No sensitivity analysis is carried out to the value of Re, since it was observed in [2] that this parameter has only a moderate impact on the results.

The numerical simulations are carried out by using the code Nek5000 that is based on a spectral-element method. Spectral element methods combine some properties of Finite Element Methods (FEM) and spectral methods. Each spectral element is rectangular, or a suitable coordinate mapping of a rectangle, as in spectral methods. The basis functions inside each element consist of Legendre polynomials of the order N for velocity, and $N-2$ for pressure, where typically $N \geq 6$; they are the Lagrangian interpolants based on the Gauss-Lobatto-Legendre quadrature points. Continuity of the velocity field over element boundaries is obtained by matching the velocities there. Thus, the derivatives of the velocity field are not continuous. As for FEM, the equations are cast into a weak form, and the integrated residual is minimized. It can be shown that the method has a spectral convergence in N (so-called p-refinement), and the convergence of a high order FEM method with respect to the number of elements (h-refinement). A third-order backward finite-difference scheme is used for time advancing.

In the present simulations $N = 6$ and the spectral element size in the streamwise and lateral directions is $\Delta x = \Delta y = 0.2D$; the spanwise resolution is varied as explained in the following. The time step is $\Delta t = 0.004$, approximately corresponding to a CFL of 0.4. As for the LES formulation, we use a simple approach based on the application of a low-pass explicit filter in the modal space. The adopted filter is a sharp cut-off for the modes up to $N-k$ (unfiltered) and it has a quadratic transfer function for the modes $N-k \leq p \leq N$, which can be tuned through a weighting parameter, w. This modal filter provides a dissipation in the highest resolved modes, which can be interpreted as a 'SGS dissipation' (e.g. [3, 5]).

The uncertain parameters for UQ are the following: the grid resolution in the spanwise direction, defined in terms of the average element size Δz, and the weight of the explicit filter, w. The latter has been chosen because it directly controls the amount of SGS dissipation; the number of filtered modes is for this study fixed to $k = 3$. The sensitivity to the grid resolution in the spanwise direction is also investigated because of the high impact of this parameter shown in the LES simulations in [1]. These two uncertain parameters are allowed to vary in the following ranges: $w \in [0.01, 0.131]$ and $\Delta z \in [0.31D, 0.67D]$. The impact of the uncertainty in these parameters is evaluated on the quantities of interest in the BARC benchmark, such as the time-average drag coefficient, $t-avg(c_x)$, the time-standard deviation of the lift coefficient, $t-std(c_y)$ and the distribution on the cylinder lateral surface of the $t-avg$ and of the $t-std$ of the pressure coefficient.

As previously said, the so-called gPC approach is adopted here in its non-intrusive form, i.e. the output variables are directly projected over the orthogonal basis spanning the random space, without any modification of the deterministic solver. The Probability Density Function (PDF) of the input uncertain parameters is assumed to be uniform; hence, this basis is made of Legendre polynomials. The polynomial expansion being truncated to the third order, 4 points for each random variable are sufficient to compute the coefficients of the expansion, i.e. a total of 16 LES simulations. The accuracy of the method is assessed by checking that the contribution of polynomials of order higher than three remains very low for all the considered quantities.

3 Results and Discussion

Figure 2a shows the stochastic mean ± stochastic standard deviation of the time-averaged drag coefficient, compared against the ensemble average and variation of the numerical contributions to BARC. It can be seen that the variance of $t - avg(c_x)$ with the considered parameters is much smaller than the ensemble dispersion of the BARC contributions. The stochastic mean value of our simulations is slightly underestimated compared to the ensemble average of BARC; this is due to numerical oscillations near the upstream corners occurring because of a too coarse grid resolution, which indeed disappear in the simulations on a more refined grid (not shown here for sake of brevity). The partial sensitivities to the single uncertain parameters, shown in Fig. 2b, indicate that this quantity is mainly sensitive to the grid refinement in the spanwise direction.

Figure 3 shows the same quantities and comparison for the standard deviation in time of the lift coefficient, together with the related PDF. For this quantity the variance with the considered parameters is larger than for the mean drag coefficient, but it is again much smaller than the overall dispersion of the BARC contributions. The PDF shows that most of the parameter combinations give values between 0.5 and 0.7, which correspond to the stochastic standard deviation, but there are large tails towards smaller values, i.e. some parameter combinations can give significantly smaller values. Finally, this quantity is mainly sensitive to the SGS dissipation.

The distribution over the cylinder side of the stochastic mean ± stochastic standard deviation of the time-averaged and side-averaged pressure coefficient, C_p, is shown in Fig. 4 and compared against the ensemble statistics of the BARC computations; the distribution of the partial variances is also reported. The same quantities and comparisons for the side-averaged standard deviation in time of C_p, $t - std(C_p)$, can be observed in Fig. 5. In both cases, the variability observed in our simulations due to the uncertainties in the considered set-up parameters is once again noticeably

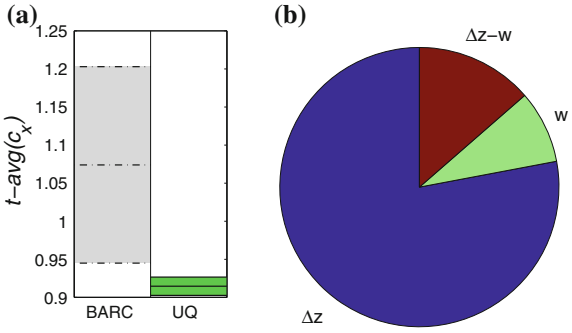

Fig. 2 **a** Stochastic mean ± stochastic standard deviation of the time-averaged drag coefficient, c_x, and comparison with the ensemble average and variation of the numerical contributions to BARC [2]. **b** Stochastic variance decomposition for the time-averaged c_x

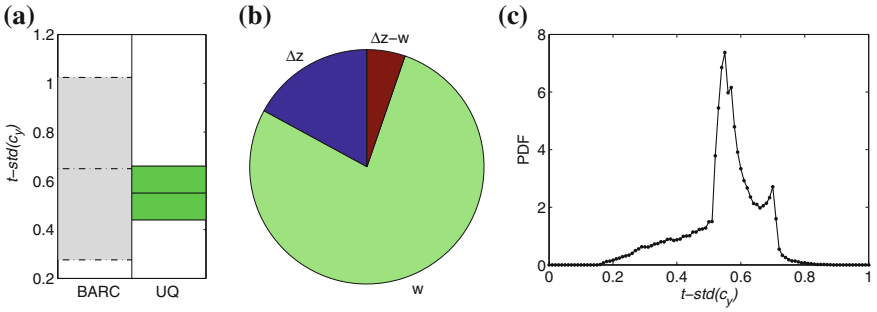

Fig. 3 **a** Stochastic mean ± stochastic standard deviation of the standard deviation in time of the lift coefficient, c_y, and comparison with the ensemble average and variation of the numerical contributions to BARC [2]. **b** Stochastic variance decomposition for the standard deviation in time of the lift coefficient. **c** PDF for the standard deviation in time of c_y

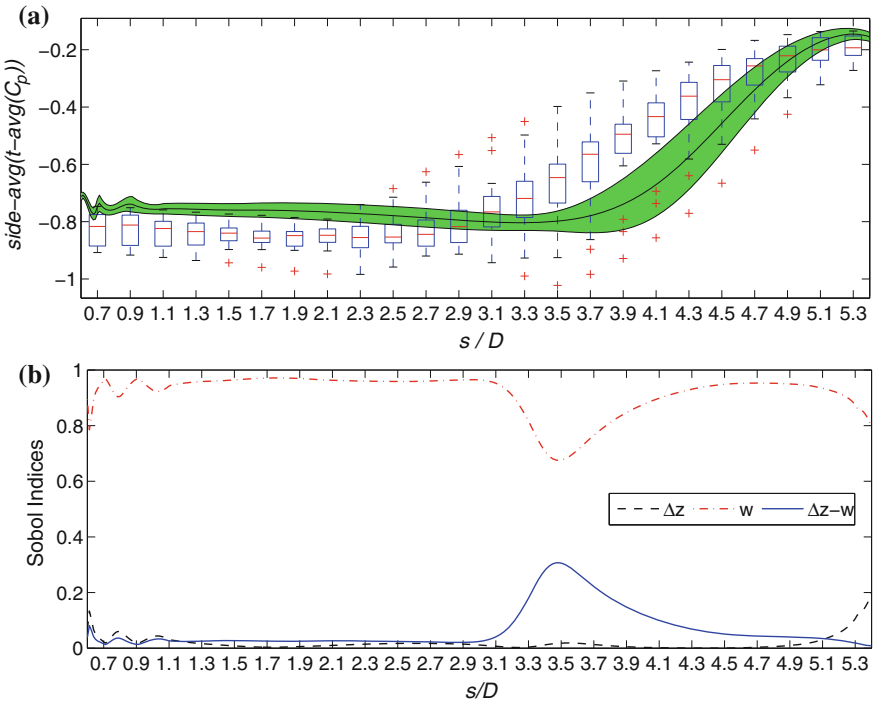

Fig. 4 **a** Stochastic mean ± stochastic standard deviation of the side-averaged and time-averaged pressure coefficient, C_p; comparison with the ensemble statistics of the BARC numerical simulations (data from [2]) **b** Stochastic variance decomposition of the time-averaged C_p

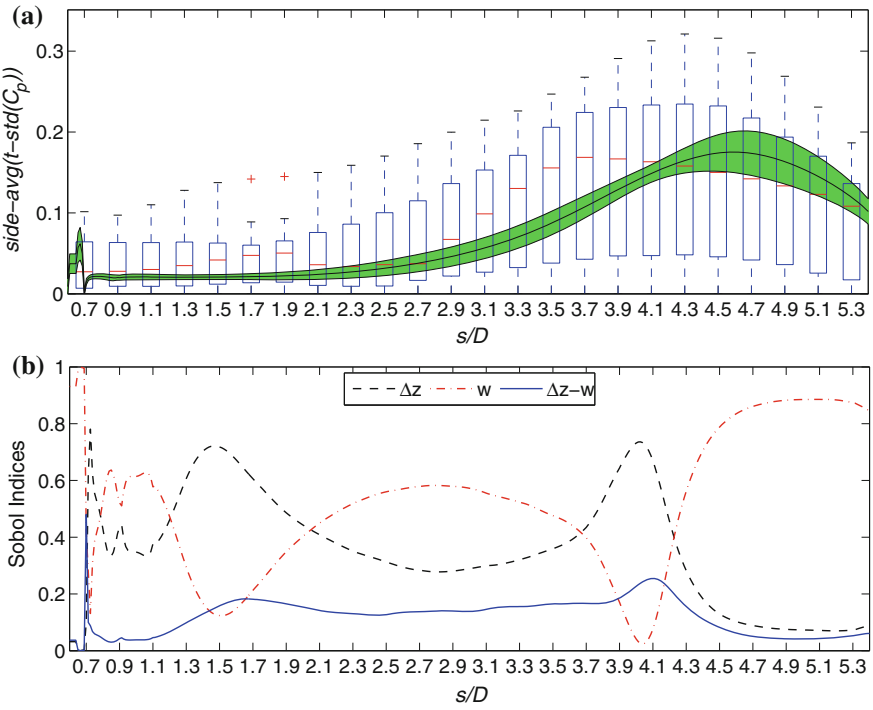

Fig. 5 **a** Stochastic mean ± stochastic standard deviation of the standard deviation in time of the pressure coefficient, C_p; comparison with the ensemble statistics of the BARC numerical simulations (data from [2]). **b** Stochastic variance decomposition of the standard deviation of C_p

smaller than the overall dispersion of the BARC simulations. The mean pressure is mainly sensitive to the SGS dissipation, while coupling between SGS dissipation and spanwise grid refinement seems to have a significant impact only in the region where the mean pressure starts to increase (see Fig. 4b). Conversely, for the $t - std(C_p)$ the sensitivity to the parameters is more complex and there is not a clear predominant effect (see Fig. 5b). The PDF distributions over the cylinder side of $t - avg(C_p)$ and $t - std(C_p)$ are reported in Fig. 6. Note how the PDF of the C_p in the zone of its largest variability has a bimodal distribution, i.e. there are two different highly probably values.

Summarizing, a stochastic approach to quantify the sensitivity of LES results to different computational set-up parameters has been described. The impact of spanwise grid resolution and of SGS dissipation have been investigated herein. The overall variance of the results of our LES is generally much lower than the BARC global dispersion. This kind of analysis may, in general, be useful to appraise the reliability of large-eddy simulations. The strong effect of spanwise grid resolution, observed by [1] has not been found in our analysis, most of the quantities being mainly sensitive to SGS dissipation.

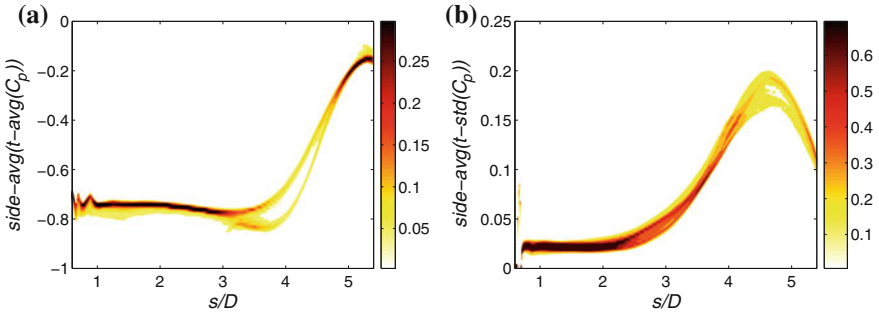

Fig. 6 PDF for the time-averaged **(a)** and for the standard deviation in time **(b)** of C_p

References

1. Bruno, L., Coste, N., Fransos, D.: Simulated flow around a rectangular 5:1 cylinder: spanwise discretisation effects and emerging flow features. J. Wind Eng. Ind. Aerod. **104–106**, 203–215 (2012)
2. Bruno, L., Salvetti, M.V., Ricciardelli, F.: Benchmark on the aerodynamics of a rectangular 5:1 cylinder: and overview after the first four years of activity. J. Wind Eng. Ind. Aerod. **126**, 87–106 (2014)
3. Domarazdki, J.A.: Large eddy simulations without explicit eddy viscosity models. Int. J. Comput. Fluid Dyn. **24**(10), 435–447 (2010)
4. Ghanem, R., Spanos, P.: Stochastic Finite Elements: A Spectral Approach. Springer, Berlin (1991)
5. Mathew, J., Lechner, R., Foysi, H., Setsterhenn, J., Friedrich, R.: An explicit filtering method for large eddy simulation of compressible flows. Phys. Fluids **15**, 2279–2289 (2003)
6. Salvetti, M.V., Bruno, L.: Reliability of LES simulations in the context of a benchmark on the aerodynamics of a rectangular 5:1 cylinder. In: Proceedings of Direct and Large-Eddy Simulations 9, April 3–5, Dresden, Germany (2013)

Effects of the Subgrid-Scale Modeling in the Large-Eddy Simulations of Wind Turbines

U. Ciri, M.V. Salvetti, K. Carrasquillo, C. Santoni, G.V. Iungo and S. Leonardi

1 Introduction

The increased demand for wind energy had led to a continuous increase in the size of wind turbines and as a consequence in the size of wind farms. A potential drawback of using large arrays of wind turbines is the decrease in efficiency due to the wake interference. Although simple wake models, based on conservation of momentum, provide a good estimate of mean quantities and overall performances when the wind direction is aligned with the turbine axis, higher fidelity codes are required to study the wake meandering and its interaction with downstream turbines. Due to the high Reynolds number in wind turbines applications, direct numerical simulations are not feasible in realistic conditions, while large-eddy simulations have shown the capability of resolving the unsteady nature of wind turbine wake. In LES, subgrid scale (SGS) models are needed to introduce the effects of the small scales of the flow, which can not be represented on the computational grids; the SGS model is expected to have a significant effect on the quality of the results. Many LES of wind farms simulations employ the classic Smagorinsky SGS model. This model is attractive because it is very simple to be implemented and it implies almost negligible additional numerical costs. On the other hand, it has a few important drawbacks, among which the most important are the following: (i) the parameter tuning the Smagorinsky model is flow dependent and, thus, should be adjusted for each particular application, (ii) the model has a wrong behavior near solid walls, and, in particular, it introduces

U. Ciri · M.V. Salvetti (✉)
Dipartimento di Ingegneria Civile e Industriale, University of Pisa, Pisa, Italy
e-mail: mv.salvetti@ing.unipi.it

K. Carrasquillo · C. Santoni · G.V. Iungo · S. Leonardi
Department of Mechanical Engineering, The University of Texas at Dallas, Dallas, United States
e-mail: valerio.iungo@utdallas.edu

S. Leonardi
e-mail: stefano.leonardi@utdallas.edu

D.G.E. Grigoriadis et al. (eds.), *Direct and Large-Eddy Simulation X*,
ERCOFTAC Series 24, https://doi.org/10.1007/978-3-319-63212-4_13

an excessive SGS dissipation in attached boundary layers. Although some LES simulations of wind farms employ more sophisticated and more recent SGS models than the Smagorinsky one, there is a lack of systematic investigations of the impact of SGS modeling in the context of wind farm simulations. A recent example can be found in [1] for a double-rotor arrangement using the actuator line technique, which compared the results obtained by the Smagorinsky model and by two different mixed-scale models. The dynamic versions of these previous SGS models were also considered. The impact of the SGS model on the flow structures and on the predicted power performance was found to be small compared to that of the rotor resolution and of the actuator line force kernel size.

In the present work, we carry out a similar study, but for large-eddy simulations in which the turbine tower and nacelle are directly simulated by using the immersed boundary (IB) method [2]. It has been shown in [3] that the simulation of tower and nacelle is important to obtain a close agreement with experiments, since virtual forces mimicking the tower do not guarantee impermeability and affect the downstream wake. In this paper, the question at issue is whether the SGS model has a larger impact than found in [1], especially in the separated flow region behind the tower. In addition, the wrong behavior of the Smagorinsky model near solid walls becomes a serious concern, because near-wall ad-hoc corrections are not suitable for complex geometries. Since we want to keep the complexity and the computational requirements of the SGS model as low as possible, we focus herein on non-dynamic eddy-viscosity models, which have been proven to have a correct behavior near solid walls, in particular, we consider the models proposed in [4–6].

2 Methodology and Flow Configuration

The non-dimensional filtered incompressible Navier-Stokes equations are considered:

$$\frac{\partial \tilde{u}_i}{\partial x_i} = 0 \quad ; \quad \frac{\partial \tilde{u}_i}{\partial t} + \frac{\partial}{\partial x_j}\left(\tilde{u}_i \tilde{u}_j\right) = -\frac{\partial p^*}{\partial x_i} + \frac{1}{\mathrm{Re}} \frac{\partial^2 \tilde{u}_i}{\partial x_j \partial x_j} - \frac{\partial \tau_{ij}^d}{\partial x_j} + F_i \quad (1)$$

where $\mathrm{Re} = UD/\nu$ is the Reynolds number based on the unperturbed inlet velocity U and the rotor diameter D, with ν being the air kinematic viscosity. The velocity component in the i-th direction is u_i and the tilde represents the filtering operation. The modified pressure p^* is the sum of the filtered pressure $\tilde{p}$ and the isotropic part of the SGS tensor $\tau_{ij} = \widetilde{u_i u_j} - \tilde{u}_i \tilde{u}_j$. The deviatoric part $\tau_{ij}^d = \tau_{ij} - \frac{1}{3}\tau_{kk}\delta_{ij}$ is modeled as described in detail later on. The term F_i represents the body forces which are applied by the turbine blades to the aerodynamic field. Indeed, because of the wide range of scales involved in wind turbines flows, modeling of the effects of the turbine rotor is required to keep the computational costs reasonable. The recently developed Rotating Actuator Disk Model (RADM) is used herein. With this method

the forces, computed through the blade element theory, are spread onto a disk with a distribution which depends on both the radial and azimuthal coordinates. As the blades rotate, such distribution is changed accordingly, thus recovering the effects of the rotor motion in the simulation. This method can be considered as a compromise in terms of accuracy and computational costs between the two most commonly employed models, the Actuator Line and the Actuator Disk models.

The discretisation method for Eq. (1) is developed from the one described in [2]. It consists of a second-order central finite-difference approximation on Cartesian staggered grid for the spatial derivatives. Integration in time is performed with a fractional step method where linear terms are treated implicitly while convective terms explicitly. The momentum equations are solved with an approximate factorisation technique which uses the pressure at the previous step. The solution is then projected onto a solenoidal space obtaining the next step velocity field.

The turbine tower and nacelle are taken into account in the simulations through the immersed boundary method, as described in [2].

As for SGS modeling, we considered eddy-viscosity models, which are based on the Boussinesq hypothesis which describes the SGS tensor as $\tau_{ij}^d = -2\nu_T \tilde{S}_{ij}$ where $\tilde{S}_{ij}$ is the filtered strain rate tensor. The expression of the eddy-viscosity differs according to the particular model considered, but has the following general structure:

$$\nu_T = (C_{\text{model}} \Delta)^2 \mathscr{D}_{\text{model}} \tag{2}$$

where C_{model} is a constant which has to be provided as an input parameter, $\mathscr{D}_{\text{model}}$ is an operator depending on the resolved field and Δ is the LES filter width.

Various models have been investigated, namely the Vreman model [5], the WALE model [4] and the σ-model [6]. The classical Smagorinsky model [7] has also been considered, because it is the most widely employed in LES of wind turbine flows. As previously mentioned, this model has an incorrect behavior near solid walls and ad-hoc damping of the eddy viscosity is usually employed to overcome this problem. However, in our case, due to the complex geometry of tower and nacelle and to the IB treatment, this would be extremely complex; therefore, no damping is used. The values of the model constant parameters used in the present study are: $C_s = 0.09$, $C_V = 2.5C_s^2$, $C_W = 0.55$ and $C_\sigma = 1.35$ for the Smagorinsky, the Vreman, the WALE and the σ models respectively.

The simulation setup is aimed at reproducing the configuration of the experiment carried out by Krogstad et al. [8] within the NOWITECH/NORCOWE blind test. A small wind turbine, having a rotor diameter $D = 0.9\,\text{m}$, is placed inside a wind tunnel; the oncoming flow velocity is $U = 10\,\text{m/s}$ and the resulting Reynolds number is $\text{Re} = UD/\nu = 6.3 \cdot 10^5$. The turbine is set to operate at a constant specified tip speed ratio $TSR = \omega R/U$, where $R = D/2$ and ω is the turbine rotational speed. TSR is set equal to 3 in all the simulations in the present work. The flow configuration and the computational domain are sketched in Fig. 1. In our simulation, a uniform velocity inflow profile is imposed at the inlet; no-slip conditions are prescribed at

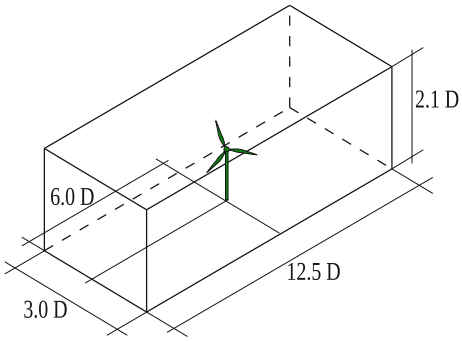

Fig. 1 Flow configuration and computational domain

the lateral boundaries of the domain as well as at upper and lower ones in order to mimic the wind tunnel walls. A radiative outflow condition is used at outlet.

3 Results and Discussion

The *a priori* tests are performed at a low Reynolds number ($Re = 10{,}000$), for which a no-model simulation was carried out on a rather fine uniform grid having $1024 \times 512 \times 512$ gridpoints in the streamwise, wall-normal and spanwise direction respectively. The velocity field obtained from this simulation was filtered in each direction with a discrete second-order filter of width equal twice the mesh spacing Δx_i. The time-averaged subgrid dissipation $\langle \varepsilon \rangle = \langle \tau_{ij} \tilde{S}_{ij} \rangle$ provided by each model in the vertical plane containing the tower axis is shown in Fig. 2. The dissipation provided by the WALE model and the σ-model is significantly larger than that of

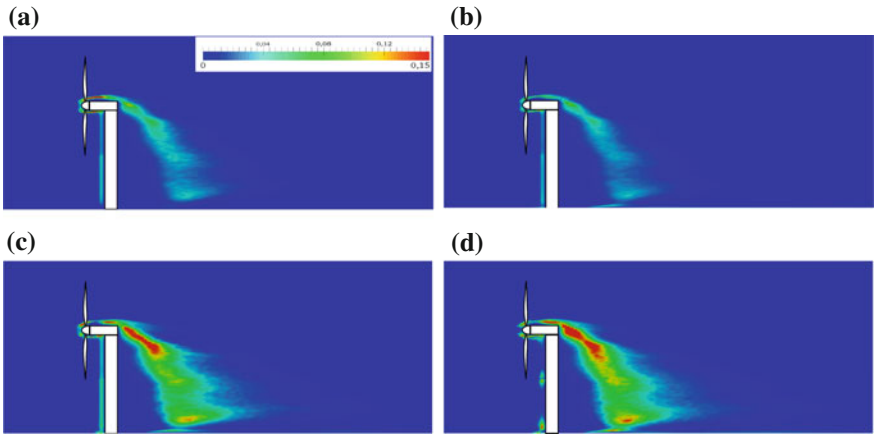

Fig. 2 **a** Smagorinsky model: $\langle \varepsilon \rangle$, **b** Vreman model: $\langle \varepsilon \rangle$, **c** WALE model: $\langle \varepsilon \rangle$, **d** σ-model: $\langle \varepsilon \rangle$

the other models, while the Vreman model is the least dissipative. These trends are consistent with the findings of other studies in the literature (see e.g. [9]). The correlation coefficient between the time-averaged 'exact' subgrid dissipation $\langle \varepsilon_{\text{exact}} \rangle$, computed from the no-model simulation, and the one predicted by each SGS model has been computed. The correlation coefficients, further averaged in space on the vertical plane containing the tower axis, are the following: 0.54, 0.71, 0.68 and 0.64 for the Vreman, WALE, σ and Smagorinsky models. It seems, thus, that the low SGS dissipation introduced by the Vreman model is also the least correlated with the 'exact' one.

Actual LES were carried out at the same Reynolds number as in the experiment ($\text{Re} = 6.3 \cdot 10^5$), on a very coarse grid having $512 \times 256 \times 256$ gridpoints in the streamwise, wall-normal and spanwise direction respectively. The Vreman model led to unstable simulations, probably because of the too low dissipative character of the model.

The time averaged thrust and power coefficients ($C_T = Thrust/0.5\rho U^2 \pi R^2$ and $C_P = Power/0.5\rho U^3 \pi R^2$ respectively) are reported in Table 1 together with the measured values and the results of the blind test. The results provided by the three models are similar and within the blind test prediction range.

The time-averaged streamwise velocity profiles $\langle \tilde{u}_1 \rangle / U$ in the spanwise direction at two different downstream locations are shown in Fig. 3. The agreement with the

Table 1 Turbine performances

		C_T	C_P
LES:			
	WALE model	0.294	0.162
	σ-model	0.302	0.171
	Smagorinsky model	0.327	0.190
Exp.		0.393	0.120
Blindtest range		0.260–0.430	0.080–0.250

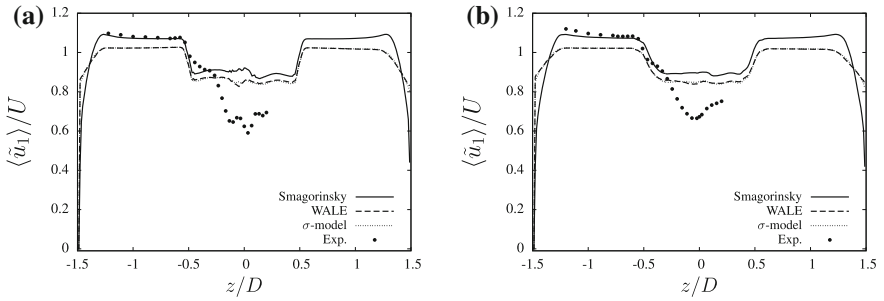

Fig. 3 **a** Spanwise profile at hub height $1D$ downstream rotor, **b** Spanwise profile at hub height $3D$ downstream rotor

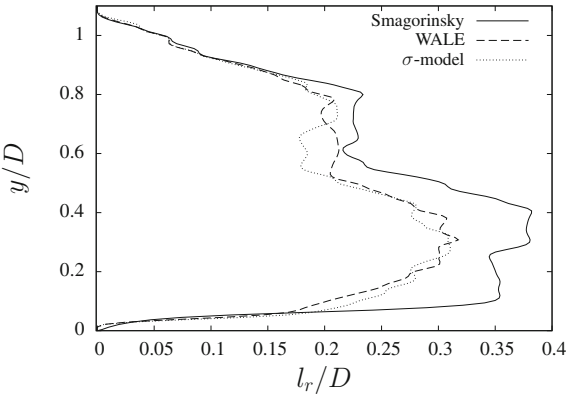

Fig. 4 Mean recirculation length l_r along the tower axis. Rotor centre is positioned at $y/D = 1.05$

experimental results is satisfactorily, though not excellent. No dramatic differences between the various models can be observed overall.

A larger impact of the SGS modeling is found when considering the recirculating region which is created behind the tower. As shown in Fig. 4, the mean recirculation length l_r decreases as the amount of dissipation provided by the model increases. Indeed, the more dissipative models cause earlier transition to turbulence of the shear-layers: the vortices form more upstream and the mean recirculation zone is shorter [9].

Summarizing, despite the different amount of SGS dissipation introduced by the considered models, in actual LES the results given by the Smagorinsky, WALE and σ models are not so different. On the other hand, the Vreman model, which is the least dissipative, led to unstable simulations. However, the small impact of SGS modeling might be due to the used model of the turbine blade effects and to the very coarse grid resolution, which only allow a crude representation of the small flow scales, on which the SGS dissipation is expected to have the largest impact. Future studies will be aimed at assessing whether the same conclusions hold for a more refined grid and for a more accurate and detailed model of the rotor, as e.g. the actuator line model.

References

1. Sarlak, H., Meneveau, C., Sørensen, J.N.: Role of subgrid-scale modelling in the large eddy simulation of wind turbine wake interactions. Renew. Energy **77**, 386–389 (2014)
2. Orlandi, P., Leonardi, S.: DNS of turbulent channel flows with two- and three-dimensional roughness. J. Turbul. **7** (2006)
3. Santoni, C., Carrasquillo, K., Arenas-Navarro, I., Leonardi, S.: Effect of tower and nacelle on the flow past a wind turbine. Wind Energ. (2017). doi:10.1002/we.2130
4. Nicoud, F., Ducros, F.: Subgrid-Scale Stress Modelling based on the Square of the Velocity Gradient Tensor. Flow Turb. Combust. **62**, 183–200 (1999)
5. Vreman, A.W.: An eddy-viscosity subgrid-scale model for turbulent shear flow: Algebraic theory and applications. Phys. Fluids **16**, 36–70 (2004)

6. Nicoud, F., Toda, H.B., Cabrit, O., Bose, S., Lee, J.: Using singular values to build a subgrid-scale model for large eddy simulations. Phys. Fluids **23**, 85–106 (2011)
7. Smagorinsky, J.: General circulation experiments with the primitive equations. Mon. Weather Rev. **3**, 99–164 (1963)
8. Krogstad, P.-Å.: Eriksen, P.E.: "Blind test" calculations of the performance and wake development for a model wind turbine. Renew. Energy **50**, 325–333 (2013)
9. Ouvrard, H., Koobus, B., Dervieux, A., Salvetti, M.V.: Classical and variational multiscale LES of the flow around a circular cylinder on unstructured grids. Comput. Fluids **7**, 1083–1094 (2010)

Part III
Multiphase

Particle Agglomeration in Turbulent Flows: A LES Investigation Based on a Deterministic Collision and Agglomeration Model

M. Breuer and N. Almohammed

1 Introduction

Dry, electrostatically neutral particles in a turbulent flow are a common example for disperse particle–laden flows playing a dominant role in many technical devices such as pulverized coal firing systems or cyclone separators. It is well-known that the complexity of these flows strongly increases with the mass loading of the disperse phase. On the one hand, this observation is related to the growing significance of various interactions between the particulate and the continuous phase. On the other hand, the interaction between the particles itself plays an increasing role if the volume fraction exceeds values of about 10^{-3}. Then, particle–particle collisions can no longer be neglected. However, the collision between particles is not the only physical process of relevance, but the first prerequisite for the agglomeration of particles. Restricting to microscopic, electrostatically neutral and dry particles in a gas flow, the second prerequisite for agglomeration is an attractive force between the particles known as the molecular van-der-Waals force.

The modeling and simulation of particle agglomeration in turbulent flows in the framework of an Euler–Lagrange approach is the topic of the present paper. The application of large–eddy simulation for the continuous flow, an efficient particle tracking scheme for the disperse phase and a deterministic collision model form the basis for investigations on the agglomeration process. For this purpose, the agglomeration model of Kosinski and Hoffmann [6] is enhanced and its application area is extended to fully three–dimensional turbulent flows [5]. In order to validate the entire simulation methodology, the turbulent particle–laden flow through a vertical plane channel is analyzed in detail investigating small and large particles, low and high numbers of the same particle size, and hence low and high mass loadings.

M. Breuer (✉) · N. Almohammed
Professur für Strömungsmechanik, Helmut–Schmidt–Universität Hamburg, Hamburg, Germany
e-mail: breuer@hsu-hh.de

D.G.E. Grigoriadis et al. (eds.), *Direct and Large-Eddy Simulation X*,
ERCOFTAC Series 24, https://doi.org/10.1007/978-3-319-63212-4_14

2 Simulation Methodology of Four–Way Coupled LES

Relying on a four–way coupled Euler–Lagrange LES approach, the continuous phase is solved in an Eulerian frame of reference taking the conservation equations of the filtered quantities [2] into account. For modeling the non-resolvable subgrid scales the well-known Smagorinsky model (C_s = 0.065) with Van Driest damping near solid walls is applied. To take the feedback effect of the particles into account, the particle-source-in-cell method is used. The solution is based on a 3-D finite–volume method [2] for arbitrary non-orthogonal and block–structured grids. The spatial as well as the temporal discretizations are second–order accurate.

The disperse phase is solved in a Lagrangian frame of reference [1, 3, 4] based on Newton's second law, where the fluid forces are derived from the displacement of a small rigid sphere in a non-uniform flow. For particles with a density much higher than the carrier fluid, only the drag, lift, gravity and buoyancy forces have to be considered. To account for the rotation of the spherical particles, Newton's second law for the angular momentum is considered. The torque acting on a rotating particle is determined analytically taking the rotation of the surrounding fluid into account.

The ordinary differential equation for the particle motion is integrated by a fourth–order Runge-Kutta scheme in physical space. To avoid time–consuming search algorithms, the second integration to determine the particle position on the grid is done in the computational space. Here, an explicit relation between the position of the particle and the cell index containing the particle exists [3], which is required to calculate the fluid forces on the particle. Thus, the result is a highly efficient particle tracking scheme allowing to predict the paths of millions of particles.

The collisions between particles (four–way coupling) are predicted deterministically by a recently developed collision algorithm [4]. The calculation of the trajectories is split into two stages. In the first stage particles are moved based on the equation of motion without particle–particle interactions. In the second stage the occurrence of collisions during the first stage is examined for all particles by a highly efficient algorithm based on virtual cells. If a collision is found, the velocities of the collision pair are replaced by the post-collision velocities without changing their position. The post-collision velocities are calculated based on a hard–sphere collision model involving friction between the colliding spheres based on Coulomb's law.

3 Agglomeration Model

Beside collisions the second prerequisite for agglomeration is a strong enough attractive force between the particles known as the molecular van-der-Waals force. In order to account for the agglomeration process of colliding particles, the classical hard–sphere model is extended by this cohesive force [5, 6]. To determine the cohesive impulse, the actual period of contact is estimated as a function of the restitution coefficient [5]. If the cohesive impulse is sufficiently large, both particles stick together

after the collision and move with a common velocity. For the agglomeration, two cases have to be distinguished [5, 6]: In case of a sticking collision the agglomeration criterion is only related to the normal component of the impulse vector, since it is already assumed that the colliding particles stop sliding during collision. In case of a sliding collision the situation is different, since a second condition has to be satisfied. That guarantees that the tangential component of the impulse is strong enough to stop the particles and prevent them from further sliding. The arising agglomerate is typically described by a volume-equivalent sphere (see, e.g., [6]), which does not take the interstitial space between the agglomerated particles into account. Improved models such as the closely–packed sphere model were suggested in [5] allowing a packing fraction of the primary particles and thus a reduced density of the agglomerate.

4 Definition of the Test Case and Numerical Setup

A particle–laden vertical plane channel flow at a Reynolds number Re = 11,900 (Re_τ = 644) based on the bulk velocity U_B and the channel half–width δ is used as a test case. The gravitational acceleration g_x points in the main flow direction ($g_x \delta / U_B = 2.4 \times 10^{-3}$). Smooth channel walls with particle–wall collisions involving friction are considered. The particles are assumed to be made of fused quartz with a particle-to-fluid density of ρ_p / ρ_f = 1814. The normal and tangential restitution coefficients ($e_{n,p} = 0.97$, $e_{t,p} = 0.44$) and the kinetic coefficient of friction ($\mu_{kin,p} = 0.092$) are taken from measurements (see [5]). An often used value of $\mu_{st,p} = 0.94$ is applied for the static friction coefficient. For the particle–wall collisions the same restitution and friction coefficients are assumed. The dimensionless Hamaker constant and Young's modulus are $H/(\rho_f U_B^2 \delta^3) = 7.92 \times 10^{-17}$ and $E/(\rho_f U_B^2) = 7.24 \times 10^8$, respectively.

The grid consists of 128 × 128 × 128 cells. In streamwise (x) and spanwise (z) direction an equidistant grid with $\Delta x^+ = 61.76$ and $\Delta z^+ = 30.88$ is used. In wall–normal (y) direction the first cell center is located at $\Delta y^+ = 0.63$ and the grid is geometrically stretched with a stretching factor of 1.05. Thus, the resolution used lies in the range of the requirements for a wall–resolved LES. The time step is set to $\Delta t^* = \Delta t \, U_B / \delta = 0.005$. Periodic boundary conditions are applied in the streamwise and spanwise directions, and the no-slip condition is used at the walls.

Three cases are studied: Case *'Large'* denotes 3×10^6 particles with $d_p = 12\,\mu\mathrm{m}$ ($\mathrm{St}^+ = \tau_p / \tau_f^+ = 15.0$ with $\tau_f^+ = \nu_f / u_\tau^2$) leading to a mass loading of $\eta = 1.66\%$. Case *'Small'* denotes the same number of particles with a smaller diameter of $d_p = 4\,\mu\mathrm{m}$ ($\mathrm{St}^+ = 1.67$). Case *'Many'* stands for the same small particles but increasing the number to 81×10^6 in order to reach the same mass loading as in the first case.

5 Results, Discussion and Conclusions

Assuming a statistically developed state for both phases after a long initialization phase, the agglomeration model is applied for a dimensionless time interval of $\Delta T^* = 200$ (about 33 flow-throughs). Figure 1 depicts the time history of the accumulated number of inter–particle collisions (N_{col}) and agglomeration processes (N_{agg}) for all three cases showing a linear increase. As expected, the number of collisions does not only depend on the mass loading but also on the particle diameter. Hence, the largest number of collisions is observed for the case *Many* including 81 million small particles. For the case *Large* with the same mass loading but 27 times less particles of $d_p = 12\,\mu$m, the collision number is more than one order of magnitude smaller. As expected, for the case *Small* the number of collisions is drastically lower. This behavior also influences the number of successful agglomeration processes, since inter–particle collisions are the first prerequisite for agglomeration. However, an additional effect is visible in Fig. 1. With respect to the number of collisions the number of agglomerations significantly drops for the case *Large*.

This phenomenon is even more clearly visible when the so-called agglomeration rate defined as the ratio of the number of agglomeration processes to the number of inter–particle collisions is displayed in Fig. 2. At $T^* = 200$ the values for N_{agg}/N_{col} are 1.74×10^{-3}, 1.07×10^{-2} and 1.17×10^{-2} for the cases *Large*, *Small* and *Many*, respectively. Thus, for the two cases with the same particle diameter the agglomeration rate is nearly identical although the total number of collisions and agglomeration processes differ by three orders of magnitude. However, for the case with the large particles the agglomeration rate is about a factor of six smaller. The reason for this

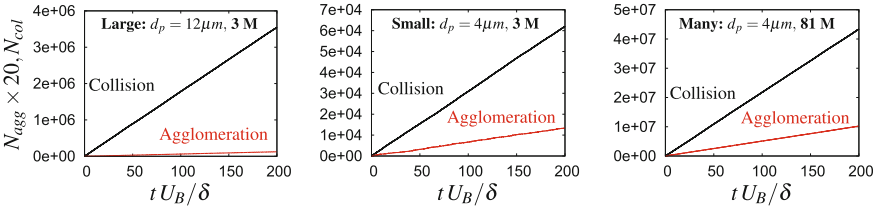

Fig. 1 Time history of the accumulated number of particle–particle collisions N_{col} and agglomeration processes N_{agg}

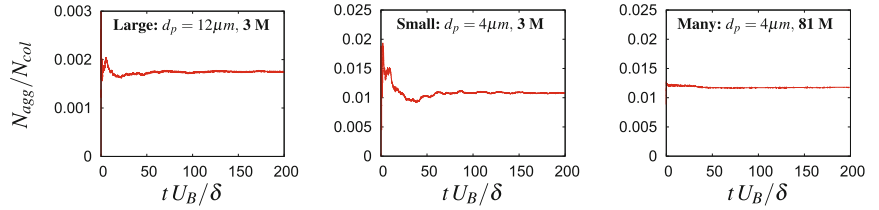

Fig. 2 Time history of the agglomeration rate N_{agg}/N_{col}

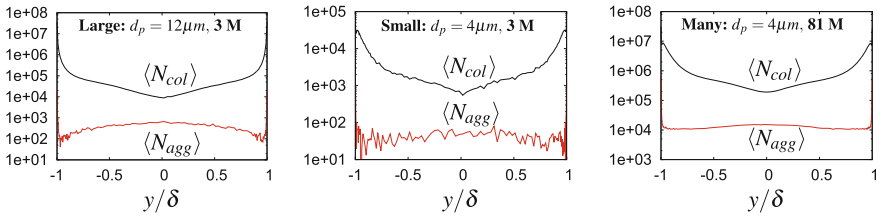

Fig. 3 Averaged number of inter–particle collisions $\langle N_{col} \rangle$ and agglomeration processes $\langle N_{agg} \rangle$

behavior can be attributed to the cohesive impulse, which is inversely proportional to the diameter of the agglomerating particles. Larger cohesive impulses found for the smaller particles can more often overcome the repulsive impulses of the collision and hence the probability of agglomeration increases significantly as visible in Fig. 2.

To get insight into the local distribution of the collision events and agglomeration processes, these quantities are accumulated during the simulation and then averaged in streamwise and spanwise directions. Figure 3 depicts the concentration of the averaged number of inter–particle collisions and agglomeration processes. Obviously, for all three cases most of the collisions and agglomeration processes take place in the near–wall region. On the one hand, the high turbulence level of the fluid and especially of the particles in this region leads to higher numbers of collisions than at other locations. On the other hand, due to turbophoresis the highest particle volume fractions (not shown here) are found in the region closest to the channel walls. Figure 3 also shows that the number of collisions and those leading to agglomeration are low at the channel center due to the low particle velocity fluctuations.

Figure 4 depicts the distribution of the averaged agglomeration rate $\langle N_{agg} \rangle / \langle N_{col} \rangle$ along the channel width. Although the largest numbers of collisions and agglomeration processes are found close to the walls, the agglomeration rate is largest in the center of the channel. That is first of all astonishing but can be explained as follows: The velocity gradient and thus the velocity difference between two particles moving in a similar distance to the wall is smallest in the center of the channel. Additionally, the velocity fluctuations are low in the center. Consequently, the impulsive force of two colliding particles is small and can be easily outplayed by the cohesive force leading to agglomeration. A comparison of the three cases reveals that the distribution of the agglomeration rates of the large and the small particles differ over the

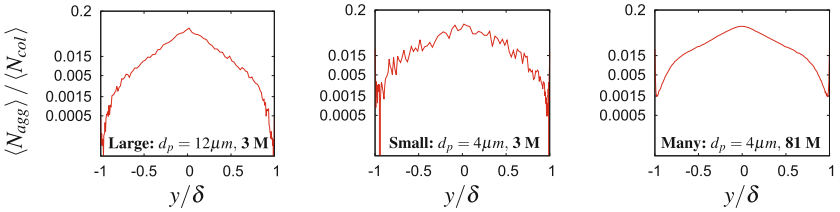

Fig. 4 Distribution of the averaged agglomeration rate $\langle N_{agg} \rangle / \langle N_{col} \rangle$ along the channel width y/δ

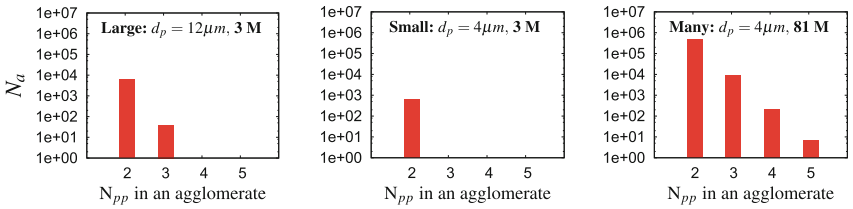

Fig. 5 Size distribution of the arising agglomerates in terms of included primary particles

entire channel width, where the deviations are smallest in the center and increase towards the walls. Overall, that explains the significant difference between the global agglomeration rates found for the small and the large particles mentioned above.

Finally, Fig. 5 depicts a statistic on the number of existing agglomerates of the same type at $T^* = 200$. The sizes of the agglomerates are given in terms of the number of primary particles included in the agglomerate. For the case *Small* solely a few two–particle agglomerates exist. Thus, although the agglomeration rate is relatively high, the probability that these agglomerates collide with primary particles or even other agglomerates is low. Hence, larger agglomerates are unlikely to appear. The situation is completely different for the case *Many*. Here, the agglomeration rate is comparable to the previous case, but due to 27 times more particles of the same size the total number of agglomerates is much higher and that also increases the probability that existing agglomerates collide and agglomerate with primary particles or even other agglomerates building up larger agglomerates consisting of up to 5 primary particles. On the contrary, for the case *Large* solely a much lower number of two– and three–particle agglomerates is observed. The reason is the decrease of the cohesive impulse for increasing particle diameters. That also hinders the formation of larger agglomerates, since the effect is strongly augmented in this case.

References

1. Alletto, M., Breuer, M.: One-way, two-way and four-way coupled LES predictions of a particle-laden turbulent flow at high mass loading downstream of a confined bluff body. Int. J. Multiph. Flow **45**, 70–90 (2012)
2. Breuer, M.: Direkte Numerische Simulation und Large-Eddy Simulation turbulenter Strömungen auf Hochleistungsrechnern. Berichte aus der Strömungstechnik. Shaker Verlag, Aachen, Habilitationsschrift, Universität Erlangen-Nürnberg (2002)
3. Breuer, M., Baytekin, H.T., Matida, E.A.: Prediction of aerosol deposition in 90 degrees bends using LES and an efficient Lagrangian tracking method. J. Aerosol Sci. **37**, 1407–1428 (2006)
4. Breuer, M., Alletto, M.: Efficient simulation of particle-laden turbulent flows with high mass loadings using LES. Int. J. Heat Fluid Flow **35**, 2–12 (2012)
5. Breuer, M., Almohammed, N.: Modeling and simulation of particle agglomeration in turbulent flows using a hard-sphere model with deterministic collision detection and enhanced structure models. Int. J. Multiph. Flow **73**, 171–206 (2015)
6. Kosinski, P., Hoffmann, A.C.: An extension of the hard-sphere particle-particle collision model to study agglomeration. Chem. Eng. Sci. **65**, 3231–3239 (2010)

DNS of the Rising Motion of a Swarm of Bubbles in a Confined Vertical Channel

N. Balcázar, O. Lehmkuhl, J. Castro and A. Oliva

1 Introduction

The motion of bubbles and droplets is ubiquitous in a variety of natural processes and technological applications, such as boiling heat transfer, steam generators of nuclear power plants, unit operations of the chemical engineering (e.g. distillation, absorption columns, bubble reactors), micro-devices, among others [8]. These technological applications have motivated many of the computational, experimental, and theoretical research of bubbly flows, some of them are summarized in [8, 14]. Although those efforts, many challenging problems remain. Therefore, this research aims to contribute to the development of numerical methodologies for simulating bubbly flows.

Due to the advances in computational technology, Direct Numerical Simulation (DNS) of two-phase flows opens the possibility to design non-invasive and controlled numerical experiments [13, 14], albeit computationally demanding. Multiple computational methods have been introduced in the last decades for DNS of multiphase flows, for instance: level set (LS) methods [1, 2, 9–11], volume-of-fluid (VOF) methods [7, 16], coupled VOF-LS methods [5, 12, 17] and front tracking (FT) methods [13, 15]. These approaches treat two-phase flow as a single flow, whereas physical properties are regularized across the interface, using a smoothed indicator function. Furthermore, the interface is captured in the framework of a Eulerian approach (VOF, LS, VOF/LS), or through a Lagrangian approach (FT). While the main idea persists in all these methods, their computational implementation differs between them. A

N. Balcázar (✉) · O. Lehmkuhl · J. Castro · A. Oliva
Heat and Mass Transfer Technological Center (CTTC), Technical University of Catalonia - BarcelonaTECH (UPC), Colom 11, 08222 Terrassa, Spain
e-mail: nestor@cttc.upc.edu

A. Oliva
e-mail: cttc@cttc.upc.edu

D.G.E. Grigoriadis et al. (eds.), *Direct and Large-Eddy Simulation X*,
ERCOFTAC Series 24, https://doi.org/10.1007/978-3-319-63212-4_15

summary of advantages and disadvantages of the methods mentioned above is presented by [6].

For the present research, the concept of multiple marker [2, 5] is combined with the conservative level-set (CLS) method deployed in [1], for simulating the motion of bubble swarms in a vertical channel, without numerical merging of their interfaces. Thus, mass conservation error of standard level-set methods is avoided, while multiple interfaces can be solved within the same control volume, allowing for simulation of bubble collisions.

2 Mathematical Formulation and Numerical Methods

The multiple marker CLS method has been introduced in [2], and here is reviewed for the sake of completeness. The Navier–Stokes equations for the continuous fluid in Ω_c and the dispersed fluid in Ω_d is written as a single set of equations in $\Omega = \Omega_d \cup \Omega_c$, with a singular source term for the surface tension force concentrated at the interface Γ:

$$\frac{\partial(\rho\mathbf{v})}{\partial t} + \nabla\cdot(\rho\mathbf{v}\mathbf{v}) = -\nabla p + \nabla\cdot\mu\left(\nabla\mathbf{v} + (\nabla\mathbf{v})^T\right) + (\rho-\rho_0)\mathbf{g} + \mathbf{f}_\sigma, \qquad \nabla\cdot\mathbf{v} = 0.$$
$$\rho = \rho_d H_d + \rho_c(1-H_d), \quad \mu = \mu_d H_d + \mu_c(1-H_d). \tag{1}$$

where $\mathbf{v}$ denote the velocity, p is the pressure, μ is the dynamic viscosity, ρ is the fluid density, $\mathbf{f}_\sigma$ is the surface tension force, $\mathbf{g}$ is the gravity, subscripts c and d refer to the continuous and dispersed fluids respectively, whereas H_d is the Heaviside step function, which is 1 in Ω_d and 0 elsewhere. Ω is periodic in parallel direction to $\mathbf{g}$ (y-axis), therefore, a force $-\rho_0\mathbf{g}$ is included in the Navier–Stokes equations, taken $\rho_0 = V_\Omega^{-1}\int_\Omega(\rho_d\phi_d + \rho_c(1-\phi_d))\,dV$ [2]. The conservative level-set method (CLS) [9] introduced in [1] is used for interface capturing on unstructured grids. Furthermore, each bubble is represented by a different CLS function. It means that the interface of the ith bubble is captured by the 0.5 iso-contour of the regularized indicator function ϕ_i, where $i = 1, 2, \ldots, n_d$ and n_d is the total number of bubbles [2]. Since the velocity field is incompressible, $\nabla\cdot\mathbf{v} = 0$, the ith interface transport equation is written in the conservative form:

$$\frac{\partial\phi_i}{\partial t} + \nabla\cdot\phi_i\mathbf{v} = 0 \tag{2}$$

Moreover, a re-initialization equation is solved for the steady state to maintain a sharp and constant interface profile of the CLS functions [1, 9]:

$$\frac{\partial\phi_i}{\partial\tau} + \nabla\cdot\phi_i(1-\phi_i)\mathbf{n}_i = \nabla\cdot\varepsilon\nabla\phi_i \tag{3}$$

Geometrical properties of the interfaces, which include normal vectors $\mathbf{n}_i$ and curvatures κ_i, are calculated as follows: $\mathbf{n}_i(\phi_i) = \nabla\phi_i/\|\nabla\phi_i\|$ and $\kappa_i(\phi_i) = -\nabla\cdot\mathbf{n}_i$. The surface tension force is treated by the continuous surface force (CSF) model introduced in [3], and extended to the multiple marker CLS methodology in [2], as follows:

$$\mathbf{f}_\sigma = \sigma\sum_i \kappa_i(\phi_i)\mathbf{n}_i\delta_{\Gamma_i} = \sigma\sum_i \kappa_i(\phi_i)\nabla\phi_i \tag{4}$$

Following the work of [2], fluid properties in Eq. 1 are regularized using a global CLS function $H_d = \phi_d$, defined as $\phi_d = max\{\phi_1, \ldots, \phi_{n_d}\}$, with the aim to prevent numerical instabilities at the interfaces. The governing equations are discretized through the finite-volume method on a collocated unstructured grid arrangement [1]. The reader is referred to [1, 2] for technical details on the discretization of the Navier–Stokes and CLS equations that are beyond the scope of this paper.

3 Numerical Results and Discussion

Validations and verifications of the multiple marker CLS method used in this research have been reported in [1, 2], in the context of 3D rising bubbles [1], drop collision against a fluid-fluid interface [2] and binary droplet collision with bouncing outcome [2]. To the best of the authors' knowledge, there are not previous DNS studies of bubbly flows in vertical pipes using a multiple marker CLS method [2], for the flow regimes explored in this work. For the present research, Ω is a vertical channel of circular cross-section, with size $D_\Omega \times H_\Omega = 5d \times 4d$, where D_Ω is the cylinder diameter, H_Ω is the cylinder height, and d is the bubble diameter. Ω is discretized by 21×10^6 hexahedral volumes, which is equivalent to the grid size $h = d/60$. No-slip boundary condition is used at the rigid wall, whereas the domain is periodic in the y-direction which is aligned to $\mathbf{g}$. As an initial condition, both bubbles and liquid are quiescent, whereas an array of 12 bubbles is placed in the periodic channel following a random pattern. This condition is equivalent to a dilute bubbly flow, with a bubble volume fraction $\alpha_\Omega = 8\%$. Finally, the flow is characterized by the Eotvos number $Eo = gd^2(\rho_c - \rho_d)/\sigma$, Morton number $Mo = g\mu_c^4(\rho_c - \rho_d)/(\rho_c^2\sigma^3)$, density ratio $\eta_\rho = \rho_c/\rho_d$, and viscosity ratio $\eta_\mu = \mu_c/\mu_d$.

Figure 1 illustrates the buoyancy-driven motion of 12 deformable bubbles at the time $t^* = t(g/d)^{1/2} = 14$, for dimensionless parameters $Eo = 3$, $Mo = 1 \times 10^{-6}$, $\eta_\rho = \rho_c/\rho_d = 10$ and $\eta_\mu = \mu_c/\mu_d = 10$. Figure 1a shows the velocity vectors on the plane $x - y$, whereas Fig. 1b and c depict the vorticity generated by both the wall and bubbles, as well as the pressure field on the plane $x - y$, respectively. The vorticity generated by the bubble-wall interactions have opposite signs as shown Fig. 1b. These vorticity interactions reduce the velocity close to the wall, while the pressure increases due to the Bernoulli's effect. Consequently, a repulsion effect directed from the wall to the bubbles is observed. Figure 2 shows the time evolution of

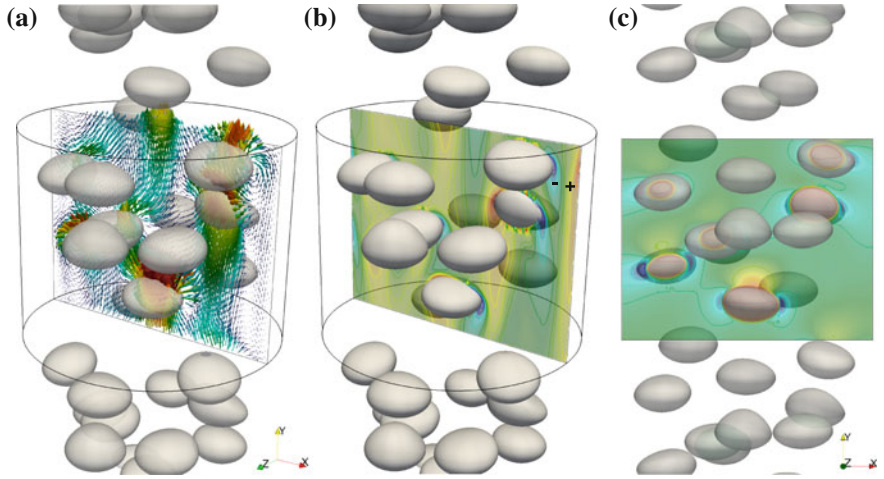

Fig. 1 Bubble swarm (12 bubbles), $Eo = 3$, $M = 1 \times 10^{-6}$, $\eta_\rho = 10$, $\eta_\mu = 10$ at $t^* = t(g/d)^{1/2} = 14$, **a** Velocity vectors on the plane $(y - x)$. **b** Vorticity $(\nabla \times \mathbf{v}) \cdot \mathbf{e}_z$ generated by the wall and bubbles on the plane $x - y$. **c** pressure field

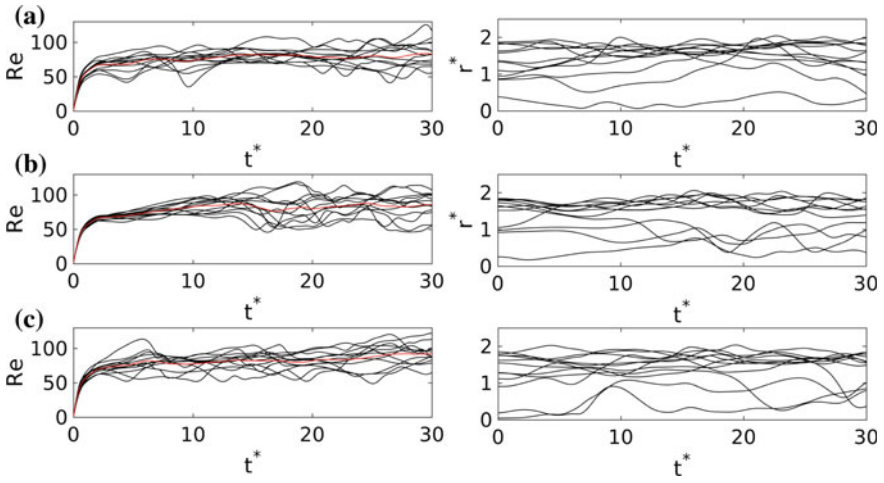

Fig. 2 Time evolution of Reynolds number $Re = \rho_c(\mathbf{v}_b \cdot \mathbf{e}_y)d\mu_c^{-1}$ and radial position $(r^* = r/d)$ of 12 bubbles. $Eo = 3$, $M = 1 \times 10^{-6}$, $\eta_\rho = 10$, $\eta_\mu = 10$. **a** Initial condition 1, **b** Initial condition 2, **c** Initial condition 3. Average Re with *red line*

the Reynolds numbers (Re_i), and radial position ($r^* = r/d$) of the bubble centroids, for three random initial conditions. Here, $Re_i = \rho_c d(\mathbf{v}_i \cdot \mathbf{e}_y)\mu_c^{-1}$ with $\mathbf{v}_i$ defined as the bubble velocity. Due to the wake interactions of the bubbles and wall, the individual rising motion is transient, whereas the average Reynolds number reaches

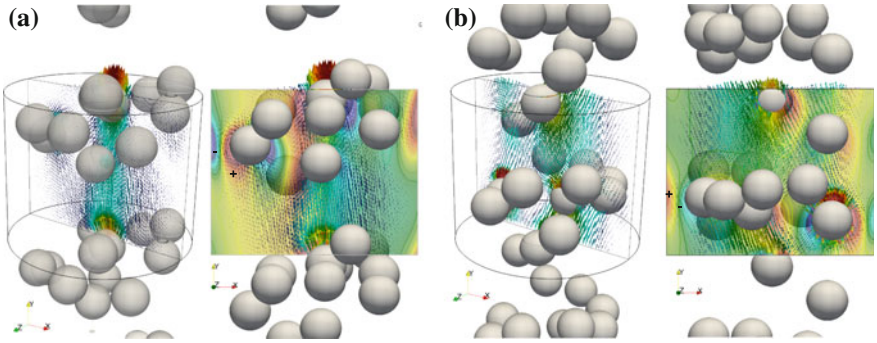

Fig. 3 12 bubbles, $Eo = 0.5$, $M = 1 \times 10^{-6}$, $\eta_\rho = 10$, $\eta_\mu = 10$, **a** Velocity vectors and Vorticity $(\nabla \times \mathbf{v}) \cdot \mathbf{e}_z$ on the plane $x - y$ at $t^* = t(g/d)^{1/2} = 16$. **b** $t^* = 26$

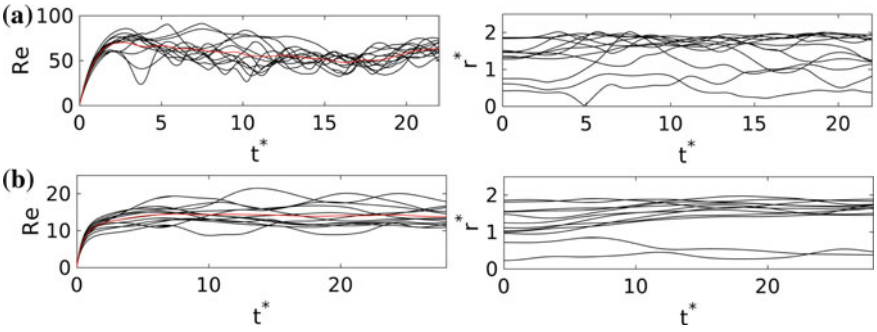

Fig. 4 Time evolution of $Re = \rho_c(\mathbf{v}_b \cdot \mathbf{e}_y)d\mu_c^{-1}$ and $r^* = r/d$ of 12 bubbles. **a** $Eo = 0.5$, $M = 1 \times 10^{-8}$, $\eta_\rho = 10$, $\eta_\mu = 10$. **b** $Eo = 0.5$, $M = 1 \times 10^{-6}$, $\eta_\rho = 10$, $\eta_\mu = 10$. Average Re with *red line*

a quasi-steady state. Figure 2b also shows that bubbles move in radial direction, and tend to concentrate close to the wall; however they do not collide with it.

A second set of experiments is performed for $Eo = 0.5$, $Mo = \{10^{-6}, 10^{-8}\}$, $\eta_\rho = \rho_c/\rho_d = 10$ and $\eta_\mu = \mu_c/\mu_d = 10$. Figure 3 depicts a sequence of images for the motion of a swarm of 12 quasi-spherical bubbles at $(Eo, Mo) = (0.5, 10^{-6})$. Due to the reduction of Eo, the droplet deformation decreases, whereas the set of bubbles tend to form a horizontal arrangement. Figure 4 shows the time evolution of Re_i, and radial coordinates of the bubble centroids. For $(Eo, Mo) = (0.5, 10^{-8})$ the average Reynolds number achieves a steady state, whereas the radial positions of the bubbles indicate a slow migration up to the wall. On the other hand, as the Morton number decrease $(Eo, Mo) = (0.5, 10^{-6})$, the Reynolds number and the radial positions present higher fluctuations, as illustrated in Fig. 4a.

4 Concluding Remarks

Direct simulations of gravity-driven motion of a swarm of bubbles in a vertical pipe have been presented. These results demonstrate the capacity of the multiple marker CLS method introduced in [2] to do long time simulations of bubbly flows, taken into account bubble collisions. For $Eo = 3$, it was observed that deformable bubbles do not collide with the wall, whereas bubble-bubble interactions follow the so-called drafting-kissing-tumbling mechanism, consistently with the front-tracking simulations reported by [4]. Furthermore, the average Re tend to the same value independently of the initial condition. For $Eo = 0.5$, the set of spherical bubbles tends to form horizontal arrangements, similar to bubble rafts. In future work, the present model will be extended to include interfacial heat and mass transfer.

Acknowledgements This work has been financially supported by the *Ministerio de Economía y Competitividad, Secretaría de Estado de Investigación, Desarrollo e Innovación*, Spain (ENE2011-28699, ENE2012-36910). Simulations were performed using the computer time awarded by PRACE 10th Call (project 2014112666) on the supercomputer MareNostrum III based in Barcelona, Spain.

References

1. Balcázar, N., Jofre, L., Lehmkuhl, O., Castro, J., Rigola, J.: A finite-volume/level-set method for simulating two-phase flows on unstructured grids. Int. J. Multiphase Flow **64**, 55–72 (2014)
2. Balcázar, N., Lemhkuhl, O., Rigola, J., Oliva, A.: A multiple marker level-set method for simulation of deformable fluid particles. Int. J. Multiphase Flow **74**, 125–142 (2015)
3. Brackbill, J.U., Kothe, D.B., Zemach, C.: A continuum method for modeling surface tension. J. Comput. Phys. **100**, 335–354 (1992)
4. Bunner, B., Tryggvason, G.: Effect of bubble deformation on the properties of bubbly flows. J. Fluid Mech. **495**, 77–118 (2003)
5. Coyajee, E., Boersma, J.B.: Numerical simulation of drop impact on a liquid-liquid interface with a multiple marker front-capturing method. J. Comput. Phys. **228**, 4444–4467 (2009)
6. Deen, N.G., Van Sint Annaland, M., Kuipers, J.A.M.: Direct numerical simulation of complex multi-fluid flows using a combined front tracking and immersed boundary method. Chem. Eng. Sci. **64**, 2186–2201 (2009)
7. Hirt, C., Nichols, B.: Volume of fluid (VOF) method for the dynamics of free boundary. J. Comput. Phys. **39**, 201–225 (1981)
8. Mudde, R.: Gravity-Driven bubbly flows. Annu. Rev. Fluid Mech. **37**, 393–423 (2005)
9. Olsson, E., Kreiss, G.: A conservative level set method for two phase flow. J. Comput. Phys. **210**, 225–246 (2005)
10. Osher, S., Sethian, J.A.: Fronts propagating with curvature-dependent speed: algorithms based on Hamilton-Jacobi formulations. J. Comput. Phys. **79**, 175–210 (1988)
11. Sussman, M., Smereka, P., Osher, S.: A level set approach for computing solutions to incompressible two-phase flow. J. Comput. Phys. **144**, 146–159 (1994)
12. Sussman, M., Puckett, E.G.: A coupled level set and volume-of-fluid method for computing 3D and axisymmetric incompressible two-phase flows. J. Comput. Phys. **162**, 301–337 (2000)
13. Tryggvason, G., Bunner, B., Esmaeeli, A., Juric, D., Al-Rawahi, N., Tauber, W., Han, J., Nas, S., Jan, Y.-J.: A front-tracking method for the computations of multiphase flow. J. Comput. Phys. **169**, 708–759 (2001)

14. Tryggvason, G., Dabiri, S., Abouhasanzadeh, B., Jaicai, L.: Multiscale considerations in direct numerical simulations of multiphase flows. Phys. Fluids **25**, 031302 (2013)
15. Unverdi, S., Tryggvason, G.: A front-tracking method for viscous, incompressible, multifluid flows. J. Comput. Phys. **100**, 25–37 (1992)
16. Van Sint Annaland, M., Deen, N.G.: Kuipers, J.A.M.: Numerical simulation of gas bubbles behaviour using a three-dimensional volume-of-fluid method. Chem. Eng. Sci. **60**, 2999–3011 (2005)
17. Wang, Z., Yang, J., Koo, B., Stern, F.: A coupled level set and volume-of-fluid method for sharp interface simulation of plunging breaking waves. Int. J. Multiphase Flow **35**, 227–246 (2009)

LES of Cavitating Nozzle and Jet Flows

F. Örley, T. Trummler, M.S. Mihatsch, S.J. Schmidt and S. Hickel

1 Introduction

Accurate, predictive simulations of fuel injection and atomization are a key requirement for meeting future emission standards with optimized combustion processes. Fuel injection is a multi-component two-phase flow that involves complex thermodynamics and fluid dynamics phenomena at different spatial and temporal scales. Atomization and vaporization are influenced by the chamber conditions (pressure, temperature and velocity) and very sensitive on the properties of the fuel jet conditioned by the injector. The highly unsteady and turbulent fuel flow inside the injector involves very energetic secondary flow structures (vortices). Current trends towards higher rail pressures lead directly to larger pressure differences and promote cavitation, that is, the local evaporation and subsequent implosion-like re-condensation of fuel in throttles, at the nozzle inlets, and in vortex cores of the secondary flow structures. Both phenomena are highly sensitive on the injector geometry and strongly affect the primary atomization.

Direct interphase resolving simulations (see [5], e.g.) of practically relevant injection processes are computationally intractable, today and in the next decades. Current state-of-the-art spray simulations therefore use computationally efficient Lagrangian particle tracking (LPT) methods, which do not attempt to capture, by design, the primary breakup of the liquid fuel jet. Engineers can calibrate LPT methods in such a

F. Örley · T. Trummler · M.S. Mihatsch · S.J. Schmidt · S. Hickel
Institute of Aerodynamics and Fluid Mechanics, Technische Universität München, Boltzmannstr. 15, 85748 Garching bei München, Germany

S. Hickel (✉)
Faculty of Aerospace Engineering, Delft University of Technology, Kluyverweg 1, 2629 HS Delft, The Netherlands
e-mail: s.hickel@tudelft.nl; sh@tum.de

D.G.E. Grigoriadis et al. (eds.), *Direct and Large-Eddy Simulation X*,
ERCOFTAC Series 24, https://doi.org/10.1007/978-3-319-63212-4_16

way that they reproduce experimentally determined spray characteristics with sufficient accuracy for full-scale combustion simulations. However, LPT methods are not designed to predict the effect of new injector geometries or modified operating conditions on the spray formation. Computational spray design requires sufficiently detailed numerical methods and physical models that can accurately predict the effects of the nozzle geometry and internal nozzle flow on the primary jet breakup and downstream spray evolution. At the same time, the methods and models must be as simple as possible and have minimum computational resource requirements to enable their application in the engineering design process. The most suitable approach is to combine Eulerian large-eddy simulation (LES) of injector flow and primary jet breakup with LPT for secondary atomization and vaporization. The LES can lead to an improved understanding of the nozzle spray interaction and provide input data for LPT in regions where liquid filaments become too small to be captured on reasonable grids.

We have developed a computationally very efficient method for the LES of injector and jet flows based on an Eulerian description with barotropic phase-equilibrium models. This new model extends our compressible framework for LES of turbulent multiphase fuel flows (fuel in a liquid and gaseous state), see, e.g., Hickel et al. [3] and Egerer et al. [1], and can now additionally capture the mixing of cavitating fuel jets with non-condensable gas [7]. In this paper, we discuss selected results from recently performed LES for the cavitating nozzle and jet flow experiment of Sou et al. [9, 10]. We consider three operating points with different cavitation characteristics and identify the main mechanisms that affect the primary jet breakup.

2 Numerical Model

The fluid considered in this work consists of three components, liquid water (W), water-vapor mixtures (M), and air as non-condensible gas (G). The flow of this fluid is governed by the compressible Navier–Stokes equations, which we discretize with the finite-volume LES model of Hickel et al. [2–4], and an additional transport equation for the mass fraction β_G of the non-condensible gas. We believe that it is essential to consider compressibility of all phases in order to capture cavitation induced wave dynamics. In this fully Eulerian, compressible, finite-volume framework, the transported volume-averaged mass density $\rho = \sum_\Phi \beta_\Phi \rho_\Phi$, is the sum of the volume-averaged densities ρ_Φ of the three components $\Phi = \{M, W, G\}$ weighted by their volume fraction β_Φ. By assuming thermodynamic and mechanical equilibrium, the cell-averaged pressure p can be computed from the equations of state (EOS) of the individual components $\Phi = \{M, W, G\}$ to close the transport equations. In this work, we use barotropic equations of state, leading to $p = p(\rho, \beta_G)$. An isothermal, ideal gas EOS $\rho_G = p/(\mathrm{R}_G T_{ref})$, with $T_{ref} = 293.15$, is used for the non-condensible gas. Liquid water is modeled as an isentropic fluid with a constant speed of sound $c_{liq} = 1482.35$ m/s at the same ambient conditions. The EOS then directly follows from $c_{liq}^2 = \partial p/\partial \rho$ by integration. This simple model is in excellent

agreement with more accurate EOS for $p \leq 200$ bar. The same EOS framework, $\rho = \rho_{s,liq} + (p - p_s)/c^2$, is used to model the formation of vapor and liquid-vapor mixtures. Suitable reference conditions are the saturation pressure p_s and saturation density $\rho_{s,liq}$ of liquid water. For $p > p_s$, i.e., pure liquid water, the speed of sound is $c = c_{liq}$. For $p < p_s$, i.e., two-phase liquid-vapor mixtures, we use a numerical value of $c = c_M = 1$ m/s as conservative upper estimate of the average of the speed of sound between a frozen and an equilibrium isentropic phase change.

This thermodynamic model assumes that phase change is fast compared to the hydrodynamic time scales and in thermodynamic and mechanical equilibrium. That is, there is only one velocity field; gas, liquid and vapor have the same (thermodynamic equilibrium) pressure and surface tension is neglected. The cavitation model has been extensively applied and validated, e.g., for LES of turbulent wall-bounded flows [1, 3], for closing control valves [6], and for the cavitating flow inside a 9-hole Diesel injector during a full injection cycle [8]. For a detailed description of the model we refer to our journal paper [7].

3 Test Setup

Sou et al. [9, 10] have performed a series of experiments for a simplified injector geometry with an optically accessible rectangular nozzle. The experimental operating points have different mean streamwise liquid velocity U_N inside the nozzle, leading to different to cavitation numbers

$$\sigma = \frac{p_\infty - p_s}{0.5 \rho_L U_N^2}, \tag{1}$$

where $p_\infty = 1$ atm $= 1.01325 \times 10^5$ Pa corresponds to the surrounding pressure, and ρ_L is the liquid density. In the following, we discuss LES results for three operation conditions: the first case with $\sigma = 1.27$ shows no cavitation; small cavitation regions are developing inside the nozzle for the second case with $\sigma = 0.78$; and supercavitation and a choked nozzle is observed for $\sigma = 0.65$.

Figure 1 shows the geometry and dimensions of the computational domain, which is meshed with an adaptive, locally refined Cartesian grid with a total number of 43×10^6 cells. The mesh is strongly refined within the boundary layers and the jet region. A large, coarsely meshed plenum is added on the right, which ensures that there are no artificial interactions with outflow boundary conditions, where we impose a constant pressure of $p_\infty = 1$ atm. The inflow boundary condition on the left is a laminar duct flow. Adiabatic no-slip wall boundary conditions are used on the top, bottom and sides.

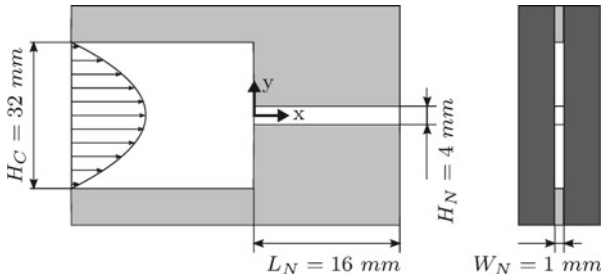

Fig. 1 Geometry of the computational domain. The flow is from left to right. The inflow duct has a width of $W_N = 1\,\text{mm}$ and a height of $H_C = 32\,\text{mm}$. The *rectangular* nozzle has the length $L_N = 16\,\text{mm}$, height $H_N = 4\,\text{mm}$, and width $W_N = 1\,\text{mm}$. The jet flow exits into a very large plenum on the right

4 Results

Instantaneous cavitation structures have been experimentally recorded as transmitted light images, which we compare with visualizations of the spanwise-integrated vapor volume fraction for three corresponding LES simulations in Fig. 2. The agreement between experiment and simulation is very good for the operating points with $\sigma = 1.27$ and $\sigma = 0.78$. The effect of cavitation damping coherent turbulence structures can be observed in Fig. 3. For the third operating point with $\sigma = 0.65$, we observe cavitation in stable vortices that develop from the corners to the nozzle center and strongly damp the turbulence. These vortices are not stable in the experiment, probably due to a high level of inflow perturbations, cf. discussion in Ref. [7].

Cavitation has a strong effect on the liquid-jet breakup; visualizations of the jet structure are presented in Fig. 4. The two lower cavitation numbers, $\sigma = 1.27$ and $\sigma = 0.78$, show a similar jet structure. The supercavitation case, $\sigma = 0.65$, shows a strongly increased jet angle, a much rougher jet surface and small detached liquid ligaments. The collapse of cavitation structures near the nozzle exit induces turbu-

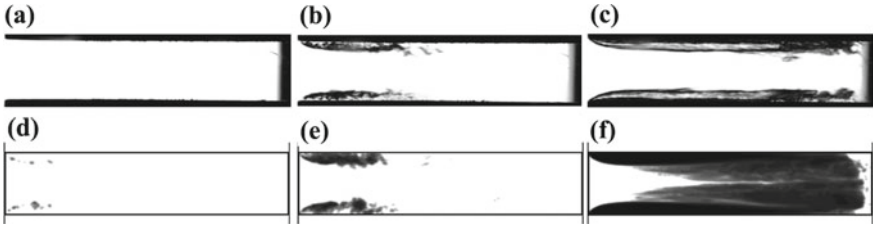

Fig. 2 Effect of cavitation number on vapor structures inside the nozzle for three cavitation numbers: The *top* row shows transmitted-light images from Sou et al. [9] for cavitation number **a** $\sigma = 1.27$, **b** $\sigma = 0.78$, and **c** $\sigma = 0.65$ (reprinted with permission from Elsevier). The *bottom* row (**d/e/f**) shows corresponding contours of the spanwise-averaged vapor fraction from our LES (adopted from Örley et al. [7])

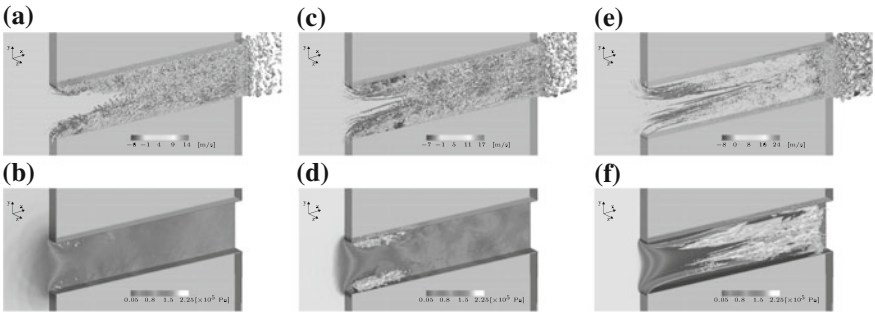

Fig. 3 Effect of cavitation on the turbulent nozzle flow for three cavitation numbers: **a/b** $\sigma = 1.27$, **c/d** $\sigma = 0.78$, and **e/f** $\sigma = 0.65$. The *top* row shows iso-surfaces of $\lambda_2 = -1 \times 10^8\ 1/\mathrm{s}^2$, visualizing instantaneous turbulent flow structures. The *bottom* row shows $\alpha = 0.1$ vapor volume-fraction iso-surfaces at the same instants in time. The walls are colored by pressure contours

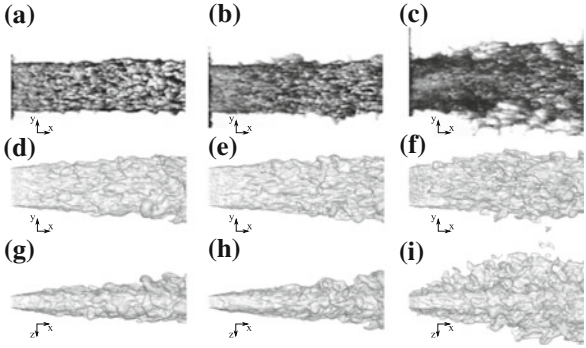

Fig. 4 Effect of cavitation on the liquid-jet breakup for three cavitation numbers: The *top* row shows transmitted-light images from the experiment of Sou et al. [9] for cavitation number **a** $\sigma = 1.27$, **b** $\sigma = 0.78$, and **c** $\sigma = 0.65$ (reprinted with permission from Elsevier). Corresponding snapshots of $\beta_G = 0.99$ iso-surfaces from our simulations are shown in the center (view on x-y plane) and *bottom* row (view on x-z plane)

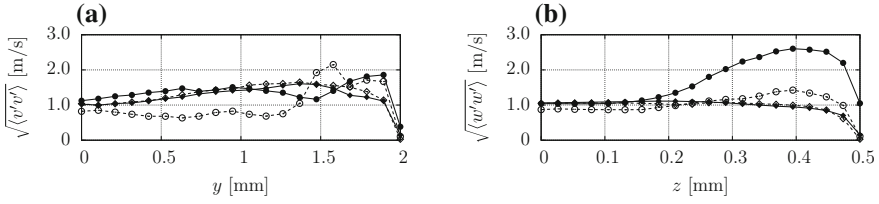

Fig. 5 Wall-normal velocity fluctuations at the nozzle outlet at $x = 15.0$ mm (*empty symbols/dashed lines*) and $x = 16.0$ mm (*filled symbols/solid lines*) for $\sigma = 0.78$ (-◇-) and $\sigma = 0.65$ (-○-)

lent fluctuations and promotes the jet breakup. Figure 5 shows LES results for the wall-normal velocity fluctuations in y- and z-direction, v' and w'. We see that the velocity fluctuations in y-direction, v', increase only slightly near the top wall, Fig. 5a, however, the velocity fluctuations in z-direction, w', increases significantly for the case with the lowest cavitation number $\sigma = 0.65$, see Fig. 5b, with an increase of approximately 150% compared to $\sigma = 0.78$.

5 Summary and Outlook

We have presented an Eulerian three-component two-phase model for the large-eddy simulation (LES) of the cavitating flow within liquid-fuel injectors and the primary breakup of injected fuel jets. The model was applied to a generic nozzle and jet flow at different cavitation numbers and Reynolds numbers, and correctly reproduced experimentally observed cavitation effects. We found that collapse events near the exit plane of the nozzle increase the turbulence level, perturb the liquid-gas interface, and enhance the jet breakup in very good agreement with experimental data. We subsequently identified two additional mechanisms that affect the jet breakup: The collapse of cavitation structures near the nozzle exit can lead to an entrainment of ambient gas into the nozzle, which then changes the effective nozzle cross section and tilts the jet. The collapse cavitation structures inside the jet near the liquid-gas interface leads to ejections of fuel into the ambient air, which increases the jet spreading angle. These mechanisms are discussed in more detail in Örley et al. [7].

Acknowledgements Computing time was granted by the Leibnitz Supercomputing Centre (LRZ) of the Bavarian Academy of Sciences and Humanities.

References

1. Egerer, C.P., Hickel, S., Schmidt, S.J., Adams, N.A.: Large-eddy simulation of turbulent cavitating flow in a micro channel. Phys. Fluids **26**(8), 085102 (2014)
2. Hickel, S., Adams, N.A., Domaradzki, J.A.: An adaptive local deconvolution method for implicit LES. J. Comput. Phys. **213**(1), 413–436 (2006)
3. Hickel, S., Mihatsch, M., Schmidt, S.J.: Implicit large eddy simulation of cavitation in micro channel flows. In: Proceedings of the WIMRC 3rd International Cavitation Forum, University of Warwick, UK (2011)
4. Hickel, S., Egerer, C., Larsson, J.: Subgrid-scale modeling for implicit large eddy simulation of compressible flows and shock-turbulence interaction. Phys. Fluids **26**(10), 106101 (2014)
5. Lauer, E., Hu, X.Y., Hickel, S., Adams, N.A.: Numerical modelling and investigation of symmetric and asymmetric cavitation bubble dynamics. Comput. Fluids **69**, 1–19 (2012)
6. Örley, F., Pasquariello, V., Hickel, S., Adams, N.A.: Cut-element based immersed boundary method for moving geometries in compressible liquid flows with cavitation. J. Comput. Phys. **283**(C), 1–22 (2015)

7. Örley, F., Trummer, T., Hickel, S., Mihatsch, M.S., Schmidt, S.J., Adams, N.A.: Large-eddy simulation of cavitating nozzle flow and primary jet break-up. Phys. Fluids **27**(8), 086101 (2015)
8. Örley, F., Hickel, S., Schmidt, S.J., Adams, N.A.: Large-eddy simulation of turbulent, cavitating flow inside a 9-hole Diesel injector including needle movement. Int. J. Engine Res. **18**, 195–211 (2017)
9. Sou, A., Hosokawa, S., Tomiyama, A.: Effects of cavitation in a nozzle on liquid jet atomization. Int. J. Heat Mass Transf. **50**, 3575–3582 (2007)
10. Sou, A., Tomiyama, A., Hosokawa, S., Nigorikawa, S., Maeda, T.: Cavitation in a two-dimensional nozzle and liquid jet atomization. JSME Int. J. Ser. B, Fluids Thermal Eng. **49**(4), 1253–1259 (2006)

Particle Laden Pipe Flows: Turbulence Modulation

R. Messina, F. Battista, P. Gualtieri and C.M. Casciola

Abstract This work deals with the Direct Numerical Simulation of a particle laden turbulent pipe flow in the two-way coupling regime where the particles back-react on the fluid leading to the so called turbulence modulation. The inter-phase momentum coupling is achieved exploiting a novel approach, namely the Exact Regularized Point Particle (ERPP) method. The turbulence modification is discussed under different coupling conditions. Results show that the flow throughput dimishes implying a global drag increasing in the two-way coupling regime. Velocity fluctuations and the Reynolds shear stress are altered in the viscous sub-layer and in the buffer region when the particles segregate in the near wall region.

1 Introduction

Particle laden turbulent flows occur in many technological applications where the carrier flow is confined by solid walls, e.g. cyclonic separators or pipelines. When the mass flow rate of the disperse phase and of the carrier fluid are comparable a significant inter-phase momentum exchange occurs (two-way coupling regime). Under these conditions a substantial alteration of the turbulent fluctuations and of the dynamics of the transported phase is observed. In such contest a renewed effort is demanded to grasp the new physics introduced by the inter-phase momentum coupling.

The simplest wall bounded turbulent flow is certainly represented by the plane channel flow or by the pipe flow. For instance, in [8] are reported experimental data in a channel documenting the turbulence modification. In wall bounded flows the turbophoresis, i.e. the preferential accumulation in the near wall region, occurs as shown in [7] where the particles are also shown to segregate in the low speed streaks leading to an alteration of the turbulence production mechanisms and to an overall decrease on the mean velocity. Other experimental data deals with the turbulent

R. Messina (✉) · F. Battista · P. Gualtieri · C.M. Casciola
Dipartimento di Ingegneria Meccanica e Aerospaziale, Sapienza Università di Roma,
via Eudossiana 18, 00184 Roma, Italy
e-mail: roberta.messina@uniroma1.it

D.G.E. Grigoriadis et al. (eds.), *Direct and Large-Eddy Simulation X*,
ERCOFTAC Series 24, https://doi.org/10.1007/978-3-319-63212-4_17

pipe flow. The measurements reported in [10] deal with an horizontal pipe flow and show how the turbulence intensity increases close to the center of the pipe while the fluctuations are depleted in the near wall region. Other data concerning the velocity fluctuations, the Reynolds stresses, mean velocity profiles of both carrier and solid phase are reported in [2].

Concerning numerical simulations of wall bounded flows in the two-way coupling regime, only few numerical studies are reported for the pipe flow [11, 12]. The results found by the different authors are pretty scattered. For instance, the data in [13] show that turbulence intensities were increased for small mass loading but the inverse behavior its observed for higher loadings. However the data in [11] show that no alteration of the mean flow is observed in the two-way coupling regime while [14] reports an overall drag reduction due to the presence of the particles.

All the above numerical simulations employed the classical Particle In Cell (PIC) approach to account for the inter-phase momentum coupling [3]. Such approach must be used with care due to numerical issues related to the implementation of the back reaction on the fluid, see e.g. the discussion in [1, 5, 6].

In this contribution we present new results of a particle laden turbulent pipe flow in the two-way coupling regime exploiting a novel momentum coupling method named Exact Regularized Point Particle (ERPP) approach [4] which overcomes the typical difficulties of the PIC.

2 Results and Discussion

In wall bounded particle laden flows the dimensionless parameters which control the particles dynamics and the inter-phase momentum coupling are the Stokes number $St_+ = \tau_p/\tau_+$, defined as the ratio between the Stokes time τ_p and the wall-unit time-scale τ_+, the mass loading ϕ, the number of particles N_p, and the friction Reynolds number Re_*. The dataset is summarized in Table 1. In all cases addressed in this paper the density ratio is fixed to $\rho_p/\rho_f = 50$ and $Re_* = 300$.

Table 1 Summary of the different simulations operated in a pipe flow at Reynolds number $Re_0 = U_0 R_0/\nu = 3000$ where U_0 is the centerline velocity and R_0 is the pipe's radius, corresponding to a friction Reynolds number $Re_* = u_* R_0/\nu = 300$ where u_* is the friction velocity. The Stokes number based on the wall-unit time-scale $\tau_* = \nu/u_*$ is defined as $St_+ = \tau_p/\tau_*$ where τ_p is the Stokes response time. Alternatively $St_0 = \tau_p U_0/R_0$ denotes the Stokes number based on the centerline velocity and the pipe's radius. N_p is the number of particles used to achieve the desired mass loading ϕ

Case	St_+	ϕ	St_0	N_p
A	10	0.15	0.75	130000
B	5	0.3	0.375	750000
C	10	0.3	0.75	265000
D	50	0.3	3.75	24000
E	100	0.3	7.5	8396

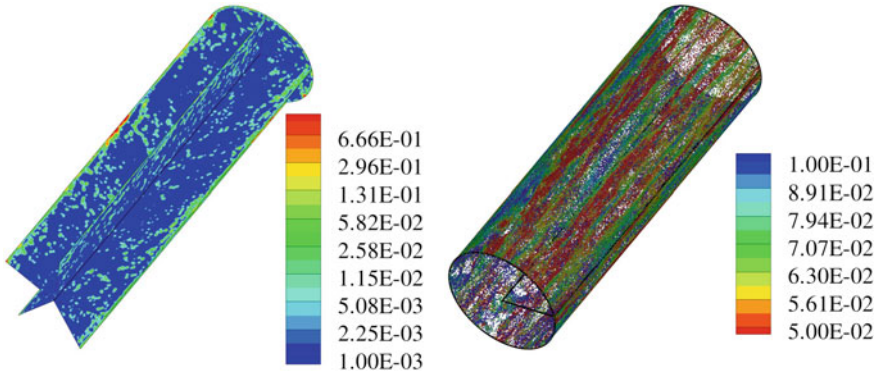

Fig. 1 *Left panel* instantaneous feedback-forcing field on the carrier phase for case B, see Table 1. *Right panel* instantaneous particle configuration in the near wall region corresponding to the snapshot of the *left panel*. The different colors of the particles correspond to the intensity of their axial velocity

Results for case A, see Table 1, are reported in the left panel of Fig. 1 where the contour plot highlights the Eulerian back-reaction field of the particles on the carrier fluid. The colors correspond to the feedback intensity which is strongly imprinted by the instantaneous particle geometrical configuration. In fact, as well known in wall bounded flows, the particles accumulate in the near wall region where the feedback is characterized by an high intensity level when compared with the imposed mean pressure gradient. The right panel shows the instantaneous particles configuration corresponding to the snapshot of the left panel where the particles show the highest concentration in the near wall region. In the figure the different colors of the particles correspond to the intensity of their axial velocity. It is worth noting how the spatial structure of this "field" strongly resembles the streaky structure of the axial fluid velocity fluctuations typical of wall bounded flows.

Figure 2 shows the semi-logarithmic plot of the normalized mean velocity profile in wall units, namely $u^+ = \langle u_z \rangle / u_*$, being u_* the friction velocity, as a function of the normalized wall distance $y^+ = (1 - r)/y_*$ with $y_* = \nu/u_\tau$ the wall unit. In both panels the violet line pertaining to the uncoupled case (no back-reaction on the fluid) is reported for comparisons. The left panel addresses the effect of the mass loading ϕ which is increased from $\phi = 0.15$ (red line) to $\phi = 0.3$ (black line) at a fixed value of the Stokes number $St_+ = 10$, cases A and C of Table 1 respectively. An increase of the mass loading results in a decrease of the flow throughput. In fact, in all the simulations the pressure gradient is imposed and any coupling effect reflects in a modification of the flow rate, i.e. in an overall drag increasing. Specifically, in cases A and C, the flow rate is diminished documenting the drag increasing effect due to the presence of the particles. The right panel of Fig. 2 addresses the effect of the Stokes number ranging from $St_+ = 5$ to $St_+ = 100$ at a fixed mass loading $\phi = 0.3$. Even in these cases, namely cases B-E of Table 1, an overall drag increasing is observed. Note that relatively light particles, i.e. $St_+ = 5$ and $St_+ = 10$ produce the higher increase

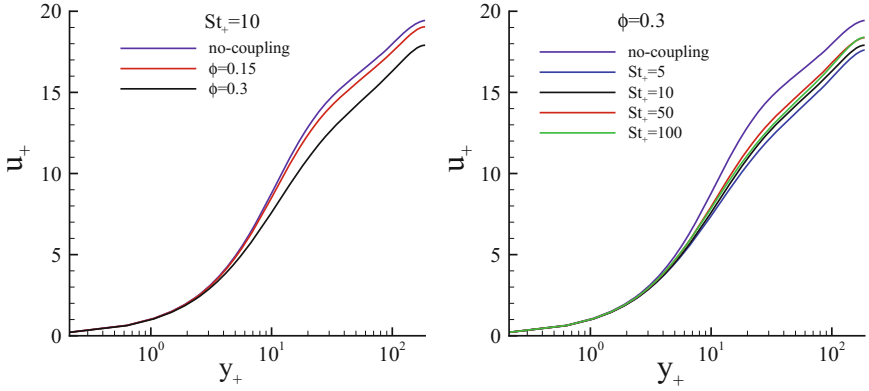

Fig. 2 Semi-logarithmic plot of the normalized mean velocity profile, $u_+ = \langle u \rangle / u_*$ with $u_* = \sqrt{\tau_w/\rho}$ the friction velocity, as a function of the normalized wall distance $y_+ = (1 - r)/y_*$ being $y_* = \nu/u_*$ the wall unit. The *violet line* denotes the uncoupled case (one-way coupling). *Left panel* the Stokes number is fixed to $St_+ = 10$ and the mass load is changed, namely $\phi = 0.15$ (case A, *red line*) and $\phi = 0.30$ (case C, *black line*). *Right panel* effect of the Stokes number at fixed mass loading $\phi = 0.30$, namely $St_+ = 5$ (case B, *light blue line*); $St_+ = 10$ (case C, *black line*); $St_+ = 50$ (case D, *red line*); $St_+ = 100$ (case E, *green line*)

of drag. Noteworthy such particles are characterized by a substantial accumulation in the near wall region.

Figure 3 addresses the fluid velocity fluctuations in comparisons with the uncoupled case (violet line). The left panel shows the normalized axial velocity fluctuations as a function of the wall normal distance for two values of the mass loading $\phi = 0.15$ (red line) and $\phi = 0.3$ (black line) at $St_+ = 10$. Overall the peak intensity is attenuated at higher mass loadings even though fluctuations are augmented in the near wall region (viscous sub-layer) as ϕ is increased. The right panel addresses the effect of the Stokes number $St_+ = 5 \div 100$ at fixed mass loading $\phi = 0.3$. In these cases, irrespective of the Stokes number, all the particles suppress the peak of axial velocity fluctuations even though the particles at $St_+ = 5$ and $St_+ = 10$ are able to augment fluctuations in the viscous sub-layer.

Probably the increase of the velocity is related to a segregation effect.

The analysis of the turbulent velocity fluctuations is completed by the Reynolds shear stresses profiles reported in Fig. 4. In case B (right panel) the Reynolds stress increases in the viscous sub-layer denoting a substantial alteration of the turbulent kinetic energy production mechanisms.

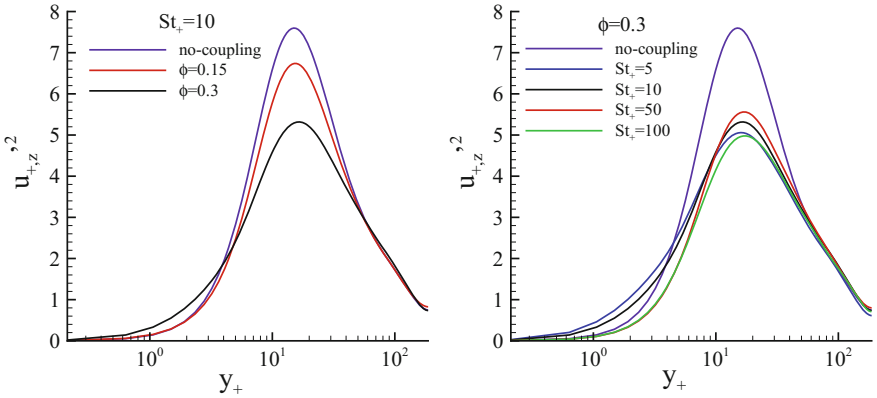

Fig. 3 Semi-logarithmic plot of the normalized axial fluctuation velocity, $u'^2_{+,z} = \langle u'^2_{+,z} \rangle / u_*^2$ with $u_* = \sqrt{\tau_w/\rho}$ the friction velocity, as a function of the normalized wall distance $y_+ = (1-r)y_*$ being $y_* = \nu/u_*$ the wall unit. The *violet line* denotes the uncoupled case (one-way coupling). *Left panel* the Stokes number is fixed to $St_+ = 10$ and the mass load is changed, namely $\phi = 0.15$ (case A, *red line*) and $\phi = 0.30$ (case C, *black line*). *Right panel* effect of the Stokes number at fixed mass loading $\phi = 0.30$, namely $St_+ = 5$ (case B, *light blue line*); $St_+ = 10$ (case C, *black line*); $St_+ = 50$ (case D, *red line*); $St_+ = 100$ (case E, *green line*)

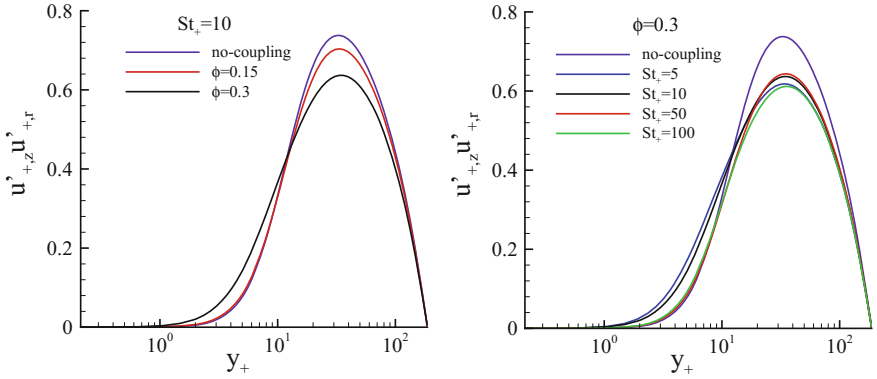

Fig. 4 Semi-logarithmic plot of the normalized Reynolds shear stresses $u'_{+,z}u'_{+,r} = \langle u'_{+,z}u'_{+,r} \rangle / u_*^2$ with $u_* = \sqrt{\tau_w/\rho}$ the friction velocity, as a function of the normalized wall distance $y_+ = (1-r)y_*$ being $y_* = \nu/u_*$ the wall unit. The *violet line* denotes the uncoupled case (one-way coupling). *Left panel* the Stokes number is fixed to $St_+ = 10$ and the mass load is changed, namely $\phi = 0.15$ (case A, *red line*) and $\phi = 0.30$ (case C, *black line*). *Right panel* effect of the Stokes number at fixed mass loading $\phi = 0.30$, namely $St_+ = 5$ (case B, *light blue line*); $St_+ = 10$ (case C, *black line*); $St_+ = 50$ (case D, *red line*); $St_+ = 100$ (case E, *green line*)

3 Final Remarks

In the present paper we have addressed Direct Numerical Simulation data of a two-way coupled particle-laden pipe flow. In the DNS the inter-phase momentum coupling was achieved by means of the ERPP model which overcomes several difficulties which arise in the classical PIC approach. In particular the available data shows that the presence of the particles globally leads to a drag increasing at least for the Stokes number and mass loadings explored in the present calculations. Concerning velocity fluctuations these are attenuated in presence of significative back-reaction of the particles on the fluid. This effect is probably due to their relatively high concentration in the near the wall.

References

1. Balachandar, S., Eaton, J.K.: Turbulent dispersed multiphase flow. Ann. Rev. Fluid Mech. **42** (2010)
2. Caraman, N., Bore, J., Simonin, O.: Effect of collisions on the dispersed phase fluctuation in a dilute tube flow: experimental and theoretical analysis. Phys. Fluids (1994-present), **15**(12), 3602–3612 (2003)
3. Crowe, C.T., Sharma, M.P., Stock, D.E.: The particle-source in cell method for gas droplet flow. J. Fluid Eng. **99** (1977)
4. Gaualtieri, P., Picano, F., Sardina, G., Casciola, C.M.: Exact regularized point particle method for multi-phase flows in the two-way coupling regime. J. Fluid Mech. http://arxiv.org/abs/1405.6969 (2015) (accepted for publication)
5. Gualtieri, P., Picano, F., Sardina, G., Casciola, C.M.: Clustering and turbulence modulation in particle-laden shear flow. J. Fluid Mech. **715** (2013)
6. Jenny, P., Roekaerts, D., Beishuizen, N.: Modeling of turbulent dilute spray combustion. Prog. Energy Combust, Sci (2012)
7. Kaftori, D., Hetsroni, G., Banerjee, S.: The effect of particles on wall turbulence. Int. J. Multiph. Flow **24**, 359–386 (1998)
8. Kulick, J.D., Fessler, J.R., Eaton, J.K.: Particle response and turbulence modification in fully developed channel flow. J. Fluid Mech. **277**, 109–134 (1994)
9. Lee, J., Lee, C.: Modification of particle-laden near-wall turbulence: effect of Stokes number. arXiv preprint arXiv:1409.1339 (2014)
10. Ljus, C., Bert, J., Alf-Erik, A.: Turbulence modification by particles in a horizontal pipe flow. Int. J. Multiph. Flow **28**, 1075–1090 (2002)
11. Rani, S., Winkler, C.M., Vanka, S.P.: Numerical simulations of turbulence modulation by dense particles in a fully developed pipe flow. Powder Technol. **141**, 80–99 (2004)
12. Vreman, A.W.: Turbulence characteristics of particle-laden pipe flow. J. Fluid Mech. **584**, 235–279 (2007)
13. Yiming, L., McLaughlin, J.B., Kontomaris, K., Portela, L.: Numerical simulation of particle-laden turbulent channel flow. Phys. Fluids **13**, 2957–29677 (2001)
14. Zhao, L.H., Andersson, H.I., Gillissen, J.J.: Turbulence modulation and drag reduction by spherical particles. Phys. Fluids **22**, 081702 (2010)

Part IV
LES Fundamentals

Physical Scaling of Numerical Dissipation for LES

T. Dairay, E. Lamballais, S. Laizet and J.C. Vassilicos

1 Introduction

In this work, we are interested in an alternative way to perform LES using a numerical substitute of a subgrid-scale model with a calibration based on physical inputs. This approach can be seen as falling within Implicit LES (ILES) because it is based on an artificial dissipation operator where the numerical error is the source of the regularization. However, the purpose here is to control explicitly this error to enable it to play the role of an explicit subgrid-scale model.

The most popular ILES are based on differentiation operators that introduce artificial dissipation in order to mimic the dissipative mechanisms of the subgrid-scales. For this ILES family, the term "implicit" can be understood in the sense that the actual equations to be solved are the Navier–Stokes equations without any extra explicit modelling as in a DNS. In practice, the numerical dissipation provided by some specific schemes (typically upwind schemes) can act at small-scales in a manner similar to an explicit subgrid-scale model. This favourable property, sometimes referred to as the "convenient conspiracy", does not hold systematically because a scheme that provides an acceptable artificial dissipation at one spatial resolution can become

T. Dairay · E. Lamballais (✉)
Institute PPRIME, Department of Fluid Flow, Heat Transfer and Combustion,
CNRS - Université de Poitiers ENSMA, Téléport 2, Boulevard Marie et Pierre Curie,
BP 30179, 86962 Futuroscope Chasseneuil Cedex, France
e-mail: eric.lamballais@univ-poitiers.fr

T. Dairay
e-mail: thibault.dairay@univ-poitiers.fr

S. Laizet · J.C. Vassilicos
Turbulence, Mixing and Flow Control Group, Department of Aeronautics,
Imperial College London, London SW7 2AZ, UK
e-mail: s.laizet@imperial.ac.uk

J.C. Vassilicos
e-mail: j.c.vassilicos@imperial.ac.uk

D.G.E. Grigoriadis et al. (eds.), *Direct and Large-Eddy Simulation X*,
ERCOFTAC Series 24, https://doi.org/10.1007/978-3-319-63212-4_18

sub- or over-dissipative at another resolution. That is why some authors have developed different versions of their schemes depending on their ILES resolution. The goal of the present study is to examine how this weakness can be overcome through flexible and accurate numerics with physical inputs.

2 General Methodology and Goal

Here, we present an ILES modelling where the artificial dissipation is introduced by the molecular dissipation operator, namely the viscous term [5]. As for standard ILES, the source of artificial dissipation is the numerical error. However, an originality of the approach is that it is based on high-order centred finite-difference schemes for the computation of the second derivatives in the Navier–Stokes equations. Importantly, these schemes are implicit in space (they are often referred to as "compact", see [6] for a comprehensive presentation) thereby enabling flexibility for the control of their artificial dissipative features. It can be easily shown that the use of a finite difference scheme with a modified square wavenumber k'' that overestimates its exact counterpart k^2 is equivalent to the introduction of a spectral viscosity $\nu_s(k)$ given by $\nu_s(k) = \nu\frac{k''(k)-k^2}{k^2}$ where ν is the kinematic molecular viscosity. The flexibility to shape k'' makes it possible to prescribe any value ν_0 to the spectral viscosity at the cutoff wavenumber $k_c = \pi/\Delta x$ while at the same time controlling the kernel $\nu_s(k)/\nu_0$ (Δx is the mesh size). For instance, [5] have used this flexibility to mimic the Spectral Vanishing Viscosity (SVV) or hyperviscous kernels while ensuring high-order accuracy.

The first calculations based on this approach have been successful for DNS as well as for LES. For the former, a moderate value of ν_0 with a very selective kernel concentrated near k_c is helpful to control spurious oscillations due to aliasing. For the latter, after the successful calculation of a turbulent channel flow by [2, 5] have shown that this kind of implicit subgrid-modelling drastically improves the prediction of heat transfer for an impinging jet flow compared to eddy viscosity subgrid-scale closures such as the dynamic Smagorinsky or the WALE models.

Even if these first LES results are encouraging, the flexibility in the prescription of $\nu_s(k)$ can also be seen as a drawback because of the arbitrariness introduced by the need to chose both ν_0 and the kernel $\nu_s(k)/\nu_0$ appropriately case by case. The aim of this study is therefore to provide ways to constrain this choice by appropriate physical scaling of the numerical dissipation. To predict the value of ν_0 required for a given LES spatial resolution, we propose an approach based on the solution of a Pao-like equation. The method is validated on DNS and LES of the 3D Taylor-Green vortex problem.

3 Pao-like Solution

In the framework of homogeneous and isotropic turbulence, and assuming that a spectral range exists where the energy spectrum is stationary,[1] the Lin equation leads to

$$T(k) = 2\nu k^2 E(k) \tag{1}$$

where $E(k)$ is the kinetic energy spectrum whereas $T(k)$ is the transfer term related to the energy flux $\Pi(k)$ by $-d\Pi(k)/dk = T(k)$. As in the Kolmogorov theory, this flux can be assumed to depend only on the dissipation ε and the wavenumber k. Then, for dimensional reasons, Eq. (1) becomes

$$\frac{d}{dk}\left(1/C_k \varepsilon^{1/3} k^{5/3} E(k)\right) + 2\nu k^2 E(k) = 0 \tag{2}$$

with the analytical solution

$$E(k) = C_k \varepsilon^{2/3} k^{-5/3} \exp\left(-3/2 C_k \left(k/k_\eta\right)^{4/3}\right) \tag{3}$$

where $k_\eta = \varepsilon^{1/4}/\nu^{3/4}$ is the Kolmogorov wavenumber (see [7] for more details).

As a tool to predict the spectrum that should be obtained by the present type of LES, a similar approach can be used by replacing k^2 on the right hand side of Eq. (2) with k''. Then, the resulting differential equation can be solved numerically in a spectral range between a wavenumber k_s (below which $\nu_s(k)$ is assumed to vanish) and infinity. This computationally inexpensive solution can be done for any value of ν_0 leading to a set of Pao-like solutions.

To illustrate the behaviour of such Pao-like solutions, the case $k_\eta/k_c = 5$ is considered with a SVV-like kernel (plotted in Fig. 2-left). First, it is interesting to investigate how the increase of ν_0/ν modifies the kinetic energy spectrum and its related dissipation spectrum (including the numerical contribution). Six kinetic energy spectra are presented in Fig. 1-left. The reference spectrum corresponds to the case $\nu_0/\nu = 0$ for which the Pao spectrum (3) is virtually recovered. Then, ν_0/ν is increased by steps of 8 up to the value 48. As ν_0/ν is increased, the overall range of the predicted spectrum is reduced. For the highest values of ν_0/ν, this reduction corresponds to a strong fall at the cutoff wavenumber $k_c = 8k_s$ considered for this example. The resulting low levels of $E(k_c)$ suggest that the corresponding LES could be done using a mesh such as $\Delta x = \pi/k_c$. For instance, to have the same kinetic energy at k_c as at k_η for the reference DNS (for which $\nu_0/\nu = 0$), a simple dichotomic search provides the value $\nu_0/\nu = 42.37$. Using the Pao-like solver, this dichotomic search ensuring $E_{LES}(k_c) = E_{DNS}(k_\eta)$ can be performed extensively for any ratio k_η/k_c. Figure 2-right presents the resulting behaviour for the range $1 \leq k_\eta/k_c \leq 30$. As expected, the

[1] Note, however, that evidence has been accumulating over the past 8 years which shows that there is no significant such range except perhaps in the directly viscous dissipation range, see [3] and references therein, but the present work is only a starting point which will evolve accordingly.

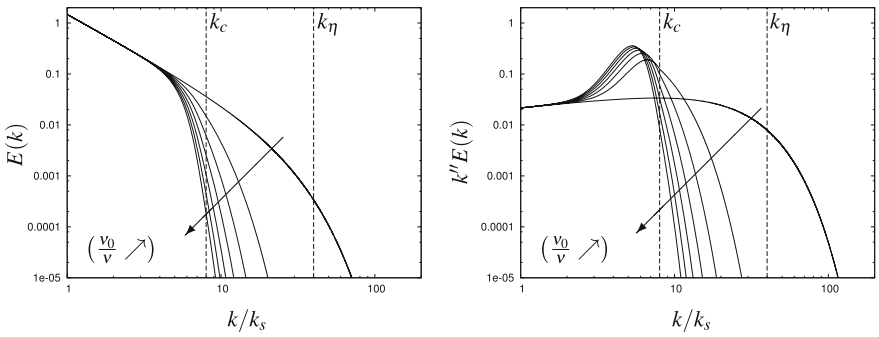

Fig. 1 Kinetic energy $E(k)$ and dissipation $k''E(k)$ spectra obtained by solving the Pao-like equation from $\nu_0/\nu = 0$ (reference Pao solution) to $\nu_0/\nu = 48$ by steps of 8

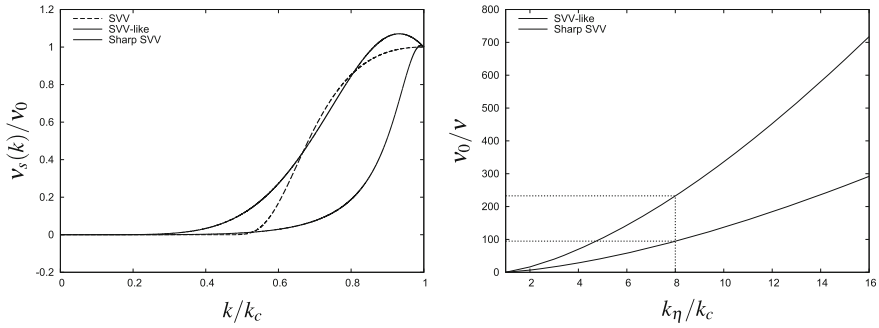

Fig. 2 *Left* SVV-like and Sharp SVV kernels. *Right* evolution of ν_0/ν with k_η/k_c to ensure $E_{LES}(k_c) = E_{DNS}(k_\eta)$ as predicted by the Pao-like solution

Sharp SVV kernel (plotted in Fig. 2-left) requires to use significantly higher values of ν_0/ν (see Fig. 2-right).

The corresponding dissipation spectra (Fig. 1-right) clearly show how the use of high-order numerical viscosity can concentrate an extra-dissipation near k_c in order to compensate the lack of dissipation for $k > k_c$ (which could not be taken into account using a discretization based on mesh size with $\Delta x = \pi/k_c$).

4 DNS and LES Results

The suitability of the present prediction of ν_0/ν is examined by performing LES of the 3D Taylor-Green vortex problem while using filtered DNS results as reference for comparison (case "DNS$_f$"). Both DNS and LES are carried out using the high-order flow solver "Incompact3d" which is based on sixth-order finite-difference schemes [4]. For the sake of clarity, only the Reynolds number $Re = 5000$ is pre-

sented here. For this fairly high value, accurate DNS results can be obtained with a regular Cartesian mesh of 1280^3 mesh odes on a triperiodic domain $2\pi^3$. For the present calculations, using the symmetries of the problem, only the flow inside the impermeable box π^3 is explicitly calculated with a reduction of the computational cost by a factor 8. Then, comparable LES are performed using 160^3 mesh nodes with $k_\eta/k_c = 8$ which represents a reduction of the computational cost by a factor of 4096 by comparison with DNS. The Pao-like solver provides the values $\nu_0/\nu \approx 95$ and 232 for the SVV-like and Sharp SVV kernels respectively (see Fig. 2-right).

When these values are used in the present type of LES, satisfactory results are obtained with a clear improvement compared to a calculation performed at the same spatial resolution but free from subgrid-scale modelling and artificial dissipation. This improvement can be illustrated by considering the time evolution of the kinetic energy E_k and its dissipation $\varepsilon = -dE_k/dt$ (that includes the numerical contribution) as presented in Fig. 3 (left). The filtered DNS data are obtained after the application of the filter $T_f(k) = \sqrt{E_{LES}(k)/E_{DNS}(k)}$ in the Fourier space where $E_{DNS}(k)$ is the Pao kinetic energy spectrum whereas $E_{LES}(k)$ is its Pao-like counterpart for a given set of ν_0 and kernel $\nu_s(k)/\nu_0$. Here, for the sake of brevity, only the Sharp SVV kernel is considered with $\nu_0/\nu = 232$.

The calculation free from extra dissipation, referred to as "LES no model" case, means that a conventional compact finite difference scheme is used to compute the viscous term. Interestingly, although this configuration is a priori sub-dissipative, an over-dissipative behaviour seems to be observed a posteriori throughout the calculation as shown in Fig. 3 (left). A close examination of the time evolution of E_k and ε reveals that in fact, the "LES no model" case is very slightly sub-dissipative just a the beginning of the simulation. This lack of dissipation is responsible of a pile-up of energy near the cutoff wave number k_c at the early transition. As a direct consequence of this pile-up, the dissipation is overestimated despite the nature of the numerical operator that is essentially sub-dissipative. At this coarse resolution, this erroneous dissipation eventually overdamps E_k for the rest of the calculation without being able to suppress the spurious energy at small scale. This behaviour is a very simple illustration of the contradictory conclusions that can be provided by a priori and a posteriori analysis of the influence of any subgrid-scale model.

Then, when the second derivatives of the Navier–Stokes equations are computed using an over-dissipative scheme with the level of numerical viscosity predicted by the Pao-like solver ("LES $\nu_0/\nu = 232$" case), the agreement with the filtered DNS is clearly improved as shown in Fig. 3 (left). The a priori/a posteriori paradox is recovered in reverse, namely the extra dissipation is found to slow down the time decrease of E_k by comparison with the "LES no model" case while matching remarkably well the "DNS$_f$" data. This matching suggests that the artificial dissipation provided by the choice $\nu_0/\nu = 232$ is able to compensate consistently the small-scale dissipation that is missed by the coarse discretization.

To better understand the role played by the artificial viscosity, it is insightful to consider the time evolution of the kinetic energy spectrum $E(k, t)$. For the "LES no model", from the start of the early transition until the end of the calculation, an unrealistic pile-up of energy can be observed in the vicinity of the cutoff wave num-

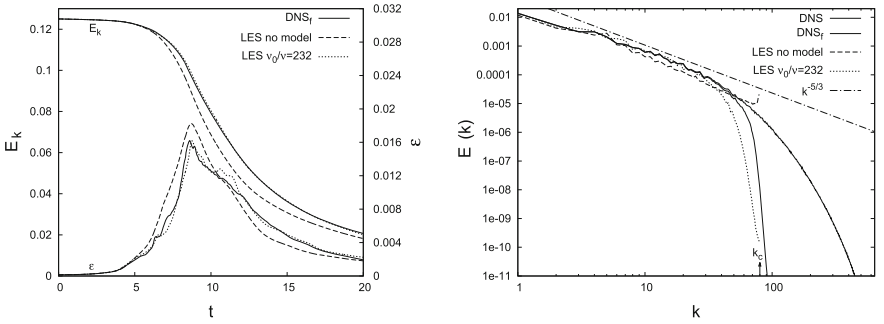

Fig. 3 *Left* time evolution of the kinetic energy E_k and its dissipation ε. *Right* 1D spectra $E(k, t)$ at $t = 14$

ber k_c. This production of small-scale oscillations leads to very unrealistic vortical structures subjected to a spurious background noise in instantaneous visualisations of, for instance, the enstrophy and the Q-criterion (not shown for reasons of space). Conversely, the use of a calibrated numerical viscosity for the "LES $\nu_0/\nu = 232$" case enables a strong decrease of $E(k, t)$ at $k \approx k_c$ throughout the simulation. These behaviours are illustrated in Fig. 3 (right) for spectra obtained at $t = 14$, a time for which the turbulence is fully developed. The spectral range where the artificial dissipation is active can be easily guessed by comparison to the non-filtered DNS results. The resulting damping of the small-scale energy ensures the regularity of the LES solution (free from spurious oscillations) as for its numerically converged DNS counterpart computed at high resolution. This feature enables the development of realistic vortices that compare very well, at least qualitatively, to those associated with the filtered DNS results (not shown for reasons of space).

It can be noticed that the damping of the kinetic energy near k_c is stronger for the "LES $\nu_0/\nu = 232$" case compared to the "DNS$_f$" data. This discrepancy means that the Pao-like solver cannot predict exactly the full dissipation as it is actually computed in the LES. The assumption of turbulence in equilibrium to simplify the Lin equation can be suspected to be responsible of this inability. Another reason could be connected to the discretization errors in the convective terms that are not taken into account. The improvement of the present Pao-like model is in progress, in particular by taking into account the pervasive non-equilibrium nature of the turbulence. The potential benefit of non-vanishing spectral viscosity as in the subgrid-scale model of [1] is also under investigation.

Acknowledgements This work was performed using HPC resources from GENCI-TGCC/IDRIS (Grant 2014-2a0912).

References

1. Chollet, J.P., Lesieur, M.: J. Atmos. Sci. **38**, 2747–2757 (1981)
2. Dairay, T., Fortuné, V., Lamballais, E., Brizzi, L.E.: Int. J. Heat Fluid Flow **50**, 177–187 (2014)
3. Goto, S., Vassilicos, J.C.: Phys. Lett. A **379**(16–17), 1144–1148 (2015)
4. Laizet, S., Lamballais, E.: J. Comput. Phys. **228**, 5989–6015 (2009)
5. Lamballais, E., Fortuné, V., Laizet, S.: J. Comput. Phys. **230**, 3270–3275 (2011)
6. Lele, S.K.: J. Comput. Phys. **103**, 16–42 (1992)
7. Pao, Y.-H.: Phys. Fluids **8**(6), 1063–1075 (1965)

A Discrete Scale-Truncation Model for LES

Roel Verstappen

1 A Template for LES

To model the dynamics of the larger eddies in turbulent flows, the Navier–Stokes (NS) equations are written as

$$\partial_t u \,+\, \nabla\cdot\overline{(\overline{u}\otimes\overline{u})} \,-\, \nu\,\nabla\cdot\nabla u \,+\, \nabla p \,=\, \nabla\cdot\Big(\overline{(\overline{u}\otimes\overline{u})} - u\otimes u\Big) \tag{1}$$

where $\overline{u}$ denotes a filtered velocity field. When the convective nonlinearity is discretized in space, the low-pass characteristics of the discrete operator effectively act as a filter. This numeric filter will inevitably interact with the explicit filter in Eq. (1). So, at the discrete level, the effective filter is not so clear, unless we use a Schumann filter [1]. Therefore, we take $\overline{u} = \frac{1}{|\Omega_h|}\int_{\Omega_h} u(x,t)\,dx$, where Ω_h denotes the computational cell. So as in Schumann's approach the spatial discretization of the convective term defines the filter. Here we use a second-order, symmetry-preserving finite-volume method [2]. Replacing the right-hand side by a 'model' yields

$$\partial_t v \,+\, \nabla\cdot\overline{(\overline{v}\otimes\overline{v})} \,-\, \nu\,\nabla\cdot\nabla v \,+\, \nabla\pi \,=\, -\nabla\cdot\overline{\tau(\overline{v})} \tag{2}$$

where the variable name is changed from u to v (and p to π) to stress that the solution of Eq. (2) differs from that of Eq. (1), because the model is not exact. This is crucial since fine details must be lost. Basically, the idea is that the modulated field v approximates the large scales of motion in the NS-solution u, whereas the tail of the modulated spectrum falls of much faster than the NS-spectrum. This idea can be formalized by introducing a second filter. If we choose

R. Verstappen (✉)
Johann Bernoulli Institute for Mathematics and Computer Science,
University of Groningen, Groningen, The Netherlands
e-mail: r.w.c.p.verstappen@rug.nl

D.G.E. Grigoriadis et al. (eds.), *Direct and Large-Eddy Simulation X*,
ERCOFTAC Series 24, https://doi.org/10.1007/978-3-319-63212-4_19

$$\widetilde{v} = \frac{1}{|\Omega_\delta|} \int_{\Omega_\delta} v(x,t)\, dx, \tag{3}$$

for that, the larger eddies are described by the part of the fluid motion with velocity $\widetilde{v}$. Notice that the length h of the (grid-)filter is supposed to be less than the length δ of the box filter (3). The model is chosen properly if the associated box-filtered modulated velocity $\widetilde{v}$ approximates the box-filtered NS-solution $\widetilde{u}$, i.e. τ is to be chosen such that $\widetilde{v} \approx \widetilde{u}$. The residual $v - \widetilde{v}$ does not have any physical significance; it represents the error resulting from the shortening of the NS-spectrum. The right-hand side of Eq. (1) does not dissipate energy, but transfers it (on average) towards smaller scales of motion that can dissipate energy at a higher rate. Here, we do not try to model the transport itself, but only just the net effect thereof. So the model should strengthen the dissipation (without producing smaller scales of motion, of course). To that end, we use the relaxation model introduced by Stolz et al. [3]. They used the relaxation

$$\nabla \cdot \tau(v) \;=\; \chi(v - \widetilde{v}) \tag{4}$$

It has the attractive feature that no (explicit) use is made of a differential operator. In fact, the tensor τ is defined through an auxiliary variable w, that is $\tau(v) = -2\chi S(w)$, where $v - \widetilde{v} = -\nabla \cdot \nabla w$. Indeed, $\nabla \cdot \tau(v) = \nabla \cdot (-2\chi S(w)) = -\chi \nabla \cdot \nabla w = \chi(v - \widetilde{v})$. Furthermore, it may be noted that in lowest order $v - \widetilde{v} \approx -(\delta^2/24)\nabla \cdot \nabla \widetilde{v}$.

2 Scale-Truncation Condition

The residual of the box filter (3), $v' = v - \widetilde{v}$, consists of scales of size smaller than δ. The closure model must be designed so that these small scales are dynamically insignificant. By applying the residual operator to Eq. (2) we find the equation for v' and from that we obtain the evolution of the $L^2(\Omega_\delta)$ norm of the small-scale field:

$$\frac{\mathrm{d}}{\mathrm{d}t} \int_{\Omega_\delta} \frac{1}{2} ||v'||^2\, dx \;=\; \int_{\Omega_\delta} \left(\nu \nabla \cdot \nabla v' \;-\; \nabla \pi' \right) \cdot v'\, dx \;-\; \int_{\Omega_\delta} \left(\nabla \cdot (\overline{\overline{v} \otimes \overline{v}}) \;+\; \nabla \cdot \overline{\tau} \right)' \cdot v'\, dx$$

The two contributions to the last integral represent the energy that is transfered from the box-filtered velocity field $\widetilde{v}$ to the residual field v' and the eddy dissipation resulting from the closure model, respectively. Equation (2) does not produce residual scales if the eddy dissipation balances the energy transfer at the scale set by the box filter. Now if the closure model is taken so that the production and eddy dissipation terms cancel each other out, then

$$\frac{\mathrm{d}}{\mathrm{d}t} \int_{\Omega_\delta} \frac{1}{2} ||v'||^2\, dx \;=\; \int_{\Omega_\delta} \left(\nu \nabla \cdot \nabla v' \;-\; \nabla \pi' \right) \cdot v'\, dx \tag{5}$$

and the evolution of the energy of v' does not depend on $\widetilde{v}$. Stated otherwise, the energy of residual scales dissipates at a natural rate, without any forcing mechanism involving $\widetilde{v}$, i.e., scales larger than δ. In this way, the scales $< \delta$ are separated from scales $\geq \delta$. Finally it may be noted that the pressure π' appears in Eq. (5), since the residual field v' is solenoidal.

Our guiding principle is that closure model keeps the residual field $v' = v - \widetilde{v}$ from becoming dynamically significant if the energy of the residual field is controlled by the action of viscosity, as described by Eq. (5). Therefore the production of small scales of motion it to be balanced by the modelled dissipation:

$$\int_{\Omega_\delta} v' \cdot (\nabla \cdot \overline{\tau(\overline{v})})' \, dx = -\int_{\Omega_\delta} v' \cdot (\nabla \cdot \overline{(\overline{v} \otimes \overline{v})})' \, dx \tag{6}$$

By substituting the relaxation model (4) into Eq. (6), we can obtain an expression for the relaxation parameter χ, that includes the residual velocity field v'. Consequently, this approach will require a fair approximation of v'. Therefore the width δ of filter (3) should be quite a bit larger than the width h of the grid. This is not very attractive from efficiency considerations. Indeed, the residual velocity v' is not dynamically significant; hence we do not want to spend large computational resources on it. In summary we are in the following dilemma: v' need be computed fairly accurate to satisfy the scale-truncation condition (6), whereas we aim to focus our computational resources on the 'relevant' part $\widetilde{v}$. Poincaré offers a way out:

3 Poincaré

In this section, Poincaré's inequality is used to develop the dissipation-production balance (6) without explicitly referring to the residual field v'. Poincaré's inequality states that the $L^2(\Omega_\delta)$ norm of the residual field v' is bounded by a constant C_δ (independent of v) times the $L^2(\Omega_\delta)$ norm of ∇v:

$$\int_{\Omega_\delta} ||v - \widetilde{v}||^2 \, dx \;\leq\; C_\delta \int_{\Omega_\delta} ||\nabla v||^2 \, dx \tag{7}$$

Consequently, we can confine the dynamically significant part of the motion to scales $\geq \delta$ by introducing a suitable amount of dissipation in the dynamics of the velocity gradient. Here we aim to convert the dissipative condition (5) to the upper bound set by the Poincaré inequality (7). According to Eq. (2) the $L^2(\Omega_\delta)$ norm of ∇v is governed by

$$\begin{aligned} \frac{\mathrm{d}}{\mathrm{d}t} \int_{\Omega_\delta} \frac{1}{2} ||\nabla v||^2 \, dx = & \int_{\Omega_\delta} \nabla \left(\nu \, \nabla \cdot \nabla v \;-\; \nabla \pi \right) : \nabla v \, dx \\ & - \int_{\Omega_\delta} \left(\nabla \cdot (\overline{v} \otimes \overline{v}) \;+\; \nabla \cdot \tau(\overline{v}) \right) : \nabla \overline{v} \, dx \end{aligned} \tag{8}$$

Thus we see that the upperbound given by Poincaré's inequality dissipates at its natural rate if the two contributions on the last line above cancel each other out. For incompressible flows, the production of fine details can be expressed in terms of the invariants $Q(v) = \frac{1}{2}\nabla v : \nabla v$ and $R(v) = -\frac{1}{3}\nabla v : \nabla v \nabla v$ of the velocity gradient. Indeed, since $\partial_k v_k = 0$, we have

$$\int_{\Omega_\delta} \nabla\cdot(\overline{v}\otimes\overline{v}) : \nabla\overline{v}\, dx \;=\; \int_{\Omega_\delta} \partial_i\partial_k\left(\overline{v}_k\overline{v}_j\right)\partial_i\overline{v}_j\, dx \;=$$
$$\int_{\Omega_\delta}\left(\partial_i\overline{v}_k\partial_k\overline{v}_j\partial_i\overline{v}_j \;+\; \frac{1}{2}\partial_k\left(\overline{v}_k\left(\partial_i\overline{v}_j\right)^2\right)\right) dx \;=\; -3\int_{\Omega_\delta} R(\overline{v})\, dx \;+\; \int_{\partial\Omega_\delta} Q(\overline{v})\,\overline{v}\cdot n\, ds$$

where n is the outward-pointing normal vector to the boundary $\partial\Omega_\delta$ of Ω_δ. So, in conclusion, the convective contribution to the evolution of the $L^2(\Omega_\delta)$ norm of ∇v is properly balanced by the modeled dissipation if

$$\int_{\Omega_\delta} \nabla\nabla\cdot\tau(\overline{v}) : \nabla\overline{v}\, dx \;=\; 3\int_{\Omega_\delta} R(\overline{v})\, dx \;-\; \int_{\partial\Omega_\delta} Q(\overline{v})\,\overline{v}\cdot n\, ds \tag{9}$$

The scale truncation condition associated with the relaxation model is obtained by substituting Eq. (4) into Eq. (9). This gives

$$\chi \;=\; \frac{3\int_{\Omega_\delta} R(\overline{v})\, dx \;-\; \int_{\partial\Omega_\delta} Q(\overline{v})\,\overline{v}\cdot n\, ds}{\int_{\Omega_\delta} \nabla(\overline{v}-\widetilde{\overline{v}}) : \nabla\overline{v}\, dx} \tag{10}$$

where it is assumed that χ is constant in Ω_δ, i.e., δ is assumed to by the smallest scale at which χ varies. Here it may be emphasized that the relaxation parameter does not depend on the subgrid velocity $v - \overline{v}$. Consequently, the model can be evaluated directly, i.e., without applying any form of deconvolution to the grid-filter; so any difficulties associated with the deconvolution procedure are circumvented.

Condition (9) ensures that the modeled dissipation counterbalances the nonlinear production of all scales that are so small that they fit in the box Ω_δ. But this balance is achieved just as well if energy is transfered from the small, box-fitting scales *to* the larger eddies. In this case, the relaxation parameter given by Eq. (10) is negative. The problem here is that the small box-fitting scales of motion do not have any physical significance; they are only there to dissipate energy in an efficient manner. Hence, data transfered from the small, box-fitting scales to the larger eddies is mostly incorrect. Therefore, the parameter χ is set to zero if Eq. (10) yields a negative value (i.e., χ is clipped just as in the dynamical procedure).

4 Discrete Scale Truncation

Probably the best discretization is obtained by taking a discrete Poincaré inequality as a starting point, and by subsequently repeating all the steps in the previous derivation in a discrete setting. This results into a natural discretization of the scale-truncation condition, whereby all the properties of the considered discretization automatically be discounted. Here we opt for a simpler approach, i.e., we directly discretize the continuous scale-truncation condition (10). As in Schumann's approach, the spatial discretization of the convective term defines the grid-filter. Here, we use a second-order, symmetry-preserving finite-volume method, see Ref. [2], e.g. In one spatial dimension, the convective term is approximated to second-order accuracy by $\partial_x \phi_i \approx (\phi^2_{i+1/2} - \phi^2_{i-1/2})/h$, where $\phi_{i\pm1/2} = (\phi_{i\pm1} + \phi_i)/2$ and $\phi = v^2$; the diffusive term is approximated using $\partial^2_{xx} v_i \approx (v_{i+1} - 2v_i + v_{i-1})/h^2$. The discrete convective term does not see a point-to-point oscillation, whereas the discrete diffusive term does see this mode. So the convection-diffusion balance is not approximated correctly at the scale h set by the grid. Therefore we take $\delta = 2h$ [4, 5]. In 1D the box filter (3) is approximated by

$$\widetilde{v}_i = \frac{1}{2} v_i + \frac{1}{4} (v_{i+1} + v_{i-1}) \tag{11}$$

This discretization rule is also applied to the Ω_δ-integrals in Eq. (10). Here it is to be stressed that we approximate all integrals using the trapezoidal rule with constant coefficients, even if the grid is non-uniform, since the point-to-point mode must be an integral part of the residue of the discrete box filter. The invariants $Q(\overline{v})$ and $R(\overline{v})$ are computed from the discrete velocity gradient, where the gradient is discretized as in the convective term, that is over a distance $2h$. Thus, the length scale δ enters the discretization.

Finally, it may be remarked that - on a 1D uniform grid - our discrete relaxation model can be related straightforwardly to a discrete Smagorinsky model. Indeed,

$$\chi (v - \widetilde{v})_i \overset{(11)}{\approx} -\frac{1}{4} \chi h^2 \frac{v_{i+1} - 2v_i + v_{i-1}}{h^2} \approx -2 \nu_t \partial^2_{xx} v_i$$

where the eddy viscosity is given by $\nu_t = \chi h^2/8$. Notice: on 3D anisotropic grids, the filter length associated to the Smagorinsky model is usually not chosen such that the corresponding factors "h^2" in the above expression cancel each other out.

5 Results

The relaxation model given by Eq. (10) has the following properties: (a) $\chi = 0$ in any part Ω_δ of the flow where $R = 0$ (no production of scales $< \delta$) and Q vanish at the boundaries (no influx of scales $< \delta$); (b) $\chi = 0$ at a wall. It goes without saying

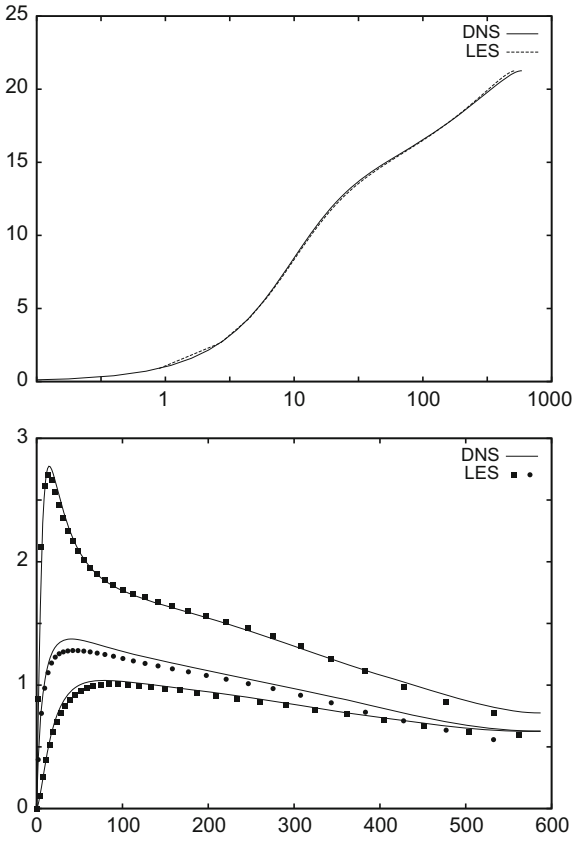

Fig. 1 The *upper* figure shows the mean velocity (in wall coordinates) obtained with the help of the 64^3 LES and the DNS [6]. The *lower* figure displays the rms of the fluctuating velocities; here the *upper* and *lower* curve represents the stream-wise and wall-normal component, respectively

that the performance of the relaxation model has to be investigated for many cases. As a first step it was tested for turbulent channel flow by means of a comparison with a direct numerical simulation (DNS). The results are compared to the DNS data of Moser et al. at $\mathrm{Re}_\tau = 590$ [6]. In fact, we should compare the LES-solution $\widetilde{v}$ to the filtered DNS-solution $\widetilde{u}$. Yet, since the filtered DNS-solution is not given by Moser et al. we will compare v directly to u. The dimensions of the channel are taken identical to those of the DNS of Moser et al. The computational grid used for the large-eddy simulation consists of 64^3 points. The DNS was performed on a $384 \times 257 \times 384$ grid, i.e., the DNS uses about 144 times more grid points than the present LES. As can be seen in Fig. 1 both the mean velocity and the root-mean-square of the fluctuating velocity are in good agreement with the DNS. Here, it may be remarked that 64^3 simulations without a LES-model predict a wall friction that differs about 10% from the DNS.

References

1. Schumann, U.: Subgrid scale model for finite difference simulations of turbulent flows in plane channels and annuli. J. Comput. Phys. **18**, 376–404 (1975)
2. Verstappen, R.W.C.P., Veldman, A.E.P.: Symmetry-preserving discretization of turbulent flow. J. Comput. Phys. **187**, 343–368 (2003)
3. Stolz, S., Adams, N.A., Kleiser, L.: An approximate deconvolution model for large-eddy simulation with application to incompressible wall-bounded flows. Phys. Fluids **13**, 997–1015 (2001)
4. Verstappen, R.W.C.P., Rozema, W., Bae, H.J.: Numerical scale separation in large eddy simulation. In: Proceedings of the Summer Program 2014, CTR, Stanford (2014)
5. Rozema, W., Bae, H.J., Moin, P., Verstappen, R.: Minimum-dissipation models for large-eddy simulation, submitted to Phys. Fluids
6. Moser, R.D., Kim, J., Mansour, N.N.: Direct numerical simulation of turbulent channel flow up to Re_τ=590. Phys. Fluids **11**, 943–945 (1999)

Building Proper Invariants for Large-Eddy Simulation

F.X. Trias, D. Folch, A. Gorobets and A. Oliva

1 Introduction

We consider the simulation of the incompressible Navier–Stokes (NS) equations

$$\partial_t u + (u \cdot \nabla)\, u = \nu \nabla^2 u - \nabla p, \qquad \nabla \cdot u = 0, \tag{1}$$

where u denotes the velocity field, p represents the kinematic pressure and ν is the kinematic viscosity. In the foreseeable future, numerical simulations of turbulent flows will have to resort to models of the small scales because the non-linear convective term produces too many scales of motion. Large-Eddy Simulation (LES) is probably the most popular example thereof. In short, LES equations result from applying a spatial filter, with filter length Δ, to the NS Eq. (1)

$$\partial_t \overline{u} + (\overline{u} \cdot \nabla)\, \overline{u} = \nu \nabla^2 \overline{u} - \nabla \overline{p} - \nabla \cdot \tau(\overline{u}), \qquad \nabla \cdot \overline{u} = 0, \tag{2}$$

where $\overline{u}$ is the filtered velocity and $\tau(\overline{u})$ is the subgrid stress (SGS) tensor and aims to approximate the effect of the under-resolved scales, i.e. $\tau(\overline{u}) \approx \overline{u \otimes u} - \overline{u} \otimes \overline{u}$. In this regard, the eddy-viscosity assumption is by far the most used closure model

F.X. Trias (✉) · D. Folch · A. Gorobets · A. Oliva
Heat and Mass Transfer Technological Center, ETSEIAT, Technical University of Catalonia, C/Colom 11, 08222 Terrassa, Spain
e-mail: xavi@cttc.upc.edu; xavitrias@gmail.com

D. Folch
e-mail: davidf@cttc.upc.edu

A. Oliva
e-mail: oliva@cttc.upc.edu

A. Gorobets
Keldysh Institute of Applied Mathematics, 4A, Miusskaya Sq., Moscow 125047, Russia
e-mail: andrey@cttc.upc.edu; cherepock@gmail.com

D.G.E. Grigoriadis et al. (eds.), *Direct and Large-Eddy Simulation X*,
ERCOFTAC Series 24, https://doi.org/10.1007/978-3-319-63212-4_20

$$\tau(\overline{u}) \approx -2\nu_e S(\overline{u}), \tag{3}$$

where ν_e is the eddy-viscosity. Following [1], the it can be modeled as follows

$$\nu_e = (C_m \Delta)^2 D_m(\overline{u}), \tag{4}$$

where Δ is a subgrid characteristic length. C_m and D_m are the constant and differential operator associated with the model.

2 A 5D Phase Space for Eddy-Viscosity Models

The essence of turbulence are the smallest scales of motion. They result from a subtle balance between convective transport and diffusive dissipation. Numerically, if the mesh is too coarse, this balance needs to be restored by a turbulence model. Therefore, the performance of these models strongly depends on the ability to capture well this (im)balance. In this respect, many eddy-viscosity models for LES have been proposed (see [3], for a review). In order to be frame invariant, most of them rely on differential operators that are based on invariants of a symmetric second-order tensor (with the proper scaling factors). Such tensors are usually derived from the gradient of the resolved velocity field, $G \equiv \nabla\overline{u}$; therefore, they are locally dependent and Galilean invariant. This is a second-order traceless tensor, $tr(G) = \nabla \cdot \overline{u} = 0$. Hence, it contains 8 independent elements and it can be characterized by 5 invariants (3 scalars are required to specify the orientation in 3D). Following the same notation as in [4], this set of invariants is given by

$$\{Q_G, R_G, Q_S, R_S, V^2\}, \tag{5}$$

where $Q_A = 1/2\{tr^2(A) - tr(A^2)\}$ and $R_A = det(A)$ are the second and third invariants of the second-order tensor A. The first invariant of A is denoted as $P_A = tr(A)$. Finally, $V^2 = 4(tr(S^2\Omega^2) - 2Q_S Q_\Omega)$, where $S = 1/2(G + G^T)$ is the symmetric part and $\Omega = 1/2(G - G^T)$ is the skew-symmetric part of the tensor G. Going back to the Smagorinsky model [5]

$$\nu_e^{Smag} = (C_S\Delta)^2|S(\overline{u})| = 2(C_S\Delta)^2(-Q_S)^{1/2}, \tag{6}$$

almost all the eddy-viscosity models for LES are based on invariants of second-order tensors derived from the gradient tensor, G. Hence, they can be re-write in terms of the 5D phase space defined in (5). For example, the WALE [6] and the Vreman's model [7] read

Table 1 Top: near-wall behavior and units of the five basic invariants in the 5D phase space given in (5) together with the invariant $Q_\Omega = Q_G - Q_S$. Bottom: near-wall behavior of the Smagorinsky, the WALE, the Vreman's, the Verstappen's and the σ-model

Invariants					
Q_G	R_G	Q_S	R_S	V^2	Q_Ω
$\mathcal{O}(y^2)$	$\mathcal{O}(y^3)$	$\mathcal{O}(y^0)$	$\mathcal{O}(y^1)$	$\mathcal{O}(y^0)$	$\mathcal{O}(y^0)$
$[T^{-2}]$	$[T^{-3}]$	$[T^{-2}]$	$[T^{-3}]$	$[T^{-4}]$	$[T^{-2}]$
Models					
Smagorinsky	WALE	Vreman's	Verstappen's	σ-model	
Eq. (6)	Eq. (7)	Eq. (7)	Ref. [2]	Ref. [1]	
$\mathcal{O}(y^0)$	$\mathcal{O}(y^3)$	$\mathcal{O}(y^1)$	$\mathcal{O}(y^1)$	$\mathcal{O}(y^3)$	

$$\nu_e^W = (C_W\Delta)^2 \frac{(V^2/2+2Q_G^2/3)^{3/2}}{(-2Q_S)^{5/2}+(V^2/2+2Q_G^2/3)^{5/4}}, \tag{7}$$

$$\nu_e^{Vr} = (C_{Vr}\Delta)^2 \left(\frac{V^2+Q_G^2}{2(Q_\Omega-Q_S)}\right)^{1/2}. \tag{8}$$

respectively, where $Q_\Omega = Q_G - Q_S$. Other eddy-viscosity models that can be re-written in terms of the above-defined invariants are the σ-model proposed in [1] and the model proposed by Verstappen [2]. The major drawback of the Smagorinsky model is that the invariant Q_S (see Eq. 6) does not vanish in near-wall regions (see Table 1). Nevertheless, it is possible to build models that do not have this limitation: the WALE, the Vreman's, the Verstappen's and the σ-model are examples thereof.

3 Building New Proper Invariants for LES Models

In this context, it is interesting to observe that new models can be derived by imposing appropriate restrictions on the differential operator. For example, we can consider models that are based on the invariants of the tensor GG^T. Namely,

$$\nu_e = (C_M\Delta)^2 P_{GG^T}^p Q_{GG^T}^q R_{GG^T}^r, \tag{9}$$

where $-6r - 4q - 2p = -1$, $6r + 2q = s$ and $P_{GG^T} = 2(Q_\Omega - Q_S)$, $Q_{GG^T} = V^2 + Q_G^2$ and $R_{GG^T} = R_G^2$, respectively. The GG^T tensor appears in the leading term (gradient model) of the Taylor series expansion of the SGS tensor $\tau(\overline{u}) = (\Delta^2/12)GG^T + \mathcal{O}(\Delta^4)$. The above-defined restrictions on the exponents follow by imposing the $[T^{-1}]$ units of the differential operator and the slope, s, for the asymptotic near-wall behavior (see Table 1), i.e. $\mathcal{O}(y^s)$. Solutions for $q(p,s) = (1-s)/2 - p$ and $r(p,s) = (2s-1)/6 + p/3$ are displayed in Fig. 1. The Vreman's

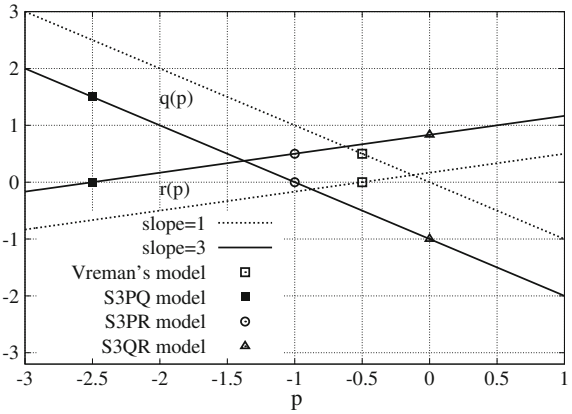

Fig. 1 Solutions for the linear system of Eq. (9) for $s = 1$ (*dashed line*) and $s = 3$ (*solid line*). Each (r, q, p) solution represents an eddy-viscosity model of the form given in Eq. (9)

model given in Eq. (7) corresponds to the solution with $s = 1$ (see Table 1) and $r = 0$. Nevertheless, solutions with the proper near-wall behavior, i.e. $s = 3$ (solid lines in Fig. 1) seem more appropriate. Then, restricting ourselves to solutions involving only two invariants of GG^T we find three new eddy-viscosity models (see Fig. 1),

$$\nu_e^{S3PQ} = (C_{s3pq}\Delta)^2 P_{GG^T}^{-5/2} Q_{GG^T}^{3/2}, \tag{10}$$

$$\nu_e^{S3PR} = (C_{s3pr}\Delta)^2 P_{GG^T}^{-1} R_{GG^T}^{1/2}, \tag{11}$$

$$\nu_e^{S3QR} = (C_{s3qr}\Delta)^2 Q_{GG^T}^{-1} R_{GG^T}^{5/6}. \tag{12}$$

Lower bounds for the model constants, C_{s3xx}, can be with found (see details in [8])

$$0 \leq \frac{(C_{Vr})^2}{(C_{s3xx})^2} \frac{\nu_e^{S3xx}}{\nu_e^{Vr}} \leq \frac{1}{3}, \tag{13}$$

where C_{Vr} is the Vreman's constant. Hence, imposing $C_{s3pq} = C_{s3pr} = C_{s3qr} = \sqrt{3}C_{Vr}$ guarantees both numerical stability and that the models have less or equal dissipation than Vreman's model, i.e.

$$0 \leq \nu_e^{S3xx} \leq \nu_e^{Vr}. \tag{14}$$

4 Results

Figure 2 shows the performance of the proposed models for a turbulent channel flow at $Re_\tau = 395$ together with the discretization methods for eddy-viscosity models proposed in [10]. The code is based on a fourth-order symmetry-preserving discretization finite volume discretization. Results are in good agreement with the DNS data [9]. To illustrate the contribution of the eddy-viscosity models to improve the

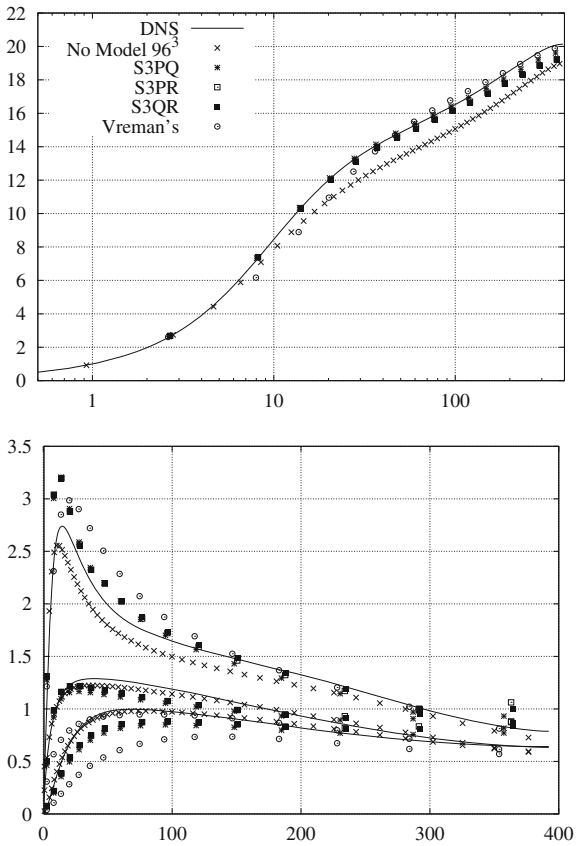

Fig. 2 Results for a turbulent channel flow at $Re_\tau = 395$ obtained with a 32^3 mesh for LES and a 96^3 mesh without model, i.e. $\nu_e = 0$. *Solid line* corresponds to the DNS by Moser et al. [9]. *Top* average stream-wise velocity, $\langle u \rangle$. *Bottom* root-mean-square of the fluctuating velocity components (from *top* to *bottom*, u_{rms}, w_{rms} and v_{rms}, respectively)

quality of the solution, the results obtained with a 96^3 mesh without model, i.e. $\nu_e = 0$, are also shown. The performance of the three models proposed here (S3PQ, S3PR and S3QR) is essentially the same. Compared with the Vreman's model, they tend to improve the results for the mean velocity in the buffer layer region ($5 < y^+ < 30$) whereas the quality of the solutions in the outer layer ($y^+ > 50$) is very similar. Although some discrepancies are observed, the root-mean-square of the fluctuating velocity components (see Fig. 2, bottom) are also in rather good agreement with the DNS data. In this case, the proposed models outperform the solution obtained with the Vreman's model. The latter does not predict accurately the position of the peak for u_{rms}, and clearly under-predict the solution for both v_{rms} and w_{rms}. In this case, the solution obtained without model may seem accurate; however, the clearly over-predicted friction velocity (if results were normalized by the mean stream-wise velocity) compensates an over-prediction of the velocity fluctuations. These results support the idea that the Vreman's model tends to dissipate too much in the near-wall region where the eddy-viscosity, ν_e, does not follow the proper cubic behavior (see Table 1). To illustrate this, the average eddy-viscosity, $\langle \nu_e \rangle$, divided by the kine-

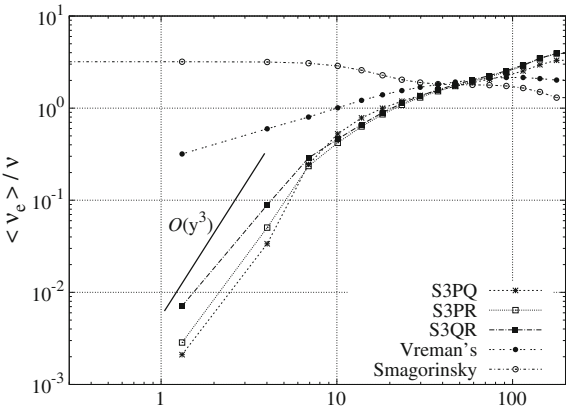

Fig. 3 Averaged eddy-viscosity, $\langle \nu_e \rangle$, divided by the kinematic viscosity, ν. Results for a turbulent channel flow at $Re_\tau = 395$ obtained with a 32^3 for different LES models

matic viscosity, ν, is displayed in Fig. 3. Results using the classical Smagorinsky model are also shown for comparison. As expected, the proposed models follow a cubic near-wall behavior whereas the Vreman's model predict much higher values in the buffer layer region ($5 < y^+ < 30$). Our current research is focused on finding a proper definition of the subgrid characteristic length, Δ which is also a key element of any eddy-viscosity model (see Eq. 4). Preliminary results in this regard can be found in [11].

Acknowledgements This work has been financially supported by the *Ministerio de Economía y Competitividad*, Spain (ENE2014-60577-R), and a *Ramón y Cajal* postdoctoral contract (RYC-2012-11996). Calculations have been performed on the IBM MareNostrum supercomputer at the Barcelona Supercomputing Center. The authors thankfully acknowledge these institutions.

References

1. Nicoud, F., Toda, H.B., Cabrit, O., Bose, S., Lee, J.: Using singular values to build a subgrid-scale model for large eddy simulations. Phys. Fluids **23**(8), 085106 (2011)
2. Verstappen, R.: When does eddy viscosity damp subfilter scales sufficiently? J. Sci. Comput. **49**(1), 94–110 (2011)
3. Berselli, L.C., Iliescu, T., Layton, W.: Mathematics of Large Eddy Simulation of Turbulent Flows, first edn. Springer (2006)
4. Cantwell, B.J.: Exact solution of a restricted Euler equation for the velocity gradient tensor. Phys. Fluids A **4**, 782–793 (1992)
5. Smagorinsky, J.: General circulation experiments with the primitive equations. Monthly Weather Rev. **91**, 99–164 (1963)
6. Nicoud, F., Ducros, F.: Subgrid-scale stress modelling based on the square of the velocity gradient tensor. Flow, Turbul. Combust. **62**(3), 183–200 (1999)
7. Vreman, A.W.: An eddy-viscosity subgrid-scale model for turbulent shear flow: algebraic theory and applications. Phys. Fluids **16**(10), 3670–3681 (2004)
8. Trias, F.X., Folch, D., Gorobets, A., Oliva, A.: Building proper invariants for eddy-viscosity subgrid-scale models. Phys. Fluids **27**(6), 065103 (2015)

9. Moser, R.D., Kim, J., Mansour, N.N.: Direct numerical simulation of turbulent channel flow up to $Re_\tau = 590$. Phys. Fluids **11**, 943–945 (1999)
10. Trias, F.X., Gorobets, A., Oliva, A.: A simple approach to discretize the viscous term with spatially varying (eddy-)viscosity. J. Comput. Phys. **253**, 405–417 (2013)
11. Silvis, M.H., Trias, F.X., Abkar, M., Bae, H.J., Lozano-Durán, A., Verstappen, R.W.C.P.: Exploring nonlinear subgrid-scale models and new characteristic length scales for large-eddy simulation. In: Proceedings of Summer Program 2016, Center for Turbulence Research, Stanford University (2016)

Boundary Layer Separation Under Strong Adverse Pressure Gradient over Smooth and Rough Walls

Pouya Mottaghian, Junlin Yuan and Ugo Piomelli

1 Introduction

Separation of the turbulent boundary layer is among the most critical phenomena that determine the efficiency of flow devices, ranging from airplane wings to turbine and compressor blades, to curved ducts. The accurate prediction of incipient separation and reattachment in these configuration is critical. A simple configuration in which separation occurs, caused by the adverse pressure gradient, is the turbulent flow over a flat plate with a suction and blowing velocity profile imposed at the freestream, a case studied experimentally [1, 8] and numerically, both in the laminar [11] and turbulent regimes [6, 10]. This velocity profile induces a strong adverse pressure gradient (APG) that causes the flow to separate and then to reattach downstream. This type of pressure-driven separation is relevant to many flows (airfoils, ducts, etc.) and, unlike the case of geometry-induced separation (such as that in the backward-facing step), both separation and reattachment locations fluctuate; the prediction of their position is, therefore, more challenging. Numerical and experimental studies have shown that large coherent structures are generated in the separation zone and lifted upward into the shear layer and over the separated-flow region. Near the reattachment point these structures impinge on the wall and break apart, generating a highly unsteady three-dimensional flow.

The studies mentioned above (and most other investigations of APG boundary layers) are confined to smooth surfaces. In many real applications, however, surface roughness is present. Its effect is to increase the wall friction, due to the contribution of pressure drag. The knowledge of the interaction between APG (which is an outer

P. Mottaghian · U. Piomelli (✉)
Department of Mechanical and Materials Engineering, Queen's University, Kingston, ON, Canada
e-mail: ugo@queensu.ca

J. Yuan
Department of Mechanical Engineering, Michigan State University, East Lansing, MI, USA

D.G.E. Grigoriadis et al. (eds.), *Direct and Large-Eddy Simulation X*,
ERCOFTAC Series 24, https://doi.org/10.1007/978-3-319-63212-4_21

layer effect) leading to separation and roughness (an inner layer effect) is, however, limited. Boundary layers subjected to strong APG on a rough wall have been studied experimentally in flows over a ramp [12] or a hill [2]; the roughness was shown to cause earlier separation, and a larger separation bubble compared to the smooth-wall flow. This has been attributed to a larger mean momentum deficit on the rough wall. However, roughness is also expected to lead to higher turbulence intensity, which should contribute to a delay of the separation. Therefore, the cause of the earlier separation is not fully understood. The APG tends to thicken the boundary layer; due to separation, furthermore, near-wall fluid is advected over the recirculation zone. It is possible, therefore, that roughness affects the flow farther from the wall, in APG boundary layers, than in the canonical zero-pressure-gradient (ZPG) case.

In this study, we carry out large-eddy simulations (LES) of flat plate boundary layers in APG to investigate the physics underlying rough-wall flow separations. Both smooth and rough walls are considered, and the roughness is resolved by the grid. Since this will allow access to the flow field inside the roughness sublayer, it will be possible to answer some questions that the experimental methods have left open. In the following, the methodology is presented; then some results are shown, and conclusions are drawn.

2 Problem Formulation

The governing equations are filtered continuity and Navier-Stokes equations for an incompressible flow:

$$\frac{\partial \overline{u_i}}{\partial x_i} = 0; \quad \frac{\partial \overline{u}_i}{\partial t} + \frac{\partial \overline{u}_j \overline{u}_i}{\partial x_j} = \nu \frac{\partial^2 \overline{u}_i}{\partial x_j \partial x_j} - \frac{1}{\rho} \frac{\partial \overline{p}}{\partial x_i} - \frac{\partial \tau_{ij}}{\partial x_j}, \tag{1}$$

which are solved using a well-validated code that employs a staggered grid and second-order, central differences for all terms, a second-order-accurate semi-implicit time advancement, and MPI (Message Passing Interface) parallelization [4]. An immersed-boundary method (IBM) based on the volume-of-fluid approach [9, 14] is applied to impose no-slip boundary condition on the rough surfaces and model the roughness as a dense distribution of randomly rotated ellipsoids (sand grains).

Roughness starts at a location downstream of the recycling plane; sufficiently far downstream (to allow the rough-wall boundary layer to become well-developed) is the reference plane, $x = 0$. Downstream of this plane, the deceleration is imposed by assigning a freestream velocity in the wall-normal direction, $V_\infty(x)$; the streamwise component, $U_\infty(x)$, is calculated by imposing zero vorticity. The resulting velocity components at the freestream are shown in Fig. 1a. A no-slip boundary condition is applied at the bottom wall; the turbulent inflow at the inlet is generated from a rescaling/recycling region [3] (which ends before roughness begins). Periodic boundary conditions are applied respectively in the spanwise direction, and a convective

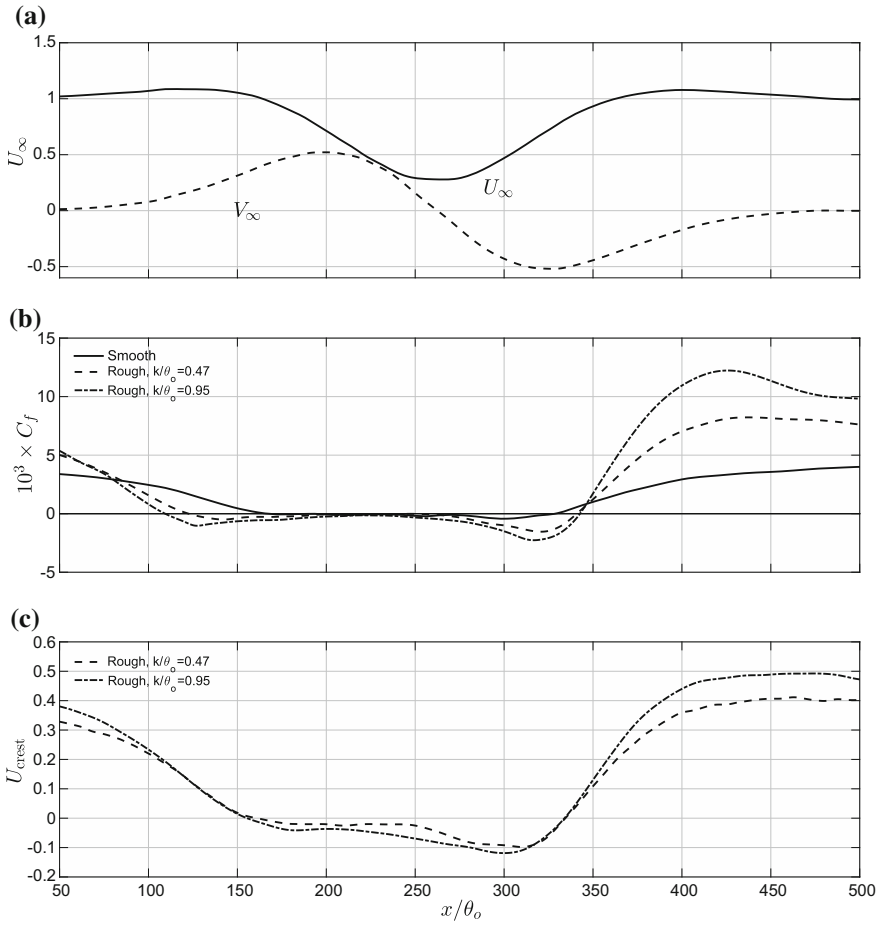

Fig. 1 Streamwise development of **a** freestream velocity U_∞ and V_∞; **b** skin friction coefficient; **c** velocity at the roughness crest

condition [7] is used at the domain outlet. The subgrid scale stresses τ_{ij} are modeled using the Lagrangian dynamic eddy-viscosity model [5].

We performed three calculations, on a smooth wall and with two roughness heights. All quantities are normalized by length and velocity scales at the reference location, indicated with a subscript o. The simulations are summarized in Table 1. The first grid point was always less than one wall unit above the roughness crest, and at least 750 grid volumes were used to resolve a single roughness element. The total simulation time is more than $120\delta_o^*/u_\tau$ for all the cases, sufficient to achieve sample convergence for second and third-order turbulent statistics. The model was validated by comparing the results of a low-Re LES to Direct Numerical Simulation (DNS) data [6]. Good agreement was obtained on all first- and second-order statistics.

Table 1 Summary of simulation parameters

Case	k/θ_o	Domain size	Grid
1	0	$760\theta_o \times 90\theta_o \times 70\theta_o$	$2560 \times 384 \times 384$
2	0.47	$760\theta_o \times 90\theta_o \times 70\theta_o$	$2048 \times 384 \times 384$
3	0.95	$760\theta_o \times 90\theta_o \times 70\theta_o$	$2560 \times 432 \times 384$

3 Results

Figure 1b shows the skin-friction coefficient for the three high-Re cases; the wall stress, in the rough cases, includes both the contributions of viscous and form drag (due to the low pressure in the separated flow behind each roughness element). If one considers the standard definition of separation ($\tau_w = 0$ and $d\tau_w/dx < 0$) we observe very early separation in the rough-wall cases. However, the flow streamlines, shown in Fig. 2, do not reflect this: the zero-velocity line does not lift up until $x/\theta_o \simeq 150$, much downstream of the point where C_f crosses zero. This is also evident in Fig. 1c, in which the mean streamwise velocity above the roughness crest, U_{crest}, is shown. The point where $U_{\text{crest}} = 0$ is much closer to the point where the smooth flow separates. Note that in experiments the occurrence of separation is usually estimated from U_{crest} [12, 13], since the wall stress is not generally known. Roughness results in a wider and taller recirculation zone (Fig. 2), and a thicker boundary layer. The early occurrence of $C_f = 0$, unaccompanied by detachment of the flow, represents a flow reversal without separation. It is due to the recirculating-flow regions that occur behind each roughness element, whose size increases in the APG region; the flow outside of the sublayer, however, is mostly unaffected and streamlines remain roughly parallel to the wall, until the recirculating regions occupy most of the roughness sublayer. At this point, the outer flow separates.

The mean streamwise-velocity profiles at two streamwise locations before separation are shown in Fig. 3. Roughness leads to lower mean momentum in the boundary

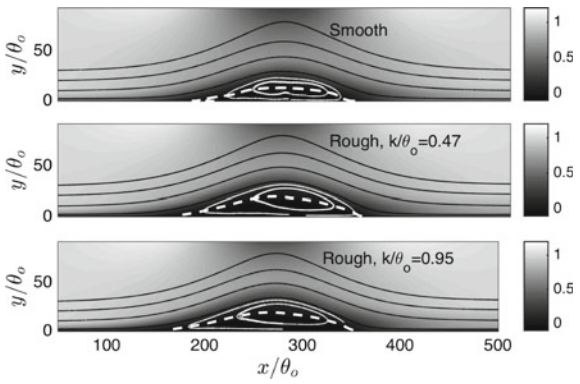

Fig. 2 Streamwise velocity contours, mean streamlines (*thin lines*) and zero-velocity line (*thick dashed line*)

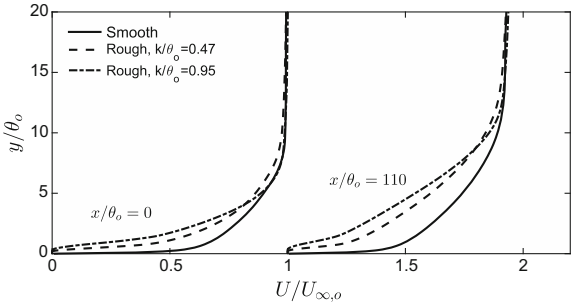

Fig. 3 Mean streamwise velocity profiles before separation

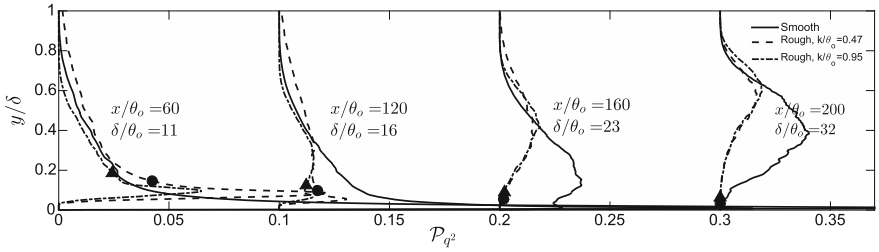

Fig. 4 Profiles of the production of q^2 at the four locations indicated in the *top* figure. The *dots* indicate the thickness of the roughness sublayer, $y/\theta_o = 3k_s$

layer due to the higher Reynolds shear stress and thicker boundary layer. The momentum deficit is the main reason of early separation at rough wall flow. The decreased mean-velocity gradient also plays a role in a marked decrease of the production of turbulent kinetic energy and Reynolds shear stresses, as will be shown later.

Figure 4 shows profiles of the production of $q^2 = \langle u_i' u_i' \rangle$ (twice the turbulent kinetic energy):

$$\mathscr{P}_{q^2} = -2\langle u'v' \rangle \left(\frac{\partial U}{\partial y} + \frac{\partial V}{\partial x} \right). \tag{2}$$

In equilibrium boundary layers, the thickness of the roughness sublayer (defined as the region where roughness causes spatial variations of time-averaged turbulent statistics) is approximately $3-5k_s$; the turbulent statistics, farther from the wall, are expected to collapse with the smooth-wall case, if properly normalized. In the present case the production profiles only collapse in the ZPG region; even a mild APG results in thickening of the roughness sublayer (at $x/\theta_o = 100$). In the region where the APG is significant the roughness effects propagate much farther from the wall, and, shortly before separation, they communicate through much of the boundary layer thickness (at this location, $\delta \simeq 21\theta_o$). Beyond separation, the advection of near-wall flow over the recirculation bubble propagates roughness effects even farther from the wall.

In the rough-wall cases the production is much lower, in the separated-flow region, than in the smooth case (even outside of the recirculating bubble). This effect is due to the decrease of the velocity gradient observed before; the Reynolds stresses along a streamline (not shown) do not decrease significantly; in fact, the $\langle v'v' \rangle$ component increases. The decrease of $\partial U/\partial y$, however, indicates that, in the rough-wall cases, turbulent fluctuations are only advected, in a quasi-frozen state, around the recirculation bubble, and no local production mechanism is present. This may be due to a different topology of the detached eddies, in the rough-wall cases; this is an item that warrants further investigation.

4 Conclusions

Large eddy simulations of separated turbulent boundary layers over a flat plate were performed to study the effects of wall roughness. Rough-wall cases have a larger separation bubble with both earlier separation and later reattachment. Roughness leads to early flow reversal upstream of the real separation (which occurs when the zero-velocity line moves away from the wall) because the small-scale separation regions downstream of the roughness elements become larger and merge together as a result of the APG. However, this flow reversal remains confined below the roughness crest. The reasons for the earlier separation are larger momentum deficit in rough-wall flows and the shut down of the production of $-\langle u'v' \rangle$ in the separated shear layer, mainly due to the decrease in the velocity gradient in the outer layer. Even before separation, however, the APG propagates the roughness effects outside of the roughness sublayer. After separation, roughness effects can be felt throughout the boundary layer because of the advection of near-wall fluid around the recirculation region.

Acknowledgements Support from Hydro Québec, the Natural Science and Engineering Research Council of Canada (NSERC), and the High Performance Computing Virtual Laboratory (HPCVL), Queen's University site, is gratefully acknowledged.

References

1. Alving, A., Fernholz, H.H.: Turbulence measurements around a mild separation bubble and downstream of reattachment. J. Fluid Mech. **322**, 297–328 (1996)
2. Cao, S., Tamura, T.: Experimental study on roughness effects on turbulent boundary layer flow over a two-dimensional steep hill. J. Wind. Eng. **94**, 1–19 (2006)
3. Keating, A., Piomelli, U., Bremhorst, K., Nešić, S.: Large-eddy simulation of heat transfer downstream of a backward-facing step. J. Turbul. **5**(N20), 1–27 (2004)
4. Lund, T.S., Wu, X., Squires, K.D.: Generation of inflow data for spatially-developing boundary layer simulations. J. Comput. Phys. **140**, 233–258 (1998)
5. Meneveau, C., Lund, T.S., Cabot, W.H.: A Lagrangian dynamic subgrid-scale model of turbulence. J. Fluid Mech. **319**, 353–385 (1996)

6. Na, Y., Moin, P.: Direct numerical simulation of a separated turbulent boundary layer. J. Fluid Mech. **370**, 175–201 (1998)
7. Orlanski, I.: A simple boundary condition for unbounded hyperbolic flows. J. Comput. Phys. **21**, 251–269 (1976)
8. Perry, A.E., Fairlie, B.D.: A study of turbulent boundary-layer separation and reattachment. J. Fluid Mech. **69**(4), 657–672 (1975)
9. Scotti, A.: Direct numerical simulation of turbulent channel flows with boundary roughened with virtual sandpaper. Phys. Fluids **18**, 31701-1–4 (2006)
10. Skote, M., Henningson, D.: Direct numerical simulation of a separated turbulent boundary layer. J. Fluid Mech. **471**, 107–136 (2002)
11. Spalart, P.R., Strelets, M.K.: Mechanisms of transition and heat transfer in a separation bubble. J. Fluid Mech. **403**, 329–349 (2000)
12. Song, S., Eaton, K.: The effects of wall roughness on the separated flow over a smoothly contoured ramp. Exp. Fluids **33**, 38–46 (2002)
13. Song, S., DeGraaff, D.B., Eaton, K.: Experimental studies of a separating, reattaching, and redeveloping flow over a smoothly contoured ramp. Int. J. Heat Fluid Flow **21**, 512–519 (2000)
14. Yuan, J., Piomelli, U.: Numerical simulations of sink-flow boundary layers over rough surfaces. Phys. Fluids **26**, 015113-1–28 (2014)

Comparison of DNS of Compressible and Incompressible Turbulent Droplet-Laden Heated Channel Flow with Phase Transition

A. Bukhvostova, E. Russo, J.G.M. Kuerten and Bernard J. Geurts

1 Introduction

Multiphase flows in which a large number of small droplets are dispersed in a gas, play an important role in a variety of applications. At sufficiently high mass and volume fraction the presence of the dispersed droplet phase directly modulates the flow through the exchange of momentum with the gas [1]. Dispersed multiphase flows may in addition show effects arising from phase transition. Turbulent spray cooling is an example in which the effect of phase transition is exploited to enhance the desired cooling rate [2]. In this contribution we study turbulent flow in a differentially heated plane channel in which the dispersed droplet phase is treated as a discrete set of point particles whose motion in the carrier gas flow is tracked. Momentum, heat and mass transfer effects between the gas and the liquid droplets are included. We consider the flow of droplets of water in a carrier gas consisting of air and water vapor.

A key assumption in the modeling of dispersed gas-liquid multiphase flows pertains to the treatment of the carrier gas as either incompressible or compressible. The compressibility assumption is of importance in case phase transitions are taken into consideration. If the carrier gas is assumed to be strictly incompressible, the inclusion of evaporation and condensation is subject to the condition that all instantaneous changes in the local mass-density of air and water vapor cancel each other precisely throughout the domain. A full simulation model can be developed for such an incompressible carrier gas [3]. Here, we complement the incompressible model

A. Bukhvostova (✉) · J.G.M. Kuerten · B.J. Geurts
Faculty EEMCS, University of Twente, Enschede, The Netherlands
e-mail: a.bukhvostova@utwente.nl

B.J. Geurts
e-mail: b.j.geurts@utwente.nl

E. Russo · J.G.M. Kuerten
Department of Mechanical Engineering, Eindhoven University of Technology, Enschede, The Netherlands

D.G.E. Grigoriadis et al. (eds.), *Direct and Large-Eddy Simulation X*,
ERCOFTAC Series 24, https://doi.org/10.1007/978-3-319-63212-4_22

by a fully compressible description, which allows to quantify the consequences of non-constant mass density of the carrier gas under a variety of thermal and turbulent conditions. We concentrate on turbulent channel flow in which the top wall is heated uniformly and the lower one is cooled. We will investigate the dependence of the thermal properties such as the mean temperature and the Nusselt number on Mach number, on the thermal forcing applied to the system and on the mean temperature within the channel and compare directly with the incompressible results.

2 Mathematical Model

We consider a water-air system in a channel, bounded by two parallel horizontal plates. The domain has a size of $4\pi H$ in the streamwise direction, which is denoted by x, and $2\pi H$ in the spanwise direction, z, where H is half the channel height. In addition, y is the coordinate in the wall-normal direction. A constant heat flux $\dot{Q}$ is applied through the walls: this heat flux is positive through the top wall and negative through the bottom wall. The flux at both walls is equal in size in order to conserve the total energy of the system. The considered system consists of two phases: the continuous and the dispersed. Initially, the droplets are randomly distributed over the total volume of the channel.

We treat the carrier phase as a compressible Newtonian fluid. We impose conservation of mass, momentum, total energy density and water vapor. The equations can be written as [2]:

$$\partial_t \rho + \partial_j(\rho u_j) = Q_m \tag{1}$$

$$\partial_t(\rho u_i) + \partial_j(\rho u_i u_j) = -\partial_i p + \partial_j\left(\mu(T) S_{ij}\right) + F_i + Q_{mom,i} \tag{2}$$

$$\partial_t e + \partial_j\left((e+p)u_j\right) = -\partial_j q_j - \partial_j(u_i \mu(T) S_{ij}) + Q_e \tag{3}$$

$$\partial_t(\rho Y_v) + \partial_j(u_j \rho Y_v) = \partial_j(J_{v,j}) + Q_m \tag{4}$$

This system is solved for mass density ρ, momentum density components ρu_i, total energy density e and vapor mass density ρY_v. The source terms Q_m, $Q_{mom,i}$, Q_e express the interaction between the phases. The term F_i is an external force density, which is chosen in such a way that the total momentum in the streamwise direction is constant in time.

In Eq. (2) S_{ij} is the compressible extension of the rate-of-strain tensor defined as $S_{ij} = \partial_i u_j + \partial_j u_i - \frac{2}{3}\Delta\delta_{ij}$ where $\Delta = \partial_k u_k$ denotes the divergence of the velocity. Here and elsewhere we adopt the summation convention implying summation over repeated indices. The dynamic viscosity of the carrier gas μ depends on temperature through Sutherland's law. In addition, q_j in (3) denotes the components of the heat flux vector, which consists of heat transport by conduction and by diffusion of vapor. The vector $\mathbf{J}_v$ defines the diffusive mass flux of water vapor with respect to the mixture velocity. The pressure and temperature of the carrier phase are denoted by p and T and are connected by the ideal gas law for the two-component mixture. An explicit

equation of state is used to connect pressure and temperature in the compressible case, the incompressible formulation solves the pressure from a Poisson equation derived from the condition of a divergence-free velocity field.

The system of ordinary differential equations for the dispersed phase is identical to the one described in [3]. The model uses a point-particle approach. We assume that the droplets are spherical and include evaporation and condensation to describe the phase-transition response of the droplets to the thermodynamic conditions found in the carrier gas along their trajectories. In addition, Q_m, $Q_{mom,i}$, Q_e are obtained from the condition that the interaction between the two phases conserves mass, momentum and energy.

3 Numerical Methods and Initial Conditions

The incompressible and compressible models are simulated using different numerical methods. The incompressible formulation adopts a pseudo-spectral method for the carrier phase as described in [3]. In the two periodic directions a Fourier-Galerkin approach is used, while a Chebyshev-collocation approach is applied in the wall-normal direction. The droplet equations are integrated in time with the same three-stage Runge–Kutta method as used for the convective terms in the carrier phase equations. The viscous terms and pressure are integrated in time with the implicit Crank–Nicolson method. The pressure is found at each time level from the divergence-free condition for the velocity. The numerical model for the compressible carrier phase adopts explicit second-order Runge–Kutta time-stepping and a second order finite volume discretization.

Two sets of simulations were chosen in order to quantify the dependence of the heat transfer properties on the value of the Mach number: the value of the heat flux through the walls and the mean temperature level within the channel.

All chosen cases are described in the Table 1. During the first set of simulations we vary the Mach number, Ma, from a value as high as 0.2 to more realistic values as low as 0.05, cases 1, 2 and 3. From these simulations we can identify the sensitivity of predictions of the compressible formulation to the adopted Mach number and its relation to truly incompressible results. In order to investigate the sensitivity to explicit compressibility further a second set of simulations is considered. In this set we examine how an increased heat flux and an increased temperature level affect the agreement between the two formulations. First, we increase the heat flux to the walls, making its absolute value 5 times bigger, case number 4. Second, we investigate a case in which the reference temperature within the channel is set equal to 323.15 K, case number 5. The chosen value of temperature is higher than the room temperature used in case 3, but still corresponds to relatively mild conditions far from the boiling point of water.

Table 1 The carrier gas conditions for the compressible simulations

Case	Ma	$\dot{Q}$, $(\mathrm{W/m^2})$	T_{ref}, (K)
1	0.2	32	293.15
2	0.1	32	293.15
3	0.05	32	293.15
4	0.05	160	293.15
5	0.05	34	323.15

4 Thermal Properties - Dependence on Mach Number

In this section the results of the compressible and incompressible formulations will be compared. The main purposes of the comparison are to see whether the compressible results converge to the incompressible if we decrease the value of the Mach number and under what flow conditions the compressible formulation is needed for accurate results. We will concentrate on heat transfer properties of the system.

The heat flux at the walls causes the development of a temperature gradient in the wall-normal direction within the channel: a region with higher temperatures forms near the top wall and a region with lower temperatures near the bottom wall. To express the efficiency of the heat transfer within the channel, it is common to use the Nusselt number. We will study this quantity for all chosen cases. The new issue of this study is the ability of the droplets to undergo phase transition. Some studies were done in order to examine how the presence of solid particles in a turbulent channel affects the Nusselt number. It is known that their presence can increase the value of the Nusselt number by more than a factor of two [4]. In the current study phase transition is considered and its effect on the value of the Nusselt number will be discussed.

The development of the mean temperature profile in time is presented in Fig. 1 for Ma $= 0.2$. After a short transient the mean profile settles robustly. In Fig. 2 the mean temperature profile averaged over time in the long-time regime is presented for different values of the Mach number and compared with the incompressible results. It can be concluded that the compressible formulation yields results converging readily to the incompressible model: Ma $= 0.05$ shows the best agreement between the two formulations out of the three values of the Mach number. However, even for the lowest Mach number, 0.05, some differences in the temperature profiles remain which are caused by differences in the numerical approaches and forcing of the flow.
The Nusselt number is defined in the following way:

$$\mathrm{Nu} = \left(\frac{d\overline{T_g}}{dy} \Big|_{wall} \right) \Big/ \frac{\Delta \overline{T_g}}{2H} \tag{5}$$

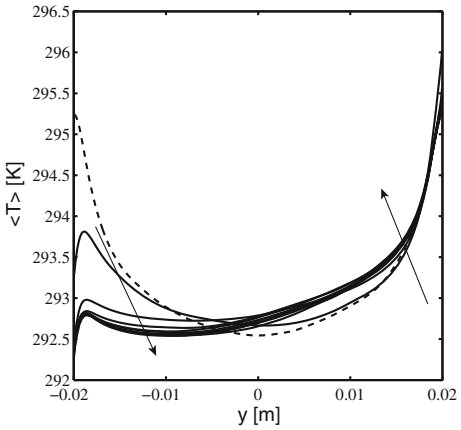

Fig. 1 Gas temperature averaged over two homogeneous directions as a function of the wall-normal coordinate at different times. The *dashed line* is the initial profile, all *solid lines* show the evolution of the profile in the time interval [0.2 s; 8 s] for case 1. The *arrows* show the direction of increasing time

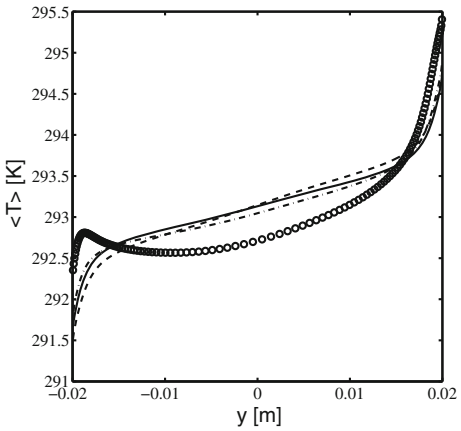

Fig. 2 Gas temperature averaged over the two homogeneous directions and the time interval [2 s; 8 s] as a function of the wall-normal coordinate. *Dashed* incompressible case; *circles* case 1; *dash-dotted* case 2; *solid* case 3

where bars denote averaging over the two homogeneous directions, ΔT_g is the difference in gas temperature between the two walls and the numerator is the average over both walls. Figure 3 shows how the Nusselt number depends on time for both formulations. We observe a close agreement with a relative difference of about 10%. The compressible formulation predicts a slightly higher value than the incompressible model. Figure 4 shows the comparison of the two formulations for cases 3, 4 and 5. The Nusselt numbers obtained from the compressible simulations are slightly higher for all three cases. Moreover, the case with the higher reference temperature gives a significant increase in the value of the Nusselt number by more than a factor of 2. Figure 4 shows that the compressible formulation is essential in this case and it is expected to be the only accurate description in cases where phase transitions play a larger role.

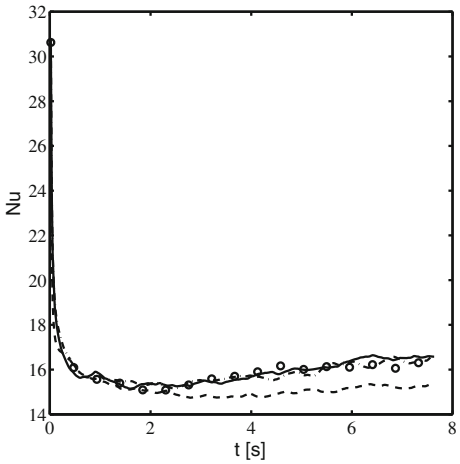

Fig. 3 The Nusselt number history. *Dashed* incompressible case; *circles* case 1; *dash-dotted* case 2; solid case 3

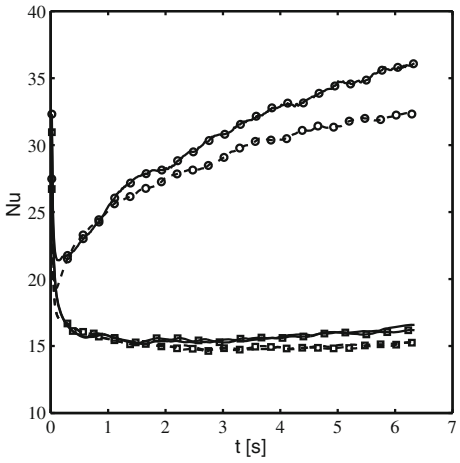

Fig. 4 The Nusselt number history. *Solid* compressible case, *dashed ones* incompressible. *Lines without markers* case 3, *square-marked* case 4, *circle-marked* case 5

5 Conclusions

We compared an incompressible and a compressible formulation for droplet-laden turbulent channel flow. The comparison involved two completely different spatial and temporal discretization methods. Three values of the Mach number were tested in the case of the compressible model and convergence of heat transfer results to the incompressible model was found with decreasing Mach number for a specific reference case. The agreement was tested further for increasing heat flux to the walls of the channel and for increasing mean gas temperature. It was found that the compressible formulation becomes essential for accurate predictions in case of a higher temperature level in the channel: the difference in the value of the Nusselt number is about 15%.

The main point of attention for future work regarding the compressible formulation will be to first implement a low-Mach specific algorithm. This will allow to extend the comparison between the incompressible and compressible models to realistically low Mach numbers at feasible computation times. In this way the question can be answered under what flow conditions the compressible formulation incorporating changes in carrier gas mass density is necessary for an accurate description of this flow.

Acknowledgements This work is supported through a PhD grant within the FOM DROP program and a PhD grant provided by the Dutch Technology Foundation STW, applied-science division of NWO (Netherlands Organisation for Scientific Research), and the Technology Program of the Ministry of Economic Affairs of the Netherlands. This work was sponsored by the Stichting Nationale Computerfaciliteiten (National Computing Facilities Foundation, NCF) for the use of supercomputer facilities, with Financial support from the Nederlandse Organisatie voor Wetenschappelijk Onderzoek, NWO (project SH-061).

References

1. Elghobashi, S.: On predicting particle-laden channel flow. Appl. Sci. Res. **52**, 309–329 (1994)
2. Mashayek, F.: Direct numerical simulations of evaporating droplet dispersion in forced low mach number turbulence. Int. Heat Mass Transfer. **41**, 2601–2617 (1997)
3. Russo, E., Kuerten, J.G.M., van der Geld, C.W.M., Geurts, B.J.: Modeling water droplet condensation and evaporation in DNS of turbulent channel flow. J Phys. Conf. Ser. **318**, 052019 (2011)
4. Kuerten, J.G.M., ven der Geld, C.W.M., Geurts, B.J.: Turbulence modification and heat transfer enhancement by inertial particles in turbulent channel flow. Phys. Fluids. **23**, 123301 (2011)

Part V
LES Modeling

A Novel Approach for Wall Modeling in LES of Wall-Bounded High-Reynolds-Number Flow via Function Enrichment

B. Krank and W.A. Wall

1 Introduction

The computational cost of wall-bounded large-eddy simulation (LES) is strongly dependent on the Reynolds number. While turbulent low-Reynolds-number flows of engineering interest may be successfully predicted with state-of-the-art computational methods, LES involving high Reynolds numbers requires very fine meshes near the wall to resolve the necessary scales. Wall models therefore represent near-wall turbulence in a statistical sense by applying artificial traction boundary conditions to the outer flow. One time step of the outer flow thus comprises many life times of near-wall eddies and a discretization cell is much larger than the typical scale of near-wall eddies.

For these statistical wall models to be accurate, the sample of near-wall eddies must however be large enough to capture the statistical properties of the inner layer. Common wall models are therefore more accurate at very high Reynolds numbers and very coarse grids [7].

On the other hand, detached-eddy simulation (DES) [9] applies RANS turbulence models in the vicinity of the wall and the velocity gradient is resolved with a relatively fine mesh in wall-normal direction making calculations of moderate to high Reynolds numbers quite expensive. Under-resolution close to the wall causes an incorrect velocity profile resulting in underprediction of the wall shear stress [6].

In this study, a method is presented that intends to fill this gap between wall models for very large Reynolds numbers and DES by applying coarse meshes but yet resolving the boundary layer gradient close to the wall. The method has recently

B. Krank (✉) · W.A. Wall
Institute for Computational Mechanics, Technical University of Munich, Boltzmannstraße 15, 85747 Garching b. München, Germany
e-mail: krank@lnm.mw.tum.de

W.A. Wall
e-mail: wall@lnm.mw.tum.de

D.G.E. Grigoriadis et al. (eds.), *Direct and Large-Eddy Simulation X*,
ERCOFTAC Series 24, https://doi.org/10.1007/978-3-319-63212-4_23

been proposed by Krank and Wall in [4] and excellent results have been obtained both for attached and separated boundary layers. In the next section, the basic idea is summarized and subsequently results of a backward-facing-step flow at a step Reynolds number of $Re_h = 5000$ are discussed.

2 Enriching the Solution Space

One of the main disadvantages of standard computational methods applied to DES is the use of low-order polynomial function spaces which cannot resolve the high velocity gradient at the wall unless fine discretizations are employed. On the other hand, wall functions are often inaccurate when used in separated flow regimes. In this study, we combine these two wall modeling approaches by enriching the function space of the computational method with a wall function such that the velocity gradient at the wall can be resolved with coarse discretizations. The solution is not prescribed, but the computational method is able to choose the correct solution among all functions available in its function space. The following advantages are expected compared to other wall modeling approaches:

- Much coarser meshes may be used compared to DES.
- Better results may be expected in separated flows compared to wall functions.
- The skin friction may be computed accurately despite the coarseness of the mesh.

We suggest the law-of-the-wall [10] as enrichment function, since it is a well-established description of the mean velocity of turbulent boundary layers. As numerical method we utilize the extended finite element method (XFEM)[1], which provides the possibility of function enrichment.

In the current approach the velocity function space $\mathbf{u}^h$ in a layer close to the wall consists of the standard linear approximation $\bar{\mathbf{u}}^h$ and an extension $\widetilde{\mathbf{u}}^h$ as

$$\mathbf{u}^h(\mathbf{x}, t) = \bar{\mathbf{u}}^h(\mathbf{x}, t) + \widetilde{\mathbf{u}}^h(\mathbf{x}, t). \tag{1}$$

The standard finite element expansion is

$$\widetilde{\mathbf{u}}^h(\mathbf{x}, t) = \sum_{B \in N^{\mathbf{u}}} N_B^{\mathbf{u}}(\mathbf{x}) \widetilde{\mathbf{u}}_B \tag{2}$$

with the shape functions $N_B^{\mathbf{u}}$ and nodal values $\bar{\mathbf{u}}_B$ and the enrichment with additional degrees of freedom $\widetilde{\mathbf{u}}_B$ is represented by

$$\widetilde{\mathbf{u}}^h(\mathbf{x}, t) = \sum_{B \in N_{enr}^{\mathbf{u}}} N_B^{\mathbf{u}}(\mathbf{x})(\psi(\mathbf{x}, t) - \psi(\mathbf{x}_B, t))\widetilde{\mathbf{u}}_B \tag{3}$$

where only a subset of nodes $N_{enr}^{\mathbf{u}} \subset N^{\mathbf{u}}$ is enriched. The enrichment function ψ is subtracted by its nodal values and represents a problem-tailored profile. As

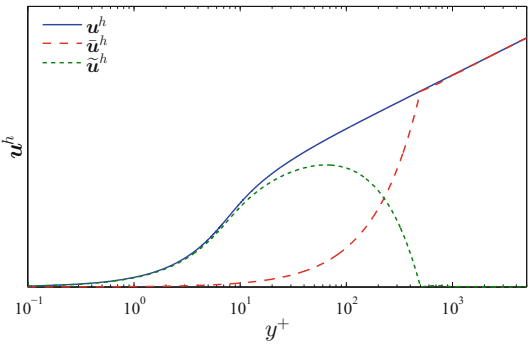

Fig. 1 Decomposition of the mean velocity profile into a linear and enrichment function space

enrichment function we propose a modification of the law-of-the-wall [10] implicitly defined by

$$y^+ = \frac{\psi}{\kappa} + e^{-\kappa B}(e^{\psi} - 1 - \psi - \frac{\psi^2}{2!} - \frac{\psi^3}{3!} - \frac{\psi^4}{4!}). \tag{4}$$

The law-of-the-wall describes the mean velocity profile of a turbulent boundary layer within the viscous sub- and buffer layer as a blending from a linear to a logarithmic profile.

Note that we do not prescribe Spalding's law a priori as velocity profile, but we provide the FEM with the ability to utilize a linearly weighted law-of-the-wall, besides the standard linear shape functions. And it is one key feature of the FEM that it tries to find the optimal solution from the whole available function space, i.e. here from standard Lagrange polynomials plus the law-of-the-wall functions.

The decomposition of a turbulent boundary layer profile into the linear and enrichment function space according to Eq. (1) is displayed in Fig. 1 using the law-of-the-wall (4) as enrichment function. The velocity gradient is predicted directly through the available finite element function space even for coarse element discretizations and does not require any additional wall model. Compared to standard equilibrium-stress wall models, pressure gradients are not an issue as the full Navier–Stokes equations are solved in the wall region. In contrast to hybrid- or two-layer models, no additional or simplified equations are solved near the wall.

The current approach is also compatible with the idea of DES. In classical DES methods, a blending of the turbulence model from RANS to LES has to be defined. In the present approach, this blending is a priori given by the idea of modeling the under-resolved eddies in a statistical sense with the enrichment and the resolved eddies with the classical linear function space. In our ongoing work, we develop a turbulence modeling approach exploiting this idea, which uses a RANS closure on the enrichment scale and an LES scheme on the standard polynomial part, although these regions are not spatially separated. The result is furthermore that a log-layer mismatch, which is typical for DES, is not observed, since the RANS model only directly affects the enrichment scale and not the LES modes.

For the backward-facing step flow discussed in the following, the incompressible Navier–Stokes equations are solved for the velocity $\mathbf{u}$ and pressure p as

$$\frac{\partial \mathbf{u}}{\partial t} + \mathbf{u} \cdot \nabla \mathbf{u} + \nabla p - 2\nu \nabla \cdot \boldsymbol{\varepsilon}(\mathbf{u}) = \mathbf{f} \tag{5}$$

$$\nabla \cdot \mathbf{u} = 0 \tag{6}$$

with the kinematic viscosity ν as well as the symmetric rate-of-deformation tensor $\boldsymbol{\varepsilon}(\mathbf{u}) = \frac{1}{2}(\nabla \mathbf{u} + (\nabla \mathbf{u})^T)$. For the numerical example presented in the following, subgrid turbulence is modeled by explicit reconstruction of the unresolved scales via a multifractal scale similarity method [8]. Since the enrichment is a feature of the spatial discretization only, any other turbulence modeling approach may be used, including hybrid RANS/LES methods.

3 Flow over a Backward-Facing Step at $Re_h = 5000$

The proposed method has been validated for turbulent channel flow at various friction Reynolds numbers on very coarse grids and the influence of mesh refinement has been studied in [4]. Excellent results have been found for this test case with the first off-wall grid point located at up to $y_1^+ = 500$ wall units. Further, the wall model has been applied to flow over periodic hills at a hill Reynolds number of $Re_H = 10{,}595$ and 19,000 as well as a backward-facing step at $Re_h = 5000$ based on the step height. Especially the skin friction is predicted accurately for these flows, which is often challenging for wall models.

In this paper, our wall model is investigated with a flow over a backward-facing step at a Reynolds number of $Re_h = 5000$ based on the step height and an expansion ratio of $ER = 1.2$ according to the experiments by Jovic and Driver [2]. The domain behind the step is of the size $30h \times 6h \times 3h$ in streamwise, wall-normal and spanwise direction, respectively, and the mesh consists of $120 \times 24 \times 20$ cells. This mesh is equal to the one discussed in [4] in streamwise and wall-normal direction but in [4] only 12 cells were used in spanwise direction. The boundary conditions are also chosen as in [4] consisting of slip boundary conditions on the top wall, no-slip

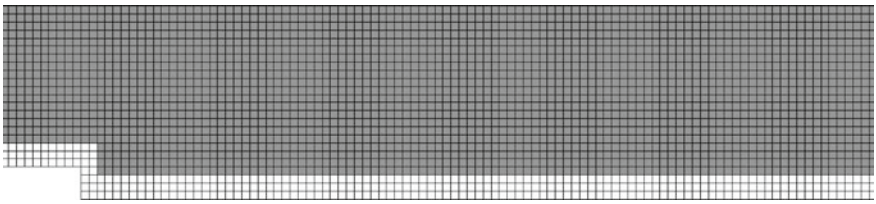

Fig. 2 Mesh of the backward-facing-step flow. Enriched cells (*transparent*), standard cells (*grey*)

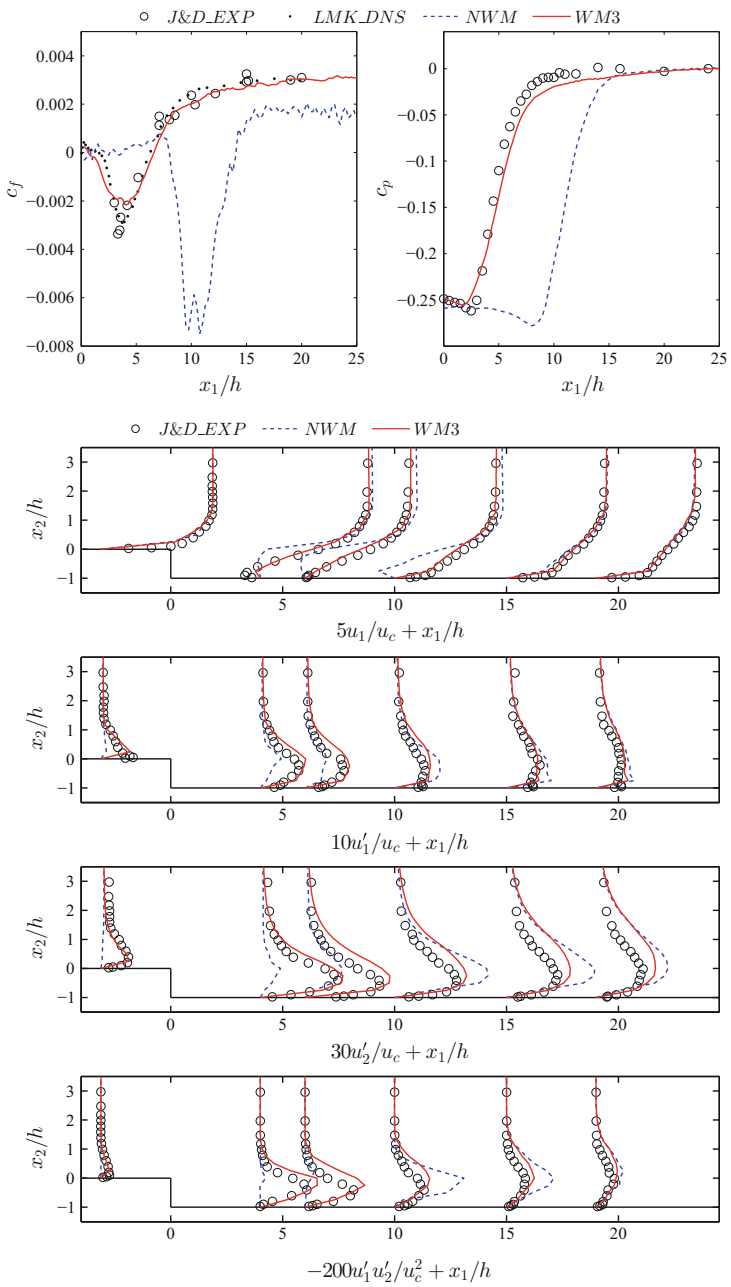

Fig. 3 Flow over a backward-facing step. *Top* skin friction and pressure coefficients. *Bottom* mean and RMS velocities as well as reynolds shear stresses. Experimental data *J&D_EXP*, DNS *LMK_DNS*, no wall model *NWM*, wall model with three layers *WM3*

boundary conditions at the bottom wall including the step and periodic conditions in spanwise direction. As displayed in Fig. 2, three element rows at the lower wall are enriched while the standard space is used for the remaining cells. The results are in the following compared to experimental data by Jovic and Driver [2], labeled $J\&D\_EXP$ and the skin friction coefficient is additionally compared to DNS data at a similar Reynolds number of Le, Moin and Kim [5], labeled LMK_DNS.

The skin friction and pressure coefficients for this mesh show excellent agreement with reference data in Fig. 3 if the wall model is included (case $WM3$). Without wall model (case NWM), the peak of the skin friction is shifted downstream by several step lengths and is massively over predicted. The pressure coefficient is also much better predicted if the enrichment-based wall model is included.

The wall model is further evaluated with the streamwise mean velocity u_1, the root-mean square velocities u_1' and u_2' as well as Reynolds shear stresses $u_1'u_2'$ in Fig. 3 at six stations. Considering the coarseness of the mesh, good results are found for the case with wall modeling while large errors are observed without wall model.

4 Concluding Remarks

A new approach to wall modeling has been presented which enables resolution of the mean boundary layer with very coarse meshes and yields excellent results under challenging conditions such as flow separation. Although the method has been presented here within FEM, it is not limited to it. Our recent developments include application of the wall modeling approach to RANS using the Spalart–Allmaras model within a Discontinuous Galerkin method [3] and its extension to hybrid RANS/LES in the same framework.

References

1. Belytschko, T., Gracie, R., Ventura, G.: A review of extended/generalized finite element methods for material modeling. Model. Simul. Mater. Sci. Eng. **17**(4), 043001 (2009)
2. Jovic, S., Driver, D.M.: Backward-facing step measurements at low Reynolds number, $Re_H = 5000$. NASA TM 108807 (1994)
3. Krank, B., Wall, W.A.: A new approach to wall modeling in LES of incompressible flow via function enrichment. J. Comput. Phys. **316**, 94–116 (2016)
4. Krank, B., Kronbichler, M., Wall, W.A.: Wall modeling via function enrichment within a high-order DG method for RANS simulations of incompressible flow. Int. J. Numer. Meth. Fluids (2017). doi:10.1002/fld.4409
5. Le, H., Moin, P., Kim, J.: Direct numerical simulation of turbulent flow over a backward-facing step. J. Fluid Mech. **330**, 349–374 (1997)
6. Piomelli, U., Balaras, E.: Wall-layer models for large-eddy simulations. Annu. Rev. Fluid Mech. **34**, 349–374 (2002)
7. Piomelli, U.: Wall-layer models for large-eddy simulations. Prog. Aerosp. Sci. **44**, 437–446 (2008)

8. Rasthofer, U., Gravemeier, V.: Multifractal subgrid-scale modeling within a variational multiscale method for large-eddy simulation of turbulent flow. J. Comput. Phys. **234**, 233–265 (2013)
9. Spalart, P.R., Jou, W.H., Strelets, M., Allmaras, S.R.: Comments on the feasibility of LES for wings and on a hybrid RANS/LES approach. In: Liu, C., Liu, Z. (eds.) Advances in DNS/LES, pp. 137–148. Ohio Greyden Press, Columbus (1997)
10. Spalding, D.B.: A single formula for the law of the wall. J. Appl. Mech. **28**, 444–458 (1961)

Influence of Periodic Forcing on Laminar Separation Bubble

E. ElJack, I. AlQadi and J. AlMutairi

1 Introduction

Flow control plays an important role in enhancing aerodynamic characteristics of airfoils such as reducing skin-friction drag, advancing or delaying transition, preventing or triggering separation, and enhancing the lift coefficient. In the review paper of Gad-el-Hak and Bushnell [6], they provided an extensive review of flow control techniques such as blowing [11], suction [13] acoustic excitation [18], periodic forcing excitation by imposing an oscillating wire or flap upstream the separation location [5, 10, 15] and utilization of magnetic field through plasma actuators as documented by Post and Corke [12] and Huang et al. [7]. Stall can be eliminated by controlling the boundary layer through the addition of momentum to fluid particles near the surface of the airfoil.

Low-frequency flow oscillation is a critical unsteady phenomenon which occurs at the onset of airfoil stall [2] causing undesirable effects. Large Eddy Simulation (LES) is an efficient numerical tool to predict the effect of periodic forcing on the performance of low-Reynolds number airfoils [1]. Flow forcing is applied to the boundary layer in order to eliminate the negative effects of laminar separation bubble (LSB) thus preventing low-frequency flow oscillation and improving the performance of low-Reynolds number airfoils.

Almutairi [1] showed that periodic forcing technique has high effectiveness in controlling flow separation. He illustrated that trailing edge flapping, at high Mach

E. ElJack (✉) · I. AlQadi
King Abdulaziz University, Jeddah, Saudi Arabia
e-mail: eljack@kau.edu.sa

I. AlQadi
e-mail: ialqadi@kau.edu.sa

J. AlMutairi (✉)
College of Technological Studies, Paaet, Kuwait
e-mail: jh.almutairi@paaet.edu.kw

D.G.E. Grigoriadis et al. (eds.), *Direct and Large-Eddy Simulation X*,
ERCOFTAC Series 24, https://doi.org/10.1007/978-3-319-63212-4_24

number ($M_\infty = 0.8$) and zero angle of attack, was eliminated with measurable enhancement in the aerodynamic performance. Almutairi [1] suggested a procedure to apply the periodic forcing for the boundary layer control utilizing the trailing edge frequency. The forcing is applied at this frequency. In the current work, large eddy simulation is carried out to investigate the influence of periodic forcing on laminar separation bubble for flow around NACA-0012 airfoil at an angle of attack $\alpha = 11.5°$ and Reynolds number 1.3×10^5. At these conditions the low-frequency flow oscillation phenomenon takes place as observed experimentally by Rinoie and Takemura [14] and numerically by AlMutairi et al. [3]. Dynamic Mode Decomposition (DMD) was used to analyze the flow field [3]. DMD was applied to a sample of instantaneous pressure recorded along the middle plane and spanning over one low-frequency cycle (25 non-dimensional time units). DMD spectrum of the flow field showed two distinct dominant modes, a low-frequency mode ($St = 0.00839$) and a high-frequency mode ($St = 0.1669$). The low-frequency mode features two distinct events; fully separated flow followed by fully attached flow. The high-frequency mode features a strong vortex shedding at the airfoil trailing edge, during the fully separated phase. The strong vortex shedding at the airfoil trailing edge generates acoustic waves that travel upstream and excite the laminar shear layer and force it into early transition and consequently force the separated flow to reattach. Once the flow is attached the strong vortex shedding dies down and the feed back mechanism via acoustic waves is cut-off, the flow separate eventually and the process repeats itself in a periodic manner. The continuous presence of the high-frequency mode would prevent bubble bursting and consequently remove the low-frequency flow oscillation. It is thus possible to replace the effect of the high-frequency mode via periodic forcing. AlMutairi et al. [3] proposed that the high-frequency mode can be used to control the separated flow and force it to reattach by means of periodic forcing applied at this frequency or combinations of it. The present study takes up Almutairi et al. [3] work and utilize their DMD results to explore various combinations of forcing frequencies based on the analysis of the simulated flow field.

2 Numerical Modeling and Computational Setup

The flow field around NACA-0012 airfoil is computed using a LES code which was extensively validated by Jones et al. [9] and Almutairi et al. [4]. The code solves the compressible Navier-Stokes equations after applying low-pass filtering and incorporating the mixed-time-scale (MTS) model constructed and validated by Inagaki et al. [8]. The computational domain is shown in Fig. 1. The width of the domain is set to 50% of the chord. This was found to be necessary to obtain accurate results [4]. The outflow boundary is located five chord lengths downstream the airfoil's trailing-edge while the far-field boundary is located over seven chord lengths from the trailing-edge line. At the upstream and far-field boundaries, the code implements the integral characteristic boundary condition of Sandhu and Sandham [17] combined with a buffer zone to further reduce reflections from the boundary. At the

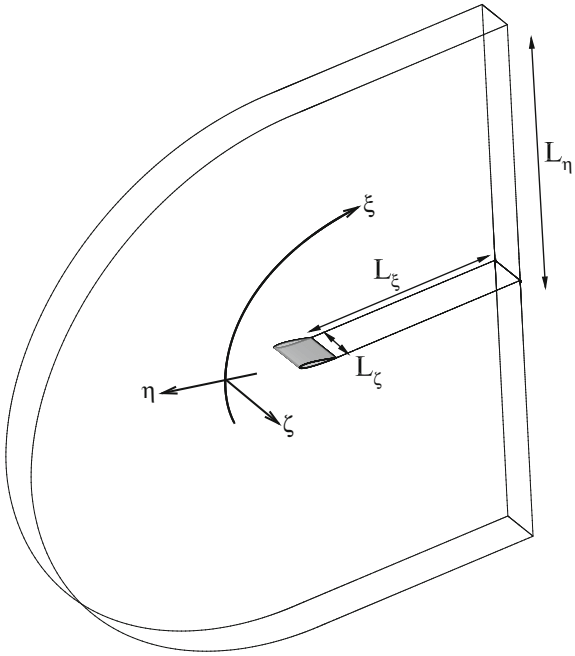

Fig. 1 Computational domain

downstream boundary, the zonal characteristic boundary condition [16] is applied. The airfoil surface is insulated and no-slip wall condition is applied. The internal branch-cut boundary is updated at each step of the Runge-Kutta scheme. A grid was constructed around NACA-0012 airfoil oriented at an angle of attack $\alpha = 11.5°$. The number of grid points along the curvilinear directions ξ, η, and ζ are 1485, 500, and 86, respectively. The resolution of the current grid is illustrated in Fig. 2. The grid resolution was computed based on mean skin friction over one cycle. The maximum grid spacings over the transitional and turbulent regions, at the airfoil surface, are $\Delta y^+ = 1.9$, $\Delta x^+ = 11$, and $\Delta z^+ = 41$.

3 Results and Discussions

Large eddy simulations incorporating a small-amplitude periodic forcing of the flow field around NACA-0012 airfoil are carried out at angle of attack $\alpha = 11.5°$, Reynolds number 1.3×10^5, and Mach number $M_\infty = 0.4$. The periodic forcing is introduced into the laminar boundary layer just upstream the location of the flow separation, ($x = 0.0128$, $y = 0.02$) measured from the airfoil leading edge. The amplitude of the forcing is set to 0.3% of the free-stream velocity. A single forcing frequency is not sufficient to energize the shear layer and force the flow to reattach. Three combinations of the trailing-edge frequency were considered as follows:

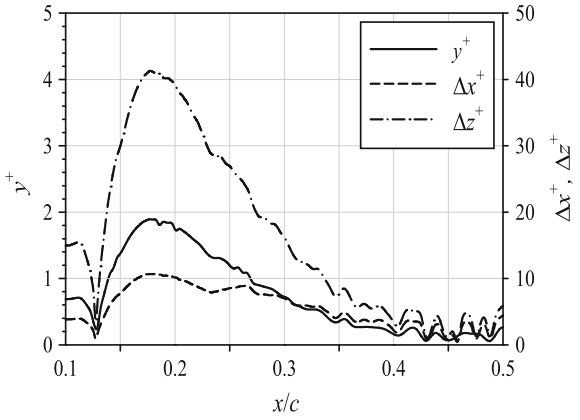

Fig. 2 Wall grid resolution

- Case I: A single forcing frequency equal twice trailing edge shedding frequency ($2f_t$).
- Case II: A combination of the trailing edge shedding frequency with its sub and super harmonics ($f_t/4,\ f_t, 4f_t$).
- Case III: A combination of twice the trailing edge shedding frequency with its sub and super harmonics ($f_t/2, 2f_t, 8f_t$).

The periodic forcing was implemented onto a fully developed flow field, i.e., the flow forcing was applied after the low-frequency flow oscillation has started and became self-sustained. Statistical data, including instantaneous and averaged flow quantities are sampled every one non-dimensional time unit. The time-step is set to 10^{-4} non-dimensional time units. The time-dependent aerodynamic forces such as lift, drag and skin-friction coefficients are sampled every 20 time-steps.

Figure 3a, b show comparison of the time histories of the lift and drag coefficients for the unforced and the forced, case I, flow fields. Data analysis, not presented here, showed that in this case the bubble is smaller in size compared to the unforced case. It is evident that the single frequency forcing affected the bubble shape and size but did not remove the low-frequency flow oscillation. For Case II, data analysis showed that the bubble size is much smaller compared to the unforced flow. The periodic forcing, in this case, damped the low-frequency flow oscillation. Consequently, the lift coefficient fluctuates near its maximum value at a higher frequency and the drag coefficient fluctuates at its minimum value as can be seen in Fig. 3c, d. The forcing has completely removed the large fluctuations in the lift and drag coefficients for Case III as shown in Fig. 3e, f. Flow forcing, in this case, has fixed the lift coefficient around its maximum value and the drag coefficient around its minimum value and greatly improved the airfoil performance. Data analysis showed that the laminar separation bubble is smaller in size and does not burst.

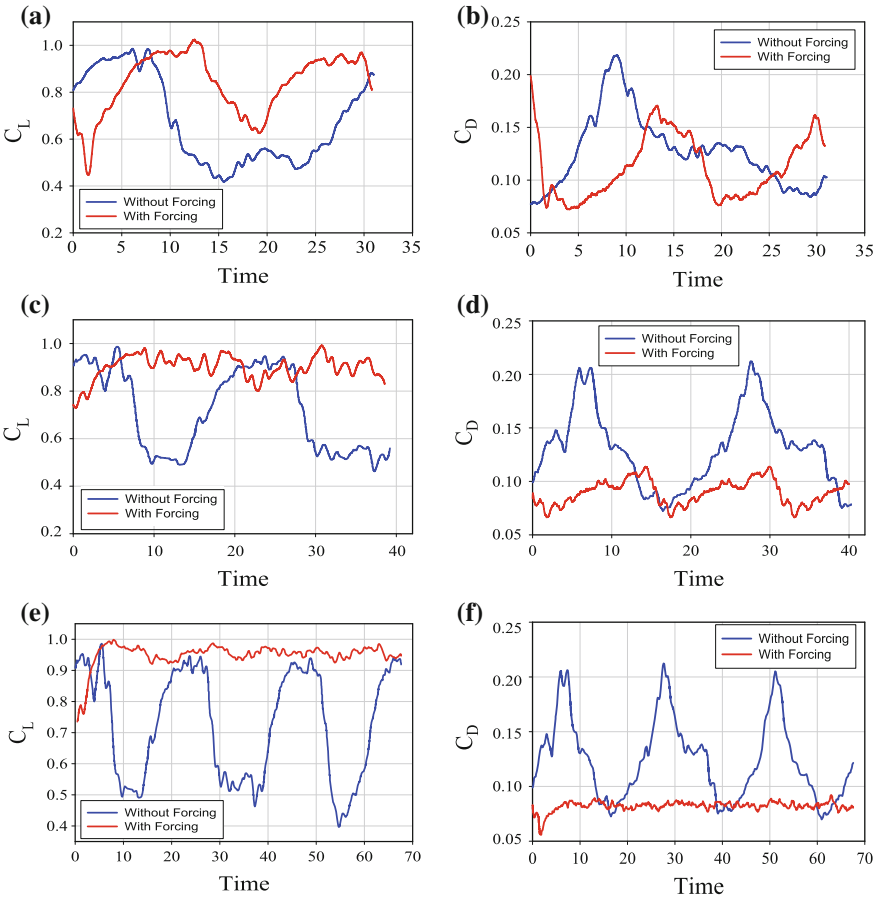

Fig. 3 Comparison of the time histories of the lift and drag coefficients with and without forcing. From *top* to *bottom* Case I; Case II; Case III

4 Conclusions

In this study, the trailing edge shedding frequency identified by the DMD analysis is utilized as a forcing frequency. Three different combinations of this frequency were used to force the flow; a single forcing frequency equal twice trailing edge shedding frequency (Case I), a combination of the trailing edge shedding frequency with its sub and super harmonics (Case II); a combination of twice the trailing edge shedding frequency with its sub and super harmonics (Case III). Case I reduced the magnitude of oscillations in both lift and drag coefficients and reduced the bubble size. Case II greatly reduced the magnitude of oscillations but with a higher frequency. Case III removed most of the lift and drag oscillations. It is concluded that flow forcing

using combinations of the trailing edge shedding frequency is effective in removing low-frequency flow oscillation and improving airfoil performance.

Acknowledgements This work was supported by King Abdulaziz City for Science and Technology (KACST) under the NSTIP strategic technologies program - Project. No. (13-SPA499-03). All computations were performed on Aziz Supercomputer at King Abdulaziz university's High Performance Computing Center (http://hpc.kau.edu.sa). The authors would like to acknowledge the computer time and technical support provided by the center.

References

1. AlMutairi, J.H.: Large-eddy simulation of flow around an airfoil at low Reynolds number near stall, Ph.D. thesis, School of Engineering sciences, Southampton University, Southampton, UK (2010)
2. AlMutairi, J.H., AlQadi, I.M.: Large-eddy simulation of natural low-frequency oscillations of separating-reattaching flow near stall conditions. AIAA J. **51**, 981–991 (2013)
3. AlMutairi, J., AlQadi, I., ElJack, E.: Large eddy simulation of a NACA-0012 airfoil near stall. Direct and Large-Eddy Simulation IX, pp. 389–395. Springer, Cham (2015)
4. Almutairi, J.H., Jones, L.E., Sandham, N.D.: Intermittent bursting of a laminar separation bubble on an airfoil. AIAA J. **48**(2), 414–426 (2010)
5. Bar-Sever, A.: Separation control on an airfoil by periodic forcing. AIAA J. **27**(6), 820–821 (1989)
6. Gad-el-Hak, M., Bushnell, D.M.: Separation control: review. J. Fluid Eng. **113**, 5–30 (1991)
7. Huang, J., Corke, T.C., Thomas, F.O.: Unsteady plasma actuators for separation control of low-pressure turbine blades. AIAA J. **44**(7), 1477–1487 (2006)
8. Inagaki, M., Kondoh, T., Nagano, Y.: A mixed-time-scale SGS model with fixed model-parameters for practical LES. J. Fluid Eng. **127**, 1–13 (2005)
9. Jones, L.E., Sandberg, R.D., Sandham, N.D.: Direct numerical simulation of forced and unforced separation bubbles on an airfoil at incidence. J. Fluid Mech. **602**, 175–207 (2008)
10. Katz, Y., Nishri, B., Wygnanski, I.: The delay of turbulent boundary layer separation by oscillatory active control. Phys. Fluids Fluid Dyn. **2**, 179–181 (1989)
11. McLachlan, B.G.: Study of a circulation control airfoil with leading/trailing-edge blowing. J. Aircr. **25**, 817–821 (1989)
12. Post, M.L., Corke, T.C.: Separation control on high angle of attack airfoil using plasma actuators. AIAA J. **42**(11), 2177–2184 (2004)
13. Purohit, S.C.: Effect of vectored suction on a shock-induced separation. AIAA J. **25**, 759–760 (1987)
14. Rinoie, K., Takemura, N.: Oscillating behavior of laminar separation bubble formed on an aerofoil near stall. Aeronaut. J. **108**, 153–163 (2004)
15. Roos, F.W., Kegelman, J.T.: Control of coherent structures in reattaching laminar and turbulent shear layer. AIAA J. **24**, 1956–1963 (1986)
16. Sandberg, R.D., Sandham, N.D.: Nonreflecting zonal characteristic boundary condition for direct numerical simulation of aerodynamic sound. AIAA J. **44**(2), 402–405 (2006)
17. Sandhu, H.S., and Sandham, N.D.: Boundary conditions for spatially growing compressible shear layers. Reptort QMW-EP-1100, Faculty of Engineering, Queen Mary and Westfield College, University of London, London (1994)
18. Zaman, K.B.M.Q., Bar-Sever, A., Mangalam, S.M.: Effect of acoustic excitation on the flow over a low-Re airfoil. J. Fluid Mech. **182**, 127–148 (1987)

Transition Location Effect on Oblique Shock-Wave/Boundary-Layer Interaction at M=1.5

A. Sansica, N.D. Sandham and Z. Hu

Abstract The effect of transition location on the interaction between an oblique shock-wave and a boundary-layer at $M = 1.5$ on a flat plate is investigated via direct numerical simulations. It is shown that the shock trips transition at the impingement location and the effect of the impingement location on the separation is studied for laminar, transitional and turbulent interactions. Qualitative agreement is obtained with the experiments, as part of the European FP7-2012 TFAST project.

1 Introduction

In high speed flows over wings and in gas turbines, shock-wave/boundary-layer interaction (SWBLI) can occur and cause separation, transition to turbulence and unsteadiness near the interaction region. SWBLI has been an important topic for the aeronautical scientific community over the past 60 years with most of the work carried out for turbulent interactions. Laminar and transitional interactions are also of interest because they can occur in wind tunnel testing, on turbine and compressor blades and on wings and intakes. The present work considers the effect of transition location on the interaction between an oblique shock-wave and a boundary-layer at $M = 1.5$ on a flat plate. Experiments conducted at the Institute of Theoretical and Applied Mechanics (ITAM) in Novosibirsk, Russia for laminar, transitional and turbulent interactions are used for comparisons.

A. Sansica (✉) · N.D. Sandham · Z. Hu
Aerodynamics and Flight Mechanics Research Group, Faculty of Engineering and the Environment, University of Southampton, Southampton SO17 1BJ, UK
e-mail: A.Sansica@soton.ac.uk; andrea.sansica@gmail.com

D.G.E. Grigoriadis et al. (eds.), *Direct and Large-Eddy Simulation X*,
ERCOFTAC Series 24, https://doi.org/10.1007/978-3-319-63212-4_25

2 Numerical Method

As part of the European Union (EU) FP7-2012 project TFAST (http://www.tfast.eu), different interaction types have been investigated numerically with a compressible in-house high-order fully-parallelised finite difference code. More details and validation of the code can be found in Sansica et al. [1]. The numerical setup is based on the experiments carried out by ITAM and three different types of interaction are studied. By moving the shock wave in the streamwise direction it is possible to obtain laminar, transitional and turbulent interactions, depending on the state of the zero-pressure gradient (ZPG) boundary-layer just upstream of the impingement location. The free-stream Mach number is $M = 1.5$, free-stream temperature $T^*_\infty = 197.93$ K and Sutherland's law is used to describe the variation of viscosity μ with the temperature (Sutherland's constant is taken as $T^*_S = 110.4$ K). For all simulations, the inflow boundary is placed at $x_0 = 0.0518$ m downstream of the flat plate leading edge where the displacement thickness is $\delta^*_{1,0} = 1.84 \times 10^{-4}$ m and giving a Reynolds number based on the displacement thickness at the inlet of $Re_{\delta^*_{1,0}} = 1971.07$. The angle of the shock generator plate is fixed to $\theta = 4°$ for all the SWBLI cases. Depending on the interaction type, the streamwise domain length, L_x, is increased in order to let the boundary-layer become either transitional or turbulent before the interaction. Thus, $L_x/\delta^*_{1,0} = 175, 250$ and 350 are selected for the laminar, transitional and turbulent interactions, respectively. For all cases, the domain height is fixed to be $L_y/\delta^*_{1,0} = 90$ in order to avoid any possible reflection of the wave system from the top boundary impinging onto the boundary-layer. The span width is $L_z/\delta^*_{1,0} = 2\pi/\beta = 31$, where β is the spanwise wavenumber of the most unstable mode predicted by local linear stability theory (LST) at the inflow. The grid is uniform in the spanwise direction and stretched in the wall-normal direction clustering about 30% of the grid points within the boundary-layer at the inlet. The grid distribution in the streamwise direction is refined at either the shock impingement or the transition location (whichever comes first). The number of grid points is $(n_x, n_y, n_z) = (1824, 288, 462)$ for the laminar interaction, $(2400, 288, 462)$ for the transitional one and $(2976, 288, 462)$ for the turbulent case. In wall units, the grid resolution in the transitional/turbulent region is $\Delta x^+ = 4.8$, $\Delta z^+ = 4.8$ and $\Delta y^+_{wall} = 0.96$. For the ZPG boundary-layer study, the same domain size and grid resolution as for the turbulent interaction are used. The boundary conditions applied to the computational domain are no-slip and fixed temperature (with temperature equal to the laminar adiabatic wall temperature) at the wall. To minimise the reflection of waves into the domain, an integral characteristic method is applied to the top boundary and a standard characteristic boundary condition at the outflow. A similarity solution profile is applied at the inlet and the boundary-layer is forced with a time-dependent boundary condition. A "broadband modal" forcing technique is used and consists in the forcing of 42 eigenmodes calculated with local LST at the inlet for different combinations of frequency and spanwise wavenumber. Random phases are added to each mode in order to break any symmetries.

3 Results

Forcing is applied to a ZPG boundary-layer with an amplitude of $A_o = 0.05$ (corresponding to a turbulence intensity at the inflow $\rho_{rms} = 0.25\%$). The time and span averaged skin friction distribution (a) and instantaneous streamwise velocity at the centre plane (b) reported in Fig. 1 show that transition starts at $Re_x = 7 \times 10^5$ and the turbulent state is reached at $Re_x = 11 \times 10^5$. An overshoot of the skin friction with respect to empirical distribution from Young (1989) [3] can be seen for $Re_x \geq 1.02 \times 10^6$ due to the high intensity structures formed during the breakdown to turbulence. The main transition scenario is a bypass breakdown where intermittent turbulent spots are generated. Figure 2 shows the contours of vertical vorticity in the vicinity of the wall for two different time instances: $t = 7,900$ (a) and $t = 8,350$ (b). The formation of a turbulent spot is visible in Fig. 2-b between $Re_x = 9 \times 10^5$ and $Re_x = 10.5 \times 10^5$. Three different impingement locations are selected and define

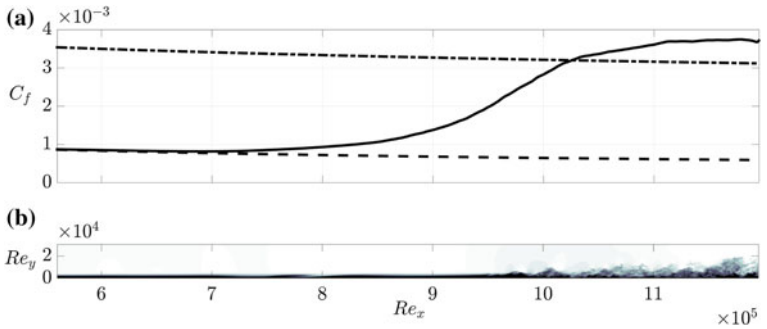

Fig. 1 ZPG boundary-layer case: **(a)** Time and span averaged skin friction distribution (*solid line*) along with laminar (*dashed line*) and turbulent (*dash-dotted line*) boundary-layer distributions by Eckert (1955) [2] and Young (1989) [3], respectively; **(b)** contours of instantaneous streamwise velocity

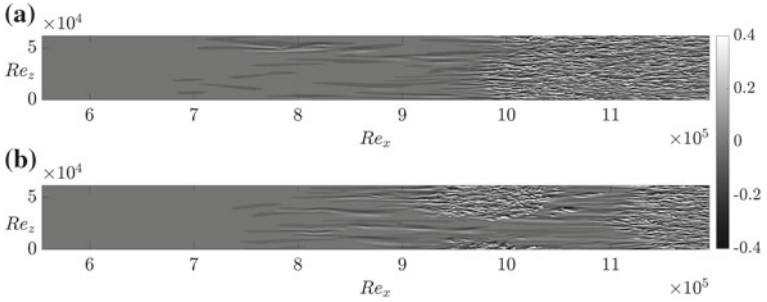

Fig. 2 ZPG boundary-layer case: Contours of vertical vorticity at time levels $t = 7,900$ **(a)** and $t = 8,350$ **(b)**

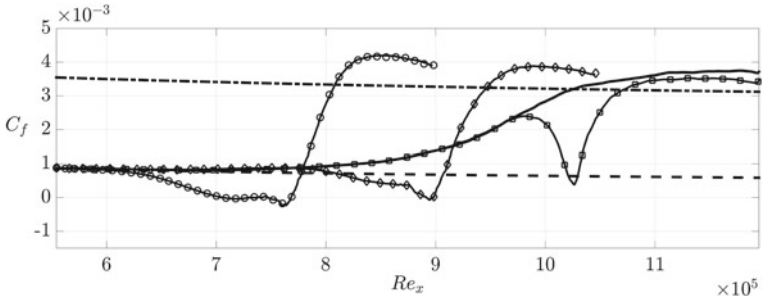

Fig. 3 Time and span averaged skin friction distribution for the laminar (*solid line with circles*), transitional (*solid line with diamonds*) and turbulent (*solid line with squares*) interactions. The ZPG boundary-layer (*solid line*) is also plotted along with laminar (*dashed line*) and turbulent (*dash-dotted line*) boundary-layer distributions by Eckert (1955) [2] and Young (1989) [3], respectively

laminar, transitional and turbulent interactions at an impingement Reynolds number $Re_{x_{imp^*}}(\times 10^5) = 7.6, 8.9$ and 10.2, respectively. Span and time averaged skin friction distributions are reported in Fig. 3 for both the ZPG boundary-layer and the interaction cases. A first main observation is that when a laminar interaction occurs the boundary-layer separates, while it remains attached for the turbulent interaction. For the transitional case, a marginal separation occurs. As part of the TFAST project, Giepman et al. [4] reported a similar situation for different SWBLIs at $M = 1.7$. While the separated region is large for the laminar interaction, for the transitional case the zone of reversed flow is significantly reduced and no mean-flow separation is present for the turbulent interaction. Another important point, in qualitative agreement with the experiments, is that a turbulent boundary-layer is detected immediately downstream of the impingement location for the laminar interaction and that transition is accelerated for the transitional and turbulent cases. The shock is very strong and the boundary-layer becomes turbulent at the shock impingement location. A useful way to determine the state of the boundary-layer is to calculate an intermittency function, Γ, calculated as the fraction of time during which the first and second time derivatives of the skin friction time series are larger than a prescribed threshold, indicating that the boundary-layer is locally turbulent. The span-averaged intermittency distributions for the ZPG boundary-layer case and the interaction cases are reported in Fig. 4-a. The intermittency distributions show a sharp increase towards unity downstream of the impingement location due to the turbulent character of the boundary-layer. Upstream of the impingement, the effect of the shock-wave differs significantly, depending on the type of interaction. For the laminar interaction, the boundary-layer quickly switches from being laminar to turbulent when passing across the shock and this causes a very localised change of the intermittency. The transitional interaction affects the boundary-layer for a longer upstream extent and the increase of intermittency is more gradual. Although the boundary-layer stays attached, the presence of the interaction changes the instability of the boundary-layer and the Γ distribution deviates from the ZPG distribution. This also happens

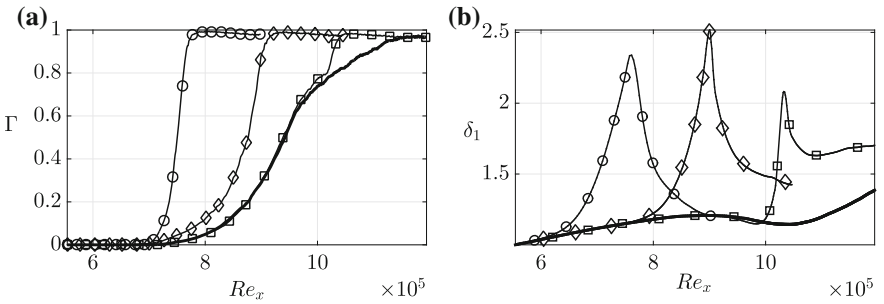

Fig. 4 Span averaged intermittency **(a)** and displacement thickness **(b)** distributions for ZPG boundary-layer case (*solid line*) and the laminar (*solid line with circles*), transitional (*solid line with diamonds*) and turbulent (*solid line with squares*) interactions

for the turbulent case but with less significant consequences since the size of the interaction is much smaller. The upstream response of the boundary-layer to the turbulent interaction is negligible and the major effects are only visible downstream of the impingement, for example on the thickening of the boundary-layer. The time and span averaged displacement thickness distributions, δ_1, reported in Fig. 4-b show that the boundary-layer thickening after the interaction increases with $Re_{x^*_{imp}}$, especially for the transitional and turbulent interactions whose thickening is significantly larger than the ZPG case. Another important difference between the three interactions is the unsteady character of the shock at the impingement. Oil flow visualisations around the shock impingement location provided by ITAM can be used for a qualitative comparison. Figure 5 compares the experimental oil flow visualisations with the DNS statistical skin friction distributions for each interaction. For better clarity, the DNS visualisations are scaled up by a factor of about 2 with respect to the original size, which is indicated in the black rectangle in the oil flow picture (the spanwise location is purely indicative). For the laminar interaction, the paint in the oil flow visualisation is spread significantly upstream of the shock impingement location due to the existence of the separation bubble. For the transitional interaction, the shock location is clearly indicated by the vertical black region. However, the presence of turbulent spots moving through the shock smear the paint and leave localised horizontal traces of paint across the vertical black line. In the same way, the DNS skin friction shows elongated structures upstream of the impingement. For the turbulent case, both experiments and DNS show a narrow vertical black line resulting from a relatively steady interaction.

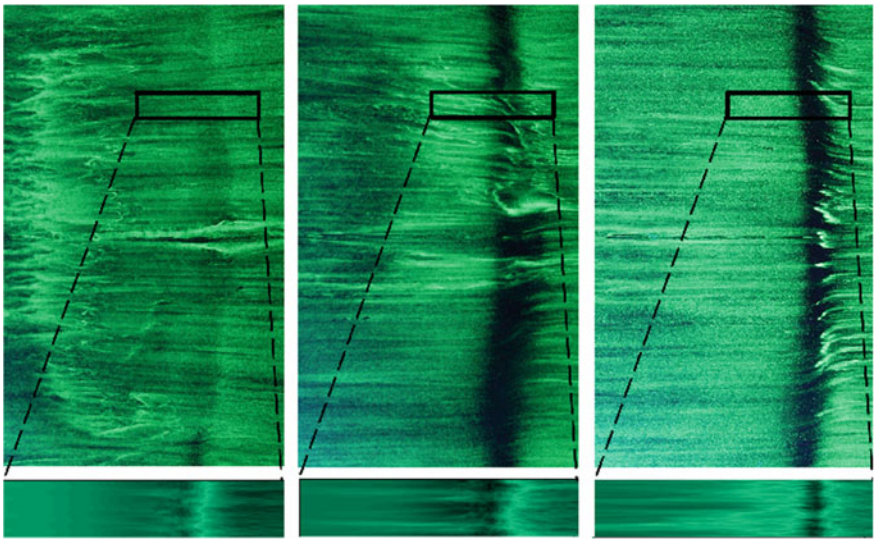

Fig. 5 Oil flow visualisations by ITAM (*top plots*) for laminar (*left*), transitional (*middle*) and turbulent (*right*) interactions. Comparisons with statistical DNS skin friction distributions (*bottom plots*). [With permission of A.A. Sidorenko and P.A. Polivanov (ITAM, Novosibirsk, Russia)]

4 Conclusions

Direct numerical simulations are performed to investigate laminar, transitional and turbulent interactions of a boundary-layer with an imposed oblique shock. Displacement thickness and intermittency distributions are used to distinguish the different types of interaction. In agreement with the experiments, the boundary-layer is separated for laminar interactions while it remains attached for transitional and turbulent ones. The oblique shock trips the boundary-layer at the impingement location for the laminar case, while it accelerates transition for the transitional and turbulent interactions. Differently to laminar and transitional cases, the effects of the turbulent interaction upstream of the impingement are minor. Qualitative agreement is achieved between the numerical simulations and experimental data.

Acknowledgements This work is supported through the European Union (EU) FP7 project TFAST. Computer time is provided by Engineering and Physical Sciences Research Council (EPSRC, UK), under Grant No. EP/L000261/1. Experimental data are provided by A.A. Sidorenko and P.A. Polivanov (ITAM, Novosibirsk, Russia).

References

1. Sansica, A., Sandham, N.D., Hu, Z.: Forced response of a laminar shock-induced separation bubble. Phys. Fluids **26**, 093601 (2014)
2. Eckert, E.R.G.: Engineering relations for friction and heat transfer to surfaces in high velocity flow. J. Aeronaut. Sci. **2**, 585–587 (1955)
3. Young, A.D.: Boundary Layers. Blackwell Science, AIAA Educational Ser (1989)
4. Giepman, R.H.M., Schrijer, F.F.J., van Oudheusden, B.W.: High resolution PIV measurements of a transitional shock wave boundary layer interaction. Exp. Fluids **56**, 120 (2015)

Adaptive LES of Immersed-Body Flows Based on Variable Wavelet Threshold Filtering

G. De Stefano, A. Nejadmalayeri and O.V. Vasilyev

1 Introduction

In the wavelet-based adaptive large-eddy simulation (LES) approach to turbulent flows, the multi-resolution wavelet threshold filtering (WTF) procedure is exploited to separate coherent energetic eddies, which are resolved, from residual background flow, which is modeled. The governing equations for incompressible LES are formally obtained by applying the WTF operator to the Navier–Stokes equations.

The wavelet transform is also used for the automatic grid adaptation since a hierarchical high-order finite difference scheme, which takes advantage of the wavelet multilevel decomposition, is used for the numerical differentiation. Due to the one-to-one correspondence between wavelets and collocation points, some grid points are omitted from the numerical mesh when the associated wavelets are omitted from

G. De Stefano (✉)
Dipartimento di Ingegneria Industriale e dell'Informazione, Università della Campania, Aversa 81031, Italy
e-mail: giuliano.destefano@unicampania.it

A. Nejadmalayeri
FortiVenti Inc., Suite 04, 999 Canada Place, Vancouver, BC V6C 3E2, Canada
e-mail: alireza.nejadmalayeri@gmail.com

O.V. Vasilyev
Center for Design, Manufacturing & Materials,
Skolkovo Institute of Science and Technology, Moscow 143026, Russia
e-mail: O.Vasilyev@skoltech.ru

O.V. Vasilyev
NorthWest Research Associates, Boulder, CO 80301, USA
e-mail: oleg.vasilyev@nwra.com

O.V. Vasilyev
Department of Mechanical Engineering, University of Colorado Boulder, Colorado 80309, USA
e-mail: oleg.vasilyev@colorado.edu

D.G.E. Grigoriadis et al. (eds.), *Direct and Large-Eddy Simulation X*,
ERCOFTAC Series 24, https://doi.org/10.1007/978-3-319-63212-4_26

the WTF representation, because the corresponding coefficients are below a given thresholding level, say, ε. This way, the method allows the numerical grid to dynamically adapt to the evolution of the resolved flow structures, in both location and scale. Higher resolution calculations are actually carried out only in the regions where sharp gradients in the flow-field exist, which leads to the high grid compression property of wavelet-based methods.

Until very recently, the wavelet-based adaptive LES method has employed a prescribed constant thresholding level to separate resolved from unresolved turbulent velocity fields, say, $u_i = \overline{u}_i^{>\varepsilon} + u_i'$. A new fully adaptive methodology that makes use of either a spatially-uniform time-dependent [1] or a spatio-temporally varying [2] threshold have been recently proposed for homogeneous isotropic turbulence.

The present work aims at extending the wavelet-based adaptive LES approach with space-time variable thresholding for the simulation of flows with immersed obstacles. The numerical methodology combines the Brinkman volume penalization technique with the parallel Adaptive Wavelet Collocation Method [3]. The former is used for imposing the flow geometry while the latter guarantees the efficient flow resolution on a continuously adaptive computational grid.

2 Space-Time Variable Thresholding

The space-time variability of the wavelet threshold is introduced to employ a physics-based coupling mechanism between computational grid and turbulence modeling that ensures the desired uniform fidelity of the numerical solution, all over the time of simulation. The main idea is to continuously adjust the threshold variable by controlling a suitable measure of the local turbulence resolution. At the same time, a feedback mechanism governing the evolution of the threshold field is provided. To achieve this aim, the ratio between modeled subgrid-scale (SGS) and resolved viscous dissipations, say $\mathscr{R} = \Pi/D$, is assumed here as the measure of the turbulence resolution of the LES solution. This ratio was demonstrated in past research to increase with the square of the thresholding level. Moreover, the threshold variation should be sufficiently smooth in order not to lead to unphysical small scales in the resolved wavelet-filtered velocity field. In order to avoid this undesirable behavior, the wavelet threshold field is prescribed to depend upon the local flow evolution on the corresponding time scale.

All that is accomplished by solving the following Lagrangian transport equation to simulate the evolution of the threshold field

$$\frac{\partial \varepsilon}{\partial t} + \left(\overline{u}_i^{>\varepsilon} + U_i\right) \frac{\partial \varepsilon}{\partial x_i} = \frac{\partial}{\partial x_i}\left[(\nu + \nu_\varepsilon)\frac{\partial \varepsilon}{\partial x_i}\right] + f_\varepsilon \,, \tag{1}$$

where U_i represents the known freestream velocity. The diffusion term with artificial viscosity coefficient ν_ε is introduced to prevent the creation of undesired high-frequency modes in the threshold field. Due to a Smagorinsky-like scaling, this coefficient is expressed in terms of the local strain-rate magnitude as follows

$$\nu_\varepsilon = C_{\nu_\varepsilon} \Delta^2 |\overline{S}^{>\varepsilon}| \,, \tag{2}$$

where Δ stands for the local characteristic WTF width, while the constant parameter C_{ν_ε} is set to 0.1 in this study. This way, the variable ε can be interpreted as the path-line diffusive averaged threshold, according to the averaging procedure proposed in [4].

The forcing term at the right hand side of Eq. (1) plays the key role in the current approach as it expresses the two-way feedback mechanism between the physical resolution of the LES field and the numerical resolution of the computational grid. In this work, the threshold field is forced so that the adaptive LES solution approaches a prescribed value $\mathscr{R}_0$ for the dissipations ratio. Namely, the following forcing definition is assumed

$$f_\varepsilon = \frac{\mathscr{H}(\Pi)}{\sqrt{\nu \mathscr{R}_0}} \left(\sqrt{\mathscr{R}_0 D} - \sqrt{\Pi} \right) \varepsilon \,, \tag{3}$$

where the presence of the Heaviside function $\mathscr{H}(\cdot)$ ensures that the threshold evolution is forced only in regions of energy forward scatter. According to this approach, in turbulent flow regions with low turbulence resolution ($\mathscr{R} > \mathscr{R}_0$), the thresholding variable is forced to decrease, which leads to local mesh refining. That leads to the subsequent growth of resolved viscous dissipation and the associate reduction of SGS dissipation. On the other hand, in regions of high resolution ($0 < \mathscr{R} < \mathscr{R}_0$), the threshold is forced to increase, which leads to mesh coarsening with the subsequent decrease of the resolved dissipation and the increase of the modeled one. It is worth noting that, in a practical calculation, the threshold must be explicitly bounded from both below and above. On the one side, the use of very low thresholds would lead to the no-model coherent vortex simulation regime while, on the other side, using very high thresholds would deteriorate the numerical accuracy of the adaptive LES solution.

The above forcing scheme inherently works in turbulent flow regions. It was found that in laminar flow regions, where both the resolved and the modeled dissipations vanish, the forcing (3) does not exhibit the right limiting behavior and needs to be switched to a different mechanism that, on the convective time scale, forces the wavelet threshold to take the maximum allowable value, which is prescribed by the user. The right limiting behavior is accomplished by following the modified forcing scheme

$$f_\varepsilon = \frac{\mathscr{H}(\Pi)}{\sqrt{\nu \mathscr{R}_0}} \left(\sqrt{\mathscr{R}_0 D} - \sqrt{\Pi} \right) \varepsilon + \max\left(\frac{U}{L} - A, 0 \right) \varepsilon \,, \tag{4}$$

where A stands for the magnitude of the velocity gradient tensor and L represents the characteristic length of the obstacle. The additional forcing term acts on the convective time scale only in regions of relatively low velocity gradients ($A < U/L$), while being absent in both the near wall and the wake regions, where the velocity gradients are generally much higher.

3 Results

The incompressible turbulent flow around a square cylinder is considered as a benchmark for the proposed numerical method. The cylinder, which has the cross-section with side length L in the (x, y) plane, is immersed in a uniform stream with velocity U along the x direction. The shear layers that separate from the sides of the cylinder become unstable and the transition to turbulence occurs at moderately high Reynolds-number [5]. The present numerical experiment is conducted at $Re = UL/\nu = 2 \times 10^3$. Eight levels of numerical resolution are used, which means that eight nested wavelet collocation grids are involved in the calcualtion. The hexahedral grid elements have a square cross section in the transverse plane with minimum size $L/128$, while the highest spanwise resolution corresponds to $L/64$. The threshold evolution equation (1) is solved along with the volume-penalized wavelet-based LES governing equations, supplied with the localized dynamic one-equation eddy-viscosity model proposed in [6]. The turbulence modeling approach that is adopted allows for negative eddy-viscosity coefficients, which corresponds to mimic the energy backscatter from unresolved to resolved motions. The threshold field may take values in the bounded interval $0.01 < \varepsilon < 0.2$.

The results of the present simulation have been successfully validated against both numerical non-adaptive solutions [7] and experimental findings [8]. For brevity, the

Fig. 1 Main vortical structures visualized through the iso-surfaces of $Q = 0.3U^2/L^2$

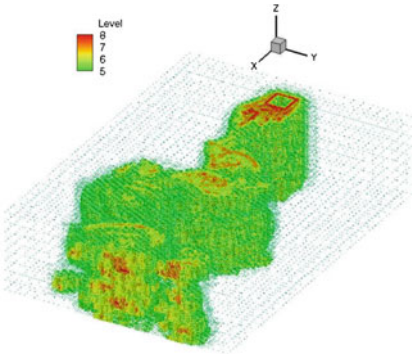

Fig. 2 Scatter plot of the retained collocation points at the highest levels of resolution ($5 \leq j \leq 8$)

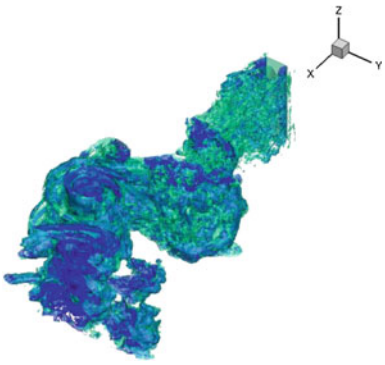

Fig. 3 Instantaneous threshold field visualized through the iso-surfaces of $\varepsilon = 0.08$ (*blue*) and 0.1 (*green*)

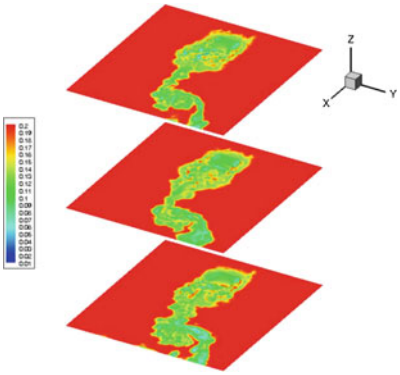

Fig. 4 Threshold contours in three volume *slice planes* along the spanwise direction

pertinent discussion is not reported in this paper. Here, it is preferred to elaborate on the space-time variability of the threshold that is achieved. The turbulent wake of the cylinder is visualized in Fig. 1, where the iso-surfaces of the second invariant of the velocity gradient tensor corresponding to the level $Q = 0.3U^2/L^2$ are depicted at a given time instant. The ability of the method to adapt to the local flow conditions is clearly demonstrated by making a comparison with the spatial distribution of the retained collocation points, which is reported in Fig. 2. For the sake of clarity, only the four finest levels of resolution are considered. Due to the two-way feedback mechanism that is employed, the evolution of the resolved flow field and the threshold distribution mutually influence each other. This is also apparent by inspection of Fig. 3, where the threshold field is visualized through the iso-surfaces corresponding to two different values that are $\varepsilon = 0.08$ (blue) and 0.1 (green). On Fig. 4, the threshold contours in three different volume slice planes along the spanwise direction are depicted, while the contours in volume slice planes along the streamwise and lateral directions are illustrated on Figs. 5 and 6, respectively. On the one hand, the structure of the threshold field closely resembles the wake structure. On the other hand, the pointwise value of the threshold dictates the local numerical resolution. In the flow regions where the threshold is relatively low, more collocation points are retained at

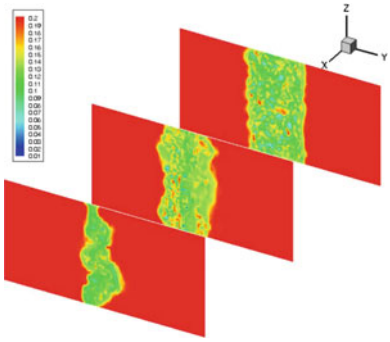

Fig. 5 Threshold contours in three volume *slice planes* along the streamwise direction

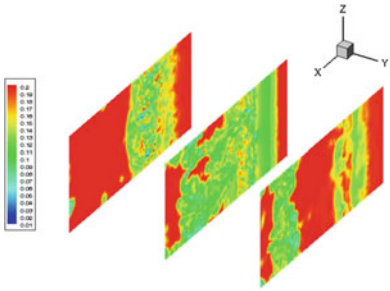

Fig. 6 Threshold contours in three volume *slice planes* along the lateral direction

the highest levels of resolution as happens, for instance, at the fluid-body interface. As expected, away from the body, the threshold takes the maximum value that is allowed, whereas close to the wall and in the turbulent wake it is adjusted so that the LES solution locally tends to achieve the prescribed resolution.

4 Conclusions

The coupled wavelet-collocation/volume-penalization method with variable thresholding is developed for the adaptive large-eddy simulation of turbulent flows around obstacles. The use of a spatio-temporally varying threshold allows numerical simulations with the prescribed turbulence resolution, on a near optimal computational mesh, to be carried out. The desired uniform fidelity is achieved thanks to the solution of a Lagrangian evolution equation for the threshold field in conjunction with the wavelet-filtered Navier–Stokes equations supplied with an energy-based eddy-viscosity model. The results obtained for a classical benchmark, which is the turbulent shedding flow past a square cylinder at supercritical Reynolds-number, demonstrate the accuracy and the efficiency of the proposed adaptive method.

Acknowledgements This work was supported by NSF under grant No. CBET-1236505 and by the Russian Science Foundation under project 16-11-10350. This support is gratefully acknowledged. Authors are also thankful for the computing time on the Janus supercomputer, which is supported by the National Science Foundation (award number CNS-0821794) and the University of Colorado Boulder. The Janus supercomputer is a joint effort of the University of Colorado Boulder, the University of Colorado Denver and the National Center for Atmospheric Research.

References

1. De Stefano, G., Vasilyev, O.V.: A fully adaptive wavelet-based approach to homogeneous turbulence simulation. J. Fluid Mech. **695**, 149–172 (2012)
2. Nejadmalayeri, A., Vezolainen, A., De Stefano, G., Vasilyev, O.V.: Fully adaptive turbulence simulations based on Lagrangian spatio-temporally varying wavelet thresholding. J. Fluid Mech. **749**, 794–817 (2014)
3. Nejadmalayeri, A., Vezolainen, A., Brown-Dymkoski, E., Vasilyev, O.V.: Parallel adaptive wavelet collocation method for PDEs. J. Comput. Phys. **298**, 237–253 (2015)
4. Vasilyev, O.V., De Stefano, G., Goldstein, D.E., Kevlahan, N.K.-R.: Lagrangian dynamic SGS model for stochastic coherent adaptive LES. J. Turbul. **9**, 1–14 (2008)
5. De Stefano, G., Vasilyev, O.V.: Wavelet-based adaptive simulations of three-dimensional flow past a square cylinder. J. Fluid Mech. **748**, 433–456 (2014)
6. De Stefano, G., Vasilyev, O.V., Goldstein, D.E.: Localized dynamic kinetic-energy-based models for stochastic coherent adaptive LES. Phys. Fluids **20**, 045102.1–045102.14 (2008)
7. Brun, C., Aubrun, S., Goossens, T.: Ravier, P: Coherent structures and their frequency signature in the separated shear layer on the sides of a square cylinder. Flow Turbul. Combust. **81**, 97–114 (2008)
8. Lyn, D.A., Einav, S., Rodi, W., Park, J.-H.: A laser-Doppler velocimetry study of ensemble-averaged characteristics of the turbulent near wake of a square cylinder. J. Fluid Mech. **304**, 285–319 (1995)

A Strip Modelling of Flow Past a Freely Vibrating Cable

Y. Bao, R. Palacios, M. Graham and S. Sherwin

1 Introduction

-induced vibration of long flexible structures with cylindrical cross-section are widely encountered in various engineering fields. For instance, deep water, string-like, marine risers are subject to strong ocean currents, undergoing large amplitude vibrations in both cross-flow and in-line directions, due to interactions of vortex shedding and structural properties of the risers. This affects the fatigue life of the structures, since when the vortex shedding frequency approaches a natural frequency of the structure, the vortex shedding process synchronizes with the structure's motion and then further strengthens the vibration responses. In such conditions, building accurate models for prediction of forces and motions of long flexible bodies becomes essential to develop efficient vortex-control device and avoid fatigue damage caused by VIV.

There are only a few numerical results in the literature on VIV for the case of long flexible cylinders at high Reynolds number flows. The main reason is that full resolutions of such 3D VIV problems with large scale flexible bodies and complex flows around them are still unfeasible under realistic conditions. For example, Yamamoto et al. [1] have developed a quasi-three-dimensional approach, in which they evaluated the hydrodynamic forces in two-dimensional strips, and performed

Y. Bao (✉) · R. Palacios · M. Graham · S. Sherwin
Department of Aeronautics, Imperial College London, South Kensington Campus, London, UK
e-mail: y.bao@imperial.ac.uk

S. Sherwin
e-mail: s.sherwin@imperial.ac.uk

R. Palacios
e-mail: r.palacios@imperial.ac.uk

M. Graham
e-mail: m.graham@imperial.ac.uk

D.G.E. Grigoriadis et al. (eds.), *Direct and Large-Eddy Simulation X*,
ERCOFTAC Series 24, https://doi.org/10.1007/978-3-319-63212-4_27

the coupling between strips via three-dimensional structural dynamics. The hydrodynamic forces were assessed from the simulation of two-dimensional incompressible viscous flow through the discrete vortex method (DVM). The simulation results were compared against the experimental one, but have shown a significant underprediction of response amplitudes, which might be actually related to the fact that two-dimensional DVM was not able to capture the rotating, stretching nature of vortices in turbulent wake at high Reynolds numbers. Willden and Graham [2] proposed a similar numerical model based upon strip theory for a long flexible riser pipe with the assumption that local fluid flows under lock-in condition are predominantly two-dimensional.

In this work, we developed a more accurate numerical VIV model in the context of high-order spectral/*hp* element framework−Nektar++ [3]. The most distinct feature of the VIV model presented here is that we established three-dimensional DNS model for each strip, assuming local periodic boundary conditions. It means that each strip has a spanwise scale, and that they are locally distributed along the flexible risers with gaps between them.

2 Strip Modeling of VIV

We consider a three-dimensional incompressible flow past a long slender cylindrical body immersed in an oncoming external flow, with aspect ratio of L_c/D, where L_c is the spanwise length of the body and D is the cross-sectional diameter. The N strips with thickness ratio of L_z/D are evenly distributed along the spanwise direction, where L_z is the thickness of the strip in z-direction, so the gap between the neighboring strips, represented by L_g, satisfy the relationship of $L_c = (L_z + L_g)N$. Next, the flow dynamics for each individual strips are modeled by viscous incompressible Navier-Stokes equations, which are represented in non-dimensional form as follows,

$$\frac{\partial \mathbf{u}}{\partial t} + (\mathbf{u} \cdot \nabla)\mathbf{u} = -\frac{1}{\rho}\nabla p + \frac{1}{Re}\nabla^2 \mathbf{u} \tag{1}$$

$$\nabla \cdot \mathbf{u} = 0 \tag{2}$$

where the vector $\mathbf{u}$ denotes the fluid velocity, p is the fluid's static pressure, $Re = U_\infty D/\nu$ (where ν is kinematic viscosity, U_∞ is the oncoming velocity) is the Reynolds number, ρ is the density of the fluid and t is the dimensionless time.

Although the flow dynamics are evaluated independently for local strips, the coupling of those strips is enforced through the calculation of three-dimensional structural dynamic model. This then indicates that the updating of time-dependent boundary conditions on the wall of moving bodies links to the solution of the three-dimensional structural dynamic equation. A tensioned beam model is employed to govern the dynamics of cylinder structure and that can be expressed by the following equation

$$\frac{\partial^2 \eta}{\partial t^2} + \frac{b}{m}\frac{\partial \eta}{\partial t} = \frac{T}{m}\frac{\partial^2 \eta}{\partial z^2} - \frac{EI}{m}\frac{\partial^4 \eta}{\partial z^4} + \mathbf{f}(z,t), \tag{3}$$

where m is the body mass ratio and normalized by fluid density ρ such that $m = \rho_c/\rho$, and ρ_c is the structural mass per unit length. b is the structural damping per unit length. The structural displacement η has two components of η_x and η_y, respectively corresponding to the streamwise and crossflow directions. T is the cable tension and EI is the beam rigidity. In this prediction model, $\mathbf{f}(z,t)$ is a hydrodynamic force acting on the body and it is evaluated from the solution of the Navier-Stokes equations. It is noted that the distribution of the hydrodynamic forces along the span direction is modeled in the basis of Fourier interpolation, since the fluid solution only provides that within the strip domain. We introduce the mode decomposition in spanwise direction to the structural variables and hydrodynamic forces, so that the partial differential equations reduce to a set of complex model ordinary differential equations, which fit the required form of direct integration schemes such as standard Newmark–β method.

The coupled system of incompressible flow and moving bodies are solved using high-order Fourier spectral/hp element method, which is implemented in the Nektar++ spectral/hp element framework. A body-fitted coordinate formulation is used to take into account the moving body effect and then avoid the difficulty of moving meshes. So that the moving body's influence upon the surrounding flows are reflected in adding acceleration term to the Navier-Stokes equations with non-inertial transformation. Details regarding coordinate transformation and time integration schemes can be found in [4].

3 Simulation Results

In this section, we present some numerical tests within the laminar flow regime (Re = 100). A 3D fully resolved simulation is conducted firstly to verify the code implementation against the previous numerical results in [4] and to be used to compare against the results of strip theory-based modelling. The vibration of the cylinder is constrained to occur only in the crossflow direction. The cylinder has a length ratio of $L_z = 4\pi$ with the tension parameter set to $T = 8.82$, choosing the same parameters with the numerical case reported in [4]. We also neglect the effect of different types of cable support by assuming an infinitely long cable and periodicity in the spanwise direction. This then indicates that the two ends of the cable move freely. The structural damping and flexural rigidity are omitted to simplify the analysis. The mass ratio, defined as the ratio of the cylinder's mass per unit length to the fluid density (i.e., $\rho_c/\rho_f D^2$ with $D = 1$), is set to be 2.

A C-type domain is used in the computation that has its semicircle upstream boundary with diameter of $20D$, its lateral boundaries located at $10D$, and extending over $12.5D$ downstream. All of the simulations use a grid of 283 spectral elements with polynomial order $P = 6$ in the (x, y) plane. For the full 3D simulation at Re =

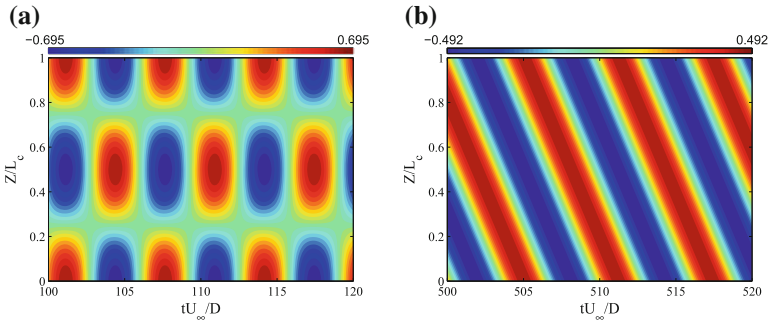

Fig. 1 **a** Temporal evolution of standing wave responses: η/D. **b** Temporal evolution of traveling wave responses: η/D

100, 32 planes (16 complex Fourier modes, i.e. $M = 16$) are used, which gives a high resolution to the homogeneous solution in the z-direction. For the strip modelling at Re $= 100$, 8 strips with thickness ratio of $L_z/D = \pi/8$ are evenly separated along the z-direction, and for each strip two planes (one pair of complex Fourier modes) are used for the local flow resolution. A standing wave perturbation $\eta = A\cos(\omega t)\cos(2\pi z/L_c)$ with $A = 0.025$, $\omega = 1.0$, is specified as an initial condition for the moving cylinder, similar to the simulations of Newman and Karniadakis [4]. The nondimensional time step used in the computations is 0.002.

3.1 Full Resolution Results

The VIV responses of the cylinder at $\rho_c/\rho_f = 2$ are presented in Fig. 1a, b. Obviously, a well-defined standing wave pattern is observed in the displacement response in the early simulation stage. However, the standing wave is not a stable response and gradually transitions to a traveling wave pattern as the simulation becomes fully saturated in time. From the comparison of these two plots, the amplitude of the displacement for this traveling wave pattern is reduced slightly from the standing wave response. A similar observation is also reported in previous numerical examination by Newman and Kaniadarkis [4].

3.2 Strip Modelling Results

In this test, we apply the strip theory to the low Reynolds number problems. As seen in the temporal evolution of VIV responses plotted in Fig. 2a, the model reproduces the standing wave that is also observed in the full 3D model. However, the wave cell in the drag and lift coefficients as shown in Fig. 3a, b are somewhat different from

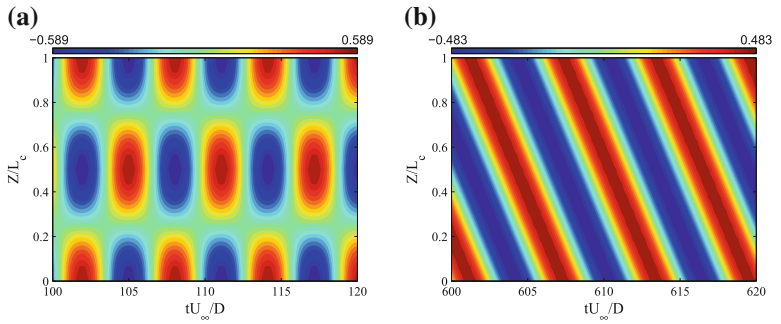

Fig. 2 **a** Converged states of η/D response for the cylinder: mixed wave response, 2D strip modelling. **b** Converged states of η/D response for the cylinder: traveling wave response, 2D strip modelling

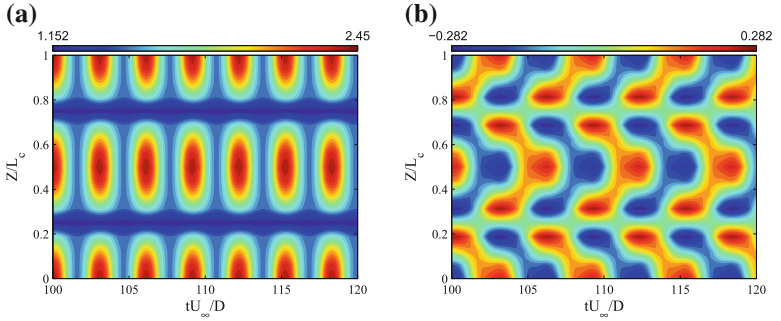

Fig. 3 **a** Temporal evolution of standing wave responses: C_D. **b** Temporal evolution of standing wave responses: C_L

their fully resolved counterparts. This is because, the communication between the flow dynamics in different strips is achieved, not directly, but through the structure dynamics. This then accounts for the principal difference between the full 3D and strip theory-based models. The predicted vibration amplitude is 0.589, which is approximately lower by 15% with respect to those in full 3D resolutions. There appears to be a relatively larger difference in prediction of the hydrodynamic forces. Taking lift coefficient as an example, its magnitudes for the cases of $\rho_c/\rho_f = 2$ is 0.296, whereas the full 3D simulations obtained the values of lift coefficient as 0.482, showing differences of 38% respectively.

In contrast to the fully resolved case, the mode may converge to different states at $\rho_c/\rho_f = 2$, depending on the initial conditions. If the simulation runs from a standing wave perturbation, the VIV saturated in a mixed state of standing wave and traveling wave (not shown here). However, if the simulation is started from an initial condition of a traveling wave with an amplitude value of $A = 2 \times 10^{-4}$, the flow converges quickly to the traveling wave state, see Fig. 2b. The amplitude of the displacement in

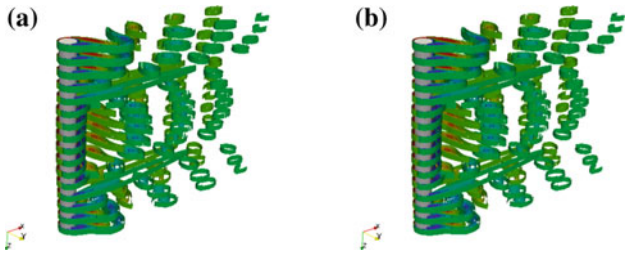

Fig. 4 **a** Spanwise vorticity contours for standing wave response. **b** Spanwise vorticity contours for traveling wave response

the traveling wave is 0.484 at $\rho_c/\rho_f = 2$, which is less than 2% from the crossflow vibration amplitude of 0.492 in the full 3D case.

The wake features of the 2D strip model are illustrated in Fig. 4a, b. The spanwise vorticity contours show a consistent convergence of the flow fields with the increase of the strip numbers. The standing wave response of the cylinder generates an interwoven structure of vortex shedding in the wake, which is consistently similar to the wake observed in full 3D simulations [4]. Again, similar to the full resolution results in [4], the traveling wave responses generate a coherent wake structure with oblique shedding of spanwise vorticity. Therefore, it can be confirmed that although the wake produced within strip-domain is two dimensional, the intrinsic three dimensionality of the wake structure as a whole is well-reproduced due to the interactions between strips through the structural dynamics.

3.3 Conclusions

In this paper, a strip model is presented for prediction of VIV responses of a long flexible cylinder. The flows in this modelling are split into a series of separated strips, which have spanwise scale to locally resolve the three dimensional effects that have a potentially influence on the VIV responses. Numerical tests were performed to evaluate the performance of this approach. The results of laminar flow simulations which essentially are equivalent to 2D strip theory showed that the model can accurately predict the major feature of the VIV responses of flexible bodies. The working principle of the 2D strip model and its suitability for low Re flow are investigated at $\mathrm{Re} = 100$. For the traveling wave responses, this model achieves the amplitude of the vibration with only 2–3% errors. For standing waves, however, we observe moderate agreement of the vibration amplitude with 11–15% errors, since the coupling between the wake modes has been lost. A much complicated flow over very long flexible riser at high Re will be presented in our future work.

Acknowledgements This work was supported by the funding EPSRC under grant EP/K037536/1.

References

1. Yamamoto, C.T., Meneghini, J.R., Saltara, F., Fregonesi, R.A., Ferrari Jr., J.A.: Numerical simulations of vortex-induced vibration on flexible cylinders. J. Fluids Struct. **19**, 467–489 (2004)
2. Willden, R.H.J., Graham, J.M.R.: Multi-modal vortex-induced vibrations of a vertical riser pipe subject to a uniform current profile. Eur. J. Mech. B-Fluid. **23**, 209–218 (2004)
3. Nektar++(2014). http://www.nektar.info
4. Newman, D.J., Karniadakis, G.E.: A direct numerical simulation study of flow past a freely vibrating cable. J. Fluid Mech. **344**, 95–136 (1997)

One-Sided Fluid–Structure–Acoustic Interaction for Turbulent Flow over a Step

M. Springer, C. Scheit and S. Becker

1 Introduction

Flow induced noise is very important regarding many technical applications. As an example, the aeroacoustic as well as the vibroacoustic noise induced by the turbulent flow field around cars or planes has an unfavorable influence on the comfort for passengers and therefore on the quality of the vehicle. Aeroacoustic noise is induced by turbulent pressure fluctuations e.g. in turbulent shear layers or recirculation areas. Vibroacoustic noise is generated by the interaction of turbulent wall bounded flows with flexible surfaces which are excited to vibrate in their characteristic eigenmodes. According to the eigenfrequencies, sound is radiated from the flexible structures surface. The goal of the current work is to compute the aeroacoustic, as well as the vibroaocustic sound radiation by the combination of a turbulent flow field behind a forward–backward facing step and a flexible plate with turbulent fluid load. The coupling between flow field and acoustic field is realized by calculating aeroacoustic source terms from the velocity field. The vibroacoustic sound radiation is based on the surface velocity of the flexible structure. Besides the numerical investigations, microphone measurements of the sound radiated by the forward–backward facing step were carried out in a low–noise wind tunnel. A comparison between numerical and experimental results will be given and discussed.

M. Springer (✉) · C. Scheit · S. Becker
Institute of Process Machinery and Systems Engineering, University Erlangen-Nuremberg, Erlangen, Germany
e-mail: sp@ipat.uni-erlangen.de

C. Scheit
e-mail: sh@ipat.uni-erlangen.de

S. Becker
e-mail: sb@ipat.uni-erlangen.de

D.G.E. Grigoriadis et al. (eds.), *Direct and Large-Eddy Simulation X*,
ERCOFTAC Series 24, https://doi.org/10.1007/978-3-319-63212-4_28

2 Numerical Setup

2.1 Fluidmechanical Setup

The three–dimensional flow field generated by the forward–backward facing step was computed by means of LES. The flow computation was carried out using the software FASTEST-3D [1]. This code solves the transient, incompressible Navier–Stokes equations on structured grids. The equations were discretised using the finite volume method (FVM). The influence of the unresolved flow scales was modeled with a Smagorinsky subgrid scale model. The Smagorinsky constant was set to 0.1. The forward–backward facing step was a quadratic obstacle attached to a flat plate with edge length of $D = 0.02$ m. The spanwise extend of the geometry was chosen to be 10 D. In spanwise direction, periodic boundary conditions were applied. The height of the computational domain was 20 D. At the outflow boundary a convective boundary condition was used. At the inflow boundary, a laminar boundary layer profile was set. This boundary layer profile origins from LDA–measurements during previous performed experimental investigations [2] of the current geometry. The velocity at the boundary layer edge was 20 m/s. This yields a Reynolds number of 26.000, based on inflow velocity and step height D. The grid size was chosen to obtain a wall normal resolution of $y^+ < 1$. The streamwise and spanwise resolution in the wake region of the step was $x^+ < 40$ and $z^+ < 20$, respectively. The overall number of hexahedron control volumes was 91.6 Millions. To get a CFL-number below 1, the time step size was chosen to be $4 \cdot 10^{-7}$ s.

2.2 Aeroacoustic Setup

Aeroacoustic source terms were computed at simulation time from the incompressible flow variables. Based on these acoustic source terms, the radiation of sound was computed using the software CFS++ [3]. This solver uses the finite–element method (FEM) to solve the Lighthill equation.

$$\frac{\partial^2 \rho'}{\partial t^2} - {c_0}^2 \frac{\partial^2 \rho'}{\partial {x_i}^2} = \frac{\partial^2 T_{ij}}{\partial x_i \partial x_j} \quad \text{with} \quad T_{ij} \approx \rho_0 u_i u_j \tag{1}$$

The acoustic pressure is computed for a 2D region. Therefore, the acoustic source terms are averaged in spanwise direction. Except the walls of the fluid domain, which are modeled as acoustically hard walls, the whole acoustic domain is surrounded by a perfectly matched layer (PML [4]) to prevent reflections of acoustic waves at the domain boundaries. Acoustic source terms are calculated at simulation time during flow computation [5]. The source terms are stored on the CFD grid. The acoustic computation is performed on a grid which is much coarser than the CFD grid. Therefore, a conservative interpolation of the acoustic sources between the fine

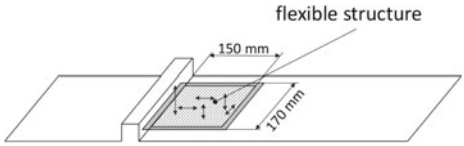

Fig. 1 Flexible structure loaded by pressure force and shear force

CFD grid and the much coarser CAA (computational aeroacoustics) grid has to be done [6]. The CAA grid is an equidistant, orthogonal, quadrilateral grid with a grid size of 2.5 mm in streamwise and wall-normal direction.

2.3 Vibroacoustic Setup

The vibration of the plate was induced by the turbulent wall pressure and wall shear fluctuations (Fig. 1). The surrounding fluid was not modified by the plates displacement. The sound radiation of the plate was described by the linear wave equation. The wall–normal velocity of the plate surface must coincide with the wall–normal component of the acoustic particle velocity v':

$$\frac{\partial \xi_i}{\partial t} n_i = v_i' n_i \tag{2}$$

Here, ξ_i are the mechanical displacements. For the calculation of the plates vibration, the plate was modeled as a aluminium plate with a thickness of 3 mm, a density of $2700\,\mathrm{kg/m^3}$ and a modulus of elasticity of $\mathrm{E} = 70 \cdot 10^9\,\mathrm{N/m^2}$. The plate was joined on a rigid baffle which resulted in an effective flexible area of 150×150 mm.

The transient mechanical computation of the plate was carried out with the FEM code CFS++. The load vector from the flow simulation which was composed of pressure and wall shear force was conservatively interpolated on the mechanical grid, which consisted of 19200 hexahedral cells of second order. The timestep size was $1 \cdot 10^{-5}$ s which was equal to the timestep size of the aeroacoustic simulation. The propagation of the vibroacoustic sound was computed in a 3–dimensional domain similar to the aeroacoustic sound computation.

3 Experimental Setup

The acoustic measurements were performed in the acoustic wind tunnel of the University of Erlangen–Nuremberg, which is equipped with sound absorbers (anechoic chamber conditions) [7]. The square cylinder obstacle with edge length of $D = 0.02$ m and a spanwise width of 35 D was attached on a flat plate. The measurements were carried out at a wind speed of 20 m/s to realize the same Reynolds

number as in the simulation. A microphone was installed directly above the step with a distance of 1 m. The microphone measurements were performed for 30 s with a sampling rate of 48 kHz.

4 Results

4.1 Flow Field

The streamlines of the time-averaged flow field generated by the forward–backward facing step in addition to the distribution of the turbulent kinetic energy k are shown in Fig. 2. Basically, the flow field can be characterized by two recirculation regions. The recirculation region in front of the obstacle is created by pressure induced boundary layer separation during the flow approaching the obstacle. It has a length of $1.6D$. The recirculation region behind the obstacle represents the obstacle's wake. Its length is $13.5D$. Based on the time–averaged distribution of the turbulent kinetic energy, it can be concluded that turbulence is mainly produced in the shear layer of the obstacle's wake. The maxima of the turbulent kinetic energy can be found in the shear layer behind the obstacle's windward edge. Here, the velocity gradients are largest.

4.2 Acoustic Results

4.2.1 Aeroacoustic

The power spectral density of the computed acoustic sound pressure level (SPL) at the monitor point 1 m above the obstacle and the comparison with experimental results is plotted in Fig. 3. The comparison is performed with the averaged experimentally determined spectrum as well as with a superposition of experimentally determined spectra evaluated equally to the computed spectrum. To compare the results of the 2D aeroacoustic simulation with experimentally obtained data, a sound pressure

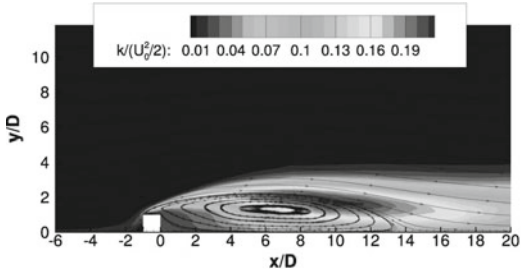

Fig. 2 Time-averaged velocity field and distribution of turbulent kinetic energy k

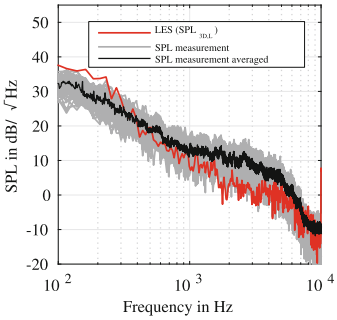

Fig. 3 Power spectral density of aeroacoustic sound pressure level at microphone point

correction from 2D to 3D had to be performed. In the current work, a correction procedure to compare simulations with infinite spanwise width to experiments with finite geometries was applied. Details are explained in [8]. The comparisons show that the numerical results are located within the region of the equivalent evaluated measurements. The flattening of the experimentally results above 1000 Hz due to the influence of the recirculation area is also visible in the numerical data. The decay in the frequency region towards 10000 Hz agrees good between simulation and measurement.

4.2.2 Vibroacoustic

A load vector composed of pressure force and wall shear force computed from the fully developed flow field is imprinted on the surface of the plate during a transient mechanical computation. The maximum plate displacement is approx. $10 \cdot 10^{-7}$ m. The frequency of the dominating oscillation is approx. 1160 Hz which is the first

Table 1 First five computed eigenfrequencies in Hz

1st	2nd	3rd	4th	5th
1160	2359	3469	4209	4232

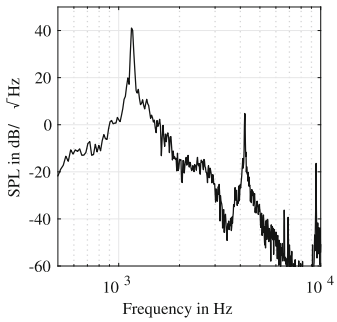

Fig. 4 Power spectral density of vibroacoustic sound pressure level at microphone point

eigenfrequency of the plate. In Table 1, the first five computed eigenfrequencies according to the boundary conditions mentioned in Sect. 2.3 are plotted.

The acoustic spectrum at the microphone point due to the plate vibration is shown in Fig. 4. The dominant modes are the first as well as the forth eigenmode.

5 Conclusion

The flow simulation of the turbulent flow over a forward–backward facing step with coupled aeroacoustic and vibroacoustic simulation was presented. The results of the aeroacoustic simulation were compared with aeroacoustic measurements. Good comparability over a wide frequency range was observed. The vibroacoustic sound radiation was based on the temporal displacement of a flexible plate located in the wake region of the step, loaded with turbulent pressure and shear stress forces. The vibroacoustic analysis showed the plate being excited mainly in its first and forth eigenfrequency. Hence, the sound radiation was dominated by these frequencies. Conclusively, the presented work showed the feasibility to capture the fluid–structure–acoustic interaction for complex turbulent flows. In addition to measurements, the simulative approach allows for detailed insight into the mechanisms of noise generation and enables the separation of aeroacoustic and vibroacoustic noise.

References

1. Durst, F., Schäfer, F.: A parallel block/structured multigrid method for the prediction of incompressible flows. Int. J. Numer. Methods Fluids. **22**, 249–565 (1996)
2. Schäfer, F., Müller, S., Uffinger, T., Becker, S., Grabinger, J.: Fluid-structure-acoustics interaction of the flow past a thin flexible structure. AIAA J. **48**, 738–748 (2010)
3. Kaltenbacher, M.: Advanced simulation tool for the design of sensors and actuators. Procedia Eng. **5**, 597–600 (2010)
4. Hüppe, A.: Spectral Finite Elements for Acoustic Field Computation. Dissertation, Vienna University of Technology, Austria (2012)
5. Scheit, C., Esmaeili, A., Becker, S.: Direct numerical simulation of a flow over a forward-facing step - flow structures and aeroacoustic source regions. Int. J. Heat Fluid Flow **43**, 184–193 (2013)
6. Kaltenbacher, M., Escobar, M., Becker, S., Ali, I.: Computational aeroacoustics based on lighthills acoustic analogy. Comput. Acoust. Noise Propag. Fluids **4**, 115–142 (2008)
7. Hahn, C., Becker, S., Ali, I., Escobar, M.: Investigation of Flow Induced Sound Radiated by a Forward Facing Step. New results in numerical and experimental fluid mechanics, pp. 438–445 (2007)
8. Oberei, A.A., Roknaldin, F., Hughes, T.J.R., S: Trailing–Edge Noise Due to Turbulent Flows, Boston University, Report No. 02–002 (2002)

Study of Stochastic Models for Subgrid Dispersion in Lagrangian-Eulerian Formulation

J. Muela, O. Lehmkuhl and A. Oliva

1 Introduction

Dispersed multiphase turbulent flows are present in many industrial and commercial applications like internal combustion engines, turbofans, dispersion of contaminants, steam turbines, etc. Therefore, there is a clear interest in the development of models and numerical tools capable of performing detailed and reliable simulations about these kinds of flows. Most numerical investigations of dispersed flows use a Lagrangian-Eulerian formulation, and therefore the present work is developed under this framework.

2 Turbulent Dispersion of Particles

The equations governing the fluid-dynamic behaviour of the carrier phase are the Navier-Stokes (NS) equations. In Large-Eddy Simulation (LES) the NS equations are filtered, appearing an extra term (the unresolved Reynolds stresses), which is unclosed and should be modelled. In order to close this term, the Dynamic One-Equation sub-grid Model (DOEM) [5] is employed. Regarding the dispersed phase, if it is considered as a large number of discrete spherical particles with density much larger than that of the surrounding ambient gas, the Lagrangian equations governing the motion of the dispersed phase are:

$$\frac{d\mathbf{x}}{dt} = \mathbf{v} \tag{1}$$

J. Muela (✉) · O. Lehmkuhl · A. Oliva
Universitat Politècnica de Catalunya - BarcelonaTech, C. Colom 11,
08222 Terrassa (Barcelona), Spain
e-mail: jordim@cttc.upc.edu
URL: http://www.upc.edu/

D.G.E. Grigoriadis et al. (eds.), *Direct and Large-Eddy Simulation X*,
ERCOFTAC Series 24, https://doi.org/10.1007/978-3-319-63212-4_29

$$\frac{d\mathbf{v}}{dt} = \frac{\mathbf{U} - \mathbf{v}}{\tau_p} + \left(1 - \frac{\rho_g}{\rho_l}\right)\mathbf{g} \tag{2}$$

where $\mathbf{v}$ is the particle velocity and $\mathbf{U}$ is the velocity of the carrier phase at particle position. When working under the framework of LES modelling, only the large scales of the flow are well-resolved, while the sub-grid scales (SGS) are modelled. In Eq. (2) the velocity of the carrier phase at particle position may be decomposed as $\mathbf{U} = \widetilde{\mathbf{U}} + \mathbf{u}_{sgs}$, where $\widetilde{\mathbf{U}}$ is the resolved velocity field and $\mathbf{u}_{sgs}$ represents the SGS velocity contribution that is lost during the filtering procedure applied in LES modelling. It is a key aspect in the development of numerical methods for dispersed multiphase flows to assess and study the influence and importance of the contribution of the sub-grid scales on the dispersed phase. In many previous works, the effect of the SGS over the particle motion is directly neglected (it is, $\mathbf{U} = \widetilde{\mathbf{U}}$), stating that in the well-resolved regions the amount of energy in the SGS is small, and the effect over the particles is negligible. In the present work, the influence of the unresolved scales of the flow has been studied using two different stochastic models. The first one is the model proposed by Bini and Jones (BJ) [1, 2], where Eq. (2) is expressed as (3) (neglecting gravity and buoyancy terms). The additional term χ provides an estimation of the force exerted over the Lagrangian particle by the unresolved velocity fluctuations and is modelled as a Wiener process. The second model studied in the present work is the one introduced by Pozorski and Apte (PA) [7], where a SGS dispersion model for locally homogeneous and isotropic turbulence is proposed. In this model, the sub-grid velocity $\mathbf{u}_{sgs}$, is tracked along the particle path. Each sub-grid velocity component $u_{i_{sgs}}$ is governed by the Langevin equation (4).

$$\frac{d\mathbf{v}}{dt} = \frac{\widetilde{\mathbf{U}} - \mathbf{v}}{\tau_p} + \chi \tag{3}$$

$$du_{i_{sgs}} = -\frac{u_{i_{sgs}}}{\tau_L}dt + bdW_i \tag{4}$$

3 Stochastic Models Analysis

The instantaneous structures of a turbulent flow influence the motion of the particles depending on their inertia. Some particles tend to correlate with certain eddy structures leading to preferential concentration effect (PCE). In the present work, the PCE is calculated using the criterion defined by Wang and Maxey [8]: $D = \sum_{n=0}^{\infty} \left[f_d(n) - f_p(n)\right]^2$, where $f_d(n)$ is the discrete pdf of the simulated particles distribution and $f_p(n)$ the discrete Poisson (random) distribution. Particle inertia is characterized using the Stokes number, which is defined as the particle relaxation time normalized by the Kolmogorov time scale $St = \frac{\tau_p}{\tau_K}$. The DNS of a forced isotropic turbulence test with periodic boundary conditions has been done in order

to study the behaviour of the dispersed phase in turbulent cases. The flow field was generated using the linear forcing technique proposed by Lundgren [6]. Particles with different weight and initial velocity equal to the gas velocity at the injected position are randomly injected inside the domain. Snapshots of particle locations in a slice for different Stokes numbers are depicted in Fig. 1. As can be seen, particles with a Stokes number close to unity tend to correlate with certain eddy structures. Specifically, particles tend to accumulate in flow regions of low vorticity and high rate of strain. These results are in agreement with previous observations found in the literature [7]. In order to study and analyse the previously presented sub-grid stochastic models, several simulations where the DNS velocity field has been spatially filtered (FDNS simulations) have been computed. For each simulation, a particle field is solved using the DNS velocity field, while other particle fields are computed using the LES-like velocity field (FDNS) for three different filter sizes: FDNS2 ($\Delta_f = 2^1\Delta_x$), FDNS3 ($\Delta_f = 2^2\Delta_x$) and FDNS4 ($\Delta_f = 2^3\Delta_x$), where Δ_x is the control volume size. The filtered cases are solved for both BJ (BJ) and PA ($Apte$) models, and without any sub-grid model ($No\ Model$). For small inertia particles, the PCE measured employing the criteria defined before (D) for different bin sizes Δ_{bin} (where $\Delta_{bin} = V_{bin}^{1/3}$ and V_{bin} is the volume employed to calculate the particles number density) is depicted in Figs. 2 and 3. As can be seen, for Stokes number less than unity, the PCE is dissipated with filtering. This is due to small-inertia particles tend to follow all the scales of the flow, including small eddies that are removed in the filtering procedure. The stochastic sub-grid models not only do not fix this issue, but also make it worse, since the models tend to introduce a scattering effect. On the other hand, as is depicted in Figs. 4 and 5, for particles with Stokes number larger than one, the PCE seems to be enhanced by the filtering. On that kind of particles the inertia effect dominates, and the small scales eddies only have a stirring effect on them, randomizing their distribution. Therefore, for this kind of particles the stochastic models help to restore the randomizing effect lost with filtering. However, for the current simulations, the randomizing effect introduced by the models is bigger than the stirring effect lost by filtering. Regarding the kinetic energy of the particles, in Figs. 6 and 7 it can be clearly seen how the filtering procedure reduce the kinetic energy of the particles. Both sub-grid stochastic models help to recover the kinetic energy level, although the models are not able to retrieve the exact kinetic energy level of the DNS simulation. These models employ a model constant C_0 in their formulation (see [1, 7]). The value of this model constant is case-dependant and its correct adjustment is still an open issue. For the present cases, employing $C_0 = 1$, the PA model slightly under-predicts the kinetic-energy, while the BJ model over-predicts it. In addition, it is worth to say that the BJ model seems to be quite more dependent on filter size Δ_f than the PA model.

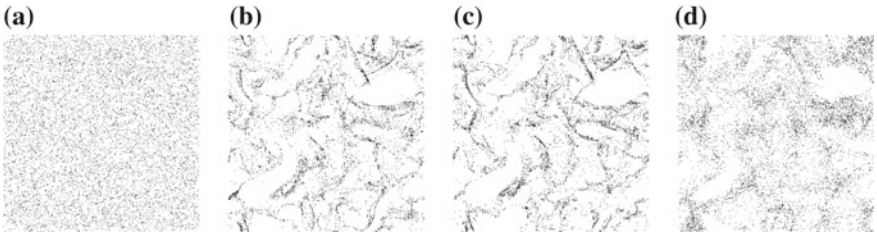

Fig. 1 **a** St = 0.001 **b** St = 0.7 **c** St = 1 **d** St = 4

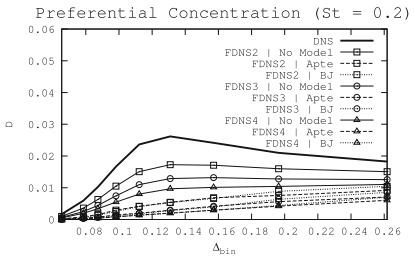

Fig. 2 Prefential concentration (St = 0.2)

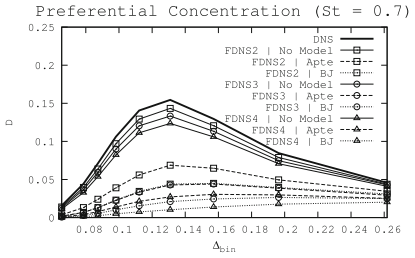

Fig. 3 Prefential concentration (St = 0.7)

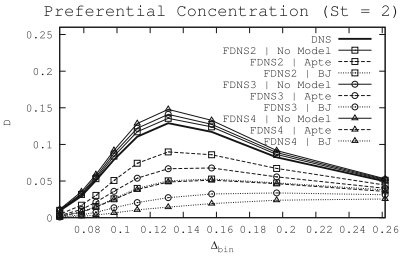

Fig. 4 Prefential concentration (St = 2)

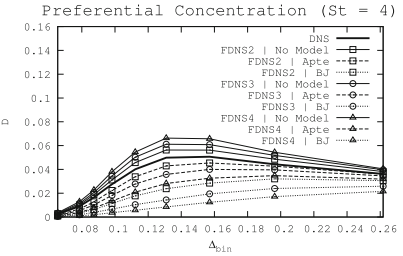

Fig. 5 Prefential concentration (St = 4)

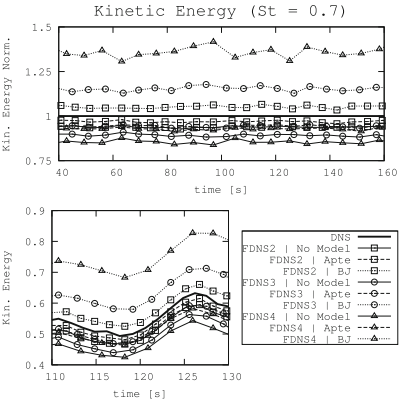

Fig. 6 Kinetic energy (St = 0.7)

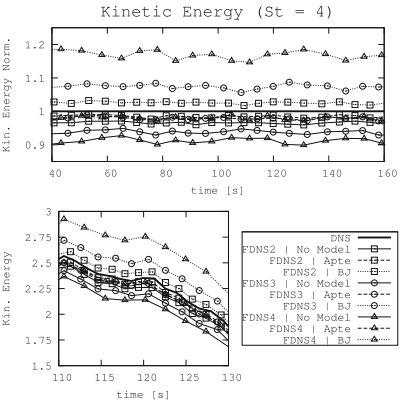

Fig. 7 Kinetic energy (St = 4)

4 Real Test Case

The real test case chosen to study the presented turbulent models is the experiment in the flow loop Hercule from Boree et al. [3], which creates an axisymmetric confined bluff body flow. The velocity of the inner jet is low in order to obtain two stagnation points on the axis of the flow. Poly-dispersed glass particles are injected in the inner pipe. In the present work, the experiment with a mass loading ratio in the inner jet of $M_i = 22\%$ has been reproduced. For the outer pipe, the mean velocity profile of the experiment has been imposed, while for the inner pipe a synthetic turbulence generator [4] has been used to reproduce the flow. Particles are injected in the inner pipe using the particle size distribution and the mean velocity of the experiment. For the walls, a no-slip boundary conditions has been imposed. Figures 8 and 9 show the mean and RMS value of the carrier phase velocity in the axis of the jet, and as can be seen, the experimental results are quite well captured by the current simulations (the minor differences between the cases are due to time-averaging reasons). The results for two different sizes of particles are shown in Figs. 10, 11, 12 and 13. Since the mean-axial velocity of the carrier phase is already slightly over-predicted, the mean axial velocity of the particles is also overestimated. This is due to the case configuration is really sensitive to inlet boundary conditions. Therefore, a more precise setting of boundary conditions and/or a refinement of the computational mesh should be done to better match the experimental results. Anyway, as could be expected from the analysis done in the isotropic turbulence test, both models increase the kinetic energy of the particles, specially the BJ model, which also seems to overestimate the RMS value between the stagnation points. This effect is more remarkable for small inertia particles.

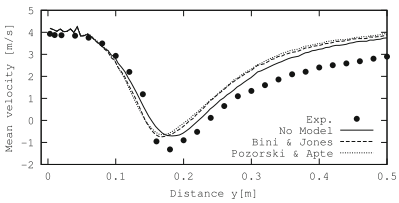

Fig. 8 Mean axial vel (carrier phase)

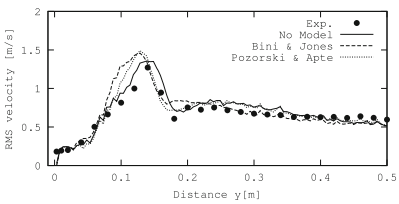

Fig. 9 RMS axial vel (carrier phase)

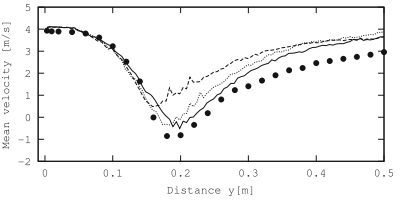

Fig. 10 Mean axial vel (particles 20 μm)

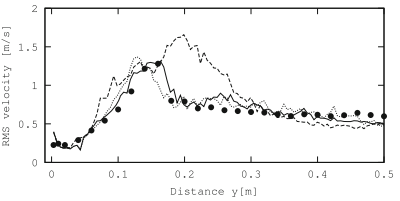

Fig. 11 RMS axial vel (particles 20 μm)

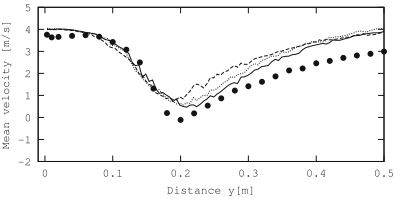

Fig. 12 Mean axial vel (particles 80 μm)

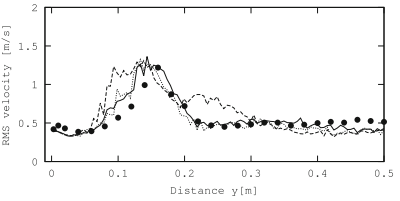

Fig. 13 RMS axial vel (particles 80 μm)

5 Conclusions and Future Work

In this paper, the behaviour of Lagrangian particles in an isotropic turbulent flow has been studied and characterized, as well as the impact of the filtering procedure on the velocity of the continuous phase over the statistics for position and velocity of the dispersed phase. Furthermore, the performance and behaviour of two different stochastic models designed to reconstruct the influence of the sub-grid velocities

lost by filtering in LES over Lagrangian particles have been examined. Both studied stochastic models are well-suited to reconstruct particle-kinetic energy for high-inertia particles, although the models have a model constant that is case-dependent and should be properly setted. For small-inertia particles, these models introduce a stirring effect that dissipates the PCE. Both models have a similar computational cost. The main lines of future work in order to develop better sub-grid stochastic models are: a smart strategy to evaluate the model constant, avoid grid dependency, addition of the sub-grid time-scale seen by the particles in function of particle inertia and new methods to capture the effect of fluid coherent structures (PCEs).

Acknowledgements This work has been financially supported by the *Ministerio de Economía y Competitividad* of the Spanish government through project ENE2014-60577-R and with the support of the *Departament d'Innovació, Universitat i Empresa* of *Generalitat de Catalunya* and the *European Social Fund*.

References

1. Bini, M., Jones, W.: Particle acceleration in turbulent flows: a class of nonlinear stochastic models for intermittency. Phys. Fluids **19**, 035104 (2007)
2. Bini, M., Jones, W.: Large-eddy simulation of particle-laden turbulent flows. J. Fluid Mech. **614**, 207–252 (2008)
3. Bore, J., Ishima, T., Flow, I.: The effect of mass loading and inter-particles collisions on the development of the polydispersed two-phase flow downstream of a confined bluff body. J. Fluid Mech. **443**, 129–165 (2001)
4. Klein, M., Sadiki, A., Janicka, J.: A digital filter based generation of inflow data for spatially developing direct numerical or large eddy simulations. J. Comput. Phys. **186**, 652–665 (2003)
5. Krajnovic, S., Davidson, L.: Large-eddy simulation of the flow around a bluff body. AIAA J. **40**(5), 927–936 (2002)
6. Lundgren, T.S.: Linearly Forced Isotropic Turbulence, pp. 461–473. Annual Research Briefs, C.T.R., Stanford (2003)
7. Pozorski, A., Apte, S.: Filtered particle tracking in isotropic turbulence and stochastic modeling. Int. J. Multiph. Flow **35**, 118–128 (2009)
8. Wang, L.P., Maxey, M.R.: Settling velocity and concentration distribution of heavy particles in homogeneous isotropic turbulence. J. Fluid Mech. **256**, 27–68 (1993)

Large Eddy Simulation of the Flow Around a Simplified Car Model

K. Nusser, S. Müller, C. Scheit, M. Oswald and S. Becker

1 Introduction

Aim of the ongoing development of passenger cars is to predict the interior acoustics early in the development process. A significant noise component results from the flow phenomena in the area of the side window. The complex turbulent flow field in the wake of the a-pillar and the side mirror is characterized by velocity and pressure fluctuations. The flow field results in sound sources which transmit noise into the passenger cabin. In addition to that, it excites the structure, resulting in a radiation of structure-borne noise into the interior of the car. In the present work, as a first step in solving this three part problem, a Large Eddy simulation (LES) of the flow was conducted to investigate the sound generation due to external air turbulence. For this purpose, a simplified model of an automobile was used. In addition to the LES, a Delayed-Detached Eddy simulation (DDES) and an unsteady RANS (URANS) simulation of the same model were carried out. All simulations are compared to experimental data which is already available for this model [6].

Up to now, different approaches were made to simulate the flow around a car. Generic models like the Ahmed body are often used with LES or DES simulations, like for example by Krajnovic et al. [4] or Minguez et al. [5], but also the flow around real car geometries is calculated, for example by Ask et al. [1].

K. Nusser (✉) · S. Müller · C. Scheit · S. Becker
Institute of Process Machinery and Systems Engineering (iPAT), University of Erlangen-Nuremberg, Erlangen, Germany
e-mail: katrin.nusser@ipat.uni-erlangen.de

M. Oswald
ANSYS Germany GmbH, Darmstadt, Germany

D.G.E. Grigoriadis et al. (eds.), *Direct and Large-Eddy Simulation X*,
ERCOFTAC Series 24, https://doi.org/10.1007/978-3-319-63212-4_30

2 Model Setup

The overflown geometry of the car model is identical to the SAE Type 4 body [7]. For this work, a side mirror with square cross section was added to the model, as shown in Fig. 1. The generic, idealized model was designed to reduce the complexity of a real vehicle and to focus on distinct regions. It is therefore very suitable for developing methods to analyze the radiation of flow-induced noise into the vehicle interior. The whole model is assumed to be acoustically insulated, such that noise can only be radiated into the interior through the side window. This area is therefore the main region of interest for the simulations.

For the LES, the flow domain was discretized using a block-structured grid with a total size of 96.7 million cells. A fine near-wall resolution could be achieved with the help of o-grids, which resulted in an average dimensionless distance of the first grid cell off the wall of $y^+ < 1$. The grid which was used for the URANS simulation was about 14 times coarser, leading to approximately 6.9 million elements. For the DDES an unstructured mesh consisting of prism layers and tetrahedral elements was used. It consisted of 87.0 million elements with a wall resolution of $y^+ < 1$.

For the LES and URANS simulation, a half body grid was used and symmetry assumed. It was assumed that this boundary condition has no major influence on the flow in the area of the side window, which is the main focus of this work. On the top, bottom and outer channel wall, a slip boundary condition was imposed. A convective outlet boundary condition was used for the LES, whereas for the URANS a pressure outlet was assumed.

In contrast to that, the DDES was conducted using a full model and no-slip boundary conditions on all four channel walls to reproduce the conditions of the experiments in the acoustic wind tunnel.

Both URANS and DDES used an inlet velocity of u_x = 150 km/h, leading to a Reynolds number based on the mirror height of 2.20×10^5. The LES was conducted at an inlet velocity of u_x = 100 km/h at $Re = 1.47 \times 10^5$ based on the mirror height.

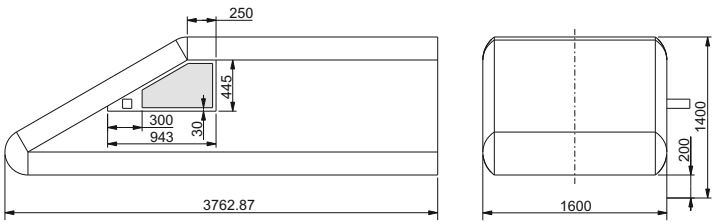

Fig. 1 Schematic drawing of the setup with dimensions of the side window (units in mm)

3 Numerical Setup

As a precursor of this work, an incompressible URANS simulation was conducted to determine the suitability of the computational grid and to get a basic understanding of the flow field on the side window. A k-ω-SST model was used to model the turbulent scales. Second order Euler time-stepping was applied in combination with a timestep of 1×10^{-4} s.

The incompressible Large Eddy simulation constitutes the main part of this work. It was executed using the in-house code FASTEST-3D, which uses a Finite Volume approach based on block-structured, co-located meshes. The Smagorinsky model was used for modeling the subgrid scales in combination with a van Driest damping in the near-wall area. A central differencing scheme with 10% upwind differencing was used for the discretization in space. Time advancement was done via an implicit Crank–Nicolson scheme, using a timestep of 6×10^{-7} s.

Additionally, a compressible simulation of the SAE body was conducted by ANSYS Germany. To account for the large-scale hydrodynamic and aeroacoustic sources in the flow, scale-resolving simulations were done by means of Delayed-Detached Eddy turbulence models with a k-ω-SST model delivering the RANS-part. A second order upwind differencing in space and an implicit second order time-stepping with a timestep of 3×10^{-5} s were used.

4 Results

To illustrate the instantaneous flow and the developing turbulent structures in the LES, isosurfaces of the instantaneous pressure fluctuations $p'(x_i, t) = p(x_i, t) - \overline{p}(x_i)$ are visualized in Fig. 3. It shows a high degree of irregularity and a great variety of sizes in the vortex structures generated by the mirror and the a-pillar. Also very small turbulent structures are resolved. In contrast to this, the pressure fluctuations resulting from the URANS approach can be seen in Fig. 2. Here, only large turbulent structures are resolved, originating from a shedding of regularly formed vortices behind the side mirror. Nearly no smaller structures occur. Furthermore, the characteristic decay in vortex size cannot be observed here. This superiority of the LES gives a good impression of the capabilities of scale-resolving simulation approaches for this application.

To give a qualitative comparison of the coherent structures in the wake of the side mirror developed in the simulations, the Q-criterion proposed by Hunt et al. [3] was used. Iso-surface plots of the second invariant of the velocity gradient tensor Q are depicted in Fig. 4 for the DDES and in Fig. 5 for the LES. The characteristic horseshoe vortex and the vortex shedding around the bluff body can be observed in both simulations, as well as the vortex breakdown in the wake of the mirror model. The LES is also able to resolve the generation of vortices due to a detachment of the flow on the a-pillar. In general the vortex structures which are resolved by the

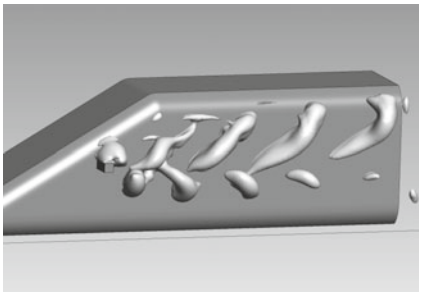

Fig. 2 Instantaneous pressure fluctuations $p' = 20$ Pa of URANS simulation

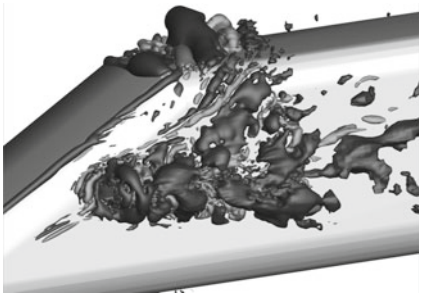

Fig. 3 Instantaneous pressure fluctuations $p' = \pm 20$ Pa of LES

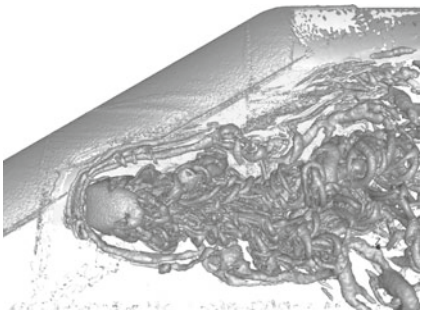

Fig. 4 Iso-surfaces of Q of DDES

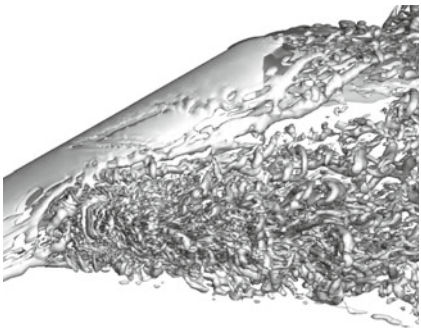

Fig. 5 Iso-surfaces of Q of LES

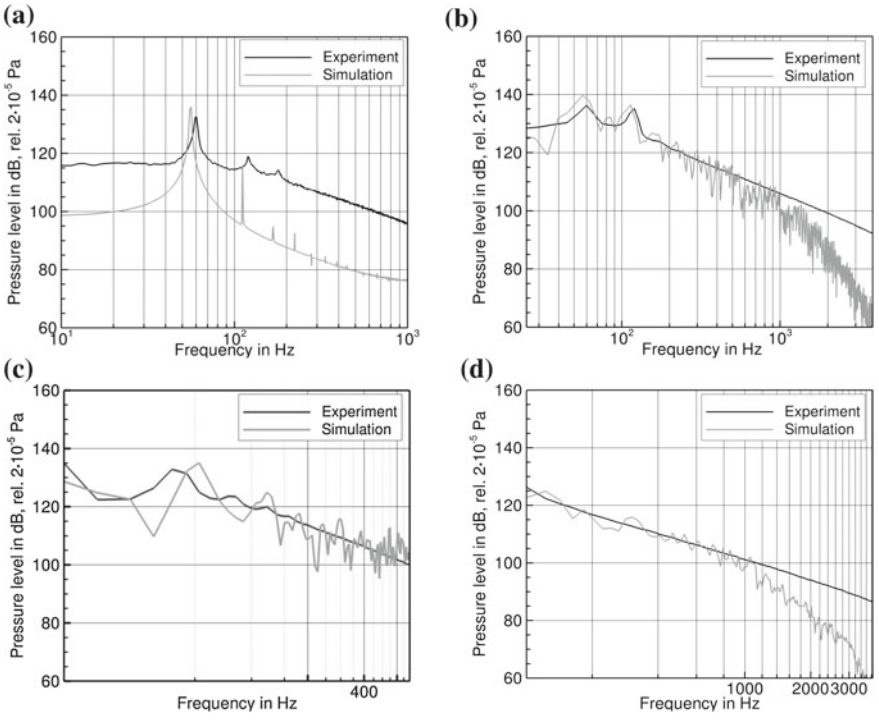

Fig. 6 Frequency spectra of the wall-pressure fluctuations at a position in the wake of the side mirror model from URANS (**a**), DDES (**b**) and LES (**c**, **d**)

LES are much smaller than those of the DDES, especially in the direct vicinity of the mirror model, but also in the wake in the area of the side window.

Due to extensive experiments in an acoustic wind tunnel, local pressure values on 39 positions on the surface of the side window are available. On the same monitoring locations, these wall-pressure values were also gathered from the three different simulations. The frequency and amplitude of these wall-pressure fluctuations were computed by an FFT and compared to the experimental data. In Fig. 6a, b, results are shown as frequency spectra for both URANS and DDES simulations for monitoring points at a position in the wake of the side mirror model. For the LES, results for the low frequency range in Fig. 6c are plotted separately to the high frequency range in Fig. 6d for the same monitoring point.

As expected, the URANS simulation is only able to resolve the first tonal component of the spectrum at around 60 Hz, which results from periodic vortex shedding on the mirror model. Components at higher frequencies are only partially resolved due to the limits of this approach regarding the resolution of smaller turbulent structures.

For the DDES, a good agreement of the results with the experimental values is found. The tonal components are well resolved in both frequency and amplitude.

The amplitude of the pressure at higher frequencies also matches the experimental results up to a frequency of approximately 800 Hz.

The low frequency part of the spectrum of the pressure fluctuations of the LES in Fig. 6c shows that the tonal components are well captured in amplitude, but slightly shifted in frequency. This can be explained by the coarse frequency resolution which results from the limited averaging time due to the small timestep of the LES. A longer averaging time is therefore expected to further improve the results for the low frequency range. Furthermore, the use of upwind differencing could also influence the frequency of the tonal components.

An analysis of the higher frequency part of the spectrum of the LES in Fig. 6d shows a good agreement with the experimental data up to a frequency of over 1000 Hz. This is important for this application, because this frequency range cannot be successfully calculated using for example the Corcos model [2]. This model is used to describe the coherence properties of a turbulent boundary layer flow to generate a synthetic field of wall-pressure fluctuations. In applications with large detachment regions, like in the case of the mirror model, it can only be applied in a limited way.

5 Conclusion

Different simulations of the flow around a simplified car model were carried out and compared to experimental data. Results of the LES show a good agreement with this reference data up to a frequency of 1000 Hz. This could not be matched by the URANS simulation due to its limited resolution of small turbulent structures. The DDES is able to resolve both low and higher frequency parts of the wall-pressure fluctuations with a slightly lower maximal resolvable frequency than for the LES.

It can also be concluded from these results, that a simulation of the full model is not necessary when only the flow in the area of the side window is of interest. The simulation of the half model in case of the LES and URANS gives sufficient results while also reducing the computational effort.

References

1. Ask, J., Davidson, L.: Flow and dipole source evaluation of a generic SUV. J. Fluid Eng. **132**(5), 051111 (2010)
2. Corcos, G.: Resolution of pressure in turbulence. J. Acoust. Soc. Amer. **35**(2), 192–199 (1963)
3. Hunt, J., Wray, A., Moin, P.: Eddies, stream and convergence zones in turbulent flows. Technical report CTR-S88, Center for Turbulent Research (1988)
4. Krajnovic, S., Davidson, L.: Flow around a simplified car, part 1: large eddy simulation. J. Fluid Eng. **127**(5), 907–918 (2005)
5. Minguez, M., Pasquetti, R., Serre, E.: High-order large-eddy simulation of flow over the ahmed body car model. Phys. Fluids **20**, 095101 (2008)

6. Müller, S., Becker, S., Gabriel, C., Lerch, R., Ullrich, F.: Flow-induced input of sound to the interior of a simplified car model depending on various setup parameters. In: AIAA Aeroacoustics Conference (2013)
7. Society of Automotive Engineers: Aerodynamic Testing of Road Vehicles in Open Jet Wind Tunnels. SAE Special Publication 1465 (1999)

Wake Prediction of a Marine Propeller: The Role of the Turbulence Closures

E. Guilmineau, G.B. Deng, A. Leroyer, P. Queutey, M. Visonneau and J. Wackers

1 Introduction

The marine propeller is the principal ship component to provide the necessary propulsion and when working at the aft of a ship, the propeller operates in a heterogeneous field because of the wake, created by the hull, which can have an effect on performance since the interaction is directly related to vibrations, noise and propulsion performances. So, the physical mechanisms that characterize the interactions between the propeller and the hull is very complex.

However, even in the simple case of an isolated propeller in a uniform flow, called open water conditions, the flow is complex. It consists of viscous phenomena as the development of the turbulent boundary on the blade and hub, flow separation on the blade, viscous-inviscid interaction, hub and tip vortices, viscous wake. Therefore, the study of these flow characteristics, in particular a better knowledge of the wake characteristics, is essential for accurate prediction of the propulsion performance. In open water conditions, the flow is characterized by two vortex systems: one generated by the tip of the blade and the second arisen from the hub. A experimental study of the flow around a propeller in a water tunnel by Felli et al. [3] shows a comprehensive description. By flow measurements and visualizations, these authors studied the mechanisms that causes the instability of the wake and the dependence of the vortex pairing and grouping is investigated.

From on a numerical point of view, the reliability of the such numerical predictions can be questioned. When intense and localized three-dimensional structures are concerned, the control of the numerical diffusion is difficult. For a tip vortex,

E. Guilmineau (✉) · G.B. Deng · A. Leroyer · P. Queutey · M. Visonneau · J. Wackers
LHEEA, CNRS UMR 6598, Ecole Centrale de Nantes, BP. 92101,
44321 Nantes Cedex 3, France
e-mail: emmanuel.guilmineau@ec-nantes.fr

D.G.E. Grigoriadis et al. (eds.), *Direct and Large-Eddy Simulation X*,
ERCOFTAC Series 24, https://doi.org/10.1007/978-3-319-63212-4_31

the flow in the core of the vortex is characterized by rotation, streamline curvature effects. These flow features are poorly modeled by classical eddy-viscosity based turbulence models. Recently, unsteady hybrid RANS-LES turbulence closures, like DES, seems to be able to predict these features, see Muscari et al. [5].

A validation of the flow around an isolated propeller is proposed in this paper. The main objective is a comparison of statistical turbulence closures and an hybrid RANS-LES methodology with the ISIS-CFD flow solver in order to draw conclusions about the requirements in term of physical modelization.

2 Test-Case

The propeller geometry is the INSEAN E779A model, i.e. a four bladed, fixed-pitch, right-handed propeller characterized by a nominally constant pitch distribution and a very low skew angle. The diameter of the propeller is $D = 0.227\,m$.

The rotational speed of the propeller will be kept fixed to a value of $n = 25\,rps$ and the different advance coefficients $J = U_\infty/(nD)$ will be obtained by changing the inflow velocity U_∞. The Reynolds number is based on the radius of the propeller ($R = 0.1135$ m) and the velocity of the tips of the blades ($U_{ref} = n\pi D \approx 17.829$ m/s) and is $Re = 1.78 \times 10^6$.

3 ISIS-CFD at Glance

ISIS-CFD, developed by the Ecole Centrale de Nantes and CNRS and available as a part of the FINE/Marine computing suite, is an incompressible unsteady Reynolds-averaged Navier-Stokes (URANS) method. The solver is based on the finite volume method to build the spatial discretization of the transport equations. The unstructured discretization is face-based, which means that cells with an arbitrary number of arbitrarily shaped faces are accepted. A second order backward difference scheme is used to discretize time. The solver can simulate both steady and unsteady flows. The velocity field is obtained from the momentum conservation equations and the pressure field is extracted from the mass equation constraint, or continuity equation, transformed into a pressure equation. In the case of turbulent flows, transport equations for the variables in the turbulence model are added to the discretization. A detailed description of the solver is given by Queutey and Visonneau [6].

The solver features sophisticated turbulence models: apart from the classical two-equation k-ε and k-ω models, the anisotropic two-equation Explicit Algebraic Reynolds Stress Model (EARSM), as well as Reynolds Stress Transport Models, are available, see Duvigneau et al. [2] and Deng and Visonneau [1]. All these are RANS models. Recently, a Detached Eddy Simulation (DES) approach has been introduced, see Guilmineau et al. [4].

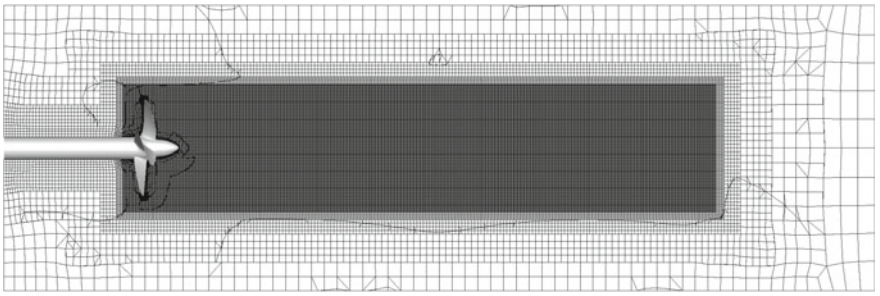

Fig. 1 View of the mesh in the symmetry plane

4 Numerical Simulation Set-Up

The computational domain consists of a cylindrical domain, whose diameter is 3D, and length is 9.18D. It starts 1.48D before the propeller plane.

The computational mesh is created with HEXPRESS, an automatic unstructured mesh generator. This software generates meshes containing only hexahedrons. The mesh consists of 21.4×10^6 cells. The number of faces for each blade is approximately 38,100. The average wall normal resolution on the blades is $y^+ = 0.6$ with a maximum around the tip, in the order of 1.8. A box including the propeller and extending up to 6D in the wake is added to capture the vortices. In this box, the cells are isotropic and the size is 0.009D, see Fig. 1.

The RANS equations are written in the rotating reference frame but written in terms of velocity components of the fixed inertial frame. For the RANS turbulence models (k-w SST and EARSM), the solution is a steady solution while for DES computations, this approach is unsteady and the time step is 3×10^{-5} s. This time step corresponds to a rotation of 0.25°. The time-averaged flow is obtained in approximately 9 rotations of the propeller for DES computations.

5 Results

5.1 Open-Water Characteristics

The open water characteristics of the propeller, the thrust and the torque, for different values of the advance coefficient J are computed for various turbulence closures and compared with the experimental data, obtained by Salvatore [7], see Fig. 2. The thrust coefficient Kt is defined by $Kt = T/(\rho n^2 D^4)$, where T is the thrust of the propeller and ρ the density of the water, the torque coefficient by $Kq = Q/(\rho n^2 D^5)$, where Q is the torque, and the propeller open-water efficiency by $\eta = Kt/Kq\ J/(2\pi)$. All numerical simulations give similar results differ by less than 5% for the low values

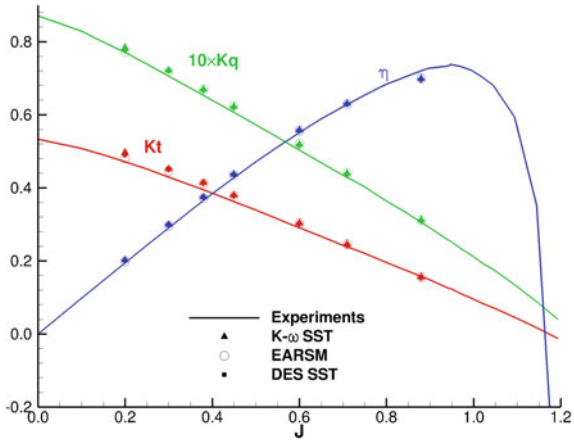

Fig. 2 Open-water characteristics of the E779A propeller

of the advance coefficient and by less than 3% for the high value of J. Moreover, the numerical results are in good agreement with the experimental data.

5.2 *Flow Field in the Wake*

The analysis of the flow field is carried out for two values of the advance coefficient, J = 0.71 and 0.20 and the results are compared with the experimental data obtained by Felli et al. [3].

5.2.1 J = 0.71

A general view of the wake of the propeller, for the advance coefficient J = 0.71, is given in Fig. 3a–c which presents an isosurface of the dimensionless value $\lambda_2 = -2$ of the second largest invariant of $S^2 + \Omega^2$ (S and Ω being the symmetric and antisymmetric component of ∇u) colored by the helicity. The acceleration of the flow behind the propeller causes a slight reduction of the radial position of the vortex cores. Then, the helices formed by the tip vortices remain located on a circular cylinder. RANS model yield tip vortices but they vanish more or less rapidly in

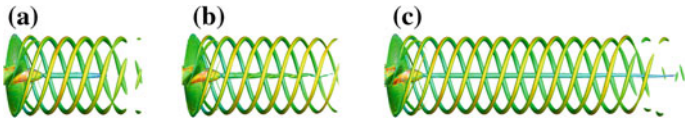

Fig. 3 **a** J = 0.71 - k-ω SST, **b** J = 0.71 - EARSM, **c** J = 0.71 - DES SST

the wake depending on the turbulence model used. With the DES approach, the tip vortices are maintained much further in the wake. These remarks are also observed by Muscari et al. [5]. Although no figure presents the turbulent kinetic energy (TKE), the RANS simulations predict a small value of TKE near the tip of the blade which grows rapidly in the vortex core. The values around the vortex core increase along the filament. On the contrary, the DES approach produces a high TKE near the tip but the level vanishes quickly in the wake and the level is lower than those observed with a RANS approach.

5.2.2 J = 0.20

The second value of the advance coefficient is J = 0.20 which corresponds to a condition of very high blade loading. The tip vortices vanish quickly in the wake of the propeller, even for the DES approach, see Fig. 4a–c.

5.2.3 Instantaneous Views

Figure 5a, b represent a view of the instantaneous isosurface of the invariant λ_2 obtained with a DES approach for both values of J. We can compare these figures with those representing the results obtained with the RANS model. For J = 0.71, the vortex grouping appears only with a DES simulation. It is located at approximately 7.2R, see the red ellipse in Fig. 5, while in the experiments, this phenomena appears at 7R. For J = 0.20, more structures are predicted with a DES approach. Even if a RANS simulation yields a good prediction of forces and moments, this approach fails to give information about the wake evolution, as unsteadiness of the wake.

Fig. 4 **a** J = 0.20 - k-ω SST, **b** J = 0.20 - EARSM, **c** J = 0.20 - DES SST

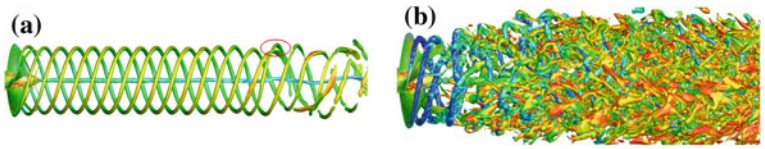

Fig. 5 **a** J = 0.71 - DES SST, **b** J = 0.20 - DES SST

6 Conclusions

In the present work, the numerical simulation of the flow past an isolated propeller was been addressed in order to compare various turbulence closures (RANS and DES) using ISIS-CFD flow solver. The geometry chosen was the INSEAN E779A. Computations were performed for various advance coefficients following experimental conditions. On the one hand, the thrust and the torque obtained with all turbulence models are in good agreement with the measured data. On the other hand, the prediction of the wake depends on the turbulence closures used. Indeed, the RANS approach dissipates the tip vortices very quickly due to the high level of the turbulence kinetic energy in the core of the vortices. On the contrary, the DES approach allows to capture the evolution of the tip vortices and the initial stages of the instability pattern, with two consecutive filaments grouping their relative position, can also be reproduced and agree reasonably well with the flow visualization. Thanks to the relaminarization of the core of the tip vortex in the wake of the propeller, the hybrid RANS-LES model performs better than the eddy-viscosity based turbulence closures.

Looking at the cost of the simulation, a DES approach is still prohibitive compared to a RANS simulation. Consequently, if the prediction of the thrust and the torque is the objective, the RANS approach is sufficient. However, if the prediction of the propeller wake is necessary, a DES approach should be used.

Acknowledgements This work was granted access to the HPC resources of CINES/IDRIS under the allocation 2014-2a0129 made by GENCI.

References

1. Deng, G.B., Visonneau, M.: Comparison of explicit algebraic stress models and second-order turbulence closures for steady flow around ships. In: Piquet, J. (ed.) 7th Inernational Conference on Numerical Ship Hydrodynamics, pp. 4.4.1–15, Nantes, France (1999)
2. Duvigneau, R., Visonneau, M., Deng, G.B.: On the role played by turbulence closures in hull ship optimization at model and full scale. J. Mar. Sci. Technol. **8**, 11–25 (2003)
3. Felli, M., Camusi, R., Di Felice, F.: Mechanisms of evolution of the propeller wake in the transition and far fields. J. Fluid Mech. **682**, 5–53 (2011)
4. Guilmineau, E., Deng, G.B., Wackers, J.: Numerical simulation with DES approach for automotive flows. J. Fluids Struct. **27**, 807–816 (2011)
5. Muscari, R., Di Mascio, A., Verzicco, R.: Modelling of vortex dynamics in the wake of a marine propeller. Comput. Fluids **73**, 69–79 (2013)
6. Queutey, P., Visonneau, M.: An interface capturing method for free-surface hydrodynamic flows. Comput. Fluids **36**, 1481–1510 (2007)
7. Salvatore, F.: D4.1.3: The INSEAN E779A propeller experimental dataset. VIRTUE European Project TIP5-CT-2005-516201 (2007)

Coherent Structures in a Flow Past a Circular Cylinder at Critical and Super-Critical Reynolds Numbers

I. Rodríguez, O. Lehmkuhl, J. Chiva, R. Borrell and A. Oliva

1 Introduction

It is well known that the wake topology in the flow past a circular cylinder remains almost unchanged up to Reynolds number $\sim 10^5$ Williamson [1]. Then, at $Re \sim 2 \times 10^5$ major changes take place entailing flow separation, turbulence transition in the detached shear layers, reattachment of the flow and further separation of the boundary layer. In the present work, large-eddy simulations of the flow past a cylinder at Reynolds numbers in the range $2.5 \times 10^5 - 10^6$ are performed. This range includes both critical and super-critical Reynolds numbers [2]. Contradicting results about the wake configuration and structures are found in the literature. These contradictions are based on the reports that vortex shedding ceases to occur at Reynolds numbers beyond $Re = 4 \times 10^5$ (see for instance [2, 3]). In this work, the coherent structures found at both critical and super-critical Reynolds numbers is analysed by means of both shear layer instabilities and vortex shedding measurements. Furthermore, the main features of the unsteady super-critical wake is also pointed out.

I. Rodríguez (✉)
Turbulence and Aerodynamics Research Group, Universitat Politècnica de Catalunya, ESEIAAT Colom 11, 08222 Terrassa, Spain
e-mail: ivette.rodriguez@upc.edu

O. Lehmkuhl · R. Borrell
Barcelona Supercomputing Center, Edificio NEXUS II, Gran Capitan 2-4, 08034 Barcelona, Spain
e-mail: oriol.lehmkuhl@bsc.es

R. Borrell
e-mail: ricard.borrell@bsc.es

J. Chiva · A. Oliva
Heat and Mass Transfer Technological Centre, Universitat Politècnica de Catalunya, ESEIAAT Colom 11, 08222 Terrassa, Spain
e-mail: jordic@cttc.upc.edu

A. Oliva
e-mail: oliva@cttc.upc.edu

D.G.E. Grigoriadis et al. (eds.), *Direct and Large-Eddy Simulation X*,
ERCOFTAC Series 24, https://doi.org/10.1007/978-3-319-63212-4_32

2 Mathematical and Numerical Models

Large eddy simulations of the flow are carried out. The methodology used for solving the flow over bluff bodies with massive separation is described in and Rodríguez et al. [4]. The governing equations are discretised on a collocated unstructured grid arrangement by means of second-order spectrum-consistent schemes. For the temporal discretisation of the momentum equation a self-adaptive two-step linear explicit scheme on a fractional-step method has been used for the convective and diffusive terms [5], while for the pressure gradient term an implicit first-order scheme has been implemented. As for the subgrid scale model, the wall-adapting local-eddy viscosity model (WALE) [6] is used. For more details the user is referred to [7].

3 Results

The flow past a circular cylinder at critical and super-critical Reynolds numbers of $Re_D = 2.5 \times 10^5$, 3.8×10^5, 5.3×10^5, 7.2×10^5, 8.5×-10^5 and 10^6 is here considered. The cases are solved in a computational domain of dimensions $x \equiv [-16D, 16D]$; $y \equiv [-10D, 10D]$ for the stream- and cross-stream directions, whereas for the span-wise direction $z \equiv [0, 0.5\pi D]$ is considered for Reynolds number up to $Re = 6.5 \times 10^5$ and $z \equiv [0, D]$ for the higher Reynolds numbers. For solving these cases meshes up to 114.7 million control volumes are used depending on the Reynolds number. For obtaining the numerical results presented, average statistics are then computed for a time span of at least 25 shedding cycles, in order to assure that the flow is statistically converged.

The variation of the drag coefficient with the Reynolds number is plotted in Fig. 1 together with the literature available measurements. A fair agreement is observed along the whole range and the steep drop in the drag is well captured by the present simulations. As it was observed in a previous work [7], in the critical regime major changes are occurring, where the drag drop off up to $C_D \approx 0.21$ at $Re = 6.5 \times 10^5$.

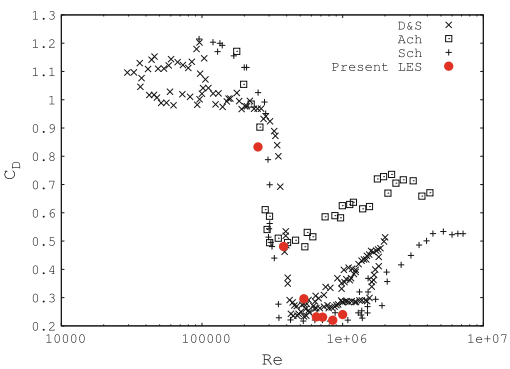

Fig. 1 Variation of the drag coefficient with the reynolds number. Comparison with literature. (*red solid circles*) Present results; (*crosses*) Delany and Sorensen [8]; (*squares*) Achenbach [9]; (*pluses*) Schewe [10]

As can be seen in the figure, in the super-critical ($Re > 6.5 \times 10^5$), a plateau in the magnitude of the drag is observed up to $Re = 10^6$.

3.1 Vortex Shedding

When it comes to coherent structures in the flow past a bluff body, the way separated shear-layers interact and how vortices are shed into the wake should be analysed. In the super-critical regime, once the drag coefficient is at its minimum, the pressure difference accelerates the flow triggering the transition just after separation, and eventually, forces the turbulent shear-layers to interact with each other in the wake centreline. This behaviour, similar at all super-critical Reynolds numbers, results in alternating shedding of vortices and the formation of a von Kármán-like vortex street (see Fig. 2). This vortex street configuration resembles those observed at subcritical Reynolds numbers, but also differences can be found. First, as a result of the delayed turbulent separation of the shear-layers, these are bent towards the wake centreline and thus, vortex formation region is limited to a reduced zone in the cylinder rear and with a length (measured from the cylinder centroid) about $\sim 1D$ at all the supercritical regime. This also causes the wake to be narrower than that of the subcritical regime. Measurements of the wake width in the super-critical regime (not shown here) yielded a value of about $d_w/D \sim 0.4$, in contrast with the values reported in the subcritical regime $d_w/D > 1$. Secondly, while in the sub-critical regime the formation region shrinks as the transition to turbulence in the shear-layers moves towards the cylinder with the increase of the Reynolds number, in the super-critical regime as the turbulent final separation of the shear-layers does occur nearly at the same position, other wake characteristic (i.e. the formation region, location of the vortices and average Reynolds stresses peaks, among others) remain almost at the same location in the wake regardless the Reynolds number.

By analysing the energy spectra of several proves located at the near-wake region, vortex shedding frequency was detected at every Reynolds number as a narrow-band

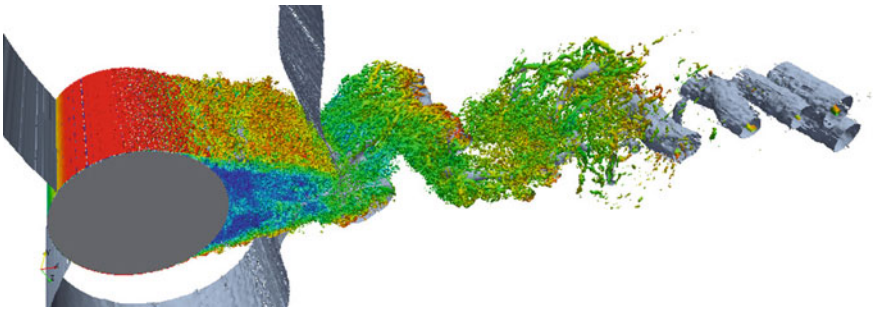

Fig. 2 Instantaneous pressure and Q iso-contours coloured by the velocity magnitude at $Re = 10^6$

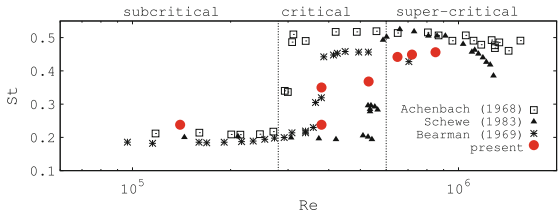

Fig. 3 Vortex-shedding frequency, comparison with the literature

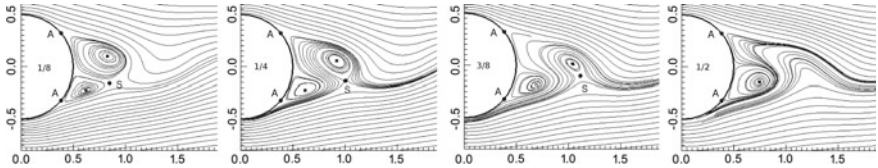

Fig. 4 Phase-average streamlines in the super-critical regime. One half of a vortex shedding is represented

peak (see Fig. 3). These observations contrast with some experimental investigations (see for instance Shih et al. [3]). Indeed, the vortex shedding frequency increases from a value of about 0.2 at critical Reynolds numbers up to about 0.44 at super-critical Reynolds numbers. One can only but speculate why vortex shedding was not detected in the super-critical regime. Several experimental issues have been reported in different experimental works, e.g. the use of a too small cylinder model (Achenbach and Heinecke [9] reported un-coherent flow for $L_z/D < 3.33$), the use of a cantilevered cylinder ([11]), instabilities introduced by small dust particles on the cylinder model (see [10]), amongst others can be the sources of the loss of coherence in the wake in the super-critical regime.

The unsteady mean flow has been analysed by means of the phase-average technique. For the ensemble average, 8 vortex shedding cycles have been used to generate each coherent component. Defined streamlines contours for half vortex shedding period at phase angles of $\phi = 1/8\ St_{vs},\ 1/4\ St_{vs},\ 3/8\ St_{vs},\ 1/2\ St_{vs}$ confirm the existence of a coherent wake flow in the super-critical regime (Fig. 4). In the figure, vortices as they form in the vortex formation region can be tracked as they travel downstream and are convected into the wake. The position of the vortex cores is also marked in the figure.

3.1.1 Shear-Layer Instabilities

Shear-layer instabilities were pointed out as the main mechanism of transition to turbulence in the critical regime [7]. An interesting trait of the vortex formation is that even at these high Reynolds numbers small scale instabilities are detected just

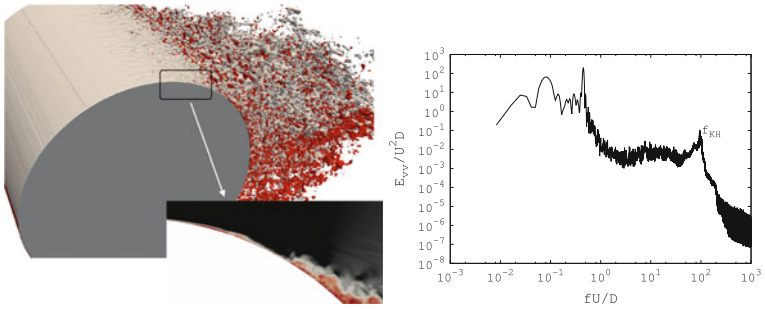

Fig. 5 (*left*) Shear-layer instabilities near the cylinder apex; (*right*) Energy spectrum of velocity fluctuations at the shear-layer, $Re = 7.2 \times 10^5$

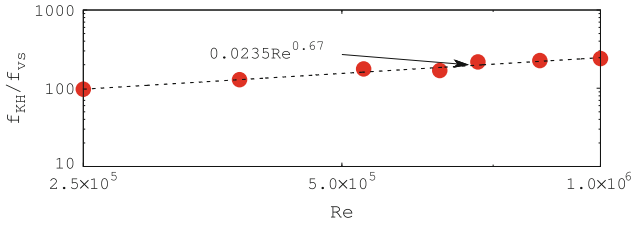

Fig. 6 f_{KH}/f_{vs}, the correlation proposed by Prasad and Williamson [12] and the $Re^{0.5}$ scaling are also plotted

close to the separation point of the shear-layers. If a close inspection of the shear-layers structures in the region close to their detachment is done, one can detect these instabilities developing near the cylinder apex (see Fig. 5 left). As they travel along the boundary layer, get amplified (see Fig. 5a inset) and eventually are the responsible of the rapid transition to turbulence once the boundary layer has detached from the cylinder surface. In Fig. 5 right, the energy spectrum of the velocity fluctuations in the detached shear-layers is depicted. In addition to the vortex shedding frequency, a high frequency broad-band peak (marked as KH) is the footprint of these instabilities. The ratio of the shear-layer frequency to the vortex shedding frequency is shown in Fig. 6 for all Reynolds numbers. It is interesting to point out the agreement with Prasad and Williamson [12] scaling. These finding thus extend the observations made for the critical regime to the super-critical zone, at least up to $Re = 10^6$.

4 Conclusions

The analysis of the flow past a circular cylinder has shown that even at super-critical Reynolds numbers the wake formed behind the cylinder is coherent. Similar to the subcritical regime, alternating vortices are detached from the separated shear layers

forming a coherent vortex street. However, the frequency at which these vortices are shed is larger than that of the subcritical regime. The supercritical wake is narrower, and vortex formation region is limited to the region behind the cylinder. The signal of the shear layer instabilities has been detected in all the super-critical regime showing that these instabilities are also the main mechanism of transition in this regime.

Acknowledgements This work has been partially financially supported by the Ministerio de Economía y Competitividad, Secretaría de Estado de Investigación, Desarrollo e Innovación, Spain (ref. ENE2009-07689) and by the collaboration project between Universitat Politècnica de Catalunya and Termo Fluids S.L. We acknowledge PRACE (project 2012071290) for awarding us access to the MareNostrum III machine based in Barcelona, Spain.

References

1. Williamson, C.H.K.: Vortex dynamics in the cylinder wake. Annu. Rev. Fluid Mech. **28**(1), 477–539 (1996)
2. Roshko, A.: Experiments on the flow past a circular cylinder at very high Reynolds number. J. Fluid Mech. **10**(3), 345–356 (1961)
3. Shih, W., Wang, C., Coles, D., Roshko, A.: Experiments on flow past rough circular cylinders at large Reynolds numbers. J. Wind. Eng. Ind. Aerodyn. **49**, 351–368 (1993)
4. Rodríguez, I., Borrell, R., Lehmkuhl, O., Pérez-Segarra, C.D., Oliva, A.: Direct numerical simulation of the flow over a sphere at Re = 3700. J. Fluid Mech. **679**, 263–287 (2011)
5. Trias, F.X., Lehmkuhl, O.: A self-adaptive strategy for the time integration of Navier-stokes equations. Numer. Heat Transf. Part B **60**(2), 116–134 (2011)
6. Nicoud, F., Ducros, F.: Subgrid-scale stress modelling based on the square of the velocity gradient tensor. Flow Turbul. Combust. **62**, 183–200 (1999)
7. Lehmkuhl, O., Rodríguez, I., Borrell, R., Chiva, J., Oliva, A.: Unsteady forces on a circular cylinder at critical reynolds numbers. Phys. Fluids **26**(12), 125110 (2014)
8. Delany, N., Sorensen, N.: Low-speed drag of cylinders of various shapes, Technical Report NACA TN3038, NACA, (1953)
9. Achenbach, E., Heinecke, E.: On vortex shedding from smooth and rough cylinders in the range of reynolds numbers 6e3 to 5e6. J. Fluid Mech. **109**, 239–251 (1981)
10. Schewe, G.: On the force fluctuations acting on a circular cylinder in crossflow from subcritical up to transcritical reynolds numbers. J. Fluid Mech. **133**, 265–285 (1983)
11. Schmidt, L.V.: Measurements of fluctuating air loads on a circular cylinder. J. Aircr. **2**(1), 49–55 (1965)
12. Prasad, A., Williamson, C.: The instability of the shear layer separating from a bluff body. J. Fluid Mech. **333**, 375–492 (1997)

Wall-Modeled Large Eddy Simulation for Rotating Flows

N.A. Loppi, J. Bodart and G. Dufour

1 Introduction

In order to carry out Large Eddy Simulations (LES) of challenging industrial systems such as turbomachines, the effects of system rotation need to be considered [9]. Moreover, high Reynolds number applications require additional modeling framework, such as DES [8] or wall-modeling [7] to maintain reasonable costs. These hybrid techniques must be able to incorporate appropriate rotation corrections, as system rotation can affect the logarithmic zone of turbulent boundary layers [6]. In this context, the spanwise rotating turbulent channel flow is a well-known test case, relevant for applications in which the rotation is not streamwise-aligned (as in centrifugal compressors, where the outflow is orthogonal to the rotation vector). However, wall-modeling for rotating flows and its ability to account for the Coriolis acceleration, is a relatively unexplored field. Precursor approaches [1] have shown some success at low Reynolds ($Re_\tau = 200$) and rotation numbers ($Ro = 0.21$) but are likely to fail at higher Reynolds and rotation number as the model does not include rotation effects. In particular, the results of Ref. [1] show difficulties in predicting the shear stress on the stabilized side as the rotation number increases.

In this study, a wall-resolved simulation was performed, using a bulk Reynolds number of 20,000 and a rotation number of 0.45. The wall-resolved computation was harnessed to *a priori* test the wall-modeling strategy based on the RANS/LES grid decoupling proposed by Kawai and Larsson [2, 4]. The standard formulation

N.A. Loppi (✉) · J. Bodart · G. Dufour
Dépt. Aérodynamique Energétique et Propulsion, ISAE-SUPAERO,
Université de Toulouse, Toulouse, France
e-mail: n.loppi15@imperial.ac.uk

J. Bodart
e-mail: julien.bodart@isae.fr

G. Dufour
e-mail: guillaume.dufour@isae.fr

D.G.E. Grigoriadis et al. (eds.), *Direct and Large-Eddy Simulation X*,
ERCOFTAC Series 24, https://doi.org/10.1007/978-3-319-63212-4_33

was found to be unable to adapt to the rotation effects on wall shear stresses which motivates modifying the expression of the eddy viscosity in the wall-model. A rotation correction, adopted from previous work in RANS framework [3] is proposed and tested against the wall-resolved reference data. The correction was found to significantly improve the shear stress prediction in the wall-modeled LES, and largely reduce the wall-model layer thickness dependency in the results.

2 Wall-Resolved Simulation Setup

A spanwise rotating channel configuration can be explicitly defined with the Reynolds number and the rotation number (inverse Rossby number), which are defined as $Re = \rho U_b h/\mu$ and $Ro = 2|\Omega|h/U_b$, in which U_b is the bulk velocity, $|\Omega|$ is the magnitude of the angular velocity vector and h is the half-channel height.

The stabilizing and destabilizing effects of the Coriolis acceleration can be characterized by a local stability parameter, the gradient Richardson number [3]:

$$Ri = S(S+1), \text{ where } \quad S = \frac{-2\Omega}{(\partial \overline{U}/\partial y)} \,. \tag{1}$$

System rotation has a destabilizing or stabilizing effect on the flow when $Ri < 0$ or $Ri > 0$, respectively. This effect locally increases or decreases turbulence production, and may partially delay or prevent transition [9].

A wall-resolved simulation (WR) was performed to provide reference data. The simulations in this study were carried out with a compressible, unstructured, and massively parallel LES solver Charles^X (see [5] for more details on the solver). Regarding compressibility effects, a global Mach number of $M = 0.2$ was specified in order to stay within the incompressible limit in the whole domain. The Vreman subgrid scale model [10] was chosen to account for transitional effects. The relevant computational and physical parameters are summarized in Table 1.

3 A *Priori* Testing

The first step towards a working wall-model is to implement its algorithm into a separate stand-alone 'sandbox'. This enables the model to be tested a priori by using the wall-resolved results as an input. The feasibility of the model can be assessed by comparing the wall-resolved shear stresses and the ones obtained by the stand-alone wall-model.

The wall-model equation that was investigated in this study is given by

$$\frac{d}{dy}\left[(\mu + \mu_t)\frac{du_{||}}{dy}\right] = 0 \,, \tag{2}$$

Table 1 Summary of the simulations carried out, both with and without a wall-model. All simulations use a $8\pi h \times 2h \times 3\pi h$ domain and a bulk Reynolds number $Re_b = 20{,}000$. RC-$x/z/xz$ indicates a simulation using the Rotation Corrected model, with coarsening in the $x/z/xz$ direction with respect to the LES resolution

		Ro	Gridpoints	$\Delta y^+_{firstcell}$	Δx^+_p	Δz^+_p	$\frac{\tau^u_{w,WM}}{\tau^u_{w,WR}}$	$\frac{\tau^s_{w,WM}}{\tau^s_{w,WR}}$
LES	WR	0.45	$350 \times 100 \times 300$	0.54	77	34		
	RC-z	0.45	$350 \times 60 \times 200$	35	75	50	0.937	0.998
	RC-x	0.45	$250 \times 60 \times 300$	36	107	33	0.961	1.010
WMLES	RC-xz	0.45	$250 \times 60 \times 200$	35	106	50	0.949	0.988
	NM (no model)	0.45	$250 \times 60 \times 200$	28	86	40	0.615	0.930
	EQ (std. formulation)	0.45	$250 \times 60 \times 200$	30	92	43	0.716	1.168

in which $u_{||}$ denotes the wall-parallel velocity. The wall-model eddy viscosity was calculated by a simple mixing length model with van Driest damping, defined as

$$\frac{\mu_t}{\mu} = \kappa y^+ (1 - e^{-y^+/A^+})^2 \,, \tag{3}$$

where the von Karman constant $\kappa = 0.41$ and A^+ is the van Driest damping constant. Following the work of Bradshaw [3], system rotation was introduced through a dependency to the Richardson number:

$$\frac{\mu_t}{\mu} = (1 - \beta Ri)\kappa y^+ (1 - e^{-y^+/A^+})^2 \,, \tag{4}$$

where $\beta = 3.6$ for a spanwise rotating channel.

The a priori analysis was carried out by using the mean velocity as a Dirichlet condition at the wall-model boundary and the no-slip condition was enforced at the wall. The analysis was based on the mean values, as it was observed that several uncorrelated time instants produced nearly identical mean results.

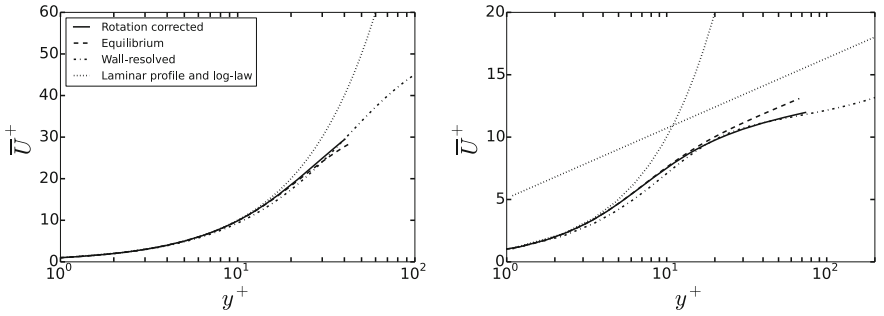

Fig. 1 Velocity profiles calculated with the stand-alone wall-model

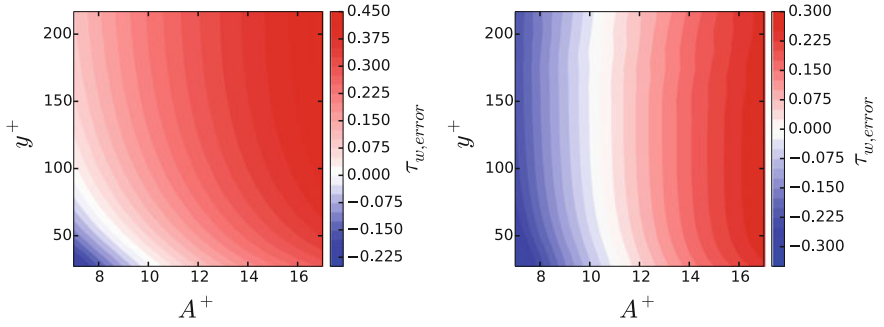

Fig. 2 Relative error in wall shear stress for standard equilibrium and rotation corrected wall-model on the unstable side

The wall-resolved result and a priori calculated velocity profiles in wall units are visualized in Fig. 1. The curves are scaled with their respective friction velocities. Firstly, the results show that the standard (uncorrected) model fails to account for the modification of the wall shear stresses, which confirms the need for rotation correction in wall-modeling. Secondly, the rotation-corrected model predictions yield the correct slope in the logarithmic region with good accuracy.

Figure 2 shows the error in the wall shear stress as a function of A^+ and the wall-model layer thickness. It appears that the standard wall-model requires strong adjustment of A^+ as a function the wall-model thickness. On the opposite, the rotation corrected model is nearly independent on the wall-model and A^+ behaves just as an off-set: the rotation-correction yields the appropriate slope, but the van Driest damping constant A^+ needs to be adjusted case specifically for high rotation rates, because the thickness of the viscous sublayer varies with Ro.

The wall-model behavior on the stable side was found to be more problematic as Ro is high (as reported in Ref. [1]), because the velocity profiles resemble the shape of the laminar profile rather than the logarithmic profile. However, with an appropriate value of A^+, high enough to enforce laminar behavior, the rotation correction improved the value of wall shear stress on the stable side as compared to the standard equilibrium model.

4 Wall-Modeled LES Computations

After the a priori analysis, the rotation correction was implemented into the Charles^X solver, and wall-modeled LES was performed at $Re = 20{,}000$ and $Ro = 0.45$. The van Driest damping constants were chosen as $A_u^+ = 11$ (unstable) and $A_s^+ = 80$ (stable side) based on the a priori tests. Thirty wall-normal cells were placed inside the auxiliary grid, whose thickness was set to be $y_{wm}/h = 0.08$ ($y^+_{wm,u} \approx 85$, $y^+_{wm,s} \approx 40$). Three different spanwise-streamwise resolution were studied and the details of the simulations as well as their relative mean wall-shear stress errors are shown in Table 1.

Concerning the values of the wall-shear stress of Table 1, it can be emphasized that the standard (EQ) model yielded errors of 28.4 and 16.8% on the unstable and stable side, respectively. The proposed correction drastically improved the results, as the errors were reduced to 5.1 and 2.2%.

Figure 3 illustrates the mean velocity profiles in outer layer scaling as well as in wall units, and the normal Reynolds stresses are shown in Fig. 4. All the rotation corrected results were in good agreement with the wall-resolved data, whereas the under-resolved and standard equilibirium wall-models yielded discrepancies. The best results were obtained with the unchanged spanwise resolution, which indicates that it is the most limiting aspect. Surprisingly, the RC-xz case, in which both mesh directions were coarsened, produced slightly better results than RC-x, where the streamwise resolution was intact. This indicates that too large streamwise-spanwise cell aspect ratios should be avoided when coarsening the mesh for wall-modeling.

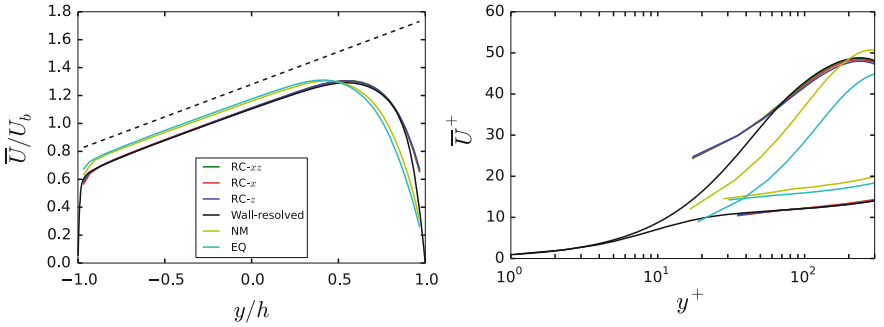

Fig. 3 Mean velocity profiles (*left*) in outer layer scaling (*right*) in wall units

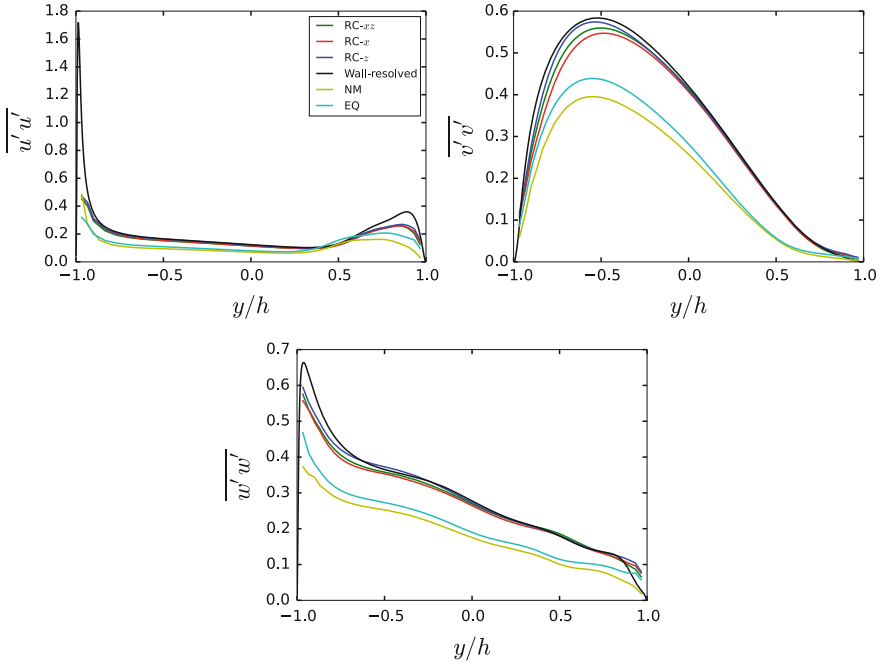

Fig. 4 Mean Reynolds stresses

5 Conclusions

In this paper, the problematic of wall-modeling for cases with system rotation has been addressed. The results first indicate that rotation needs to be accounted for in the framework of wall-modeling. Indeed, for a spanwise rotating plane channel, the standard approach fails to reproduce the rotation effect on the shear stresses, both on the stable and unstable sides.

A simple correction to the consitutive relation of the eddy viscosity model is thus proposed, and first assessed with a priori testing. Comparisons against wall-resolved results then show that the correction significantly improves the prediction of the wall shear stresses and velocity profiles. It also reduces wall-model layer thickness dependency in the results, which is a practical advantage.

Further work will involve generalization of the correction to complex flows, and an assessment of its behavior for radial turbomachinery applications.

Acknowledgements Authors are grateful for the computational resources that were provided by (i) CNRS on the BlueGene/Q system Turing, through the GENCI-IDRIS grants x20142a7178 and x20152a7178 and (ii) CALMIP on the Eos system through the p1425 allocation.

References

1. Balaras, E., Benocci, C., Piomelli, U.: Two-layer approximate boundary conditions for large eddy simulations. AIAA J. **34**, 1111–1119 (1996)
2. Bodart, J., Larsson, J.: Sensor-based computation of transitional flows using wall-modeled large eddy simulation. In: Center for Turbulence Research Annual Briefs, pp. 229–240 (2012)
3. Bradshaw, P.: The analogy between streamline curvature and buoyancy in turbulent shear flow. J. Fluid Mech. **36**, 177–191 (1969)
4. Kawai, S., Larsson, J.: Wall-modeling in large eddy simulation: length scales, grid resolution, and accuracy. Phys. Fluids **24**(1), 015105+ (2012)
5. Moreno, Iván B.: Campo, L., Larsson, J., Bodart, J., Helmer, D., Eaton, J.K.: Confinement effects in shock wave/turbulent boundary layer interactions through wall-modelled large-eddy simulations. J. Fluid Mech. **758**, 5–62 (2014)
6. Nickels, T.B., Joubert, P.N.: The mean velocity profile of turbulent boundary layers with system rotation. J. Fluid Mech. **408**, 323–345 (2000)
7. Piomelli, U.: Wall-layer models for large-eddy simulations. Prog. Aerosp. Sci. **44**(6), 437–446 (2008)
8. Spalart, P.R.: Detached-eddy simulation. Annu. Rev. Fluid Mech. **41**(1), 181–202 (2009)
9. Tritton, D.J.: Stabilization and destabilization of turbulent shear flow in a rotating fluid. J. Fluid Mech. **241**, 503–523 (1992)
10. Vreman, A.W.: An eddy-viscosity subgrid-scale model for turbulent shear flow: algebraic theory and applications. Phys. Fluids **16**(10), 3670–3681 (2004)

Part VI
Industrial Applications

Hybrid LES of a High Pressure Turbine Nozzle/Blade Interaction

J.E. Kopriva, G.M. Laskowski and M.R.H. Sheikhi

1 Introduction

Turbulence plays an important role in the flow physics through the high pressure turbine (HPT), yet its evolution through the stage is still poorly understood. Furthermore, achieving high values, on the order of 10–20%, can be both challenging and costly in an experimental facility. Numerous experimental efforts have been undertaken to mimic the turbulence levels exiting a combustor. Barringer et al. [1] achieved intensity of 18% and non-dimensional integral length scale of 0.11 with a combustor simulator and large jets.

The impact of turbulence levels on nozzle flow physics has received renewed attention recently. Arts and Rouvroit [2] conducted a detailed study of an uncooled, transonic nozzle at exit Reynolds numbers for $5 \times 10^5 - 2 \times 10^6$; exit Mach numbers of 0.7–1.12 for turbulence intensities of 1, 4 and 6%. The wall heat transfer measurements clearly demonstrated the free-stream condition impact on boundary layer (BL) state (laminar, transitional, and turbulent). On the same geometry, LES was preformed by Bhaskaran [3] then Morata et al. [4] demonstrating predictive capability of heat transfer coefficient (HTC). In a similar study, Laskowski et al. [5] showed improved metal temperature predictions compared to measurements on the suction side surface for a conjugate heat transfer analysis by including a transition model.

J.E. Kopriva (✉) · G.M. Laskowski (✉)
Thermal System Design, GE Aviation, Lynn, MA 01905, USA
e-mail: james.kopriva@ge.com

G.M. Laskowski
e-mail: laskowsk@ge.com

M.R.H. Sheikhi (✉)
Department of Mechanical and Industrial Engineering, Northeastern University, Boston, MA 02115, USA
e-mail: sheikhi@me.com

D.G.E. Grigoriadis et al. (eds.), *Direct and Large-Eddy Simulation X*,
ERCOFTAC Series 24, https://doi.org/10.1007/978-3-319-63212-4_34

In general, the impact of turbulence has a pronounced effect on it's BL development and resulting heat transfer. Furthermore, it is well documented that the BL plays an important role in downstream wake mixing [6]. Rehder [7] demonstrated that the contribution of loss due to the BL represented up to 50% of the overall loss for a trail-edge cooled transonic nozzle. Clearly free stream turbulence impacts BL development which, in turn, impacts downstream wake mixing.

The effect of the upstream nozzle wake on blade heat transfer was studied by Ou [8]. An upstream wake generator was used to generate the wakes and in general had a stronger impact on suction side HTC than on pressure side HTC. Fully coupled HPT nozzle/blade interaction studies at engine relevant Mach and Reynolds numbers are challenging and costly. However, they prove very insightful. Didier et al. [9] conducted an experimental evaluation of an HPT nozzle/rotor interaction at realistic engine conditions. They found that leading edge heat transfer was significantly higher than a stationary blade subjected to high values of isotropic turbulence due to periodic fluctuations of shocks and wakes. As with the nozzle, turbulence and unsteadiness play an important role in the development of the BL and downstream wake formation. Recently, Wang et al. [10] reported a LES result for an HPT nozzle/blade sliding mesh simulation. The analysis was for an entire nozzle/blade including endwall and tip effects utilizing unstructured grids and wall-functions. Wang et al. [10] acknowledge further work is required on near wall modeling and grid resolution, but their analysis demonstrates the feasibility of conducting such simulations.

2 Approach

The current study presents the first set of systematic computational studies to understand the impact of turbulence on an uncooled HPT nozzle and downstream blade. Doing so will provide a much better understanding of stage mixing losses and wall heat transfer which, in turn, can allow for improved engine performance. The current study will explore both LES and hybrid LES methods focused on the following objectives:

- Impact of turbulence on surface heat transfer and wake formation in absence of downstream blade interaction (Sect. 4).
- Blade wall heat transfer in the presences of an upstream nozzle wake (Sect. 5).

CFD predictions of surface heat transfer and wake mixing are presented first for no inlet turbulence in Sect. 4. The inlet turbulence is increased to 6% to then show the impact of BL transition on surface heat transfer. Upstream bars are included in the domain as seen in Fig. 1a, matching the experimental setup, to generate elevated inlet turbulence and matching decay rate. The local bar mesh is shown in Fig. 1b. Further detail of the setup and inlet conditions for the HPT nozzle only cases are discussed in the next section.The numerical approach is grounded to experimental measurements of Arts and Rouvroit [2] before including the interaction of the downstream blade.

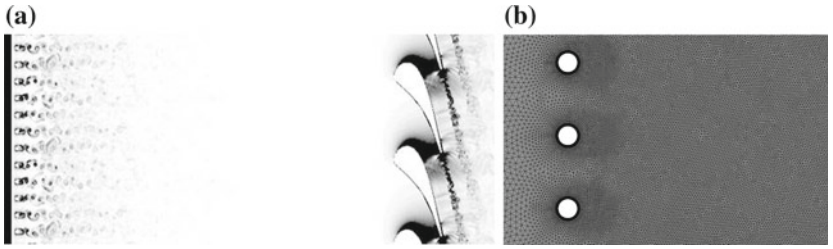

Fig. 1 **a** HPT Nozzle domain including upstream bars for turbulence generation. **b** Zoomed in mesh for upstream bars

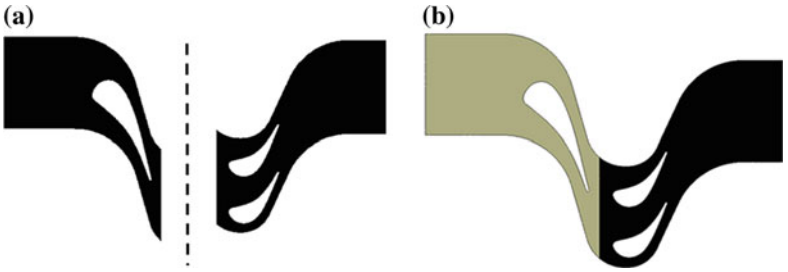

Fig. 2 **a** Uncoupled geometry **b** Coupled geometry.

Section 5 presents the impact of nozzle/blade interaction on blade surface heat transfer. The downstream blade has been designed for this study to be coupled with the upstream uncooled nozzle of Arts and Rouvroit [2]. A detailed description of the design and blade coordinates are provided by Kopriva et al. [11]. The computational domain is held to a pitchline section that includes no centrifugal forces (linear sliding-mesh). The stage geometry is intended to study the fundamental nozzle/blade interaction in a computationally cost efficient manner. Blade/nozzle count of 2:1 is designed to maintain computational periodic boundary conditions for the coupled problem. Representation of the uncoupled and coupled geometry can be found in Fig. 2a, b.

Computational studies are performed using ANSYS Fluent v15.0 using both the WALE (Wale Adapted Local Eddy) model and IDDES (Improved Delayed Detached Eddy Simulation). In order to address BL development, IDDES-T (IDDES with SST including $\gamma - Re_\theta$ transition model) is compared to the standard IDDES with SST model. These hybrid models are appealing due to their reduced computational cost as scale resolve models become more practical for HPT design.

Given the complexity of typical turbine designs, the study focuses on (1) a robust commercial solver predictive capability using scale resolved methods and (2) unstructured meshing. Simulations are preformed at engine scaled conditions requiring a compressible solver. The WALE model uses bounded central differencing in space and bounded 2nd order implicit in time. IDDES switch to 2nd order upwind for RANS turbulent transport equations. Additional details are provided by Kopriva et al. [11].

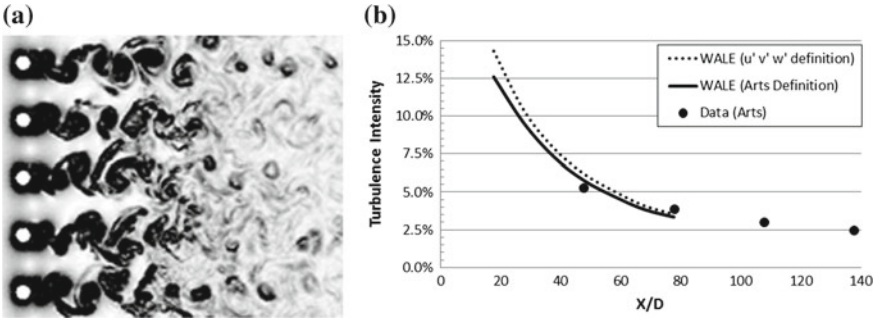

Fig. 3 **a** Numerical Schlieren of upstream bar's generated turbulence for case MUR235 **b** LES compared to measured turbulence level and decay [12]

3 Computational Study

The uncooled HPT nozzle numerical predictions are compared to measurements of Arts and Rouvroit [2] before moving to the coupled blade geometry. This is done to ground the approach to measurement before moving to the expanded computational study. The cases selected for comparison are:

- Case MUR129 with inlet TI 0%, RE=1.16x10^6, and exit Mach=0.84.
- Case MUR235 with inlet TI=6.0%, RE=1.17x10^6, and exit Mach=0.93.

RE and exit Mach are based on exit conditions and airfoil chord. Nozzle surface HTC and downstream total pressure wake profile were measured for case MUR129. Case MUR235 is unique due to the elevated level of turbulence generated by upstream bars shown in Fig. 3a. These bars are included and resolved in the computational domain. Excellent agreement between the LES resolved turbulence and measurement is shown in Fig. 3b. The experimental turbulent kinetic energy is defined $K = \frac{1}{2}((\overline{u'})^2 + 2 * 0.75(\overline{u'})^2)$, where only the streamwise fluctuating component was measured [12]. LES results are presented matching the experimental and conventional definition ($K = \frac{1}{2}((\overline{u'})^2 + (\overline{v'})^2 + (\overline{w'})^2)$). Agreement in turbulence decay rate and level, provides confidence that the proper characteristics are being passed to the downstream nozzle.

4 Uncoupled Nozzle Results

Nozzle surface HTC are presented for WALE, IDDES, and IDDES-T models and compared to measurements for case MUR129 (Fig. 4a) and case MUR235 (Fig. 4b). HTC measurements for MUR129, show no transitional BL behavior resulting in a laminar surface heat transfer over the majority of airfoil. Only at the very trail-edge does the unsteady wake shedding impact the measured HTC. This highlights the

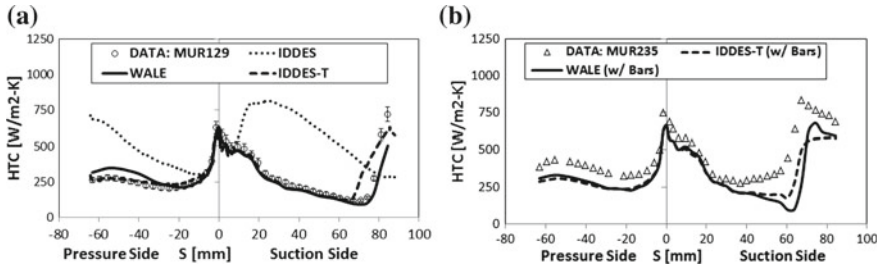

Fig. 4 **a** MUR129 HTC predictions **b** MUR235 HTC predictions

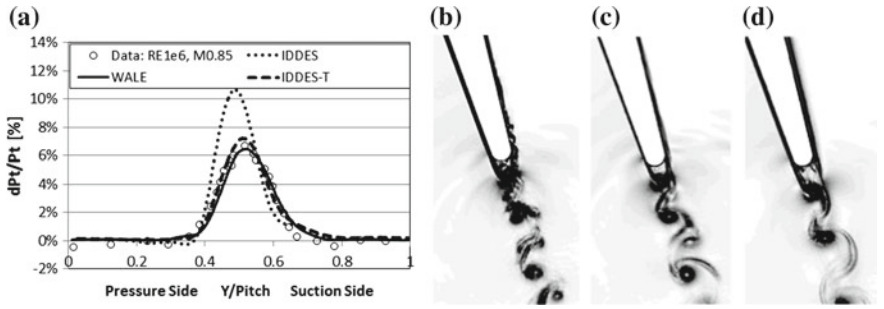

Fig. 5 **a** Prediction of wake total pressure wake profile normalized to inlet total pressure **b** WALE **c** IDDES-T **d** IDDES

importance of transition modeling. By not accounting for transitional BL behavior with a hybrid LES approach, HTC will be significantly over-predicted.

Figure 4b shows under prediction of HTC for both WALE and IDDES-T models. Similar under-prediction of transition and HTC was found by Bhaskaran [3] using a structure mesh and low dissipative 6th order LES code. At Re = 1.0×10^6 and above, Arts showed significant sensitivity of the transition point between TI of 4 and 6%. Both the current study and Bhaskaran [3] are in excellent agreement with the case at TI = 4% (not shown). Influence of turbulent length scale and surface roughness may be possible contributions to the variation from measurement.

Figure 5a shows total pressure wake profile predictions of WALE, IDDES, and IDDES-T for case MUR129. The profile measurement is located $X/C_{ax} = 43\%$ downstream of the nozzle trail-edge, where X is the axial distance and C_{ax} is the axial chord. Excellent agreement is found for both the WALE and IDDES-T. This can be explained by the correct prediction of BL state at the trail-edge of the nozzle for the two modeling approaches. The IDDES-T model results in similar separation zone and wake formation to the WALE model as shown in Fig. 5b, c and d.

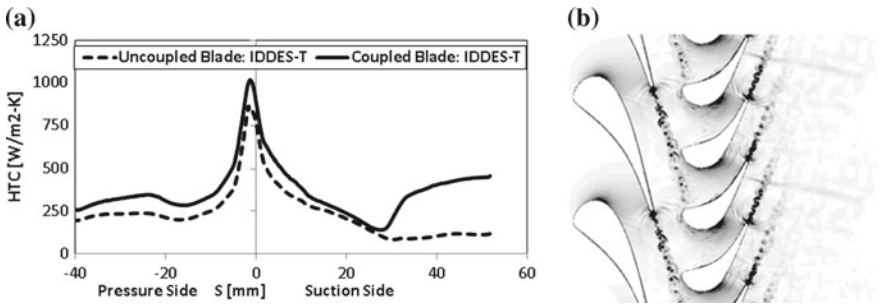

Fig. 6 **a** Coupled & uncoupled blade HTC predictions **b** IDDES-T Numerical Schlieren of coupled nozzle/blade

5 Uncoupled Versus Coupled Blade Results

The coupled and uncoupled downstream blade's BL development impact on wall heat transfer is presented in Fig. 6a and b. HTC is found to increase over the entire blade for the coupled case due to the impact of the nozzle wake consistent studies of Didier et al. [9]. The deterministic passing wake induces transition on the suction side of the downstream blade showing the importance of the nozzle and blade interaction. The uncoupled blade applies no inlet turbulence to show the result of ignoring inlet turbulence and deterministic unsteadiness.

References

1. Barringer, M.D., Richard, O.T., Walter, J.P., Stitzel, S.M., Thole, K.A.: Flowfield simulatios of a gas turbine combustor. J. Turbomach. **124**, 508–516 (2002)
2. Arts, T., Rouvroit, M.L.: Aero-thermal performance of a two-dimensional highly loaded transonic turbine nozzle guide vane: a test case for inviscid and viscous flow computations. J. Turbomach. **114**, (1992)
3. Bhaskaran, R.: Large eddy simulation of high pressure turbine cascasde. Ph.D. Dissertation, Stanford University (2010)
4. Morata, E.C., Gourdain, N., Duchaine, F., Gicquel, Y.: Effects of free-stream turbulence on high pressure turbine heat transfer predicted by structured and unstructured LES. Int. J. Heat Mass Transf. **55**, 5754–5768 (2012)
5. Laskowski, G.M., Ledezma, G., Tolpadi, A., Ostrowski, M.: CFD simulations and conjugate heat transfer analysis of a high pressure turbine vane utilizing different cooling configurations. ISROMAC-12. Honolulu, HI (2008)
6. Mee, D.J., Baines, N.C., Oldfield, M.L.G.: An examination of the contributions to loss on a transonic turbine blade in a cascade, ASME Paper No 90-GT-264 (1990)
7. Rehder, H.J.: Investigation of trailing edge cooling concepts in a high pressure turbine cascade - aerodynamic experiments and loss analysis. J. Turbomach. **134**, (2012)
8. Ou, S., Han, J.C.: Unsteady wake effect on film effectiveness and heat transfer coeffiecient from a turbine blade with one row of air and Co_2 film injection. J. Turbomach. (1994)
9. Didier, F., Denos, R., Arts, T.: Unsteady rotor heat transfer in a transonic turbine stage. J. Turbomach. **124**, (1994)

10. Wang, G., Papadogiannis, D., Duchaine, F., Gourdain, N., Gicquel, L.: Towards massively parallel large eddy simulation of turbine stages, GT2013-94852 (2013)
11. Kopriva, J.E., Laskowski, G.M., Sheikhi, M.R.H.: Computational assessment of inlet turbulence on boundary layer development and momentum/thermal wakes for high pressure turbine nozzle and blade, IMECE2014-38620 (2014)
12. Arts, T.: Private communication (2014)

Turbulent Fluid Flow over Aerodynamically Rough Surfaces Using Direct Numerical Simulations

M. Thakkar, A. Busse and N.D. Sandham

Abstract Incompressible turbulent fluid flow in aerodynamically rough channels is investigated using direct numerical simulations. A comprehensive database of simulation data for rough surfaces with different topographical properties has been developed for 17 industrially relevant rough surface samples. It includes numerous commonly-seen industrial rough surfaces such as concrete, graphite, carbon-carbon composite and ground, shotblasted and spark-eroded steel. Other surfaces such as cast, filed and gritblasted steel are also studied, along with replicas of ship propeller surfaces eroded by periods of service. The Reynolds number considered is $Re_\tau = 180$, for which the flow is in the transitionally rough regime. A study with variable δ/S_q ratio, while keeping S_q^+ constant, where S_q is the root mean squared roughness height, is conducted for one of the samples with the mean profiles showing convergence for $\delta/S_q >\approx 25$. A Reynolds number dependence study is conducted for two of the samples with Re_τ up to 720 showing a more complete range up to the fully rough flow regime, allowing the equivalent sandgrain roughness height, k_s, to be computed. A correlation based on the frontal and wetted roughness area is found to be superior to the surface skewness in predicting ΔU^+ based on the topographic surface parameters.

1 Introduction

In many boundary layer flows (especially geophysical flows), surface roughness is not the exception but the norm. A wide range of practical applications show the presence of roughness at various scales, including industrial finishing processes such

M. Thakkar (✉) · N.D. Sandham
University of Southampton, Southampton, UK
e-mail: mnt2g11@soton.ac.uk

N.D. Sandham
e-mail: n.sandham@soton.ac.uk

A. Busse
University of Glasgow, Glasgow, UK
e-mail: angela.busse@glasgow.ac.uk

D.G.E. Grigoriadis et al. (eds.), *Direct and Large-Eddy Simulation X*,
ERCOFTAC Series 24, https://doi.org/10.1007/978-3-319-63212-4_35

as grinding and shotblasting [2], industrial heat exchangers, ship propellers and hulls due to marine fouling, plant canopies on the earth's surface and urban flows over cities. The primary effect of roughness is an increase in the surface friction compared to a smooth wall, which is seen as a downward shift in the mean streamwise velocity profile when plotted in wall units. This shift is quantified by the roughness function, ΔU^+. Roughness also causes an increase in the exchange of momentum in the near-wall regions and in the wall heat and mass transfer rates.

Most previous experimental and numerical studies of flows over rough walls have dealt with geometries that were artificially constructed from simple roughness elements, e.g. bars, cubes and spheres, arranged in regular patterns. Such surfaces typically possess a small number of characteristic length scales and their surface properties such as roughness heights and spacing can be easily evaluated. They are also simple to construct for the purpose of experimentation or computational simulations. However, most rough surfaces encountered in practice are irregular in nature and have features on a large number of length scales and a complex topography. They bear limited resemblance to the above-mentioned regular rough surfaces and it is not guaranteed that ideas developed from studies over regular rough surfaces can be applied to irregular rough surfaces.

The overall aim of this research is to understand the fluid flow characteristics over irregular and more realistic roughness, as opposed to the regular and idealised rough surface geometries studied extensively in the past. This is done by studying incompressible turbulent flow through rough channels using direct numerical simulations (DNS).

2 Methodology

A three step methodology [1] is used to conduct the rough wall channel flow simulations. In the first step, surface data is acquired from the physical sample by using a variable focus microscope. The second step involves data pre-processing where the raw data is filtered in Fourier space in order to eliminate any measurement noise. Filtering also removes the smallest roughness length scales (which can be regarded as aerodynamically irrelevant [6]) and provides a periodic tile required for the DNS. The final step involves using the periodic tile as a no-slip boundary condition in the DNS of turbulent channel flow. The study is conducted at $Re_\tau = u_\tau \delta/\nu = 180$, where u_τ is the friction velocity, δ is the channel half-height and ν is the kinematic viscosity. The rough surface is resolved using an immersed boundary method that is an iterative modification of [9]; details of the method are given in [1]. The mean surface height is set as the mean reference plane, $z = 0$ (where z is the wall-normal direction). The distance between the bottom and top mean reference planes is 2δ. Uniform grid spacing is used in x and y taking the minimum of two criteria: (a) $\Delta x^+ = \Delta y^+ \approx 5$ and (b) $\Delta x = \Delta y \approx \lambda_{min}/12$, where λ_{min} is the smallest wavelength of the rough surface after filtering. A stretched grid is used in the wall-normal direction with $\Delta z^+_{min} < 1$ close to the rough walls and $\Delta z^+_{max} \leq 5$ toward the channel centre. All rough surfaces

are scaled to the same physical roughness height, defined by the mean-peak-to-valley height, $S_{z,5\times5}$,[1] such that $\delta/S_{z,5\times5} = 6$ (and $20 < \delta/S_q < 31$). The roughness height, k is defined by $S_{z,5\times5}$ unless stated otherwise.

3 Results

The mean profiles for $Re_\tau = 180$ for all surfaces are shown in Figs. 1 and 2. Due to the large number of surfaces, these results have been spread out over two plots; Fig. 1 shows profiles from previous studies [2] and Fig. 2 shows additional profiles from the present study. All surfaces have a clear effect on the mean flow as can be seen from the downward shift, ΔU^+, in the mean velocity profile, compared to a smooth wall. ΔU^+ is generally measured as the vertical shift of the log region of the mean velocity profile but since the Reynolds number in this study is low, no clearly defined log region is present. Hence ΔU^+ is obtained by subtracting the centreline velocity for a given sample from the corresponding smooth-wall centreline velocity [3]. Table 1 displays the ΔU^+ values for all surfaces. There is a wide range, from 1.3 to 5, despite all the surfaces being scaled to the same roughness height. This is a clear indication that the roughness function depends not only on the roughness height for a given surface but also on the detailed roughness topography.

It is commonly assumed that universal behaviour emerges only when the roughness height is considerably smaller than the macroscopic length scale of the flow, i.e. for high δ/k [5]. In order to check the sensitivity of the results to δ/k, a study is conducted for the gritblasted sample. Here the roughness height is chosen as the root mean squared roughness height, S_q. The ratio δ/S_q is varied but the roughness height Reynolds number, $S_q^+ = S_q u_\tau/\nu$, is kept constant for all cases. For instance, $S_q^+ \approx 6.44$ at $Re_\tau = 180$, for which $\delta/S_q \approx 28$. Other cases include $Re_\tau = 120$ and 360, with corresponding $\delta/S_q \approx 19$ and 56 respectively, obtained by

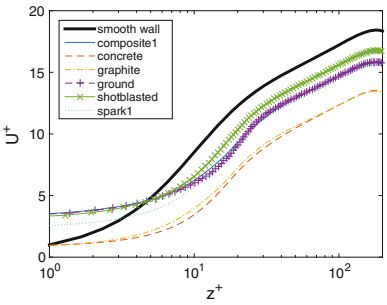

Fig. 1 Mean profiles for $Re_\tau = 180$ (6 surfaces)

[1] To compute $S_{z,5\times5}$, a surface is divided into 5×5 sections of equal size. For each section, the maximum and minimum surface height is found. The mean-peak-to-valley height is the difference between the mean of the maxima and the mean of the minima.

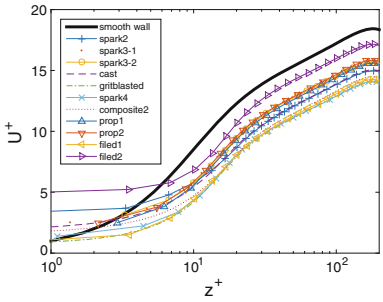

Fig. 2 Mean profiles for $Re_\tau = 180$ (11 surfaces)

Table 1 ΔU^+ for all samples

	Composite1	Concrete	Graphite	Ground	Shotblasted	Spark1	Spark2	Spark3–1	Spark3–2
ΔU^+	2.7	4.9	5.0	2.6	1.7	2.8	3.5	2.7	2.8
	Cast	Gritblasted	Spark4	Composite2	Prop1	Prop2	Filed1	Filed2	
ΔU^+	3.4	4.4	4.4	3.9	2.8	2.6	4.2	1.3	

scaling the $Re_\tau = 180$ case. Due to the small roughness height in the $Re_\tau = 360$ case, the domain size may be too small for proper flow development. Hence this sample was replicated in x and y to give a tiled sample with a larger domain size. Both cases were simulated. The need for this replication motivated the choice of S_q instead of $S_{z,5\times5}$ for the roughness height as the latter does not scale by exactly the same factor as the irregular surface. As seen from Fig. 3, the mean profiles for all cases are similar. It can also be seen from Fig. 4, which shows ΔU^+ against δ/S_q, that convergence for ΔU^+ is obtained for $\delta/S_q >\approx 25$. The dashed lines in this figure represent 5% tolerance bands around the $Re_\tau = 180$ case.

Figure 5 shows the dependence of ΔU^+ on Re_τ for two surfaces, graphite and gritblasted. It also shows Colebrook's universal interpolation formula [5], given by $\Delta U^+(k_s^+) = \kappa^{-1}\log(0.3k_s^+ + 1)$, and the fully rough asymptote line, given by $\Delta U^+(k_s^+) = \kappa^{-1}\log(0.3k_s^+)$, where k_s is the equivalent sand grain roughness height and $\kappa \approx 0.41$ is the von Kármán constant. The range of $Re_\tau = 90, 120, 180, 240, 360, 540, 720$ gives corresponding $k^+ = 15, 20, 30, 40, 60, 90, 120$ (with $\delta/k = 6$ for all Re_τ) respectively. This curve is expected to asymptote to a straight line at high k^+ corresponding to the fully rough regime, and allowing the definition of an equivalent sand grain roughness height, k_s^+, as was also noted by Yuan & Piomelli [10]. Thus in Fig. 6, points for graphite have been shifted horizontally by 4/3 such that points in the fully rough regime fall on the asymptote. This gives $k_s^+ \approx (4/3)k^+$ for the graphite surface and $k_s^+ \approx k^+$ for the gritblasted surface. For $k^+ <\approx 30$, the points depart from the expected trend probably due to low Reynolds number effects.

A number of numerical models that relate ΔU^+ to the surface topographical properties of three-dimensional rough surfaces have been proposed in the past [4]. The generalised Sigal-Danberg parameter, Λ_s [7], as modified by van Rij et al. [8] is a geometrical parameter that captures information about the roughness shape as well as direction with respect to the mean flow. It is defined as $\Lambda_s = \left(S/S_f\right)\left(S_f/S_s\right)^{-1.6}$,

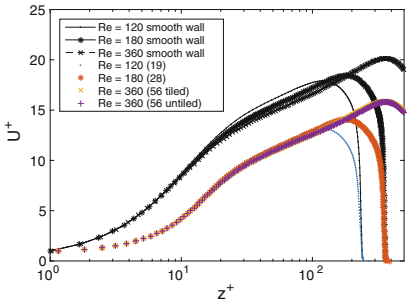

Fig. 3 Mean profiles for the δ/S_q study (gritblasted surface). Numbers in brackets in the legend indicate δ/S_q values

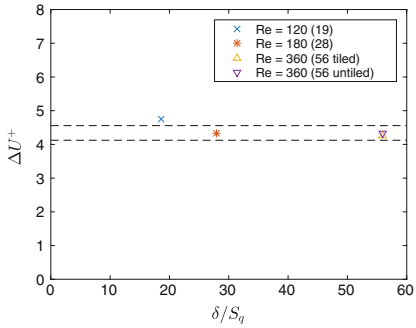

Fig. 4 ΔU^+ against δ/S_q (gritblasted surface). Numbers in brackets in the legend indicate δ/S_q values

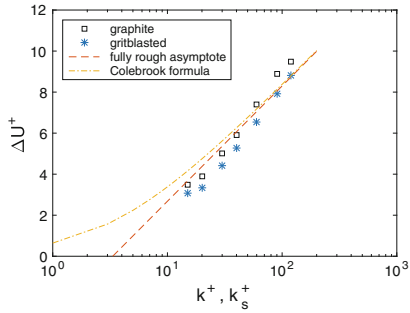

Fig. 5 Re_τ dependence study

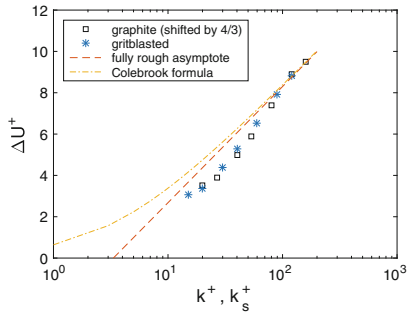

Fig. 6 Re_τ dependence study. Graphite sample results shifted horizontally by applying a factor of 4/3

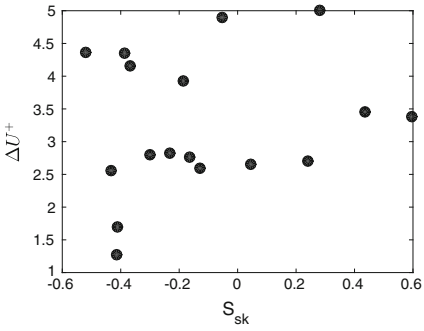

Fig. 7 ΔU^+ against surface skewness, S_{sk}. Symbols indicate different rough surfaces

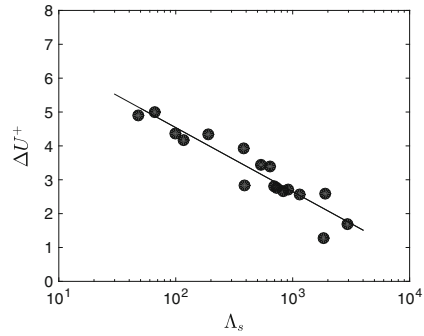

Fig. 8 ΔU^+ against Sigal-Danberg parameter, Λ_s. Symbols indicate different rough surfaces

where S is the planform area of the corresponding smooth surface, S_f is the total projected frontal area of all the roughness elements and S_s is the total area of all roughness elements wetted by the flow. S/S_f is a roughness density parameter and S_f/S_s is a roughness shape parameter. As shown in Figs. 7 and 8, surface skewness, S_{sk} fails to correlate the current data whereas ΔU^+ decreases with increasing Λ_s. The best fit is given by $\Delta U^+ = \log(\Lambda_s)^{-1.89} + 8.32$.

4 Conclusions

Incompressible turbulent channel flow over a large variety of industrially-relevant rough surfaces has been studied using direct numerical simulations. Mean velocity profiles for the surfaces show significant variation in terms of ΔU^+, despite all surfaces being scaled to the same physical roughness height, clearly indicating that the roughness effect depends on the detailed surface topography as well as the roughness height. A sensitivity study on δ/S_q, while keeping S_q^+ constant, for one sample showed that similar mean profiles are obtained for the cases considered and convergence for ΔU^+ is obtained for $\delta/S_q >\approx 25$. Simulations over a wide range of Re_τ from the transitionally rough regime up to the fully rough regime for two of

the samples allowed the calculation of an equivalent sand grain roughness height, k_s. The Sigal-Danberg parameter, Λ_s was found to correlate much better with ΔU^+ than the surface skewness, S_{sk}.

References

1. Busse, A., Lützner, M., Sandham, N.D.: Direct numerical simulation of turbulent flow over a rough surface based on a surface scan. Comput. Fluids. **116**, 129–147 (2015)
2. Busse, A., Tyson, C.J., Sandham, N.D., Lützner, M.: DNS of turbulent channel flow over engineering rough surfaces. In: Eight international symposium on turbulence and shear flow phenomena (TSFP-8), August 28–30, Poitiers, France (2013)
3. Busse, A., Sandham, N.D.: Parametric forcing approach to rough-wall turbulent channel flow. J. Fluid Mech. **712**, 169–202 (2012)
4. Flack, K.A. & Schultz, M.P. Review of hydraulic roughness scales in the fully rough regime. J. Fluids Eng. **132**: 041203-1–041203-10 (2010)
5. Jiménez, J.: Turbulent flows over rough walls. Annu. Rev. Fluid Mech. **36**, 173–196 (2004)
6. Mejia-Alvarez, R., Christensen, K.T.: Low-order representations of irregular surface roughness and their impact on a turbulent boundary layer. Phys. Fluids **22**, 015106 (2010)
7. Sigal, A., Danberg, J.E. Analysis of turbulent boundary-layer over rough surfaces with application to projectile aerodynamics. Technical Report BRL-TR-2977. Army ballistic research lab, Aberdeen proving grounds, MD (1988)
8. van Rij, J.A., Belnap, B.J., Ligrani, P.M.: Analysis and experiments on three-dimensional irregular surface roughness. J. Fluids Eng. **124**(3), 671–677 (2002)
9. Yang, J., Balaras, E.: An embedded-boundary formulation for large-eddy simulation of turbulent flows interacting with moving boundaries. J. Comput. Phys. **215**, 12–40 (2006)
10. Yuan, J., Piomelli, U.: Estimation and prediction of the roughness function on realistic surfaces. J. Turbul. **15**(6), 350–365 (2014)

Wall Modeled Large Eddy Simulation of the VFE-2 Delta Wing

C. Zwerger, S. Hickel, C. Breitsamter and N. Adams

1 Introduction

Delta wing configurations are commonly employed for high agility supersonic aircraft and aerodynamic devices such as vortex generators, and have thus been a focus of extensive investigations over the past decades. A large data base of experimental and computational investigations is provided by the international vortex flow experiments VFE-1 and VFE-2, which constitute major collaborative efforts regarding these flows [4, 12]. Two aspects of the flow field are of particular interest: (1) leading edge bluntness effects on the primary vortex separation [14], and (2) vortex breakdown above the wing and its control [15]. The present study addresses both aspects.

With regard to aspect (1), the VFE-2 delta wing [2] with sharp leading edge (SLE) and medium radius round leading edge (MRLE) are investigated. The latter configuration is computationally more challenging than the sharp leading edge, since separation occurs closely behind the leading edge and is not geometrically fixed at the leading edge [14]. Numerical results are analyzed for three angles of attack α leading to different overall flow characteristics. For the MRLE and $\alpha = 13°$, there is a partially developed primary vortex, starting approximately at one third chord length. For $\alpha = 18°$, the primary vortex is fully developed for both leading edge geometries. For $\alpha = 23°$, the primary vortex breaks down above the wing for both SLE and MRLE, the breakdown positions differ depending on the leading edge geometry, however.

C. Zwerger (✉) · S. Hickel · C. Breitsamter · N. Adams
Technische Universität München, Institute of Aerodynamics and Fluid Mechanics,
Boltzmannstr. 15, 85748 Garching, Germany
e-mail: christian.zwerger@tum.de

S. Hickel
Technische Universiteit Delft, Faculty of Aerospace Engineering,
Kluyverweg 2, 2629, HT Delft, The Netherlands

D.G.E. Grigoriadis et al. (eds.), *Direct and Large-Eddy Simulation X*,
ERCOFTAC Series 24, https://doi.org/10.1007/978-3-319-63212-4_36

With regard to aspect (2), two possible flow control mechanisms are considered for the SLE and $\alpha = 28°$: active flow control by oscillating control surfaces at the leading edges in the front part of the wing, and passive flow control by a geometric modification of the wing, leading to the injection of fluid from the pressure side.

RANS approaches, which are commonly used in industry, have shown only moderate success in investigations of the massively separated flow around a delta wing, notably regarding the correct prediction of vortex breakdown at high angles of attack [3, 5]. LES seems to be a more suitable approach for such flows, but is still prohibitively expensive when considering high-Reynolds number wall bounded flows. Therefore, we use wall modeled implicit large eddy simulation (WMLES), which relaxes the grid resolution requirements of LES close to walls. The influence of the wall model and different refinement levels of the grid are investigated.

For comparison we use experimental data available from measurements carried out at the Technische Universität München [6, 7, 13].

2 Numerical Approach and Setup

The implicit subgrid-scale model employed is based on the adaptive local deconvolution method (ALDM) [9, 10], and the wall model is based on the thin boundary layer equations (TBLE) [1]. For comparison we also performed LES with a simple no-slip boundary condition. The wing geometry [2] with root chord length $c_r = 1$ is mapped onto the Cartesian grid via a conservative immersed-interface method (CIIM) [8]. The computational domain is a cubic box with dimensions $-4 < x/c_r < 6$, $-5 < y/c_r < 5$, and $-5 < z/c_r < 5$. The wing tip is located at the point of origin. At the inflow, a uniform veloctiy profile is prescribed, and at the outflow, a static pressure of $P_{stat} = 1/(Ma^2 \cdot \gamma)$ is imposed, where Ma and γ denote Mach number and heat capacity ratio, respectively. Effects of wind tunnel walls are not simulated, and a slip condition is imposed at the remaining boundaries. The grids have been generated using an adaptive mesh refinement (AMR) technique. The cell size has been chosen such that the wall model coupling position lies within the logartihmic layer. Hereafter, results will be presented for two grids, denoted by Grid 1 and Grid 2. They are identical apart from the near wall region close to the apex, where Grid 2 is further refined. The grids had up to $74.2 \cdot 10^6$ cells. All investigations have been conducted for a Reynolds number based on the mean aerodynamic chord $(2/3 \cdot c_r)$ of $Re = 2.0 \cdot 10^6$ and a Mach number of $Ma = 0.14$. Hereafter, if not otherwise specified, all quantities are nondimensionalized by free stream velocity U_∞ and root chord length c_r.

3 Results

With respect to leading edge bluntness effects, the numerical simulations predict the main flow phenomena qualitatively correctly for both leading edge geometries and for all angles of attack considered, see Fig. 1, leading to the characteristic pressure coefficient distribution with a suction peak below the axis of the primary vortex on the upper wing surface, see Fig. 2. However, there is no secondary vortex in any of the simulations due to the insufficient grid resolution, which does not allow for the prediction of such a small scale flow feature [11]. Quantitatively, the results show reasonable to good agreement with experimental measurements of steady (see Fig. 3) and unsteady surface pressures, velocity distributions, and vortex breakdown position and frequency. As expected, the agreement is overall better for the SLE due to the geometrically fixed separation at the leading edge. For the MRLE, the discrepancies between numerical and experimental results are largest in the apex region, where the leading edge crossflow bluntness, defined by the ratio of leading edge radius r_{le} and local half span width b_{loc}, is highest.

With respect to flow control, our numerical results show that oscillating control surfaces have only a minor effect on vortex breakdown, which is in agreement with experimental observations (Fig. 4). In the simulation, the vortex breakdown position was shifted from $x/c_r = 0.73$ to $x/c_r = 0.75$. Injecting fluid via the suggested geometric modification, however, significantly delays vortex breakdown. For this approach, the vortex breakdown position was shifted from $x/c_r = 0.73$ to

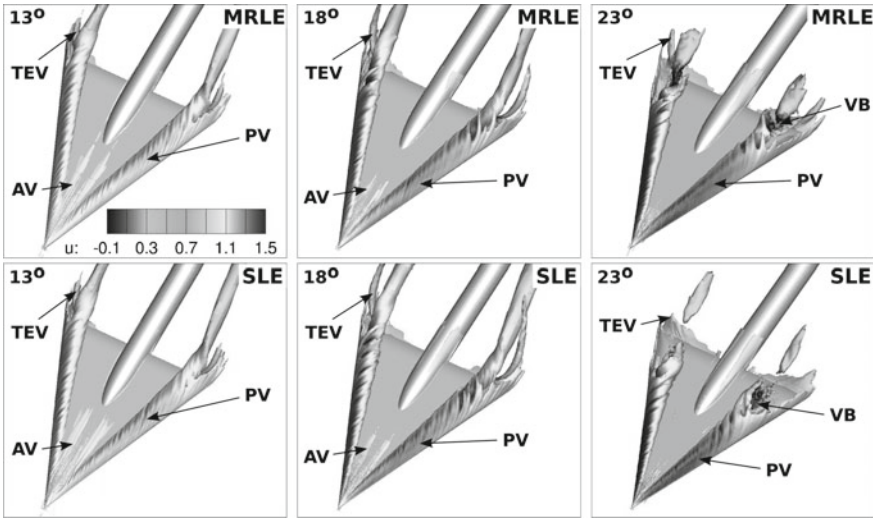

Fig. 1 Main flow characteristics at angles of attack of 13° (*left*), 18° (*center*), and 23° (*right*), obtained with Grid 1. AV - apex vortex, PV - primary vortex, TEV - trailing edge vortex, VB - vortex breakdown. *Top* and *bottom* row show isosurfaces of streamwise vorticity colored by streamwise velocity for MRLE and SLE, respectively

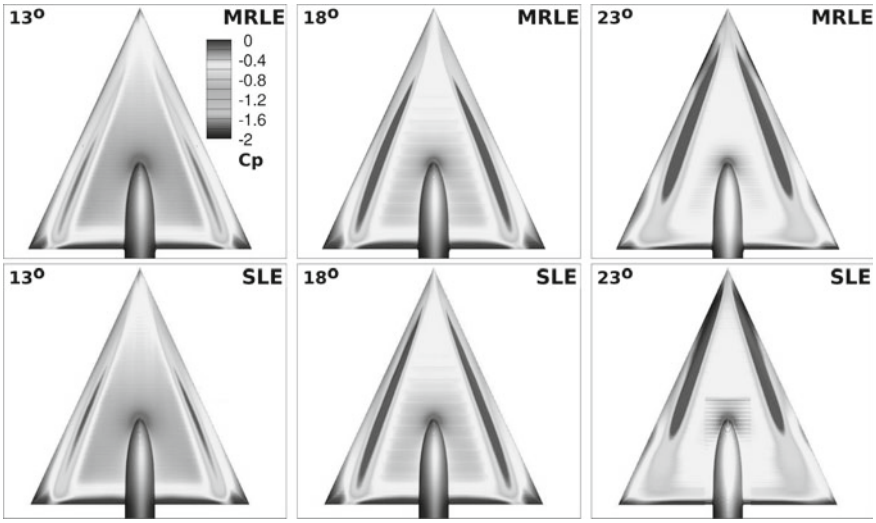

Fig. 2 Main flow characteristics at angles of attack of 13° (*left*), 18° (*center*), and 23° (*right*), obtained with Grid 1. *Top* and *bottom* row show surface pressure coefficient distributions for MRLE and SLE, respectively

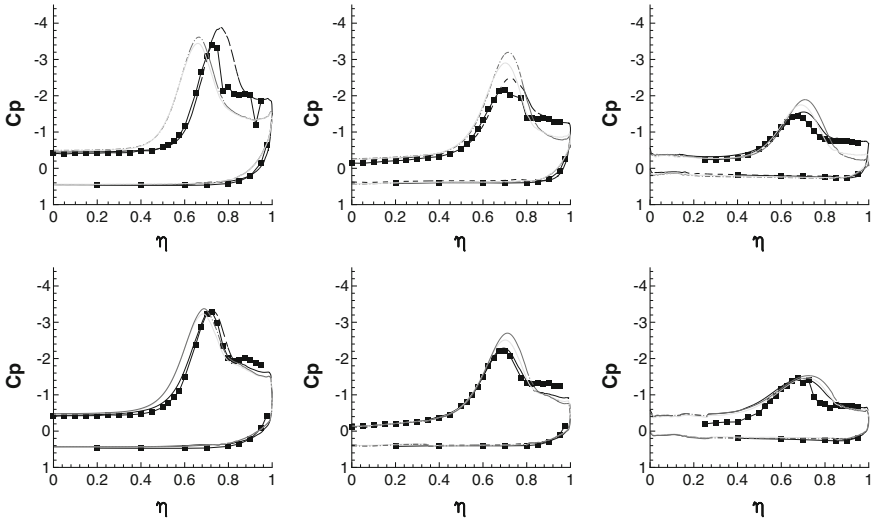

Fig. 3 Surface pressure distribution C_p at cross sections $x/c_r = 0.4, 0.6,$ and 0.8 (from *left* to *right*) for MRLE (*top*) and SLE (*bottom*) and $\alpha = 23°$. Grid 1 with no-slip condition - *dash-dotted*; Grid 1 with TBLE wall model - solid; Grid 2 with no-slip condition - *dashed*; Experiments [6, 7] - solid with *squares*. η denotes normalized local half span width

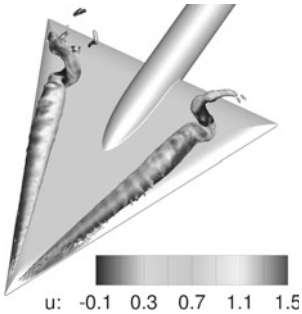

Fig. 4 Characteristic helical form of vortex breakdown. Rotation of vortex axis is opposite to rotation of primary vortex [12]. Figure shows isosurface of pressure coefficient ($C_p = -2$) colored by streamwise velocity for SLE and $\alpha = 23°$

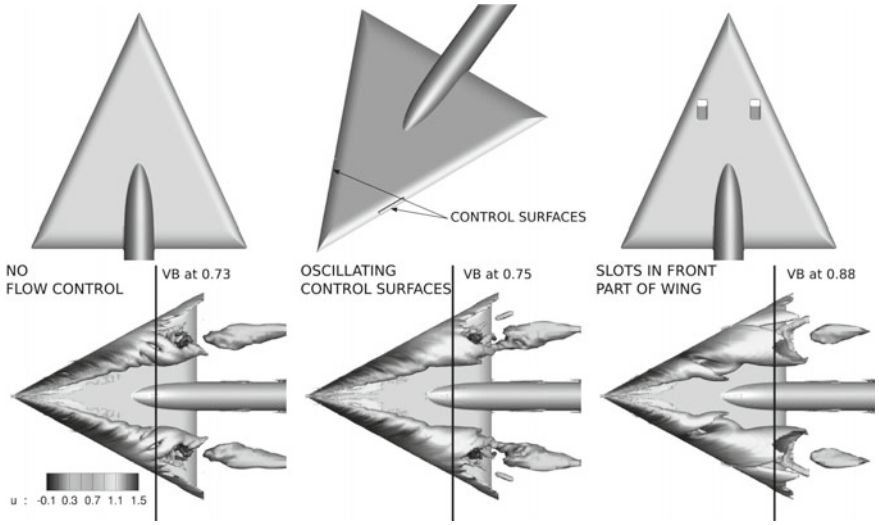

Fig. 5 No flow control (*left*), control surfaces in the front part of the wing (*center*), and slots in the front part of the wing (*right*). *Bottom* row figures show isosurface of streamwise vorticity colored by streamwise velocity. Vortex breakdown (VB) position indicated by *black line*

$x/c_r = 0.88$. Figure 5 shows the baseline configuration with no flow control (left), the configuration with oscillating control surfaces (center), and the configuration with a geometric modification (right), and the respective effects on the vortex breakdown position (bottom row).

4 Conclusion

We used wall modeled LES to investigate the flow field around the VFE-2 delta wing, focusing on (1) leading-edge bluntness effects and (2) vortex breakdown and its control.

With regard to (1) leading edge bluntness effects, our three main conclusions are: First, the main flow characteristics are predicted qualitatively correctly for all angles of attack and both SLE and MRLE, apart from the secondary vortex, which is not predicted due to the insufficient grid resolution. Second, quantitatively, the numerical predictions of velocity distributions, steady and unsteady surface pressures, and position and frequency of the vortex breakdown are overall in reasonable to good agreement with experimental data. Due to the geometrically fixed separation, the agreement is generally better for the SLE. Third, using a TBLE based wall model instead of a simple no-slip boundary condition leads only to a minor improvement of the results. However, refining the grid leads to a much more significant improvement suggesting that the TBLE based wall model contains too many approximations for the complex flow considered.

With regard to (2) vortex breakdown and its control, our two main conclusions are: First, flow control by oscillating control surfaces seems to have a minor impact on the vortex breakdown location for the configuration considered, which confirms experimental observations. Second, geometric modifications leading to the injection of fluid from the pressure side can have an effect resembling active blowing mechanisms and significantly delay vortex breakdown.

References

1. Chen, Z.L., Hickel, S., Devesa, A., Berland, J., Adams, N.A.: Wall modeling for implicit large-eddy simulation and immersed-interface methods. Theor. Comput. Fluid Dyn. **28**, 1–21 (2014)
2. Chu, J., Luckring, J.M.: Experimental surface pressure data obtained on 65° delta wing across reynolds number and mach number ranges. In: NASA technical memorandum 4645, vol. 3 - Medium-Radius Leading Edge (1996)
3. Crivellini, A., D'Alessandro, V., Bassi, F.: High-order discontinuous Galerkin RANS solutions of the incompressible flow over a delta wing. Comput. Fluids **88**, 663–677 (2013)
4. Drougge, G.: The international vortex flow experiment for computer code validation. In: ICAS-Proceedings, Jerusalem (1988)
5. Fritz, W., Cummings, R.M.: Lessons learned from the numerical investigations on the VFE-2 configuration. In: NATO STO, Summary Report of Task Group AVT-113, Chapter 34 (2009)
6. Furman, A., Breitsamter, C.: Experimental Investigations on the VFE-2 Configuration at TU Munich, Germany. In: NATO STO, Summary Report of Task Group AVT-113, Chapter 21 (2009)
7. Furman, A., Breitsamter, C.: Turbulent and unsteady flow characteristics of delta wing vortex systems. Aerosp. Sci. Tech. **24**, 32–44 (2013)
8. Grilli, M., Hickel, S., Hu, X.Y., Adams, N.A.: Conservative immersed boundary method for compressible viscous flows. In: Annual Report 2009 of the Sonderforschungsbereich/Transregio 40 (TRR40), Technische Universität München (2009)

9. Hickel, S., Adams, N.A., Domaradzki, J.A.: An adaptive local deconvolution method for implicit LES. J. Comput. Phys. **213**, 413–436 (2006)
10. Hickel, S., Egerer, C.P., Larsson, J.: Subgrid-scale modeling for implicit Large Eddy Simulation of compressible flows and shock turbulence interaction. Phys. Fluids **26**, 106101 (2014)
11. Hummel, D.: Effects of boundary layer formation on the vortical flow above slender delta wings. In: RTO symposium on enhancement of NATO military flight vehicle performance by management of interacting boundary layer transition and separation, Prague (2004)
12. Hummel, D.: The international vortex flow experiment 2 (VFE-2): objectives and overview. In: NATO STO, summary report of task group AVT-113, Chapter 17 (2009)
13. Kölzsch, A., Breitsamter, C.: Vortex-flow manipulation on a generic delta-wing configuration. J. Aircr. **51**, 1380–1390 (2014)
14. Luckring, J.M.: Initial experiments and analysis of blunt-edge vortex flows. In: NATO STO, summary report of task group AVT-113, Chapter 18 (2009)
15. Mitchell, A., Délery, J.: Research into vortex breakdown control. Prog. Aerosp. Sci. **37**, 385–418 (2001)

An Embedded Flow Simulation Methodology for Flow over Fence Simulations

K. Anupindi and R.D. Sandberg

1 Introduction

In this paper, we report the development of embedding a flow simulation methodology (FSM) [1, 7] region in a global Reynolds-averaged Navier-Stokes (RANS) region and its application to flow over a fence. The open-source computational fluid dynamics software OpenFOAM [8] is used to develop the proposed framework. FSM belongs to the type of unified hybrid RANS/large-eddy simulation (LES) models [2]. As opposed to segregated or embedded hybrid RANS/LES models, unified models are dynamically adaptive and can switch between the considered modelling approaches on a cell-by-cell basis. Unified models rely on numerical instabilities to trigger transition in the LES region of the flow and this sometimes produces poor quality results in cases involving insufficient instabilities. For segregated or embedded approaches, a relatively fine mesh needs to be used in the eddy-resolving regions of the flow field and a coarse mesh can be used in the regions that are modelled using RANS. Usage of a non-conformal mesh at the interface between the two regions makes it easier to generate the required mesh. In order to benefit from this feature as well as to be able to provide sufficient level of synthetic turbulence at the interface, we propose to combine a unified model with an embedding approach, i.e. embed an FSM region inside a global RANS region. As a major portion of the domain is selected *a priori* and solved using RANS on a coarse mesh, it is expected that as this would reduce the turnover time required for such simulations at the same time enable the use of synthetic turbulence generation at the inlet to the FSM region. The paper is

K. Anupindi (✉) · R.D. Sandberg
Faculty of Engineering and the Environment, University of Southampton,
Southampton S017 1BJ, UK
e-mail: K.Anupindi@soton.ac.uk; kamesh.a@gmail.com

R.D. Sandberg
e-mail: R.D.Sandberg@soton.ac.uk

D.G.E. Grigoriadis et al. (eds.), *Direct and Large-Eddy Simulation X*,
ERCOFTAC Series 24, https://doi.org/10.1007/978-3-319-63212-4_37

organised as follows. The numerical method is discussed in Sect. 2 and the results obtained for a spatially developing turbulent channel flow, flow over a vertical fence and a summary are presented in Sect. 3.

2 Numerical Method

Embedding of an FSM region inside a RANS region is implemented in the OpenFOAM solver [8]. It is based on a cell-centered, finite-volume discretisation and specifically the *rhoPimpleFoam* solver is used in the present work to develop the embedding strategy. The governing equations are the unsteady, three-dimensional, compressible Navier-Stokes equations. A schematic of the proposed embedding together with the synthetic turbulence generation at the interface is shown in Fig. 1. As shown in this figure, two separate mesh regions Ω_{RANS} and Ω_{FSM} are used for each of the RANS and the FSM regions respectively and are coupled, using arbitrary mesh interfaces, for flow and turbulence quantities through the interface boundaries Γ_{RANS} and Γ_{FSM}. A digital filter method (DFM) [3] is used to provide synthetic fluctuations at the inflow interface to the FSM region. In the present work, the DFM is modified such that it extracts the mean flow and Reynolds stresses from the upstream RANS region in a fully coupled manner so that the synthetic fluctuations are sensitive to the upstream unsteady effects from the LES region. In the RANS region Menter's $k-\omega$ shear stress transport (SST) turbulence model [4] is used. The same turbulence model is used in the FSM region when it works in the RANS mode. In the present version of FSM the turbulent viscosity is damped using a blending function that produces a continuous distribution between the RANS and a resolving simulation, this can be represented as [1, 6, 7], $\overline{u_i'u_j'} = F.\ \overline{u_i'u_j'}^{RANS}$, where F is the blending function and the super-script RANS denotes the Reynolds-stress tensor calculated from the underlying RANS model used. In the present work we use the modified damping function that was introduced in Weinmann et al. [7] given as follows, $F = min\left[f_\eta f_\Delta f_z, 1\right]$. This modified damping function contains a product of three individual functions f_η, f_Δ and f_z. The first one f_η is the same as the original damping function proposed in Speziale [6] given as $f_\eta = \left[1 - exp\left(\frac{-\beta\Delta}{L_\eta}\right)\right]^n$ where

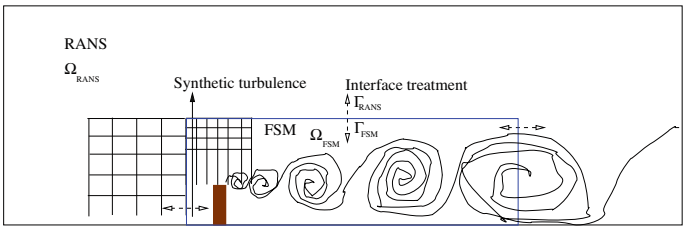

Fig. 1 A schematic of embedded FSM zone in a global RANS zone

β and n are model parameters, Δ is the local grid spacing and L_η is the Kolmogorov length scale, the second one $f_\Delta = C_\alpha \Delta / L_T$ ensures that a correct value of damping is provided when the model operates in LES mode, where C_α is a calibration constant and L_T is the characteristic length scale, and the final one $f_z = 1/(1 - F_z)$ ensures the switch from RANS to LES occurs outside the boundary layer, where F_z is the blending function from the underlying $k - \omega$ SST turbulence model.

3 Results

3.1 Turbulent Channel Flow

In order to validate the synthetic turbulence generation as an interface condition a spatially developing turbulent channel flow was simulated using the present solver. The friction Reynolds number of the channel was $Re_\tau = 395$ with half-depth of the channel δ as the length scale and the friction velocity u_τ as the velocity scale. The simulation domain for the channel is composed of two channels placed one after the other with the outlet of the first channel directly coupled to the inlet of the second channel. The channel in the fore is solved using RANS and the one in the aft is solved using LES. The DFM extracts mean velocities and Reynolds stresses from the RANS region in a coupled manner and feeds the fluctuations to the LES inflow interface. The low Re $k - \varepsilon$ model was used as the RANS turbulence model and the constant coefficient Smagorinsky model was used as the sub-grid scale model in the LES region. The near-wall mesh resolution satisfies $y^+ = 1$ and the mesh resolution in the stream-wise and span-wise directions were $\Delta x^+ = 39.5$ and $\Delta z^+ = 19.8$. The domain of the RANS channel was $15\delta \times 2\delta \times 3.5\delta$ and that of the LES channel was $45\delta \times 2\delta \times 3.5\delta$ in the streamwise, wallnormal and spanwise directions respectively. The number of grid points for the RANS channel were $150 \times 80 \times 70$ and for the LES channel $450 \times 80 \times 70$. The time-averaged and spanwise-averaged mean velocity profiles are shown in Fig. 2 and the Reynolds stresses are shown in Fig. 3. The mean velocity and Reynolds stresses obtained from the present simulation show a good match with the results obtained by Kim et al. [3]. using the same DFM in a full LES simulation. The variation of wall shear stress (not shown here) along the streamwise distance shows an adaptation length of 20δ. However, the Reynolds stress profiles extracted at several locations downstream of the LES interface collapse on to self-similar profiles beginning with a distance of 6δ (not shown here). The restoration of shear stresses is thought to be more important than the wall shear stress, thus a length of around 6δ appears to be necessary in order to obtain profiles that represent realistic turbulence.

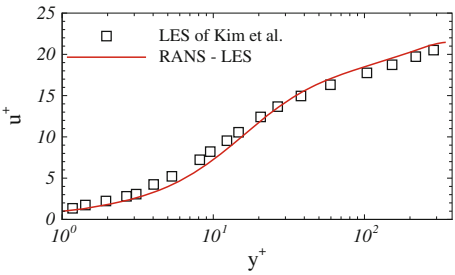

Fig. 2 Mean velocity

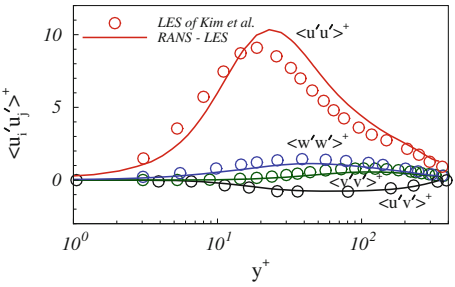

Fig. 3 Turbulent stresses

3.2 *Flow over a Vertical Fence*

The problem considered here is the flow over a vertical fence configuration which was previously studied both experimentally and numerically using direct numerical simulation (DNS) and LES [5]. The incoming boundary layer thickness is equal to the height of the fence (h), the Reynolds number is based on h, and the maximum inlet velocity U is equal to 3000. At the inlet to the domain we apply the turbulent velocity profile together with the turbulent kinetic energy and frequency profiles taken from the DNS data [5]. At the far-field boundary a slip boundary condition on the velocity is specified. At the outlet of the RANS domain a zero-gradient boundary condition on velocity is prescribed and non-reflective boundary condition on pressure are applied. No-slip boundary conditions are applied on the bottom wall including the fence boundaries. As shown in Fig. 1 an FSM region is embedded in a global RANS region. Four simulations are performed namely (a) FSM interface at $-3h$ and without feeding synthetic fluctuations, black dotted line (b) FSM interface at $-3h$ with fluctuations, green dash-dot line (c) FSM interface at $-6h$ with fluctuations, red solid line (d) FSM interface at $-6h$ with fluctuations on a coarse mesh, blue dash line, and the results are shown in Figs. 4, 5 and 6 for $\langle u \rangle$, u_{rms} and $\langle u'v' \rangle$ respectively. The DNS results [5] are represented using circular symbols in all of the figures. From Fig. 4 it can be seen that case (a) laminarises in front of the fence and does not match with the reference data at all the downstream locations. The u_{rms} and $\langle u'v' \rangle$ profiles for the case (a) are essentially zero until $x/h = 2.75$, thereafter the peak values of these profiles quickly grow and are over-predicted at all downstream locations beginning at $x/h = 7.74$. Mean velocity profiles obtained from case (b) also follow

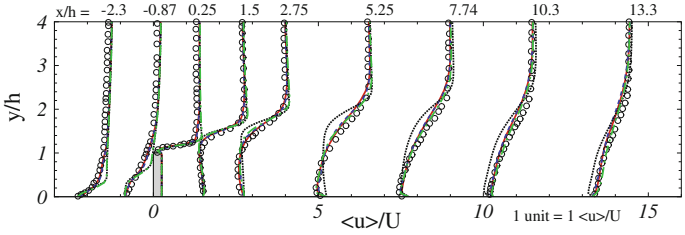

Fig. 4 Profiles of $\langle u \rangle$ at indicated streamwise locations

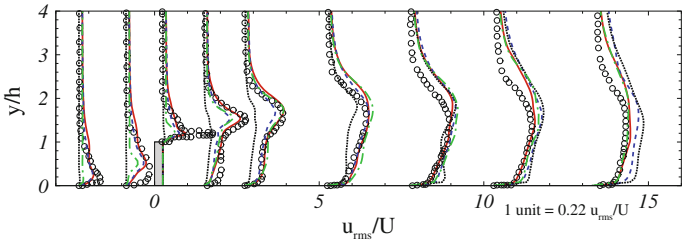

Fig. 5 Profiles of u_{rms} at several streamwise locations

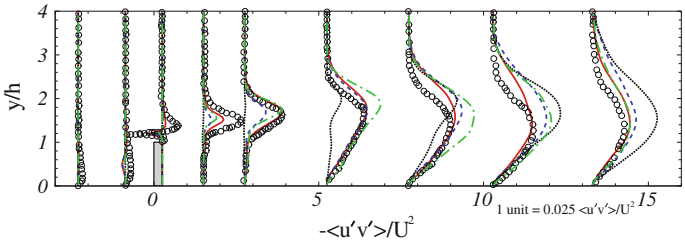

Fig. 6 Profiles of $\langle u'v' \rangle$ at several streamwise locations

the same trend as the case (a) for the two locations upstream of the fence, however, they show good agreement with the reference data at downstream locations beginning at $x/h = 2.75$. The u_{rms} and $\langle u'v' \rangle$ profiles for the case (b) do not reach sufficient levels upstream of the fence and they also result in over-prediction at all downstream locations beginning at $x/h = 5.25$. Surprisingly, the second-order statistics show a good match at the location $x/h = 2.75$ for the case (b) in their transition from under-prediction to over-prediction. These two cases (a and b) indicate the need to feed synthetic fluctuations and the case (b) in particular shows that the interface where the fluctuations are fed is not far enough upstream for them to grow to maintain a turbulent velocity profile. The mean velocity profiles obtained from case (c) show a good match at all the locations upstream and downstream of the fence. The second-order statistics also show a good match with the reference data except at the location exactly on the fence. This is attributed to the underlying FSM damping function

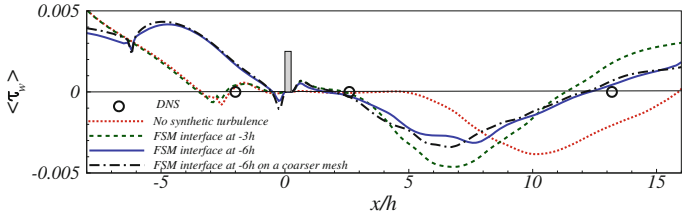

Fig. 7 Variation of wall shear stress along the streamwise direction

operating in a RANS mode. This result obtained from case (c) indicates that feeding the synthetic fluctuations with the FSM interface placed at $6h$ upstream of the fence is sufficient to produce a good match with the reference data. In a final simulation in case (d) the mesh is coarsened to 0.8 million cells (one-third of the mesh size of all the previous cases) keeping the location of feeding the synthetic fluctuations the same at $-6h$. The mean velocity profiles for case (d) show a good match at all the locations, similar to that of case (c) and u_{rms} and $\langle u'v' \rangle$ profiles also show a good match until $x/h = 7.74$ beyond which a slight over-prediction is observed. This final case indicates the benefit of using a damping model such as FSM as it gives good results even on coarse meshes. The variation of wall shear stress is computed for all the cases and is shown in Fig. 7. Cases (a) and (b) do not correctly capture the location of the primary recirculation bubble behind the fence and the cases (c) and (d) seem to be predicting this location better and their spatial variation follows a similar path. All the cases show differences for the location of the recirculation bubble upstream of the fence and this could be attributed to the synthetic fluctuations.

3.3 Summary

A framework is developed within the OpenFOAM [8] solver to embed an FSM region inside a RANS region. Spatially developing turbulent channel flow is simulated to validate the method. Flow over a vertical fence is simulated using the developed embedded FSM method and the mean and second-order statistics are compared with the reference data. The results indicate that the location where synthetic fluctuations are fed needs to be placed sufficiently far upstream in order to obtain a good match and that good results can be obtained at reduced computational cost when replacing the embedded LES region with an embedded unified hybrid RANS/LES approach.

Acknowledgements This work is performed with support from Airbus Group Innovations and BAE Systems through the "Simulations at Off-Design (SimOD) conditions" project. The authors also acknowledge the computational support provided through the IRIDIS4 High Performance Computing Facility at the University of Southampton, and the ARCHER Supercomputer facility at the University of Edinburgh through the UK Turbulence Consortium under ESPRC grant EP/L000261/1.

References

1. Fasel, H.F., von Terzi, D.A., Sandberg, R.D.: A methodology for simulating compressible turbulent flows. J. Appl. Mech. **73**(3), 405–412 (2006)
2. Fröhlich, J., von Terzi, D.: Hybrid LES/RANS methods for the simulation of turbulent flows. Prog. Aerosp. Sci. **44**(5), 349–377 (2008)
3. Kim, Y., Castro, I.P., Xie, Z.-T.: Divergence-free turbulence inflow conditions for large-eddy simulations with incompressible flow solvers. Comput. Fluids **84**, 56–68 (2013)
4. Menter, F.R.: Two-equation eddy-viscosity turbulence models for engineering applications. AIAA J. **32**(8), 1598–1605 (1994)
5. Orellano, A., Wengle, H.: Numerical simulation (DNS and LES) of manipulated turbulent boundary layer flow over a surface-mounted fence. Eur. J. Mech. B/Fluids **19**(5), 765–788 (2000)
6. Speziale, C.G.: A combined large-eddy simulation and time-dependent RANS capability for high-speed compressible flows. J. Sci. Comput. **13**(3), 253–274 (1998)
7. Weinmann, M., Sandberg, R.D., Doolan, C.: Tandem cylinder flow and noise predictions using a hybrid RANS/LES approach. Int. J. Heat Fluid Flow **50**, 263–278 (2014)
8. Weller, H.G., Tabor, G., Jasak, H., Fureby, C.: A tensorial approach to computational continuum mechanics using object-oriented techniques. Comput. Phys. **12**(6), 620–631 (1998)

LES of a Simplified HVAC System Used for Aeroacoustic Predictions

S. Rolfo, C. Moulinec, D.R. Emerson and J. Lirvat

1 Introduction

In recent years noise emissions have been strongly regulated in many industries in order to reduce noise pollution and to improve comfort. A typical example of noise generated by a turbulent flow inside a Heat and Ventilation Air Conditioning (HVAC) system of a vehicle is presented. In this case, besides the blower, most of the flow-induced noise is generated by obstacles present in the ducts and pipes of the system. To study this problem a consortium of car manufacturers have proposed a simplified test case. They wanted to assess the accuracy of several Computational Fluid Dynamics (CFD) and Computational Aero-Acoustics software in performing noise simulations. In this paper a simplified HVAC duct, as the one proposed in [1] is investigated by means of wall resolved Large Eddy Simulations (LES).

2 Test Case Definition

The geometry under consideration is constituted of a bend square duct with a flap positioned downstream of the bend. The duct exits into a plenum, which contributes to create a squared cross section jet. Figure 1 sketches the geometry with all the main

S. Rolfo (✉) · C. Moulinec · D.R. Emerson
Scientific Computing Department, STFC Daresbury Laboratory, Cheshire, UK
e-mail: stefano.rolfo@stfc.ac.uk

C. Moulinec
e-mail: moulinec@stfc.ac.uk

D.R. Emerson
e-mail: david.emerson@stfc.ac.uk

J. Lirvat
Aeroacoustic Research Team, Dyson Limited, UK
e-mail: jimmy.lirvat@dyson.com

D.G.E. Grigoriadis et al. (eds.), *Direct and Large-Eddy Simulation X*,
ERCOFTAC Series 24, https://doi.org/10.1007/978-3-319-63212-4_38

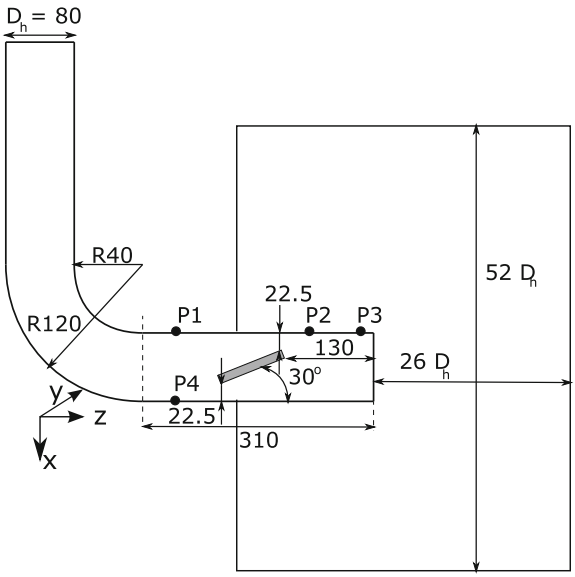

Fig. 1 Sketch of the HVAC geometry and relative dimensions (in mm) in the mid-plane. The dimensions of the plenum refers to the one used in the computational domain. The dimension of the plenum in the spanwise direction is $52D_H$ and the length of the incoming pipe is $10D_H$

features and relative dimensions. The experimental apparatus has a very long inlet duct before the bend, therefore a fully turbulent flow can be assumed at the domain inlet. The inlet bulk velocity is kept constant at 7.5 m/s which corresponds to a bulk Reynolds number, based on the hydraulic diameter $D_H = 0.08$ m, of $Re = 40{,}000$.

3 Numerical Methods

The open source CFD software *Code_Saturne* [2, 3] (www.code-saturne.org) has been used for all the simulations presented herein. The equations are discretised using a cell centred co-located finite volume approach. Velocity and pressure coupling is ensured by a prediction/correction method similar to the SIMPLEC algorithm and the Poisson equation is solved using an algebraic multigrid solver. The code handles completely unstructured grids, including polyhedral cells and embedded refinements. In Large Eddy Simulation mode the time and space discretisation are second order accurate. A Smagoringky model [4] with Van Driest damping [5], for the turbulent viscosity at the wall, has been employed to model the subgrid scales. The mean inlet velocity profile has been computed with a precursor RANS simulation using a 4 equations BL$v^2 - k$ RANS model [6]. A Divergence-Free Synthetic Eddy Method [7] has been used to reconstruct the turbulent fluctuations at the inlet.

Particular care has been placed in implementing the boundary conditions for the outlet and the side of the plenum. Homogeneous Neumann boundary condition is applied to the velocity, whereas the dynamic pressure (p_f) at the boundary face is

evaluated solving a Bernoulli type of equation assuming that the velocity at infinity is $\underline{u}_\infty = 0$. Consequently the dynamic pressure can be rearranged as:

$$p_f = -\frac{1+K}{2}\rho_f \underline{u}_f \cdot \underline{u}_f, \tag{1}$$

with K being a head loss applied to the boundary face to improve the stability of the calculation, ρ_f the density at the boundary face and $\underline{u}_f$ the velocity vector.

4 Results

The domain that has been described in Sect. 2 has been meshed using a fully conformal block structured approach. The first cells at the duct wall and on the flap are 0.07 mm high. This guarantees a y^+ at the wall of 1 or below everywhere in the domain. The aspect ratio between the first cell height and the length in the tangential direction varies between 3.5 and 22. In the streamwise direction the aspect ratio is maintained below 30 for part of the duct after the bend, whereas it can reach 100 in the part before the bend, just down-stream of the inlet. The total mesh size is of the order of 28 million cells.

The simulations were performed on the Hartree Centre Blue Gene/Q system using 16,384 MPI tasks (512 nodes with 32 ranks per node or 1024 nodes with 16 ranks per node). The time step used is $1.25 \cdot 10^{-5}$ s, which gives an average CFL number over all the domain of the order of 0.1. Statistics have been collected for more than 1.5 s of physical time, which corresponds to about 10 passes through the duct and more than 2 flow-through from the inlet of the duct to the outlet of the plenum.

4.1 Flow Features and Comparison with Experiments

Figure 2 shows the streamlines and the p_{rms} in the symmetry plane ($2y/D_h = 0$) of the geometry and the main flow features read as follows: (a) a small separation on the top wall just down-stream the bend and (b) a very large wake behind the flap, which

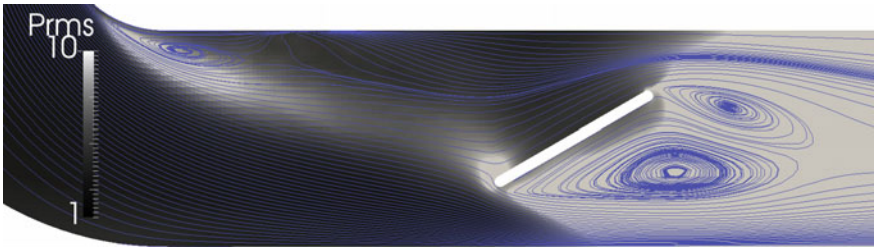

Fig. 2 Streamlines and p_{rms} in the symmetry plane ($y = 0$)

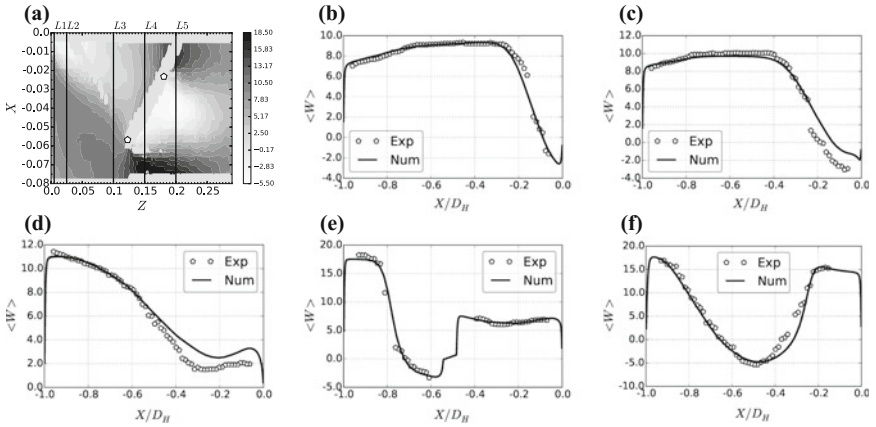

Fig. 3 **a** Average velocity in z direction from the experiments [1]. **b** Comparison between experiments and numerical results at $L1$. **c** Comparison between experiments and numerical results at $L2$. **d** Comparison between experiments and numerical results at $L3$. **e** Comparison between experiments and numerical results at $L4$. **f** Comparison between experiments and numerical results at $L5$

is composed by two counter-rotating vortices. These two areas are also characterized by the highest level of pressure fluctuations along with the leading edge of the flap. Indeed, these areas are the ones where most of the noise sources are located.

Experimental data are available from [1] for the W velocity component. Since the raw data are not available, they have been extracted from contours plots in [1]. Contours plots and relative legends have been converted into RGB triplets and a linear interpolation has been used to correlate the RGB of the contours with the closest in the legend to obtain a single value for the velocity. The results of the contour digitalization is shown in Fig. 3a along with the locations of 5 different lines for comparison between experimental data and numerical results. The numerical results are in very good agreement with the experimental data (see Fig. 3b–f), particularly: (a) the maximum velocities in the two acceleration areas above and below the flap are very well predicted in both locations and magnitude and (b) the recirculation, with relative location of the two vortices, is very well captured (see Fig. 3e, f). However, some discrepancies are observed in the recirculation bubble located on the top wall particularly in the region between $L2$ and $L3$ (see Fig. 3c, d), suggesting an underestimation of the reattachment length.

The flow is fully 3D and flow features can largely vary along the span-wise direction as demonstrated in Fig. 4a–d. The separation bubble progressively becomes smaller, moving towards the side wall of the duct and completely disappears at about $2y/D_h = 0.85$. The wake behind the flap progressively change with the span-wise direction, more precisely the smaller top vortex tends to disappear, whereas the lower larger vortex moves upwards. At $2y/D_h = 0.85$ only one remains (see Fig. 4d)

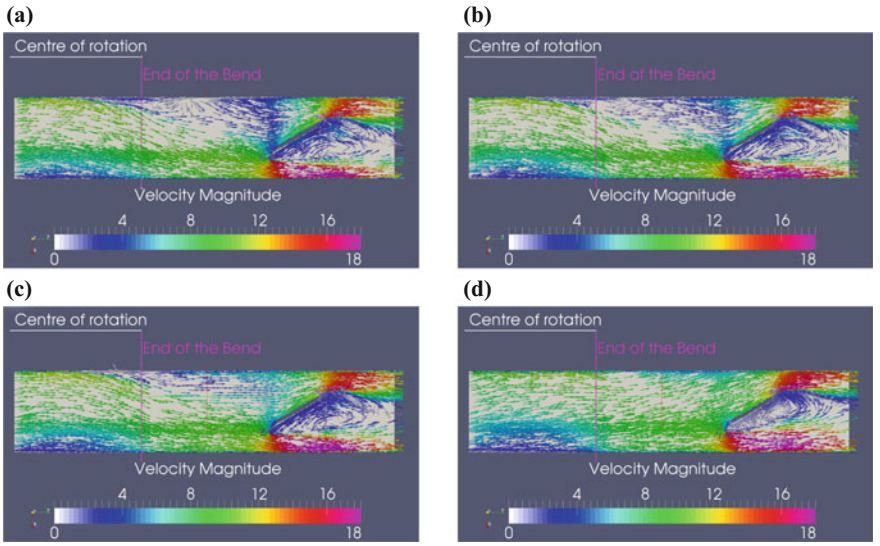

Fig. 4 **a** Mean velocity vectors in the midplane $2y/D_h = 0$. **b** Mean velocity vectors in the plane $2y/D_h = 0.5$. **c** Mean velocity vectors in the plane $2y/D_h = 0.75$. **d** Mean velocity vectors in the plane $2y/D_h = 0.85$

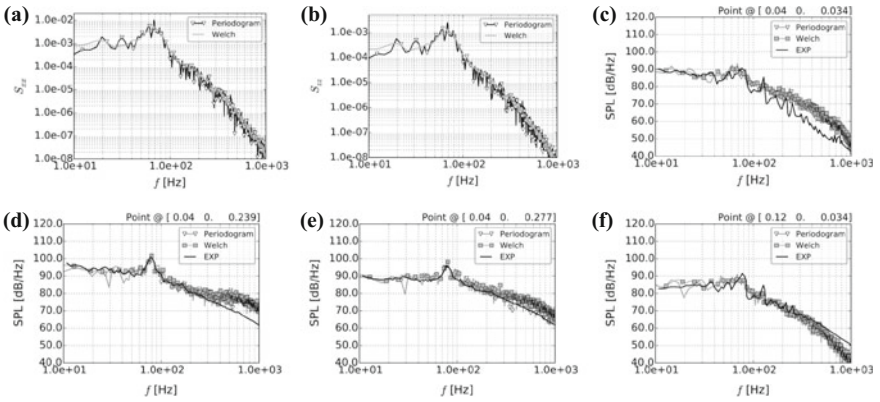

Fig. 5 **a** PSD of lift force S_{xx}. **b** PSD of drag force S_{zz}. **c** SPL at point $P1$. **d** SPL at point $P2$. **e** SPL at point $P3$. **f** SPL at point $P4$

4.2 Frequency Analysis

Power spectral density (PSD) of lift (i.e. x-direction) and drag (i.e. z-direction) is shown in Fig. 5a, b respectively. The data are sampled at 80 kHz and the length of the time signal is around 1.64 s (2^{17} points). FFTs are computed using the periodogramm

and the Welch method using an Hanning window of width 2^{15} points. Different windowing (triangular and flattop) and sizes (2^{14} and 2^{16}) have also been tested for both methods, producing very similar spectra. The PSD for the forces shows in both case a peak at about 69 Hz. The same dominant frequency can be also observed in the Sound Pressure Level (SPL) of $P1$ (see Fig. 5c), which is located upstream of the flap on both top and bottom wall. The dominant frequency for both lift and drag PSD has exactly the same value and does not exhibit the factor of two typical of flows around bluff body, i.e. circular cylinder.

On the other hand, SPLs at points downstream the obstacles (i.e. $P2$ and $P3$) present a peak at about 79 Hz, which is in excellent agreement with the value provided experimentally.

Instantaneous flow visualisations (not reported here because of limited space available) show that the detached flow is impinging on the obstacle, and the vortex shedding downstream the flap are relatively independent. This might explain the presence of the two different dominant frequencies reported above.

5 Conclusions

The flow inside a simplified HVAC has been investigated by means of LES. Comparison of the hydrodynamic results is in very good agreement with the experimental values, with the only exception of the recirculation bubble on the top wall, which is shorter in the numerical simulation.

The dominant frequency of 79 Hz, which has been identify in the SPL at microphones located downstream the flap is properly captured as well as the correct noise level. On the other hand, the Power Spectral Density of forces on the obstacle and the SPL at point upstream the flap show also a dominant frequency at 69 Hz that might be related to the detached flow from the bend that is impinging on the flap.

Further work is on-going in order to test: (a) the effect of the sub-grid modelling, (b) the cell aspect ratio effect if increasing the mesh size up to 60 million cells and (c) the influence of the inlet definition.

References

1. Jager, A., et al.: Numerical and experimental investigations of the noise generated by a flap in a simplified HVAC duct. In: 29th AIAA Aeroacoustics Conference (2008)
2. Archambeau, F., Mechitoua N., Sakiz, M.: Code_Saturne: a finite volume code for the computation of turbulent incompressible flows - industrial applications. Int. J. Finite Vol. vol. 1 (2004)
3. Fournier, Y., Bonelle, J., Moulinec, C., Shang, Z., Sunderland, A., Uribe, J.: optimizing code_saturne computations on petascale systems. Comp. Fluids **45**, 103–108 (2011)
4. Smagorinsky, J.: General circulation experiments with the primitive equations: I. the basic experiment. Mon. Wea. Rev. **91**, 99–164 (1963)

5. Van Driest, E.R.: On turbulent flow near a wall. J. Aerosp. Sci **23**, 1007–1011 (1956)
6. Billard, F., Laurence, D.: A robust $k - \varepsilon - \overline{v^2}/k$ elliptic blending turbulence model with improved predictions in near-wall, wake, separated and buoyant flows. IJHFF **33**, 45–58 (2012)
7. Poletto, R., Craft, T., Revell, A.: A new divergence free synthetic eddy method for the reproduction of inlet flow conditions for les. Flow Turbul. Combust. **91**(3), 519–539 (2013)

High-Order Hybrid RANS/LES Strategy for Industrial Applications

G. Pont, P. Brenner, P. Cinnella and J.-C. Robinet

1 Introduction

Turbulent flows of industrial interest are often dominated by large turbulent structures. A typical example is provided by launcher base flows, combining one or more extended and interacting separated regions with strong compressibility effects. Such flow features represent a challenge for CFD simulations, since, on the one hand, well established Reynolds-Averaged-Navier-Stokes (RANS) solvers cannot represent such highly unsteady and three-dimensional large scales and, on the other hand, Large Eddy Simulation (LES) approaches remain too expensive for routine production use in industry. In fact, LES methods can lead to inaccurate results if the mesh size and/or the scheme accuracy are not good enough to resolve correctly most of the relevant flow scales. In complex industrial applications, the energy spectrum is often ill defined and changes from one point to another of the simulation, so that it is difficult to warrant a sufficient resolution everywhere, unless extremely fine meshes are used. Mesh resolution requirements become particularly severe if industrial codes based on low order, low resolution discretization schemes are used. In this work we assess a recently developed hybrid RANS/LES strategy, combining a self-adaptive hybrid turbulence model [6] and a hybrid high-order finite volume scheme [7], for flow around industrial geometries, namely, the Ariane 6 and Ariane 5 space

G. Pont · P. Brenner
Airbus Defense and Space, Les Mureaux, France
e-mail: gregoire.pont@astrium.eads.net

P. Brenner
e-mail: pierre.brenner@astrium.eads.net

P. Cinnella (✉) · J.-C. Robinet
Laboratoire DynFluid, Arts et Métiers ParisTech, Paris, France
e-mail: paola.cinnella@ensam.eu

J.-C. Robinet
e-mail: jean-christophe.robinet@ensam.eu

D.G.E. Grigoriadis et al. (eds.), *Direct and Large-Eddy Simulation X*,
ERCOFTAC Series 24, https://doi.org/10.1007/978-3-319-63212-4_39

launchers. Increasingly complex geometrical details are included in the simulation and the results are compared with the experimental data available for the average and root mean square (rms) of the longitudinal distribution of the pressure coefficient, which represent a significant quantity of interest for launcher design.

2 Numerical Methodology

The simulations are carried out by using a high-order unstructured finite volume solver. The space discretization scheme uses k-exact reconstructions of the variables over each cell to obtain high-order approximations of the fluxes at cell interfaces. Precisely, the reconstruction process requires approximations of the solution derivatives up to order two, leading to a third-order accurate approximation on generic grids. Derivative approximations are obtained by means of an efficient successive reconstruction technique [3]. An exact Riemann solver is then applied to the reconstructed solution at cell interfaces. The resulting numerical scheme is suitable for highly compressible flows since it has good shock capturing capabilities. Nevertheless, it appears to be too dissipative for scale-resolving simulations since it overdamps the vortical structures associated to LES regions of the computational domain. To overcome this difficulty, a hybrid numerical scheme is constructed by locally recentering the third-order scheme in vortex-dominated regions according to a blending function involving Ducros' compressibility/vorticity sensor [2] and a stability criterion involving the grid Reynolds number based on the sum of the local molecular and turbulent viscosity. The fully centered scheme is fourth-order accurate. If the stability criterion is not satisfied, the blending function partly re-centers the scheme while keeping a minimal amount of numerical dissipation to ensure stability. The proposed scheme is referred-to as vortex-centered (VC) scheme. More details can be found in Ref. [7]. The proposed strategy has been implemented within FLUSEPA, the unstructured finite-volume solver developed by Airbus Defence & Space (ADS) to calculate compressible, multidimensional, unsteady, viscous and reactive flow over bodies in relative motion. Time integration is carried out by means of the explicit second-order accurate Heun scheme, along with a time-consistent local time stepping technique.

Unresolved turbulence effects on the resolved scales are taken into account by means of a self-adaptive hybrid RANS/LES model, initially developed by Perot and Gadebusch [6], based on a modification of the well known $k - \epsilon$ model. The model is referred-to as PG hereafter. Such a model acts as a subgrid model in well-resolved regions while keeping a classical $k - \epsilon$ model in under-resolved regions, via a sensor based of the local amount of resolved kinetic energy compared to the modeled one. When the amount of resolved kinetic energy is low compared to an indicator of the local grid resolution, the model switches automatically from the RANS to the LES mode. The original model was developed for free turbulence. In order to apply

the model to wall-bounded flows, we introduce a shielding function near the wall, similar to that introduced in [10]. Wall functions are used near the wall [5] to avoid too severe restrictions on the maximum allowable time step.

The proposed numerical methodology was assessed against well documented test cases [7, 8]. In particular, simulations of the flow around 2D and axi-symmetric backward facing steps showed that the proposed approach provides satisfactory results by using relatively coarse computational grids compared to similar calculations available in the literature.

3 Application to the RANS/LES Simulation of Industrial Launcher Configurations

3.1 Flow Around the Shrinkage of Ariane 6

We simulate a 1/60 scale of the wind tunnel model of Ariane 6 space launcher, with an angle of attack and yaw angle equal to 0. Simulations are carried out for a Reynolds number, based on the main diameter D of the launcher equal to 9.1×10^5 and a Mach number equal to 0.9. Figure 1 shows the composite grids used to discretize the computational domain. The total number of cells is about 15×10^6. The mesh resolution in the wall-normal and longitudinal directions is of approximately 30 and 50 wall units, respectively. An azimuthal step of 2 degrees is used. The calculations are started from a partially converged $k - \epsilon$ solution. Statistics are collected over a non-dimensional duration $T \times U_\infty/(D - d) = 200$ (with U_∞ the freestream velocity and D and d the diameters upstream and downstream of the shrinkage). Figure 2 a shows the instantaneous Q criterion around the shrinkage of the launcher colored by Mach number. In the recirculation area, the heads of Kelvin-Helmholtz vortices

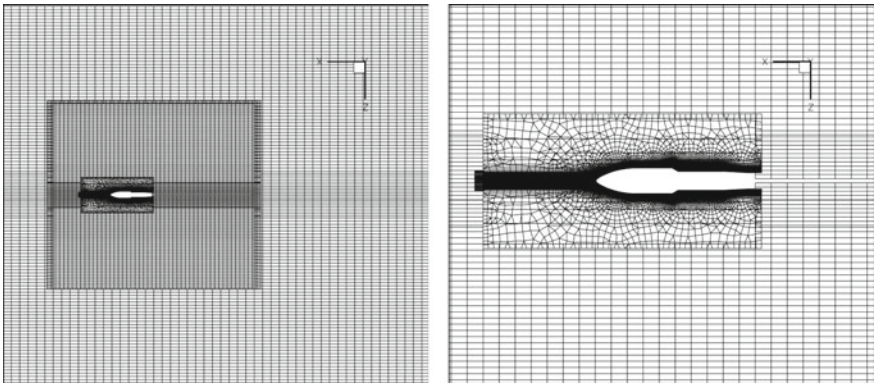

Fig. 1 Details of the overlapping grid around the Ariane 6 shrinkage

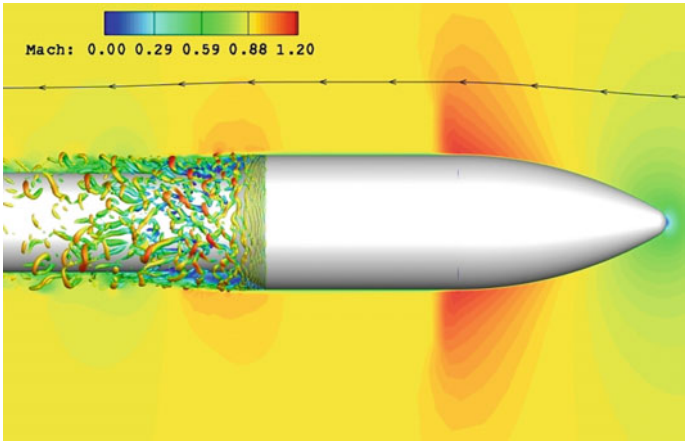

Fig. 2 Instantaneous Q criterion *colored* by the Mach number

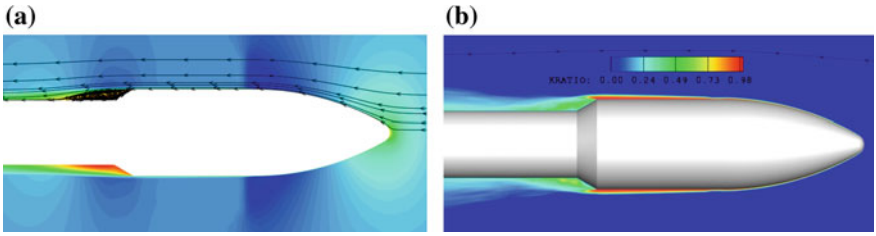

Fig. 3 Mean flow around the Ariane 6 launcher: **a** mean longitudinal velocity and streamlines, **b** modeled to total kinetic energy ratio

are supersonic and induce local compressibility effects. A shock/boundary layer interaction occurs on the fairing of the launcher. The proposed numerical approach accurately captures Kelvin–Helmholtz instabilities while ensuring robustness. The present results are compared to the experiments available for a slightly different configuration [4]. In the mean flow, see Fig. 3a, the predicted reattachment length, normalized with shrinkage height ($h = (D - d)/2$), is equal to 6.1, the experimental value being 5.8. Finally, Fig. 3b shows that the kinetic energy is fully modeled in the attached upstream boundary layer, while in the shear layers and recirculation bubble the modeled kinetic energy is gradually replaced by the resolved one. Figure 4 shows the evolution of mean pressure and rms pressure coefficients along the shrinkage, versus the longitudinal coordinate normalized by the recirculation length. Both are in good agreement with the experiments. The Strouhal number based on the buffeting frequency, the recirculation length x_r and U_∞ is about 0.63, a value close to the experiments and other calculations in the litterature.

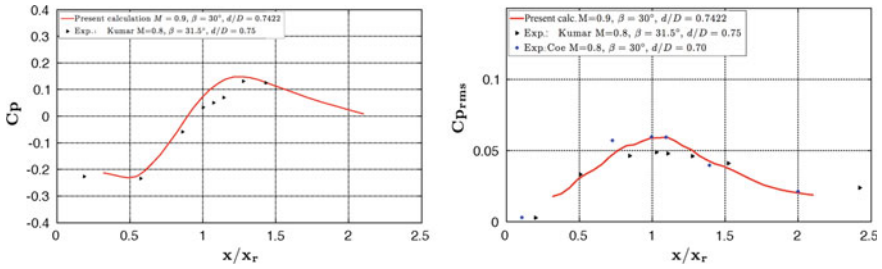

Fig. 4 Distributions of the average (*left*) and rms (*right*) pressure coefficient along the shrinkage

3.2 Flow Around the Ariane 5 Launcher with Boosters

The next application is a 1/60 scale model of the Ariane 5 launcher at zero angle of attack. The freestram Mach number is equal to 0.8 and the Reynolds number based on the diameter of the central body is 2×10^{-6}. The computational mesh, shown in Fig. 5 is composed by 20×10^6 cells. The y^+ is about 20 at the beginning of the separated region. The azimuthal resolution equal to 2 degrees. The simulation is initialized with a partly converged RANS solution, and the statistics are collected over a non-dimensional duration $T * U_\infty / H$ equal to 40 after the numerical transient. This is not long enough to fully converge the statistics, so that results hereafter are to be taken with caution. Figure 6 gives an overview of the instantaneous field at the base of the launcher. The Kelvin–Helmholtz instabilities are clearly visible and are triggered without delay. Figure 7 compares present results for the average and rms pressure coefficient with experimental data collected at ADS the recirculation area of the launcher. The overall agreement is reasonably good.

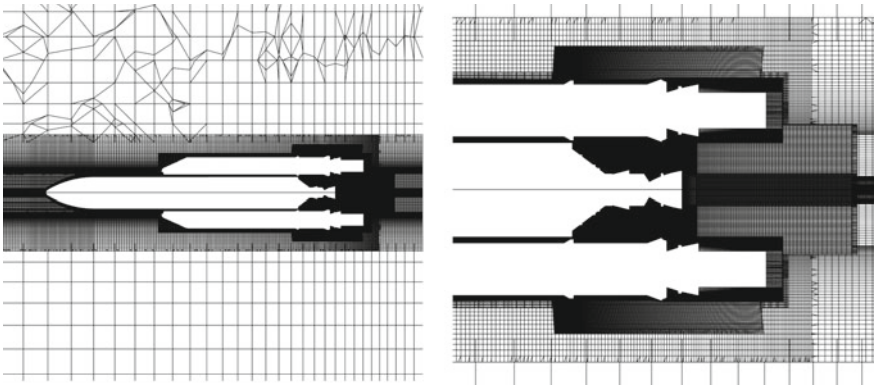

Fig. 5 Details of the overlapping grid around the Ariane 5 launcher

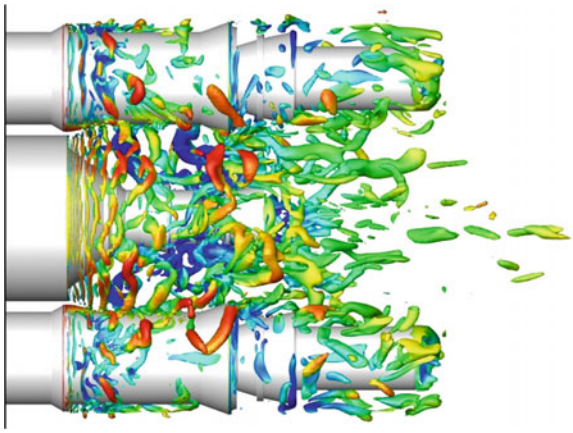

Fig. 6 Instantaneous Q criterion *colored* by the Mach number

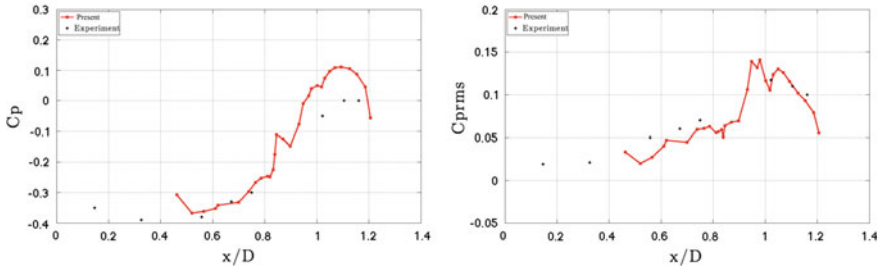

Fig. 7 Distributions of the average (*left*) and rms (*right*) pressure coefficient along the nozzle

4 Conclusions

The present work demonstrated the capability of a hybrid high-accurate industrial solver to successfully predict complex launcher configurations to within engineering accuracy, while ensuring the necessary robustness. Using a low-dissipative scheme in conjunction with a hybrid RANS/LES model is found to be crucial for triggering flow instabilities and obtaining correct average and rms wall pressure levels.

References

1. Chauvet, N.: Simulation numérique et analyse physique d'un jet propulsif contrôlé par des injections radiales. PhD Thesis, University of Poitiers (2007)
2. Ducros, F., et al.: Large eddy simulation of the shock/turbulence interaction. J. Comput. Phys. **152**, 517–549 (1999)

3. Haider, F., Brenner, P., Courbet, B., Croisille, J.P.: Efficient implementation of high order reconstruction in finite volume methods. Finite Volumes for Complex Application VI-Problem & Perspectives, Springer Proceedings in Mathematics **4**, 553–560 (2011)
4. Kumar, R., Viswanath, P.R.: Mean and fluctuating pressure in boat-tail separated flows at transonic speeds. J. Spacecr. Rocket. **19**(3), 430–438 (2002)
5. Launder, B., Spalding, D.: Application of the energy-dissipation model of turbulence to the calculation of flow near a spinning disc. Lett. Heat Mass Transf. **1**, 131–138 (1974)
6. Perot, B., Gadebush, J.: A self-adapting turbulence model for flow simulation at any mesh resolution. Phys. Fluids **19**, 1–11 (2007)
7. Pont, G., Cinnella, P., Brenner, P., Robinet, J-C.: Development of numerical schemes for hybrid turbulence modelling in an industrial CFD solver, AIAA Paper 2013–2440
8. Pont, G., Cinnella, P., Brenner, P., Robinet, J-C.: Assessment of automatic hybrid RANS/LES models for industrial CFD. AIAA Paper 2014–2691
9. Pont, G., Cinnella, P., Brenner, P., Robinet, J-C.: An efficient k-exact reconstruction method for robust and high-order finite volumes on any grid. Submitted (2015)
10. Spalart, P.R.: Detached eddy simulation. Ann. Rev. Fluid Mech. **41**, 181202 (2009)

Numerical Investigation of Flow Dynamics of Turbulent Flow Through Ribbed Pipes

A. Twerda and B.J. Boersma

1 Introduction

Now the oil reserves are decreasing other sources of energy are being used. Next to the more sustainable solar and wind energy also Natural Gas is more being used as fuel for heating or transportation. The transport of Natural Gas is mostly done via pipe lines but when distances become large, transporting it as a liquid, i.e. Liquified Natural Gas (LNG) is a cost-efficient option. The transport of LNG is mainly done via ships. The transfer of LNG from ship to ship or from ship to shore is carried out using so called flexible hoses. The flexibility of the hoses is needed to cope with the (small) movements of the ships. The prediction of pressure drop is important because the LNG is at or near its boiling point. If the pressure drop becomes too high, too much boil-off gas will occur, having a bad effect on the transfer rate. The particular flexible hose considered in this paper, consist of two metal spirals with multi-layered composite section in between. This makes the inner geometry of the pipe to have large corrugations.

Pressure drop in smooth pipelines is well known and documented in for instance the Moody diagram. In this diagram also the wall roughness is included. However, the wall roughness is assumed to be small compared to the pipe diameter. That assumption does not hold for our case. The case of large wall roughness is investigated before, but mainly for channel flows. For example, work has been done by [4] in which different flow regimes for the pressure drop are found depending of the distance/height ratio of the ribs. In this work we will use LES simulations to calculate the pressure drop and we want also to determine the influence of the distance

A. Twerda (✉) · B.J. Boersma
Process and Energy of Delft University of Technology, Delft, Netherlands
e-mail: a.twerda@tudelft.nl

B.J. Boersma
e-mail: b.j.boersma@tudelft.nl

D.G.E. Grigoriadis et al. (eds.), *Direct and Large-Eddy Simulation X*,
ERCOFTAC Series 24, https://doi.org/10.1007/978-3-319-63212-4_40

between the restrictions on the pressure drop. We will focus on pipe flow and will therefore use a LES code which has been written in cylindrical coordinates, using a hexahedral grid. This method is described in [5].

In this paper we will describe a numerical model to be able to predict the pressure drop of those flexible hoses with high roughness

2 Numerical Model

The model is a LES code written in cylindrical coordinates. The Navier-Stokes equations for an incompressible fluid with constant density are implemented.

The equations are discretized using a staggered grid arrangement using second order discretizations for both the convective and diffusive fluxes. For time integration the second order Adams-Bashforth scheme is applied. Periodic boundaries are applied to simulate fully developed flow. LES turbulence model was used to simulate the high Reynolds which are typical in the order of $Re = \frac{\rho U L}{\mu} = 10^4 \sim 10^5$ for our specific application.

The specific LES model applied is the standard Smagorinsky model using a constant value for $C_s = 0.1$. Standard wall functions are used to bridge the gap between the turbulent flow in the center of the pipe and the flow near the walls. To correct for the high turbulence near the wall the van Driest damping function was applied for the eddy viscosity.

The corrugations are modelled using the Immersed Boundary method (IBM) which is detailled in [2]. The diameter of the pipe is $D = 1$ and the length of the pipe was $L = 2.5$. The grid consisted of $(144 \times 256 \times 724)$ number of cells. A cross section of *half* the geometry is shown in Fig. 1. Here also the width (w) and height (h) of the ribs are shown.

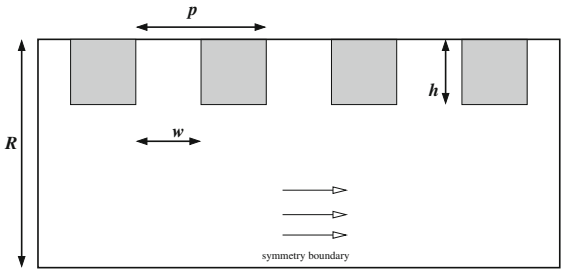

Fig. 1 Side view of *half* the geometry. R is the radius of the pipe. The width and height of the obstructions are d and h. The width of the corrugation is w. And the pitch $p = w + d$

3 Results

First the code has been validated by simulating flow in a smooth pipe. The dimensionless averaged flow profile is plotted in Fig. 2. The lines $u^+ = y^+$ and the log law are also plotted in this figure for comparison.

Additionally to the simulations, PIV experiments have been performed in the Aero and Hydro laboratory at the TUD, measuring the pressure drop and flow profile. The liquid used was water and the pipe diameter 50mm. Flow speeds, pitch length, shape and number of ribs were varied during the measuring campaign. We will compare our LES calculations with measurement set using eight square ribs at various distances [3].

Next, simulations with the corrugations are performed. The height of the corrugations and width of the ribs are fixed with the values $h = 0.15$ and $d = 0.18$, while the width w of the corrugation is varied. Four values of are simulated $w = 0.24, 0.32, 0.65$ and 1.07. This results in the pitch of the corrugations of $p = 0.41, 0.5, 0.83$ and 1.25.

Figure 3 shows the measured pressure drop over 8 ribs, ΔP scaled with $\frac{1}{2}\rho u^2$ for different pitches together with the scaled pressured drop from the LES simulations. As the LES simulations has respectively 6, 5, 3, and 2 ribs in the section the calculated pressure drop has been corrected for 8. In this figure we see that the trend in the pressure drop is nicely captured by the simulations but there is an offset, which is constant. This offset could be explained by the fact that in experimental setup set-up an additional pressure drop at the first rib is measured, which is not present in the simulation because we have applied a periodic boundary condition. The pressure drop is increasing as the pitch is increased as should be expected. However, the

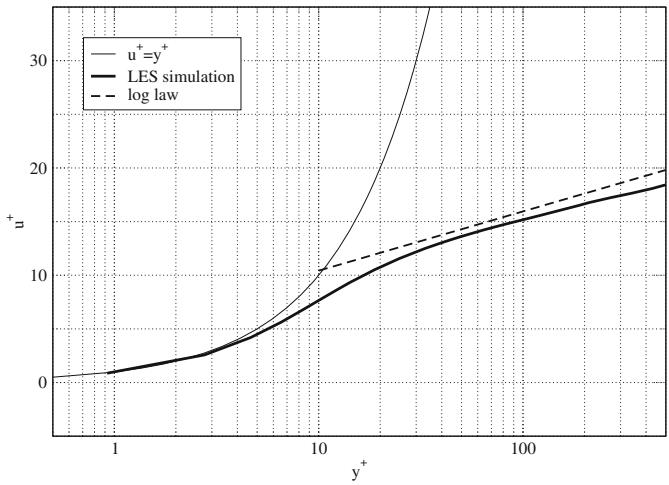

Fig. 2 Averaged axial velocity profile of the straight pipe (*solid line*) together with the log law and the viscus sublayer

increase should stop because, if the pitch becomes very large the pressure drop over each rib will be unrelated and we should get the pressure drop over one single rib. The value over one single rib or orifice can be calculated using:

$$K = \frac{2.7(1-m)(1-m^2)}{m^2} \tag{1}$$

where m is the ratio between the large and the small area, which is in our case 0.49. Hence, according to Eq. 1 the maximum pressure drop we should get for very large w is $K = 4.36$.

Furthermore, the velocity profiles of the PIV experiments and LES simulation are compared. See Fig. 4. In this figure the scaled averaged axial velocity is plotted as function of radial position for the case of $w/h = 4.35$. The velocity profiles match nicely and have a parabolic profile.

4 Discussion and Conclusion

The LES simulations over a number of ribs have been simulated and compared with experiments. Regarding the pressure drop we see that it is increasing when the pitch is increasing, it should go to a plateau of around 4, which has not been observed. Comparing the pressure drop with experiments we observe that the LES simulations are under predicting. This can be explained by the higher pressure drop of the first rib in the experiment, which is not present in the simulation.

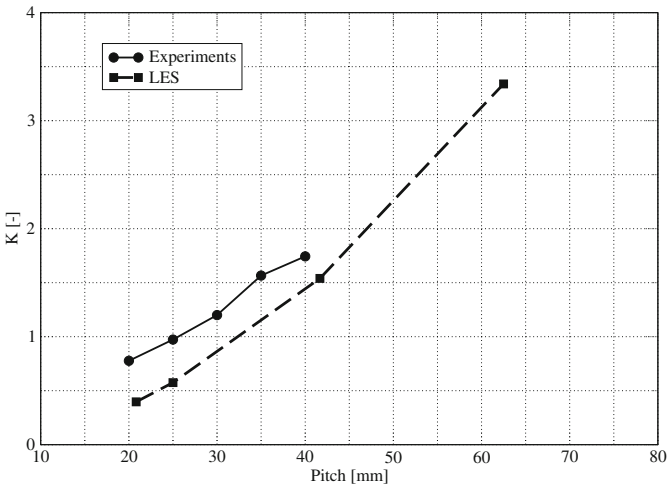

Fig. 3 Dimensionless pressure drop, $K = \frac{\Delta P}{1/2\rho v^2}$ over 8 ribs for different pitches for the experiments and LES simulation

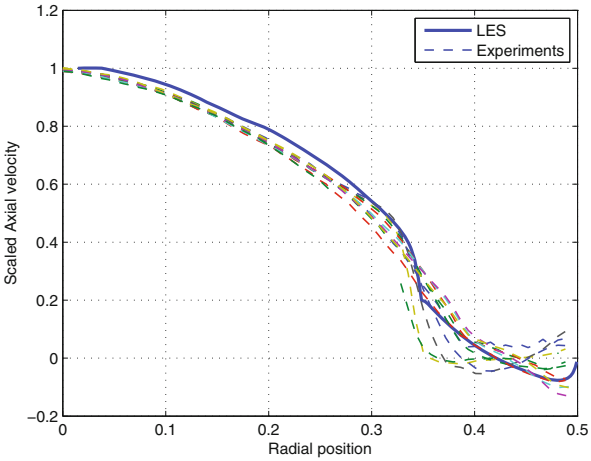

Fig. 4 Scaled averaged Axial velocity profile for the LES (*solid blue line*) and the experiments, *coloured dashed line* on several locations. $w/h = 4.35$

The parabolic profile of the velocity field which matches the PIV measurements suggests that the turbulent scales between the ribs are uniform and do not depend on the radial distance. Further investigations will therefore focus on the turbulent statistics analysis.

References

1. Werner, H., Wengle, H.: Large-eddy simulation of turbulent flow over and around a cube in a plate channel. Eighth Symposium on Turbulent Shear Flows, Munich, Germany (1991)
2. Breugem, W.P., Boersma, B.J.: Direct numerical simulations of turbulent flow over a permeable wall using a direct and a continuum approach. Phys. Fluids **17**(025103), 15 (2005)
3. Schenker, M. Delfos, R. Wester weel, J. Twerda, A. Bokhorst, E. van: The influence of cavitation on turbulent flow through a ribbed geometry, ExHFT-8, Lissbon, June 2013
4. Leonardi, S., Orlandi, P., Antonia, R.A.: Properties of d- and k-type roughness in a turbulent channel flow. Phys. Fluids **19** (2007)
5. Eggels, J. G. M.: Direct and Large Eddy Simulation of Turbulent Flow in a Cylindrical Pipe Geometry Ph.D. thesis TU-Delft(1994)

Direct Numerical Simulations of the Shock-Induced Separation of a Laminar Boundary Layer

G. Fournier, A. Chpoun, Y. Fraigneau and C. Tenaud

1 Introduction

In the aeronautical and aerospace industries, the flow configurations where an incident oblique shock wave impinges upon a boundary layer are very common. The supersonic flow around an aircraft, in a rocket nozzle or in a supersonic inlet are some examples among others. Under certain circumstances (High Mach number, large shock angle …), the interaction between the incident shock wave and the boundary layer may create an unsteady separation bubble. This separation bubble as well as the subsequent reflected shock that occurs around the separation point, are known to oscillate in a low-frequency streamwise motion that can spread over several tenth of the boundary layer thickness [12]. The origin of those oscillations, however still unclear, has been related either to the shedding of vortices in the mixing layer downstream of the separation, both for a flat-plate [2] or a ramp configuration [9], or to the turbulent structures in the incoming boundary layer [5]. Thanks to the tremendous increase of the computational power that has occured in the last two decades, many numerical studies of the shock wave/boundary layer interactions (SWBLI) have been performed recently using Large Eddy Simulations (LES) [1, 7, 14], RANS/LES hybrid methods [6] or Direct Numerical Simulations (DNS) [4, 15].

G. Fournier (✉) · A. Chpoun
Laboratoire de Mécanique et d'Energétique d'Evry, 40 Rue du Pelvoux,
91020 Evry Cedex, France
e-mail: guillaume.fournier@ufrst.univ-evry.fr

A. Chpoun
e-mail: a.chpoun@iut.univ-evry.fr

Y. Fraigneau · C. Tenaud
LIMSI-CNRS, Rue John von Neumann,
91045 Orsay Cedex, France
e-mail: Yann@limsi.fr

C. Tenaud
e-mail: Christian.Tenaud@limsi.fr

D.G.E. Grigoriadis et al. (eds.), *Direct and Large-Eddy Simulation X*,
ERCOFTAC Series 24, https://doi.org/10.1007/978-3-319-63212-4_41

Most of these studies however dealt with turbulent boundary layer and only a very few of them considered the laminar case [10, 11]. The streamwise motion being potentially related to the turbulent behavior of the incoming boundary layer, the aim of the present study is therefore to show that the streamwise motion could also be recovered with an incoming laminar boundary layer. To investigate this streamwise motion, the interaction between a laminar boundary layer and an oblique shock has been studied using DNS.

2 Numerical Methods

In this study, Direct Numerical Simulations (DNS) of the interaction between an oblique shock wave and a laminar boundary layer have been performed using an in-house parallel (MPI) Finite-Volume based DNS/LES solver developed at LIMSI-CNRS [13]. A Monotonicity-Preserving shock-capturing scheme, based on the Lax-Wendroff method through a 7th order accurate coupled space and time approximation is used for the convective fluxes [3]. The diffusive fluxes are discretized by a second order centered scheme.

The incoming laminar boundary layer is modelled using a 4th order polynomial approximation of the Blasius profile, defined by $\frac{u(z)}{U_\infty} = \frac{z}{\delta_0}\left(2 - 2\left(\frac{z}{\delta_0}\right)^2 + \left(\frac{z}{\delta_0}\right)^3\right)$ where z is the wall-normal direction and δ_0 the boundary layer thickness. This function has the advantage to verify the boundary conditions both for the velocity at the wall and outside the boundary layer, and for the first-order derivative at $z = \delta_0$ and for $z \to \infty$. The Rankine–Hugoniot relations are used to create an oblique shock at the inlet plane, which freestream Mach number and angle with respect to the horizontal plane fit the conditions from [8] and are respectively $M = 2.23$ and $\beta = 33.1°$. Finally, an adiabatic no-slip condition is applied on the lower boundary at the solid wall. The Reynolds number based on the inlet boundary layer thickness is chosen to be $Re = 1,800$ for the 2D case and $Re = 1,000$ for the 3D simulations.

3 Results

2D simulations have first been conducted. The computational domain is discretised using $M = 1000 \times 252$ cells and extends over $D = 500\delta_0 \times 200\delta_0$. In the wall-normal direction, a 3% geometrical stretching is applied in order to save CPU time without spoiling the space order of the scheme. An instantaneous field of the numerical schlieren is represented in Fig. 1 and clearly underlines the shock-induced separation of the laminar boundary layer and the subsequent recirculation bubble.

A qualitative comparison between these results and the reference studies shows that every aspects of such interactions are recovered. The incident shock, the reflected shock, the expansion fan and the reattachment shock are obvious, forming a very

Fig. 1 Instantaneous contours of the numerical schlieren from a 2D simulations

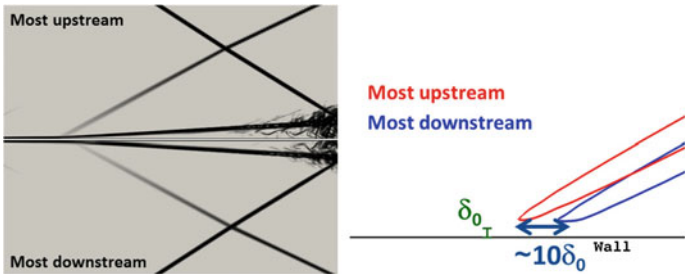

Fig. 2 Comparison of the most upstream and most downstream locations of the reflected shock, obtained for two different timesteps and revealed by contours of the numerical schlieren (*left*) and of the divergence of the velocity (*right*)

complex shock system. It is noteworthy that because of the laminar aspect of the incoming boundary layer, the extent of the recirculation zone is overestimated in the present simulations with respect to other numerical investigations, performed for a turbulent boundary layer. In addition, it can be seen in Fig. 2 that the reflected shock is submitted to an oscillatory motion that spreads over several δ. This observation, though in qualitative agreement with results from [12], is also overestimated since Selig et. al. noted that the shock moved for only around one inlet boundary layer thickness. This quantitative discrepency could be partially explained by the laminar aspect of the boundary layer but some further investigations are in progress in order to conclude. However, these slight discrepencies should not minimise the fact that an oscillatory motion is found even with 2D simulations of a laminar boundary layer, that tends to prove that it is not solely due to the incoming turbulent structures.

3D simulations have then be performed in order to show that the oscillatory motion that have been found in 2D simulations is not an artefact due to the lack of the third component. The analysis of the numerical schlieren (not shown in this paper) clearly shows that the reflected shock is subjected to a streamwise motion. However, no oscillations have been found and the reflected shock is just moving upstream.

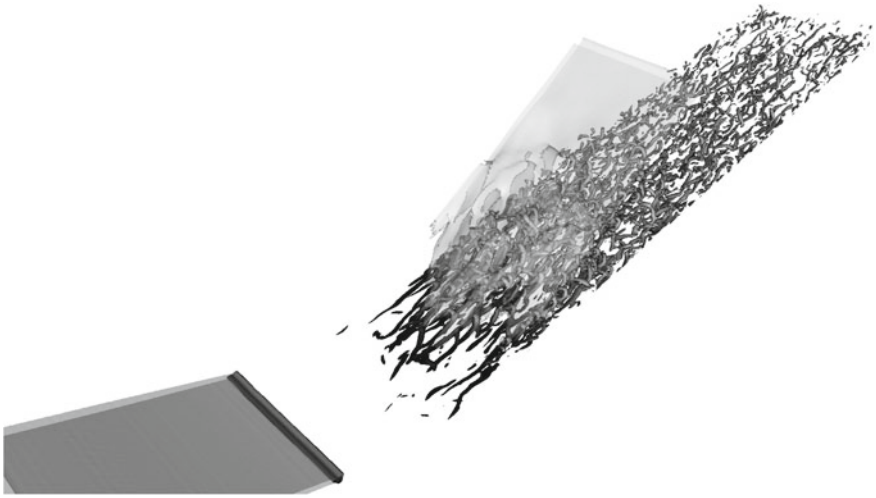

Fig. 3 Vortical structures in the interaction region, represented by Q criterion isosurfaces and coloured with the streamwise velocity (Low velocities are in *black* while the high velocities are in light *gray*). The shock system (*translucent gray*) is made visible by isosurfaces of the divergence of the velocity

The isosurfaces of the Q-criterion, coloured by the streamwise velocity are shown in Fig. 3. Isosurfaces of the divergence of the velocity are used to reveal the shock system (in light gray). Despite the 2D aspect of the inlet boundary layer, due to its laminar nature, a fully three-dimensional flow can be observed. The shock impinging the boundary layer leads to the creation of a highly three-dimensional separation bubble. The separation is first laminar and no vortical structures are observed. Then, the shear layer becomes unstable and the transition to turbulence occurs. This transition takes place just a few boundary layer thicknesses upstream of the reattachment point, as emphasised by the dark colour of the vortical structures, corresponding to low velocities. Once the boundary layer is reattached, they are elongated by the reacceleration occuring through the boundary layer and eventually evolve into large hairpin vortices, typical of wall-bounded turbulent flows.

This shedding is however very irregular. As shown in Fig. 4, the vortical structures are not uniformly shed over the span but it takes place at different locations at different timesteps, creating some spots with no structures. Those no-vorticity spots are clearly recovered on the time evolutions of the spanwise velocity for two probes, located in the vicinity of the reattachment point, at midspan and 20% of the span (Fig. 5). At mid span, three occurences of these spots can be seen. Two very large spots can be found for $t\frac{U_\infty}{\delta_0} \in [0; 200]$ and $t\frac{U_\infty}{\delta_0} \in [800 : 1000]$. In those cases, the spots seem to be limited to the midspan since the signal at the 20%-span location does not exhibit any peculiar behaviour and therefore correspond to the configuration represented in Fig. 4-Left. On the other hand, the shedding cases of Figs. 4-Center and 4-Right are found either for $t\frac{U_\infty}{\delta_0} \sim 1100$ or $t\frac{U_\infty}{\delta_0} \sim 2500$. In addition to the

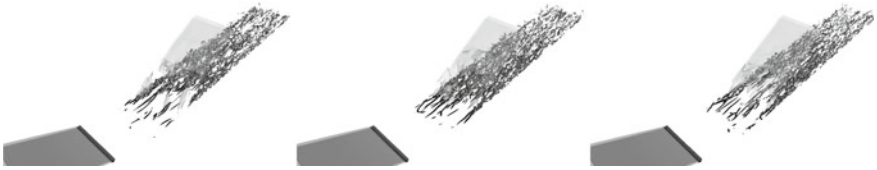

Fig. 4 Vortical structures for three different timesteps. *Left* Vortices shed only on the sides. *Centeri* Vortices shed only on the left part. *Right* Vortices only shed at midspan

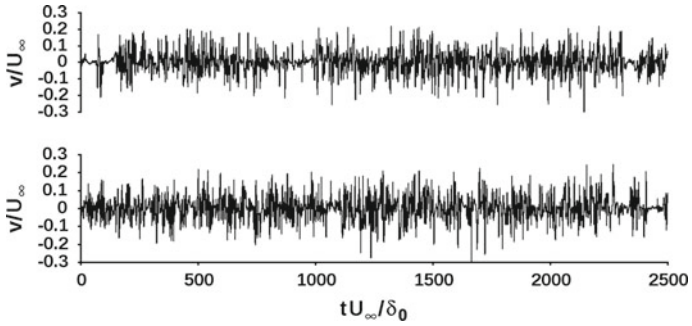

Fig. 5 Time history of the spanwise velocity for two probes located at midspan (*Top*) and at 20% of the span (*Bottom*)

large shedding frequency, the signals exhibit at least two more frequencies. The first one corresponds to no-vortices spots passing around the probe while the other one is more likely related to the oscillations of the reattachment shock. Spectral analysis is currently in progress to precisely define those frequency and to find a more physical insight.

4 Conclusions

DNS have been performed in the case of the interaction between an oblique shock and a laminar boundary layer developing along a flat plate. The aim was to determine whether the oscillation motion of the separation bubble and the reflected shock is related to the turbulent aspect of inlet boundary layer or if it can happen even in for a laminar boundary layer. The preliminary 2D simulations have found that streamwise oscillations are recovered for the reflected shock. These promising preliminary results leaded us to perform 3D simulations. Up to date, no oscillations have yet been recovered with these simulations. The reflected shock has been shown to move upstream but no clear frequency has been found. Investigations are under way to see if the fact that the oscillations do not occur in the 3D case can be related to the different Reynolds numbers in 2D and 3D. The 3D simulations have however highlighted another interesting phenomenon. Even if the transition occurs in the

shear layer just upstream of the reattachment point, the vortex shedding is not uniform after the boundary layer reattaches. Instead, some no-vorticity spots are created that highly increase the three-dimensionality of the flow and therefore increases the non-uniformity of the stresses.

Acknowledgements This work has been performed using HPC resources from GENCI-IDRIS, France (Grant 2015-i20152a7195).

References

1. Agostini, L., Larchevêque, L., Dupont, P., Debiève, J.-F., Dussauge, J.-P.: Zones of influence and shock motion in a shock/boundary-layer interaction. AIAA J. **50** (2012)
2. Aubard, G., Gloerfelt, X., Robinet, J.-C.: Large-Eddy simulation of broadband unsteadiness in a shock/boundary-layer interaction. AIAA J. **51** (2013)
3. Daru, V., Tenaud, C.: High order one-step monotonicity preserving schemes for unsteady flow calculations. J. Comp. Phys. **193** (2004)
4. Fang, J., Yao, Y., Li, Z., Lu, L.: Investigation of low-dissipation monotonicity-preserving scheme for direct numerical simulation of compressible turbulent flows. Comput. Fluids **104** (2014)
5. Ganapathisubramani, B., Clemens, N.T., Dolling, D.S.: Effects of upstream boundary layer on the unsteadiness of shock-induced separation. J. Fluid Mech. **585** (2007)
6. Garnier, E.: Stimulated detached eddy simulation of three-dimensional shock/boundary layer interaction. Shock Waves **19** (2009)
7. Grilli, M., Schmid, P. J., Hickel, S., Adams, N. A.: Analysis of unsteady behaviour in shockwave turbulent boundary layer interaction. J. Fluid Mech. **700** (2012)
8. Pirozzoli, S., Grasso, F.: Direct numerical simulation of impinging shock wave/turbulent boundary layer interaction at M=2.25. Phys. Fluids **18** (2006)
9. Priebe, S., Martín, M. P.: Low-frequency unsteadiness in shock wave-turbulent boundary layer interaction. J. Fluid Mech. **699** (2012)
10. Robinet, J. C.: Bifurcations in shock-wave/laminar-boundary-layer interaction: global instability approach. J. Fluid Mech. **579** (2007)
11. Sansica, A., Sandham, N.D., Hu., Z.: Forced response of a laminar shock-induced separation bubble. Phys. Fluids **26** (2014)
12. Selig, M. S., Andreopoulos, J., Muck, K. C., Dussauge, J.-P., Smits, A. J.: Turbulence structure in a shock wave/turbulent boundary-layer interaction. AIAA J. **27** (1989)
13. Tenaud, C., Fraigneau, Y., Daru, V.: Numerical simulation of the turbulent separation reattachment flow around a thick flat plate. J. Phys. Conf. Ser. **318** (2011)
14. Touber, E., Sandham, N. D.: Large-eddy simulation of low-frequency unsteadiness in a turbulent shock-induced separation bubble. Theor. Comp. Fluid Dyn. **23** (2009)
15. Wu, M., Martín, M. P.: Analysis of shock motion in shockwave and turbulent boundary layer interaction using direct numerical simulation data. J. Fluid Mech. **594** (2008)

Secondary Instability and Subcritical Transition in the Leading-Edge Boundary Layer

M.O. John, D. Obrist and L. Kleiser

1 Introduction

The leading-edge boundary-layer (LEBL) flow is found in the front part of swept airplane wings where the flow is subject to strong acceleration. It is prone to subcritical instability [1–4], i.e., transition may regularly be observed even though the flow is stable according to linear stability theory. Understanding this instability is particularly important to avoid turbulent flow emanating from the front part of swept wings, which might contaminate large portions of the wing chord downstream [5].

The transition Reynolds number $Re_{\mathrm{tr}} \approx 250$ is known from experiments [5] and DNS [6]. However, a theoretical explanation for this value or for the causes of transition are still missing, but are required for transition prediction, flow control and drag reduction. Recent findings [3, 7] suggest that a vortex/shear-layer configuration is a cause for secondary modal instability and subsequent bypass transition if a pronounced high-speed streak (HSS) is located at the attachment line. This transition scenario is analogous to a self-sustained instability process known from two-dimensional flat-plate boundary layers [8].

In this paper we demonstrate that a low-speed streak (LSS) of comparable amplitude is not able to trigger this bypass transition. We carry out direct numerical simulations (DNS) of the swept Hiemenz boundary layer (SHBL) with HSS and with LSS disturbances of finite amplitude to investigate the influence on flow transition. The remainder of this paper is structured as follows: In Sect. 2 the baseflow and the

M.O. John (✉) · L. Kleiser
Institute of Fluid Dynamics, ETH Zurich, 8092 Zurich, Switzerland
e-mail: john@ifd.mavt.ethz.ch

L. Kleiser
e-mail: kleiser@ifd.mavt.ethz.ch

D. Obrist
ARTORG Center, University of Bern, 3010 Bern, Switzerland

D.G.E. Grigoriadis et al. (eds.), *Direct and Large-Eddy Simulation X*,
ERCOFTAC Series 24, https://doi.org/10.1007/978-3-319-63212-4_42

primary disturbance types are introduced. Section 3 explains the secondary perturbation and numerical methods and Sect. 4 reports the transition behavior for the various disturbance types. Section 5 concludes this paper.

2 Baseflow and Primary Disturbance

In the present work, the LEBL is modeled by the SHBL past a flat plate. The Reynolds number is $Re = W_\infty/\sqrt{\nu a}$ [5], where W_∞ is the far-field sweep velocity in the z-direction, a the far-field strain rate in the chordwise x-direction and ν the kinematic viscosity (cf. Fig. 1).

The wall-normal similarity coordinate is $\eta = \sqrt{a/\nu} \cdot y$ and the flow field reads

$$u = x \cdot f'(\eta)/Re \qquad v = -f(\eta)/Re \qquad w = g(\eta),$$

where f and g are the solutions of the equations

$$f''' + ff'' - f'^2 + 1 = 0 \qquad g'' + fg' = 0,$$

subject to the boundary conditions $f(0) = f'(0) = g(0) = 0$, $f'(\eta \to \infty) = g(\eta \to \infty) = 1$.

This SHBL is disturbed with steady, counterrotating streamwise vortices next to the attachment line as a primary disturbance. These vortices advect baseflow shear and lead to streaks (cf. Fig. 2). Three different primary disturbances are investigated [9]: Either, two counter-rotating vortices which propel high-speed fluid from the far-field towards the attachment line, leading to a pronounced HSS above the attachment line (cf. Fig. 2). Or, the sense of rotation of the counter-rotating vortices is inverted, leading to a pronounced LSS at the attachment line. Or, three streamwise counter-rotating vortices are investigated with one localized above the attachment line and two vortices adjacent to it on either side, leading to a HSS and a LSS on either side of the attachment line. All three disturbance types are steady and decay slowly in the streamwise direction (cf. Fig. 2) for the linearly subcritical Reynolds numbers that we are investigating here, $Re < Re_c \approx 583$ [10].

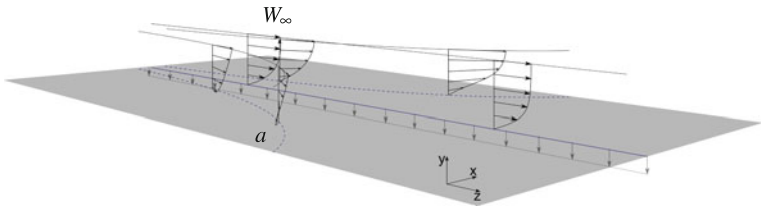

Fig. 1 The SHBL baseflow with coordinate system

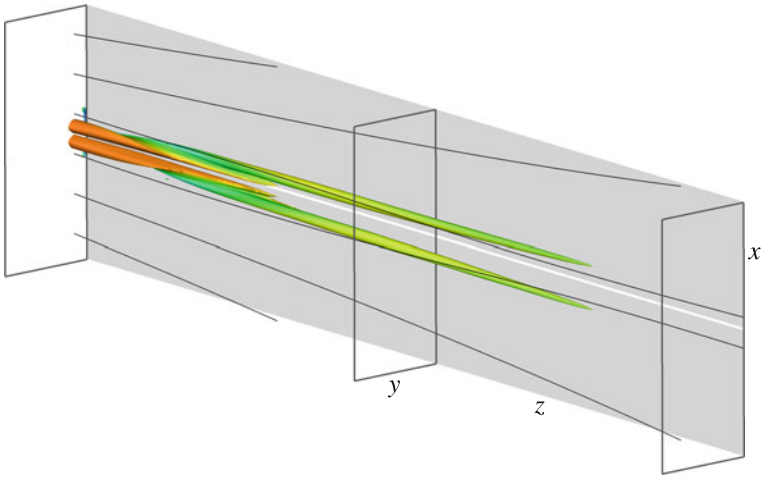

Fig. 2 Illustration of a SHBL flow disturbed by a pair of primary vortices illustrated by λ_2 isosurfaces, leading to a high-speed streak. $Re = 250$

3 Secondary Perturbation and Instability

All three primary disturbances (streamwise vortices) are perturbed with an additional weak, time-dependent secondary perturbation to trigger instability and bypass transition. To this end, a weak oscillation of small amplitude A_2 is superimposed onto the primary vortex amplitude $|A_1|$ at some secondary disturbance frequency ω_2 [3, 11]. The amplitude of this secondary disturbance is very small ($A_2/A_1 \approx 10^{-3}$). For a given primary vortex amplitude A_1, this secondary perturbation may lead to instability and transition, depending in particular on Re and ω_2 [3, 7, 11].

We employ two different techniques to study the evolving instability and the subsequent subcritical transition. First, direct numerical simulations (DNS) of the disturbed flow evolution are carried out. Second, a secondary temporal linear stability analysis is carried out. Details are reported in [7, 9].

3.1 Numerical Methods

Following [3, 4], we perform DNS of incompressible flow using our in-house code IMPACT [12]. The Navier–Stokes equations are discretized in all three spatial directions by sixth-order finite differences on a stretched Cartesian grid. The time integration is semi-implicit (explicit Runge–Kutta scheme for nonlinear terms, Crank–Nicolson for linear terms). A typical domain size is $L_x \times L_y \times L_z = 75 \times 30 \times 600$ discretized with $N_x \times N_y \times N_z \approx 750 \times 150 \times 3000$ grid points. The SHBL solution is set as initial condition in the entire computational domain. The SHBL

together with the disturbances at the inflow plane $z = 0$ and the exact SHBL solution at the top inflow plane $y = L_y$ are prescribed as Dirichlet boundary conditions. At the remaining three open boundaries we prescribe advective outflow conditions for the velocity disturbances (i.e. deviations from the SHBL) in the direction normal to the boundary [9].

4 Transition Behavior

The first and the third configuration, each containing a HSS, are found to be unstable to small secondary, unsteady disturbances at Reynolds numbers far below Re_c. For a pure HSS disturbance, exponentially growing secondary modes and subsequent bypass transition to turbulence are observed [3, 7, 9]. The modes emerge from the

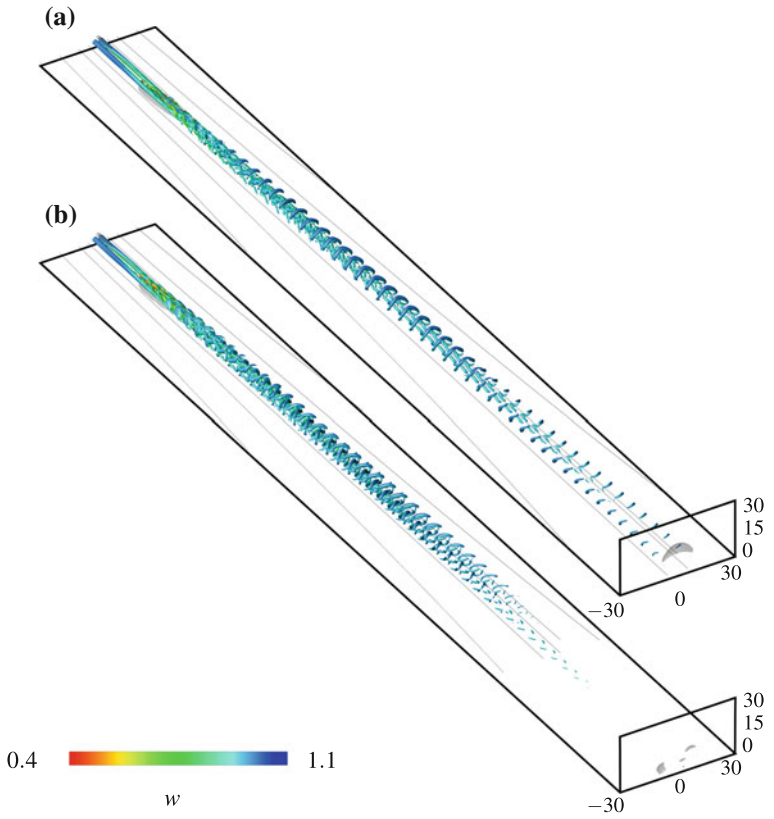

Fig. 3 Secondary **a** symmetric and **b** antisymmetric disturbances in the LSS configuration, visualized with λ_2 vortices (isosurfaces $\lambda_2 = -3 \cdot 10^{-3}$), *colored* by the local streamwise velocity component $w(x, y, z)$, $Re = 500$, primary amplitude $A_1 = -0.10$, secondary frequency $\omega_2 \approx 0.63$

shear layers surrounding the vortices at Reynolds numbers as low as $Re = 200$. Transition to turbulent flow is observed above $Re_{\mathrm{tr}} \approx 250$ [7], which coincides well with the experimentally known value [5].

To the contrary, no transition to turbulent flow is observed for the second configuration (LSS at the attachment line) for comparable disturbance amplitudes, even at the substantially higher Reynolds number $Re = 500$. Even though secondary flow structures are observed, they do not grow exponentially and decay quickly without leading to breakdown. This holds both for symmetric (varicose) and antisymmetric (sinuous) disturbances (cf. Fig. 3). The LSS configuration is substantially less prone to secondary instability than the corresponding HSS configuration.

The third, combined HSS/LSS case confirms this behavior. It reveals an instability emerging from the HSS side (cf. Fig. 4). Farther downstream this instability spreads to the opposing LSS side as well.

An additional temporal stability analysis of the HSS [7, 9] confirms the existence of unstable eigenmodes in the shear layers surrounding the vortices found in our DNS. The upper branch of the secondary neutral curve illustrates unstable eigenmodes at Reynolds numbers as low as $Re = 175$. Their geometrical shape, the growth rate and frequency dependence are in good agreement with the DNS results.

For the pure LSS case, on the other hand, no exponentially growing secondary eigenmodes were found by linear stability analysis [9].

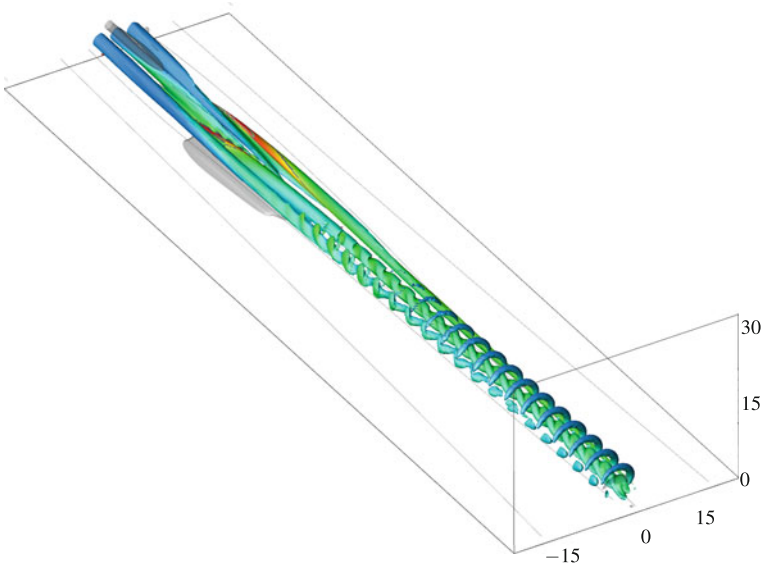

Fig. 4 Secondary instability in the mixed HSS/LSS configuration, illustrated by λ_2 vortices, *colored* by the local streamwise velocity component $w(x, y, z)$ (see Fig. 3), $Re = 400$, $A_1 = 0.10$, $\omega_2 \approx 1.26$. Surfaces of constant pressure are illustrated in gray

5 Summary and Conclusions

We investigated the secondary stability of various finite-amplitude primary disturbances of the swept Hiemenz boundary layer (SHBL). The flow is prone to a secondary modal instability at Reynolds numbers as low as $Re \approx 175$ which may lead to transition to fully turbulent flow at values as low as $Re \approx 250$. This instability is observed when the SHBL is disturbed with a pair of counter-rotating vortices that lead to a dominant high-speed streak (HSS). A secondary linear stability analysis confirms the existence of these modes.

When the sense of rotation of these primary vortices is inverted, leading to a pronounced low-speed streak (LSS) at the attachment line, no such secondary modal instability could be observed, even at higher subcritical Reynolds numbers. Accordingly, no unstable eigenmodes could be found by secondary linear stability analysis of the LSS disturbance configuration.

We conclude that the secondary instability of the SHBL, subject to a dominant HSS disturbance, may serve as a model explaining the experimentally observed subcritical transition in the LEBL. Furthermore, the LSS configuration is substantially less prone to secondary instability than the corresponding HSS configuration and is not expected to lead to turbulent flow.

References

1. Pfenninger, W.: Special Course on Concepts for Drag Reduction. Laminar Flow Control. Laminarization, NATO-AGARD, Technical Report 654, (1977)
2. Arnal, D., Juillen, J.C., Reneaux, J., Gasparian, G.: Effect of wall suction on leading edge contamination. Aerosp. Sci. Technol. **1**(8), 505–517 (1997). doi:10.1016/S1270-9638(97)90000-6
3. Obrist, D., Henniger, R., Kleiser, L.: Subcritical spatial transition of swept Hiemenz flow. Int. J. Heat Fluid Flow **35**, 61–67 (2012). doi:10.1016/j.ijheatfluidflow.2012.01.012
4. John, M.O., Obrist, D., Kleiser, L.: Stabilization of subcritical bypass transition in the leading-edge boundary layer by suction. J. Turbul. **15**(11), 795–805 (2014). doi:10.1080/14685248.2014.933226
5. Poll, D.I.A.: Transition in the infinite swept attachment line boundary layer. Aeronaut. Q. **30**, 607–629 (1979)
6. Spalart, P.R.: Direct numerical study of leading-edge contamination. In: NATO-AGARD, Conference Proceedings, 438 (1988)
7. John, M.O., Obrist, D., Kleiser, L.: Secondary instability and subcritical transition of the leading-edge boundary layer. J. Fluid Mech. **792**, 682–711 (2016). doi:10.1017/jfm.2016.117
8. Waleffe, F.: On a self-sustaining process in shear flows. Phys. Fluids **9**(4), 883–900 (1997). doi:10.1063/1.869185
9. John, M. O.: Stability of homogeneous flat-plate boundary layers and attachment-line transition, Dissertation no. 22316, ETH Zurich (2014). doi:10.3929/ethz-a-010345115
10. Hall, P., Malik, M.R., Poll, D.I.A.: On the stability of an infinite swept attachment line boundary layer. Proc. R. Soc. Lond. A Math. **395**(1809), 229–245 (1984)
11. John, M.O., Obrist, D., Kleiser, L.: A class of exact Navier-Stokes solutions for homogeneous flat-plate boundary layers and their linear stability. J. Fluid Mech. **752**, 462–484 (2014). doi:10.1017/jfm.2014.346

12. Henniger, R., Obrist, D., Kleiser, L.: High-order accurate solution of the incompressible Navier-Stokes equations on massively parallel computers. J. Comput. Phys. **229**(10), 3543–3572 (2010). doi:10.1016/j.jcp.2010.01.015

Part VII
Biological Flows

The Effect of Flow Rate and Electrostatic Charge on Aerosol Deposition in a Realistic Lung Geometry

P.G. Koullapis and S.C. Kassinos

1 Introduction

To be able to predict the fate of therapeutic or pollutant xenobiotic inhaled particles in the human lungs, we need to understand the nature of airflow as it occurs throughout the entire respiratory tract. Airflow in human lung airways may undergo different flow regimes in different airway segments: it may be laminar in the oral cavity, become transitional and turbulent after the constriction formed by the laryngeal glottis and eventually turn into laminar again after several generations in the bronchial tree because the local Reynolds number gradually decreases. Computational Fluid-Particle Dynamics (CFPD) techniques can be a valuable tool in understanding the airflow and particle deposition characteristics in the lungs. Most CFPD simulations rely on Reynolds Averaged Navier–Stokes (RANS) solutions because of the significantly lower computational cost [7]. Nowadays, Large Eddy Simulations (LES) and Direct Numerical Simulations (DNS) approaches have become affordable tools and are used more and more in research studies as they can track the instantaneous turbulent fluctuations [2, 6, 8].

An important parameter affecting both the airflow and particle transport is the inhalation flowrate. A higher flowrate causes earlier transition to turbulence in the upper airways with turbulent fluctuations in a wide range of length and time scales [3]. Turbulent fluctuations make aerosol particles move erratically and turbulent effects can be advected to several generations of the airway tree. Flow rates of 15, 30 and 60 l/min are considered to correspond to sedentary, light and heavy activity conditions [10].

P.G. Koullapis (✉) · S.C. Kassinos
Department of Mechanical and Manufacturing Engineering, Computational Sciences Laboratory, University of Cyprus, University Avenue 1, 2109 Nicosia, Cyprus
e-mail: koullapis.g.pantelis@ucy.ac.cy

S.C. Kassinos
e-mail: kassinos@ucy.ac.cy

D.G.E. Grigoriadis et al. (eds.), *Direct and Large-Eddy Simulation X*,
ERCOFTAC Series 24, https://doi.org/10.1007/978-3-319-63212-4_43

A second important determinant of deposition is the electrostatic charge carried by inhaled particles. Charge carried by particles can enhance the deposition in the lung considerably [11]. This is not desirable for drugs intended for systemic uptake, which must pass into the blood through the alveolar epithelium, but might be desirable for maximising the drug dose in certain upper regions of the airway tree or even leveraged for the removal of pollutant particles using charge effects [1]. Medical devices often generate electrostatically charged aerosols [5] but even environmental aerosols may have significant charge levels.

The aim of this study is to quantitatively assess the distinct effects of inhalation flowrate and aerosol charge on particle deposition enhancement in a realistic geometry of the human respiratory system using LES and Euler–Lagrangian approach.

2 Airway Geometry

The physical domain in which flow is simulated can be simplified by representing the airways as a network of smooth circular cylinders [9]. Recent advancements in medical imaging have afforded us detailed views of the complex structures of the lung, especially of the conducting airways. The geometry considered in this study, shown in Fig. 1, is reconstructed from Multi-detector Computed Tomography scans and it represents a non-smoking 20 year old female. Geometrical (cross-sectional areas and hydraulic diameters) and flow (average velocities and Reynolds numbers) properties on the cross-sections of interest can be found in [4].

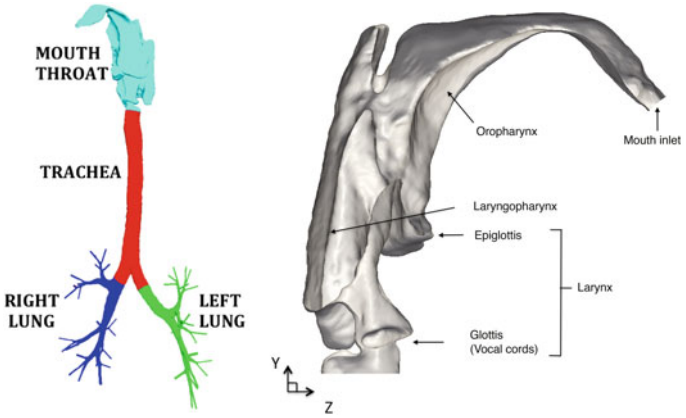

Fig. 1 Realistic human airway tree geometry (resolution limitations restrict further CT-reconstruction of lower airway generations) [2]. *Left* Full geometry and sub-regions. *Right* Inside oblique view of the upper airways

3 Numerical Methods

We are employing LES with a dynamic Smagorinsky subgrid scale model in order to solve the filtered set of incompressible Navier–Stokes equations in OpenFOAM (Open Source CFD toolbox). Uniform velocity at the inlet and zero pressure at the outlets were set as boundary conditions [7]. The discretization of the equations is done using the finite volume method and second order discretization schemes. The PISO algorithm is employed for the treatment of the pressure-velocity system.

Spherical, rigid and non rotating particles are introduced at the mouth inlet. At each time step, the flow equations are solved first and then the motion of each particle is individually computed (Lagrangian approach) by integrating Newton's equations using an implicit Euler scheme. The forces acting on each particle include drag ($\mathbf{F}_D$), gravity ($\mathbf{F}_G$), Brownian ($\mathbf{F}_B$) and electrostatic image charge forces ($\mathbf{F}_{image}$). Brownian force is important for particles with diameter less than 1 μm while image charge force is an attractive force experienced by a particle with a charge q near a conducting wall (Coulomb's law). A particle is considered deposited if the shortest distance from the center of the particle to the airway wall is less than the particle radius. One-way coupling is taken into account.

4 Results - Flow Field

In this section, we show the effect of inhalation rate (15.2, 30, 60 l/min) on the characteristics of the flow field. Figure 2 shows the contours, secondary component vectors as well as the velocity profiles in black at the lines of intersection of the cut-planes of normalised mean velocities. For the sake of brevity results are shown for the flowrates of 15.2 and 30 l/min (moderate differences between the cases of 30 and 60 l/min).

Mean flow structures are qualitatively similar for the three flowrates regardless of Reynolds number. The normalized mean velocity initially exhibits a high speed jet in the oral region and then decelerates when passing through the wide and curved passage of the oropharynx and the laryngopharynx. The jet entering the oral cavity causes a recirculation zone close to the anterior wall. The laryngeal jet is formed starting slightly upstream of the glottis due to the constricted cross-sectional area and it impinges on the tracheal front wall. This jetting effect creates a large recirculation zone near the dorsal wall of the upper trachea. Asymmetric counter-rotating secondary motions are generated as we move downstream in the trachea (slices B and C), which agrees with experimental observations [3]. Further downstream, the jet is dispersed and the secondary motions are weakened.

Figure 3 shows the contours of normalised turbulent kinetic energy (TKE) in a vertical and three horizontal cut-planes. TKE in the oral region rises rapidly after the constriction due to the soft palate. The location of maximum TKE in this region depends on the Reynolds number. Further downstream in the oropharynx and laryn-

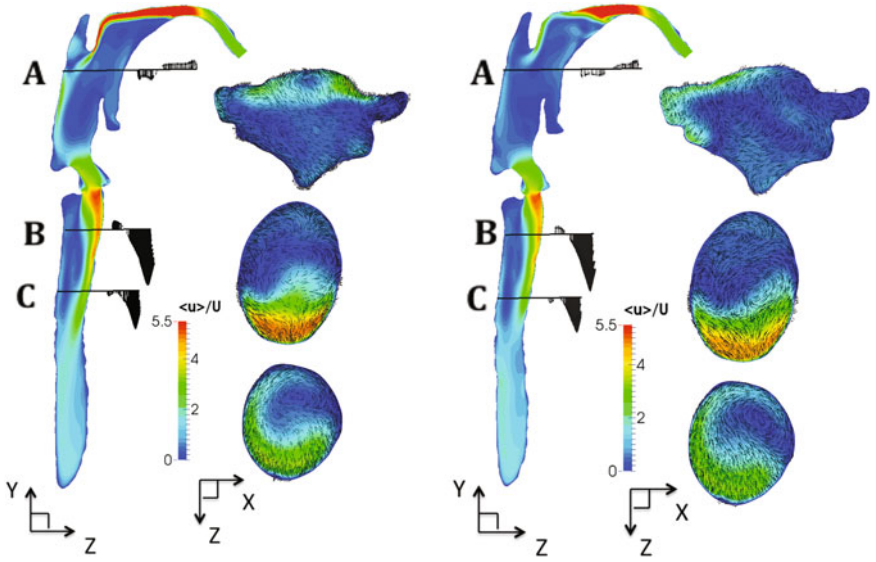

Fig. 2 Contours and vectors of normalised mean velocity. *Left* $\dot{Q} = 15.2$ l/min. *Right* $\dot{Q} = 30$ l/min

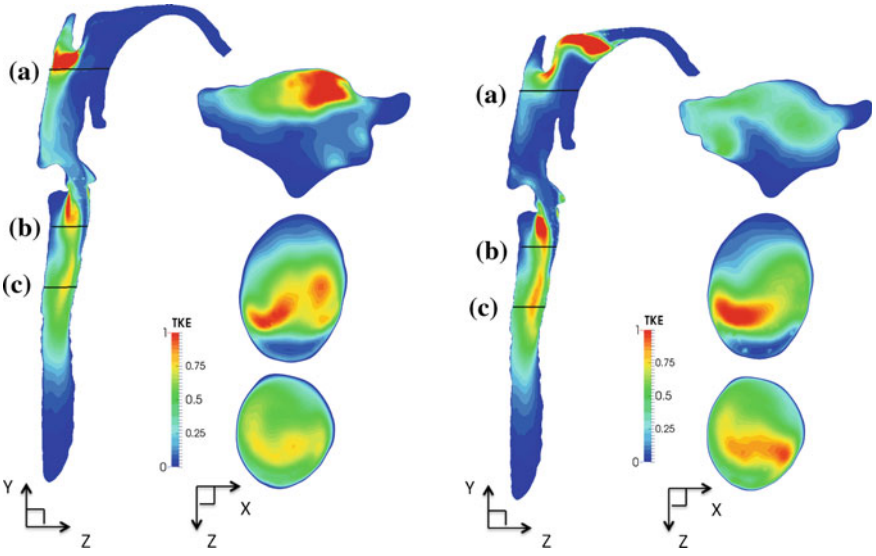

Fig. 3 Contours of normalised TKE. *Left* $\dot{Q} = 15.2$ l/min. *Right* $\dot{Q} = 30$ l/min

gopharynx, TKE is suppressed due to the increased flow cross section, but it is augmented again by the glottis constriction. A high TKE region is found at the mixing layer between the cavity-like flow in the recirculation zone and the free stream velocity. A second region of high TKE in the trachea is located near the end of the jet core and is attributable to the transition of the jet to turbulence. These two regions extend in greater areas as Reynolds number is increased. TKE is reduced as we move further downstream to the lower part of the trachea.

5 Results - Particle Transport and Deposition

In this section, simulation results for the effects of flowrate and particle charge on aerosol transport and deposition are discussed. The particle sizes considered are: 0.1, 0.5, 1, 2.5, 5 and 10 μm. The level of charge on particles depends on the size and physical properties of these aerosols (larger particles can hold more charge). In the current study five charge levels, i.e. 0, 50, 250, 500 and 1000 elementary charges (e) were considered. These charge levels are below the Rayleigh charge limit, which is the maximum amount of charge a liquid droplet can carry.

Figure 4 presents the overall Deposition Fractions (DF) of particles as a function of the particle charge at the three flow rates considered. Independently of the flowrate and the charge level, almost all of the 10 μm particles are deposited in the upper airways of the mouth. The deposition hot spots for these particles are the curvatures of the mouth-throat region. Due to their high inertia, larger particles deviate from the fluid streamlines and impact at the curved airway walls in the mouth region.

The effect of flowrate is more pronounced on the deposition of 2.5 and 5 μm diameter particles. Increasing the flowrate from 15.2 to 30 l/min augments the overall DF of 5 μm particles by approximately 40%, while for 2.5 μm particles, increasing the flow rate from 15.2 to 60 lt/ min causes a rise in DF of about 70%. As the flow rate is increased, electrostatic precipitation becomes negligible and inertial impaction is the dominant deposition mechanism for these particle sizes. Most of deposition enhancement occurs in the mouth throat region. Considerable deposition also occurs on the sidewalls of the larynx and the upper trachea.

0.1, 0.5 and 1 μm particles without charge have similar DF at a given flow rate, while DF is slightly increased as the flow rate is increased. The effect of charge is more important as the particle size is decreased: the overall DF of 0.1 μm with 1000 elementary charges at a flow rate of 15 l/min is approximately 7 times greater than that with no charge. The impact of charge is reduced as the particle size is increased. For all particles sizes, most of the deposition enhancement due to electrostatic charge occurs in the mouth-throat region. The distribution of deposition enhancement in this region is mostly uniform and results from the large residence times in the oropharynx and the laryngopharynx, due to both low velocities and recirculation regions. Similar enhancement in deposition is observed at the three flow rates as the charge level of particles is increased, indicating a relatively small impact of flow rate on the deposition of charged particles with sizes ranging from 0.1 to 1 μm.

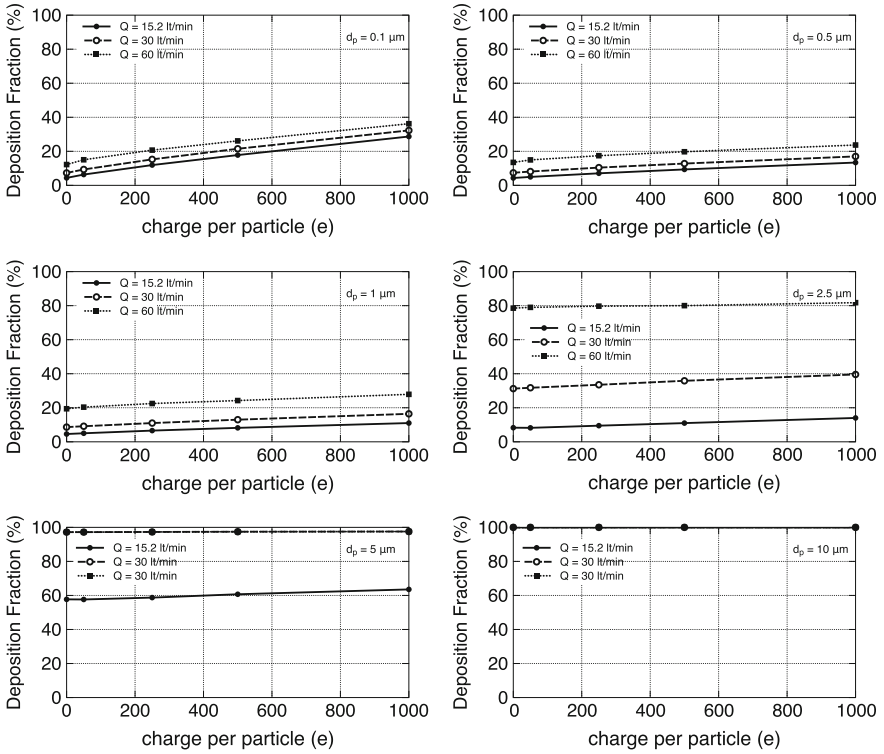

Fig. 4 Overall DF of particles as a function of the electrostatic charge at various flowrates

6 Conclusions

LES were used to investigate the transport and deposition of inhaled aerosol particles carrying electrostatic charge in a CT-scan derived geometry of the human lungs under three steady inhalation flowrates. The mean flow structures at the three flowrates are found to be qualitatively similar regardless of Reynolds number. The DF of particles is increased with flowrate due to greater inertial impaction. The effect of flowrate is more pronounced on the deposition of 2.5 and 5 μm diameter particles. The effect of charge is more significant for smaller particles; the overall DF of 0.1 μm with 1000 elementary charges at a flow rate of 15.2 l/min is approximately 7 times greater than that with no charge. The impact of inhalation flow rate on the deposition of charged particles is negligible for smaller particles (0.1–1 μm), while in the case of 2.5 and 5 μm diameter particles inertial impaction prevails over electrostatic deposition mechanism.

Acknowledgements The present study was funded by the European Union 7th framework program HEXACOMM FP7/2007–2013 under grant agreement *N*° 315760.

References

1. Ali, M., Reddy, R.N., Mazumder, M.K.: Electrostatic charge effect on respirable aerosol particle deposition in a cadaver based throat cast replica. J. Electrost. **66**, 401–406 (2008)
2. Choi, J., Tawhai, M.H., Hoffman, E.A., Lin, C.-L.: On intra- and intersubject variabilities of airflow in the human lungs. Phys. Fluids **21**, 101901 (2009)
3. Johnstone, A., Uddin, M., Pollard, A., Heenan, A., Finlay, W.H.: The flow inside an idealised form of the human extra-thoracic airway. Exp. Fluids **37**, 673–689 (2004)
4. Koullapis, P.G., Kassinos, S.C., Lin, C.-L.: Computational fluid dynamic simulations of aerosol deposition in the lungs. In: 9th Symposium on Turbulence and Shear Flow Phenomena (TSFP-9), The University of Melbourne, Australia, 2015
5. Kwok, P.C.L., Chan, H.K.: Electrostatics of pharmaceutical inhalation aerosols. Aerosol Sci. Technol. **61**, 1587–1599 (2009)
6. Lin, C.-L., Tawhai, M.H., McLennan, G., Hoffman, E.A.: Characteristics of the turbulent laryngeal jet and its effect on airflow in the human intra-thoracic airways. Respir. Physiol. Neurobiol. **157**, 295–309 (2007)
7. Luo, H.Y., Liu, Y.: Modeling the bifurcating flow in a CT-scanned human lung airway. J. Biomech. **41**(12), 2681–2688 (2008)
8. Radhakrishnan, H., Kassinos, S.: CFD modeling of turbulent flow and particle deposition in human lungs. In: 31st Annual International Conference of the IEEE EMBS Mineapoolis, Minnesota, USA, 2009
9. Weibel.: Morphometry of the Human Lung. Springer, Berlin (1965)
10. Xi, J., Longest, W.: Transport and deposition of micro-aerosols in realistic and simplified models of the oral airway. Ann. Biomed. Eng. **35**, 560–581 (2007)
11. Yu, C.P.: Theories of electrostatic lung deposition of inhaled aerosols. Ann. Occup. Hyg. **29**, 219–227 (1985)

Particle-Laden Flow in a Physiologically Realistic Human Airway Bifurcation

F.S. Stylianou and S.C. Kassinos

1 Introduction

Predicting regional deposition patterns of inhaled aerosols is important for the design and optimization of pharmaceutical formulations. Variabilities in the respiratory tracts of patients complicate the efforts to understand patterns of regional deposition and point towards the need for patient-specific airflow analysis. In this regard, computer simulations can be used to predict regional deposition, thus helping in the development of targeted inhalation therapies that are customized, if not to individuals, at least to classes of patients. Such computations need to be affordable for use in routine medical evaluations of patients. Direct Numerical Simulations (DNS) are computationally too demanding for routine use, while Large Eddy Simulations (LES) are now becoming barely affordable. Thus, for routine computations the emphasis remains on modeling approaches, such as Reynolds-Averaged Navier–Stokes (RANS) closures. Nevertheless, DNS and LES can be used to elucidate the regional flow characteristics in the conducting airways, thus helping to ensure that RANS computations are properly tuned to capture the most important flow features.

The upper airways are composed of building blocks that can be represented by idealized geometries in benchmark studies, e.g. straight and bend pipes, tubular constrictions and expansions, and bifurcations. For most of the aforementioned building blocks, RANS models can be validated, and if necessary tuned, using turbulent benchmark data in the scientific literature. The bifurcation geometry is an exception. In this study we perform LES and DNS of fully developed turbulent flow through a human airway bifurcation, emulating steady prolonged inspiration and expiration

F.S. Stylianou (✉) · S.C. Kassinos (✉)
Department of Mechanical and Manufacturing Engineering, Computational Sciences Laboratory (UCY-CompSci), University of Cyprus, University Avenue 1, 2109 Nicosia, Cyprus
e-mail: stylianou.fotos@ucy.ac.cy

S.C. Kassinos
e-mail: kassinos@ucy.ac.cy

D.G.E. Grigoriadis et al. (eds.), *Direct and Large-Eddy Simulation X*,
ERCOFTAC Series 24, https://doi.org/10.1007/978-3-319-63212-4_44

conditions. We examine the flow characteristics and the vortical structures formed at laminar and turbulent Reynolds numbers. We report particle deposition patterns and deposition efficiencies for representative Stokes numbers.

2 Geometry and Computational Details

We consider fully developed turbulent flow in a human airway bifurcation. Distinct geometries are used to simulate steady prolonged inspiration and expiration conditions (Fig. 1). The construction of the geometries is based on the Physiologically Realistic Bifurcation model of Heistracher and Hofmann [3] with the exception of the carinal ridge region. The geometric parameters correspond to the airway generations G3-G4 in the model of Weibel [5] (for more detail see Table 1 of [4]).

To achieve fully developed turbulent inlet profiles (for the DNS/LES) we use the recycling boundary conditions at the corresponding entries of the flow. To avoid upstream effects from the bifurcation and the outlet regions, the lengths of the parent and daughter branches (L_p and L_d) are extended from the original values given by Weibel (L_p^W and L_d^W). For the laminar simulations we use parabolic inlet profiles.

For the DNS/LES the Reynolds number, based on the local bulk velocities (u_b^p, u_b^d) and the local pipe diameters ($D_p = 2R_p$, $D_d = 2R_d$), at the parent branch is $Re_b^p = 8517.86$ and at the daughter branches is $Re_b^d = 5300$. These Reynolds numbers are 5–10 times larger than what is expected at the G3-G4 airway generations for inhalation flow rates of 30–60 l/min. For the laminar simulations the values of the Reynolds numbers are 5 times lower with respect to the DNS/LES.

We have employed a multiblock unstructured hexahedral mesh with prismatic grid patches at the bifurcation point to increase the density of the mesh as we move from the low to the high Reynolds number region (see Fig. 2 of [4]). The mesh densities

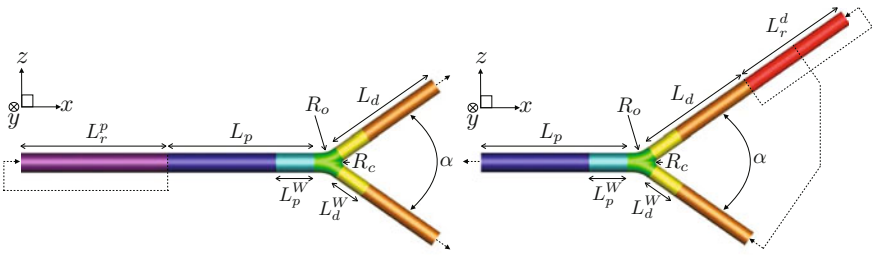

Fig. 1 Computational geometries for steady inspiration (*left*) and steady expiration (*right*). Recycled-inlet and convective-outlet boundary conditions are illustrated with *dotted arrows*. Only the DNS geometries are shown. For the LES, the lengths of the parent L_p and daughter branches L_d are twice larger. For the laminar simulations the recycling segments are discarded, the inlet sections are reduced to the original values given by Weibel, and the outlet sections are reduced to 2/3 of the respective DNS lengths

at the straight pipe sections are given in Table 2 of [4]. The total number of control volumes for the LES simulations is 9.56/8.42 million for the inspiration/expiration geometry. Almost one level of refinement of the LES mesh leads to the DNS mesh with 46.0/37.2 million control volumes for the inspiration/expiration geometry (note that the DNS geometries are shorter than the LES geometries). For the laminar simulation we use almost the same mesh density with the LES, which leads to 2.61/2.90 million control volumes for the inspiration/expiration geometries (note that the Laminar geometries are even shorter than the DNS geometries).

3 Eulerian Fluid Flow

In this section, we compare the results from our DNS, LES, and laminar simulations. It is evident from Fig. 2 that the LES results (based on the Dynamic Smagorinsky model) are in excellent agreement with the DNS results. The shape of the in-plane averaged velocity streamlines are almost identical. For the inspiration condition two symmetric, counter rotating, axially oriented secondary vortices are formed at each daughter branch, while for the expiration condition four secondary vortices are formed at the parent branch; note that for each of the aforementioned vortex-systems only one vortex is captured in the cross-sections shown. These secondary vortices (refer to as *Dean vortices*) are present even in the laminar regime, their formation being due to centrifugal effects. Dean secondary vortices are formed whenever a straight geometry starts to curve (for flow in a curved pipe see [1, 2]). As the flow moves away from the pipe merging region, curvature effects will no longer con-

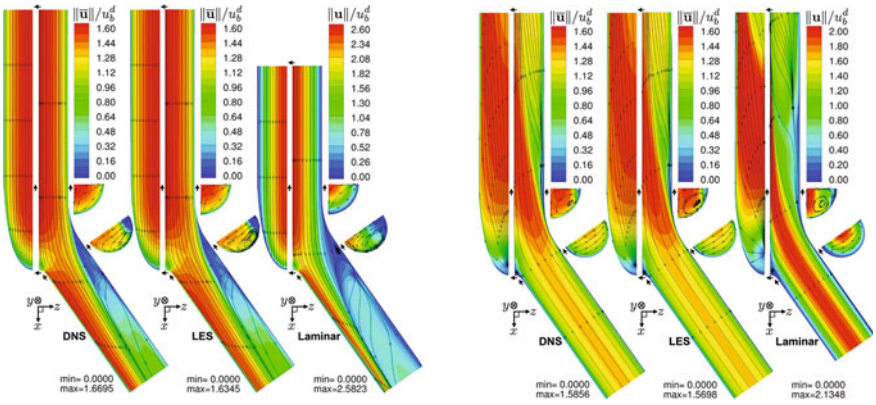

Fig. 2 Four different slices of a small part (slightly greater than Weibel's regime) of one quarter of the inspiration and expiration geometries. Contour plots of the averaged velocity magnitude from DNS/LES and velocity magnitude from laminar simulations under steady inspiration (*left*) and expiration (*right*) conditions. The minimum and maximum values of each contour field are given. The streamlines are constructed from the in-plane velocities of each slice

tribute to the secondary motion and will eventually dissipate. For the inspiration case a stagnation point is formed at the head of carina. This forces the incoming flow from the parent branch to split into the two daughter branches. The maximum velocity is deflected away from the center and towards the inner walls of the daughter branches. In the outer walls of the daughter branches velocity is very small, while at the same time there is a short region with backflow (see also the 3D streamlines in Figs. 3 and 4). The backflow region is formed just after the incoming flow from the parent branch separates from the outer wall of the daughter branches. In the backflow region of the laminar flow there is an extra recirculation feature that is not present in the turbulent flow. For the expiration case a high pressure point is formed in front of the carina head. This forces the incoming flow that is traveling close to the inner walls of the daughter branches to form two small vortices at the head of carina; note that only one is shown (see also the 3D streamlines in Figs. 3 and 4). The rest of the incoming flow from the daughter branches merges at the center of the parent branch. It is evident that the secondary flow field in the bifurcation domain is a result of the bifurcation curvature and of the carinal ridge shape.

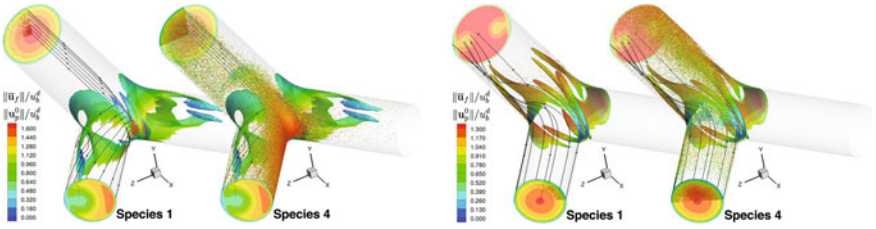

Fig. 3 From the DNS simulations, initial release locations and final deposition locations of particles from Species 1 and 4 under steady inspiration (*left*) and expiration (*right*) conditions. Only the Weibel's regime is shown. The slices, *colored* with the mean fluid velocity magnitude, represent the inlet and outlet locations of Weibel's geometry. Particles are *colored* by their initial velocity magnitude (obtained from the instantaneous fluid velocity at the time and location of release). Only the particles that stuck in the Weibel's regime and had initial release location with $y_p^0 \geq 0$ and $z_p^0 \geq 0$ are shown. For these particles their initial and final locations are illustrated. The iso-surfaces of the mean flow vortical structures, identified with the Q-criterion, are colored with the mean fluid velocity magnitude. Representative streamlines based on the mean velocity vector field are shown

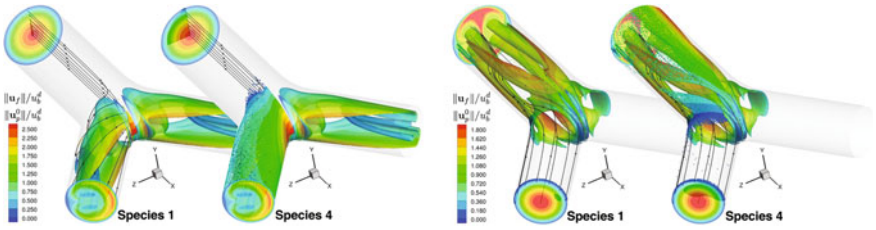

Fig. 4 From the Laminar simulations, initial release locations and final deposition locations of particles from Species 1 and 4 under steady inspiration (*left*) and expiration (*right*) conditions. Same as in Fig. 3, but using steady state velocities instead of instantaneous and mean velocities

4 Lagrangian Particle Dispersion

In the bronchial airways, carinal ridges of airway bifurcations are primary hot spots for deposition of inhaled particles. Particulate suspensions inhaled by humans are typically dilute and hence the effect of dispersed particles on the carrier fluid, as well as the interactions between particles, can be ignored. We use DNS to capture all small and large scale flow features that directly affect the motion of particles. The unsteadiness of turbulent conditions demands the time advancement of flow and particle motions to be carried at the same time. For the laminar cases the particles are advanced using the steady state velocity field.

The dispersed phase is simulated by a Lagrangian approach where particles are continuously released and tracked throughout the domain. The motion of each particle is governed by Newton's second law. As a first approximation, we have considered spherical rigid particles that experience only the drag force. We approximate the bifurcation walls as sticky; a particle is deposited by the interception mechanism if its center of mass falls within a distance of one particle radius from the wall surface. For more details on the model used for the particle tracking see [4].

We have simulated particles of five different Stokes numbers with values smaller and larger than unity. For the turbulent simulations we have used the fixed particle to fluid density ratio $\rho_p/\rho_f = 750$. For the laminar simulation we have used five times greater density ratio $\rho_p/\rho_f = 3750$, in order to achieve the same Stokes numbers with the turbulent simulations. The variability of the Stokes numbers comes from the diameter of the particles d_p (see Table 1). During steady inspiration, the particles were released uniformly and randomly at a cross section normal to the flow direction located at the starting point of the parent pipe branch as defined in Weibel's model. Similarly, for the expiration condition the particles were released at the starting points of the daughter pipe branches as defined in Weibel's model. The initial velocity of a particle was chosen to be the same with the fluid velocity field at its location of release. The total number of particles released for each one of the five species considered and for each simulation (inspiration and expiration) is 0.5 million. Deposition fractions (DF) for the different particle species and flow conditions considered are summarized in Table 1.

Figures 3 and 4 illustrate the correlation between particle deposition sites and vortical structures. In the inspiration case, the carina region becomes the primary particle deposition site due to direct impaction. High speed incoming particles reaching the carina cannot turn to follow the local streamlines. For the heavier particles, at turbulent conditions, deposition takes place even at the straight parent branch due to the presence of ejections and sweeps. Increased deposition at the top and bottom walls of the carina are due to the contraction of geometry which blocks the incoming particles with high inertia. On the other hand, the regions where the side walls of the parent branch meet the diverging external side walls of the daughter branches correspond to particle-free areas. The deposition of heavier particles downstream of the carina, on the inner walls of the daughter branches, is due to a combination of direct impaction and centrifugal/drifting effects. In the expiration case, the carinal vortices

Table 1 Particle species (defer in diameter d_p) released and tracked in the bifurcation geometry. The Stokes numbers, St, span a range of smaller and larger values than unity. If our geometries are scaled based on the physical size of the airway generations G3-G4 (in the model of Weibel where $R_d^W = 2.25$ mm), the physical size of the particles, d_p^W, is in the range of μm. Deposition fractions (DF) for steady inspiration and expiration, under turbulent and laminar conditions are tabulated

Species	d_p^W [μm]	d_p [$\times 10^{-3}$ R_d]	$St = \frac{1}{9}\frac{\rho_p}{\rho_f}\frac{d_p^2}{D_d^2}Re_b^d$	Inspiration		Expiration	
				DF_{turb}[%]	DF_{lam}[%]	DF_{turb}[%]	DF_{lam}[%]
Species 1	2.0	0.88888	0.08724	0.83	1.99	2.07	3.55
Species 2	4.0	1.77777	0.34897	20.60	32.00	16.94	31.36
Species 3	6.0	2.66666	0.78519	53.53	58.27	29.14	46.32
Species 4	8.0	3.55555	1.39588	75.34	69.71	35.24	51.10
Species 5	10.0	4.44444	2.18107	87.70	76.70	38.94	54.18

drive low speed particles towards the wall and thus increase the deposition in this region. No deposition occurs on the side walls of the pipe merging region since local velocity tends to drift the particles away form these walls. For the heavier particles, at turbulent conditions, the deposition in the straight daughter sections is the result of sweeps and ejections. There is an increased deposition at the top wall, where the daughter branch starts to bend, because the local flow turns before the geometry starts to bend, drifting the particles towards the wall. The enhanced deposition at the top wall (towards $z < 0$ in the parent branch section) is due to the rotational sense of the Dean and carinal vortices that turn particles towards the wall. In the laminar case, the heavier particles form a distinct deposition-free band which is not present in the turbulent case. The streamlines reaching this region have a history of high curvature that high inertia particles can not follow.

5 Summary and Conclusions

We have performed DNS, LES, and Laminar simulations in a human airway bifurcation emulating steady inspiration and expiration conditions. Our simulations show that the predictions of the Dynamic Smagorinsky LES model are in very good agreement with the DNS results. The flow features at laminar and turbulent regime are similar. From the averaged DNS results we have observed the Dean vortices present also at the laminar level. Using Lagrangian particle tracking we have estimated the deposition fractions for five particle species (deferring in diameter). Preferential deposition sites have been identified and a correlation with the mean flow characteristics has been established at the turbulent and laminar regimes. Our results can be used as reference in modeling studies of particle laden flows in airway bifurcations.

References

1. Dean, W.R.: XVI. Note on the motion of fluid in a curved pipe. Lond. Edinb. Dublin Philos. Mag. J. Sci. **20**(4), 208–223 (1927)
2. Dean, W.R.: LXXII. The streamline motion of fluid in a curved pipe. Lond. Edinb. Dublin Philos. Mag. J. Sci. **30**(5), 673–695 (1928)
3. Heistracher, T., Hofmann, W.: Physiologically realistic models of bronchial airway bifurcations. J. Aerosol Sci. **26**(3), 497–509 (1995)
4. Stylianou, F.S., Kassinos, S.C.: Fully turbulent flow in a physiologically realistic human airway bifurcation. In: Proceedings of TSFP-9, Melbourne, Australia (2015)
5. Weibel, E.R.: Morphometry of the Human Lung. Springer, Berlin (1963). doi:10.1007/978-3-642-87553-3

Part VIII
Reacting Flows and Combustion

The Implementation of 5-D FGM for LES of a Gas Turbine Model Combustor with Heat Loss

A. Donini, R.J.M. Bastiaans, J.A. van Oijen and L.P.H. de Goey

1 Introduction

The interest in numerical simulation of combusting flows for industrial applications has gained a wide growth in the past decade. This applies particularly for applications for which experimental investigations are expensive because of their complexity, such as burners of gas turbines. Numerical simulation is foreseen to provide a great improvement in the design, efficiency and quality of gas turbine combustors over the coming future. However, the numerical simulation of stationary gas-turbine combustor is a very complex task. The interaction of turbulence, chemical reactions and thermodynamics in reactive flows is of phenomenal complexity. The direct simulation of the entire practical combustion system remains still prohibited, because of current and future limitations in computing power. This problem demands for an appropriate treatment in the combustion chemistry modeling, as well as the modeling of its interaction with turbulence. The Flamelet-Generated Manifold (FGM) [1] technique is adopted in this work. The modeling approach of FGM is based on the idea that the internal structure of the flame front must be taken into account. In this view, a low-dimensional chemical manifold is created on the basis of single-dimensional flame structures, including a good representation of all of the transport and chemical phenomena as observed in three-dimensional flames. The structure of the flame is described by transport equations for a limited number of control variables. In the present paper all the features that are typically observed in stationary gas-turbine combustion are included. These consist of stratification effects, heat loss to the walls and turbulence. Three control variables are included for the representation of the chemistry: the reaction evolution is described by the reaction progress variable, the heat loss is described by the enthalpy and the stratification effect is expressed by the mixture fraction. The interaction between chemistry and turbulence is considered

A. Donini (✉) · R.J.M. Bastiaans · J.A. van Oijen · L.P.H. de Goey
Eindhoven University of Technology, Eindhoven, The Netherlands
e-mail: andrea.donini@gmail.com

D.G.E. Grigoriadis et al. (eds.), *Direct and Large-Eddy Simulation X*,
ERCOFTAC Series 24, https://doi.org/10.1007/978-3-319-63212-4_45

through a presumed probability density function approach, which is considered for progress variable and mixture fraction. This results in two extra control variables: progress variable variance and mixture fraction variance. The resulting manifold is five-dimensional, in which the dimensions are progress variable, enthalpy, mixture fraction, progress variable variance and mixture fraction variance.

2 Flamelet Generated Manifolds - Five Dimensional Implementation

In this study, partially premixed methane/air combustion at atmospheric pressure conditions is considered. The progress variable $\mathscr{Y}$ is chosen to be a linear combination of species mass Y_i: $\mathscr{Y} = \sum_{i=1}^{N_s} \alpha_i Y_i$. The weighting factors α_i are chosen to be: $\alpha_{CO_2} = M_{CO_2}^{-1}$, $\alpha_{H_2} = M_{H_2}^{-1}$, $\alpha_{H_2O} = M_{H_2O}^{-1}$, $\alpha_{O_2} = -M_{O_2}^{-1}$ and $\alpha_i = 0 \; \forall \; i \notin \{CO_2, H_2, H_2O, O_2\}$. The enthalpy is not conserved throughout the domain [2, 3] because of the loss of heat towards the combustion chamber walls, and by means of radiation. Furthermore, fuel and oxidizer are not perfectly mixed. In order to take this into account in the tabulation process, the laminar flamelets have to be solved for different values of enthalpy h and mixture fraction Z, introducing these two as control variables. The procedure for the chemistry tabulation with enthalpy and mixture fraction inclusion follows the description given in [4]. Chemistry is represented by the GRI-Mech 3.0 reaction mechanism [5]. A unity Lewis number assumption is chosen during the calculation of the flamelets [6]. The turbulence-chemistry interaction is accounted for progress variable and mixture fraction by convolution of the laminar database using a β-function shaped PDF [7]. The integration operation generates an increase of two dimension in the manifold, which will finally reach the number of five dimensions. The final dimensions for the manifold are: progress variable $\widetilde{\mathscr{Y}}$, enthalpy $\widetilde{h}$, mixture fraction $\widetilde{Z}$, variance of progress variable $\widetilde{\mathscr{Y}''^2}$ and variance of mixture fraction $\widetilde{Z''^2}$. The chemistry data obtained by the tabulation procedure is rearranged through a coordinate transform, and the tabulated data is then directly retrievable as a function of the control variables. A generic overview of the outcoming manifold is shown in Fig. 1. Here, the progress variable source term is shown at the maximum level of enthalpy and zero variance of mixture fraction, as a function of the progress variable and equivalence ratio (i.e. mixture fraction, under the assumption of unity Lewis number), for different levels of variance of progress variable. The latter are given in transparency. The described database is gathered in memory and linked to the CFD code. Together with the momentum and continuity equations, the CFD code solves the conservation equations for the progress variable, enthalpy and mixture fraction [4] during runtime. For the progress variable variance calculation $\widetilde{\mathscr{Y}''^2}$ and of mixture fraction $\widetilde{Z''^2}$ a gradient-based model is used, as described in [2, 7].

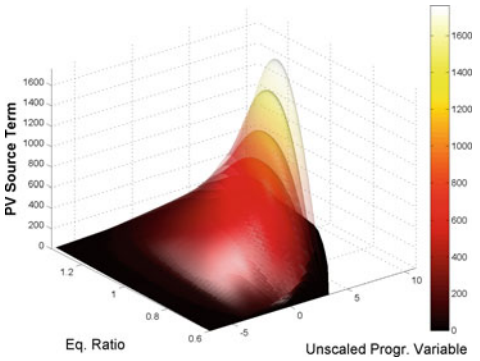

Fig. 1 Representation of the 5D manifold at the highest enthalpy level and zero variance of mixture fraction. The surfaces show the progress variable source term [$\mathrm{kg\,m^{-3}s^{-1}}$] profile as a function of unscaled progress variable and equivalence ratio, at different levels of variance of the progress variable, shown with different transparencies

3 Test-Case Geometry, Scales and Numerical Methods

In this section the test case is described: a highly turbulent and swirling flame in a gas turbine model combustor which is simulated by means of 5-D FGM. The gas-turbine test combustor, which was extensively studied by means of experiments e.g. in [8, 9], is schematically displayed in Fig. 2 (left). Dry air at room temperature and atmospheric pressure is fed to the combustion chamber by means of two concentric co-swirling nozzles. The central nozzle has a diameter of 15 mm, the annular nozzle has an inner diameter of 17 mm and outer diameter of 25 mm, with an outer exit diameter of 40 mm. Non-swirling methane is fed through a non-swirled annular inlet, radially located between the air swirlers. The combustion chamber downstream the nozzle consists of a square section measuring 85 × 85 mm with a height of 114 mm. The exit plane of the fuel and central air nozzle is positioned 4.5 mm below the outer air nozzle plane of exit. The latter is defined as reference plane $\mathscr{H} = 0$. The outlet is formed by a conical top plate with a central exhaust tube (diameter 40 mm, length 50 mm). The operating condition is characterized by the following global parameters: air mass flow rate $\dot{m}_{air} = 0.01825\,\mathrm{kg\,s^{-1}}$, fuel mass flow rate $\dot{m}_{fuel} = 0.696\,\mathrm{g\,s^{-1}}$, thermal power $P_{th} = 34.9\,\mathrm{kW}$, global equivalence ratio $\phi_{global} = 0.65$ and global adiabatic flame temperature $T_{ad,global} = 1750\,\mathrm{K}$. The ratio of split between air mass passing through the annular and central nozzle is roughly 1.5. The swirl number is $S = 0.9$, calculated from the experimental velocity profile above the nozzle exit. Heat loss to the walls is imposed by enforcing a temperature $T_w = 800\,\mathrm{K}$ to the walls. The solver used for the simulations is Ansys-CFX 14.5 [10], coupled with the above described five-dimensional FGM implementation. A custom framework for the FGM coupling has been created for the solver. This includes a table upload to the parallel stack memory and an efficient data retrieval with multi-dimensional interpolation, with an automatic management of the boundaries of the

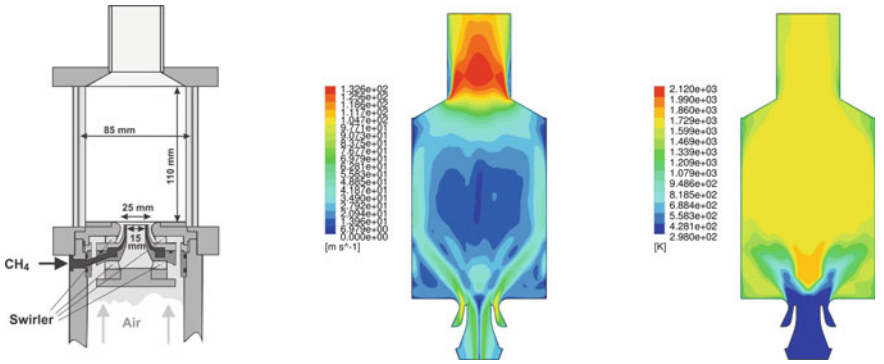

Fig. 2 *Left* schematic representation of the gas turbine model combustor geometry. *Center* view of the time-averaged velocity magnitude at a central section plane [m s^{-1}]. *Right* averaged temperature at a central section plane [K]

tabulated data. The approach used for turbulence is LES with Smagorinsky sub-grid scale model. The algorithm of the software is implicit and pressure-based, and the solver makes use of a conservative finite-element-based control volume method. The solver chosen for the computations of this work is incompressible. For the progress and control variable transport equations the turbulent Schmidt number is considered to be constant and equal to $Sc_T = 0.7$. The mesh is composed of 9 400 000 hexahedral/tetrahedral elements over 6 300 000 nodes, with the characteristic of an adequate refinement on the inlet ducts and flame zone.

4 Test Results

Figure 2 (center) displays the averaged velocity field in the combustor. The inlet gas stream develops a cone-shaped flow which reaches to the outer wall. Centrally over the nozzle an inner recirculation zone (IRZ) opposes to the inlet gas stream, and an outer recirculation zone (ORZ) appears externally to the nozzle at the dump plane edges. The effects of the rotating motion creates a vortex tube along the centerline of the combustor, which begins in the IRZ and extends to the outlet. This is in accordance with the experimental observations [8, 9]. Figure 2 (right) displays the averaged temperature field in the combustor. The temperature of the outer recirculation zone is in good agreement with the experimental data. In this region the temperature is highly influenced by the heat loss to the wall. A comparison between the profiles of transient averaged velocity (axial and radial components) and temperature from the experimental data and LES is given in Fig. 3. The results are compared at five probe lines in the domain, which are located on the midplane at different distances from the reference plane, as described at the side of each plot. As commonly observed in highly swirled flows, the sudden radial expansion of the velocity field right after the nozzle

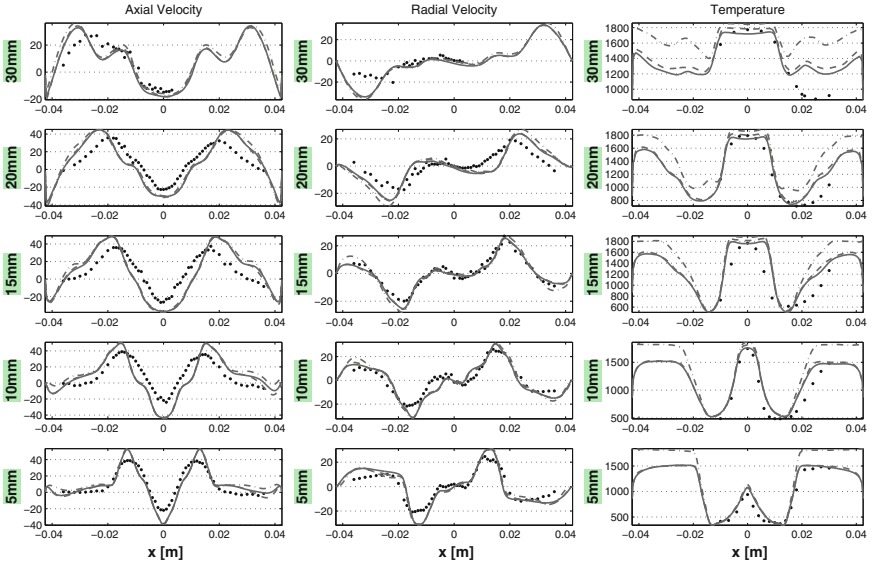

Fig. 3 Averaged results comparison along *central lines* located at different axial distances from the nozzle. **a** Axial velocity [$\mathrm{m\,s^{-1}}$]. **b** Tangential velocity [$\mathrm{m\,s^{-1}}$]. **c** Temperature [K]. The *solid lines* represent the results obtained with the full model, the *dashed lines* are results obtained omitting radiative heat loss, the *dashed-dotted lines* represent results omitting both radiative and wall heat loss, while the *black dots* the averaged experimental data. The coordinate x here refers to the radial direction

exit generates a pressure gradient. This pressure gradient causes the formation of the IRZ, which serves as flame stabilization mechanism. Overall, the present formulation reproduces satisfactorily the mean flow-field, as well as the averaged temperature profiles. It is clearly noticeable how in the IRZ the fast mixing leads to averaged temperatures which are consistent with the burned value of laminar premixed flames at $\phi = \phi_{global}$.

5 Conclusions

The well established FGM combustion model is progressively developed for the inclusion of all the combustion features that are generally found in stationary gas-turbine combustion. These consist of stratification effects, heat loss and turbulence. A highly turbulent and swirling flame in a gas turbine combustion chamber is computed by means of the present FGM implementation coupled to an LES turbulence model, and the results are compared with experimental data. In general, the model has demonstrated a very good agreement with experimental data. It is shown that the inclusion of heat loss greatly improves the temperature predictions in the whole

burner and leads to slightly better velocity predictions at downstream positions. This model sets the basis for the simulation and development of current and future gas turbine burners at high power conditions, for the alternative fuel usage in a cleaner and more efficient combustion.

Acknowledgements The authors would like to express their gratitude to Wolfgang Meier, for providing the test data. The financial support of the Dutch Technology Foundation (STW), Siemens Power Generation and Rolls-Royce Deutschland by means of the ALTAS project is gratefully acknowledged.

References

1. van Oijen, J.A., de Goey, L.P.H.: Modelling of premixed laminar flames using flamelet-generated manifolds. Combust. Sci. Technol. **161**(1), 113–137 (2000)
2. Donini, A., Martin, S.M., Bastiaans, R.J.M., van Oijen, J.A., de Goey, L.P.H.: Numerical simulations of a premixed turbulent confined jet using the flamelet generated manifold approach with heat loss inclusion. In: Proceedings of the ASME Turbo Expo, GT2013-94363 (2013). doi:10.1115/GT2013-94363
3. Donini, A., Martin, S.M., Bastiaans, R.J.M., van Oijen, J.A., de Goey, L.P.H.: High pressure jet flame numerical analysis of CO emissions by means of the flamelet generated manifolds technique. AIP Conf. Proc. **1558**, 136 (2013). doi:10.1063/1.4825439
4. A. Donini, Advanced Turbulent Combustion Modeling for Gas Turbine Application. Technische Universiteit Eindhoven, (2014) ISBN:978-90-386-3619-1
5. Smith, G.P., Golden, D.M., Frenklach, M., Moriarty, N.W., Eiteneer, B., Goldenberg, M., Bowman, C.T., Hanson, R.K., Song, S., Gardiner, W.C., Lissianski, V.V., Qin, Z.: GRI-Mech 3.0. http://www.me.berkeley.edu/gri_mech/
6. Peters, N.: Reducing mechanisms. Reduced Kinetic Mechanisms and Asymptotic Approximations for Methane-Air Flames, pp. 48–67. Springer, Berlin (1991)
7. Vreman, A., van Oijen, J.A., de Goey, L.P.H., Bastiaans, R.J.M.: Subgrid scale modeling in large-eddy simulation of turbulent combustion using premixed flamelet chemistry. Flow Turbul. Combust. **82**(4), 511–535 (2009)
8. Weigand, P., Meier, W., Duan, X.R., Stricker, W., Aigner, M.: Investigation of swirl flames in a gas turbine model combustor I. Flow-field, structures, temperature and species distributions. Combust. Flame **144**, 205–224 (2006)
9. Meier, W., Duan, X.R., Weigand, P.: Investigation of swirl flames in a gas turbine model combustor II: turbulence-chemistry interactions. Combust. Flame **144**, 225–236 (2006)
10. Ansys CFX Software, General Purpose Fluid Dynamics Program. http://www.ansys.com

LES-IB Study of Mixing Enhancement by Polygonal Orifices and Wavy Walls

A. Tyliszczak, M. Ksiezyk and Bernard J. Geurts

1 Introduction

Control of mixing in turbulent flow may lead to considerable improvement of efficiency, safety and performance of various technological devices. In so-called passive control methods, shapes of control elements (bluff-bodies, swirlers, etc.) are often a result of trial-and-error based on geometrical modifications.

In the present study we apply passive control to enhance mixing of fuel issuing from a pipe into a hot co-flowing stream. Near the outlet of the pipe plates with polygonal orifices are mounted. The role of these objects is to intensify mixing of large and small scales which potentially will lead to better mixing characteristics between the fuel and co-flow downstream of the pipe exit. We confront the gain in the mixing efficiency inside the pipe with the power required to keep the assumed flow rate. Next we focus on the mixing characteristics downstream the pipe. In particular we look at what happens with the flame as function of the orifice shape.

The research is performed using the LES (Large Eddy Simulation) approach combined with the IB (Immersed Boundary) method. The advantage of the IB method over the classical approach with body-fitted meshes is that flow problems can be solved on Cartesian grids and the objects immersed in the flow domain may be of arbitrary complexity as there is no need to create the mesh around it. The combustion

A. Tyliszczak (✉) · M. Ksiezyk
Department of Mechanical Engineering and Computer Science, Czestochowa University of Technology, Al. Armii Krajowej 21, 42-201 Czestochowa, Poland
e-mail: atyl@imc.pcz.pl

M. Ksiezyk
e-mail: mksiezyk@imc.pcz.pl

B.J. Geurts
Multiscale Modelling and Simulation, University of Twente, Box 217, 7500 AE Enschede, The Netherlands
e-mail: b.j.geurts@utwente.nl

D.G.E. Grigoriadis et al. (eds.), *Direct and Large-Eddy Simulation X*,
ERCOFTAC Series 24, https://doi.org/10.1007/978-3-319-63212-4_46

process is modelled applying the CMC (Conditional Moment Closure) model which allows for analysis of very complex physical phenomena, including auto-iginition and flame lifting which occur in the present study.

2 Modelling and Computational Setup

Governing equations and implementation issues of the LES-CMC approach, together with the solution procedure applied in the present study may be found in [4, 5]. We use an academic LES solver called SAILOR which was previously validated in various studies including wall bounded flows, jet flows and flames [5]. The Navier-Stokes and continuity equations are discretized using a 6th order compact difference method for half-staggered meshes [6]. In the equation for the mixture fraction 5th order WENO (Weighted Essentially Non-Oscillatory) and 6th order compact schemes are used for the convection and diffusion terms, respectively. The time integration employs the Adams-Bashforth / Adams-Moulton predictor-corrector method. Resolutions are such that near-DNS accuracy is achieved.

The CMC equations were solved applying the operator splitting approach where the transport in physical space, transport in mixture fraction space and chemistry are solved separately. The convective terms were discretized using the 2nd order TVD (Total Variation Diminishing) method with van Leer limiters. The diffusive terms were discretised using the central finite difference scheme. The hydrogen chemistry was modelled with the detailed mechanism of Mueller et al. [3] with 9 species and 19 reactions.

The IB method is implemented according to a direct forcing approach [2] which involves adding a source term to the Navier-Stokes equations. Its role is to act on a fluid in such a way as if there were a solid object immersed in the flow domain.

Figure 1 presents the computational configuration used in this study. It corresponds closely to the so-called Cabra flame [1]. The fuel jet is a mixture of hydrogen and nitrogen with molar fraction $X_{H_2} = 0.254$, $X_{N_2} = 0.746$. The fuel temperature is 305K, the mean velocity at the nozzle exit is equal to $U = 107$m/s, and the noz-

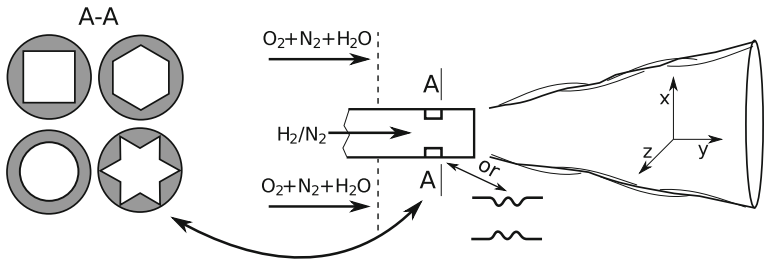

Fig. 1 Schematic view of the test case geometry with shown schematically wavy wall and plates with various orifices (*circle*, *square*, *hexagram*, *hexagon*)

zle diameter is $D = 4.57$mm. The co-flow consists of oxygen $X_{O_2} = 0.147$, water $X_{H_2O} = 0.1$ and nitrogen $X_{N_2} = 0.753$. Its temperature and velocity are equal to $T_c = 1045\text{K}\pm30\text{K}$ and $U_c = 3.5$m/s. We use the geometry and flow conditions of the Cabra flame as reference case which we modify by mounting plates with polygonal orifices or wavy wall upstream of the exit section of the pipe. The shapes of these orifices (circle, square, hexagram, hexagon) are shown in Fig. 1. The length of the plates is taken equal to $L = 0.2D$ and a blockage ratio, i.e., *(Cross-section area of the orifice)/(Cross-section area of the pipe)* to 0.5 for all orifices is used. The length of the wavy wall is $1D$, its shape corresponds to two periods of the sinus function with the amplitude giving the blockage ratio 0.5.

3 Passive Control over Mixing and Combustion

The solution procedure consists of two parts. In the first part the flows inside the pipes is computed as separate problem without considering the flow downstream of the pipes. A time varying velocity component obtained from these simulations is used in the second part of the simulations as the inlet boundary conditions. The velocity signal was extracted from the unsteady 3D results at the cross-section A-A located near the end of the orifices, as shown in Fig. 1, or at the end of the wavy wall.

The simulations were performed at Reynolds numbers equal to $\text{Re} = 1000$ and $\text{Re} = 23{,}600$, with Re defined based on the pipe diameter and inlet velocity. The computations for $\text{Re} = 1000$ were performed to assess accuracy of the applied IB method while the case with $\text{Re} = 23{,}600$ corresponds to the Cabra configuration. It was found that for $\text{Re} = 23{,}600$ the impact of the shape of the orifice is much smaller than at $\text{Re} = 1000$. The flow structures downstream the orifices were very complex, but the velocity contours at a distance of $2D$ behind the plates showed only limited dependence on the orifice shape.

Accuracy of the IB method was verified in test computations performed for two simple orifices, i.e., a circle and a square. As reference results we used the solution obtained with the ANSYS Fluent package and a body-fitted mesh. The dimensions of the computational domain were $6D$ in the axial direction (y) and $1.1D \times 1.1D$ in the perpendicular directions (x, z). Note that in the rectangular domain we not only model the orifices using the IB method but also the walls of the pipe. For the SAILOR code two Cartesian meshes were used with $192 \times 160 \times 160$ and $320 \times 160 \times 160$ nodes compacted axially in the vicinity of the orifices. In the computations performed with Fluent the mesh was matched to the orifices. It consisted of 2.5×10^6 nodes to reach a solution that is quite grid-independent.

Isosurfaces and contours of the instantaneous streamwise velocity obtained in simulations using the IB method at $\text{Re} = 1000$ are presented in Fig. 2. It can be seen that for the circular orifice the flow is ‘smooth’ up to the end of the domain and the only effect of the orifice is a local narrowing of the main stream. The flow through the square orifice is more complex. Behind the corners of the orifice four recirculation regions develop with negative velocities. Close to the outflow elongated structures

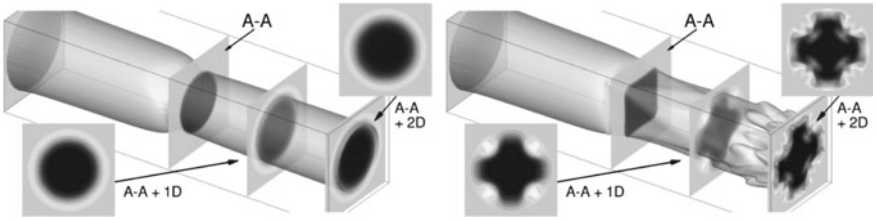

Fig. 2 Isosurface $0.5U$ of instantaneous streamwise velocity and the cross-sections showing its contours ($-0.5U \div 2.5U$) downstream the orifices. Results for circular (*left* figure) and square (*right* figure) orifices with Re = 1000

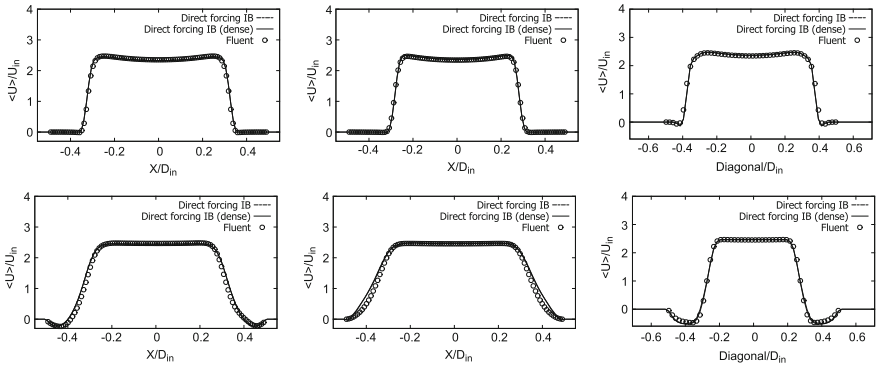

Fig. 3 Profiles of the axial velocity at Re = 1000, for the circular (*left* column) and square orifices (the central and *right* column). *Upper row* location at the A-A cross-section. *Bottom row* $1D$ downstream

form in the corners. In the center of the pipe the flow resembles as if it were issuing from the orifice with a cross shape.

Figure 3 shows profiles of the streamwise velocity at locations corresponding to the end of the plate (upper figures) and also $1D$ downstream (bottom figures). The results for the circular orifice (figures on the left) are presented along the x-direction only while for the square orifice the results are presented along the x-direction (figures in the centre) and along the diagonal direction (figures on the right). The results agree very well with the reference solution. The influence of the mesh density is very small.

The simulations for Re = 23,600 were performed using a mesh with $320 \times 160 \times 160$ nodes. The length of the velocity signals recorded as input boundary data for subsequent simulations was equal to $50D/U$. Figure 4 shows the evolution of the pressure drop along the centerline of the pipe and turbulent kinetic energy $TKE(y)$ integrated over cross-section planes Ω along the pipe with $TKE(y) = \int (u^2_{\mathrm{rms}} + v^2_{\mathrm{rms}} + w^2_{\mathrm{rms}}) \mathrm{d}\Omega$. The level of $TKE(y)$ is used here as indicator of mixing efficiency while the pressure drop is related to the power required to drive the flow at the assumed flow rate. The location of the orifices and wavy wall are also shown in Fig. 4. It is seen that except for the wavy wall the results are quite similar. The largest

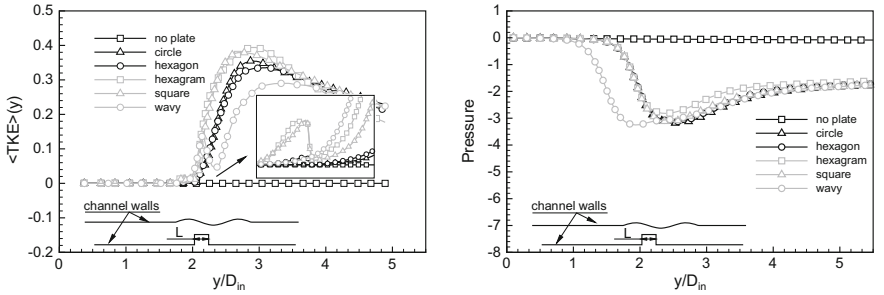

Fig. 4 Profiles of TKE and pressure along the axial direction for Re = 23600

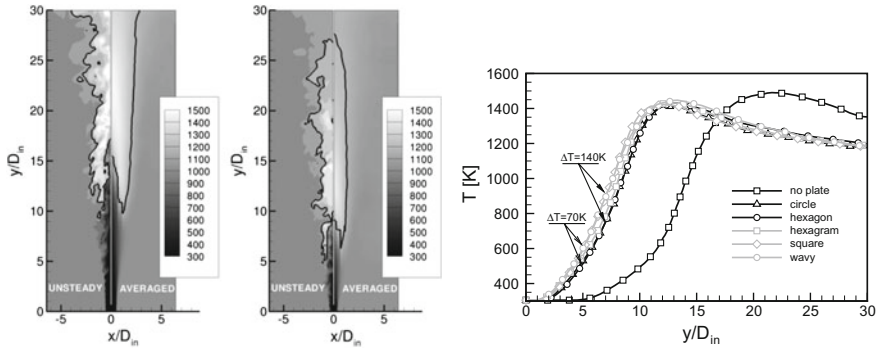

Fig. 5 Contours of instantaneous and time-averaged temperature in the main cross-section plane (two figures on the *left*) and the temperature distribution along the flame axis

$TKE(y)$ is obtained for the square and hexagram orifices. Taking into account that the hexagram orifice leads to the smallest pressure drop this shape seems to be the most efficient, although difference between orifices are small.

In the second part of the simulations combustion is included. The dimensions of the computational domain were increased to $30D \times 14D \times 14D$. The computational grids consisted of $256 \times 160 \times 160$ nodes for the Navier-Stokes equations and $60 \times 21 \times 21$ nodes for the CMC equations. In all analysed cases the flame developed in the domain according to the following scenario. The cold fuel issued from the pipe into the high temperature co-flowing stream and auto-ignited. Auto-ignition spots appeared at axial locations $y{>}20D$. Next, the flame quickly spread in the domain, propagated upstream and eventually stabilised a few diameters downstream the inlet. Sample results showing the contours of instantaneous and time-averaged temperature are presented in Fig. 5. These results were obtained for the original Cabra configuration (the left figure) and for the case with the hexagram orifice, where significant difference appear. In the original configuration the lift-off height of the flame (L_H) is approximately $10D$ while in the flame issuing from the hexagram orifice L_H is shortened by 50%. Here, L_H is measured as the distance from the inlet to

the point where the temperature exceeds the co-flow temperature by 1%. Surprisingly, neither the flame shape nor L_H are affected substantially by the type of orifice. This is confirmed by the temperature profiles along the flame axis shown in Fig. 5 on the right hand side. It can be seen that the maximum values are the same for all analysed cases and the maxima are located at $y = 10D - 12D$. Upstream of these locations the fastest temperature growth is obtained for the pipe with wavy wall and square orifice. For instance, compared to the case with the hexagonal orifice, for which the temperature rise is slowest, the temperature difference at $y = 7D$ is approximately 140 K.

4 Conclusions

The present paper showed how LES-IB can be successfully applied to study mixing characteristics in pipes with complex shaped orifice plates. The simulations of flames issuing from such pipes revealed significantly improved mixing which, compared to the flame issuing from a straight pipe, manifested itself by shortening of the lift-off heights of the flames. The results did not show an evident advantage of a particular shape of the orifice. Taking into account that the hexagram shape leads to the smallest pressure drop in the pipe, this shape seems optimal.

Acknowledgements This work has been partially supported by the Polish National Science Center under grant DEC-2012/07/B/ST8/03791 and statutory funds of the Czestochowa University of Technology. The authors are grateful to the computing centres SARA in the Netherlands (NWO project SH-061) and Cyfronet in Poland (computational resources within PL-Grid infrastructure).

References

1. Cabra, R., Myrvold, T., Chen, J.-Y., Dibble, R.W., Karpetis, A.N., Barlow, R.S.: Simultaneous laser Raman-Rayleigh-LIF measurements and numerical modeling results of a lifted turbulent H_2/N_2 jet flame in a vitiated co-flow. Proc. Combust. Inst. **29**, 1881–1888 (2002)
2. Mittal, R., Iaccarino, G.: Immersed boundary methods. Annu. Rev. Fluid Mech. **37**, 239–261 (2005)
3. Mueller, M.A., Kim, T.J., Yetter, R.A., Dryer, F.L.: Flow reactor studies and kinetic modelling of the H2/O2 reaction. Int. J. Chem. Kinet. **31**, 113–125 (1999)
4. Triantafyllidis, A., Mastorakos, E.: Implementation issues of the conditional moment closure in large eddy simulations. Flow Turbul. Combust. **84**, 481–512 (2009)
5. Tyliszczak, A.: Assessment of implementation variants of conditional scalar dissipation rate in LES-CMC simulation of auto. Arch. Mech. **65**, 97–129 (2013)
6. Tyliszczak, A.: A high-order compact difference algorithm for half-staggered grids for laminar and turbulent incompressible flows. J. Comput. Phys. **276**, 438–467 (2014)

Instability of Supersonic Ramp Flow with Intermittent Transition to Turbulence

Kangping Zhang, Neil D. Sandham and Zhiwei Hu

Abstract This paper investigates the global instability of supersonic ramp flow at Mach number 4.8 at different Reynolds numbers through direct numerical simulations. It is found that a critical Reynolds number exists for the flow to become globally unstable. Transition to turbulence happens downstream of the ramp with strong intermittency and is due to the breakdown of streaky structures fed by instability from the ramp separation region.

1 Introduction

Ramp flows are commonly seen in high-speed vehicle control surfaces and engine intakes. Flow separation, transition and shock-wave/boundary-layer interaction (SWBLI) may exist simultaneously in such flows and influence each other. Instability studies with SWBLI have been carried out in the context of flow transition [1]. Balakumar et al. [2] studied the stability of high speed compression corners using both direct numerical simulation (DNS) and linear stability theory, and showed that the added disturbances grew exponentially both upstream and downstream of the separated region but remained neutral across the separation area. Transition to turbulence only occurs downstream, due to the second-mode (called the Mack mode) of instability. Ludeke and Sandham [3] studied ramp flow with Mach number 4.8 at different Reynolds numbers. A small secondary recirculation zone was found at a Reynolds number of 3,422. They observed a convective transition process in a three-dimensional (3D) ramp flow. This paper investigates, using DNS, the instability of ramp flow at Mach number 4.8 at higher ramp angle for different Reynolds numbers and considers the mechanism of transition to turbulence in the presence of global instability.

K. Zhang
CARDC, Mianyang, China

N.D. Sandham · Z. Hu (✉)
AFM Group, Faculty of Engineering and the Environment, University of Southampton, SO17 1BJ Southampton, UK
e-mail: z.hu@soton.ac.uk

D.G.E. Grigoriadis et al. (eds.), *Direct and Large-Eddy Simulation X*,
ERCOFTAC Series 24, https://doi.org/10.1007/978-3-319-63212-4_47

2 Numerical Method and Computational Setup

The simulations presented in this paper solve the unsteady, 3D compressible Navier-Stokes equations using DNS, made dimensionless using the inflow freestream velocity U^*_∞, density ρ^*_∞, temperature T^*_∞ and viscosity μ^*_∞, together with the inflow boundary layer displacement thickness δ^*_0 as reference. The dynamic viscosity μ is assumed to follow Sutherland's law, with the Sutherland temperature set to 110.4 K. The Reynolds number is defined as $Re = \rho^*_\infty u^*_\infty \delta^*_0 / \mu^*_\infty$. A constant Prandtl number $Pr = c^*_p \mu^* / k^*$ of 0.72 is used.

A fourth-order central difference scheme is employed to discretize internal points with a stable boundary treatment. Time marching is performed using a low-storage third-order explicit compact Runge-Kutta method. The non-linear inviscid flux is split into conservative and non-conservative parts for stability improvement. A TVD scheme with a Ducros sensor, which only switches on the TVD scheme outside the boundary layer, is used for shock capturing. Details can be found in Sandham et al. [4].

Simulations are run at a ramp angle of 12° with freestream Mach number 4.8 and static temperature 55.4 K. Two cases with Reynolds numbers of 3,422 and 6,843, based on the inflow boundary layer displacement thickness, are simulated. After some tests the computational domain is chosen to extend 215.2 and 325 (in non-dimensional unit) before and after the ramp corner, respectively, and has a height of 50 in the wall-normal direction. The domain is meshed with stretched grids in both the streamwise and the wall-normal directions. A mesh convergence study found that a mesh of 1,800×250 gives grid independent results. Meshes for 3D simulations are extruded from the two-dimensional (2D) mesh with the span equal to one wavelength of the added disturbance, ranging from 3 to 24. To resolve the flow in the spanwise direction, 16 points are used across the span for the study of the exponential stage of 3D global instability. This is considered to be sufficient to resolve the flow at linear growth stage as only one wave is added in the span. A finer mesh with $Nz = 64$ is used for the transition study.

Similarity solutions for laminar boundary layer are applied at the inflow. Characteristic boundary conditions are applied at the outflow and top boundaries. The wall is considered to be isothermal with temperature equal to its laminar adiabatic wall temperature. A periodic boundary condition is used in the spanwise direction.

3 Results

Code validation and a grid independence study is first carried out. A 2D case is run for a 6° compression ramp at $M = 4.8$ and $Re = 6{,}843$. Good agreement is obtained with Ludeke and Sandham [3] and Pagella et al. [5]. Simulations are then run in 2D at 12° at $M = 4.8$ and $Re = 3{,}422$ and 6,843. Steady solutions are obtained for both cases, as shown in Fig. 1, with recirculation zones clearly seen in both cases. The

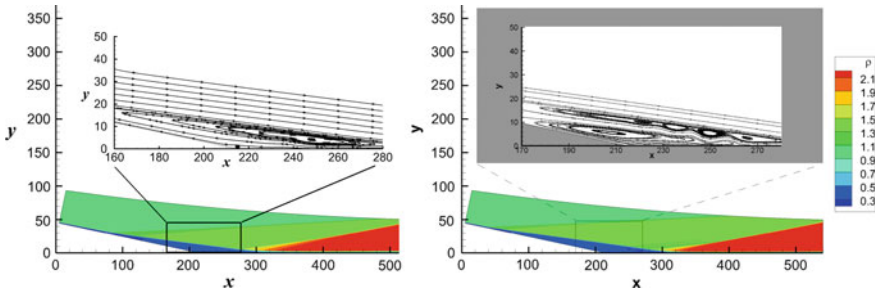

Fig. 1 The separated flow for the 12° ramp at reynolds number 3,422 (*left*) and 6,843 (*right*)

separation region is $L_s = 241$, extending from $x = 84$ to 325 for the low Reynolds number case. A larger separation region appears for the higher Reynolds number case with $L_s = 292$ (from $x = 40$ to 332). Small secondary recirculation zones can also be found for this case.

The steady 2D solution is used as a base flow for a 3D stability study. The 3D base flow is obtained by extending the 2D base flow in the spanwise direction. Small disturbances are added to the base flow in the spanwise velocity component to study the global instability. The disturbance is confined within a small patch above the ramp corner in the $x - y$ plane with a Gaussian profile and a single wave along the span, in the form of

$$w'(x, y, z) = Ae^{-\frac{1}{4}[(x-x_c)^2+(y-y_c)^2]} \sin\left(\frac{2\pi z}{L_z}\right) , \tag{1}$$

where $(x_c, y_c) = (234.7, 2.81)$ is the centre of the Gaussian profile, and the amplitude is chosen as $A = 3.5 \times 10^{-12}$. Development of flow three-dimensionality is monitored by a statistical measure of the growth of the disturbances via

$$\varepsilon(x, y) = < w(x, y, z)^2 > - < w(x, y, z) >^2 , \tag{2}$$

where $< \ . \ >$ denotes averaging over span.

Simulations are run for $L_z = 12$ at both Reynolds numbers. The growth of disturbances at a monitor point upstream of the ramp corner at (196.76, 6.7) is shown in Fig. 2. It can be seen the flow is stable for the low Reynolds number case, however it becomes unstable at high Reynolds number, suggesting that there exists a critical Reynolds number for flow instability, with the threshold in between the two Reynolds numbers. Further analysis of the flowfield showed the instability firstly developed at the centre of the secondary recirculation zone. The magnitudes of the maximum reverse flow reaches 19.5 and 26% of the freestream speed at the low and high Reynolds number, respectively. So the high Reynolds number flow is likely to be absolutely unstable in three dimensions, while the low Reynolds number case is neutral or, at most, weakly unstable.

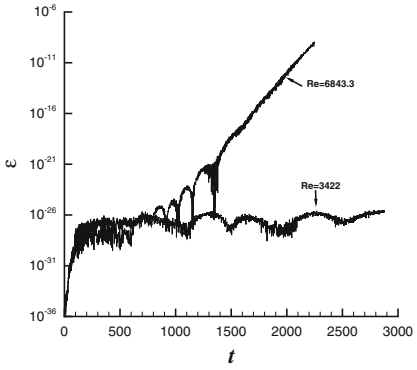

Fig. 2 Growth of disturbances ε with time for L_z=12 at different reynolds numbers for a monitor point at (196.76, 6.70)

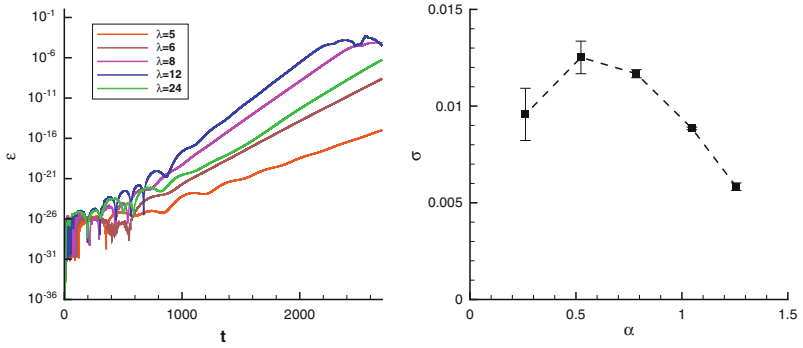

Fig. 3 Statistical measures of instability for ramp flow with different spanwise lengths: **a** variation of ε, defined by Eq. (2) at monitor point (246.86, 2.81) with time, **b** the growth rate against wavenumber, with error bars measured from growth rate at different monitor points

The high Reynolds number case is further studied with added disturbances for different spanwise lengths L_z of 5, 6, 8, 12 and 24. The growth of disturbances for all cases is illustrated in Fig. 3a. It is found that the growth rate of disturbances varies with the wavelength of the added perturbation. By measuring the slopes in the exponential stage, variation of the growth rate is shown against wavenumber in Fig. 3b. The peak of the growth rate corresponds to the case with $L_z = 12$. Error bars in the growth rate are calculated from the growth rates for different monitor points. The flow is most unstable with a spanwise length of 12 times the inflow boundary layer displacement thickness.

In the exponential stage of disturbance growth, the development of the added w-velocity perturbation still follows the single-spanwise harmonic structure, with the highest amplitudes appearing in the region from $x = 230$ to 320 and $y = 0$ to 20, within the flow recirculation zone.

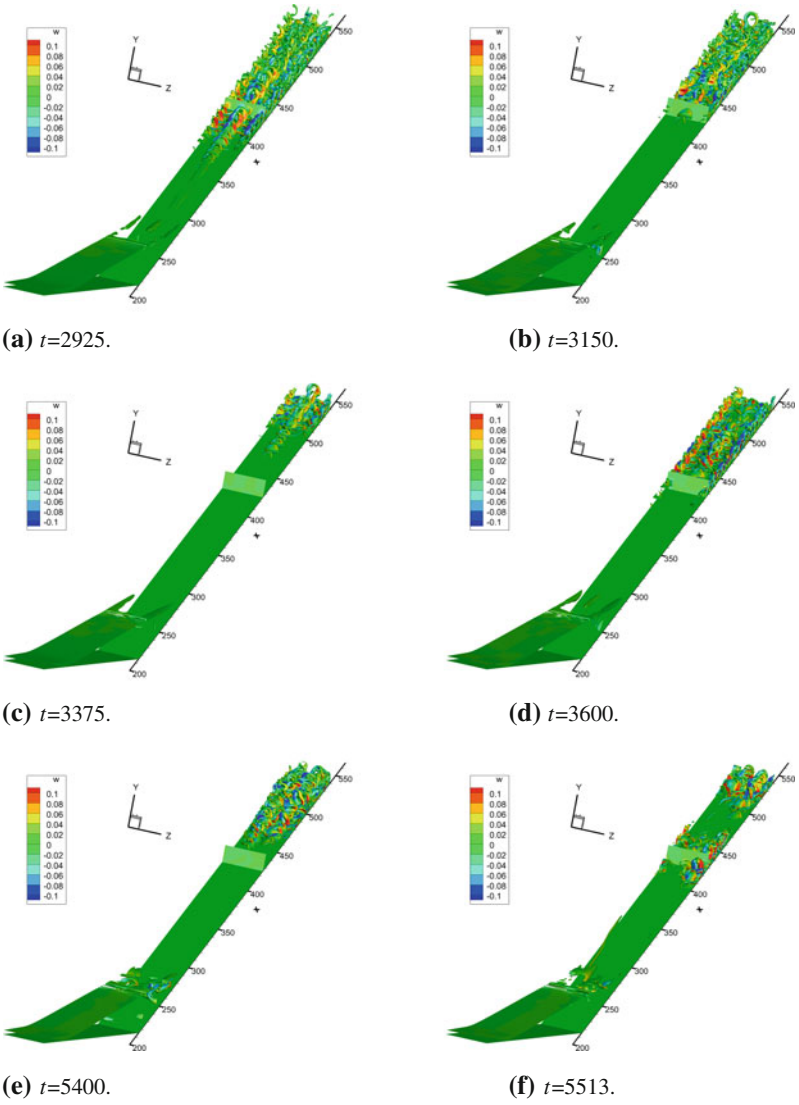

(a) t=2925. **(b)** t=3150.

(c) t=3375. **(d)** t=3600.

(e) t=5400. **(f)** t=5513.

Fig. 4 Iso-surface of the normalized second invariant of the velocity grandient vector at $Q = 0.01$, coloured by the spanwise velocity at different time instances

Flow transition is further studied for $Re = 6{,}834$ for the most unstable case with $L_z = 12$. The spanwise grid points are increased to $N_z = 64$ for improved resolution. Flow structures at different time instances are shown in Fig. 4. It can be seen that disturbances start to grow in the recirculation zone near the ramp corner, which leads to the formation of streamwise vortices. Visualization of the flow at different streamwise locations (not shown here due to space limitation) shows that the shear

flow and reattachment shock push the vortices towards the wall and lead to streaks. As the flow develops the streaks grow in strength. Streak amplitudes of more than 29.5% of the freestream speed are observed and breakdown to turbulence happens further downstream. This is consistent with existing studies [6] that a streak amplitude of about 26% was needed for streak breakdown to occur. It is also observed that the turbulence flow is strongly intermittent.

4 Conclusions

Direct numerical simulations are performed for supersonic ramp flow at Mach number 4.8 to investigate the instability and transition process. A critical Reynolds number exists, between the two cases study for $Re = 3{,}422$ and 6,843, for the global instability. For the ramp flow with the high Reynolds number, disturbances with a spanwise wavelength equal to 12 times the incoming boundary layer displacement thickness is found to be most unstable. The disturbances generated by the recirculation zone do not lead directly to transition to turbulence. Instead, streamwise vortices are formed. Because of the shear flow and reattachment shock, the vortices are pushed towards the wall and lead to streamwise velocity streaks. The streaks reach high amplitude and breakdown to turbulence happens further downstream with strong intermittency.

Acknowledgements The computer time is provided by the UK Turbulence Consortium under Engineering and Physical Sciences Research Council (EPSRC, UK) Grant No. EP/G069581/1.

References

1. Robinet, J.-C.: Bifucations in shock-wave/boundary-layer interaction: global instability approach. J. Fluid Mech. **579**, 85–112 (2005)
2. Balakumar, P., Zhao, H., Atkins, H.: Stability of hypersonic boundary layers over a compression corner. AIAA J. **43**, 760–767 (2005)
3. Ludeke, H., Sandham N.D.: Direct numerical simulation of the transition process in a separated supersonic ramp flow, AIAA Paper, pp. 2010–4470 (2010)
4. Sandham, N.D., Li, Q., Yee, H.C.: Entropy splitting for high-order numerical simulation of compressible turbulence. J. Comput. Phys. **178**(2), 307–322 (2002)
5. Pagella, A., Babucke, A., Rist, U.: Two-dimensional numerical investigations of small-amplitude disturbances in a boundary layer at $Ma = 4.8$: compression corner versus imping shock wave. Phys. Fluids **16**(7), 2272–2281 (2004)
6. Andersson, J., Brandt, L., Bottaro, A., Henningson, D.S.: On the breakdown of boundary layer streaks. J. Fluid Mech. **138**, 93–127 (2001)

Direct Numerical Simulation of Biomass Combustion in a Turbulent Particle-Laden Channel Flow

A. Awasthi, J.G.M. Kuerten and Bernard J. Geurts

1 Introduction

Renewable energy is the key to meet the ever-increasing global energy needs in a climate-constrained world. Biomass, being the only carbon based renewable energy fuel, is gaining importance in order to satisfy environmental concerns about fossil fuel usage. Biomass co-firing with coal is one of the main methods in achieving the objectives of increasing sustainable energy production. The present paper is aimed at the development of a computational model for biomass pyrolysis and combustion in a compressible gas flow. The model will enable the optimization of process parameters like conversion time, oxygen-fuel ratio and biomass fraction in the co-firing process.

2 DNS Model

The model is based on an Eulerian-Lagrangian approach in which gas and particle phases are treated in different ways. Owing to the wide range of temperatures involved in the process which results in significant variations in mass density, the gas phase

A. Awasthi (✉) · J.G.M. Kuerten
Department of Mechanical Engineering, Eindhoven University of Technology,
P.O. Box 513, 5600 Eindhoven, The Netherlands
e-mail: A.Awasthi@tue.nl

J.G.M. Kuerten · B. Geurts
Multiscale Modeling and Simulation, Faculty EEMCS, University of Twente,
Enschede, The Netherlands
e-mail: J.G.M.Kuerten@tue.nl

B.J.Geurts
Anisotropic Turbulence, Department of Applied Physics, Eindhoven University
of Technology, Eindhoven, The Netherlands
e-mail: b.j.geurts@utwente.nl

D.G.E. Grigoriadis et al. (eds.), *Direct and Large-Eddy Simulation X*,
ERCOFTAC Series 24, https://doi.org/10.1007/978-3-319-63212-4_48

is described by the compressible Navier-Stokes equations. The governing equations are based on conservation of mass, momentum, total energy and species mass. Apart from the convective and viscous fluxes, the governing equations also involve the terms which account for the two-way gas-particle interactions. To model the interaction between the gas and chemically reacting particles, single particle models for pyrolysis and combustion are developed.

Each particle is modeled as a point particle. A set of equations, tracking the char front and temperature distribution inside the particle, is developed to account for the evolving internal temperature profile of the particle during pyrolysis. A simplified pyrolysis model as developed by Haseli et al. [3] and modified for time dependent surrounding gas temperature by Russo et al. [4] is used to model the process of pyrolysis. The single particle model for combustion includes the char combustion (with O_2) and char gasification (with CO_2) reactions. It is formulated as a shrinking core model [2] with varying particle surface temperature due to convective heat exchange between the gas and the particle, radiative heat exchange between particle and reactor walls, and heat generated (or consumed) during the combustion and gasification reactions.

For particle tracking, a Lagrangian formulation is used. We use the Schiller-Naumann drag correlation, valid for particle Reynolds numbers between 0 and 1000, for calculating the drag force on the particles which are assumed to be spherical. The effect of gravity is neglected while calculating forces on the particles. The small size and very short residence time of particles inside the combustor motivate to neglect the effects of gravity.

3 Numerical Method and Setup of Simulations

Gas phase equations are spatially discretized using a second order accurate finite volume method. For time-integration, Russo et al. [4] used a low-storage second-order explicit Runge-Kutta scheme to simulate the process of biomass pyrolysis. However, it is observed that the process of combustion is quite fast in comparison to pyrolysis. The fast nature of the combustion process presents itself in the form of stiffness of the system of equations. This renders the explicit Runge-Kutta scheme (as could be used during pyrolysis) inefficient for solving the particle model equations, as a large number of time steps is required to achieve stability. To resolve this problem, a hybrid implicit-explicit method [5] is used here. As the stiffness is due to the combustion model, the implicit scheme is used only during this stage of the particle conversion. To keep the simulation time low and reduce the complexity of the numerical algorithm, the explicit part of the hybrid scheme is used for the gas phase equations and particle tracking, and during particle pyrolysis.

We consider the gas-particle system inside a channel, bounded by two parallel horizontal plates. The domain size is $4\pi H$ in streamwise direction and $2\pi H$ in spanwise direction, where H is half the channel height. The domain is divided into 128^3 control volumes. The grid spacing is uniform in streamwise and spanwise

direction, whereas it is non-uniform in the wall-normal direction with clustering of grid points near the walls. The two-way coupling terms for the gas equations account for all the particles present in a grid cell.

Simulations are performed with frictional Reynolds number approximately equal to $Re_\tau = 150$, which is based on friction velocity $u_\tau = \sqrt{\tau_w/\rho_g}$ and half the channel height. Here, τ_w is the wall shear stress based on the mean streamwise velocity component, averaged over the two homogeneous directions and time. The grid resolution is fine enough to capture the flow characteristics without any need for a turbulence model. In the simulations, we vary the volume fraction of particles, keeping it always smaller than $O(10^{-3})$, so that particle-particle collisions can be neglected [1].

For the simulations, the flow is initialized with a turbulent velocity field in the statistically steady state obtained from a simulation without particles. The initial oxygen mole fraction is $X_{O2} = 0.1$ with nitrogen the remainder. The initial gas temperature is set equal to 1400 K, and the particles are initialized with a temperature of 300 K which is constant within the particle. The walls of the channel are maintained at a temperature of 1400 K. Initially, the particles are randomly, and uniformly, distributed over the channel and the particle velocity is equal to the gas velocity at the location of the particle. With these initial conditions we simulate the pyrolysis and combustion of biomass particles in a turbulent channel flow.

4 Effects of Model Parameters on Particle Conversion Time

One of the key parameters in designing a combustor is the conversion time of the fuel particles. The total conversion time (t_{conv}) represents the time required by the particles to undergo pyrolysis (t_{pyro}) and combustion (t_{comb}). This time includes the time needed to heat the particle from its initial temperature (300 K) to the pyrolysis temperature at which point the virgin biomassgets converted into char. As a final step, upon completion of the pyrolysis stage the char burns in the presence of oxygen.

4.1 Effect of Two-Way Coupling

We analyze the effect of two-way coupling between gas and particles on the particle conversion time. Figure 1 shows the effect of two-way coupling on the time taken for pyrolysis (t_{pyro}). It can be seen that two-way coupling effects are noticeable at volume fractions $\phi > 10^{-5}$. At higher volume fractions ($\phi > 5 \times 10^{-4}$), the conversion time for two-way coupling is significantly higher (around 1.6 times) compared to one-way coupling. In case of one-way coupling the conversion time for pyrolysis remains constant with changing volume fraction. This is because the gas temperature is not affected by the presence of particles in one-way coupling.

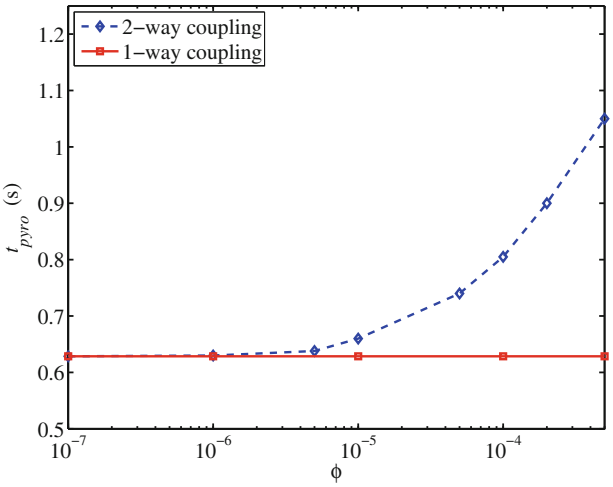

Fig. 1 Pyrolysis time (t_{pyro}) at different volume fractions ϕ with particle diameter 1 mm, for one-way and two-way coupling

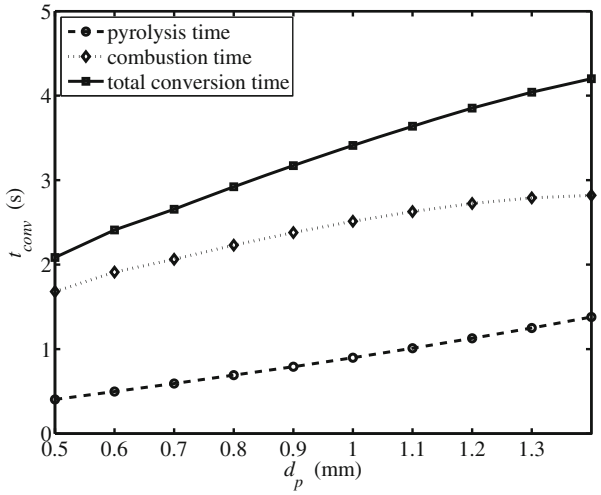

Fig. 2 Conversion (t_{conv}), combustion (t_{comb}), and pyrolysis (t_{pyro}) time vs particle diameter (d_p) at constant volume fraction ($\phi = 2.5 \times 10^4$) and initial gas temperature of 1400 K

4.2 Effect of Particle Size

To analyze the effect of particle size on conversion time, we performed simulations at constant volume fraction and variable particle size. Figure 2 shows the conversion time dependence on particle diameter. It can be seen that the combustion time is the major contribution to the total conversion time. Figure 2 shows that both pyrolysis

and combustion time increase with increasing particle diameter. However, at larger particle sizes, the change in combustion time is reduced, while the pyrolysis time keeps on increasing as also observed by Russo et al. [4]. The key difference between the pyrolysis and combustion processes is the way both are modelled. The process of pyrolysis is governed by the convective heat exchange between the hot surrounding gas and colder particles. At constant volume fraction, larger particles result in lower total surface area compared to smaller particles and so a decrease in the heat transfer between the gas and the particles, which increases the pyrolysis time.

Combustion is modelled using a shrinking core model (the particle radius decreases during the reactions), where heat is generated on the particle surface by chemical reactions and is then transferred to the gas phase. The plateauing of combustion time at larger particle sizes is probably caused by two opposing mechanisms. On one hand, at larger particle sizes, less heat is transferred from the particles to the gas due to the reduced surface area. This contributes to heating the particles to higher temperatures, thus increasing the surface reaction rates and reducing the combustion time. On the other hand, larger particles imply that the core will take more time to shrink, which would suggest a longer combustion time. These opposing factors are the probable cause for the plateauing of the combustion time at larger particle sizes.

4.3 *Effect of Volume Fraction*

To investigate the effects of particle volume fraction on the conversion time, we perform simulations varying the particle volume fraction and keeping the particle size constant. The results in Fig. 3 show the total conversion time, pyrolysis time

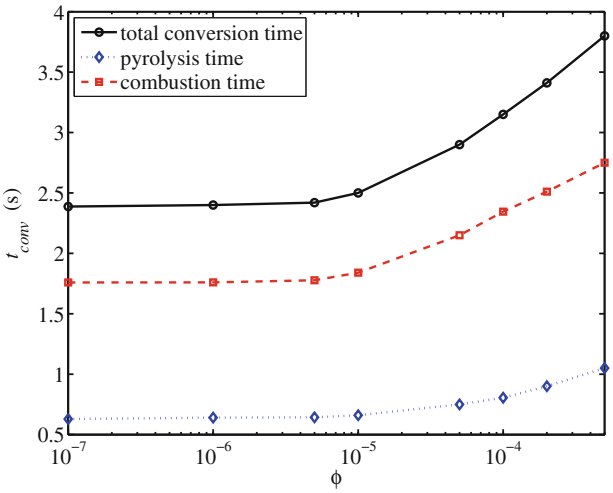

Fig. 3 Conversion (t_{conv}), combustion (t_{comb}), and pyrolysis (t_{pyro}) time vs particle volume fraction ϕ at initial gas temperature of 1400 K

and combustion time as a function of volume fraction. When two-way coupling is applied the time taken for pyrolysis increases with increasing volume fraction. The convective heat exchange between the gas and particle phases affects the gas temperature. During the pyrolysis stage, the gas heats the particles by convective heat transfer. More particles extract more heat from the gas phase which slows down the process of pyrolysis.

The combustion time increases with higher volume fraction, due to the fact that the higher number of particles consume the surrounding oxygen more quickly, after which the particle undergoes the slower gasification process. At lower volume fractions there is enough oxygen and particles lose most of the mass during the fast oxidation process.

5 Conclusion and Future Work

In this paper, we have extended the DNS model of biomass pyrolysis of Russo et al. [4] and extended it by including particle combustion reactions. We use Haseli's [2] simplified model for biomass combustion which is suitable for DNS implementation in case of simulations with a large number of point particles. It was observed that the conversion time increases with increasing particle volume fraction, for both pyrolysis and combustion stages. However, at lower volume fractions, $\phi < 10^{-5}$, the particle effect on the gas phase is negligible. The conversion time is also very sensitive to particle diameter and increases for larger particles.

Future research is devoted to the inclusion of reactions for gas phase combustion of gas species (released during pyrolysis) to present a more complete model of reaction chemistry inside the combustor.

Acknowledgements This work is part of the research program of the Foundation for Fundamental Research on Matter (FOM), which is part of the Dutch Organisation for Scientific Research (NWO).

References

1. Elghobashi, S.: On predicting particle-laden turbulent flows. Appl. Sci. Res. **52**, 309–329 (1994)
2. Haseli,Y.: Modeling combustion of single biomass particle. Ph.D. thesis, Eindhoven University of Technology, The Netherlands (2012)
3. Haseli, Y., van Oijen, J.A., de Goey, L.P.H.: A simplified pyrolysis model of a biomass particle based on infinitesimally thin reaction front approximation. Energy Fuels **26**, 3230–3243 (2012)
4. Russo, E., Kuerten, J.G.M., Geurts, B.J.: Delay of biomass pyrolysis by gas-particle interaction. J. Anal. Appl. Pyrolysis **110**, 88–99 (2014)
5. Spalart, P.R., Moser, R.D., Rogers, M.M.: Spectral methods for the Navier-Stokes equations with one infinite and two-periodic conditions. J. Comput. Phys. **96**, 297–324 (1991)

DNS of Premixed Turbulent Hydrogen Flames in Distributed Burning Regime

Z.H. Zhang, Y. Chen and K.H. Luo

1 Introduction

There has been increasing interest recently in adopting hydrogen or hydrogen-rich fuel in combustors in lean-burn mode due to the potential for zero carbon dioxide emissions. Lean combustion has advantages in reducing the burnt gas temperature and consequently the NOx emissions. Depending on the ratio between turbulence and flame characteristic time and length scales, the combustion diagram has been drawn up to characterize different modes following the work by Borghi [3] and Peters [4]. The widely adopted non-dimensional turbulent premixed combustion parameter is the turbulent flame Reynolds number $Re_T = u'l/S_L\,\delta_L$ where u' and S_L are respectively the turbulent fluctuation velocity and unstretched laminar flame speed, l and δ_L are respectively the turbulence integral scale and laminar flame thickness. Large scale turbulent motions are responsible for the flame wrinkling and convolving, thus determine the turbulent flame brush structures, which broaden the flame area and give rise to turbulent burning velocity. However, with an integral length that is several time larger than the laminar flame thickness, the large scale turbulent eddies are not able to penetrate the flamelets. In that case, the burning area is consisted of wrinkled flamelets, where the combustion models based on flamelets assumptions can be applied. On the other hand, turbulent motions of scales small enough may penetrate the flamelets and survive in the preheat zone or even the reaction zone, thus significantly affecting the diffusion and reaction behaviors.

Z.H. Zhang (✉) · Y. Chen
Thermal Science and Power Engineering of Ministry of Education Key Laboratory,
Center for Combustion Energy, Tsinghua University, Beijing 100084,
People's Republic of China
e-mail: zhangzh15@mails.tsinghua.edu.edu.cn

K.H. Luo (✉)
Department of Mechanical Engineering, University College London,
Torrington Place, London WC1E 7JE, UK
e-mail: k.luo@ucl.ac.uk

D.G.E. Grigoriadis et al. (eds.), *Direct and Large-Eddy Simulation X*,
ERCOFTAC Series 24, https://doi.org/10.1007/978-3-319-63212-4_49

The turbulent velocity fluctuation in realistic combustion devices is reported to be 150 times higher than the lean hydrogen laminar flame speed [6]. Direct numerical simulation of high turbulent Reynolds number can contribute to the understanding and physical insight into combustion characteristics, such as local extinction and scalar transport in broken flame zone. Aspden et al. [1, 2] conducted DNS cases of turbulent premixed hydrogen flames exposed to high turbulent intensities and revealed the effect of fuel Lewis number on flame characteristics. Poludnenko et al. [5] studied the interaction of turbulence and flame using one-step chemistry and discussed the turbulent flame brush effect on burning velocity and overall flame structures. However, direct numerical simulation of turbulent premixed flames with turbulent velocity to laminar flame speed ratio larger than 100 is still rare as the high hydrogen flame speed requires high resolution to achieve the turbulent Reynolds number for realistic turbulent flames.

This work is to gain detailed understanding of the structure and statistical quantities of premixed turbulent hydrogen/air flames in an unconfined three dimensional domain in the presence of homogenous, high speed turbulence using DNS with detailed chemical mechanisms. A particular focus is placed on the flame transition from thin reaction zone to distributed zone with increasing turbulence intensity. The turbulent velocity to laminar flame speed ratio is between 11.5 and 171, corresponding to a maximum turbulent Reynolds number of 171.

2 Numerical Approach

The reacting Navier–Stokes equations are solved with six-order spatial differential scheme and third order Runge–Kutta scheme for time advancing. A forcing term is added to the momentum equations to initialize the cold flow of hydrogen and air mixture with the equivalence ratio of 0.35 until a developed turbulent field is obtained. The one dimensional unstretched laminar flame is computed incorporating chemical, transport and thermodynamics models, and then superimposed to the turbulent field. A cuboid computation domain is used in the present study. The lateral boundary conditions are treated to be periodical and the flow direction boundary conditions are inflow and outflow respectively, which allows the turbulence to flow into and out of the domain. A hydrogen/air mixture of an equivalence ratio of 0.35 under atmospheric conditions ($T = 298\,\mathrm{K}$) enters the domain at the inlet with velocity equal to twice the laminar flame speed to compensate for the effects of turbulence. The inlet and the outlet are specified using the Navier–Stokes characteristic boundary conditions (NSCBC). Chemical reactions are treated with a 8 step and 8 species mechanism developed by Strohle et al. [7]. Three cases with turbulent flame Reynolds number from 11.5 to 171 are presented in this study. The corresponding Karlovitz number is between 39 and 2238, where Ka, representing the ratio between characteristic chemical time scale and Kolmogorov time scale, is defined as $Ka = (u'/S_L)^{3/2}(\delta_L/l)^{1/2}$.

Table 1 Key parameters in the simulation

Case	Flame A	Flame B	Flame C
Equivalence ratio	0.35	0.35	0.35
Flame speed (cm/s)	21.2	21.2	21.2
Flame thickness (cm)	6.28×10^{-2}	6.28×10^{-2}	6.28×10^{-2}
Domain width (cm)	3.14×10^{-1}	3.14×10^{-1}	3.14×10^{-1}
Domain length (cm)	6.28×10^{-1}	6.28×10^{-1}	6.28×10^{-1}
Integral length scale (cm)	6.28×10^{-2}	6.28×10^{-2}	6.28×10^{-2}
Turbulent intensity (cm/s)	244	681	3627
Re_T	11.5	32.1	171
Ka	39	182	2238
Da	8.7×10^{-2}	3.1×10^{-2}	5.84×10^{-3}
Resolution	$512 \times 265 \times 256$	$512 \times 265 \times 256$	$512 \times 265 \times 256$

The spatial mesh length is one fifth of the laminar flame thickness and the integral length, which is considered to be fine enough. An aspect ratio of 1:1:2 is used to give flame sufficient space to interact with the turbulence in the flow direction. Key parameters are shown in Table 1.

3 Results and Discussion

Exposed to the turbulent field, the planar laminar flame starts to be wrinkled by turbulent eddies, and the turbulent flame brush gradually develops. After $t = 4\tau$, where τ is the turbulent turnover time, the flame brush properties reach a quasi-steady state where its averaged width and speed do not change. The global flame brush structures are shown in Fig. 1. The flame zone is bounded by progress variable

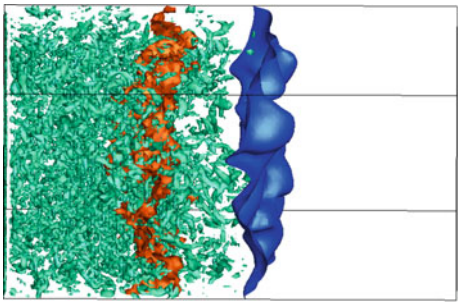

Fig. 1 Isosurfaces of the progress variable c = 0.1 (*Red*), c = 0.9 (*Blue*) and vorticity (*Green*) for flame C

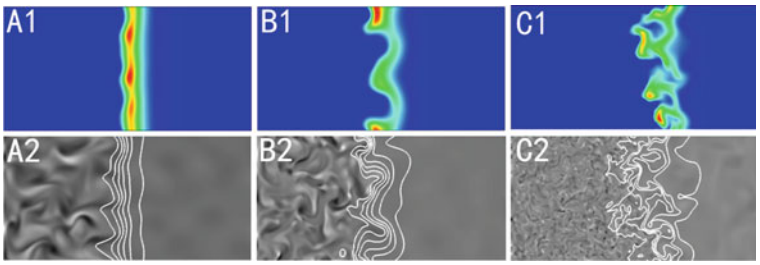

Fig. 2 Two-dimensional slices at $t = 5\tau$ of fuel consumption rate (A1, B1, C1) and vorticity (A2, B2, C2) for Flame A, B and C, respectively. The *white lines* denote the temperature contours

$c = 0.1$ and $c = 0.9$, where $c = (Y_{H_2,u} - Y_{H_2})/(Y_{H_2,u} - Y_{H_2,b})$, $Y_{H_2,u}$ is the mass fraction of unburnt mixture and $Y_{H_2,b}$ is the mass fraction of burnt mixture.

The computational domain edge is marked with black line. The flame front is highly convoluted by large scale turbulent structures, indicating that cellular burning patterns dominate the burning area. It is worth noting that small turbulent eddies survive in the reaction zone, thus laminar flamelet assumption does not apply in this case. The effect of small scale eddies on the flame will be discussed below in detail.

Figure 2 shows the fuel consumption rate and vorticity of all the three cases at $t = 5\tau$. For low turbulent Reynolds number flame case, the turbulent eddies have been consumed up before they can enter the flame front. The preheat zone is wrinkled by turbulence in the unburned side. However, as turbulence decays rapidly in the hot gas owing to the increased viscosity, the reaction zone remains unaffected by the turbulent eddies. For the moderate turbulent Reynolds number flame, turbulence is able to carry the hot gas to the unburned side, thus broadening the preheat zone. The reaction zone is also wrinkled but still remains continuous and laminar. As turbulent Reynolds number increases further to 171, the behavior of Flame C is categorically different where no obvious flamelet structures are observed. The reaction takes place in a significantly broadened area in the flow direction as a result of the turbulent eddies inside the reaction zone and holes on the flame surface appears. As the vorticity contours show, the turbulent structures at the high turbulent Reynolds number appear to have finer graularity.

In order to quantitatively demonstrate the turbulence effects on flame properties, the PDF files of density gradient and flame front curvature are shown in Fig. 3. The density gradient PDF of high Re_T flame contains regions with much larger gradients. The largest density gradient increases by a factor of 20, with an increase in Re_T from 11.5 to 117. This behaviour implies that there are much sharper interfaces between the fresh and burned gases. This is consistent with the observation that small turbulent eddies can penetrate the flame front and carry unburned gas pockets into the reaction zone, thus sharpening the interface between fresh gases and products. In the previous study by Aspen et al. [2], a similar trend was also observed, but the ratio of the largest density gradient between the high and low Re_T flames is about 2 as broken reaction mode was not achieved. In this situation, the density gradient is not determined by the

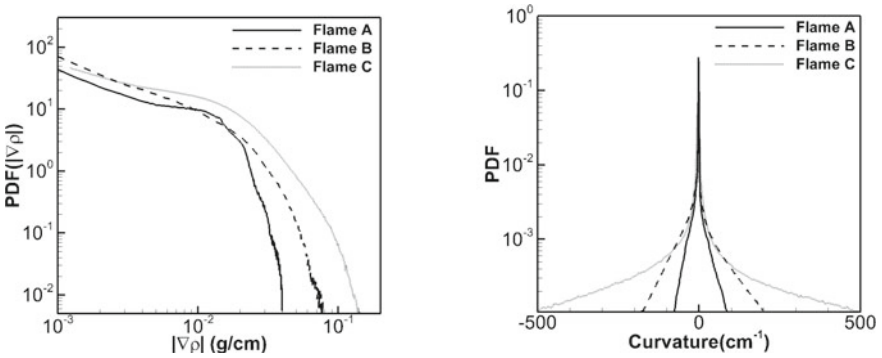

Fig. 3 PDF files of density gradients and flame front curvature

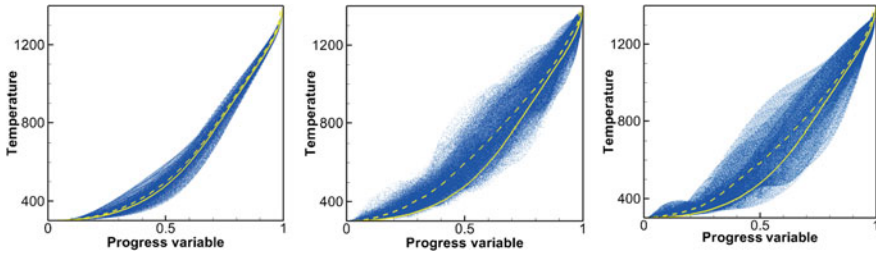

Fig. 4 Scatter plots for progress variable and temperature for Flames A (*left*), B (*middle*) and C (*right*). *Solid line* represents for 1D unstretched conditions and *dashed line* for conditional means

flame thermal thickness but by the turbulent eddy scale which can be several times smaller than the former. Consequently, the flame front wrinkles at a higher curvature due to smaller turbulent structures. For low Re_T flame, the curvature radius is on the order of initial turbulent integral scale, indicating that turbulent eddies smaller than the integral scale has been consumed up before they can wrinkle the flame front. As turbulent intensity is increased, the flame curvature radius is much smaller, indicating that the Taylor scale or even Kolmogorov scale eddies are able to convolve the flame front.

Carrying mass and heat at the same rate, turbulent structures inside the reaction zone change the convection behavior of hydrogen/air premixed flame where Lewis number is not unity. Figure 4 shows the conditional mean of temperature as a function of progress variable. In each plot, the conditional mean temperature is shown by the dashed line, and the steady unstretched laminar flame is shown by the solid curve. The unstretched laminar flame and low Re_T flame lines are highly curved due to the non-unity Lewis number and therefore the differential diffusion. As Re_T increases, the distribution is broadened, and the correlation between temperature and progress variable trends to be linear, resulting in an effectively unity Lewis number.

4 Concluding Remarks

Three 3D hydrogen/air turbulent premixed flames are simulated with detailed chemistry at turbulent fluctuation velocity to laminar flame speed ratio up to 171. For low Re_T turbulent flames, the turbulent eddies are consumed up by flame or dissipate duo to the high viscosity in the hot gas. Preheat zone and reaction zone remain unaffected by turbulence. In the case where Re_T is 171, the flame belongs to the broken reaction zone, and the turbulent eddies inside the reaction zone is well captured. Vortex-flame interactions inside the reaction zones significantly broaden the turbulent flame brush thickness. The large density gradient implies sharper interface between the fresh and burned gases, therefore enhanced diffusion terms. The obtained physical insight and statistical analysis can be incorporated into hydrogen turbulent flame modeling in future.

Acknowledgements This work is supported by the National Science Foundation of China (Grant No. 91441120) and the Center for Combustion Energy at Tsinghua University. Computing resources from the UK Engineering and Physical Sciences Research Council under Grant No. EP/J016381/2 are gratefully acknowledged.

References

1. Aspden, A.J., Day, M.S., Bell, J.B.: Lewis number effects in distributed flames. Proc. Combust. Inst. **33**, 1473–1480 (2011)
2. Aspden, A.J., Day, M.S., Bell, J.B.: Turbulence flame interactions in lean premixed hydrogen: transition to the distributed burning regime. J. Fluid Mech. **680**, 287–320 (2011)
3. Borghi, R.: Mise au point sur la structure des flammes turbulentes. J. Chim. Phys. **81**, 361–370 (1984)
4. Peters, N.: Turbulent Combustion. Cambridge University Press, Cambridge (2000)
5. Poludnenko, A.Y., Oran, E.S.: The interaction of high-speed turbulence with flames: global properties and internal flame structure. Combust. Flame **157**, 995–1011 (2011)
6. Strakey, P., Sidwell, T., Ontko, J.: Investigation of the effects of hydrogen addition on lean extinction in a swirl stabilized combustor. Proc. Combust. Inst. **31**(2), 3173–3180 (2007)
7. Strohle, J., Myhrvold, T.: An evolution of detailed reaction mechanisms for hydrogen combustion under gas turbine conditions. Int. J. Hydrogen Energy **32**, 125–135 (2007)

DNS of Burning N-Heptane Droplets: Auto-Ignition and Turbulence Modulation Mechanisms

Abouelmagd Abdelsamie and Dominique Thévenin

1 Introduction

Safety-relevant auto-ignition by n-heptane droplets exiting as a turbulent jet within a combustible gas mixture is investigated under different conditions by means of Direct Numerical Simulations (DNS). The objectives of this study are (1) to investigate the interaction between droplets and flow and (2) examine the impact of pressure, jet speed, jet width and number of droplets on the ignition process. Existing publications on the subject can be roughly categorized into four groups. First, those investigating in 3D the two-way coupling of a non-reactive turbulent flow with droplets (e.g., [6]). The second group examined reacting cases, but using a single-step reaction mechanism [9, 10]. A third approach takes into account detailed chemistry but only in 2D turbulent flows [2, 3, 12]. In the last category, both 3D flows and detailed chemistry were considered, like in [4, 7, 8] but with relatively simple configurations. In the current paper, the configuration in Refs. [1, 11] is employed with some modifications in order to examine auto-ignition and turbulence-droplet interaction.

2 Numerical and Mathematical Approaches

Here, droplets, being smaller than the grid resolution, are modeled as point droplets, while the Navier–Stokes equations are solved in the low-Mach number regime. Detailed models are employed to describe chemical reaction and molecular trans-

A. Abdelsamie (✉) · D. Thévenin
Laboratory of Fluid Dynamics and Technical Flows, University of Magdeburg
"Otto von Guericke", Universitätsplatz 2, 39106 Magdeburg, Germany
e-mail: abouelmagd.abdelsamie@ovgu.de

D. Thévenin
e-mail: thevenin@ovgu.de

D.G.E. Grigoriadis et al. (eds.), *Direct and Large-Eddy Simulation X*,
ERCOFTAC Series 24, https://doi.org/10.1007/978-3-319-63212-4_50

port in the gas phase. The continuous (gas) phase is simulated in a standard manner (Eulerian frame) whereas the discontinuous (droplet) phase is tracked in a Lagrangian frame. Two-way coupling between both phases is quantified via the exchange of mass, momentum and energy. The Stokes drag force is dominant in the droplet momentum equation, Eq. (1):

$$\frac{d\mathbf{V}_k}{dt} = \frac{\tilde{\mathbf{U}}_g - \mathbf{V}_k}{\tau_k^v}, \tag{1}$$

$$\frac{d\mathbf{X}_k}{dt} = \mathbf{V}_k, \tag{2}$$

$$\tau_k^v = \frac{\rho_k a_k^2}{18\gamma_k \tilde{\mu}_g}. \tag{3}$$

In Eqs. (1)–(3), $\mathbf{V}_k$ and $\tilde{\mathbf{U}}_g$ are the velocity of the kth droplet and of the surrounding gas at droplet location. Also, $\mathbf{X}_k$, ρ_k, γ_k, a_k and $\tilde{\mu}_g$ are droplets position vector, density, non-linear drag coefficient, diameter and gas viscosity at the particle position, respectively.

The evaporation process is computed using an infinite conduction model inside the droplet and a variable Spalding mass transfer number, B_k (Eqs. 4–10):

$$\frac{dT_k}{dt} = \frac{\tilde{T}_g - T_k - \mathrm{B}_k L_v/C_p}{\tau_k^T}, \tag{4}$$

$$\frac{da_k^2}{dt} = -\frac{a_k^2}{\tau_k^a}, \tag{5}$$

$$\tau_k^T = \frac{\mathrm{P}_r^k}{6\mathrm{Nu}_c^k}\frac{C_p^k}{C_p}\frac{\rho_k a_k^2}{\tilde{\mu}_g}\frac{\mathrm{B}_k}{\ln(1+\mathrm{B}_k)}, \tag{6}$$

$$\tau_k^a = \frac{\mathrm{Sc}^k}{4\mathrm{Sh}_c^k}\frac{\rho_k}{\tilde{\mu}_g}\frac{a_k^2}{\ln(1+\mathrm{B}_k)}, \tag{7}$$

$$\mathrm{B}_k = \frac{Y_k^s - \tilde{Y}_g^f}{1 - Y_k^s}, \tag{8}$$

$$Y_k^s = \frac{W_f}{W_f + W_o\left(\tilde{P}_g/P_k^s - 1\right)}, \tag{9}$$

$$P_k^s = P_{\mathrm{ref}}\,\exp\left[-\frac{L_v}{\mathrm{R}_f}\left(\frac{1}{T_k^s} - \frac{1}{T_{\mathrm{ref}}}\right)\right]. \tag{10}$$

In this set of equations, T_k, Y_k^s, P_k^s, P_{ref}, $\tilde{Y}_g^f$, $\tilde{P}_g$ and $\tilde{T}_g$, are the temperature of droplet k, gaseous fuel mass flux at the droplet surface, partial pressure of fuel at the droplet surface, reference pressure, fuel mass fraction in the surrounding gas mixture, surrounding gas pressure and gas temperature at droplet location, respectively. Also, Pr, C_p, Nu, Sc, Sh_c, L_v, W_f and W_o are Prandtl number, specific heat at

constant pressure, Nusselt number, Schmidt number, Sherwood number, latent heat of evaporation, molecular weight of fuel and oxidizer, respectively.

The in-house 3D DNS solver called DINO is used for the current simulations. DINO is a low-Mach number solver, relies on a 6th order finite-difference scheme for spatial discretization. For the time integration, by default a 4th order explicit Runge–Kutta method is used for non-stiff terms of the equations, while the stiff parts of these same equations, those associated to chemistry, are integrated by RADAU-5 or DVODE implicit integrators. In this manner, the timestep can be noticeably increased. Furthermore, the time integration could be performed by using a semi-implicit additive method (modified Rosenbrock technique) as an additional user option. The user also has the possibility to solve the whole system with an explicit solver if the mixture does not require implicit integration for chemistry. All kinetic and transport properties are handled in DINO using Cantera 1.8 and Eglib 3.4. Generally, DINO is a very powerful DNS tool, which is able to deal with different engineering problems. For instance, it relies on the Immersed Boundary Method to take into account complex geometries and large, fully-resolved particles. It is able to deal with incompressible and low-Mach number flows, non-reacting and reacting flows, single-phage and two-phase flows involving solid particles or evaporated droplets, etc. DINO was tested on different supercomputers and showed excellent parallel scalability. The Poisson equation is solved in DINO by a standard parallel FFT even for non-periodic boundary conditions using a pre- and post-processing technique for the involved array, before and after supplying it to a standard FFT solver. This is one of the most attractive features of DINO and this makes the code computationally very fast and highly scalable.

In order to investigate auto-ignition for safety predictions, droplets with diameter, a_k, and initial temperature, T_k, are distributed randomly in the middle of the DNS domain. The whole domain contains a hot oxidizer (air) with initial temperature $T_0 = 1500$ [K]. The droplets are distributed in a slab with width H. The surrounding gas inside this slab is moving with jet velocity U_j, whereas the surrounding co-flow moves with velocity U_{co}. The turbulence is triggered by initializing with an isotropic turbulent flow field. The turbulence signals are filtered to be imposed only in the middle of the domain (central slab), using a top-hat filter. This arrangement is equivalent to a temporally-evolving jet, the domain being periodic in streamwise and spanwise directions. Outflow conditions are applied in the transverse direction. This setting is shown in Fig. 1. The simulations are conducted over a domain with size of $1.28 \times 2.56 \times 2.56\,\text{mm}^3$, in spanwise, streamwise, and transverse directions, respectively. The overall mesh contains 1 065 024 grid points to keep a resolution of 20 μm in all directions. In the present work, a n-heptane skeletal mechanism accounting for 44 species and 114 reactions [5] is used for kinetics.

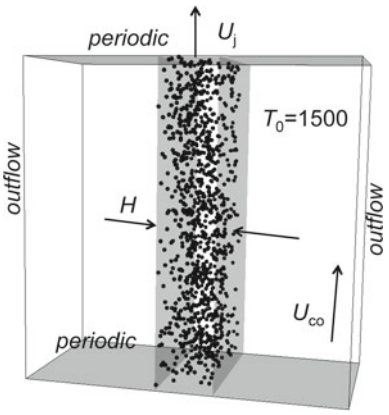

Fig. 1 schematic diagram of droplets arrangement in the computational domain, where U_j and U_{co} represent the jet and co-flow velocities of the mixture, respectively

3 Results

In this section, the interaction between the mixture and the droplets is examined for a basis case with properties and initial conditions listed in Table 1. Then, the impact of four different parameters (flow pressure, jet velocity, jet width, number of droplets) on the auto-ignition process are investigated.

3.1 Basis Case Analysis

To investigate the interactions between the droplets and the surrounding mixture, averages of streamwise velocity and temperature are depicted in Figs. 2 and 3, respectively. These average values are gathered over the spanwise and streamwise directions. Due to the diffusion and the droplets interactions (drag effect), the streamwise velocity decreases in the middle of the domain ($t = 11.5$ and $22.9\ \tau_{jet}$). At these two times, the droplets are still evaporating as it can be observed from Fig. 3. As soon as ignition happens, the temperature increases over all the domain ($t = 45.2$ and $67.5\ \tau_{jet}$). The minimum temperature is located in the middle of the domain where some evaporation process is still ongoing. Due to the ignition and dilatation the streamwise velocity increases overall the transverse direction except in the middle where liquid

Table 1 Initial conditions and properties of basis case

P [bar]	T_0 [K]	U_j [m/s]	U_{co} [m/s]	H [mm]	T_k [k]	a_k [μm]	N_k	τ^*_{jet} [μs]
3.0	1500	100	10	0.4	300	11.0	1200	4.44

*Jet time scale, $\tau_{jet} = H/(U_j - U_{co})$

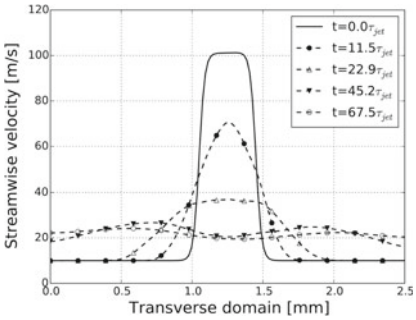

Fig. 2 Time-evolution of average streamwise velocity of the mixture versus the transverse direction

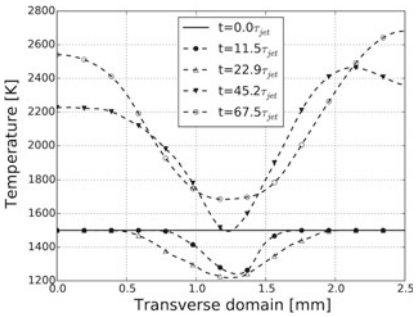

Fig. 3 Time-evolution of average temperature of the mixture versus the transverse direction

droplets still interact with the flow and induce relatively large drag forces, reducing turbulence kinetic energy and streamwise velocity as seen from Fig. 2.

3.2 Parametric Analysis

Impact of pressure (Fig. 4 top-left), jet velocity (Fig. 4 top-right), jet width (Fig. 4 bottom-left) and number of droplets in the slap (Fig. 4 bottom-right) are shown in Fig. 4. It is observed that when increasing the oxidizer pressure the auto-ignition occurs faster. An increasing pressure leads to an increase in density and Reynolds number, which enhances reaction rate, evaporation and mixing. The same conclusion can be drawn concerning the impact of the jet velocity and jet width, which directly increase the Reynolds number. On the other hand increasing the droplets number will delay the auto-ignition process, due to the increasing time required for the evaporation associated to a larger heat loss. Although the total heat release induced by a larger amount of droplets will be larger than that generated by less droplets, the priority for safety predictions is only to know the auto-ignition delay.

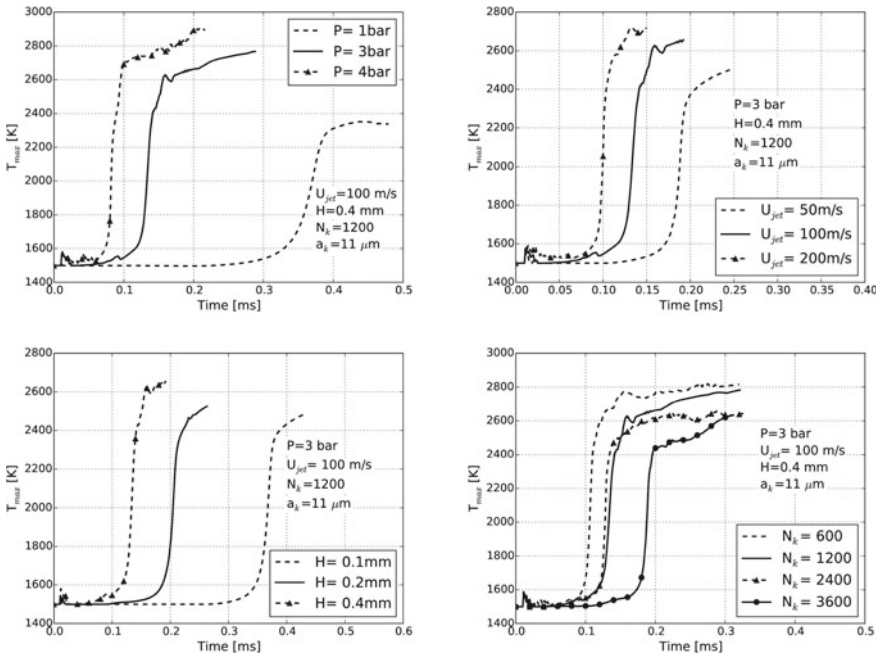

Fig. 4 Impact of different parameters on ignition process [pressure (p), jet velocity (U_j), jet width (H), number of droplets (N_k)]

4 Conclusion

The auto-ignition of n-heptane liquid droplets and their interaction with a turbulent jet flow have been investigated in the current work by means of Direct Numerical Simulations involving detailed physico-chemical models. The main processes controlling the interaction and their impact on auto-ignition delay have been studied by examining eleven cases obtained when varying pressure, jet velocity, jet width, and number of droplets. Further computations are obviously needed to deliver results suitable for safety prediction. Nevertheless, this first study already demonstrates the interest of DNS to support safety research by "numerical experiments".

Acknowledgements The financial support of the DFG (Deutsche Forschungsgemeinschaft) within the Forschergruppe (Research unit) number 1447 as well as the computer resources provided by the Gauss Center for Supercomputing/Leibniz Supercomputing Center Munich under grant pro84qo are highly acknowledged.

References

1. Borghesi, G., Mastorakos, E., Cant, E.: Complex chemistry DNS of n-heptane spray autoignition at high pressure and intermediate temperature conditions. Combust. Flame. **160**, 1254–1275 (2013)
2. Fujita, A., Watanabe, H., Kurose, R., Komori, S.: Two-dimensional direct numerical simulation of spray flames - Part 1: effects of equivalence ratio, fuel droplet size and radiation, and validity of flamelet model. Fuel **104**, 515–525 (2013)
3. Kitano, T., Nakatani, T., Kurose, R., Komori, S.: Two-dimensional direct numerical simulation of spray flames - Part 2: effects of ambient pressure and lift, and validity of flamelet model. Fuel **104**, 526–535 (2013)
4. Kitano, T., Nishio, J., Kurose, R., Komori, S.: Effects of ambient pressure, gas temperature and combustion reaction on droplet evaporation. Combust. Flame **161**, 551–564 (2014)
5. Liu, S., Hewson, J.C., Chen, J.H., Pitsch, H.: Effects of strain rate on high-pressure nonpremixed N-heptane autoignition in counterflow. Combust. Flame **137**, 320–339 (2004)
6. Mashayek, F.: Direct numerical simulations of evaporating droplet dispersion in forced low Mach number turbulence. Int. J. Heat Mass Trans. **41**(17), 2601–2617 (1998)
7. Neophytou, A., Mastorakos, E., Cant, R.S.: Complex chemistry simulations of spark ignition in turbulent sprays. Proc. Combust. Inst. **33**, 2135–2142 (2011)
8. Neophytou, A., Mastorakos, E., Cant, R.S.: The internal structure of igniting turbulent sprays as revealed by complex chemistry DNS. Combust. Flame **159**, 641–664 (2012)
9. Reveillon, J., Demoulin, F.-X.: Evaporating droplets in turbulent reacting flows. J. Fluid Mech. **583**, 273–302 (2007)
10. Reveillon, J., Vervisch, L.: Analysis of weakly turbulent dilute-spray flames and spray combustion regimes. J. Fluid Mech. **537**, 317–347 (2005)
11. Wang, H., Luo, K., Fan, J.: Effects of turbulent intensity and droplet diameter on spray combustion using direct numerical simulation. Fuel **121**, 311–318 (2014)
12. Wang, Y., Rutland, C.J.: Direct numerical simulation of ignition in turbulent n-heptane liquid-fuel spray jets. Combust. Flame **149**, 353–365 (2007)

DNS of Turbulent Lean Premixed Syngas Flames at Elevated Pressures

K.K.J. Ranga Dinesh, H. Shalaby, K.H. Luo and D.Thevenin

1 Introduction

The use of low carbon content fuels as replacements or supplement for petroleum fuels offer the advantage of a much cleaner fuel with little added atmospheric carbon dioxide greenhouse burden with a low potential sulfer content. In this context, combustion of high-hydrogen content (HHC) alternative fuels with a broader reaction class such as significant quantities of hydrogen diluted with carbon monoxide is undoubtedly significant [1]. Particularly, turbulent lean premixed combustion of HHC fuels at elevated pressure is of both fundamental and practical importance for the future internal combustion engines and gas turbine engines [2].

Although various Direct Numerical Simulation (DNS) studies with simple finite-rate and complex detailed chemistry provide insights into structure and dynamics of turbulent lean premixed hydrogen and hydrogen-enriched alternative fuel combustion at atmospheric pressure conditions [3, 4], DNS investigations on structure and propagation of turbulent lean premixed HHC alternative fuels at elevated pressure are performed seldom in the past. For example, there is no conclusive DNS work

K.K.J. Ranga Dinesh (✉) · H. Shalaby
Energy Technology Research Group, Faculty of Engineering and the Environment, University of Southampton, Southampton SO17 1BJ, UK
e-mail: dinesh.kahanda-koralagel@soton.ac.uk

H. Shalaby
e-mail: h.shalaby@soton.ac.uk

K.H. Luo
Department of Mechanical Engineering, University College London, Torrington Place, London WC1E 7JE, UK
e-mail: k.luo@ucl.ac.uk

D. Thevenin
Laboratory of Fluid Dynamics and Technical Flows, University of Magdeburg Otto von Guericke Universitatsplatz 2, 39106 Magdeburg, Germany
e-mail: thevenin@ovgu.de

D.G.E. Grigoriadis et al. (eds.), *Direct and Large-Eddy Simulation X*,
ERCOFTAC Series 24, https://doi.org/10.1007/978-3-319-63212-4_51

on influence of pressure at constant turbulent Reynolds number, and influence of turbulent Reynolds number at constant pressure on flame structure and propagation for HHC lean premixed syngas flames in the thin reaction zone regime. Thus, there is a need for DNS investigation on HHC syngas turbulent lean premixed flames at different turbulent Reynolds numbers and different pressure levels.

The outwardly propagating cylindrical flame at elevated pressure is adopted as a model flame for the present investigation. In all the considered cases, two-dimensional DNS were performed for HHC lean premixed hydrogen-rich hydrogen-carbon monoxide syngas fuel mixture with an equivalence ratio of 0.7. This paper will focus on answering following question: How does pressure elevation at constant turbulent Reynolds number and turbulence intensification at constant pressure couple with preferential diffusion effect on heat release rate, flame strain and curvature of lean premixed HHC syngas turbulent flame?

2 DNS Governing Equations, Chemistry and Numerical Details

The set of governing equations solved in DNS is the time-dependent compressible flow Navier-Stokes equations coupled with detailed chemistry and mixture-averaged transport model via coupling with chemkin, transport and eglib. In this study an equation is solved explicitly for each and every chemical species with comprehensive detailed chemistry, simultaneously with the Navier-Stokes equations. In this investigation we have employed a hydrogen-carbon monoxide kinetic scheme developed by Goswami et al. [5]. This reaction model incorporates the thermodynamic, kinetic, and species transport properties related to elevated pressure H_2/CO and oxidation, consisting of 14 species and 52 individual reactions. Furthermore, we employed the mixture-averaged transport model supplemented with a model for Soret effect (thermal diffusion) to compute the diffusive process. The full compressible governing equations together with considered thermodynamical relations, chemistry and transport models are solved using the parallel DNS flame solver, Parcomb [6]. The equations are discretised in space on a two-dimensional Cartesian grid with high-order finite difference numerical schemes. Derivatives are computed using centered explicit schemes of order six except at boundaries where the order is progressively reduced to four. Temporal integration is realized with a Runge–Kutta algorithm of order four.

A Courant-Friedrichs-Levy (CFL) condition for the convective terms and a Fourier condition pertaining to the diffusion terms are treated to ensure the stability of the explicit integration and determine a suitable time step. Boundary conditions are treated with the help of improved non-reflecting inflow/outflow Navier-Stokes characteristics boundary condition (NSBC) by considering additional terms in the definition of the wave amplitudes, and the relaxation treatment for the transverse gradient

terms in analogy with the pressure relaxation. The initial isotropic turbulent velocity field for each case was initialised using a combined approach of digital filtering (DF)and random noise diffusion.

The square box had a length of 1.5 cm on each side with 1600 and 1600 computational nodes on each direction. A time step of approximately 1.8ns was used for all simulations. To understand the individual effects of pressure elevation at constant turbulent Reynolds number and turbulence intensification at constant pressure on flame characteristics, six DNS test cases with the inclusion of non-unity Lewis numbers were performed by employing detailed chemical mechanism of Goswami et al. [5]. In the present study, two different pressure values of p = 2 and 4bar at constant turbulent Reynolds number, and three different turbulent Reynolds number of Re = 50, 100 and 150 at constant pressure value were considered.

3 Results and Discussion

Figure 1 shows instantaneous images of the expanding spherical flame temperature couple with preferential diffusion at constant pressure values ranging from p = 2 to 4bar under constant turbulent Reynolds number conditions ranging from Re = 50 to 150. Two observations are made. First, it can be seen that the onset of flame cells is dominated by elevated pressure than increased turbulence. For example, it is evident from Fig. 1 that pressure increase from p = 2 to 4bar at constant Re = 50 has greatly enhanced fine scale flame cells at the flame front compared to its formation due to turbulence intensification from Re = 50 to 150 at constant pressure of p = 2bar. Similar behaviour is also observed for other cases as well. Second, we observed that cellular instabilities occurring earlier for p = 4bar compared p = 2bar.

The evolution of flame cells at elevated pressures is strongly linked with both hydrodynamic and diffusive-thermal instabilities. In particular, we observed that lean premixed HHC syngas flames tend to exhibit cellular instabilities immediately after initiation of propagation because of simultaneous excitation of the diffusive-thermal cellular instability via non-unity Lewis number. It is also believed that the onset of hydrodynamic instability is influenced by the density ratio between unburned and burned gas, and the flame thickness. These observations are consistent with previous experimental findings for appearance of hydrodynamic and diffusive-thermal cellular instabilities in outwardly expanding hydrogen/propane spherical flames at elevated pressure reported by Law et al. [7].

Figure 2 shows the scattered heat release rate data plotted versus progress variable at pressure levels p = 2 and 4bar under constant Re conditions, and at increased turbulence levels ranging from Re = 50 to 150 at constant pressure conditions. Several observations can be made: the scattered data of heat release rate between different pressure values and turbulent Reynolds numbers show noticeable differences highlighting the individual effects of pressure elevation at constant Re and turbulent intensification at constant pressure on heat release rate distributions. The scattered data of heat release rate display a large populated area at elevated pressure,

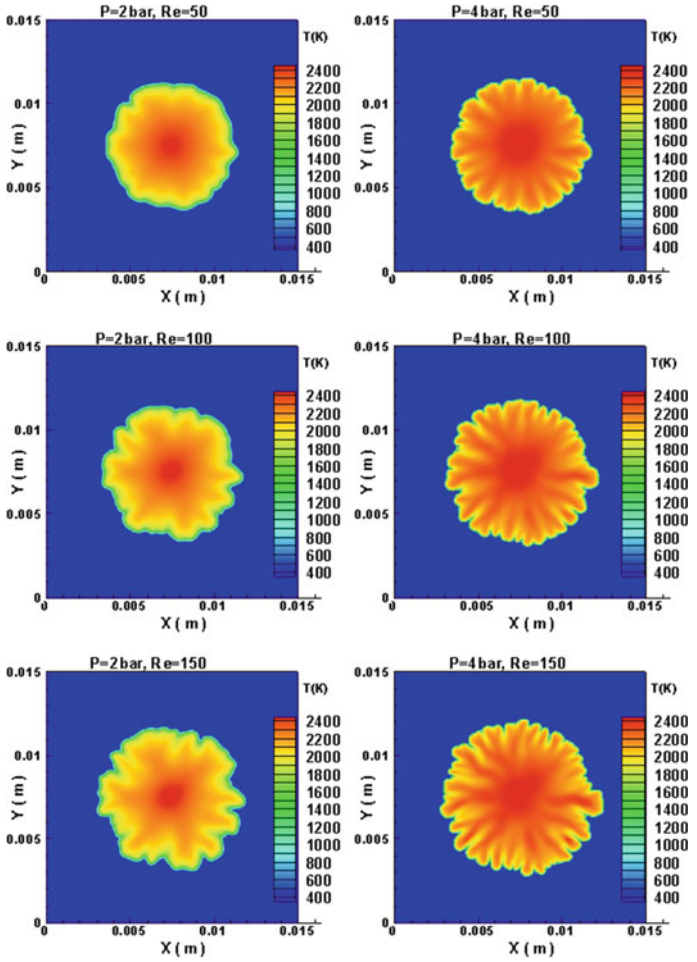

Fig. 1 Instantaneous snapshots of flame temperature at two different elevated pressure, and three different turbulent Reynolds number conditions displaying individual influence of pressure elevation at constant Reynolds number and turbulence growth at constant pressure

p = 4bar and Re = 50. Also, heat release rates show large differences in its maximum value with increased pressure. Similarly, the maximum value of heat release rate is also increased with turbulence intensification at constant pressure, but the margin is lower than that observed at elevated pressure. The turbulence intensification (Re = 150) at constant pressure also shows more populated scattered data compared to low turbulence level, Re = 50 at similar constant pressure. However, it is evident that turbulence intensification becomes less influential on forming widely spread population of heat release rate at elevated pressure compared to atmospheric pressure.

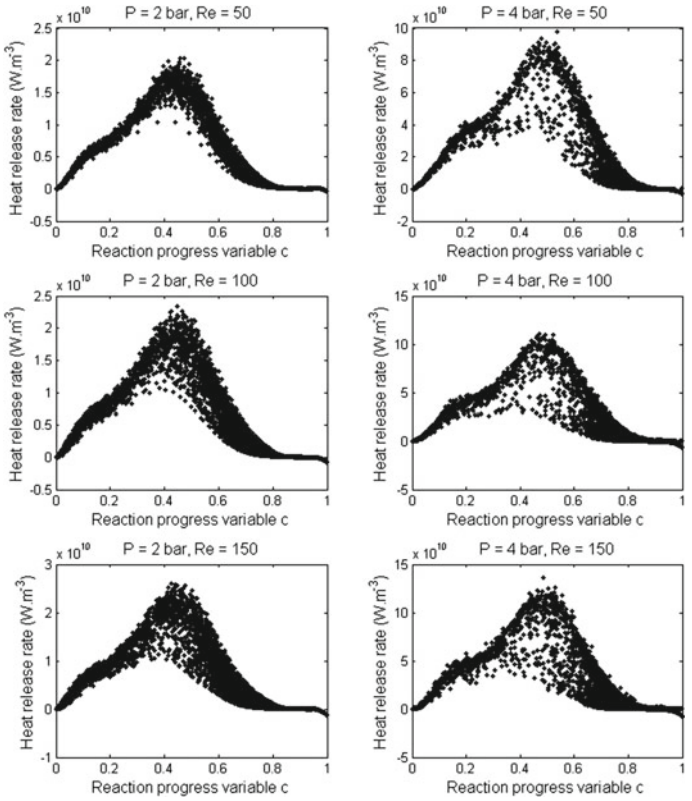

Fig. 2 Scatterplots of heat release rate across the flame at two pressures varying from p = 2 to 4bar at constant Re, and three turbulent Reynolds numbers varying from Re = 50 to 150 at constant pressure

To understand the effect of stretch on the flame structure at different pressure levels, it is worth investigating strain rate and curvature effects on the flame front propagation. As to the analysis of strain rate and curvature effects, scattered data of strain rate and surface density function, and scattered data of curvature and surface density function are analysed. Figure 3 shows the scattered data of tangential strain rate plotted versus SDF at different pressure levels ranging from p = 2 to 4bar under constant Re, and at turbulence levels ranging from Re = 50 to 150 at constant pressure. Generally, the scattered plots of SDF and tangential strain rate show positive correlation for all cases ranging from p = 2 to 4bar and Re = 50 to 150. It is evident that increased pressure at constant Re becomes more influential than turbulence intensification at constant pressure on generating strong positive correlation between SDF and tangential strain rate.

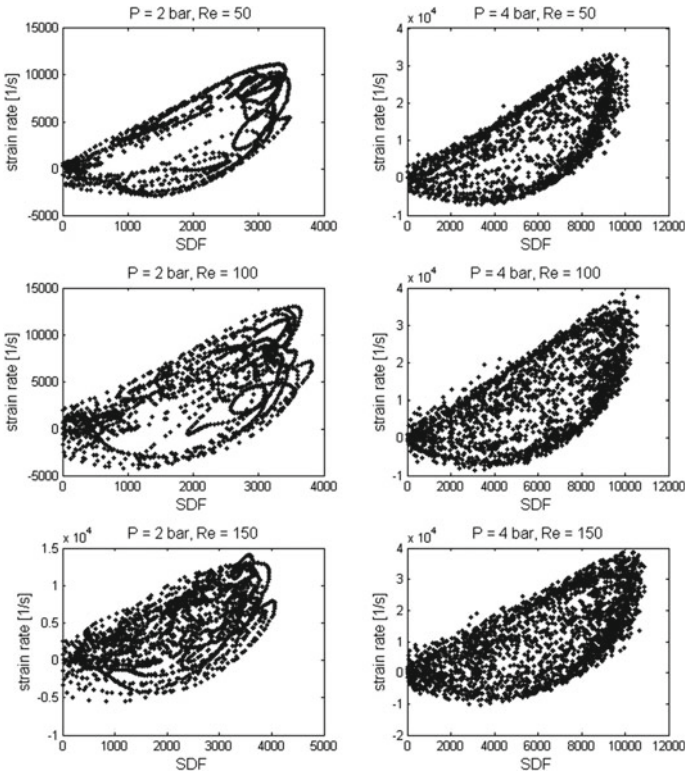

Fig. 3 Scatterplots of surface density function (SDF) with tangential strain rate at two pressures varying from p = 2 to 4bar at constant Re, and three turbulent Reynolds numbers

4 Conclusions

DNS of turbulent lean premixed high hydrogen content (HHC) syngas flame with detailed chemistry and multi-component transport models has been carried out for outwardly propagating cylindrical flames in the thin reaction zone regime. Under constant turbulent Reynolds number and elevated pressure conditions, highly wrinkled cellular flame structures are observed. It is found that increased pressures significantly influence distributions of hear release rate, surface density function, and correlations between surface density function and tangential strain rate, surface density function and curvature in the thin reaction zone.

References

1. Wall, T.F.: Combustion processes for carbon capture. Proc. Combust. Inst. **31**, 31–47 (2007)
2. Verhelst, S., Wallner, T.: Hydrogen-fueled internal combustion engines. Prog. Energy Combust. Sci. **35**, 490–527 (2009)
3. Hawkes, E.R., Chen, J.H.: Direct numerical simulation of hydrogen-enriched lean premixed methane-air flames. Combust. Flame **138**, 242–258 (2004)
4. Aspden, A.J., Day, M.S., Bell, J.B.: Lewis number effects in distributed flames. Proc. Combust. Inst. **33**, 1473–1480 (2011)
5. Goswami, M.: Bastiaans, R.J.M., Konnov, A.A. and de Goey, L.P.H.: Laminar burning velocity of lean hydrogen-carbon monoxide mixtures at elevated pressure. Int. J. Hydrogen Energy **39**, 1485–1498 (2014)
6. Hilbert, R., Tap, F., El-Rabii, H., Thevenin, D.: Impact of detailed chemistry and transport models on turbulent combustion simulations. Prog. Energy Combust. Sci. **30**, 165–193 (2004)
7. Law, C.K., Jomaas, G., Bechtold, J.K.: Cellular instabilities of expanding hydrogen/propane spherical flames at elevated pressures. Proc. Combust. Inst. **30**, 159–167 (2005)

Analysis of the Interactions of the Precessing Vortex Core with a Spray Flame in a Swirl Burner

L. Guedot, G. Lartigue and V. Moureau

1 Background and Motivation

Swirling jet flows are widely used in combustion devices for the stabilization of premixed or partially premixed flames. The swirl generates a pressure drop near the axis that leads to the formation of an axial recirculation zone. In such flows, the incoming gases are slowed down by the recirculation zone, and the reaction zone is fed with recirculating hot gases ensuring the stability of the flame [1]. In some conditions, the swirl may lead to the formation of coherent structures such as the Precessing Vortex Core (PVC) [1, 2], single or multiple helical vortices.

Based on modal analysis of experimental data, some authors showed that the PVC may be responsible of local extinction of the flame or auto-ignition [3]. The PVC may also wrinkle the premixed flame front, creating isolated flame pockets and periodic fluctuations of the heat release rate, that might affect the acoustic behavior of the chamber [2]. Some recent studies [4] showed that the PVC can either amplify or damp acoustic instabilities, according to the respective position of the PVC and the flame. In the case of spray flames, the PVC also influences the distribution of fuel mass fraction as it leads to preferential segregation of fuel droplets [5]. Some recent work [6] showed that the high level of turbulence due to the PVC close to the fuel injection helps the atomization process, improving the efficiency of the device. The analysis of this large-scale feature that plays an important role in the flow dynamics is mandatory to improve the understanding of swirl stabilized combustion.

L. Guedot · G. Lartigue · V. Moureau (✉)
CORIA - CNRS UMR 6614, Normandy Université, Saint Etienne du Rouvray, France
e-mail: vincent.moureau@coria.fr

L. Guedot
e-mail: lola.guedot@coria.fr

G. Lartigue
e-mail: ghislain.lartigue@coria.fr

D.G.E. Grigoriadis et al. (eds.), *Direct and Large-Eddy Simulation X*,
ERCOFTAC Series 24, https://doi.org/10.1007/978-3-319-63212-4_52

In well refined simulations that feature a large range of turbulent scales, the Q-criterion [7] of the smallest vortices is important due to the higher velocity gradient. Large scales structures are completely masked by the smaller vortices. Spatial low pass filters are a solution to alleviate this problem, and to perform scale separation of the different coherent structures. High-order filters, characterized by their good selectivity, have been adapted to three dimensional unstructured grids and implemented in the LES solver YALES2 [8]. Their implicit formulation is interesting since it allows to write high-order filters from low order derivative operators on compact stencils. The filtering operation removes the small-scale structures, leaving only the large scale vortices. By chosing the appropriate filter size, the PVC can be extracted in the case of swirl burners.

2 Analysis of Spray-Flame-PVC Interaction in a Swirl Burner

2.1 Description of the MERCATO Burner and Numerical Setup

The geometry of the MERCATO burner, dedicated to the study of two-phase combustion, features a plenum, a swirler, and a square combustion chamber. The operating conditions are summarized in Table 1 [9]. The Reynolds number based on the diameter of the swirler exit and the bulk velocity is approximately $Re = 54\,000$ and the swirl number $Sw = 0.7$. Axial velocity measurements are available in sections located at 10, 26, 56 and 116 mm from the injection plane. The LES profiles will be compared to these experimental data, and to numerical profiles from the Euler-Lagrange simulation performed with the AVBP code [10].

The simulation was performed with the LES code YALES2, that solves the low-Mach Navier-Stokes equations [11]. Sub-grid scale turbulence closure is achieved with the dynamic Smagorinsky model [12] and no-slip wall conditions are imposed on the chamber walls. The mesh features 40 million tetrahedra.

The dispersed phase is described with Lagrangian particles. The gas and the particles are two-way coupled with mass, momentum and energy exchanges. A discrete probability density function of 50 classes of droplet diameters is used to reproduce a Rosin-Rammler distribution. The evaporation model assumes an infinite thermal conductivity of the liquid, the temperature is supposed uniform in the droplet.

A two-step chemical scheme was used to describe the reaction [13]. It accounts for a kerosene oxidation reaction and the CO-CO_2 equilibrium, and uses a correction

Table 1 Operating conditions

T_{air} (K)	T_{fuel} (K)	$\dot{m}_{air}$ (g/s)	$\dot{m}_{fuel}$ (g/s)	P (Pa)
293	300	35	2.25	101 300

function to reproduce the laminar flame speed and the burnt gases temperature over a wide range of conditions. To encounter for the flame/turbulence interaction, the TFLES model was used [14] to thicken the flame front according to a dynamic flame sensor based on the source terms of species CO, CO_2 and H_2O. The kerosene is modeled by a single species composed (in volume) of 74% of $C_{10}H_{22}$, 15% of C_9H_{12} and 11% of C_9H_{18} [13]. The thermodynamic properties of this equivalent species are computed as an average of individual kerosene component properties.

2.2 Results

Mean axial velocity profiles are displayed in Fig. 1. The flow is characteristic of swirl burners, with a large central recirculation zone (CRZ). The global flow topology and the amplitude of the mean and RMS velocity profiles is well reproduced. The size of the CRZ is over-estimated in the two first planes, but in good agreement with the simulation of Hannebique [10].

Figure 2 shows the kerosene mass fraction and heat release rate in the mid-plane. The M-shaped flame is anchored at the external wall of the swirler exit, and in the central recirculation zone, close to the rotation axis. The fuel mass fraction is not homogeneous, and tends to accumulate in isolated pockets arranged in the chamber in helical PVC-like patterns.

2.3 Flame Anchoring Stability

The flow dynamics is characterized by a periodic motion close to the injection, where the anchoring point of the flame periodically oscillates in the CRZ from top to bottom in the mid-plane. The flame anchoring is a key parameter for the stability of the combustor. To track the location of this point over several PVC periods, the PVC and the flame surface were isolated using a levelset segmentation algorithm [8]. The extraction algorithm consists in filtering the Q-criterion and the temperature,

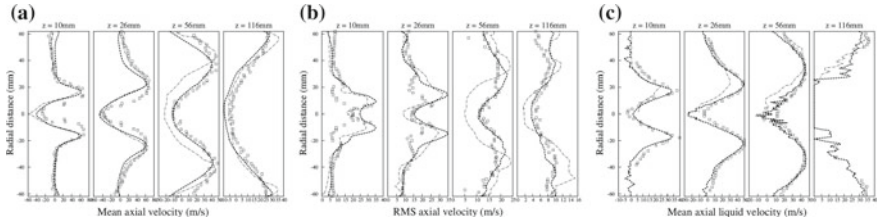

Fig. 1 Axial gaseous (a,b) and liquid (c) velocity profiles in the 4 measurement planes (Symbols: Exp [9] - dash-dot line : AVBP [10] - dash line : YALES2)

Fig. 2 Kerosene mass fraction (*left*) and heat release rate (*right*) and circles highlighting the influence of the PVC on the flame topology

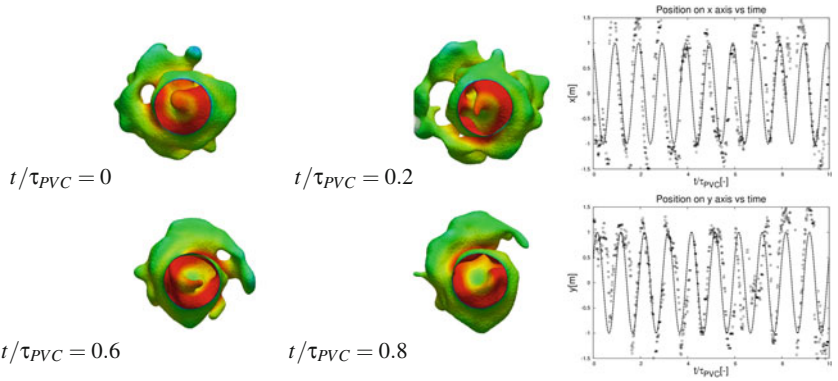

Fig. 3 Rotation of the anchoring point, visualized with isosurfaces of filtered temperature (*left*), and temporal evelotion of the flame anchoring point coordinates (*right*)

and defining a levelset fonction based on the $\overline{Q} = 2 \times 10^8\ \mathrm{s}^{-2}$ and $\overline{T} = 1100\,\mathrm{K}$ isosurfaces. The anchoring point is defined as the mesh point in the burnt gases ($\overline{T} > 1100\,\mathrm{K}$) with smaller axial coordinate in the close injection area. The flame surface (*i.e.* $\overline{T} = 1100\,\mathrm{K}$ iso-surface) is represented in Fig. 3: the rotation of the flame anchoring point is clearly visible. The direction of rotation matches the PVC precession and the swirl. The flame surface however wraps around the CRZ in the opposite direction. The anchoring point is collected over 10 PVC periods. The points are located around 6 mm from the rotation axis, and at 10 mm from the combustor head, with small fluctuations in the axial direction. The frequency of the coordinates oscillation matches the PVC frequency (around 1050 Hz).

2.4 Spray-PVC-Flame Interaction Mechanism

Figure 4 shows iso-surfaces of $\overline{Q} = 2 \times 10^8\ \mathrm{s}^{-2}$ (PVC) and $\overline{T} > 1100\,\mathrm{K}$ (flame surface). The temperature isosurface follows the helical shape of the PVC. Figure 4a,c shows that the spray is swept away by the PVC, and particles are concentrated in the azimuthal portion of the plane oposite the the PVC. This phenomenon, combined

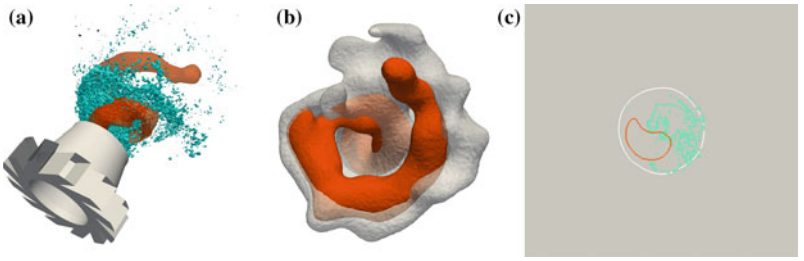

Fig. 4 Flame surface, PVC, and spray : 3D view (a,b), and slice at 6 mm of the injection plane (c)

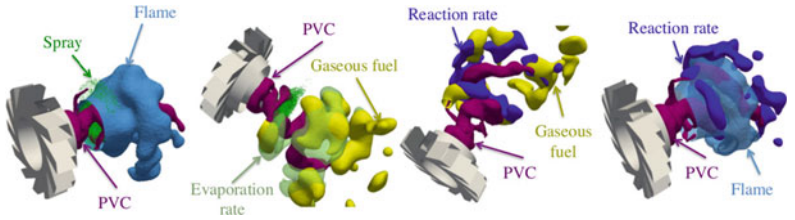

Fig. 5 PVC, flame, spray, and filtered fuel mass fraction, evaporation rate and heat release rate

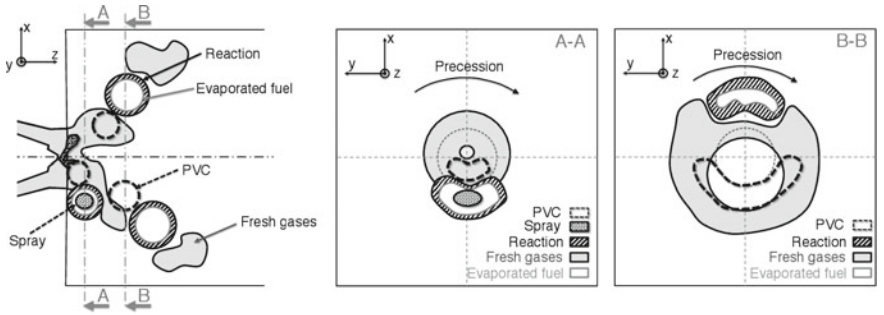

Fig. 6 Sketch of the PVC-spray-flame interaction mechanism

with the precessing movement of the PVC, imparts a helical shape to the spray that rotates around this axis with the PVC.

Iso-surfaces of filtered main variables are displayed in Fig. 5, to show the interaction mechanism between the PVC and the spray flame. The spray is asymmetric and droplets are gathered away from the rotation axis. Radial expansion convects the particules to the burnt gases, where heating and evaporation are enhanced by the high temperatures. Droplets start evaporating close to the external wall of the swirler exit. The precession of the PVC gradually shifts this process in the azimuthal direction, generating local emission of gaseous fuel that periodically rotates around the external wall of the swirler exit, at the basis of the combustor head, were the flame is anchored. The spatial distribution of the evaporated kerosene is thus helical-shaped

and follows the PVC with a phase difference. This mecanism is sketched in Fig. 6. The reaction, which is initiated by the local production of fuel, follows this mechanism. The fuel released in these rich pockets starts burning in diffusion regime, hence the helical shape of the flame surface observed earlier. The remaining fuel is then mixed by turbulent activity and burns in premixed regime further downstream.

3 Conclusions

This work, based on high-order filtering [8] proposes an original approach to study the interaction of the PVC with the flow, and the spray flame, when most of the methods are based on modal analysis and phase averaging. The analysis performed on the MERCATO burner showed that the PVC generates large scale fluctuations of all the main variables and drives the flame topology. The interaction mechanism is initiated close to the injection, where the PVC affects the spray dynamics in a decisive manner for the flow further dowstream. This perturbation of the spray topology impacts the spatial distribution of the fuel, and, by extension, the flame structure.

Acknowledgements Computational time was provided by GENCI, and all simulations were performed on the HPC ressources of IDRIS and CINES

References

1. Lucca-Negro, O., O'Doherty, T.: Vortex breakdown: a review. Prog. Energy Combust. Sci. **27**(4), 431–481 (2001)
2. Syred, N.: A review of oscillation mechanisms and the role of the precessing vortex core (PVC) in swirl combustion systems, Prog.v Energy. Combust. Sci. **32**(2), 93–161 (2006)
3. Boxx, I., Stohr, M., Carter, C., Meier, W.: Temporally resolved planar measurements of transient phenomena in a partially premixed swirl flame in a gas turbine model combustor. Combust. Flame **157**(8), 1510–1525 (2010)
4. Steinberg, A.M., Boxx, I., Stöhr, M., Meier, W., Carter, C.D.: Effects of flow structure dynamics on thermoacoustic instabilities in swirl-stabilized combustion. AIAA j. **50**(4), 952–967 (2012)
5. Sanjose, M., Senoner, J.M., Jaegle, F., Cuenot, B., Moreau, S., Poinsot, T.: Fuel injection model for Euler-Euler and Euler-Lagrange large-eddy simulations of an evaporating spray inside an aeronautical combustor. Int. J. Multiph. Flow **37**(5), 514–529 (2011)
6. Jones, W.P., Lettieri, C., Marquis, A.J., Navarro-Martinez, S.: LES of the two-phase flow in an experimental swirl-stabilized burner. Int. J. Heat Fluid Flow **38**, 145–158 (2012)
7. Hunt, J.C., Wray, A. A, Moin, P.: Eddies, streams, and convergence zones in turbulent flows, Center for turbulence research report CTR-S88, pp. 193–208 (1988)
8. Guedot, L., Lartigue, G., Moureau, V.: Design of implicit high-order filters on unstructured grids for the identification of large-scale features in large-eddy simulation and application to a swirl burner. Phys. Fluids **27**(4) (2015)
9. Lecourt, R., Linassier, G., Lavergne, G.: Detailed characterisation of a swirled air kerosene spray in reactive and non-reactive conditions downstream from an actual turbojet injection system. ASME : Turbine Tech. Conf. Expos. 185–194 (2011)
10. Hannebique, G.: Etude de la structure des flammes diphasiques dans les bruleurs aeronautiques, Ph.D. thesis (2014)

11. Moureau, V., Domingo, P., Vervisch, L.: Design of a massively parallel CFD code for complex geometries. C. R. Mec. **339**(2), 141–148 (2011)
12. Germano, M., Piomelli, U., Moin, P., Cabot, W.H.: A dynamic subgrid scale eddy viscosity model. Phys. Fluids **3**(7), 1760–1765 (1991)
13. Franzelli, B., Riber, E., Sanjose, M., Poinsot, T.: A two-step chemical scheme for kerosene air premixed flames. Combust. Flame **157**(7), 1364–1373 (2010)
14. Colin, O., Ducros, F., Veynante, D., Poinsot, T.: A thickened flame model for large eddy simulations of turbulent premixed combustion. Phys. Fluids **12**(7), 1843–1863 (2000)

The Turbulent Flame Speed of Premixed Spherically Expanding Flames

G.K. Giannakopoulos, C.E. Frouzakis, M. Matalon and A.G. Tomboulides

Abstract Premixed syngas/air flames expanding in turbulent flow fields are investigated using large scale direct numerical simulations. A parametric analysis is performed in circular and spherical geometries for the detailed investigation of the interaction between the flame front and the turbulent flow field. A stoichiometric syngas-air mixture with molar ratio $CO/H_2 = 3$ is considered at conditions relevant to internal combustion engines. The dependence of the integral heat release rate on the characteristics of the flow field (integral length scale and turbulent intensity) is discussed. The long-term evolution of important global flame quantities is analyzed, and the mechanisms that dominate the growth of the flame kernel are identified. An expression for the speed of turbulent premixed spherical flames is formulated, based on the rate of change of the surface area of the flame.

Keywords Turbulent premixed flame · Turbulent flame speed · Spherically expanding flame · Syngas flames

G.K. Giannakopoulos (✉) · A.G. Tomboulides
Department of Mechanical Engineering, University of Western Macedonia,
Kozani, Greece
e-mail: gkgiannakopoulos@uowm.gr

A.G. Tomboulides
e-mail: atompoulidis@uowm.gr

C.E. Frouzakis
Aerothermochemistry and Combustion Systems Laboratory, ETH Zurich, Switzerland
e-mail: frouzakis@lav.mavt.ethz.ch

M. Matalon
Department of Mechanical Science and Engineering, University of Illinois,
Urbana-champaign, USA
e-mail: matalon@illinois.edu

D.G.E. Grigoriadis et al. (eds.), *Direct and Large-Eddy Simulation X*,
ERCOFTAC Series 24, https://doi.org/10.1007/978-3-319-63212-4_53

1 Introduction

The development of new combustion systems depends crucially on the availability of predictive models that incorporate the relevant physico-chemical processes and can account for the flow/chemistry interactions in the regimes of interest. Plagued by empiricism (adjustable parameters) drawn primarily from existing knowledge, current engineering models are incapable of delivering reliable predictive results. The growth of high-performance computing has enabled high-fidelity direct numerical simulations (DNS) which capture the details of the intricate aero-thermo-chemical interactions in laminar and turbulent combustion with a spatial and temporal resolution that cannot be achieved by other means. In addition to the simplified descriptions of chemistry that was employed in most of the DNS works so far, relatively small square or cubic periodic domains of sizes up to approximately $50\delta_{th}$ and mainly equidiffusive (unity Lewis number) mixtures were considered. In this work, a first effort is made to analyze the data of a series of large-scale parametric DNS in open spherical domains, in order to study the early growth of the flame initiated at the ignition kernel, and the long-term development of the corrugated flame surface as it interacts with turbulent eddies of different size and intensity.

2 Definitions

The laminar flame speed S_L of a premixed flame is conventionally defined as the propagation speed relative to the incoming fresh mixture. The flame speed is affected by the flame curvature and the local hydrodynamic strain, effects that are said to stretch the flame surface [4]. According to [5], at the limit of low stretch, the relation of flame speed with stretch is linear and is modulated by the so-called Markstein length, a parameter on the order of the flame thickness that measures the sensitivity of flame speed to stretch, and incorporates the effects of mixture composition and stoichiometry.

A key challenge in the study of turbulent flames is the proper definition of the turbulent flame speed S_T and its correlation with the characteristics of the turbulent flow field (integral length scale L_T and turbulence intensity u'). Unlike the laminar flame speed which is a thermochemical property of a given combustible mixture, the turbulent flame speed also depends on the local flow conditions and is affected by both flame area increase due to turbulence, as well as local flame speed variation due to stretch. Damköhler [8] formulated an expression for the flame speed of a planar turbulent flame as

$$\frac{S_T}{S_L} = \frac{A_T}{A} \tag{1}$$

The above expression shows that the increase of the turbulent flame speed S_T compared to the planar laminar flame speed S_L is equal to the ratio of the total surface of the wrinkled flame A_T and its cross-section A. Despite the fact that this relation is

able to describe the kinematics of a planar turbulent flame, it is yet unclear how it can be applied to cylindrical or spherical flames, and, in particular, how the cross section A is defined in this case. In the present work, an attempt to adapt the above relation is made, in order to better describe the kinematics of circular and spherical flames.

3 Numerical Methodology

The conservation equations of mass, momentum, species and energy are integrated in their low-Mach number form [9, 10], which accounts for density variations due to heat release and temperature rise while removing time step restrictions due to acoustic wave propagation. The gaseous mixture is assumed to be ideal and the species diffusion velocities are given by Fick's law based on the mixture-average formulation for the species diffusivities. The equations are discretized in space using the spectral element method [11], in a computational domain that is split into curved conforming quadrilateral or hexahedral elements. The solution and geometry are expressed as Nth-order tensor product Lagrange polynomials based on the Gauss-Lobatto-Legendre quadrature points. The discretized equations are integrated in time with a highly-efficient parallel code based on $nek5000$ [12] and a high-order splitting scheme for low-Mach number reactive flows [13]. A semi-explicit integration scheme is used for continuity and momentum, while the energy and species equations are integrated implicitly using CVODE [14].

Parametric 2D and 3D simulations were performed, with the focus being on the investigation of the early flame kernel development and its long-term interaction with the turbulent flow field. The adjustable parameters were the fuel composition (molar CO/H_2 ratio), the equivalence ratio and the integral length scale L_T, and intensity of turbulence u'. In this paper, only the effect of the turbulence characteristics in the propagation of the flame kernel is investigated. The fuel CO/H_2 ratio is 3:1 and the mixture is stoichiometric, whereas the temperature and pressure of the unburned mixture are T_u=750 K and p=8 atm, respectively. For the chemistry description, the detailed 12 species/35 reactions mechanism proposed in [15] is used. The CHEMKIN transport and thermo-chemistry libraries are used for the evaluation of the transport and thermodynamic properties and chemical reaction rates. The flame thickness $\delta = (T_b - T_u)/(\partial T/\partial x)_{\max}$, the laminar flame speed S_L and the burned gas composition and temperature T_b are calculated using PREMIX for the corresponding planar adiabatic flame. Unless otherwise noted, all reported velocities, lengths and times are rendered non dimensional using S_L, δ_{th} and δ_{th}/S_L. The circular/spherical grids employed in the 2-D/3-D simulations offer the advantage of using zero-Neumann (outflow) BC for all variables. Thus, an open, constant pressure domain is simulated, eliminating confinement effects due to pressure increase. The domain extends up to a diameter of $200\delta_{th}$ and consists of 33,660 (2D) and 1.5×10^6 (3D) spectral elements of polynomial order $N = 9$, resulting to a total number of grid points equal to 3.37×10^6 and 1.5×10^9, respectively. The average (and almost uniform) mesh resolution is approximately 10 points/δ_{th}.

4 Effect of Turbulence on the Global Growth Rate

The results from the reactive calculations and the effect of turbulence on the early flame kernel propagation and the integral heat release rate (iHRR) are presented in this section. The turbulent flame propagation can be characterized by two distinct time scales, the time scale of turbulence (L_T/u') and of chemistry (δ_{th}/S_L), with their ratio defining the Damköhler number $Da = t_{flow}/t_{flame}$. The temporal evolution of the integral heat release rate is shown in Fig. 1(left) for a series of 2D calculations with the turbulence length scale and intensity summarized in Table 1. In general, greater turbulence intensity leads to increased rate of heat release. For low intensities the iHRR evolution is almost linear, in contrast to the exponential growth observed at higher intensities. The dominant mechanism for this increase is demonstrated in Fig. 1(right), where the evolution of the iHRR for selected cases of Fig. 1(left) is plotted along with the calculated area (length in 2D) of the flame front (defined by the $T = 3T_u$ iso-surface). As observed, the two quantities are directly proportional.

In the inset graph of Fig. 1(left), the early stages of the calculations are magnified ($t_{flame} = 1.5 - 2.5$). This time corresponds to the transition phase of the flame kernel from laminar to turbulent, due to the flow-flame interactions. As noted, cases are grouped depending on Da (see also Table 1). Furthermore, with decreasing Damköhler number, an enhanced interaction between the flame kernel and the turbulent eddies is observed, resulting in the overall increase of the iHRR.

Table 1 Simulation parameters for the 2D cases considered in this study

Cases	C1	C2	C3	C4	C5	C6	C7	C8	C9	C10
u'/S_L	0.8	1.3	0.8	1.3	1.9	1.3	2.0	3.5	2.0	3.6
L_T/δ_{th}	1.6	1.6	2.5	2.6	2.7	4.0	4.0	4.2	6.7	6.4
Da	2.0	1.2	3.1	2.0	1.4	3.1	2.0	1.2	3.4	1.8

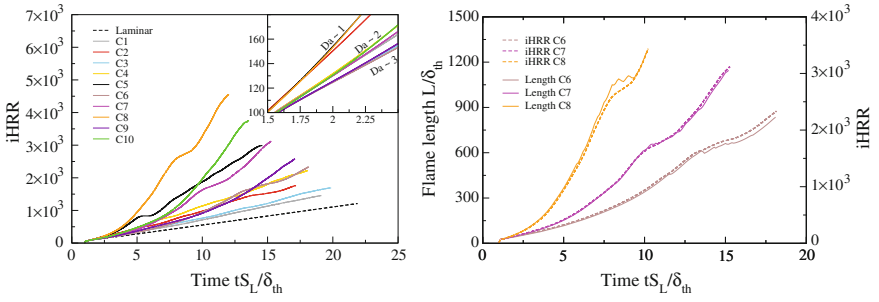

Fig. 1 (*Left*) Temporal evolution of the iHRR for simulations with different turbulence characteristics (see also Table 1) and (*Right*) correlation between the flame area (length in 2D) and iHRR for selected cases

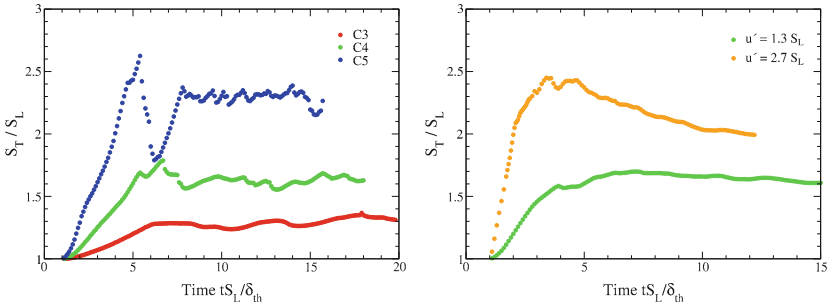

Fig. 2 Temporal evolution of the calculated turbulent flame speed S_T using (1) and (2) for cases with different turbulence intensity in 2-D (*left*) and 3-D (*right*) simulations

5 Turbulent Flame Speed

The flame speed of a turbulent premixed flame can be expressed in numerous ways that can be based on local or global flame characteristics. As stated before, the heat release rate is directly related to the increase of the flame surface. It is therefore logical to seek a definition that can incorporate this relation. The focus of this section is on the formulation of an expression which is based on the Damköhler relation (1), but is adapted appropriately to describe the motion of spherically expanding turbulent premixed flames. The problem lies on the proper description of the cross-section area A in equation (1). In a spherical (cylindrical) flame, this area can be expressed as the surface area (length) of a laminar spherical (circular) flame kernel, whose radius is equal to the mean radius R_m of the turbulent flame. Therefore,

$$A_{2D} = 2\pi R_m \qquad and \qquad A_{3D} = 4\pi R_m^2 \tag{2}$$

for 2-D and 3-D flames, respectively. In Fig. 2, the time history of the resulting turbulent flame speed S_T is plotted using the combination of Eqs. (1) and (2) for selected 2-D simulations defined in Table 1 (left) and for 3-D (right) with $L_T/\delta_{th} = 2$ and $u'/S_L = 1.3$ and 2.7. The speed initially increases at a rate which is higher as the intensity of the turbulent flow field increases, and then it levels off and fluctuates around a certain value. Therefore, by normalizing the total flame area with an equivalent laminar flame area of the same mean radius, the effect of turbulence on the flame speed can be isolated from the mean flame propagation. In addition, it is interesting to note that the turbulent flame speed balances for all cases at the same time ($t_{flame} \approx 5$).

6 Discussion

Parametric direct numerical simulations of premixed, spherically expanding turbulent syngas-air flames were performed to investigate the effect of the turbulence characteristics (integral length scale L_T and intensity u') on the integral of the heat release rate in the whole domain. It was found that the transition of the flame kernel from laminar to turbulent is dominated by the relation between the chemical time scale (t_{flame}) and the flow time scale (t_{flow}), which is expressed through the Damköhler number. The subsequent propagation of the flame kernel is determined by the significant increase of the effective flame front area resulting from increased wrinkling and the higher flame stretch rate. An expression for the turbulent flame speed based on Damköhler's formulation was examined, adapted appropriately to cylindrical and spherical flame geometries, allowing for comparison with the results obtained from statistically stationary planar turbulent flames.

The data from the parametric direct numerical simulations performed can contribute significantly to our understanding of the complex phenomena that take place during turbulent premixed combustion. Further global and local analysis of the propagating front and the effect of fuel composition and equivalence ratio are the subjects of ongoing efforts.

References

1. Jenkins, K.W., Cant, S.: Curvature effects on flame kernels in a turbulent environment. Proc. Combust. Inst. **29**, 2023–2029 (2002)
2. Thévenin, D.: Three-dimensional direct simulations and structure of expanding turbulent methane flames. Proc. Combust. Inst. **30**, 629–637 (2005)
3. Fru, G., Thévenin, D., Janiga, G.: Impact of turbulence intensity and equivalence ratio on the burning rate of premixed methane-air flames. Energies **4**, 878–893 (2011)
4. Matalon, M.: On flame stretch. Combust. Sci. Tech. **31**, 169 (1983)
5. Markstein, G.H.: Nonsteady Flame Propagation. Pergamon Press, (1964)
6. Veynante, D., Poinsot, T.: Theoretical and Numerical Combustion. Edwards, (2001)
7. Williams, F.A.: Combustion Theory. Benjamin/Cummings, (1985)
8. Damköhler, G.: On self-acceleration of outward propagating wrinkled flames. Z. Elektrochem. und Angewandte Physikalische Chemie **46**, 601 (1940)
9. Rehm, R.G., Baum, H.R.: Equations of motion for thermally driven, buoyant flows. J. Res. Natl. Bur. Stand. **83**, 97–308 (1978)
10. Chu, B.T., Kovasznay, X.: Non-linear interactions in a viscous heat conducting compressible gas. J. Fluid Mech. **3**, 494–514 (1958)
11. Patera, A.T.: A spectral element method for fluid dynamics: laminar flow in a channel expansion. J. Comp. Phys. **58**, 468–488 (1984)
12. Fischer P.F., Lottes J.W., and Kerkemeier S.G. nek5000 Web page, 2008. http://nek5000.mcs.anl.gov
13. Tomboulides, A.G., Lee, J., Orszag, S.A.: Numerical simulation of low Mach number reactive flows. J. Sci. Comp. **12**, 139–167 (1997)
14. Byrne, G.D., Hindmarsh, A.C.: PVODE, an ODE solver for parallel computers. Int. J. High Perform. Comput. Appl. **13**, 345–365 (1999)

15. Kéromnès, A., Metcalfe, W.K., Heufer, K.A., Donohoe, N., Das, A.K., Sung, C.J., et al.: An experimental and detailed chemical kinetic modeling study of hydrogen and syngas mixture oxidation at elevated pressures. Combust. Flame **160**(6), 995–1011 (2013)
16. Smirnov, S., Shi, A., Celik, I.: Random flow generation technique for large-eddy simulations and particle-dynamics modeling. Trans ASME. J. Fluids Eng. **123**, 359 (2001)

Part IX
Numerics

Boundary Data Immersion Method for DNS of Aero-vibro-acoustic Systems

S.C. Schlanderer and R.D. Sandberg

1 Introduction

The enormous growth of computational power in recent years has enabled the consideration of multi-physics phenomena, complicated shaped and moving bodies in the framework of high-fidelity numerical simulations. In the field of airfoil self-noise recent analytical studies [2, 3] suggest that a prescribed motion or a motion due to elastic deformation of the airfoil or the trailing-edge section has an effect on the scattered noise. Therefore it would be preferable to include the effects of moving bodies into compressible direct numerical simulations (DNS) which directly solve for the hydrodynamic near-field and the acoustic far-field. However, the representation of moving bodies in compressible high-fidelity numerical simulations remains a challenge.

The use of boundary conditions that can represent bodies immersed into a fluid flow independently of the background mesh make such investigations feasible and are well known as immersed boundary methods (IMBM). However such methods are commonly first-order accurate only or computationally too expensive to be used for moving bodies where the IMBM needs to be reinitialized for each timestep. Additionally, sharp interface IMBM have shown to produce non-physical pressure fluctuations due to the fresh cell problem which needs additional treatment [4]. This increases the complexity and computational cost of the method. Furthermore, to the authors' knowledge, there is no method for compressible flows that yields accurate results in aeroacoustic applications featuring moving bodies.

S.C. Schlanderer (✉) · R.D. Sandberg
Aerodynamics and Flight Mechanics Group, University of Southampton, England, UK
e-mail: stefan.schlanderer@soton.ac.uk

R.D. Sandberg
e-mail: r.d.sandberg@soton.ac.uk

D.G.E. Grigoriadis et al. (eds.), *Direct and Large-Eddy Simulation X*,
ERCOFTAC Series 24, https://doi.org/10.1007/978-3-319-63212-4_54

2 Concept of the Boundary Data Immersion Method

In the current work the Boundary Data Immersion Method (BDIM), recently presented for incompressible flows by Maertens & Weymouth [5], is extended to be used for compressible flows. The BDIM allows smooth coupling between the governing equation of a solid body subdomain Ω^B and a compressible fluid subdomain Ω^F as shown in Fig. 1a. As a result a meta equation that is valid in the whole domain under consideration can be derived. The solid body domain is not required to coincide with the background grid. The general formulation for a meta equation of an arbitrary field variable Φ is

$$\Phi_M(\mathbf{x},t) = \begin{cases} \Phi = b & \text{for } \mathbf{x} \in \Omega_b \\ \Phi = f(\Phi) & \text{for } \mathbf{x} \in \Omega_f, \end{cases} \tag{1}$$

where b and f are the governing equations for the body and fluid subdomains, respectively. In the fluid domain this equation is simply the compressible Navier-Stokes equation. For the solid body domain it is assumed that the field quantity Φ is known, e.g., from a structural solver, a flow control framework or simply prescribed.

Both subdomains can be smoothly coupled with interpolation functions μ that act in a smoothing region of size 2ε where both domains overlap as indicated in Fig. 1a by the dashed lines. Using these interpolation functions and taking advantage of the symmetries the meta equation is

$$\Phi_\varepsilon = f(\Phi,\mathbf{x},t)\,\mu_0^\varepsilon + b(\Phi,\mathbf{x},t)\,\left(1-\mu_0^\varepsilon\right) \tag{2}$$

$$+\,\mu_1^\varepsilon \tfrac{\partial}{\partial \mathbf{n}}\left(f(\Phi,\mathbf{x},t) - b(\Phi,\mathbf{x},t)\right) \quad . \tag{3}$$

The interpolation functions μ_0^ε and μ_1^ε are shown in Fig. 1b and depend on d only, which is the signed distance from the surface. The formulation allows for a higher order interpolation between both domains due to the derivative $\frac{\partial}{\partial \mathbf{n}}$ in the wall normal direction. When the derivative term is neglected the method is denoted first-order BDIM, when it is used as in (2) we refer to the method as second-order BDIM. In the current framework, the velocity and temperature fields are mapped directly with Eq. (2) whereas the continuity equation is not changed. The BDIM was implemented into our well-validated compressible in-house DNS code described in [6].

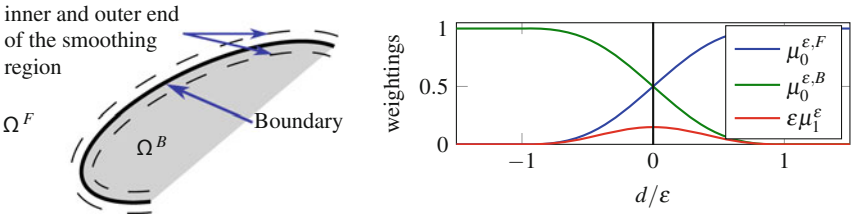

Fig. 1 **a** Illustration of the two subdomains including the smoothing region. **b** Weighting functions for the interpolation between the two subdomains

For more details on the concept of the BDIM, the derivation of the derivative correction and for the exact expressions for $\mu_0^\varepsilon(d)$ and $\mu_1^\varepsilon(d)$ please see reference [5].

3 Validation

In this section the BDIM approach for compressible flows will be validated. Since near-wall accuracy is crucial for direct noise computations the simulation of Tollmien-Schlichting waves has been chosen. This is a very challenging test case and very sensitive to the representation of the near-wall physics. Therefore this case will be used to analyse the formal order of convergence. Thereafter aero-acoustic validation cases will be considered.

For the Tollmien-Schlichting waves (TS-waves) validation-case periodic volume forcing was introduced into a Blasius boundary layer. The disturbances will initially decay before they are amplified. The exact forcing location, amplitude and the details of the computational grid can be found in [6]. The maximum disturbance amplitude of the streamwise velocity component at each streamwise location is then recorded and normalized by the minimum amplitude of all streamwise locations. In order to establish the formal order of convergences the maximum deviation of the disturbance amplitude for $800 < Re_\delta < 1025$ from the reference case with the highest resolution and body-fitted boundary conditions is plotted over the wall grid-spacing in Fig. 2. In addition a first and second-order exponential slope are plotted for comparison. It can be clearly seen that the first order BDIM framework converges with first-order when the resolution is refined. In contrast to that the convergence is improved to second-order when using the derivative correction introduced in Eq. (2).

In order to analyse why the convergence is improved the near-wall velocity profiles and velocity derivatives are presented as a function of the wall normal coordinate normalized by the smoothing region half-width ε in Fig. 3. For the profile of the streamwise velocity component it can be observed that the second-order BDIM takes better advantage of the whole smoothing region $-\varepsilon < d < \varepsilon$ compared to the first-order BDIM. As a result the first-order BDIM leads to an upward shift of the

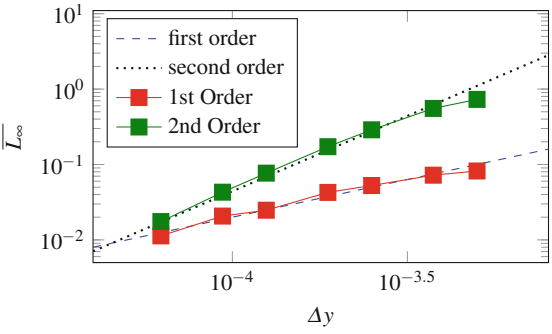

Fig. 2 Convergence of the amplitude error in the growth of TS-waves with varying resolution using the first and second-order BDIM approach to represent the wall boundary

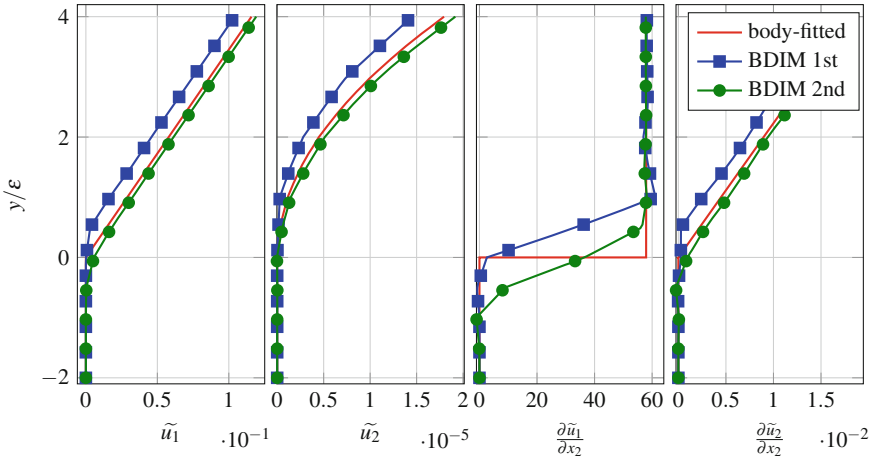

Fig. 3 Velocity profiles and their gradients for different boundary conditions at the wall

velocity profile in the wall normal direction whereas the second-order BDIM shows a reasonably good agreement with the body-fitted reference. The same general trends can be observed for the wall normal velocity component $\widetilde{u_2}$ and its derivative $\frac{\partial \widetilde{u_2}}{\partial x_2}$. In contrast to the quantities discussed so far the streamwise velocity derivative is not continuous at the wall. This can be clearly seen in the profile from the body-fitted simulation. For the first-order BDIM the discontinuity is represented only in the second part of the smoothing region and leads to an overshoot outside the smoothing region whereas the second-order BDIM shows a smooth representation of the discontinuity within the smoothing region.

Thus it can be summarized that the derivative correction allows to take better advantage of the whole smoothing region and thereby represent the velocity profiles and even the discontinuity of the derivative more smoothly and more accurately.

The first of the aeroacoustic validation cases focusses on the BDIM's capability to represent the acoustic noise generation of a moving body which is demonstrated by the simulation of a transversely oscillating cylinder in a medium at rest, employing the first-order BDIM. The cylinder has an infinite extension in the spanwise direction, hence the problem can be considered to be 2D. The cylinder's diameter d_{cyl} was set to unity and the vibration amplitude was 5% of the diameter and the vibration velocity amplitude $v_{vib} = 0.0094$. With $Ma = 1$ these parameters result in an acoustic wave length of $\lambda = 33.3 d_{cyl}$. The cylinder was discretized with 160 equispaced grid points per diameter and surrounded by another $1.25 d_{cyl}$ of equispaced grid in each direction. For the far-field the grid is then stretched over 200 grid points to a resolution of 20 grid points per acoustic wave length. In order to avoid any reflections from the boundaries, around the acoustic far field another 40 grid points were appended in

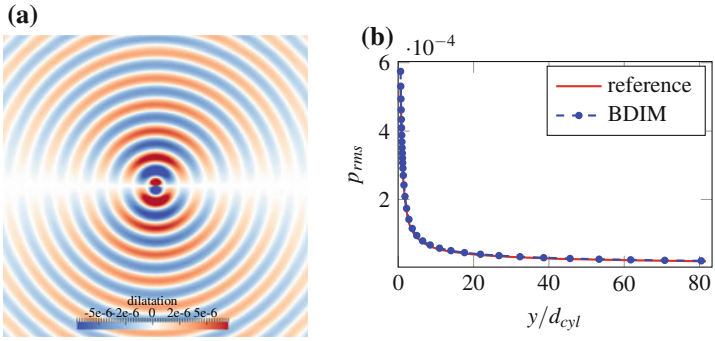

Fig. 4 **a** Instantaneous dilatation contours from the vibrating cylinder validation case. **b** Pressure fluctuations from the analytical prediction and the simulation results

each direction with strong grid stretching.

The analytical solution for the pressure fluctuations p_{rms} of this radiation problem is

$$p_{rms} = Re\left\{\left|-j\rho_0 v_{vib} cos(\theta)\frac{H_1^{(2)}(kr)}{Ma\, H_1^{(2)'}(ka)}e^{j\omega_{vib}t}\right|\right\} \quad , \tag{4}$$

where $H_1^{(2)}$ is a Hankel function of the second kind and first order and $H_1^{(2)'}$ its derivative. Furthermore ρ_0 is the mean density of the medium at rest [1].

Figure 4a presents the dilatation contours at an arbitrary instance of time. The dilatation contours show the expected dipole like radiation pattern with no signs of any spurious oscillations from either the domain boundaries or the BDIM. Figure 4b compares the p_{rms} profile from a simulation with the analytical solution. The data was extracted along the radial direction aligned with the cylinder's motion. The results from the simulation show excellent agreement with the analytical solution in the near and the acoustic far field. This demonstrates that the BDIM is an appropriate method to perform high-fidelity simulations featuring noise radiation from moving bodies.

Finally the scattering of trailing-edge noise from a trailing-edge extension of an airfoil in two dimensions is considered. The relevant parameters are given with the chord based Reynolds number $Re_c = 5 \times 10^4$, Mach number $M = 0.4$ and angle of attack $AoA = 5°$. At these flow conditions the flow separates on the suction side and forms a laminar separation bubble as can be clearly seen in the spanwise vorticity contours presented in Fig. 5b. The simulation of the trailing-edge noise from the airfoil with extension was carried out using the grids derived from the grid G3 in Jones et al. [7]. As indicated in Fig. 5b only the trailing-edge extension was represented by the BDIM.

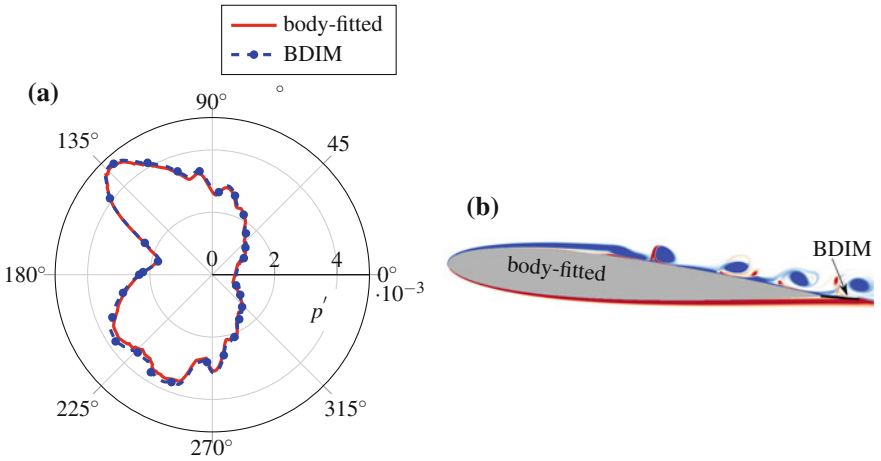

Fig. 5 **a** Noise levels at a radial distance of $r = 5$ chord lengths comparing simulation results with body-fitted boundary conditions and the BDIM. **b** Snapshot of the spanwise vorticity field indicating where the BDIM is employed and the separation on the suction side

Figure 5a compares the noise directivity when the flat plate extension is represented by body-fitted boundary conditions and by the BDIM. This plot shows excellent agreement between the two cases for the noise level as well as for the directivity shape. This demonstrates that the BDIM is able to represent the acoustic scattering of pressure disturbances from a trailing-edge accurately.

4 Conclusions

This paper introduced the boundary data immersion method (BDIM) for compressible flows. The method features a derivative correction which leads to second-order convergence when refining the grid. The novel approach was validated for near-wall accuracy, noise radiation from a moving body and scattering of trailing-edge noise.

References

1. Blackstock, D.: Fundamentals of Physical Acoustics. Wiley, New Jersey (2000)
2. Jaworski, J., Peake, N.: Aerodynamic noise from a poroelastic edge with implications for the silent flight of owls. J. Fluid Mech. **723**, 456–479 (2013)
3. Manela, A., Huang, L.: Point vortex model for prediction of sound generated by a wing with flap interacting with a passing vortex. J. Acoust. Soc. Am. **133**, 1934–1944 (2013)
4. Yang, J., Balaras, E.: An embedded-boundary formulation for large-eddy simulation of turbulent flows interacting with moving boundaries. J. Comput. Phys. **215**, 12–40 (2006)

5. Maertens, A., Weymouth, G.: Accurate cartesian-grid simulations of near-body flows at intermediate Reynolds numbers. Comput. Meth. Appl. M. (2014)
6. Schlanderer, S.C., Sandberg, R.D.: DNS of a Compliant Trailing Edge Flow, in 19th AIAA/CEAS Aeroacoustics Conference. AIAA Paper 2013–2013 (2013)
7. Jones, L.E., Sandberg, R.D., Sandham, N.D.: Direct numerical simulations of forced and unforced separation bubbles on an airfoil at incidence. J. Fluid Mech. **602**, 175–207 (2008)

DNS and ILES of Wall Bounded Flows Using a Discontinuous Galerkin Method and Inlet Synthetic Turbulence

S. Zeoli, C. Carton de Wiart, K. Hillewaert, B. Colassin, M. Rasquin and L. Bricteux

1 Introduction

High pressure turbine (HPT) blades are cooled partly by guiding air from the compressor through internal ducts. The massive boundary layer separations in their bends are the main source of head losses and may have a significant impact on the local heat transfer distribution. To capture such physics accurately, scale-resolving simulations such as Direct Numerical Simulation (DNS) or Large Eddy Simulation (LES) are required. Nevertheless, due to the complex configurations of cooling channels in turbomachinery and the level of accuracy required by scale-resolving simulations, standard industrial or academic solvers may not be able to predict efficiently this type of flow. It was shown in recent literature that discontinuous Galerkin method (DGM) combines the accuracy of academic solvers and the flexibility of industrial codes. These methods have shown large potential to perform efficient scale-resolving simulations (see e.g. [5]). In this paper, the capability of a DGM to perform fluid flow analysis of HPT cooling channels will be investigated. For internal flow configurations, the flow forcing strategy to obtain fully developed turbulence occurring at industrial conditions is an issue of primary importance. The generation of synthetic fluctuations, as described in [7], [3] will be tested. The first validation case is the turbulent channel flow at $Re_\tau = 590$. The second part of the study will address a problem relevant in the framework of turbines cooling passages: the turbulent flow in a serpentine duct at $Re_\tau = 180$.

S. Zeoli (✉) · B. Colassin · L. Bricteux
University of Mons, Fluids and Machines Dpt., Mons, Belgium
e-mail: stephanie.zeoli@umons.ac.be

C. Carton de Wiart · K. Hillewaert · M. Rasquin
Cenaero, Rue des Frères Wright 29, 6041 Gosselies, Belgium
e-mail: koen.hillewaert@cenaero.be

D.G.E. Grigoriadis et al. (eds.), *Direct and Large-Eddy Simulation X*,
ERCOFTAC Series 24, https://doi.org/10.1007/978-3-319-63212-4_55

2 The Discontinuous Galerkin / Symmetric Interior Penalty Method

The discontinuous Galerkin method [2] is a Galerkin finite element method based on an interpolation space Φ, composed of functions v that are polynomials of order p on each of the elements e in the mesh $\mathscr{E}$, but not required to be continuous across any of the interfaces f between elements. All DGM computations performed in this work use a third order interpolation (p=3) leading to a fourth order accuracy.

After choosing an appropriate set of basis functions ϕ_i for $\Phi = \text{span}\{\phi_0, \ldots, \phi_N\}$, with N the number of degrees of freedom per element, DGM then approximates the different components $\tilde{w}_m$ of $\tilde{w}$ by $w_m = \sum_i W_{im}\phi_i$.

As for any Galerkin method, the expansion weights W_{im} are found by requiring that the residual of the model equations, evaluated with w, is orthogonal to any function $v \in \Phi$. This principle is further complemented with consistent and penalty terms on the element interfaces, using, as Riemann solver $\mathscr{H}$, the Roe upwind flux for the convective terms whilst the diffusive terms are discretised according to the *Symmetric Interior Penalty (SIP)* method:

$$\begin{aligned}
&\forall \phi_i \in \Phi\ ,\ \forall m : \sum_e \int_e \phi_i \tfrac{\partial w_m}{\partial t} dV - \sum_e \int_e \tfrac{\partial \phi_i}{\partial x^k} (\mathscr{F}^k_m + \mathscr{D}^k_m)\, dV \\
&+ \underbrace{\sum_f \int_f [[\phi_i]]^k\, n^k\, \mathscr{H}_m\left(w^-, w^+, \mathbf{n}\right) dS}_{CI} + \underbrace{\sum_f \int_f [[\phi_i]]^k \left\{ D^{kl}_{mn}\, \frac{\partial w_n}{\partial x^l} \right\} dS}_{DI} \\
&+ \underbrace{\sum_f \int_f [[w_n]]^k \left\{ D^{kl}_{nm} \cdot \frac{\partial \phi_i}{\partial x^l} \right\} dS}_{DS} + \underbrace{\sum_f \sigma \int_f [[w_m]]^k\, [[\phi_i]]^k\, dS}_{DP} = 0.
\end{aligned}$$

$\mathscr{F}$ and $\mathscr{D}$ respectively stand for the convective and diffusive fluxes, D^{kl}_{mn} for the Jacobian of the diffusive fluxes with respect to the solution gradients. {.} and [[.]] denote the interface average and jump operators. The penalty parameter σ must be chosen large enough to guarantee stability. Sharp bounds for the value of σ have been elaborated for simplices and recently for hybrid meshes [4]. The influence of the sigma parameter on the dissipation of the ILES approach has been investigated on the turbulent channel flow and the HIT. Results showed that the sigma parameter does not significantly impact the results (it will impact the stiffness of the problem though). On the other hand, the choice of the Riemann solver will change the dissipation properties of the approach leading to different ILES models.

3 Synthetic Turbulence Inlet

In this work, synthetic turbulent fluctuations will be generated at the inlet plane of each computational domain. Only the principal components of the method will be presented here, for further informations, see e.g. [3, 7]. An isotropic synthetic velocity field defined by Eq. (1) is generated using N random Fourier modes.

$$\mathbf{u}'(\mathbf{x}) = \sum_{n=1}^{N} 2\,\hat{u}_n\,\cos(\kappa_n \mathbf{x} + \psi_n)\sigma_n\,, \tag{1}$$

where $\hat{u}_n$, ψ_n and σ_n are respectively the amplitude, the phase and the direction of the mode n. The wave number vector for each mode n is κ_n. To determine these parameters, it is necessary to prescribe the energy spectrum and the turbulent length scale. To ensure time coherence from independent realizations of $\mathbf{u}'$, the new fluctuating velocity fields $(\mathscr{U}')^m$, are computed using an asymmetric time filter,

$$(\mathscr{U}')^m = a(\mathscr{U}')^{m-1} + b(\mathbf{u}')^m, \tag{2}$$

where,

$$a = \exp\left(-\frac{\Delta t}{\tau_t}\right),\ b = \left(1 - a^2\right)^{\frac{1}{2}}\ . \tag{3}$$

Δt and τ_t are respectively the time step size and a relevant time scale. The anisotropy of the synthesized turbulence is introduced using a prescribed Reynolds stress tensor R_{ij}. The velocity field is build using $u_i = \overline{u_i} + a_{ij}\,\mathscr{U}'_j$, where $\overline{u_i}$ is the mean velocity profile and

$$a_{ij} = \begin{pmatrix} (R_{11})^{1/2} & 0 & 0 \\ R_{21}/a_{11} & (R_{22} - a_{21}^2)^{1/2} & 0 \\ R_{31}/a_{11} & (R_{32} - a_{21}a_{31})/a_{22} & (R_{33} - a_{31}^2 - a_{32}^2)^{1/2} \end{pmatrix}. \tag{4}$$

4 ILES of the Channel Flow at $Re_\tau = 590$

As a first validation, the wall-resolved ILES of the fully developed turbulent flow between two parallel walls at $Re_\tau = \frac{u_\tau \delta}{\nu} = 590$ is performed. $u_\tau = \sqrt{\tau_w/\rho}$ is the friction velocity based on the wall shear stress τ_w whereas δ is the channel half height. The flow is assumed to be periodic in the spanwise direction. the computational domain dimensions are $8\pi\delta \times 2\delta \times \pi\delta$ whereas the number of degrees of freedom in the respective directions is $144 \times 64 \times 96$. The downstream development of the Turbulent kinetic energy (TKE) is presented in Fig. 1. As the synthetic turbulence is not in equilibrium, the flow needs some distance to develop. One observes in Fig. 1, that the TKE profiles are fairly converged from $x \geq 6\pi\delta$. The statistics are

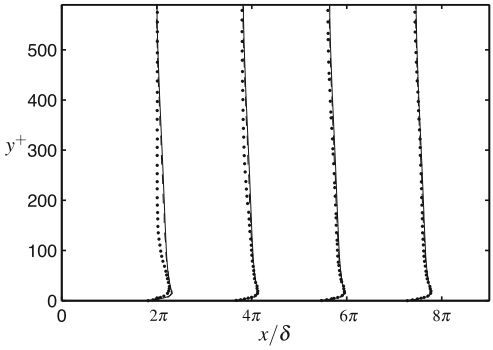

Fig. 1 TKE profile development. DGM/ILES using synthetic fluctuations (*bullets*), DGM/ILES periodic [1] (*dash*), DNS [8] (*solid*)

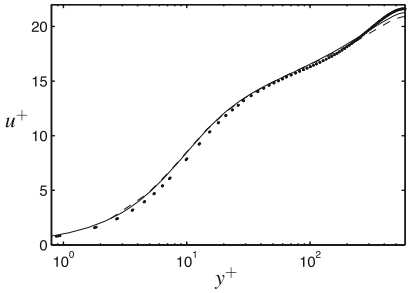

Fig. 2 Mean velocity profile. DGM/ILES using synthetic fluctuations (*bullets*); DGM/ILES periodic [1] (*dash*); DNS [8] (*solid line*)

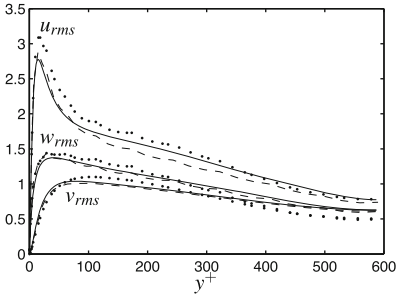

Fig. 3 Fluctuations profiles. DGM/ILES using synthetic fluctuations (*bullets*); DGM/ILES periodic [1] (*dash*); DNS [8] (*solid line*)

therefore gathered in a crossplane located at $x = 6\pi\delta$. The mean velocity (Fig. 2) and fluctuations (Fig. 3) profiles obtained using synthetic fluctuations are in good agreement with the fully periodic ILES and the reference DNS. Since the flow is developing, one can not exploit spatial homogeneity in the flow direction to accelerate convergence of the statistics, and therefore only spatial averaging in the spanwise direction is possible. Therefore small oscillations remain in the correlation profiles.

5 DNS of the Serpentine Flow at $Re_\tau = 180$

In this test case, two DNS of the flow in a serpentine passage are performed and compared. The first is a fully periodic computation (spanwise and streamwise), while the second (non-periodic streamwise) computation uses synthetic fluctuations. The computational domain dimensions are $14\pi H \times 2H \times \pi H$, H being the channel half width. The number of degrees of freedom in the respective directions is $900 \times 129 \times 87$. The main features of the flow topology are illustrated in Fig. 4. One observes the development of synthetic turbulent structures generated at the domain inlet and the massive boundary layer separation in the successive bends leading to intense vortical structures. The TKE map for the simulation with the synthetic turbulent inlet is presented at Fig. 5. It can be observed that after the first bend the TKE peak is spread over a longer distance than that following the second bend. This is due to the influence of synthetic turbulent fluctuations. The turbulent kinetic energy is certainly not zero at the inlet but its amplitude is much lower than that in the separation region. Comparison of cross correlation profiles at stations 2 & 6 are presented in Fig. 6. It is observed that at station 2, the simulation using synthetic fluctuations doesn't match the reference DNS neither the periodic DNS because the influence of synthetic fluctuations is still felt. At station 6 the three DNS results are very close of each other, discrepancies between our DNS and the reference are probably due to the forcing strategy (here using a constant pressure gradient vs recycling inflow for the reference) and the spanwise extent of the domain (3 times longer for the reference). The skin friction coefficient is displayed in Fig. 7. It can be seen that the prediction of this quantity is coherent between the different simulations except in the entry region $[0,\ 2\pi]$ where the turbulent flow is not yet developed.

Fig. 4 DNS of serpentine flow using DGM and synthetic fluctuations. Vorticity iso-surfaces

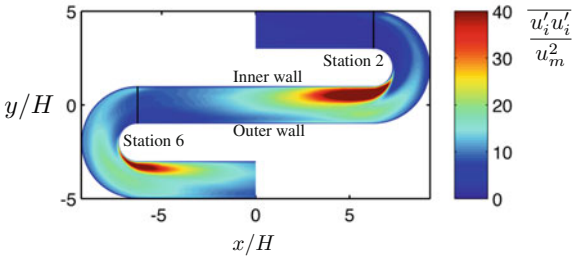

Fig. 5 DNS of serpentine flow using DGM and synthetic fluctuations. Turbulent kinetic energy map time and spanwise averaged

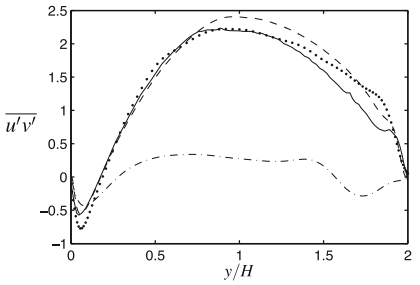

Fig. 6 Cross correlation profiles. DGM and synthetic fluctuations station 2 (*dash-dot*), DGM and synthetic fluctuations station 6 (*bullets*), DGM/periodic (*dash*), DNS [6] (*solid*)

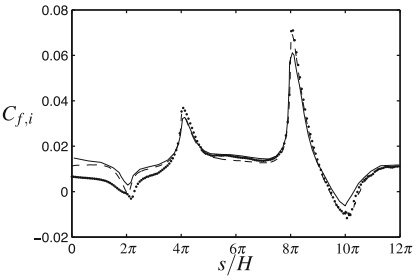

Fig. 7 Skin friction coefficient on the inner wall. DGM and synthetic fluctuations (*bullets*), DGM/periodic (*dash*), DNS [6] (*solid*)

6 Conclusion

The use of synthetic fluctuations to generate a realistic turbulent inflow with a DGM solver has been assessed. The results on channel and serpentine flows have shown the capability of the methodology to correctly predict both averages and fluctuating quantities. However the synthetic fluctuations influence a large part of the flow. The guidelines to determine the buffer zone needed to have a developed turbulence at the inlet have to be investigated in future work. This method will also be investigated considering other effects like rotation, heat transfer and more realistic cooling passage geometries.

References

1. Carton de Wiart, C., Hillewaert, K., Bricteux, L., Winckelmans, G.: Implicit LES of free and wall-bounded turbulent flows based on the discontinuous Galerkin/symmetric interior penalty method. Int. J. Numer. Methods Fluids **78** (2015)
2. Cockburn, B., Karniadakis, G.E., Shu, C.-W.: The development of discontinuous Galerkin methods. In: Cockburn, B., Karniadakis, G.E., Shu, C.-W. (eds.) Discontinuous Galerkin Methods, p. 350. Springer, Berlin (2000)
3. Davidson, L.: HYBRID LES-RANS: Inlet boundary conditions for flows including recirculation. In 5th International Symposium on Turbulence and Shear Flow Phenomena, vol. 2, pp. 689–694, 27–29 August, Munich, Germany (2007)
4. Hillewaert, K.: Development of the discontinuous Galerkin method for large scale/high-resolution CFD and acoustics in industrial geometries, Ph.D. Thesis, Université catholique de Louvain (2013)
5. Kroll, N., Hirsch, C., Bassi, F., Johnston, C., Hillewaert, K.: IDIHOM: Industrialization of High-Order Methods - A Top-Down Approach. Springer, Berlin (2015)
6. Laskowski, G., Durbin, P.A.: Direct numerical simulations of turbulent flow through a stationary and rotating infinite serpentine passage. Phys. Fluids **19**, 015101 (2007)
7. Lund, T.S., Wu, X., Squires, K.D.: Generation of turbulent inflow data for spatially-developing boundary layer simulations. J. Comput. Phys. **140**, 233–258 (1998)
8. Moser, R., Kim, J. and Mansour, N.: Direct Numerical Simulation of turbulent channel flow up to $Re_\tau = 590$ (1998)

Investigation of High-Order Methods in Large-Eddy Simulation of Separated Flow in a Channel with Periodic Constrictions

X. Gloerfelt and P. Cinnella

1 Introduction

In large-eddy simulations (LES), only the dynamics of large scales is computed and the effect of smaller scales is modelled. Scale separation is however difficult to establish since the low-pass filtering arises from a complex combination of implicit filtering by the grid and the discretization schemes. Even when explicit filtering is performed, the implicit filtering due to the application of discretization methods changes the shape of the filter function. The question of the intricate interactions between numerical errors, leading to this badly-defined filter, and subgrid-scale modelling errors has retained the attention of numerous authors since the studies of Ghosal [5] or Kravchenko and Moin [6]. Even with high-order schemes the subgrid contribution can be dominated by numerical errors in the high-wavenumber range. Meyers et al. [7] use error-landscapes to provide a more systematic assessment of computational errors. In explicitly-filtered LES, the filter shape plays a key role [10]. Since SGS models require informations from the smallest resolved scales, it is essential to ensure a high-accurate numerical approximation near the filter cutoff.

In the present study, several LES of the flow in a channel with streamwise-periodic constrictions are presented. This is a particularly challenging benchmark case for the prediction of separation of turbulent flows from curved surface and subsequent reattachment. It has been designed to test LES or RANS/LES models [4, 9], and an ERCOFTAC database [8] is available for the hill geometry, reference LES and

X. Gloerfelt (✉) · P. Cinnella
Arts et Métiers ParisTech, DynFluid Laboratory, Paris, France
e-mail: xavier.gloerfelt@ensam.eu

P. Cinnella
Università del Salento, via per Monteroni, Lecce, Italy
e-mail: paola.cinnella@ensam.eu

D.G.E. Grigoriadis et al. (eds.), *Direct and Large-Eddy Simulation X*,
ERCOFTAC Series 24, https://doi.org/10.1007/978-3-319-63212-4_56

measurements. A large variety of numerical methods, meshing strategies, subgrid-scale (SGS) models, wall modelling assumptions (through either RANS equations or wall functions) have been investigated in the past [3, 4, 9, 11]. The principal objective of the current study is to identify the sensitivity of the predictive accuracy to resolution and modelling issues. Simulations were performed for six different finite-difference schemes, six explicit filters and five subgrid-scale models on a coarse grid. It is shown in particular that the dissipative part of the discretization scheme plays a determinant role and overwhelms the choice of a SGS closure.

2 Flow Configuration and Numerical Strategy

The chosen configuration corresponds to the streamwise-periodic-hill channel flow, as described in the ERCOFTAC website [8]. The Reynolds number based on the hill height and the bulk velocity at the top of the hill is $Re_h = 10\,595$, and we choose a relatively low value for the Mach number, $\mathrm{M} = 0.2$. The dimensions of the domain are $L_x = 9h$; $L_y = 3.035h$; $L_z = 4.5h$, with h the hill height. The upper and lower boundaries are isothermal solid walls, where no-slip velocity boundary conditions apply. Periodic boundary conditions are implemented in the streamwise (x) and spanwise (z) directions. A forcing function is used to impose a constant mass flux. The governing equations are the compressible Navier-Stokes equations written for a curvilinear domain by using a coordinate transformation. They are integrated in time using an explicit low-storage six-step Runge-Kutta scheme, optimised in the frequency space [2]. Space derivatives are approximated in the Cartesian regular computational space by using centered finite differences (FD), which are not dissipative. A filtering procedure is employed to remove spurious high-wavenumber oscillations. The filters have symmetric coefficients, and thus are non-dispersive. In the present work, several finite-difference and filtering schemes are tested to show the effect of the scheme resolvability on the quality of the LES simulations. A similar study has been done for a Taylor-Green vortex and a turbulent boundary layer [1]. Table 1 summarizes the different simulations discussed in the following.

The present LES strategy combines a finite-difference scheme with good spectral properties with the use of a selective filtering, which has many advantages. It prevents aliasing error and removes grid-to-grid oscillations. Moreover, the selective filtering provides the necessary regularization. The effect of SGS motions is taken into account implicitly in the high-wavenumber range thanks to the smooth truncations of the filter and finite-difference schemes in the wavenumber space. That is why this kind of approaches is considered as an implicit LES. In the following, the strategy is referred to as RT (for Regularization Term). The explicit-filter strategy can be used alone as in the RT strategy, or in conjunction with a SGS model. The first model tested is the classical Smagorinsky model supplemented by a van Driest damping function near the walls. Second, the dynamic version (DSM) with a Laplacian test filter is investigated. The dynamic constant is also filtered with a Laplacian to avoid too fast variations. Third, the multiscale model (MSM) is tested. Scale separation

Table 1 Summary of computational cases

Cases	Grid	FD scheme	Filter	SGS	Symbol/Line
Grid convergence	$64 \times 33 \times 32$	DRP11	DRP11	RT	*Black dash-dotted*
	$128 \times 64 \times 64$	DRP11	DRP11	RT	
	$256 \times 128 \times 128$	DRP11	DRP11	RT	
Influence of discretization and filter order	$64 \times 33 \times 32$	o2	o2	RT	*Grey dashed*
	$64 \times 33 \times 32$	o4	o4	RT	*Grey solid*
	$64 \times 33 \times 32$	o6	o6	RT	*Grey dash-dotted*
	$64 \times 33 \times 32$	o8	o8	RT	*Black dashed*
	$64 \times 33 \times 32$	o10	o10	RT	*Black solid*
Influence of discretization alone	$64 \times 33 \times 32$	o2	DRP11	RT	*Grey dashed*
	$64 \times 33 \times 32$	o4	DRP11	RT	*Grey solid*
	$64 \times 33 \times 32$	o6	DRP11	RT	*Grey dash-dotted*
	$64 \times 33 \times 32$	o8	DRP11	RT	*Black dashed*
	$64 \times 33 \times 32$	o10	DRP11	RT	*Black solid*
Influence of filter order alone	$64 \times 33 \times 32$	DRP11	o2	RT	*Grey dashed*
	$64 \times 33 \times 32$	DRP11	o4	RT	*Grey solid*
	$64 \times 33 \times 32$	DRP11	o6	RT	*Grey dash-dotted*
	$64 \times 33 \times 32$	DRP11	o8	RT	*Black dashed*
	$64 \times 33 \times 32$	DRP11	o10	RT	*Black solid*
Influence of SGS modeling	$64 \times 33 \times 32$	DRP11	DRP11	SM $C_S = 0.18$	*Circle/black solid*
	$64 \times 33 \times 32$	DRP11	DRP11	SM $C_S = 0.1$	*Circle/black dashed*
	$64 \times 33 \times 32$	DRP11	DRP11	DSM C_d	*Square/grey solid*
	$64 \times 33 \times 32$	DRP11	DRP11	DSM $C_d/2$	*Square/grey dashed*
	$64 \times 33 \times 32$	DRP11	DRP11	MSM-ls	*Diamond/black solid*
	$64 \times 33 \times 32$	DRP11	DRP11	MSM-ss	*Diamond/black dashed*
Ref. LES [8]	$280 \times 200 \times 220$	FV[a]	FV[a]	DSM	*White triangle/solid*

[a]FV: second-order finite volume (code LESSOC)

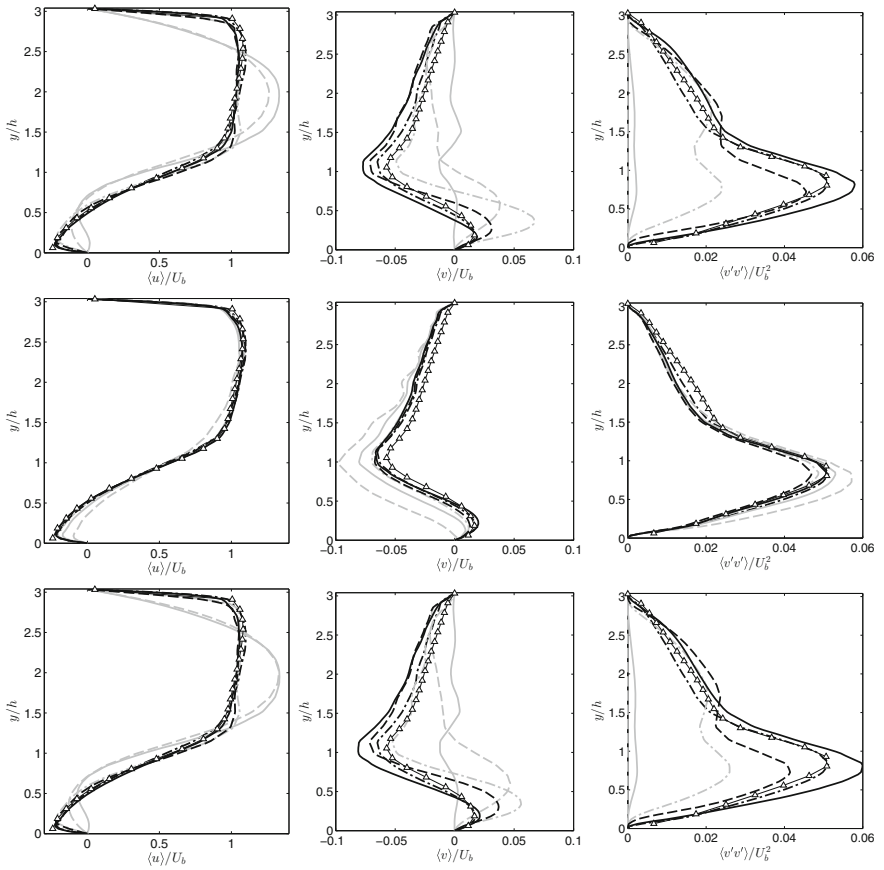

Fig. 1 From *left* to *right*, profiles of $\langle u \rangle$; $\langle v \rangle$ and $\langle v'v' \rangle$ in the recirculation region at $x/h = 2$. *First row* coupled influence of finite-difference and selective-filtering schemes; *second row* influence of finite-difference schemes supplemented by the DRP11 filter; *third row* influence of selective-filtering schemes along with the DRP11 scheme. Line legend is provided in Table 1

is performed by applying an 11-point filter with cutoff at $k\Delta x = \pi/3$ [2]. In the small-small version (MSM-ss), both the SGS tensor and the eddy viscosity are based on the filtered strain-rate tensor, whereas in the large-small version (MSM-ls), the SGS tensor alone is based on the filtered strain-rate tensor.

3 Influence of Numerical Schemes

The first investigation concerns the spatial discretization scheme on the coarsest grid. Two families of central finite-difference schemes are considered, namely standard second- to tenth-order schemes, denoted hereafter o2 to o10, and a DRP-type

optimized scheme with an 11-point stencil [2] (DRP11). For brevity, only profiles along a vertical line at $x/h = 2$, i.e. in the middle of the separated zone, are plotted in Fig. 1. The first row of Fig. 1 shows the coupled influence of finite-difference and selective-filtering schemes. The separate role of the dispersive (FD) and dissipative (filter) parts are presented in the second and third row, respectively. Concerning the influence of the order of the standard finite-difference schemes, the mean flow profiles are affected by the high phase error introduced by the 2nd and 4th -order scheme. The curves obtained beyond the 6th-order are rather similar, showing that the quality of the solution becomes independent of the spatial scheme order. The influence of the filter order in the RT method are shown in the second row of Fig. 1, where standard filters compared to the optimised filter and a reference LES [3]. The 2nd -order filter dissipates all of the turbulent structures. The 4th -order and 6th -order filters are highly overdissipative. Contrary to the results obtained for finite differences schemes, a major influence is found up to the 10th -order for the filters. The similarity with the results of the first row, where the FD and filter schemes are changed simultaneously, indicates that the accuracy of the LES solution is highly dependent on the choice of a sufficiently sharp filter. The strong influence of the filter choice on the numerical resolvability is clearly illustrated in Fig. 2 for the instantaneous vorticity: using a sharper filter allows capturing smaller structures.

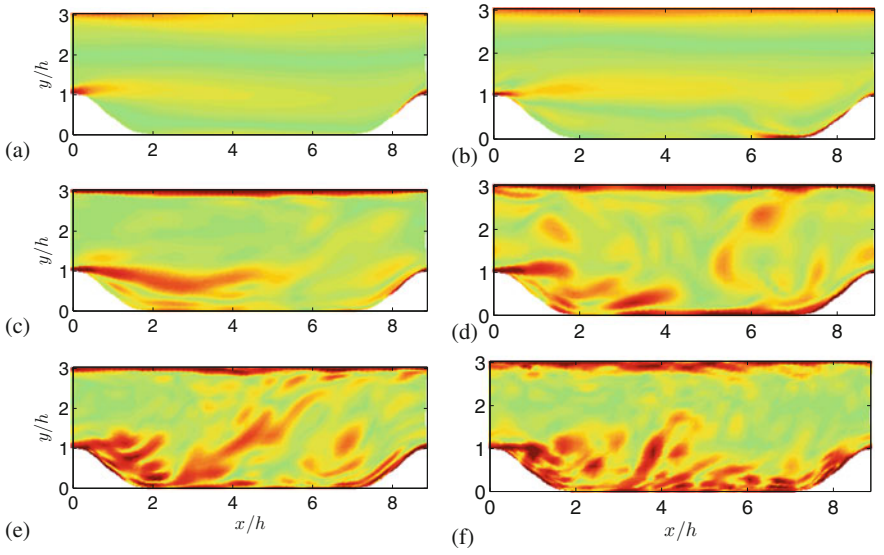

Fig. 2 Instantaneous snapshots of the vorticity norm: **a** FDo2/SFo2; **b** FDo4/SFo4; **c** FDo6/SFo6; **d** FDo8/SFo8; **e** FDo10/SFo10; **f** FD DRP11/SF DRP11

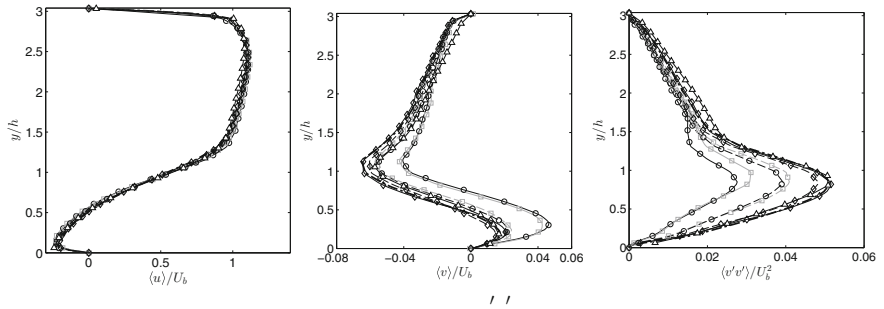

Fig. 3 From *left* to *right*, profiles of $\langle u \rangle$; $\langle v \rangle$ and $\langle v'v' \rangle$ in the recirculation region at $x/h = 2$. Influence of subgrid-scale models. Line legend is provided in Table 1

4 Influence of Subgrid-Scale Models

Results for several SGS models are presented in Fig. 3. This series of simulations uses the 11-point optimised finite-difference and filter schemes with $\chi = 0.2$ (see Table 1). The Smagorinsky model with $C_S = 0.18$, even in its dynamic form, appears to be too dissipative. As shown by several authors (e.g. [7]), the optimal values for the constant is lower. Taking $C_S = 0.1$ or dividing by a factor of 2 the value of the dynamical constant yield results in fair agreement with the reference. In the same way, the use of multiscale models allows a significant improvement of the quality of the solution, but shows results similar to those obtained with the RT strategy alone. Overall the effect of the SGS model is weak and confirms that the numerical errors tend to be more influential than the SGS-model.

5 Conclusion

The separated flow in a channel with periodic constrictions is a good candidate to investigate the quality of LES. Coarse-grid LES have been conducted and show a fair agreement with the references for this benchmark case. It is shown that the dissipative part of the numerical discretization has a significant impact on the quality of the results. In particular its selectivity in the wavenumber space is of the utmost importance for increasing the resolved part of the dynamics. The influence of different SGS models has been tested and found to be relatively weak. This confirms that the numerical errors can dominate the role of the SGS-model.

Acknowledgements This work was granted access to the HPC resources of IDRIS and CCRT under the allocation 2014–1736 made by GENCI (Grand Equipement National de Calcul Intensif).

References

1. Aubard, G., Stefanin Volpiani, P., Gloerfelt, X., Robinet, J.-C.: Comparison of subgrid-scale viscosity models and selective filtering strategy for large-eddy simulations. Flow Turbul. Combust. **91**(3), 497–518 (2013)
2. Bogey, C., Bailly, C.: A family of low dispersive and low dissipative explicit schemes for noise computation. J. Comput. Phys. **194**, 194–214 (2004)
3. Breuer, M., Peller, N., Rapp, C., Manhart, M.: Flow over periodic hills - Numerical and experimental study in a wide range of Reynolds numbers. Comput. Fluid. **38**, 433–457 (2009)
4. Fröhlich, J., Mellen, C., Rodi, W., Temmerman, L., Leschziner, M.: Highly resolved large-eddy simulation of separated flow in a channel with streamwise periodic constrictions. J. Fluid Mech. **526**, 19–66 (2005)
5. Ghosal, S.: An analysis of numerical errors in large-eddy simulations of turbulence. J. Comput. Phys. **125**, 187–206 (1996)
6. Kravchenko, A., Moin, P.: On the effect of numerical errors in large eddy simulations of turbulent flows. J. Comput. Phys. **131**, 310–322 (1997)
7. Meyers, J., Sagaut, P., Geurts, B.: Optimal model parameters for multi-objective large-eddy simulations. Phys. Fluids **18**, 095103 (2006)
8. Rapp, C., Breuer, M., Manhart, M., Peller, N. 2D periodic hill flow. ERCOFTAC QNET-CFD. http://qnet-ercoftac.cfms.org.uk/w/index.php/UFR_3-30
9. Xia, Z., Shi, Y., Hong, R., Xiao, Z., Chen, S.: Constrained large-eddy simulation of separated flow in a channel with streamwise-periodic constrictions. J. Turbul. **14**(1), 1–21 (2013)
10. Yang, X., Fu, S.: The effect of filtering on truncated Navier-Stokes equations. J. Turbul. **8**(8), 1–18 (2007)
11. Ziefle, J., Stolz, S., Kleiser, L.: Large-eddy simulation of separated flow in a channel with streamwise-periodic constrictions. AIAA J. **46**(7), 1705–1718 (2008)

DNS of a Lower Curved Wall Channel: Turbulent Separation

J.-P. Mollicone, F. Battista and C.M. Casciola

1 Introduction

Direct numerical simulations (DNS) are carried out to study turbulence dynamics in the separation bubble in lower curved wall channels. Boundary layer separation consists of fluid flow around bodies becoming detached, which causes the fluid closest to the object's surface to flow in reverse or different directions, most often giving rise to turbulent flow. The study of turbulence and boundary layer separation has long been of interest to many scientists [1], but despite its importance, this classic subject is still incompletely explored in turbulent conditions, and is especially challenging for numerical simulations. The separation of fluid flow from objects inevitably results in effects such as drag, increased mixing, momentum and energy transfer and vortex shedding. For instance, an understanding of such effects is helpful to improve road vehicle performance, in the study of structure-fluid interactions, to regulate air mixing with other substances e.g. pollutants or in the study of boundary layer control [2, 3] which is a large area of interest to researches ranging from classical technological applications up to bioengineering such as in hemodynamics, where a decrease in blood vessel section may be induced by the local degeneration of the arterial wall (atherosclerosis).

The aim is to study boundary layer separation induced by the lower curved wall with varying aspect ratios and heights to address basic issues concerning turbulence production and self-sustainment in the separation bubble and how these vary with

J.-P. Mollicone (✉) · F. Battista · C.M. Casciola
Department of Mechanical and Aerospace Engineering, Sapienza University of Rome, via Eudossiana 18, 00184 Rome, Italy
e-mail: jp.mollicone@uniroma1.it

F. Battista
e-mail: francesco.battista@uniroma1.it

C.M. Casciola
e-mail: carlomassimo.casciola@uniroma1.it

D.G.E. Grigoriadis et al. (eds.), *Direct and Large-Eddy Simulation X*,
ERCOFTAC Series 24, https://doi.org/10.1007/978-3-319-63212-4_57

geometry changes. The basic issue of turbulence sustainment, although well understood for canonical wall bounded flows, is still not exhaustively investigated for even mildly complex geometries able to induce separation such as ours. Only a few lower curved wall channels have been simulated, see e.g. [4] containing a smoother profile than ours together with different boundary conditions. We intend to capture all the turbulent scales, investigate the correlation between separation phenomena and localisation of TKE production, transport and dissipation at high Reynolds numbers for the different lower curved wall geometries.

2 Simulations

Figure 1 shows a contour plot of velocity magnitude of our reference simulation with dimensions $(L_x \times L_y \times L_z) = (24 \times 2 \times 10) \times h$ where L_i is the length in the ith direction and $h = 1$ is half the channel height. Flow is from left to right with periodic boundary conditions in both stream-wise and span-wise directions with wall boundary conditions at the top and bottom walls.

The domain consists of over 600,000 spectral elements with a spectral order of $N = 9$ for a total of over 600 million grid points. The Reynolds number based on half the channel height, $Re_h = 10000$, with a corresponding $Re_\tau = 430$. The simulation took over 5 million core hours to obtain enough uncorrelated data sets for statistical analysis. The number of cores used for a simulation ranges from a minimum requirement of 8192 cores (due to memory requirements with 1GB of RAM per core) up to 32768 cores.

The simulations are carried out using Nek5000 [5] that is a computational fluid dynamics solver based on the spectral element method (SEM). Patera [6] describes the SEM as a "...method that combines the generality of the finite element method with the accuracy of spectral techniques...". The SEM is the application of the spectral methods to elements by combining Galerkin spectral elements and finite element methods. Highly accurate numerical approaches for the simulation of wall bounded turbulent flows is crucial since it is desirable that the numerical error does not contaminate the multi-scale non-linear interactions which are at the basis of the energy cascade up to the smallest dissipative scales.

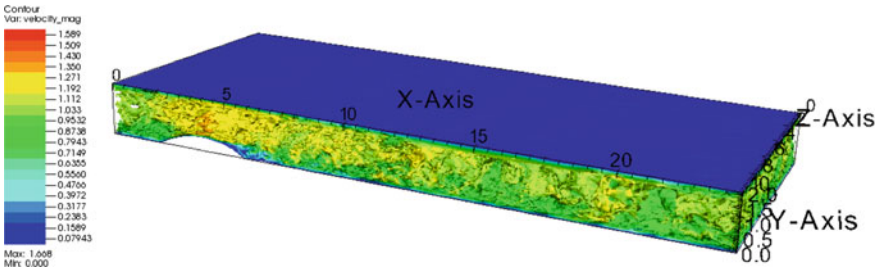

Fig. 1 Three dimensional velocity magnitude contour plot of all the computational domain

3 Results

Figure 2 shows two dimensional xz-plane velocity magnitude contour plots at three different channel heights. A significant length was used in the x-direction (streamwise direction) to allow the flow to settle and be able to impose periodic boundary conditions in this direction. Periodic boundary conditions were used in the streamwise direction to have incoming turbulent flow which was not obtained from different conditions or models and to avoid the need of a companion simulation of a turbulent plain channel flow to enforce inlet boundary conditions.

The top panel of the figure shows the xz-plane close to the bottom wall at $y = 0.015$, where the region with no flow represents the lower curved wall. The middle panel of the figure shows the xz-plane that just touches the top of the lower curved wall which is indicated by the line of zero velocity in the contour plot. Both plots show an evident separation region which extends for some distance after the bump and then settles to show the typical velocity streaks expected in channel turbulent flow. Finally, the bottom panel shows the xz-plane close to the top wall at $y = 1.99$ where the effect of the bump on the velocity is less evident but still present with a slight increase in velocity.

Following satisfactory results from the first large-scale simulation, a similar flow domain and mesh were simulated but with varying parameters with regards to the bump. In particular, we intend to see the effect of (1) varying the bump's geometry by increasing the bump's height with constant aspect ratio and (2) changing the aspect ratio and keeping the bump height constant. The different cases and their averaged x-velocity contour plots are shown in Fig. 3 where (1) and (2) are the top and bottom panel, respectively, and are referred to as the 'Higher' and 'Thinner' cases whilst the original case, which is the middle panel, is referred to as 'Default'.

Even though all the cases show an evident recirculation bubble behind the bump, the 'Thinner' case has a significantly larger separation region considering its size. The 'Default' and 'Higher' cases show similar behaviour which are expected to scale with the bump's geometrical scaling. The 'Higher' case clearly shows that fluid at the top wall slightly detaches itself after the bump with this being less evident in the 'Default' and 'Thinner' cases.

Figure 4 shows turbulent kinetic energy (TKE) line plots over a vertical line extended from the end of the bump to the top wall for the three cases. The TKE is defined as $k = \overline{u_i'^2}/2$ where u' is the velocity fluctuation with respect to the mean velocity. The evident effect of the Thinner case (blue line) is seen in the upward shift of the line plot of TKE for the Thinner case where the TKE starts increasing at a higher y-value. The TKE in the Higher and Default (red and green respectively) line plot cases drastically drops at around 0.75 and 0.5, which are the heights of the bump for each case respectively. The latter two cases tend to show similar behaviour which scales with the height of the bump when keeping the aspect ratio constant.

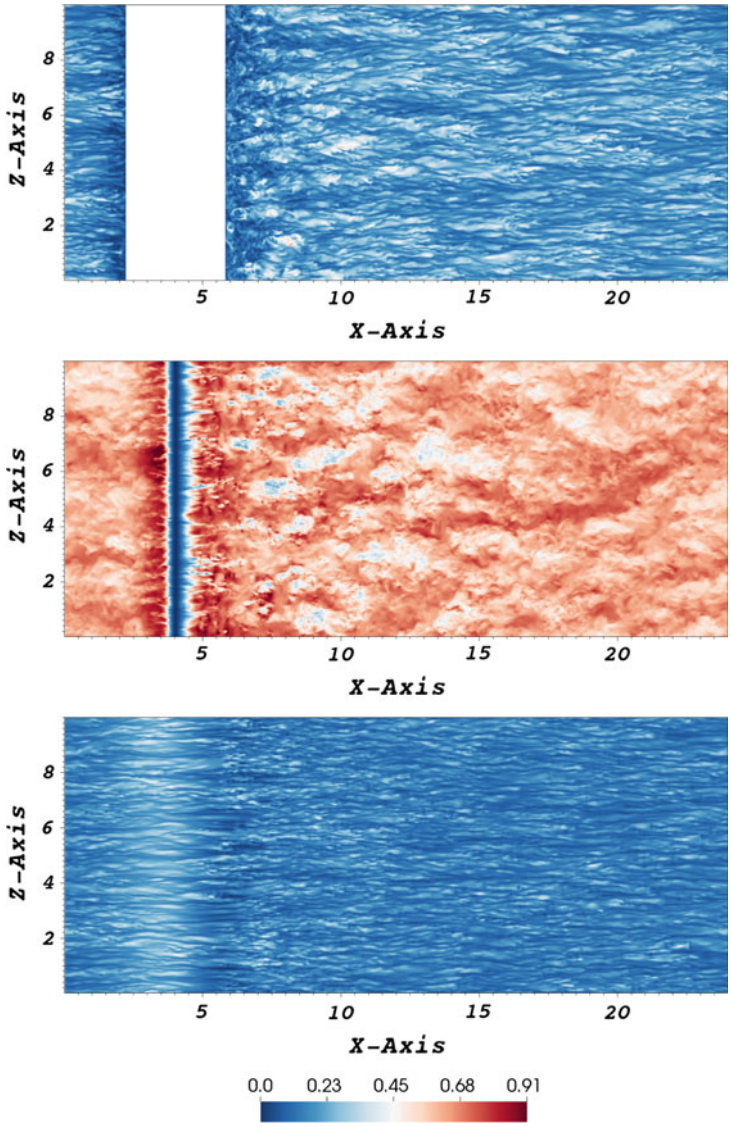

Fig. 2 Two dimensional xz-plane streamwise velocity contour plots at y = 0.015, y = 0.5 and y = 1.99 (from *top* to *bottom* respectively)

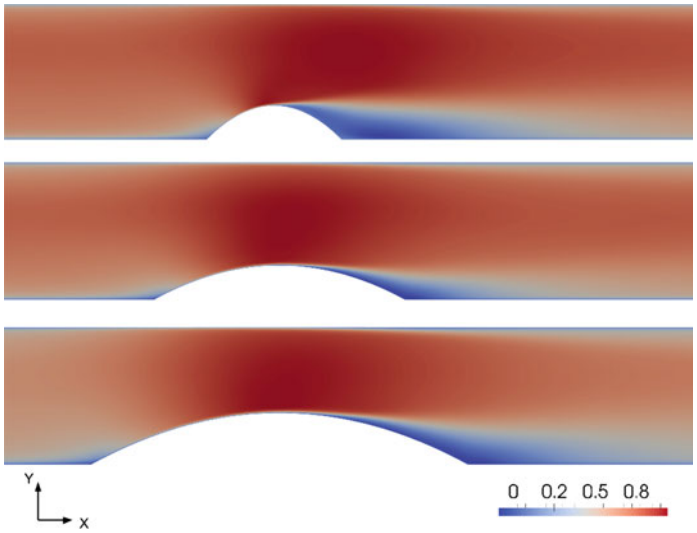

Fig. 3 Details of geometry variations with stream-wise velocity contour plots. *Top* 'Thinner' geometry, *Middle* 'Default' geometry, *Bottom* '*Higher*' geometry

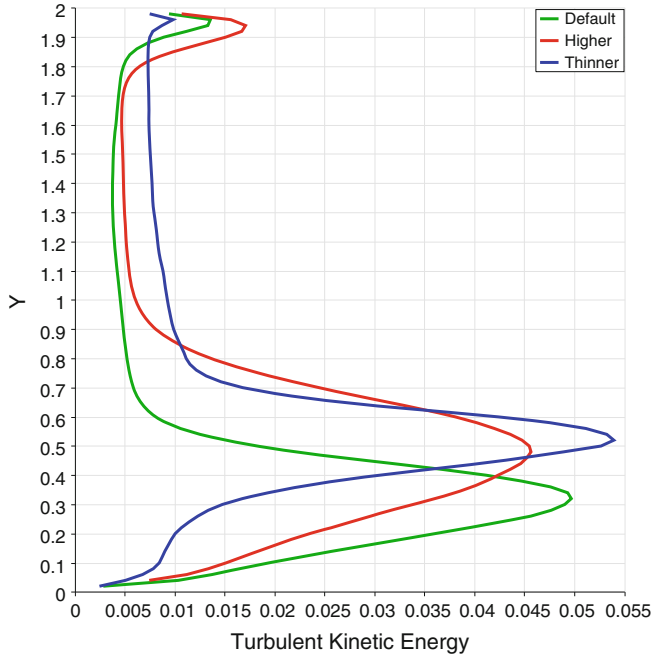

Fig. 4 Averaged turbulent kinetic energy over a vertical line extended from the end of the bump to the *top* wall for each geometry. Thinner in *blue*, Default in *green* and Higher in *red*

4 Conclusions

Three channels with different lower curved wall geometries were simulated using direct numerical simulations. More pronounced fluid flow separation effects are seen for the Thinner case when compared to the Higher and Default cases. The effect of increasing the bump's size whilst keeping its aspect ratio constant (Higher case) has less effect on fluid flow separation than making the body more bluff (Thinner case). The Thinner case shows larger and longer separation bubbles, higher peak statistical values and strong shifting of, for example, velocity profiles. The Higher and Default cases exhibit similar trends which scale with the bump's size. The Higher case makes the flow accelerate more with respect to the other cases due its increased height which in turn changes the boundary layer behaviour on the top wall. The use of periodic boundary conditions to avoid synthetic or prescribed inlet conditions is feasible, granted that the channel domain is long enough to allow the flow to recuperate to channel-like flow conditions downstream. These preliminary results are encouraging for the understanding of this phenomenon that is complex from both theoretical and practical points of view. Through the use of classical velocity statistics and TKE budgets, we intend to understand where turbulence in the separation bubble is generated, how it diffuses to the outer flow and where it is dissipated to provide a deeper understanding of the fundamental physics concerning separation dynamics.

Acknowledgements We acknowledge PRACE for awarding us access to resource FERMI based in Bologna, Italy. PRACE project no. 2014112647.

References

1. Simpson, R.L.: Turbulent boundary-layer separation. Ann. Rev, Fluid Mech (1989)
2. Marusic, I., Talluru, K.M., Hutchins, N.: Controlling the large-scale motions in a turbulent boundary layer. In: Fluid-Structure-Sound Interactions and Control (2014)
3. Bai, H.L., Zhou, Y., Zhang, W.G., Xu, S.J., Wang, Y., Antonia, R.A.: Active control of a turbulent boundary layer based on local surface perturbation. J. Fluid Mech. (2014)
4. Marquillie, M., Laval, J-P., Dolganov, R.: Direct numerical simulation of a separated channel flow with a smooth profile. J. Turbul. **9** (2008)
5. Fischer. P., et al.: Nek5000 - open source spectral element CFD solver. In: Argonne National Laboratory. Mathematics and Computer Science Division, Argonne, IL (2008). https://nek5000.mcs.anl.gov
6. Patera, A.T.: A spectral element method for fluid dynamics. J. Comput. Phys. **54**, 468–488 (1984)

Turbulence Modification in a Pipe Flow Due to Superhydrophobic Walls

R. Costantini, F. Battista and C.M. Casciola

1 Introduction

Superhydrophobic surface features could be used to obtain significant drag reduction in turbulent confined flows [1–3]. Superhydrophobic surfaces are obtained by means of chemical coating and micro/nano structures [4], involving scale sensibly smaller than the typical Kolmogorov scale in the turbulent flows. At macroscopic scales superhydrophobic features produce a wall slip velocity induced by air bubbles entrapped in surface asperities, see Cassie Baxter–Wenzel state [5, 6].

Our intent is to address the drag reduction induced in wall-bounded flows by superhydrophobic surfaces. In particular we will study the effects on wall turbulent structures and on transport, production, and dissipation of the turbulent kinetic energy. Our aim will be pursued by performing direct numerical simulations of a turbulent pipe flow equipped with perfect-slip/no-slip, PS-NS, boundary conditions mimicking the presence of stream-wise grooves characterised by stable Cassie Baxter state.

This topic has been addressed in several works dealing with wall-turbulence, see e.g. [1, 7, 8] for numerical simulations and [3, 9, 10] for experimental measurements on turbulent channel flows. However, according to us, a deeper understanding is necessary to obtain the maximum benefits from superhydrophobic patterned surfaces. As stated before we believe that a concrete step forward requires understanding the effects of the modified boundary conditions on the turbulent wall structures and on the mechanisms of production, dissipation, and transport of the turbulent kinetic energy.

R. Costantini (✉) · F. Battista · C.M. Casciola
Department of Mechanical and Aerospace Engineering, University La Sapienza,
via Eudossiana 18, 00184 Roma, Italy
e-mail: roberta.costantini@uniroma1.it

D.G.E. Grigoriadis et al. (eds.), *Direct and Large-Eddy Simulation X*,
ERCOFTAC Series 24, https://doi.org/10.1007/978-3-319-63212-4_58

Table 1 Thickness of the perfect-slip/no-slip regions of the superhydrophobic cases

Case	$N_{PS} - N_{NS}$	$\delta^+_{PS} - \delta^+_{NS}$	$\delta_{PS} - \delta_{NS}$ [μ m]
(b)	2 – 2	10.5 – 10.5	34 – 34
(c)	3 – 3	15.7 – 15.7	51 – 51
(d)	4 – 4	20.9 – 20.9	68 – 68
(e)	8 – 8	41.9 – 41.9	136 – 136
(f)	16 – 16	83.8 – 83.8	273 – 273

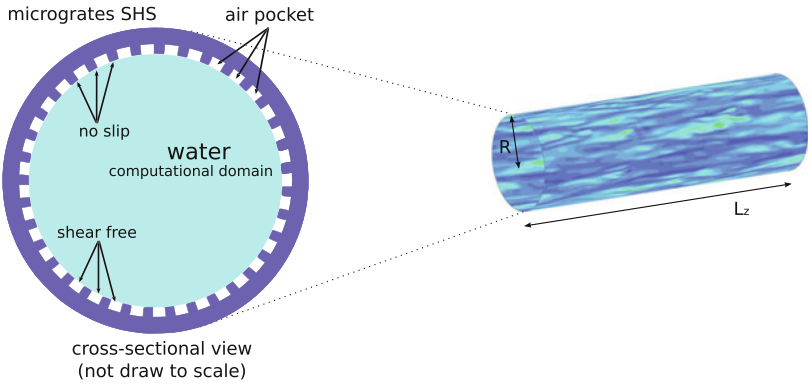

Fig. 1 Description of the computational domain. The *left* part represents a cross-sectional view of the pipe. *Cyan* colour highlights the actual computational domain surrounded by the pipe grooved wall which effect is enforced by perfect-slip/no-slip alternated boundary conditions. The *right* part reports the contour of the axial velocity, u_z, in the near wall region, $y^+ = 5$

2 Methodology

The incompressible system of Navies Stokes equations,

$$\nabla \cdot \mathbf{u} = 0$$

$$\frac{D\mathbf{u}}{Dt} = -\nabla p + \frac{1}{\mathrm{Re}}\nabla^2 \mathbf{u},$$

is discretized in a cylindrical domain to investigate the effects of superhydrophobic surfaces on the turbulent wall structures and on the flow rate in the turbulent pipe flow [11]. A reference simulation, case (a), is performed with no-slip boundary condition, while additional simulations are obtained by enforcing alternating perfect-slip/no-slip, PS/NS, boundary conditions at the pipe wall, the patterning is aligned with the axis of the pipe (Table 1). A schematic representation of the computational domain is reported in Fig. 1. The thickness of the perfect-slip/no-slip regions, here called grooves, $\delta_{PS} = \delta_{NS}$, is varied as shown in the table. We highlight that the solid fraction is $\Phi = 50\%$ in all the superhydrophobic simulations, this means that half

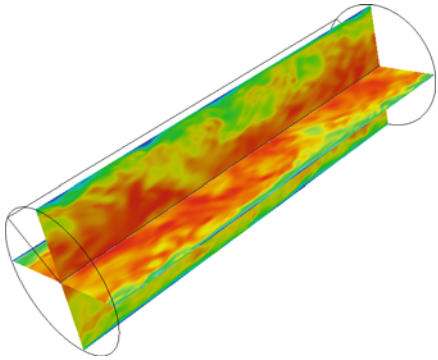

Fig. 2 Instantaneous axial velocity of the turbulent periodic pipe flow. The snapshot refers to the reference simulation with no-slip boundary conditions

of the pipe wall has no-slip conditions and the other half has perfect slip conditions. The thickness is reported in grid node size (second column from left), in wall unit size (third column from left), and in physical size (fourth column from left) assuming a radius of 1 mm. The flow is obtained by keeping constant the mean pressure gradient in all simulations $\overline{\partial_z p} = 7.88 \cdot 10^{-3}$ (z pipe axis), producing a substantially constant friction Reynolds number $Re_\tau = u_\tau R/\nu = 308$, where $u_\tau = \sqrt{\tau_w/\rho}$ is the friction velocity, R the pipe radius and ν the cinematic viscosity. Hence the boundary conditions will produce different flow rates corresponding to different drag reduction/increasing.

The simulations are performed by employing about 12.5 million of collocation points and the domain dimensions are equal to $[2\pi R \times R \times 2\pi R]$ in the azimuthal, radial and axial direction, respectively. Figure 2 shows the instantaneous configuration of the axial velocity, concerning the reference simulation with no-slip boundary conditions. About 2 hundred instantaneous fields, every $t = 2.5\, t_0$, with $t_0 = R/U_b$ the reference time, R the pipe radius and U_b the bulk velocity, are stored in order to perform an accurate statistical analysis.

3 Result and Discussion

Figure 3 (left panel) shows the normalised mean axial velocity $\langle u_z \rangle / u_\tau$, with u_τ the friction velocity, as a function of the wall distance $y^+ = (1 - r)/y^*$, with $y^* = \nu/u_\tau$ the viscous length scale. The increase of the flow rate due to the slip boundary conditions is evident by comparing the cases (b)–(f) with the reference case (a). For cases (b)–(e) the grooves dimension weakly influences the flow rate while a sensible increase is apparent for grooves dimension approaching the typical streaks spacing, case (f).

The flow rate variation can be ascribed to two different mechanisms: the wall slip velocity and the wall turbulent structures modification. Although the two causes are strongly correlated, in first approximation, we separate the two effects splitting the

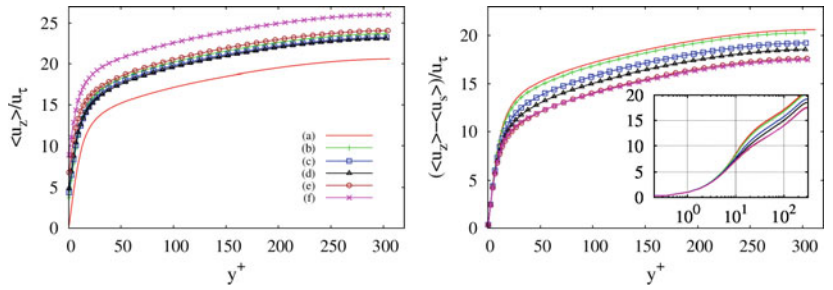

Fig. 3 Radial profile of the normalised mean axial velocity as a function of the radial distance from the wall normalised with the wall viscous length scale r^+. *Left* panel normalised mean axial velocity $< u_z > /u_\tau$ (where $u_\tau = \sqrt{\tau_w/\rho}$ is the friction velocity); *right* panel normalised mean axial velocity purged of the mean slip velocity, $(< u_z > - < u_s >)/u_\tau$, the inset is the semi-log representation of the same plot

whole flow rate variation into two contribution $\Delta Q = \Delta Q_s + \Delta Q_T$, ΔQ_s due to the wall-slip velocity and ΔQ_T due to the turbulent wall-structures modification.

The new mean axial velocity $(\langle u_z \rangle - \langle u_s \rangle)/u_\tau$ is reported in the bottom panel of Fig. 3 and shows the effects of the modified turbulent wall structures on the flow rate.

The cases (a) and (b) show similar behaviour, namely turbulent structures modifications have negligible effects on the flow rate. The increase of the flow rate, observed in the top panel of figure, is completely ascribed to the wall slip velocity, $\Delta Q \simeq \Delta Q_s$, $\Delta Q_T \simeq 0$.

The other cases show the monotone decrease of the flow rate with the increasing of the grooves dimension, see bottom panel of Fig. 3. This tendency carries on up to the case (f) characterised by a groove dimension of the order of the typical streaks spacing. This means that for cases (c)–(f) the wall structures modification has an opposite effect with respect to the slip velocity on the flow rate, $\Delta Q_T < 0$ whilst $\Delta Q_s > 0$. Since the whole flow rate increases, the former effect results to be lower than the latter, $|\Delta Q_T| < |\Delta Q_s|$.

The azimuthal repetition of the superhydrophobic texture motivates the definition of an azimuthal phase, allowing to distinguish the perfect slip from no-slip regions, in order to separately analyse the effect on the turbulent flow close to the grooves and the wall. In this context the phase-averaging of the generic variable q reads,

$$\langle q|\varphi \rangle = \int_{-\infty}^{\infty} p(q|\varphi) q dq \, . \tag{1}$$

Figure 4 shows the mean conditioned axial velocity profiles as a function of the radial distance from the wall. The left and the right panels of Fig. 4 show the profiles in correspondence of the no-slip and perfect slip sections, respectively.

Dealing with the no-slip region, as expected, all the mean velocity profiles reach zero value at the wall. On the other hand, different wall shear stress τ_w values are

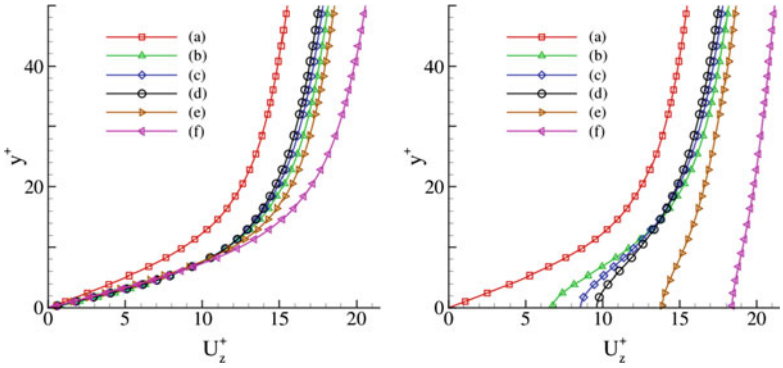

Fig. 4 Profiles of the mean conditioned axial velocity as a function of the radial distance from the wall. Both velocity and radial distance are expressed in wall unit. *Left* and *right* panels report the profiles in correspondence of the no-slip and perfect slip boundary condition, respectively

observed between the case (a) and all the other cases, in particular, the value of τ_w in cases (b)–(f) is greater with respect to τ_w in the reference case.

To better understand this behaviour it is necessary to recall the mean momentum balance in the turbulent flow. Actually the integral of the mean pressure gradient on the inlet/outlet section of the pipe is balanced by the integral of the mean shear stress on the wall. Since the mean pressure gradient is kept constant and the solid fraction is lower with respect to the reference case the SH cases present a greater wall shear stress. This explains also the evidence that the τ_w is constant among the SH cases.

Dealing with the perfect slip region (right panel of Fig. 4), as expected, the mean axial velocity at the boundary assumes non negligible values, while the wall shear stress is zero as enforced with boundary conditions. In particular the mean slip velocity at the boundary increases with the increase of the grooves dimensions.

These preliminary results show the turbulence modification induced by the unconventional texture of the wall. In particular the alternating perfect-slip/no-slip boundary conditions, reproducing the pipe wall alternated to the liquid-gas interface in correspondence of the grooves, play an important role on the overall drag variation. Actually two phenomena influence the overall drag variation in the turbulent pipe flow: the slip at the wall producing an increase of the flow rate and the induced turbulent structures modifications producing a slightly drag increasing. The overall effect of the two phenomena consists in the increase of the flow rate corresponding to a drag reduction.

Acknowledgements The research leading to these results has received funding from the European Research Council under the European Unions Seventh Framework Programme (FP7/2007-2013)/ ERC Grant agreement n. [339446].

References

1. Min, T., Kim, J.: Effects of hydrophobic surface on skin-friction drag. Phys. Fluids. **16**(7), L55 (2004)
2. Fukagata, K., Kasagi, N., Koumoutsakos, P.: A theoretical prediction of friction drag reduction in turbulent flow by superhydrophobic surfaces. Phys. Fluids **18**, 051703 (2006)
3. Aljallis, E., Sarshar, M.A., Datla, R., Sikka, V., Jones, A., Choi, C.H.: Experimental study of skin friction drag reduction on superhydrophobic flat plates in high Reynolds number boundary layer flow. Phys. Fluid. **25**, 025103 (2013)
4. Li, X.M., Reinhoudt, D.: Crego-Calama. M.: What do we need for a superhydrophobic surface? A review on the recent progress in the preparation of superhydrophobic surfaces. Chem. Soc. Rev. **36**(8), 1350–1368 (2007)
5. Lafuma, A., Qur, D.: Superhydrophobic states, Nature Materials, **2**:457–460
6. Giacomello, A., Meloni, S., Chinappi, M., Casciola, C.M.: Cassie Baxter and Wenzel states on a nanostructured surface: Phase diagram, metastabilities, and transition mechanism by atomistic free energy calculations, Langmuir. **28**:10764–10772
7. Park, H., Kim, J.: A numerical study of the effect of superhydrophobic surface on skin-friction drag in turbulent channel flow. Phys. Fluids **25**, 110815 (2013)
8. Turbulent flow over superhydrophobic surfaces with streamwise grooves: T*ü*rk, S.T., Daschiel, G. Stroh, A., Hasegawa, Y., Frohnapfel, B. J. Fluid Mech. **747**, 186–217 (2014)
9. Daniello, R.J., Waterhouse, N.E., Rothstein, J.P.: Drag reduction in turbulent flows over superhydrophobic surfaces. Physics of Fluids **21**, 085103 (2009)
10. Henoch, C., Krupenkin, T.N., Kolodner, P., Taylor, J.A., Hodes, M.S., Lyons, A.M., Peguero, C., Breuer, K.: Turbulent drag reduction using superhydrophobic surfaces. In: 3rd AIAA Flow Control Conference, 2006–3192 (2006)
11. Picano, F., Sardina, G., Casciola, C.M.: Spatial development of particle-laden turbulent pipe flow. Phys. Fluid (1994-present) **21**(9) (2009). 093305

Part X
Environmental Flows

Conditional Averaging for the Onset of Erosion of Single Particles in a Turbulent Open-Channel Flow

B. Vowinckel, R. Jain, T. Kempe and Jochen Fröhlich

1 Introduction

Erosion and incipient motion of individual particles in a turbulent open channel flow is an important aspect of numerous industrial and environmental applications, such as sediment transport or the mobilisation of pollutants. Despite the long history of research on this topic, formulas that are based on mean quantities like the one proposed by Shields [6] are of low predictive power to understand erosion events and incipient motion of inertial particles [2]. As a consequence, the complex situation related to incipient motion raises the need for transient data with high resolution, both in space and time, to gain insight into the relevant mechanisms of particle erosion. In recent time, sufficient computational power has become available to conduct numerical simulations of such a configuration. The present paper employs data generated by using Direct Numerical Simulations (DNS) in [7] and continues a previous study [8] by further analysis.

B. Vowinckel · R. Jain · T. Kempe · J. Fröhlich (✉)
Institute of Fluid Mechanics, TU Dresden, Dresden, Germany
e-mail: jochen.froehlich@tu-dresden.de

B. Vowinckel
e-mail: bernhard.vowinckel@tu-dresden.de

R. Jain
e-mail: ramandeep.jain@tu-dresden.de

T. Kempe
e-mail: tobias.kempe@tu-dresden.de

D.G.E. Grigoriadis et al. (eds.), *Direct and Large-Eddy Simulation X*,
ERCOFTAC Series 24, https://doi.org/10.1007/978-3-319-63212-4_59

2 Numerical Method and Computational Setup

The continuous phase is governed by the unsteady, three-dimensional Navier-Stokes equations for incompressible fluids. The numerical method is based on an Euler-Lagrangian approach i.e. the particle path is tracked in time while the fluid is computed on a fixed grid. The IBM of [3] is used to resolve the spatial geometry of the particles. For particle contact, the Adaptive Collision Model (ACM) [4] was used, which accounts for all relevant mechanisms during the collision process comprising short-range lubrication forces, normal forces, and tangential forces due to friction between particles. This method has already been employed in several studies and produced results in good agreement with experimental evidence while exhibiting excellent numerical performance [5, 7].

Here, a turbulent open-channel flow with periodic boundary conditions in streamwise and spanwise direction is considered with a free-slip condition on the top and a no-slip condition on the bottom wall and the particle surfaces (Fig. 1). The sediment is constituted of a single layer of fixed spheres with diameter D in a hexagonal packing and the same amount of mobile particles with identical shape on top. The restitution coefficient for dry collisions is $e = 0.97$ corresponding to the natural value for sand. The particles have a mobility below their nominal threshold of incipient motion and settle onto the rough bed. If all mobile particles were distributed regularly on top of the layer of fixed particles, the first layer would be entirely covered and the sediment would have a total thickness of $H_{sed} = 1.82D$. This position is taken as the origin of the vertical coordinate [7]. The computational domain is $L_x \times L_y \times L_z = 24H \times (H + H_{sed}) \times 6H$ with a relative submergence of $H/D = 9$. The bulk Reynolds number $Re_b = U_b H/\nu_f$ is 2941 with U_b the bulk velocity and ν_f the kinematic viscosity. The bulk flow is imposed by a volume force maintaining U_b at a constant value. The resulting particle Reynolds number $D^+ = u_\tau D/\nu_f$ is 21. Each particle is resolved with more than 22 grid cells per

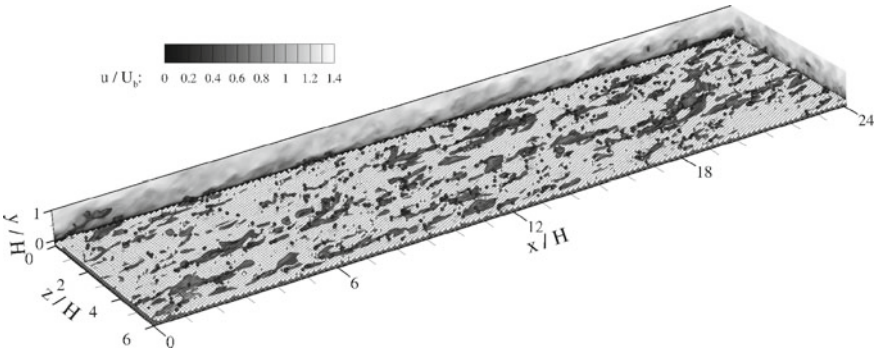

Fig. 1 Instantaneous particle distribution of the considered setup. Contour plots of u/U_b on the backward and downstream side of the domain, 3d-iso-surfaces of fluid fluctuations with $u'/U_b = -0.3$ in *grey* inside the domain. Particle colours *grey* = fixed, *white* = $|\mathbf{u}_p| < 1.5u_\tau$, *black*= $|\mathbf{u}_p| > 1.5u_\tau$

diameter. This simulation was run for more than 292 bulk units H/U_b to detect erosion events. It is one of the largest and best resolved simulations of this phenomenon existing to date.

3 Conditional Averaging

It was reported in [7] that about 3% of the mobile particles in the simulation are travelling with a high velocity on top of a layer of temporally resting particles, which is the desired situation for the present study. Due to a modified sampling strategy during the course of the simulation, data was gathered for the streamwise velocity component for the last 140 bulk units and 111 bulk units for the spanwise and wall-normal components, respectively. This yields a total of 157 velocity fields for the streamwise component and 97 samples for the wall-normal and spanwise component of the fluid velocity vector. These events constitute the statistical sample size to perform conditional averaging of the fluid phase at the instant of erosion.

An example of an erosion event of a single particle is depicted in Fig. 2. For the present scenario, erosion is typically triggered by a collision with a fast moving particle that is already eroded [8]. The erosion event itself, however, takes place at a later time and is related to a characteristic flow structure which exerts a lift force onto the particle in question over a considerable duration. The particle then starts to travel across the inactive bed with a saltating motion (Fig. 3).

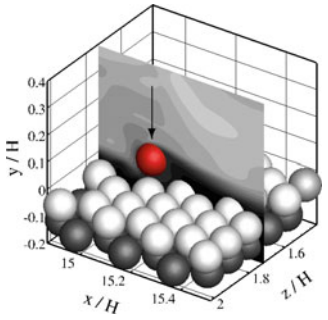

Fig. 2 Zoom into the domain shown in Fig. 1, displaying an example of a single erosion event directly after particle mobilisation. Contour plot and particle colouring as in Fig. 1. The eroded particle investigated is highlighted with an *arrow*

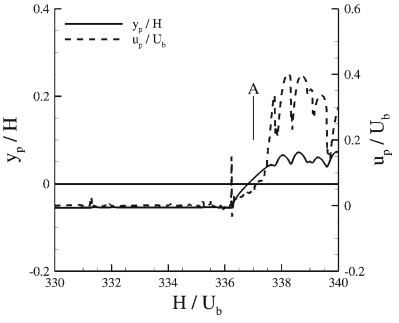

Fig. 3 Particle trajectory and related particle velocity during the event shown in Fig. 2. The picture in Fig. 2 corresponds to the situation at time A

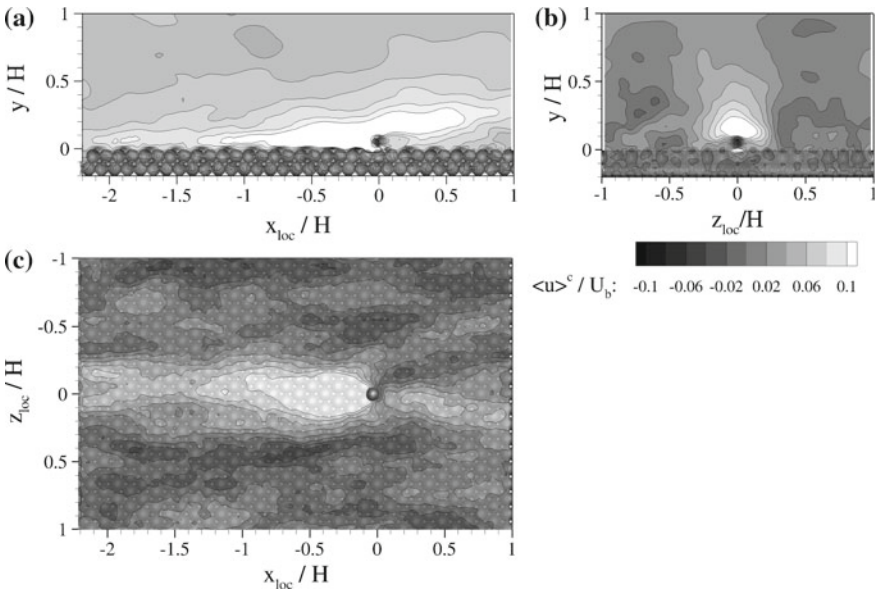

Fig. 4 Ensemble averaged information before accounting for asymmetry on the streamwise fluid velocity at the instant of an erosion event. **a** Streamwise Velocity $\langle u \rangle^c$ in the centre plane at $z_{loc} = 0$, **b** the same in the cross plane at $x_{loc} = 0$, **c** the same in the *top-view* with contour at $y_{loc} = 0.34D$

The flow fields at the instant of the erosion events were conditionally averaged to determine the characteristic flow features responsible for dislodging the particle out of its pocket. Conditional averaging of the velocity field raises the need for a local grid with a local coordinate system x_{loc} and z_{loc} at the time of erosion $t_{loc} = t_e$. To obtain the fluid information on the local grid, linear interpolation from the original grid was performed. In [8], conditional averaging of fluid structures of all the erosion events was performed and a result symmetric with respect to $z_{loc} = 0$ was obtained as shown in Fig. 4. However, if equally probable fluid structures with their centroid in $z_{loc} < 0$ and the fluid structures with their centroid in $z_{loc} > 0$ are averaged together, the final result must be symmetrical around the plane $z_{loc} = 0$ as a consequence of the procedure. Therefore, another evaluation was undertaken. To detect possible asymmetrical fluid structures, fluid fields with a centroid of the streamwise velocity in $z_{loc} < 0$ were mirrored along the symmetry planes $z_{loc} = 0$ before averaging. With this mirroring, the spanwise coordinate is named z_{sym}.

4 Results

The result of the asymmetry-sensitive conditional averaging is shown in Fig. 5. It is seen that the result does not exhibit substantial asymmetry and is similar to the one in Fig. 4. There is a slight large-scale asymmetry in the channel (Fig. 5b) but in the

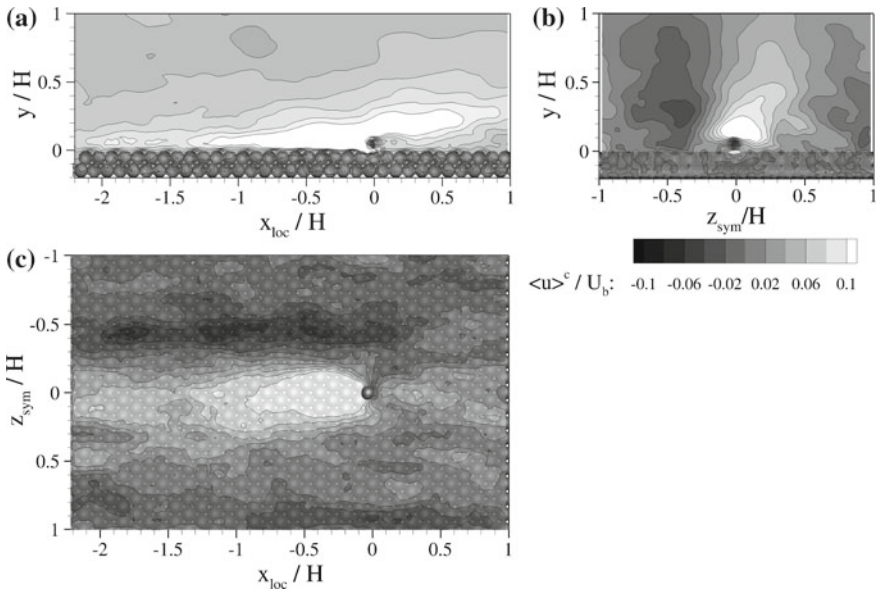

Fig. 5 Ensemble averaged information after considering asymmetry of the streamwise fluid velocity at the instant of an erosion event. **a** Streamwise Velocity $\langle u \rangle^c$ in the centre plane at $z_{sym} = 0$, **b** the same in the cross plane at $x_{loc} = 0$, **c** the same in the *top-view* with contour at $y_{loc} = 0.34D$

near wall region, i.e. at $y_{loc} = 0.34D$, the centroid of the averaged fluid structure is very close to $z_{sym} = 0$ (Fig. 5c). This is relevant as the flow features in this region are expected to play a bigger role in an erosion event.

Furthermore, there is another asymmetry that has to be accounted for, geometrical in nature, i.e. the possible position of a hole in the sediment bed. In Fig. 5, only those erosion events were considered where the eroded particle was surrounded by six other particles. There are events where the eroded particle is surrounded by only five particles. The presence of a hole upstream to the eroded particle provides more space for the fluid structure to seep into the sediment bed, therefore such events were considered in the further analysis. Presumably, presence of a hole in $z_{sym} < 0$ should provide enhanced exposure of the eroding particle to flow structures with centroid also in $z_{sym} < 0$, thereby increasing chances of an erosion and vice versa. With the arrangement of the sediment bed and the centroid of the fluid structure as conditions, these erosion events were detected and conditionally averaged. The sample size for this analysis is not significant enough for a good statistical interpretation as shown in Table 1. A total of 38 events with an upstream hole were detected for which the fluid information was available. Out of these, there are only 23 events when both asymmetries i.e. in the sediment bed and in the fluid structure are on the same side and only 15 events when either a hole is present in $z_{sym} < 0$ and the centroid of the corresponding fluid is in $z_{sym} > 0$, or vice versa. Preliminary results after conditional averaging of both the cases do not show significant changes in the fluid structure

Table 1 Number of erosion events for which particle and fluid data is available. The total number of erosion events was further sub-divided based on the number of surrounding particles

	Particle data	Fluid data of streamwise velocity
Total erosion events	340	157
Eroded particle surrounded by 6 particles	198	92
Eroded particle surrounded by 5 particles		
Hole anywhere	116	53
Hole upstream, i.e. $x_{loc} < 0$	75	38
Eroded particle surrounded by 4 particles		
Hole anywhere	22	10
Hole upstream, i.e. $x_{loc} < 0$	6	2
Others	4	2

(figures not included due to space constraints). The cases where the eroded particle is surrounded by less than five particles were not analyzed due to the very small sample size.

Acknowledgements The present work was funded by the German Research Foundation (DFG) via the project FR 1593/5-2. The authors gratefully acknowledge the Gauss Centre for Supercomputing (GCS) for providing computing time on the supercomputer JUQUEEN at the Jülich Supercomputing Centre (JSC), Grant 5122.

References

1. Adrian, R.J.: Hairpin vortex organization in wall turbulence. Phys. Fluids **19**(4), 041301 (2007)
2. Bathurst, J.C.: Effect of coarse surface layer on bed-load transport. J. Hydraul. Eng. **133**, 1192–1205 (2007)
3. Kempe, T., Fröhlich, J.: An improved immersed boundary method with direct forcing for the simulation of particle laden flows. J. Comp. Phys. **231**(9), 3663–3684 (2012a)
4. Kempe, T., Fröhlich, J.: Collision modelling for the interface-resolved simulation of spherical particles in viscous fluids. J. Fluid Mech. **709**, 445–489 (2012b)
5. Kempe, T., Vowinckel, B., Fröhlich, J.: On the relevance of collision modeling for interface-resolving simulations of sediment transport in open channel flow. Int. J. Multiph. Flow **58**, 214–235 (2014)
6. Shields, A.: Anwendung der Ähnlichkeitsmechanik und der Turbulenzforschung auf die Geschiebebewegung. *Preussische Versuchsanstalt für Wasserbau und Schiffbau*, (in German) (1936)
7. Vowinckel, B., Kempe, T., Fröhlich, J.: Fluid-particle interaction in turbulent open channel flow with fully-resolved mobile beds. Adv. Water Resour. **72**, 32–44 (2014)
8. Vowinckel, B., Jain, R., Kempe, T., Fröhlich, J.: Incipient motion of inertial particles in a turbulent open channel flow. ETMM10 Marbella, Spain, 17–19.9.2014, CD-Rom

Simulation of Large Wind Farms in the Conventionally Neutral Atmospheric Boundary Layer Using LES

D. Allaerts and J. Meyers

1 Introduction

In large wind farms, wakes of individual wind turbines combine into an aggregated wind-farm wake that interacts with the atmospheric boundary layer (ABL). This three-dimensional turbulent flow is influenced by many external factors such as, e.g., the earth's rotation and thermal stratification. Modelling the complex wind-farm–ABL interaction therefore requires a detailed spatial and temporal resolution of atmospheric turbulence. In recent years, large-eddy simulations (LES) have been successfully applied in the study of large wind farms in the ABL (e.g. by Calaf et al. [2]).

In the current study, the large-eddy simulations are used to model large wind farms in the atmospheric boundary layer, including Coriolis effects and thermal stability. More specifically, we consider wind farms in a neutral ABL developing against a stably-stratified background. This atmospheric condition is called a conventionally neutral atmospheric boundary layer (CNBL) and is shown schematically in Fig. 1. In between the neutral boundary layer and the stably-stratified free atmosphere, an inversion layer or capping inversion often forms. Inside this layer, a strong positive temperature jump occurs, which gives the inversion layer a strong thermal stability. As a consequence, the inversion layer acts as a rigid lid on top of the boundary layer and strongly influences the turbulent boundary layer flow. Accordingly, the performance of a wind farm will depend on the characteristics of the overlying capping inversion. The details of this interaction form the main scope of this study.

D. Allaerts (✉) · J. Meyers
Department of Mechanical Engineering, KU Leuven, Celestijnenlaan 300-Bus 2421, B3001 Leuven, Belgium
e-mail: dries.allaerts@kuleuven.be

J. Meyers
e-mail: johan.meyers@kuleuven.be

D.G.E. Grigoriadis et al. (eds.), *Direct and Large-Eddy Simulation X*,
ERCOFTAC Series 24, https://doi.org/10.1007/978-3-319-63212-4_60

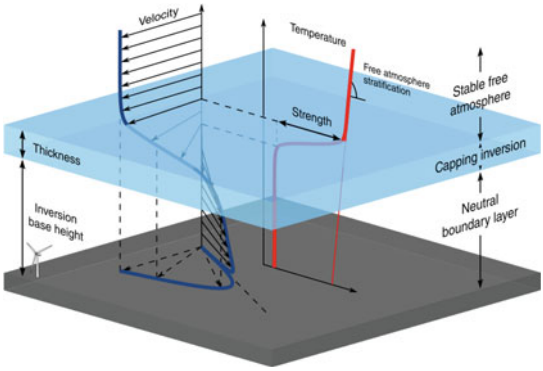

Fig. 1 Three-dimensional schematic view of the conventionally neutral atmospheric boundary layer, showing profiles of the potential temperature and the velocity vector as a function of height

2 LES Methodology

Large-eddy simulations of wind farms in the CNBL are performed with the LES code SP-Wind, which is briefly discussed in Sect. 2.1. A description of the various cases is given in Sect. 2.2.

2.1 SP-Wind Code

The in-house LES code SP-Wind [1, 3] is used to solve the governing LES equations, i.e., the filtered continuity, momentum and potential temperature equations. Coriolis forces are added in the momentum equation, causing the wind direction to vary with height (see also Fig. 1). The subgrid-scale stress and heat flux are modelled with a stability-dependent mixing-length model [4], and the effect of the wind turbines on the flow is modelled using a non-rotating Actuator Disk Method [2]. Details can be found in Ref. [1]. In order to allow LES of developing wind farms, we apply the concurrent-precursor method [5] and extend it to include inflow conditions for the potential temperature.

The flow is forced by imposing a geostrophic wind speed above the boundary layer. However, the angle between the geostrophic wind vector and the wind at hub height depends on the total energy dissipation in the ABL, which is not known a priori. In order to ensure a constant inflow direction at hub height, the geostrophic wind angle is set by an angle controller in the precursor domain. In the case of fully-developed wind farms, the angle controller is applied in the main domain.

2.2 Case Setup

An overview of the various LES cases is presented in Table 1. Cases A1-A4 simulate a fully-developed wind farm under conventionally-neutral conditions. As the CNBL depends heavily on its history, the influence of the capping inversion on the

Table 1 Overview of various LES cases. The specified inversion height h and $\Delta\theta$ are values at the start of the simulation

	$L_x \times L_y \times L_z$ [km×km×km]	$N_x \times N_y \times N_z$	h [m]	$\Delta\theta$ [K]	$\|\nabla(p_\infty/\rho)\|$ [m/s^2]
A1	$6 \times 3 \times 1$	$160 \times 320 \times 256$	500	2.5	1.00×10^{-3}
A2	$6 \times 3 \times 1$	$160 \times 320 \times 256$	500	10	1.00×10^{-3}
A3	$6 \times 3 \times 1.75$	$160 \times 320 \times 448$	500	0	1.00×10^{-3}
A4	$6 \times 3 \times 1.75$	$160 \times 320 \times 448$	1000	2.5	1.00×10^{-3}
A5	$6 \times 3 \times 0.655$	$160 \times 320 \times 160$	–	–	0.57×10^{-3}
B	$28.8 \times 4.8 \times 5.0$	$960 \times 320 \times 320$	250	4.0	1.20×10^{-3}

wind-farm–ABL interaction can be studied by varying the initial potential-temperature profile. With respect to the baseline case, cases A2 and A3 vary the inversion strength, and case A4 varies the inversion height. A simulation of an equivalent neutral pressure-driven boundary layer (A5) is also included (cf. further discussion in Sect. 3.1).

Case B considers a developing wind farm. The streamwise domain size is chosen such that it can hold a large wind farm with 20 rows of turbines and include a sufficiently large downstream region as well. The domain of the precursor differs only in the streamwise dimension, which is one third of the main domain to reduce computation costs. In total, this simulation uses approximately 130 million grid cells, for the combination of main and precursor domain.

3 Wind Farms in the CNBL

The study of wind farm behaviour in the CNBL is split into two parts. First, fully-developed wind-farm boundary layers are considered in Sect. 3.1. Subsequently, developing wind farms are discussed in Sect. 3.2.

3.1 Fully-Developed Wind-Farm Boundary Layer

First of all, some essential differences exist between the fully-developed wind-farm boundary layer in the presence of an inversion layer and the classic neutral pressure-driven approach as used, e.g., by Calaf et al. [2]. In Fig. 2a, the typical double-log layer does not reach up to the top of the domain in the CNBL. Instead, the velocity increases faster near the inversion compared to a neutral pressure-driven boundary layer. Further, the expected shear stress deviates from the well-known linear profile near the inversion, see Fig. 2b. The lower part of the CNBL shows a close to linear shear stress profile and can therefore be approximated by a classical pressure-driven

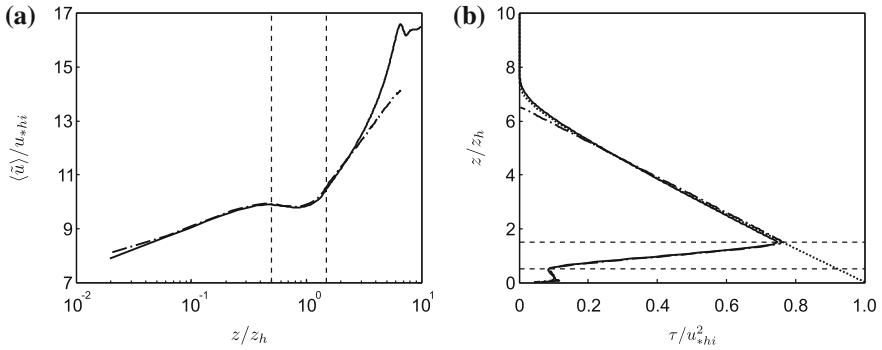

Fig. 2 *Vertical* profiles of **a** mean *horizontal* velocity and **b** shear stress magnitude in the CNBL (case A1, *solid line*) and in the equivalent pressure-driven boundary layer (case A5, *dash-dotted line*). *Dashed lines* mark the *bottom* and *top* of the turbine region. The expected stress profile for the CNBL is indicated by the dotted line in **b**

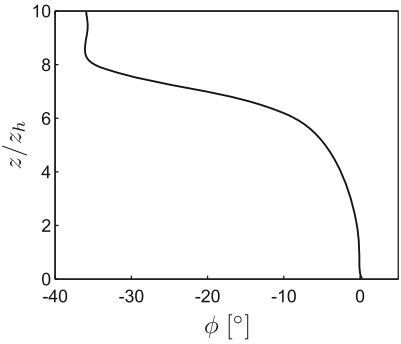

Fig. 3 *Vertical* profile of mean wind direction in the CNBL for case A1

boundary layer. The equivalent height should be chosen between the bottom and center of the inversion layer, and the corresponding pressure gradient is about 30% lower than the streamwise CNBL pressure gradient.

Figure 3 shows the vertical variation of the wind direction. We observe that the CNBL with wind turbines and a low capping inversion is marked by a large geostrophic angle, which for this case is equal to $-36°$. About 75% of this directional change occurs in the capping inversion, giving rise to a sharp directional jump. Inside the boundary layer, the wind direction is nearly constant.

The total wind-farm power extraction as a function of time is shown in Fig. 4 for various LES cases. We observe that varying the inversion-layer characteristics gives rise to a change in wind-farm performance, i.e. increasing the inversion layer height or decreasing the inversion strength results in an increase in wind-farm power production.

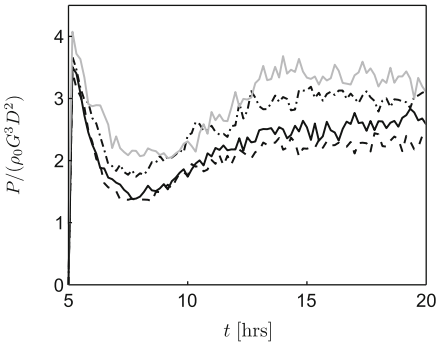

Fig. 4 Total wind-farm power extraction as a function of time for various LES cases: baseline case (A1, *solid black line*), increased inversion strength (A2, *dashed black line*), zero inversion strength (A3, *dash-dotted black line*) and increased base height (A4, *solid grey line*)

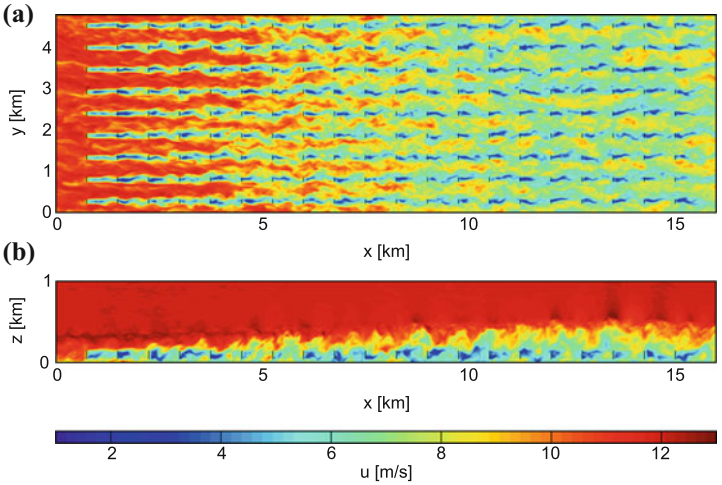

Fig. 5 Instantaneous contours of velocity magnitude for a developing wind farm (case B); **a** An $x - y$ plane at $z = 100$ m through the wind-turbine centers (The location of the wind-turbine disks are shown with *vertical black lines*). **b** An $x - z$ plane cutting through the middle of a column of wind turbines

3.2 Developing Wind-Farm Boundary Layer

In wind farms of finite length, the turbulent boundary layer gradually adapts to the increased drag caused by the wind turbines. This streamwise development is visible in Fig. 5, showing instantaneous contours of the velocity magnitude in case B. In Fig. 5a, the velocity decreases with streamwise distance as the turbine wakes increase in size and strength. After about three turbine rows, the individual turbine wakes start interacting with each other, and a fully-developed regime is attained after

approximately ten turbines. Due to the slowing down of the flow, an internal boundary layer grows above the wind farm (see, e.g., the side view in Fig. 5b). This internal boundary layer induces two additional effects. A first effect can simply be attributed to the conservation of mass, i.e., as the mass flux through the wind farm decreases, air is pushed upwards, thereby causing the inversion layer to rise as well. A second effect is related to the Coriolis forces, which scale linearly with the wind velocity. As the wind slows down throughout the wind farm, the flow changes direction due to the decreasing Coriolis forces (i.e., similar to the direction change with height due to the lower velocity near the ground).

4 Conclusion

In the current study, we showed how the complex wind-farm–ABL interaction can be modelled using large-eddy simulations. The LES code SP-Wind allows for an accurate simulation of atmospheric turbulence, and the concurrent-precursor method can be applied to investigate developing wind farms.

The results indicated that there are considerable difference between the wind farm behaviour in a CNBL and in a neutral pressure-driven approach. It was also shown that the variation of the wind direction with height is important in the CNBL, and that it induced the need for a wind angle controller when simulating wind farms. Finally, developing wind farms showed a clear streamwise evolution of the boundary layer flow. The energy extraction of the turbines was shown to slow down the flow, causing the growth of an internal boundary layer above the wind farm.

Acknowledgements The authors acknowledge support from the European Research Council (FP7–Ideas, grant no. 306471). The computational resources and services used in this work were provided by the VSC (Flemish Supercomputer Center), funded by the Hercules Foundation and the Flemish Government – department EWI.

References

1. Allaerts, D., Meyers, J.: Large eddy simulation of a large wind-turbine array in a conventionally neutral atmospheric boundary layer. Phys. Fluids **27**, 065108 (2015)
2. Calaf, M., Meneveau, C., Meyers, J.: Large eddy simulation study of fully developed wind-turbine array boundary layers. Phys. Fluids **22**, 015110 (2010)
3. Goit, J., Meyers, J.: Optimal control of energy extraction in wind-farm boundary layers. J. Fluid Mech. **768**, 5–50 (2015)
4. Stevens, B., Moeng, C.-H., Sullivan, P.P.: Entrainment and subgrid lengthscales in large-eddy simulations of atmospheric boundary-layer flows, In Kerr, R.M., Kimura, Y.(eds.) IUTAM Symposium on Developments in Geophysical Turbulence of Fluid Mechanics and Its Applications, vol. 58, pp. 253–269 (2000)
5. Stevens, R.J.A.M., Graham, J., Meneveau, C.: A concurrent precursor inflow method for large eddy simulations and applications to finite length wind farms. Renew. Energy **68**, 46–50 (2014)

Direct and Large Eddy Simulations of Droplet Condensation in Turbulent Warm Clouds

G. Sardina, F. Picano, L. Brandt and R. Caballero

1 Introduction

A cloud is a complex multiphase system constituted by a huge number of different substances such as water droplets, ice droplets, water vapor, organic vapors, air. Warm clouds produce 30% of the total rainfall of the planet (70% at the tropics). The clouds are crucially important for Earth's climate, climate changes, rain formation and water cycle. Clouds are considered the largest source of uncertainty in climate prediction because it is very difficult to accurately parameterize the small-scale dynamics and turbulence effects (microphysical processes) affecting clouds in a global climate model where grid boxes used in simulations are typically 250 km wide and 1 km high while processes important for cloud formation happen at much smaller scales, ranging from meters to micrometers. Turbulence affects the cloud microphysics (ensemble of processes that create rain formation) by entrainment, stirring, and mixing, resulting in strong fluctuations and intermittency in temperature, humidity, aerosol concentration, and cloud particle growth and decay [1]. Nowadays a fundamental open question is the rapid growth of cloud droplets in the size range 15–40 μm in radius where the gravitational collision mechanism is not effective. This phenomenon is called condensation-coalescence bottleneck problem or size gap. Rain is activated when a wide droplet radius distribution is generated and turbulence is believed to accelerate this by creating an intermittent supersaturation field and promoting collisions modifying the local droplet concentration (particle inertial clustering) and relative velocity between colliding droplets (sling effect). These

G. Sardina (✉) · R. Caballero
Department of Meteorology and SeRC, Stockholm University, Stockholm, Sweden
e-mail: gaetano.sardina@misu.su.se; gaetano@mech.kth.se

F. Picano
Department of Industrial Engineering, University of Padova, Padova, Italy

L. Brandt
Linné FLOW Centre and SeRC, KTH Mechanics, Stockholm, Sweden

D.G.E. Grigoriadis et al. (eds.), *Direct and Large-Eddy Simulation X*,
ERCOFTAC Series 24, https://doi.org/10.1007/978-3-319-63212-4_61

processes are difficult to capture because of the multi scale nature of the turbulent flows given by the high Reynolds number inside a cloud. Clearly at the moment, the complete turbulence/cloud dynamics are impossible to capture theoretically, in laboratory experiments, Direct Numerical Simulations (DNS) and direct measurements inside real clouds because of the limited resolution and control of the experimental devices. Here we will analyze the impact of turbulence on the droplet growth by water vapor condensation a possible key to understand the bottleneck problem. In the last 15 years, the increase of the computational capabilities allowed the first DNS simulations of turbulence/cloud interactions where individual droplets experience different supersaturations [2, 3] but up to now the results have been underestimated for the difficulties to run simulations up to 20 min, typical time of rain formation.

2 Methodology

The warm cloud that we want to investigate is up to order of $L = 100\,\mathrm{m}$ so that we can initially neglect the effects of spatial inhomogeneity and large scale variations of the thermodynamic parameters. Typical value of the turbulent kinetic energy dissipation ε is order $10^{-3}\,\mathrm{m^2\,s^{-3}}$ so that the cloud Kolmogorov scale $\eta = (\nu/\varepsilon)^{1/4} = 1\,\mathrm{mm}$ where ν is the air kinematic viscosity. Under these conditions the flow field $\mathbf{u}$ can be described by the incompressible Navier–Stokes equations in homogeneous isotropic configurations and the supersaturation field s is transported by the fluid according to the Twomey model, as described in [3]:

$$\frac{\partial \mathbf{u}}{\partial t} + \mathbf{u}\cdot\nabla\mathbf{u} = -\frac{\nabla p}{\rho} + \nu\nabla^2\mathbf{u} + \mathbf{f_u} \tag{1}$$

$$\frac{\partial s}{\partial t} + \mathbf{u}\cdot\nabla s = \kappa\nabla^2 s + A_1 w - \frac{s}{\tau_s} \tag{2}$$

where p is the pressure, ρ is the air density, $\mathbf{f_u}$ is an external forcing able to maintain a statistically stationary state, κ is the diffusivity of water vapor in air, w is the third component of the velocity field acting in the gravity direction, $A_1 w$ is source/sink term of supersaturation resulting from the variation in temperature and pressure with height. The parameter τ_s is the relaxation time scale of the supersaturation field and depends on droplet concentration and dimensions [4] $\tau_s^{-1} = 4\pi\rho_w A_2 A_3 \sum R_i / V$ where R_i are the radii of the droplets in the volume V, ρ_w is the water density, A_1, A_2 and A_3 are functions of thermodynamic quantities. The droplets are evolved in a Lagrangian framework: under the hypothesis of small spheres with dimensions smaller than Kolmogorov scale, low mass fraction to neglect two-way coupling effects on the carrier flow, the only forces acting on the droplets are gravity and the Stokes drag:

Table 1 Parameters of the simulations. The resolution is N, the cloud size L_{box}, the root mean square of the turbulent velocity fluctuations v_{rms} and Taylor Reynolds number Re_λ

Label	N^3	L_{box} [m]	v_{rms} [m/s]	Re_λ
DNS A1/2	64^3	0.08	0.035	45
DNS B1/2	128^3	0.2	0.05	95
DNS C1/2	256^3	0.4	0.066	150
DNS D1	1024^3	1.5	0.11	390
LES E1	512^3	100	0.7	5000

$$\frac{d\mathbf{v_d}}{dt} = \frac{\mathbf{u}(\mathbf{x_d}, t) - \mathbf{v_d}}{\tau_d} - g\mathbf{e_z} \tag{3}$$

$$\frac{d\mathbf{x_d}}{dt} = \mathbf{v_d} \tag{4}$$

$$\frac{dR_i}{dt} = A_3 \frac{s(\mathbf{x_d}, t)}{R_i} \tag{5}$$

where $\mathbf{x_d}$ is the droplet position, $\mathbf{v_d}$ is the droplet velocity, $\mathbf{u}(\mathbf{x_d}, t)$ is the fluid velocity at droplet position, $\tau_d = 2\rho_w R_i^2/(9\rho\nu)$ is the droplet relaxation time, g is the gravity acceleration and $s(\mathbf{x_d}, t)$ the supersaturation at droplet position.

We performed different simulations by gradually increasing the size of the computational clouds from few centimeters to 100 m by keeping constant the small scales. We used both Direct Numerical Simulations (DNS) for the smaller clouds and a Large Eddy Simulation with a classic Smagorinsky model for the subgrid stress tensor. The governing Eqs. (1)–(5) are solved with a classical pseudo-spectral code for the fluid phase coupled with a Lagrangian algorithm for the droplets. All cases share the same turbulent kinetic energy dissipation $\varepsilon = 10^{-3}\mathrm{m}^2\,\mathrm{s}^{-3}$, a value typically measured in stratocumuli. This corresponds to the same small-scale dynamics, with Kolmogorov scale $\eta = (\nu^3/\varepsilon)^{1/4} \approx 1\,\mathrm{mm}$, Kolmogorov time $\tau_\eta = (\nu/\varepsilon)^{1/2} \approx 0.1\mathrm{s}$ and velocity $v_\eta = \eta/\tau_\eta \approx 1\,\mathrm{cm/s}$. We examine droplets with 2 different initial radii, 13 and 5 μ m, denoted as case 1 and 2, with supersaturation relaxation time $\tau_s = 2.5$ and 7s, and same concentration (130 droplets per cm^3). The reference temperature and pressure are $T = 283\,\mathrm{K}$ and $P = 10^5\,\mathrm{Pa}$, with $A_1 = 5E-4\,\mathrm{m}^{-1}$, $A_2 = 350\,\mathrm{m}^3/\mathrm{kg}$, $A_3 = 50\,\mu\,\mathrm{m}^2/\mathrm{s}$. The simulation parameters are reported in Table 1. Note that simulation DNS D1 represent the largest Direct Numerical Simulation of a warm cloud up to now. For computational reasons, the cases DNS C2 and DNS D1 have been integrated with a computational time less than 20 min.

3 Results

A sketch of the simulation is shown in Fig. 1. The computational domain represents a portion of a warm cloud in correspondence of its core region. In the cloud core, the turbulence can be approximated as homogeneous and isotropic and the effects of

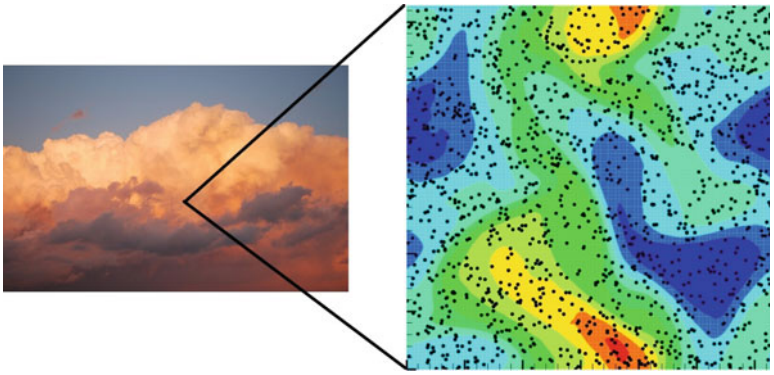

Fig. 1 Sketch of the simulations. The contours represent the supersaturation fluctuations while the discrete *dots* are the droplet positions

entrainment of dry air from the cloud boundaries can be neglected. The plot show a slice of the computational domain where the contours represents the supersaturation fluctuation field. The position of the droplets are superimposed to the contours, since the droplet relaxation time is much smaller than the Kolmogorov time, the droplets tend to be randomly distributed across the domain without preferential accumulation in specific flow regions.

In order to quantify the droplet spectral broadening, we will analyze the behavior of the root main square of the square droplet radius fluctuations indicated as $\sigma_{R^2} = \sqrt{\langle (R^{2'})^2 \rangle}$ where the symbol $\langle \cdot \rangle$ indicates the ensemble average between all the droplets in a given configuration and the apostrophe indicates the fluctuation respect to the mean value $\langle R^2 \rangle$ that in all cases is always equal to its value at time zero $\langle R_0^2 \rangle$ since the mean supersaturation is always zero $\langle s \rangle = 0 \Longrightarrow s = s'$.

The behavior of σ_{R^2} is shown in a log-log plot for all the DNS simulations (Fig. 2) and LES (Fig. 3). From the graphs we can observe for the first time in literature some important issues: (1) the most important is that the droplet spectral distribution never reach a statistical steady state but its rms continues always to increase due to turbulent fluctuations even if s has reached its quasi-steady state value s_{qs}. This implies that at infinite times all the clouds will precipitate because a sufficient spectral broadening will be reached unless external factors will influence the global cloud dynamics; (2) the rms increases according to a power law with exponent 0.5 for all the simulations independently from the Reynolds number; (3) the spectral broadening increases with the Reynolds number and so with the large/small scale separation, confirming previous results [3] where just the large scale turbulent fluctuations have a dominant role on the droplet spectral broadening. These behaviors can be easily explained by writing Eq. (5) for the square radius fluctuations, multiplying for itself and averaging:

$$\frac{d\langle (R_i^{2'})^2 \rangle}{dt} = \frac{d\sigma_{R^2}^2}{dt} = 2A_3 \langle s' R^{2'} \rangle \tag{6}$$

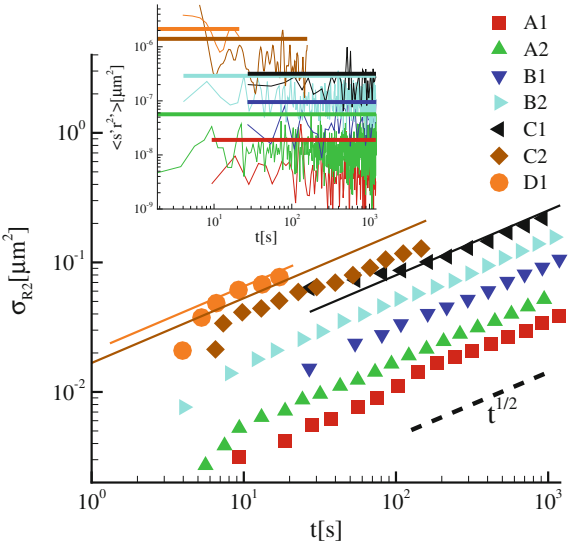

Fig. 2 Root main square of the square droplet radius fluctuations σ_{R^2} versus time for the DNS simulations. *Inset* correlation $\langle s' R^{2'} \rangle$ versus time

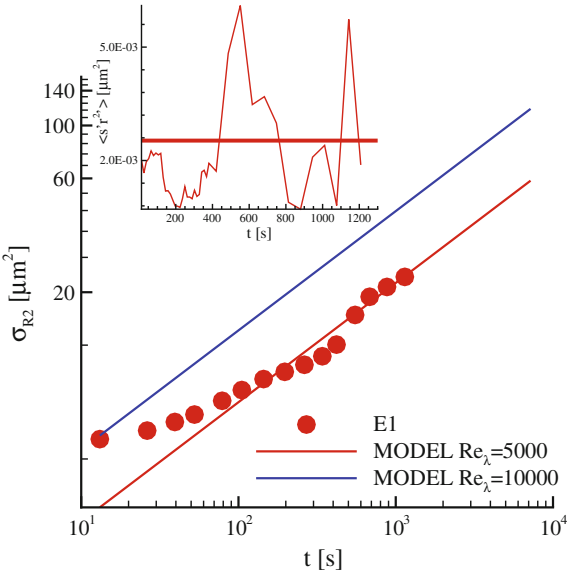

Fig. 3 Root main square of the square droplet radius fluctuations σ_{R^2} versus time for the LES simulations. *Inset* correlation $\langle s' R^{2'} \rangle$ versus time

the droplet square radius variance can linearly increase with time and consequently its rms can grow as $t^{1/2}$ if and only if the correlation $\langle s' R^{2'} \rangle$ reaches a temporal steady state. The previous correlation has been measured in the simulations and the results are plotted in the insets of Figs. 2 and 3. In all the cases the values of $\langle s' R^{2'} \rangle$ reach a statistical steady state fluctuating around a constant value that fixes the slope of σ_{R^2}. Essentially the role of turbulence in droplet condensation/evaporation is to create a constant correlation between supersaturation and square radius fluctuations that increases by increasing the scale separation and consequently the cloud sizes. LES results give us a value of σ_{R^2} order 25 μ m^2 after 20 min a value more close to the experimental observations found in stratocumuli. A 1-D stochastic model can be derived to compare the numerical results and predict the behavior at larger Reynolds number. The complete stochastic model is described in [5]. In particular the stochastic model predicts the value of the correlation $\langle s' R^{2'} \rangle$ and consequently of σ_{R^2}:

$$\langle s' R^{2'} \rangle_{qs} = 2A_3 A_1^2 v_{rms}^2 \langle \tau_s \rangle^2 T_0 = 2A_3 \langle s'^2 \rangle_{qs} T_0 \tag{7}$$

$$\sigma_{R^2} = \sqrt{8} A_3 A_1 v_{rms} \langle \tau_s \rangle (T_0 t)^{1/2} = 0.7 A_3 A_1 \nu^{1/2} \langle \tau_s \rangle Re_\lambda t^{1/2} \tag{8}$$

where T_0 is the turbulence integral time scale. The previous expression shows that the droplet/turbulence condensation dynamics does not depend on the turbulent small scales but is determined by the large flow scales. The results of the model are plotted in Fig. 2 in solid lines, the agreement improves by increasing the Reynolds number of the simulation and it is completely superimposed to the LES case. With the model prediction at higher Reynolds number can be obtained as it is shown in Fig. 3 for a case with $Re_\lambda = 10{,}000$.

4 Conclusions

We performed state of the art Direct and Large Eddy numerical simulation to study the impact of turbulence on cloud droplet growth by condensation. We show that the variance of the droplet size distribution increases indefinitely in time as $t^{1/2}$, with growth rate proportional the large-to-small turbulent scale separation and to the turbulence integral scales but independent of the smallest turbulence scale. Our results give finally a correct estimation of the impact of turbulence on the rain droplet condensation mechanism previously highly underestimated.

Acknowledgements The authors acknowledge computer time provided by SNIC (Swedish National Infrastructure for Computing).

References

1. Bodenschatz, E., Malinowski, S.P., Shaw, R.A., Stratmann, F.: Can we understand clouds without turbulence? Science **327**, 970–971 (2010)
2. Vaillancourt, P.A., Yau, M.K., Grabowski, W.W.: Microscopic approach to cloud droplet growth by condensation. Part I. J. Atmos. Sci. **58**, 1945–1964 (2001)
3. Lanotte, A., Seminara, A., Toschi, F.: Cloud droplet growth by condensation in homogeneous isotropic turbulence. J. Atmos. Sci. **66**, 1685–1697 (2009)
4. Pruppacher, H.R., Klett, J.D.: Microphysics of Clouds and Precipitation, (J. Atmos. Sci.) Springer, New York (1997)
5. Sardina, G., Picano, F., Brandt, L., Caballero, R.F.: Continuous growth of droplet size variance due to condensation in turbulent clouds. Phys. Rev. Lett. **115**, 184501 (2015)

Large Eddy Simulation of Flow over Dunes Laden with Inertial Particles

E.N. Fonias and Dimokratis G.E. Grigoriadis

1 Introduction

Waves and currents are the basic mechanisms that set sediment in motion affecting the morphology of erodible beds in coastal flows. Large-Eddy Simulations (LES) provide a significant frame of reference for the study of sediment transport because they can accurately represent the resolved scales of the flow.

There have been extensive attempts to simulate those motions. Previous studies provide empirical formulas [4] for unidirectional flows correlating the shear stress exerted on the bed with the sediment transport rate. A great number of experimental works have been also conducted for the oscillatory flow over rippled or horizontal beds [10, 11]. In those studies, the basic mechanisms that set the sediments in motion were investigated and models to predict the geometrical characteristics of ripples were proposed. The majority of the numerical works so far, focused on the accurate description of the sediment motion using two different approaches: Eulerian [13] and Lagrangian models [12]. In the former, the advection-diffusion equation for the sediment concentration field is solved, whereas in the latter, the trajectory of each particle [9] is tracked. For the Lagrangian tracking approach considered here, the treatment of the sedimenting particles is crucial because depending on their inertia and mass fraction, their interaction with the flow and between them (4-way coupling), may have significant effects [3], especially in the coastal environment.

In the present work, the unidirectional flow over dunes will be simulated with Large Eddy Simulation (LES) for Reynolds number $Re_{max} = 17{,}500$ based on maximum velocity. The no-slip boundary condition was imposed using the Immersed

E.N. Fonias (✉) · D. G. E. Grigoriadis
Department of Mechanical and Manufacturing Engineering, University of Cyprus, Nicosia, Cyprus
e-mail: fonias.efstratios@ucy.ac.cy

D.G.E. Grigoriadis et al. (eds.), *Direct and Large-Eddy Simulation X*,
ERCOFTAC Series 24, https://doi.org/10.1007/978-3-319-63212-4_62

Boundary Method (IBM) [1]. The particle phase has been represented by sandy sediments released within a thin layer over the impermeable dune-shaped bed. The results demonstrate the basic mechanisms responsible for sediment movement.

2 Numerical Model and Validation

The LES equations of motion for the resolved variables are rendered dimensionless with the maximum velocity scale U_{max} and the wall-normal domain dimension d, defining the flow Reynolds number $\mathrm{Re}_{max} = U_{max} d/\nu$,

$$\frac{\partial \overline{u}_i}{\partial x_i} = 0 \quad , \quad \frac{\partial \overline{u}_i}{\partial t} + \frac{\partial \overline{u}_i \overline{u}_j}{\partial x_j} = -\frac{\partial p}{\partial x_i} - \frac{\partial \tau_{ij}}{\partial x_j} + \frac{1}{\mathrm{Re}_{max}} \frac{\partial^2 \overline{u}_i}{\partial x_j \partial x_j} + f_i + f_i^p \qquad (1)$$

where the subgrid scale stresses τ_{ij} were modeled according to [5]. Here x_i ($i = 1, 2, 3$) are the Cartesian coordinates denoted as x (streamwise), y (spanwise) and z (wall-normal) directions, respectively, p the pressure and $\overline{u}_i$ the velocity components. An external forcing function term f_i is added enforcing proper wall boundary conditions on solid bodies that do not coincide with grid points according to the Immersed Boundary Method [1]. The term f_i^p represents the momentum exchange between fluid and dispersed phases. A Lagrangian particle tracking approach was considered for particles using the equation of Maxey and Riley [9] in dimensionless form:

$$\frac{du_p}{dt} = -\frac{1}{St}(u_p - \overline{u}_i) - \frac{1}{S}\frac{(S-1)}{Fr_i} \equiv H_i^p \quad , \quad f_i^p = \frac{1}{m_{f,i}} \sum_{p=1}^{N} m_p H_i^p \qquad (2)$$

where u_p is the particle's local velocity and the terms on the right hand side represent the Stokes drag and gravity forces. The particle to fluid density ratio is $S = \rho_p/\rho_f$. $St = S(d_p^2/h^2)(\mathrm{Re}_{max}/18)$ is the particle Stokes number, d_p is the particle diameter and $Fr_i = U_{max}^2/g_i d$ the Froude number. Equation (2) provides the velocity of particles whereas their position is determined simply by $u_p = dx_i^p/dt$. The term f_i^p is computed by summing up the momentum terms of H_i^p for all N particles which belong to cell i, i.e. using a point force approximation. $m_{f,i}$ is the fluid mass of the cell i and m_p is the mass of each particle. In cases where the volume fraction of the particles exceeds locally the critical value of 10^{-2} [3], apart from collisions of particles with the solid boundaries of the domain, the effect of inter-particle collisions was taken into account using a hard-sphere model by Hoomans [7].

The proposed model was validated using DNS data from [2] for a vertical turbulent channel flow at $\mathrm{Re}_\tau = 170$ laden with 87,500 heavy particles. The streamwise velocity comparison in Fig. 1 indicates a satisfying agreement.

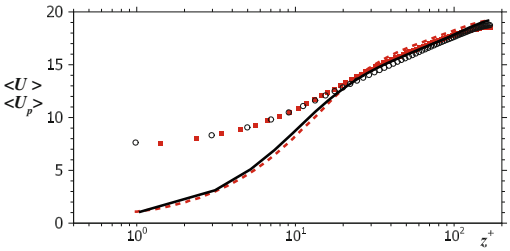

Fig. 1 Mean streamwise fluid velocity for particle-laden (*lines*) flow and particle velocity (*points*): current formulation (*continuous line - white circles*), validation data [2] (*dashed line - red squares*)

3 Simulation Set-Up

The equations of motion are discretized on a three-dimensional staggered grid arrangement and time-advancement is achieved by a fully explicit Adams-Bashforth scheme. Figure 2 shows the computational domain along with the boundary conditions for the pressure, namely homogeneous Neumann condition at the top, non-slip condition at the bed and periodic condition along the streamwise x and spanwise y directions. The flow is imposed by a dynamically-computed pressure gradient preserving a flow rate at Re_{max} =17,500, initiated by random perturbations superimposed on a log-law distribution of velocities. The dune geometry is $20h = 5d$ long in the streamwise direction, where h is the dune height. The length of the domain along the y and z directions, was set to $2.4d = 9.6h$ and $d = 4h$ respectively. A total of 600,000 particles of diameter $0.018d$ were released evenly up to a level of $2h$ over the dune's crest. The particle to fluid density ratio was set equal to $S = 2.65$, representing the density ratio of quartz sand to water. After an initial transient, particles may accumulate in regions with a local mass fraction exceeding 10^{-2} where a 4-way coupling regime should be considered [3]. Previous simulations for the fluid phase only [5] indicated that a numerical resolution of $(512, 96, 128)$ cells with proper refinement in solid boundaries ($\Delta z_{min} = 0.003d$, aspect ratio 1:10) was sufficient for a reasonable agreement with the experimental data set of Kadota and Nezu [8].

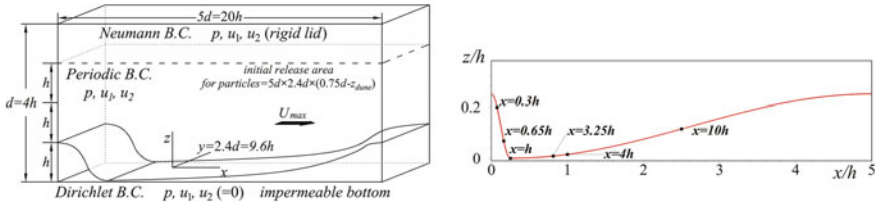

Fig. 2 (*Left*) Sketch of the computational domain with geometric parameters and boundary conditions, (*right*) Position of vertical profiles of flow variables in terms of the dune height h

4 Results

The particle-laden simulation results were compared against the free flow results presented by [5]. Profiles of mean streamwise and wall-normal velocity components are examined in Fig. 3 at the dune's downslope, concluding that the inertia of particles affects equally the velocity components. This phenomenon is mostly visible in the wall normal velocity profiles because of the velocity magnitude.

The effect of the particles in the carrier fluid is more obvious from the profiles of the velocity fluctuations of the spanwise and wall-normal velocity components (Fig. 4). The turbulent kinetic energy $q^2 = (u_{rms}^2 + v_{rms}^2 + w_{rms}^2)/2$ is clearly reduced compared to the free flow case. Finally, it appears that the recirculation region observed for the free flow case in [5] is not affected by the particles motion, having a length of $1.4d = 5.6h$, since the effect of particles on the flow is weak. Thus, the secondary recirculation bubble observed within, also retains its shape (Fig. 5).

The time averaged relative particle velocities are shown in Fig. 6. For the streamwise component, the ejection and settling regions are evident along with the particles lift-off in the upslope preceding the dune's crest. The wall-normal component indicates the settling (blue colour) and the resuspension regions (red colour).

The most important outcome is the quantification of volumetric concentration of the particles over the dune. Figure 7 shows a stable concentration of 0.18 far from the boundary layer, and extended clustering of particles onto the dune's upslope region (red colour). The different behaviour in the recirculation region can be investigated through the corresponding wall-normal profiles in six different sections: two in the dune's downslope, two sections in the recirculation region and two more sections in

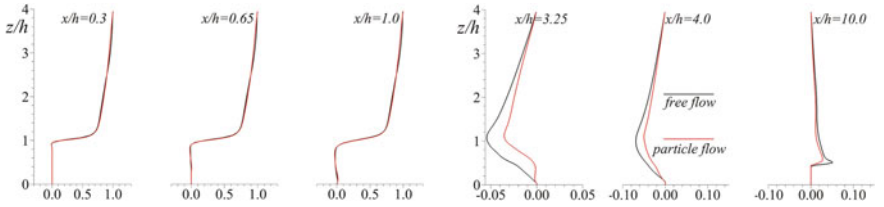

Fig. 3 Profiles of the mean streamwise velocity component $< u >$ (*left*) and mean wall-normal velocity component $< w >$ (*right*)

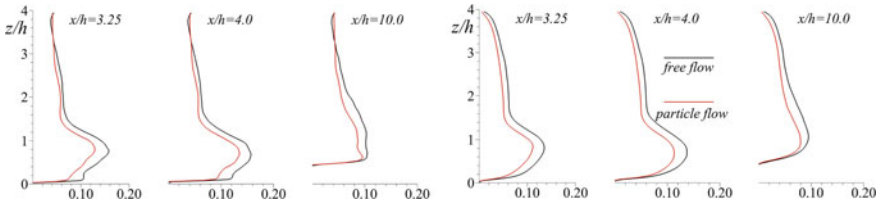

Fig. 4 Profiles of the mean spanwise velocity fluctuations $< v_{rms} >$ (*left*) and mean wall-normal velocity fluctuations $< w_{rms} >$ (*right*)

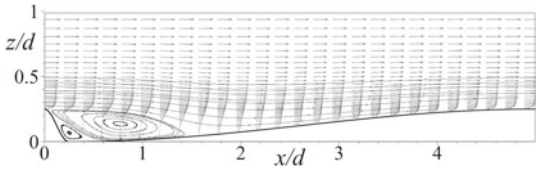

Fig. 5 Streamlines and mean velocity vectors for unidirectional, particle-laden flow

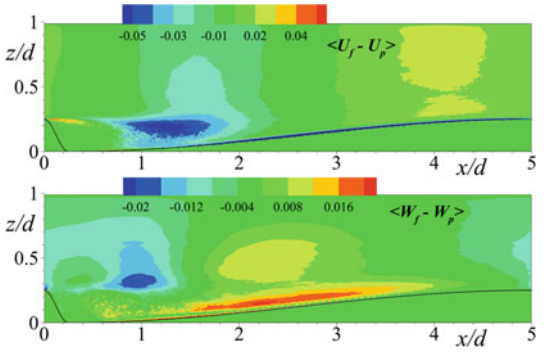

Fig. 6 Contour plot of ensemble averaged velocity components in the streamwise $< U_f - U_p >$ and wall-normal directions $< W_f - W_p >$

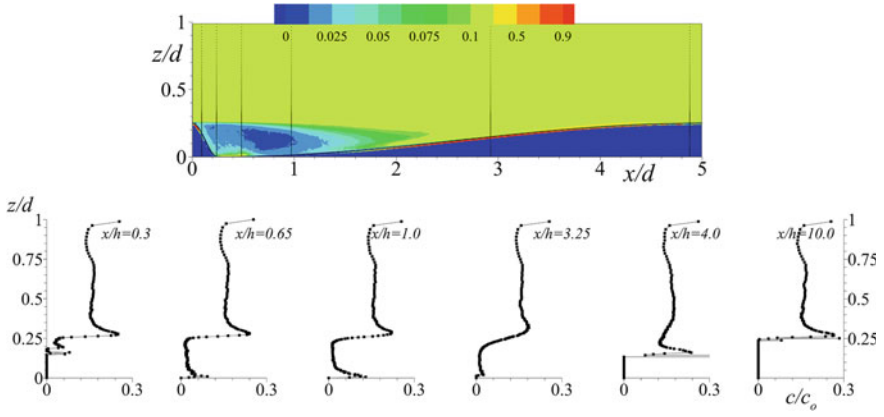

Fig. 7 (*up*) Contour plot of particle volumetric concentration and (*down*) profiles of ensemble averaged volumetric concentration of particles along the dune

the resuspension region. From those profiles it can be observed that the maximum concentration is equal to 0.3 which is approximated at the three first profiles in the recirculation region (maximum value of 0.25) and in the last profile just before the ejection point of the dune's crest. It can be also observed that within the recirculation region ($x/h = 0.3, 0.65, 1.0, 3.25$) the particle concentration is relatively low and in addition, there is a relatively high concentration of particles right over the impermeable boundary of the dune at $x/h = 4.0$.

5 Conclusions

The uniform flow over dunes laden with sand particles has been investigated by means of Large Eddy Simulations. The dune shaped bed was implemented using the Immersed Boundary Method (IBM) and the sandy sediment motion has been simulated with a Lagrangian approach using a four-way coupled regime. Turbulent statistics for the fluid phase indicate the reduction of mean velocity values along with the mean velocity fluctuations and hence the turbulent kinetic energy, in the presence of particles. Particle mean relative velocity values provide clear indications of regions where particles are settling down or set into suspension. Finally, concentration plots and profiles indicate the clustering of particles in the upslope dune region and low concentration in the recirculation region. In future works, the evolution of an erodible bed morphology due to sediment will be included.

Acknowledgements The research leading to these results has received funding from the People Programme (Marie Curie Actions) of the European Union's Seventh Framework Programme FP7/2007–2013/ under REA grant agreement n^o 607394-SEDITRANS.

References

1. Balaras, E.: Modeling complex boundaries using an external force field on fixed Cartesian grids in large-eddy simulations. Comput. Fluids **33**, 375–404 (2004)
2. Dritselis, C.D., Vlachos, N.S.: Numerical study of educed coherent structures in the near-wall region of a particle-laden channel flow. Phys. Fluids **20**, 055103 (2008)
3. Elghobashi, S.: An updated classification map of particle-laden turbulent flows. In: Proceedings of the IUTAM Symposium on Computational Multiphase Flow, Springer, Netherlands (2006)
4. Engelund, F., Fredsøe, J.: A Monograph on Sediment Transport in Alluvial Streams. Teknisk Vorlag, Copenhagen (1967)
5. Grigoriadis, D.G.E., Balaras, E., Dimas, A.A.: Large-eddy simulations of unidirectional water flow over dunes. J. Geophys. Res. **114**, F02022 (2009)
6. Grigoriadis, D.G.E., Balaras, E., Dimas, A.A.: Large-eddy simulation of wave turbulent boundary layer over rippled bed. Coast. Eng. **60**, 174–189 (2012)
7. Hoomans, B.P.B.: Granular dynamics of gas-solid two-phase flows. University of Twente, Ph.D.-Thesis (1999)
8. Kadota, A., Nezu, I.: Three-dimensional structure of space-time correlation on coherent vortices generated behind dune crest. J. Hydraul. Res. **37**, 59–80 (1999)

9. Maxey, M.R., Riley, J.J.: Equation of motion for a small rigid sphere in a nonuniform flow. Phys. Fluids **26**(4), 883–889 (1983)
10. O'Donoghue, T., Doucette, J.S., van der Werf, J.J., Ribberink, J.S.: The dimensions of sand ripples in full-scale oscillatory flows. Coast. Eng. **53**(12), 997–1012 (2006)
11. Ribberink, J.S.: Bed-load transport for steady flows and unsteady oscillatory flows. Coast. Eng. **34**(1–2), 59–82 (1998)
12. Vreman, B., Geurts, B.J., Deen, N.G., Kuipers, J.A.M., Kuerten, J.G.M.: Two- and four-way coupled Euler-Lagrangian large-eddy simulation of turbulent particle-laden channel flow. Flow Turbul. Combust. **82**(1), 47–71 (2009)
13. Zedler, E.A., Street, R.L.: Sediment transport over ripples in oscillatory flow. J. Hydraul. Eng. ASCE **132**(2), 1–14 (2001)

Large-Wave Simulation of Breaking Waves Over a Beach

A.A. Dimas, A.S. Dimakopoulos and G.A. Kolokythas

1 Introduction

Wave transformation and breaking on a beach are associated with important coastal processes like wave-generated currents, sediment transport and coastal erosion.

Spilling breaking and transformation of waves in the surf zone have been studied by both physical modeling [12, 13] and numerical simulations. For the latter, methods are based either on the Boussinesq equations where the flow is depth-averaged [10, 11] or the Navier–Stokes equations where the flow is resolved along the depth. The second category includes RANS [1, 9, 14] and LES models [4, 5, 15].

The primary objective of this work is the adaptation and application of the large-wave simulation (LWS) formulation, which was originally developed for two-dimensional, deep-water breaking [7], in three-dimensional, coastal breaking [6, 8]. LWS is based on the decomposition of flow scales, related to velocity, pressure and free-surface elevation, into resolved (large) and subgrid (small) scales. In LWS, the effect of SGS velocity and pressure fluctuations is treated according to LES formulation, while the effect of SGS free-surface fluctuations is also introduced in the flow equations by using a boundary-fitted transformation. The latter is in contrast to pure LES where the particular free surface treatment (for example VOF) does not allow for the effect of SGS free-surface fluctuations during breaking to be accounted for.

A.A. Dimas (✉)
Department of Civil Engineering, Laboratory of Hydraulic Engineering,
University of Patras, Patras, Greece
e-mail: adimas@upatras.gr

A.S. Dimakopoulos
Coastal Structures, HR Wallingford, Wallingford, UK
e-mail: a.dimakopoulos@hrwallingford.com

G.A. Kolokythas
Department of Mobility and Public Works, Flanders Hydraulics Research,
Flemish Government, Antwerp, Belgium
e-mail: gerasimos.kolokythas@mow.vlaanderen.be

D.G.E. Grigoriadis et al. (eds.), *Direct and Large-Eddy Simulation X*,
ERCOFTAC Series 24, https://doi.org/10.1007/978-3-319-63212-4_63

Another advantage of LWS is that no special boundary conditions are required to incorporate breaking generated turbulence [2, 3], since SGS free-surface fluctuations are included in the flow equations. The desirable properties of the numerical model are: (a) automatic activation of breaking model at incipient breaking without additional information about wave direction, and (b) prediction of surface roller formation after breaking and wave dissipation in the surf zone.

2 Methodology

The formulation is based on the filtering of the three-dimensional Navier–Stokes equations including a filtering of the free-surface elevation which is consistent with the velocity and pressure filtering (Fig. 1).

The process is facilitated by the use of a boundary-fitted approach, and the resulting governing equations are:

$$\frac{\partial \bar{u}_j}{\partial x_j} = 0 \tag{1}$$

$$\frac{\partial \bar{u}_i}{\partial t} + \frac{\partial (\bar{u}_i \bar{u}_j)}{\partial x_j} = -\frac{\partial \bar{p}}{\partial x_i} + \frac{1}{Re}\left(\frac{\partial^2 \bar{u}_i}{\partial x_j \partial x_j}\right) - \frac{\partial \tau_{ij}}{\partial x_j} + \frac{x_3 + d}{d + \bar{\eta}} \frac{\partial}{\partial x_3}\left(\tau^{\eta}_{i3} - \tau_{ik}\frac{\partial \bar{\eta}}{\partial x_k}\right) \tag{2}$$

where τ_{ij} are the eddy SGS stresses, which are identical to the ones resulting from an LES formulation, and τ^{η}_{ij} are the wave SGS stresses, which result from the unresolved free-surface fluctuations. Similar approach is followed for the free-surface boundary conditions, which are enforced at $x_3 = \bar{\eta}$, i.e., the filtered free-surface level.

The eddy and wave SGS stresses of Eq. (2) are modeled using the following eddy viscosity models:

$$\tau_{ij} = -2\nu_\tau \bar{S}_{ij} = -2C^2 \Delta^2 |\bar{S}| \bar{S}_{ij} \tag{3}$$

$$\tau^{\eta}_{ij} = -2\nu_\tau \bar{S}^{\eta}_{ij} = -2(C^{\eta})^2 \bar{\Delta}^2 |\bar{S}^{\eta}| \bar{S}^{\eta}_{ij} \tag{4}$$

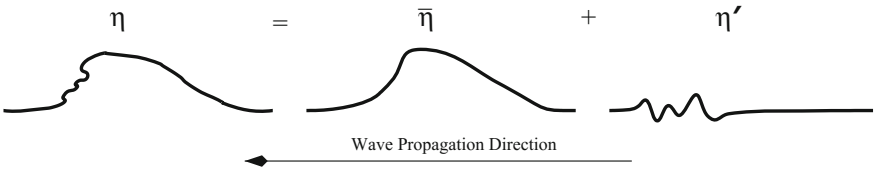

Fig. 1 Free surface decomposition for a spilling breaker

where C and C^{η} are model parameters, $\Delta = (\Delta_1 \Delta_2 \Delta_3)^{1/3}$ is the smallest resolved scale based on the grid size Δ_i, S_{ij} is the strain-rate tensor of resolved scales

$$\bar{S}_{ij} = \frac{1}{2}\left(\frac{\partial \bar{u}_i}{\partial x_j} + \frac{\partial \bar{u}_j}{\partial x_i}\right) \tag{5}$$

$|\bar{S}| = \left(2\bar{S}_{ij}\bar{S}_{ij}\right)^{1/2}$ is its magnitude, S^{η}_{ij} is a modified strain-rate tensor of resolved scales

$$\bar{S}^{\eta}_{ij} = \delta_{3j} S_{ik} \left|\frac{\partial \bar{\eta}}{\partial x_k}\right| \tag{6}$$

$|\bar{S}^{\eta}| = \left(2\bar{S}^{\eta}_{ij}\bar{S}^{\eta}_{ij}\right)^{1/2}$ is its magnitude, δ_{ij} is the Kronecker delta, and the absolute value of the free surface slope ensures the model invariance on the wave propagation direction.

For the numerical solution of Eqs. (1) and (2), a σ-transformation was used in the vertical direction to render the computational domain time-independent. A operator-splitting scheme was used for the temporal discretization. For the spatial discretization, central finite differences were used in the streamwise direction, a pseudo-spectral scheme with Chebyshev polynomials in the vertical direction and a pseudo-spectral scheme with Fourier modes in the spanwise direction.

3 Results

The method was applied on the propagation of regular waves over a beach of constant bed slope equal to 1/35.

First, the case where the wave direction is normal to the shoreline, i.e., the wave propagation angle at deep water is $\theta_o = 0°$, was examined. The wave conditions were identical to the experiments in [12]. In Fig. 2, snapshots of the resolved free-surface elevation are presented for $C = 0.1$ and $C^{\eta} = 0.4$, and compared to experimental data of maximum (crest) and minimum (trough) values of free-surface elevation [12]. The comparison shows that the LWS predicts accurately the incipient breaking parameters (wave height, H_b and depth, d_b) and the wave dissipation rate in the outer surf zone, while it overestimates the wave dissipation rate in the inner surf zone.

Next, cases where the wave direction is oblique to the shoreline were examined. A typical snapshot of the free-surface elevation, for the case of $\theta_o = 42.5°$, is shown in Fig. 3. The wave transformation in the outer coastal zone is a result of the combined action of nonlinear refraction and shoaling of waves as the water depth decreases. In the surf zone, wave transformation is dominated by the gradual spanwise wave breaking, due to the oblique propagation, and the wave energy dissipation.

According to the LWS formulation, wave breaking and dissipation in the surf zone are modeled by eddy and wave SGS stresses. It was found that the appearance and the magnitude of these SGS stresses is correlated to the wave breaking

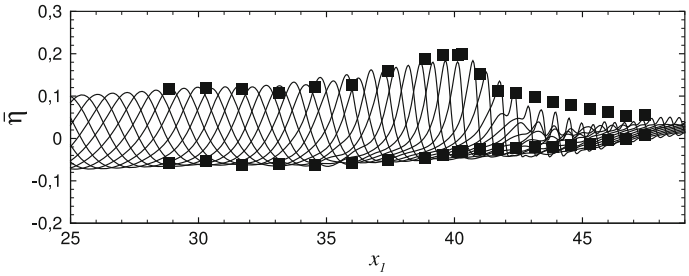

Fig. 2 Free-surface elevation at several time instants, during shoaling and in the surf zone, over beach of slope 1/35, which starts at $x_1 = 15$, for $C^\eta = 0.4$. Symbols correspond to experimental data of the free-surface elevation envelope [12]

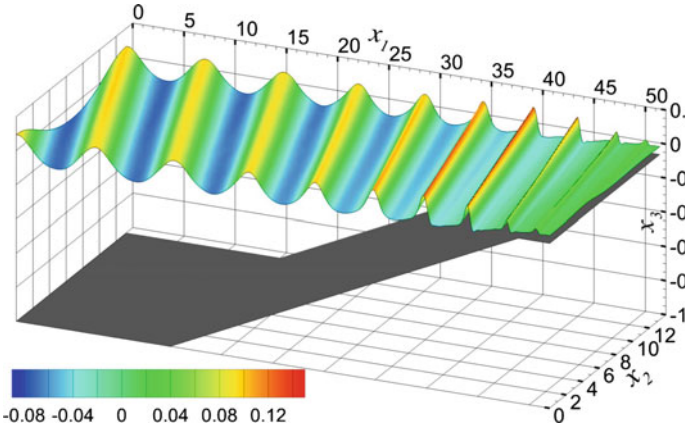

Fig. 3 Snapshot of resolved free-surface elevation contours over beach of slope 1/35, for the case of oblique incoming waves at an angle of $\theta_o = 42.5°$ at deep waters

process. Specifically, it was found that the most significant SGS stresses in terms of their magnitude were τ_{13}^{η} and τ_{23}^{η}, and they developed exclusively in the vicinity of the breaking wavefront (Fig. 4). After breaking, the development of the surface roller, which was accompanied by vorticity production (Fig. 5), was connected to the appearance and growth of the wave SGS stresses at the obliquely breaking wavefront. The magnitude of the wave SGS stresses reaches its maximum value at depth $d/d_b \approx 0.7$. For shallower water depths, the strength of the SGS stresses attenuates and practically vanishes in the inner surf zone. The generation of spanwise vorticity is clearly associated to the formation of the surface roller in the surf zone (Fig. 5), while significant spanwise vorticity generation occurs in the wave boundary layer as well.

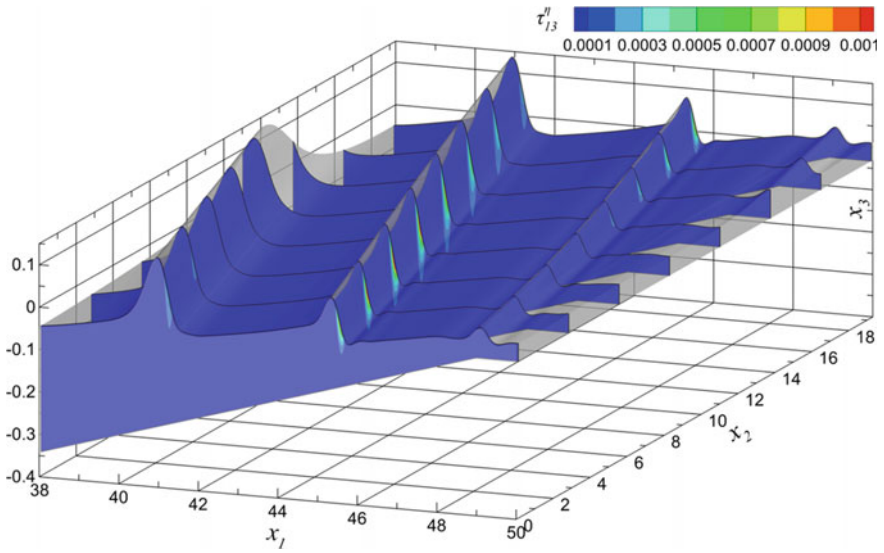

Fig. 4 *Vertical slices* show the distribution of the τ_{13}^{η} SGS stress in the surf zone over beach of slope 1/35, for the case of oblique incoming waves at an angle of $\theta_o = 42.5°$ at deep waters

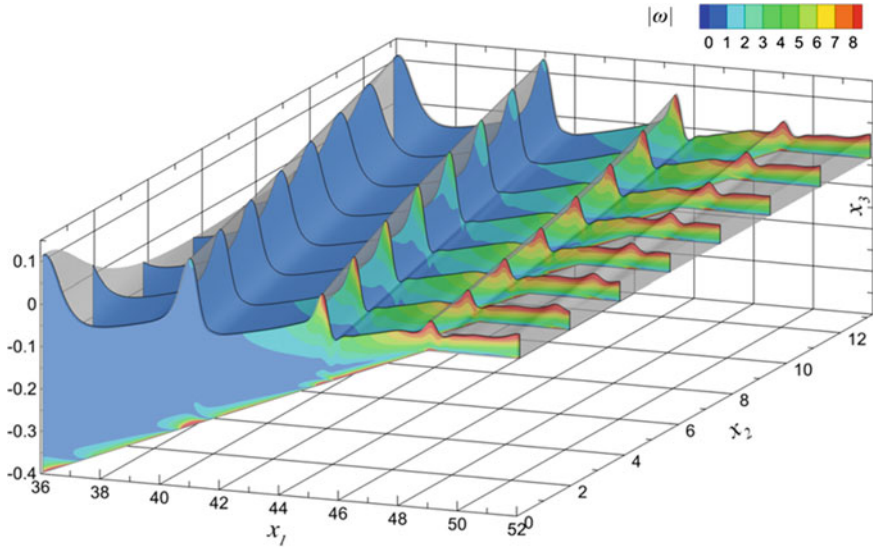

Fig. 5 *Vertical slices* show the distribution of the spanwise vorticity in the surf zone over beach of slope 1/35, for the case of oblique incoming waves at an angle of $\theta_o = 42.5°$ at deep waters

4 Conclusions

The LWS of wave transformation and breaking over a constant slope beach was successful in capturing and accurately predicting all the relevant processes of refraction, breaking, surface roller, and wave boundary layer.

Acknowledgements This paper is part of the research project ARISTEIA I - 1718, implemented within the framework of the program Education and Lifelong Learning, and co-financed by the European Union (European Social Fund) and Hellenic Republic funds.

References

1. Bradford, S.F.: Numerical simulation of surf zone dynamics. J. Waterw Port Coast. Ocean Eng. **126**(1), 1–13 (2000)
2. Brocchini, M., Peregrine, D.H.: The dynamics of strong turbulence at free surfaces. Part 1. Description. J. Fluid Mech. **449**, 225–254 (2001)
3. Brocchini, M., Peregrine, D.H.: The dynamics of strong turbulence at free surfaces. Part 2. Free-surface boundary conditions. J. Fluid Mech. **449**, 255–290 (2001)
4. Christensen, E.D.: Large eddy simulation of spilling and plunging breakers. Coast. Eng. **53**(5–6), 463–485 (2006)
5. Christensen, E.D., Deigaard, R.: Large eddy simulation of breaking waves. Coast. Eng. **42**(1), 53–86 (2001)
6. Dimakopoulos, A.S., Dimas, A.A.: Large-wave simulation of three-dimensional, cross-shore and oblique, spilling breaking on constant slope beach. Coast. Eng. **58**(8), 790–801 (2011)
7. Dimas, A.A., Fialkowski, L.T.: Large-wave simulation (LWS) of free-surface flows developing weak spilling breaking waves. J. Comput. Phys. **159**(2), 172–196 (2000)
8. Kolokythas, G.A., Dimas, A.A.: Numerical simulation of oblique wave breaking and wave-induced currents in the surf zone. In: Proceedings 33rd International Conference Offshore Mechanics and Arctic Engineering, OMAE2014-24125, pp. 1–9, San Francisco, USA (2014)
9. Lin, P., Liu, P.L.-F.: A numerical study of breaking waves in the surf zone. J. Fluid Mech. **359**, 239–264 (1998)
10. Madsen, P.A., Sorensen, O.R., Schäffer, H.A.: Surf zone dynamics simulated by a Boussinesq type model. Part I. Model description and cross-shore motion of regular waves. Coast. Eng. **32**(4), 255–287 (1997)
11. Musumeci, R.E., Svendsen, I.A., Veeramony, J.: The flow in the surf zone: a fully nonlinear Boussinesq-type of approach. Coast. Eng. **52**(7), 565–598 (2005)
12. Ting, F.C.K., Kirby, J.T.: Observation of undertow and turbulence in a laboratory surf zone. Coast. Eng. **24**(1–2), 51–80 (1994)
13. Ting, F.C.K., Kirby, J.T.: Dynamics of surf-zone turbulence in a spilling breaker. Coast. Eng. **27**(3–4), 131–160 (1996)
14. Torres-Freyermuth, A., Losada, I.J., Lara, J.L.: Modeling of surf zone processes on a natural beach using Reynolds-averaged Navier-Stokes equations. J. Geophys. Res. **112**, C09014 (2007)
15. Watanabe, Y., Saeki, H., Hosking, R.J.: Three-dimensional vortex structures under breaking waves. J. Fluid Mech. **545**, 291–328 (2005)

Part XI
Heat and Mass Transfer

Natural Convection in Ventilated Building Facades Using LES

Dimokratis G.E. Grigoriadis

1 Introduction

Understanding the buoyancy-driven flow in gas gap enclosures can provide significant physical insight into a variety of technological applications ranging from cooling of electronic equipment to energy related components and systems. Typical examples of these flows also appear in several passive-solar systems such as ventilated building facades [5], Trombe walls [8] or solar-chimneys. In all of these problems, it is crucial to estimate the convective heat transfer rate for a given geometry under a specific solar-flux intensity. For these configurations, most of the studies so far use a Reynolds averaged (RANS) approach [7, 8].

In the present study, Large Eddy Simulations (LES) and Direct Numerical Simulations (DNS) are employed to investigate the flow and the associated heat transfer rates for the buoyancy-driven flow in building facades. A C-type geometry is examined as shown in Fig. 1 using the immersed boundary method. A realistic range of parameters is investigated for Rayleigh numbers in the range 10^5–7.5×10^{10} based on the temperature difference and the wall height H.

2 Formulation and Numerical Method

For natural convection mode of heat transfer, using the Boussinesq's approximation to include buoyancy effects, the resulting equations of motion for the resolved field of an incompressible flow read,

D. G. E. Grigoriadis (✉)
Department of Mechanical and Manufacturing Engineering, Ucy-compsci,
University of Cyprus, Nicosia, Cyprus
e-mail: grigoria@ucy.ac.cy

D.G.E. Grigoriadis et al. (eds.), *Direct and Large-Eddy Simulation X*,
ERCOFTAC Series 24, https://doi.org/10.1007/978-3-319-63212-4_64

$$\frac{\partial \overline{u}_i}{\partial x_i} = 0 \tag{1}$$

$$\frac{\partial \overline{u}_i}{\partial t} + \frac{\partial \overline{u}_i \overline{u}_j}{\partial x_j} = -\frac{\partial \overline{p}}{\partial x_i} \frac{Pr}{\sqrt{Ra}} \frac{\partial^2 \overline{u}_i}{\partial x_j \partial x_j} - \frac{\partial \tau_{ij}}{\partial x_j} + Pr\overline{\Theta}\delta_{ik} + f_{u,i} \tag{2}$$

$$\frac{\partial \overline{\Theta}_i}{\partial t} + \frac{\partial \overline{\Theta} \overline{u}_j}{\partial x_j} = \frac{1}{\sqrt{Ra}} \frac{\partial^2 \overline{\Theta}}{\partial x_j \partial x_j} - \frac{\partial q_j}{\partial x_j} + f_\theta \tag{3}$$

where x_i ($i = 1, 2, 3$) are the three Cartesian coordinates (denoted as x, y, z, hereafter), and $\overline{u}_i$ are the resolved velocity components in the corresponding directions (denoted as u, v, w, hereafter). Gravity is assumed to act along the vertical, z direction. The last terms $f_{u,i}$ and f_θ in Eqs. 2 and 3 are the external forcing functions, used to dynamically model the existence of solid boundaries within the immersed boundary method approach [2]. Ra is the Rayleigh number defined with respect to the temperature difference,

$$Ra_{\Delta T,H} = \frac{g\beta(T_w - T_\infty)H^3}{\nu\alpha} = Gr_{\Delta T,H} Pr \tag{4}$$

where $Gr_{\Delta T,H}$ is the associated Grashof number. The characteristic scales used to non-dimensionalise the equations are the wall's height H for length, $V_o = \frac{\alpha}{H}\sqrt{Ra}$ for velocity, $t_o = H/V_o$ for time and $P_o = \rho {V_o}^2$ for pressure. The non-dimensional temperature is defined as $\Theta = \frac{T - T_\infty}{\Delta T_o}$ where the temperature difference between the wall and the ambient $\Delta T_o = T_w - T_\infty$ is used as a characteristic scale. For the highest Ra numbers considered, using LES, the sgs stresses τ_{ij} were modelled with the filtered structure function or the Smagorinsky model. The sgs heat fluxes q_j were modelled using a simple algebraic eddy diffusivity model with $Pr_t = 0.6$.

The numerical method consists of a fully explicit Adams-Basforth scheme for the time advancement on Cartesian staggered grids utilising a direct pressure solver [2]. A finite difference, second order accurate scheme is used for space discretisation of the velocity field. For the temperature Eq. 3, a hybrid linear parabolic approximation (HLPA) scheme was implemented [3]. The resulting algorithm is implemented in a very efficient numerical code reaching run-time performances of 100 MDOF/s on personal computers, demanding less than 100 MB of physical memory per million computational nodes.

3 Results & Conclusions

The numerical method has been first validated against the experimental study of Betts and Bokhari [1] for the case of a tall, differentially heated cavity with aspect ratio $H/s = 28.26$ (Fig. 1). Two different Rayleigh numbers based on the wall distance s were examined, $Ra_{\Delta T,s} = 0.86 \times 10^6$ and 1.43×10^6, with Prandtl numbers $Pr = 0.704$ and 0.697 respectively. The hot and cold walls were assumed to be isothermal,

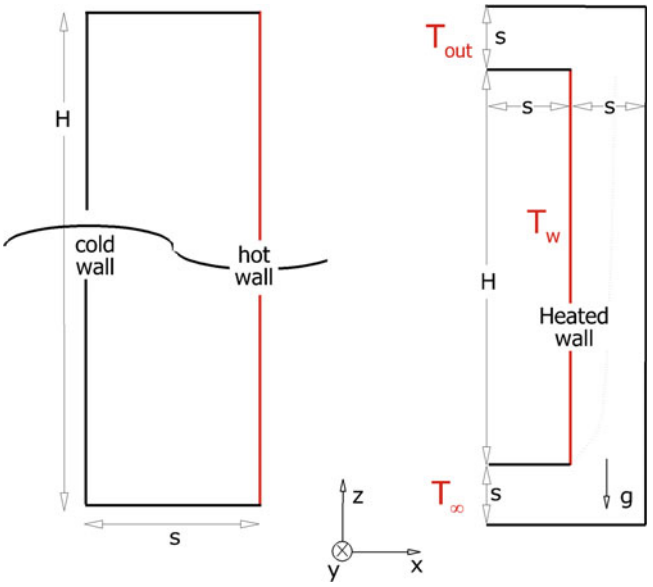

Fig. 1 (*Left*) geometrical configuration for the validation in a differentially heated cavity [1], (*right*) ventilated facade geometry

while all other surfaces were considered as adiabatic. A quite satisfactory agreement with the experimental data was reached for the finer grids, as shown in Fig. 2. The same quality of agreement was also reached for the average values of the Nusselt numbers which were computed as $Nu = 5.84$ and $Nu = 7.50$, against $Nu_{exp} = 5.85$ and $Nu_{exp} = 7.50$ reported experimentally by Betts and Bokhari [1] for the lower and higher values of the two Ra numbers respectively.

For the C-type channel, the geometrical configuration and the computational domain considered are shown in Fig. 1. The numerical resolution used for each case assumed an equidistant grid within the boundary layers, according to the resolution requirements proposed by Shishkina et al. [6]. The corresponding numerical resolution requirements translate to approximately three to eleven nodes to resolve the thermal and velocity boundary layers for the range of Rayleigh numbers considered here. Neumann boundary conditions were applied at the lower vent and a convective outflow condition at the upper, outlet vent. The isothermal hot wall was maintained at a temperature T_w, while all other surfaces were assumed to be adiabatic. Periodic boundary conditions were used along y direction. Based on preliminary simulations, the width of the wall was set to $0.3–0.6H$. Three different aspect ratios H/s were examined: $H/s = 15.3$, 20.8 and 34.67. A subset of the computed results is presented in Table 1.

Figure 3 presents a typical instantaneous (a, b) and time-averaged (c) flow field generated inside the C-type cavity. In accordance with the experimental observations, the flow becomes turbulent at $\approx$ 20–30% from the lower vent, forming several

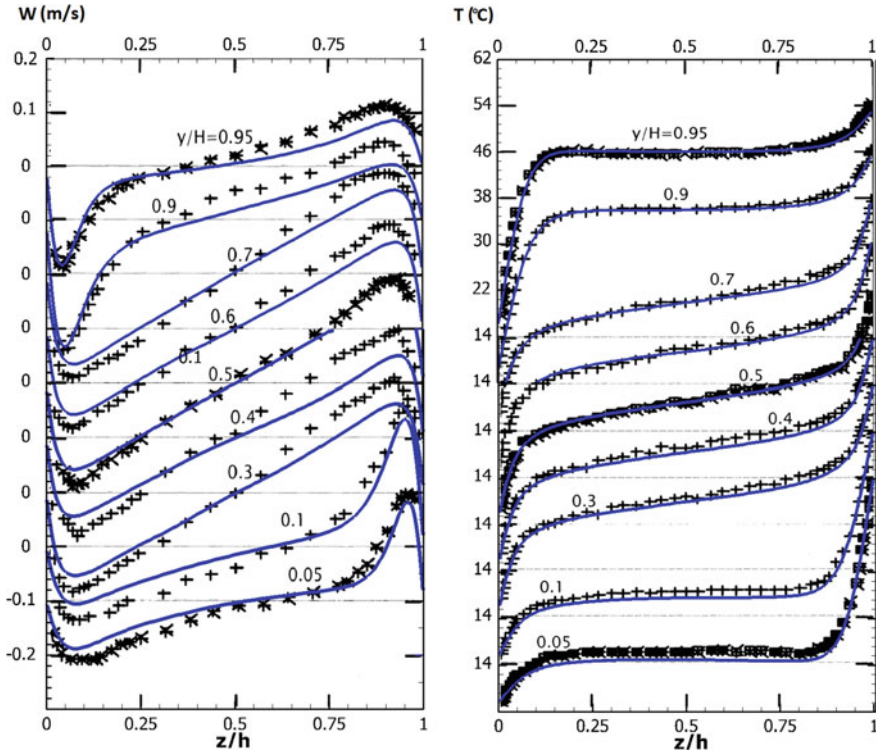

Fig. 2 Comparison against experimental data (symbols) for the flow in a differentially heated cavity [1] at $Ra_{\Delta T} = 1.43 \times 10^6$ using $1536 \times 192 \times 192$ cells. (*Left*) velocity profiles across the cavity, (*right*) temperature in the cavity

Table 1 Subset of computational cases considered and summary of computed results for the flow inside the facade, for various gas-gap spacings s (Fig. 1). Values inside parentheses correspond to the experimental work of La Pica et al. [4]. Reynolds numbers are defined based on the bulk flow velocity u_b and the channel width s, as $Re = \frac{u_b s}{\nu}$. The wall-averaged mean Nusselt numbers $< Nu >$ are defined here as $< Nu >= \frac{<h>H}{k_f}$ where k_f is the thermal conductivity of air and $< h >$ the mean heat transfer convection coefficient

Case	s/H	$Ra_{\Delta T} \div 10^{-10}$	Re_{LES} (Re_{exp})	$< Nu >_{LES}$ ($< Nu >_{exp}$)
A1	0.0288	1.68	1180 (1280)	291 (432)
A2	0.0288	3.00	1513 (1650)	404 (520)
A3	0.0288	5.14	2050 (2030)	568 (588)
A4	0.0288	7.49	2112 (2210)	433 (611)
B1	0.0481	1.68	2960 –	650 –
C1	0.0654	1.68	2161 –	510 –

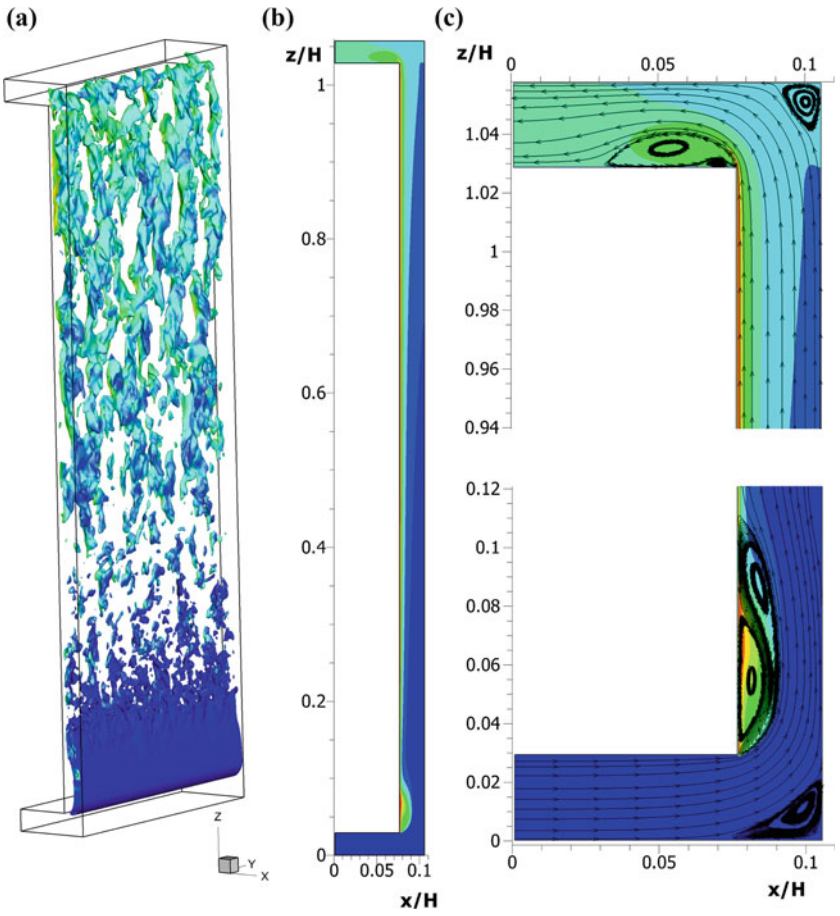

Fig. 3 Computed LES results at $Ra_{\Delta T} = 1.68 \times 10^{10}$ using a numerical grid of $144 \times 192 \times 648$ cells. **a** iso-surfaces of instantaneous vertical velocity $w = 0.32$, **b** mean temperature in the cavity, **c** mean streamlines at the outlet and the inlet vent

recirculating regions -primary and secondary- within the cavity. Their size was found to increase with s/H as shown in Fig. 4. The optimum value of Nusselt number was also found to significantly depend on the gas gap ratio s/H. Based on the simulations conducted, the ratio s/H for optimum convective heat transfer was found to reduce with Ra number.

The computed values of the bulk velocity and the generated Reynolds numbers were -always slightly lower but- found in general in a very good agreement with the reference experimental data. On the other hand, Nusselt numbers were significantly underestimated by $\approx$20–40%. This was partially due to lower outlet velocities predicted by the LES simulations, in a systematic manner. The main reason for this discrepancy is the imposition of isothermal conditions instead of isoflux conditions at the experiments of La Pica et al. [4], which will be the subject of future work.

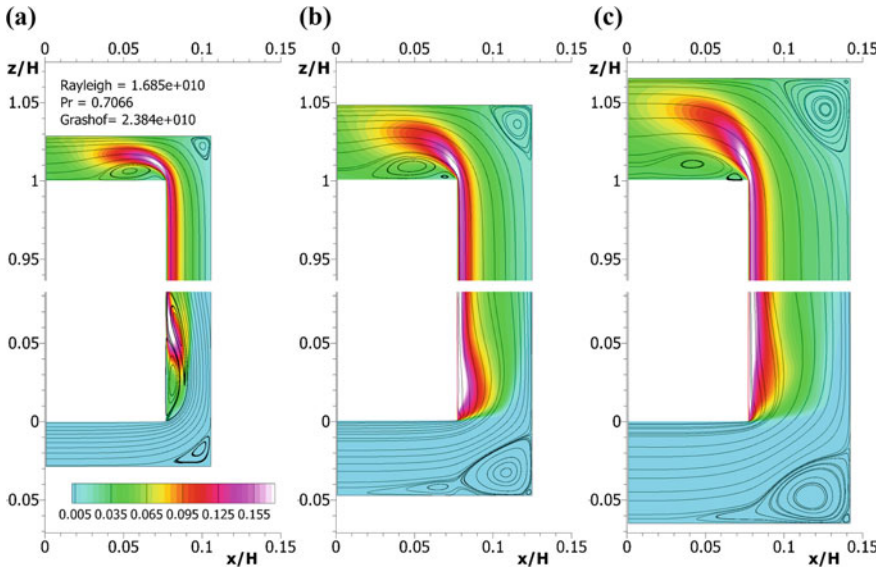

Fig. 4 Effect of wall spacing on the generated flow-field in the cavity for $Ra_{\Delta T,s} = 1.68 \times 10^{10}$. **a** case A1, $s/H = 0.0654$ **b** case B1, $s/H = 0.0654$, **c** case C1, $s/H = 0.0654$. *Colors* correspond to time averaged fluctuations of temperature

References

1. Betts, P.L., Bokhari, I.H.: Experiments on turbulent natural convection in an enclosed tall cavity. Int. J. Heat Fluid Flow **21**, 675–683 (2000)
2. Grigoriadis, D.G.E., Kassinos, S.C., Votyakov, E.V.: Immersed boundary method for the MHD flows of liquid metal. J. Comput. Phys. **228**(3), 903–920 (2009)
3. Kaloudis, E., Grigoriadis, D.G.E., Papanicolaou, E., Panidis, T.: Large eddy simulations of turbulent mixed convection in the charging of a rectangular thermal storage tank. Int. J. Heat Fluid Flow **44**, 776–791 (2013)
4. La Pica, A., Rodono, G., Volpes, R.: An experimental investigation on natural convection of air in a vertical channel. Int. J. Heat Mass Transf. **36**(3), 611–616 (1993)
5. Puangsombuta, W., Hirunlabha, J., Khedarib, J., Zeghmatic, B., Win, M.M.: Enhancement of natural ventilation rate and attic heat gain reduction of roof solar collector using radiant barrier. J. Fluid Mech. **42**(6), 2218–2226 (2007)
6. Shishkina, O., Stevens, R.J.A.M., Grossmann, S., Lohse, D.: Boundary layer structure in turbulent thermal convection and its consequences for the required numerical resolution. New J. Phys. **12**(7), 075022 (2010)
7. Zamora, B., Kaiser, A.S.: Thermal and dynamic optimization of the convective flow in Trombe Wall shaped channels by numerical investigation. Heat Mass Transf. **45**, 1393–1407 (2009)
8. Zamora, B., Kaiser, A.S.: 3D effects in numerical simulations of convective flows in cubical open cavities. Int. J. Therm. Sci. **77**, 172–185 (2014)

Velocity Profiles over Hypothetical Urban Areas in Unstable Stratification: Large-Eddy Simulation Approach

Chun-Ho Liu and Man-Chung Chan

1 Introduction

Atmospheric surface layer (ASL) is characterized by its relatively uniform fluxes with height z in which the dimensionless velocity gradient ϕ_m is expressed as

$$\frac{\kappa z}{u_\tau}\frac{\mathrm{d}\,\langle\overline{u}\rangle}{\mathrm{d}z} = \phi_m \tag{1}$$

where $\kappa\,(=0.4)$ is the von Kármán constant, u_τ the surface friction velocity and u the wind speed [1]. In this paper, over bars $\overline{\bullet}$ and angular brackets $\langle\bullet\rangle$ represent resolved scales and ensemble averages, respectively, of the large-eddy simulation (LES) data in the horizontally homogeneous domain. In isothermal conditions, $\phi_m = 1$, resulting in the logarithmic law of the wall in engineering application [2]. On the other hand, in thermal stratification, ϕ_m is a function of local thermal stability parameter $\zeta\ (=z/L)$, where $L\ (=u_\tau^2\Theta/(\kappa g\theta_\tau))$ is the Obukhov stability length, Θ the average/reference temperature, g the gravitational acceleration, $\theta_\tau\ (=\langle w''\theta''\rangle/u_\tau)$ the surface friction temperature and double prime $\bullet''$ the deviation from LES ensemble average, that leads to the well-received Monin–Obukhov similarity theory (MOST) [3]. MOST has been tested extensively using field observational data over flat, open terrain with small-scale surface roughness only [4–6]. However, studies over urban areas with roughness elements of appreciable length scales are rather limited. This study is thus conceived, using LES, to examine the applicability of MOST to hypothetical urban areas in (unstable) thermal stratification when the size of roughness elements is no longer negligible compared with the ASL thickness.

C.-H. Liu (✉) · M.-C. Chan
Department of Mechanical Engineering, 7/F Haking Wong Building,
The University of Hong Kong, Pokfulam Road, Pokfulam, Hong Kong
e-mail: liuchunho@graduate.hku.hk

M.-C. Chan
e-mail: stoneagechung@gmail.com

D.G.E. Grigoriadis et al. (eds.), *Direct and Large-Eddy Simulation X*,
ERCOFTAC Series 24, https://doi.org/10.1007/978-3-319-63212-4_65

2 Methodology

Incompressible flows are assumed in this paper. Boussinesq approximation is used to handle the buoyant flows. A box filter is employed in the LES so the resolved-scale continuity, momentum equation and thermal energy conservation are solved for the flows and temperature. The subgrid-scale (SGS) fluxes of momentum and temperature are modeled by the Smagorinsky SGS model [7]. The SGS turbulent kinetic energy (TKE) conservation is calculated by the one-equation SGS model [8].

The spatial domain ($24h$ long $\times$ $5h$ wide $\times$ H ($= 8h$) high) consists of 12 identical square ribs of size h at the bottom to simulate the dynamics over an array of hypothetical urban roughness elements (Fig. 1). The ribs, spanning the full spanwise extent, are placed at equal distance b ($= h$) apart in the streamwise direction so the aspect ratio is $h/b = 1$ and the blockage is $h/H = 0.125$. The Reynolds number based on the domain height H and the surface friction velocity u_τ is $\mathrm{Re}_\tau = 4{,}700$.

The prevailing flows are driven by a background pressure gradient normal to the ribs. Cyclic boundary conditions (BCs) are assigned to the horizontal domain extent, simulating an infinitely large array of roughness elements. Open-channel flows ($\partial\overline{u}/\partial z = \partial\overline{v}/\partial z = \overline{w} = 0$) and a constant temperature ($\overline{\theta} = \Theta - \Delta\Theta/2$) are applied at the domain top. No-slip BCs ($\overline{u} = \overline{v} = \overline{w} = 0$) and a (higher) constant temperature ($\overline{\theta} = \Theta + \Delta\Theta/2$) are applied at the bottom solid boundaries. Here, u, v and w are the velocity components in the streamwise x, spanwise y, and vertical z directions, respectively, and the (vertical) temperature difference is $\Delta\Theta$. Apart from neutral stratification ($L = -\infty$), 7 unstable scenarios ($L := -41.403h$; $-17.253h$; $-7.363h$; $-2.955h$; $-1.699h$; $-1.141h$ and $-0.840h$) are considered in the LES.

The three-dimensional (3D) spatial domain is discretized into structured mesh of 4.5 million brick elements. Each street canyon is partitioned into $16 \times 80 \times 16$ cells in the x, y and z direction, respectively. The grids are stretched away from the solid boundaries in which the stretching ratios are 2 and 3 in the street canyons and in the ASL above the roughness elements, respectively. The time increment is

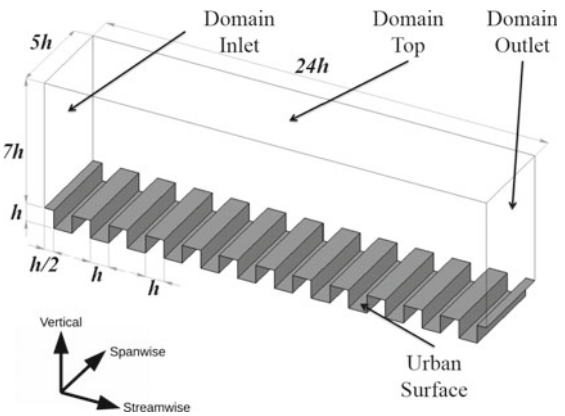

Fig. 1 Computational domain and boundary conditions adopted in the current LES

$\Delta t = 0.0012h/u_\tau$ in the temporal domain. All the scenarios are initiated by uniform flows $\overline{u} = 17u_\tau$ in isothermal conditions $\overline{\theta} = \Theta$ based on a coarse mesh (halved the spatio-temporal resolution mentioned above) for a period of $240\,h/u_\tau$. Afterward, the LES is switched to the aforementioned (fine) resolution and run for another period of $60h/u_\tau$ in which 1,000 instantaneous snapshots are archived for data analysis.

The open-source computational fluid dynamics (CFD) code OpenFOAM 2.1.0 [9] is used in this paper in which the finite volume method (FVM) is used to discretize the mathematical models. The implicit 2nd-order-accurate backward differencing is used in the time integration. The gradient, divergence, and Laplacian terms in the spatial domain are calculated by the 2nd-order-accurate Gaussian finite volume integration. The pressure-implicit with splitting of operators (PISO) pressure-velocity coupling scheme is used in the pressure correction. The pre-conditioned conjugate gradient (PCG) method is used to solve the (symmetric) system of linear equations of pressure while the pre-conditioned bi-conjugate gradient (PBiCG) method is used to solve for velocity, SGS TKE, and temperature.

3 Results and Discussion

Figure 2 depicts the dimensionless velocity gradient ϕ_m calculated by the current LES dataset as functions of the local thermal stability parameters ζ. The data in the ASL collapse onto a single curve regardless of the (unstable) thermal stratification, signifying that the current LES findings are consistent with those of MOST. Unlike the conventional ones [10], the newly proposed functional form of ϕ_m is divided into two regimes. The best-fit LES-calculated dimensionless velocity gradient is

$$\phi_m(\zeta) = \begin{cases} \phi_{m,\text{linear}} = 1 + 5.5\zeta & \text{slightly unstable} \quad \zeta_m < \zeta < 0 \\ \phi_{m,\text{power}} = 0.27\,(-\zeta)^{-1/3} & \text{moderately unstable} \quad -1 < \zeta \leq \zeta_m \end{cases} \tag{2}$$

with transition $\zeta_m = -0.05$, dividing the slightly and moderately unstable regimes.

The dimensionless velocity gradient approaches unity $\phi_m = 1$ asymptotically in neutrally stratified limit ($L \to -\infty$ or $\zeta \to 0$). In both slightly and moderately unstable stratification, the LES-calculated ϕ_m is smaller than that calculated by the existing empirical formulae $\phi_m = 0.613\,(-\zeta)^{-1/5}$ [4], $\phi_m = 1 + 4.5\zeta$ [5] and $\phi_m = (1 - 19\zeta)^{-1/4}$ [6] based on field measurements. The more slowly increasing velocity gradient and the more uniform ASL velocity profile in the current LES are likely the results of the enhanced turbulent transport induced by both the explicitly resolved roughness elements on the surface and the buoyancy-generated turbulence.

Integration of Eq. (1) using ϕ_m Eq. (2) yields the ASL velocity profiles

$$\frac{\langle \overline{u} \rangle}{u_\tau} = \frac{1}{\kappa}\left[\int_{\zeta_0}^{\zeta} \frac{1}{\zeta}\,\mathrm{d}\zeta - \int_{\zeta_0}^{\zeta} \frac{1-\phi_m(\zeta)}{\zeta}\,\mathrm{d}\zeta\right] = \frac{1}{\kappa}\left[\ln\left(\frac{\zeta}{\zeta_0}\right) - \Psi(\zeta, \zeta_0)\right] \tag{3}$$

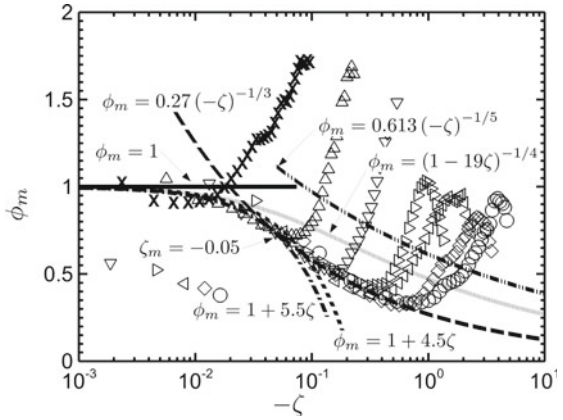

Fig. 2 ϕ_m plotted against ζ at different $L := -41.403$ ($\times$); -17.253 ($\triangle$); -7.363 (∇); -2.955 ($\triangleright$); -1.699 ($\triangleleft$); -1.141 ($\diamond$); and -0.840 ($\circ$). Also shown are the analytical solutions $\phi_m = 1$ at $L = -\infty$ (——); $\phi_m = 0.613\,(-\zeta)^{-1/5}$ ($- \cdot \cdot - \cdot \cdot -$) [4]; $\phi_m = 1 + 4.5\zeta$ ($-\ -\ -$) [5]; $\phi_m = (1-19\zeta)^{-1/4}$ ($\cdot\cdot\cdot\cdot\cdot\cdot$) [6]; and Eq. (2) for slightly unstable $\phi_m = 1 + 5.5\zeta$ ($- \cdot - \cdot -$); and for moderately unstable $\phi_m = 0.27\,(-\zeta)^{-1/3}$ (—— —— ——) stratification

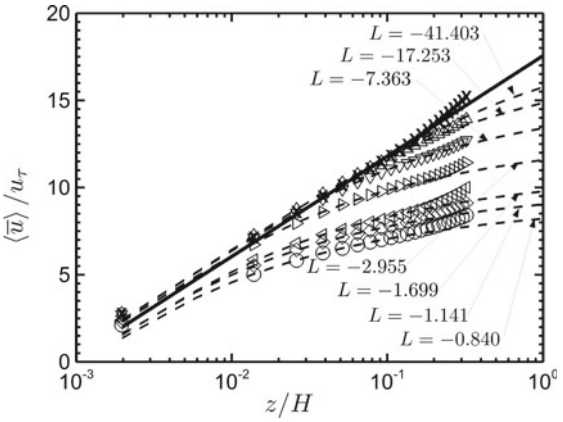

Fig. 3 Dimensionless velocity profile $\langle \overline{u} \rangle / u_\tau$ plotted against dimensionless height z/H at different unstable thermal stratification $L := -41.403$ ($\times$); -17.253 ($\triangle$); -7.363 (∇); -2.955 ($\triangleright$); -1.699 ($\triangleleft$); -1.141 ($\diamond$); and -0.840 ($\circ$). Also shown are the analytical solution in the corresponding thermal stratification Eq. (3) ($- - - - - -$) and the theoretical logarithmic law of the wall in neutral stratification $\langle \overline{u} \rangle / u_\tau = 1/\kappa \times \ln(z/z_0)$ (——)

in different thermal stratification which are compared well with the current LES-calculated results for $z \leq 0.15H$ (Fig. 3). The behavior of Eq. (3) is similar to that of the well-known log-linear wind law [11] in which a more uniform velocity is developed because of enhanced convective transport in unstable stratification.

It is noteworthy that the 1st term on the right-hand side (RHS) of Eq. (3) resumes the logarithmic law of the wall approaching neutrally stratified limit ($L \to -\infty$,

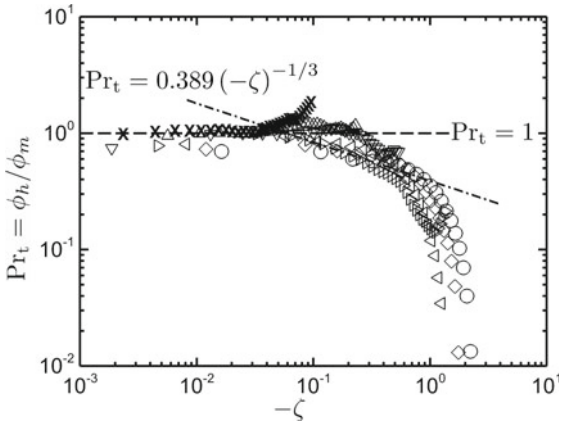

Fig. 4 Turbulent Prandtl number $\mathrm{Pr_t}$ (ratio of temperature gradient to velocity gradient ϕ_h/ϕ_m) plotted against local thermal stability parameters ζ at different unstable thermal stratification $L :=$ -41.403 ($\times$); -17.253 ($\triangle$); -7.363 (∇); -2.955 ($\triangleright$); -1.699 ($\triangleleft$); -1.141 ($\diamond$); and -0.840 ($\circ$). Also shown are the analytical solution Eq. (5) $\mathrm{Pr_t} = 1$ ($- - - - - -$) and $\mathrm{Pr_t} = 0.389\,(-\zeta)^{-1/3}$ ($- \cdot - \cdot -$)

$\zeta \to 0$ or $\zeta_0 \to 0$; where $\zeta_0 = z_0/L$ and z_0 is the roughness length scale) because $\phi_m \to 1$. Likewise, Eq. (3) approaches the behavior in neutrally stratified limit in the vicinity to surface roughness because the 2nd term on RHS of Eq. (3), which handles the buoyant flows, tends to vanish for $\zeta \to \zeta_0$ also.

Not shown here is the derivation of the functional form of dimensional temperature gradient ϕ_h, which is indeed analogous to its ϕ_m counterpart, as follows

$$\phi_h(\zeta) = \begin{cases} \phi_{h,\mathrm{linear}} = 1 + 5.5\zeta & \text{slightly unstable} \quad \zeta_m < \zeta < 0 \\ \phi_{h,\mathrm{power}} = 0.105\,(-\zeta)^{-2/3} & \text{moderately unstable} \quad -1 < \zeta \le \zeta_m \end{cases} \tag{4}$$

that is helpful to characterize another 2 commonly used dimensionless parameters.

Turbulent Prandtl number $\mathrm{Pr_t}$ is the ratio of the eddy diffusivities of momentum to heat that is equal to ϕ_h/ϕ_m after some algebraic manipulation. Hence,

$$\mathrm{Pr_t}(\zeta) = \frac{\phi_h}{\phi_m} = \begin{cases} \mathrm{Pr_{t,linear}} = 1 & \text{slightly unstable} \quad \zeta_m < \zeta < 0 \\ \mathrm{Pr_{t,power}} = 0.389\,(-\zeta)^{-1/3} & \text{moderately unstable} \quad -1 < \zeta \le \zeta_m \end{cases} \tag{5}$$

that is compared well to the current LES (Fig. 4). It is about 1 in the slightly unstable stratification so is in line with the classic Reynolds analogy.

The gradient Richardson number, which measures thermal stratification, is

$$\mathrm{Ri} = \frac{g}{\langle\overline{\theta}\rangle} \frac{\mathrm{d}\langle\overline{\theta}\rangle/\mathrm{d}z}{(\mathrm{d}\langle\overline{u}\rangle/\mathrm{d}z)^2} = \frac{\phi_h}{\phi_m^2}\zeta\ . \tag{6}$$

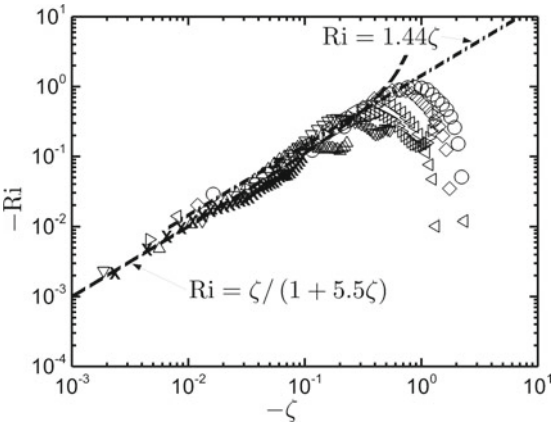

Fig. 5 Gradient Richardson number Ri plotted against local thermal stability parameter ζ in different unstable thermal stratification $L := -41.403$ ($\times$); -17.253 ($\triangle$); -7.363 (∇); -2.955 ($\triangleright$); -1.699 ($\triangleleft$); -1.141 ($\diamond$); and -0.840 ($\circ$). Also shown are the analytical solution Eq. (7) $\mathrm{Ri} = \zeta/(1 + 5.5\zeta)$ ($- - - - -$) and $\mathrm{Ri} = 1.44\zeta$ ($- \cdot - \cdot -$)

Substituting the functional forms Eqs. (2) and (4) into (6) yields

$$\mathrm{Ri}(\zeta) = \begin{cases} \mathrm{Ri}_{\mathrm{linear}} = \zeta/(1 + 5.5\zeta) & \text{slightly unstable} \quad \zeta_m < \zeta < 0 \\ \mathrm{Ri}_{\mathrm{power}} = 1.44\zeta & \text{moderately unstable} \quad -1 < \zeta \leq \zeta_m \end{cases} \tag{7}$$

that agrees with the current LES as well (Fig. 5).

4 Conclusion

A series of LES is performed to study the functionality of MOST for the dynamics over an array of explicitly resolved roughness elements. The current LES results are consistent with those available in literature that suggest the new functional forms of dimensionless velocity/temperature gradient in the MOST framework. The velocity profile obtained exhibits a behavior similar to that of the log-linear wind law. $\mathrm{Pr_t}$ and Ri are derived theoretically that agree well with the current LES data. Additional work is undertaken to elucidate the coherent structure in thermal stratification.

Acknowledgements This research is conducted using the HKU Information Technology Services research computing facilities that are supported in part by the Hong Kong UGC Special Equipment Grant (SEG HKU09). This project is partly supported by the RGC GRF HKU 714913E.

References

1. Garratt, J.R.: The Atmospheric Boundary Layer. Cambridge University Press, Cambridge (1992)
2. Schlichting, H.: Boundary-Layer Theory. Springer, Berlin (2000)

3. Obukhov, A.M.: Turbulence in an atmosphere with a non-uniform temperature. Bound. Layer Meteorol. **2**, 7–29 (1971)
4. Swinbank, W.C.: A comparison between prediction of the dimensional analysis for the constant-flux layer and observations in unstable conditions. Q. J. R. Meteorol. Soc. **94**, 460–467 (1968)
5. Webb, E.K.: Profile relationships: the log-linear range, and extension to strong stability. Q. J. R. Meteorol. Soc. **96**, 67–90 (1970)
6. Högström, U.: Non-dimensional wind and temperature profiles in the atmospheric surface layer: a re-evaluation. Bound. Layer Meteorol. **42**, 55–78 (1988)
7. Smagorinsky, J.: General circulation experiments with the primitive equations I: the basic experiment. Mon. Weather Rev. **91**, 99–165 (1963)
8. Schumann, U.: Subgrid scale model for finite difference simulations of turbulent flows in plane channels and annuli. J. Comput. Phys. **18**, 376–404 (1975)
9. OpenFOAM.: The Open Source CFD Toolbox. http://openfoam.com (2015). Accessed 12 June 2015
10. Foken, T.: 50 years of the Monin-Obukhov similarity theory. Bound. Layer Meteorol. **119**, 431–447 (2006)
11. Monin, A.S., Yaglom, A.M.: Statistical Fluid Mechanics: Mechanics of Turbulence, vol. 1. Dover Publications Inc., Mineola (1971)

Buoyancy Effects on Turbulent Heat Transfer Behind a Backward-Facing Step in Liquid Metal Flow

M. Niemann and Jochen Fröhlich

1 Introduction

Heat transfer is one the most important technical applications in fluid mechanics. Heat transfer behind sudden changes of the cross section such as a backward-facing step flow is particularly important in many devices such as the in- and outflow of thermal storage containers, collectors of power conversion systems, as well as highly heat loaded surfaces like those in concentrated solar power (CSP) plants, to name but a few examples.

With common transport media such as water or air having Prandtl numbers of order unity or above large thermal gradients are usually required to realize given heat fluxes. Low Prandtl number fluids like liquid metals feature much larger thermal conductivities and, hence, allow smaller temperature gradients to realize the same heat flux. This is especially interesting for the receivers of CSP plants where extremely large heat fluxes occur. The low Prandtl number leads to a scale separation between the thermal and viscous boundary layers and in turbulent flow to a separation of the turbulent scales of temperature and velocity field.

In technical applications the heat flux usually is chosen so that the maximum allowed temperature difference is exploited. These temperature differences generate buoyancy effects which have an additional impact on heat transfer. Particularly interesting is the mixed buoyancy regime between forced and natural convection where externally applied flow and internally generated buoyancy effects interact. However, information in this respect is still scarce for liquid metals. In this contribution heat transfer behind a backward-facing step is investigated for a buoyancy-affected flow of liquid sodium. Several cases for buoyancy impact are compared to the purely

M. Niemann (✉) · J. Fröhlich
Institute for Fluid Mechanics, Technische Universität Dresden, Dresden, Germany
e-mail: Martin.Niemann@tu-dresden.de

J. Fröhlich
e-mail: Jochen.Froehlich@tu-dresden.de

D.G.E. Grigoriadis et al. (eds.), *Direct and Large-Eddy Simulation X*,
ERCOFTAC Series 24, https://doi.org/10.1007/978-3-319-63212-4_66

forced convection case as reference. The present study is a continuation of the work presented in [3, 4] at lower Reynolds number.

2 Mathematical Model

The non-dimensional Navier-Stokes equations for an incompressible fluid with heat transfer in the mixed convection regime read [2]

$$\frac{\partial u_i}{\partial x_i} = 0 \tag{1}$$

$$\frac{\partial u_i}{\partial t} + u_j \frac{\partial u_i}{\partial x_j} = -\frac{\partial p}{\partial x_i} + \frac{1}{Re} \frac{\partial^2 u_i}{\partial {x_j}^2} + Ri\theta g_i^* \tag{2}$$

$$\frac{\partial \theta}{\partial t} + u_j \frac{\partial \theta}{\partial x_j} = \frac{1}{RePr} \frac{\partial^2 \theta}{\partial {x_j}^2}, \tag{3}$$

where u_i is the velocity component in coordinate direction x_i, p the pressure, and $\theta = (T - T_0)/(T_\mathrm{w} - T_0)$ the non-dimensional temperature. Re, Pr, and Ri denote the Reynolds, the Prandtl, and the Richardson number, respectively, while g_i^* is the unit vector in direction of gravity. In the above equations, buoyancy is considered by applying the Boussinesq approximation: effects due to density variations are neglected in all terms except for the buoyancy force term $Ri\theta g_i^*$. The Richardson number can be calculated from the Grashof and the Reynolds number as $Ri = Gr/Re^2 = g\beta h \Delta T / U_\mathrm{b}^2$. The equations are solved by a finite volume method of second order on a staggered grid with a second-order predictor-corrector approach in time [1].

3 Computational Setup

The configuration is a backward-facing step flow as depicted in Fig. 1 with an expansion ratio of $E = H/(H - h) = 2$. The Reynolds number in all simulations is $Re = U_\mathrm{b} h/\nu = 10,000$. The Prandtl number is chosen as that of liquid sodium at $T = 150\,^\circ\mathrm{C}$, which is $Pr = 0.0088$. The domain length is $L/h = 30$ behind the step with additional $L_\mathrm{in}/h = 2$ in front of the expansion. Height and width are $H/h = 2$ and $W/h = 4$, respectively.

The domain is periodic in the spanwise z-direction. At the walls a no-slip condition is applied. It is supplemented with an adiabatic condition except at the wall behind the step. Here, a constant temperature gradient is applied over the extent $L_\mathrm{q}/h = 20$ behind the step. Further downstream, the boundary condition is switched to an adiabatic wall for the remaining part. The prescribed temperature derivative corresponds to a heat flux of $\dot{q} = 38\,\mathrm{kw/m^2}$. The inlet condition for the velocity is generated

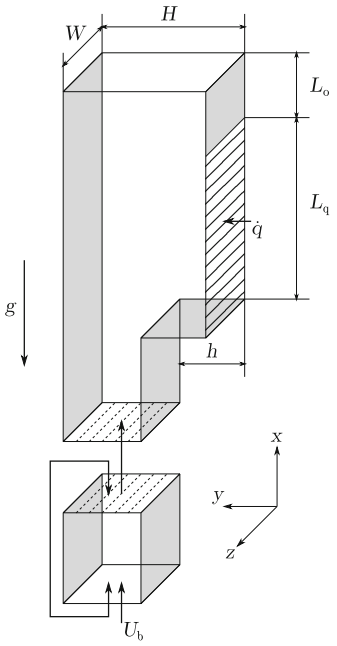

Fig. 1 Configuration investigated with nomenclature as used in the text

Table 1 Runs, grid, and averaging time

Ri	N_x	N_y	N_z	N_{tot}	$t_{aver}U_b/h$
0	1955	448	480	$420 \cdot 10^6$	102
0.12	1955	476	480	$447 \cdot 10^6$	72
0.2	2175	476	480	$497 \cdot 10^6$	55

by a separate channel flow simulation, Fig. 1. For the temperature, the inlet value is $\theta_{in} = 0$. The outlet is modeled by a convective outflow condition for both, velocity and temperature.

This configuration is investigated for several values of the buoyancy parameter in the regime of mixed convection, namely a case at the transition from forced to mixed convection, $Ri = 0.12$, and a case with more pronounced buoyancy impact, $Ri = 0.2$. As a reference, the corresponding forced convection case with $Ri = 0$ is used.

The grid employed is cartesian with points clustered towards the walls in such a way that the viscous sub-layer is resolved. Further information concerning the grid is provided in Table 1. The time step was adjusted to yield $CFL = 0.6$.

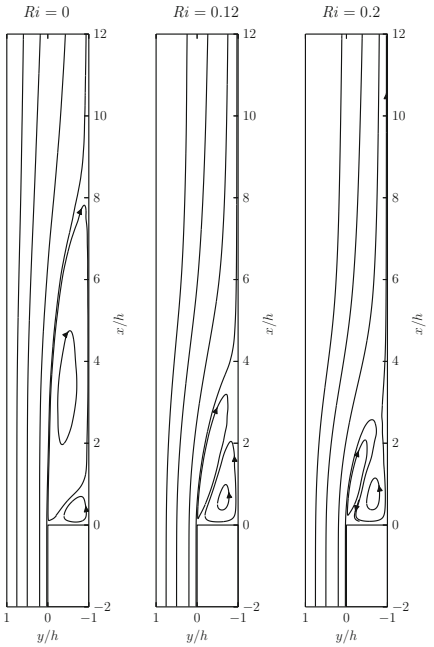

Fig. 2 Streamlines of average velocity obtained for the cases under investigation

4 Results and Discussion

Due to buoyancy forces, warm fluid at the heated wall is accelerated in vertical direction. The streamlines of average velocity in Fig. 2 illustrate the impact of this effect on the recirculation zone. Here, the corner eddy grows to the detriment of the main recirculation vortex as buoyancy acts against the backward flow in the recirculation zone. Since warm fluid at the wall is accelerated, a wall jet develops as is clearly visible in the profiles of streamwise velocity $\langle u \rangle$ depicted in Fig. 3. The strength of this wall jet in terms of the maximum velocity increases with increasing Ri. For reasons of mass conservation, fluid from the opposite part of the domain is hence drawn towards the wall and entrained into the developing wall jet. This is also obvious from the velocity profiles in Fig. 3.

Profiles of turbulent kinetic energy (TKE) $\langle k \rangle = \frac{1}{2} \left\langle u_i' u_i' \right\rangle$ are depicted in Fig. 3 (right). In the forced convection case, TKE is primarily located in the shear layer between the forward flow and the recirculation zone. For increased $Ri > 0$, a different situation is found due to the shorter recirculation zone and the increasing inclination of the shear layer towards the wall, as palpable at $x/h = 3$ and $x/h = 6$. Overall, a decrease of TKE is notable. As a consequence of increased shear at the heated wall, a small peak in the region of the attached wall jet emerges, visible at $x/h = 12$ and $x/h = 15$. Due to the entrainment of the wall jet, substantial shear develops near the left wall at $x/h = 6$ and beyond generating a second peak between $0.5 > y/h > 0$. This peak is not present in the profiles for $Ri = 0$.

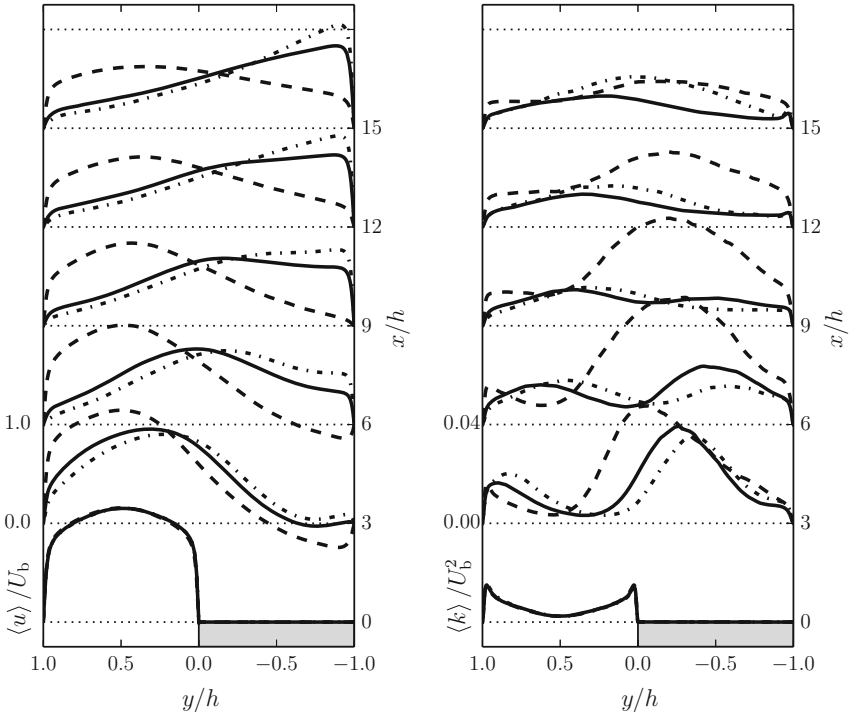

Fig. 3 Profiles of average streamwise velocity $\langle u \rangle / U_\mathrm{b}$ (*left*) and turbulent kinetic energy $\langle k \rangle / U_\mathrm{b}^2$ (*right*). - - : $Ri = 0$; — : $Ri = 0.12$; - · - : $Ri = 0.2$

Profiles of the mean temperature $\langle \theta \rangle$ are depicted in Fig. 4 (left). For $Ri = 0$ the mean temperature reaches very large values behind the step due to the reduced heat transfer in the recirculation zone. Recirculation transports hot fluid into the separating shear layer which is visible up to $x/h = 6$ and results in an overall higher level of $\langle \theta \rangle$ than for $Ri > 0$. In the latter cases the temperature field is altered according to the modified flow field and heat transfer changes substantially. The thickness of the temperature boundary layer is reduced for increasing Richardson number. Figure 5 (left) shows that the wall temperature θ_w is reduced for increasing Ri. Furthermore, the location of maximum wall temperature is shifted downstream for the mixed convection cases compared to the case with $Ri = 0$. As a result, heat transfer is enhanced due to the buoyancy force. This is also supported by the Nusselt number which increases with Ri, as shown in Fig. 5 (right).

Temperature fluctuations are depicted in Fig. 4 (right). For $Ri = 0$, these are large directly behind the step, but occur mainly in the shear layer at $x/h = 3$. At $x/h = 6$ and further behind reattachment, fluctuations increase with x due to turbulent convective transport in the attached boundary layer. For the mixed convection cases considered, mean temperature fluctuations are almost identical. At the end of the shortened recirculation zone, buoyancy affects heat transfer substantially as can be

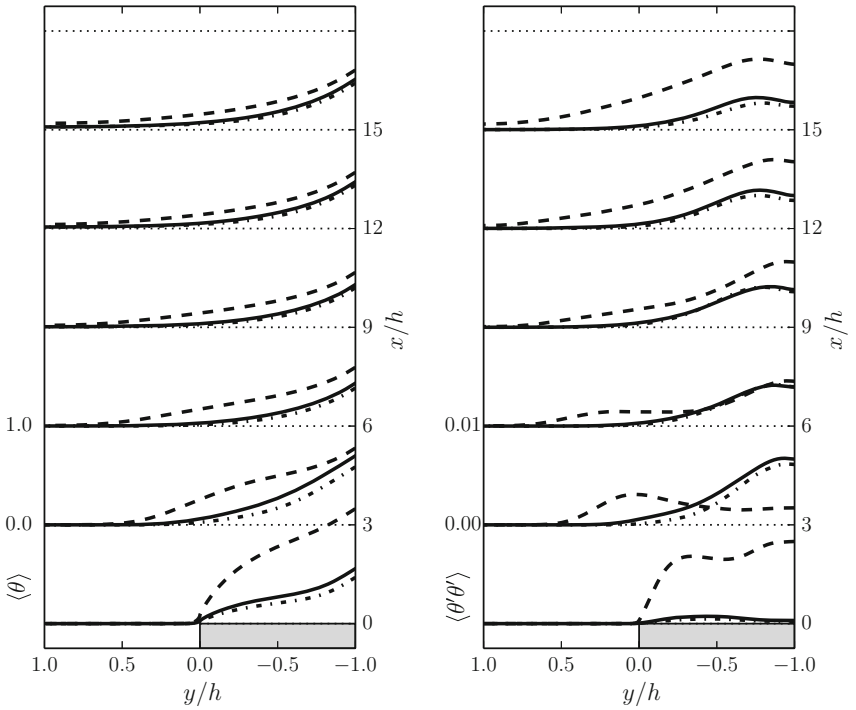

Fig. 4 Profiles of average non-dimensional temperature $\langle\theta\rangle$ (*left*) and temperature fluctuation $\langle\theta'\theta'\rangle$ (*right*). - - : $Ri = 0$; — : $Ri = 0.12$; - · - : $Ri = 0.2$

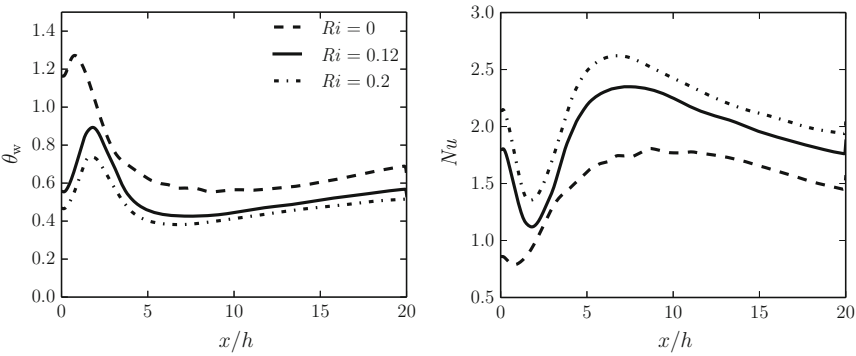

Fig. 5 Mean wall temperature θ_w (*left*) and Nusselt number *Nu* (*right*)

inferred from the profiles of temperature fluctuation at $x/h = 3$. Investigation of instantaneous results shows that, in the buoyancy-affected cases with $Ri = 0.12$ and $Ri = 0.2$, hot fluid rises in plume-like structures from the detached flow region producing large temperature and velocity fluctuations at this location.

Acknowledgements The present work is funded by the Helmholtz Society through project A1 of the Helmholtz Alliance LIMTECH. Computational time was provided by the Center for Information Services and High Performance Computing (ZIH) at TU Dresden.

References

1. Kempe, T., Fröhlich, J.: An improved immersed boundary method with direct forcing for the simulation of particle laden flows. J. Comp. Phys. **231**, 3663–3684 (2012)
2. Lin, J., Armaly, B., Chen, T.: Mixed convection in buoyancy-assisting, vertical backward-facing step flows. Int. J. Heat Mass Transf. **33**, 2121–2132 (1990)
3. Niemann, M., Fröhlich, J.: Direct numerical simulation of turbulent heat transfer behind a backward-facing step at low prandtl number. Proc. Appl. Math. Mech. **14**, 659–660 (2014)
4. Niemann, M., Fröhlich, J.: Heat transfer in a buoyancy-affected vertical liquid metal flow over a step. In: Fröhlich, J., Vogeler, K., Odenbach, S. (eds.) Strömungstechnische Tagung 2014, Schriftenreihe aus dem Institut für Strömunsmechanik, 10, 231–238. TUDpress, Dresden (2014)

Heat Transfer in Droplet-Laden Turbulent Channel Flow with Phase Transition in the Presence of a Thin Film of Water

A. Bukhvostova, J.G.M. Kuerten and Bernard J. Geurts

1 Introduction

In the field of multiphase systems droplet-laden channel flow presents a challenging topic not only because of how turbulent flow influences the mass and heat transfer properties of droplets but also how droplets modulate the flow. In this contribution we focus on droplet-laden turbulent channel flow with phase transition generalizing earlier work by [1, 2] and introducing gravity in the wall-normal direction which acts both on the flow and on the droplets. Gravity leads to a mean motion of droplets towards the bottom wall where they accumulate and form a film of water.

We introduce a thin film of water at the bottom wall and account for droplets which fall into the film. In this paper we keep the film height constant by draining water from the film at the bottom wall and keep the surface of the film stationary. The total mass of water is kept constant by continuously adding droplets at the top wall.

We investigate the case for the flow conditions considered in [1] using 1 million droplets initially distributed randomly in the channel. We consider statistically averaged heat and mass transfer properties of the droplets and gas, obtained by averaging over all droplets present in the channel and over the periodic directions, respectively. The computational setting is similar to a simple heat exchanger widely used in industry. The better understanding of heat transfer enhancement for liquids and gases made it possible to incorporate different types of heat exchangers into gas

A. Bukhvostova (✉) · J.G.M. Kuerten (✉) · B. J. Geurts
Faculty EEMCS, University of Twente, Enschede, The Netherlands
e-mail: a.bukhvostova@utwente.nl

J.G.M. Kuerten
Department of Mechanical Engineering, Eindhoven University of Technology, Eindhoven, The Netherlands
e-mail: j.g.m.kuerten@tue.nl

B. J. Geurts
e-mail: b.j.geurts@utwente.nl

D.G.E. Grigoriadis et al. (eds.), *Direct and Large-Eddy Simulation X*,
ERCOFTAC Series 24, https://doi.org/10.1007/978-3-319-63212-4_67

turbines to improve their efficiency [3]. In our situation the heat exchange between the channel walls at a given temperature difference between the walls is an important property to study.

2 Mathematical Model

We consider a water-air system in a channel, bounded by two parallel horizontal plates. In particular, a two-phase system, consisting of a carrier phase of dry air and water vapor and a dispersed phase of liquid water droplets next to a continuous water film will be investigated. The mixture of air and water vapor will be referred to as the carrier gas or gas and the liquid droplets as the dispersed phase. We use an Eulerian approach for the gas and track every droplet individually in a Lagrangian manner. In addition, we treat the carrier gas as compressible. The computational domain has a size of $x_l = 4\pi H$ in the streamwise direction, which is denoted by x, and $z_l = 2\pi H$ in the spanwise direction, z, where H is half the channel height. In addition, y is the coordinate in the wall-normal direction. The top wall of the channel is located at $y = H$ and the bottom wall at $y = -H$. A thin film of water of a fixed thickness h is maintained at the bottom wall, such that $h \ll H$. The temperatures at the top and bottom walls of the channel are denoted by T_t and T_b, respectively, and kept fixed such that $T_t < T_b$.

We consider the carrier phase to be a Newtonian fluid, whose behavior is described by the continuity equation, Navier-Stokes equation, energy conservation equation and vapor mass conservation equation. Droplets are described in a Lagrangian manner by a set of ordinary differential equations for the position, mass, velocity and temperature of each droplet. All details of the model can be found in [1]. The presence of gravity leads to some small changes in the equations of motion for the two phases and to an additional contribution to the energy from the potential energy. Two-way coupling between the two phases is implemented via momentum, energy and mass source terms in the governing equations of the carrier phase by requiring conservation of mass, momentum, energy and water mass [1].

2.1 Simplified Model for the Film

Formally, the thin film at the bottom channel wall requires the solution of a partial differential equation for its temperature as a function of time and the spatial coordinates. Along with the film temperature T_f we also consider the film energy per unit area E_s since for the carrier gas we solve the system of equations for the conservative variables and for the film we also choose a conservative variable.

The film is assumed to be sufficiently thin so that derivatives of its temperature parallel to the film are small compared to derivatives in the wall-normal direction such that they can be neglected. At the same time when droplets merge with the film, they bring locally diffusive and convective fluxes in the periodic directions parallel to the walls, which can not be neglected. The film is assumed not to move, consequently, the convective flux is not taken into account. These assumptions and simplifications permit to write the change in the film energy per unit area as:

$$\frac{\partial E_s}{\partial t}(x, z) = q_2 - q_1 + s_2 - s_1 \tag{1}$$

where q_1 and q_2 represent the fluxes in the wall-normal direction at the bottom wall $y = -H$ and at the film interface $y = -H + h$, respectively. The terms q_1 and q_2 reflect the thermal conduction. The thickness of the film can change because of two reasons: (1) the film evaporates or water vapor condenses on the film and (2) droplets fall and merge with the film because of gravity. These two contributions compose the source term s_2 at the interface of the film with the carrier gas.

In order to maintain a constant film thickness we extract or add water at the bottom of the film. This defines the source term s_1 in (1).

In order to maintain on average a constant mass of water in the channel we distribute new droplets at the top wall according to the following procedure. The diameter of the inserted droplets is taken equal to the initial diameter d_0 and the corresponding mass of one droplet is denoted by m_0. Each stage of a time step we determine the mass of droplets that should be inserted to keep the total mass of water in the system constant. This mass will in general not correspond to an integer number of droplets of mass m_0. Therefore, we insert the nearest integer just below this value and keep the remainder for the next stage. In this way, on average the total mass of water is kept constant. The droplets are inserted at random locations at the top wall at the temperature of the top wall T_t. The stream- and spanwise velocity components of these droplets are equal to zero and the wall-normal component is equal to the terminal velocity of the droplet.

The film temperature T_f enters into the proposed model, for example, into the conductive fluxes q_1 and q_2. That is why we also need to determine the film temperature. Since the film height is very small compared to the height of the channel, instead of discretizing the film, we approximate the film temperature by a second-order polynomial in the wall-normal coordinate, closely following [4]. The coefficients in this polynomial are found from the boundary condition at the bottom channel wall, continuity of flux at the film interface and the relation between the film temperature and its known energy per unit area.

3 Numerical Details and Initial Condition

The spatial discretization of the equations in the gas is based on a finite volume method which follows the approach in [1]. The geometry is divided into rectangular cells. A uniform grid is used in the two periodic directions. In the wall-normal direction a non-uniform grid is applied which is finer near the walls in order to resolve the boundary layers. We apply the same non-uniform grid in the wall-normal direction as in [1] but the height of the first cell is smaller since it starts from the film interface $y = -H + h$. The film thickness is taken equal to 1/3 of the height of the first cell. The variables are stored in the centers of the cells. We use 128 cells in each direction.

We use the time integration procedure proposed by [5]. It is a hybrid implicit-explicit time iteration method. For the nonlinear terms each stage is analogous to forward Euler or second-order Adams-Bashforth but with different coefficients while for the linear part the method is similar to the Crank-Nicolson scheme but again with different coefficients. The coefficients are derived from the condition of highest possible order of the algorithm. In the present work we only use the explicit part of the algorithm and this guarantees the third-order accuracy of the scheme.

We start the simulations from turbulent velocity, density and temperature fields obtained from a simulation without droplets and with adiabatic boundary conditions at the walls [1]. This simulation was performed until a statistically steady state was reached. In the present study we keep the wall temperatures constant. We keep the temperature difference between the walls equal to 3K choosing $T_b = 293.15$K and $T_t = 290.15$K. This temperature difference is the same as in the steady state in the reference case in [1]. The reference scales of the system define the non-dimensional parameters, such as the Reynolds number based on the bulk velocity $\mathrm{Re_b}$, the Mach number Ma, the Prandtl number Pr and the Schmidt number Sc, along with the thermodynamic parameters of the simulations. We choose the same reference scales as in the reference case in [1]. Initially, we take the film temperature uniform and equal everywhere to T_b.

We randomly distribute droplets over the volume of the channel. We define a reference case in which the initial number of droplets is equal to 1,000,000 and the initial diameter d_0 is 3.09×10^{-3} in non-dimensional units.

4 Results

We focus on the heat and mass transfer results of the gas and droplets. We consider the evolution of mean quantities which are averaged over the periodic directions. The averaging is denoted by brackets, $\langle \cdot \rangle$. All quantities are presented in dimensional units. In all figures where results at different times are shown, the arrow denotes the direction of time.

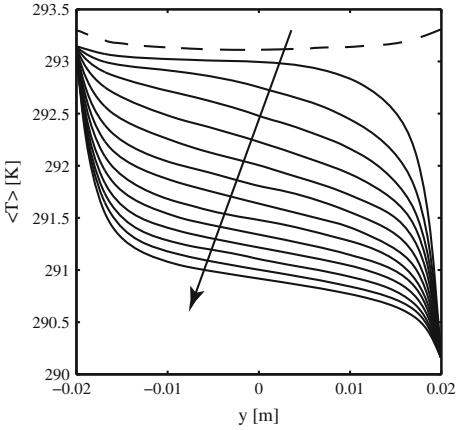

Fig. 1 Mean gas temperature as a function of the wall-normal coordinate plotted every 0.2 s in the interval [0 s, 3 s]. The dashed line corresponds to $t = 0$

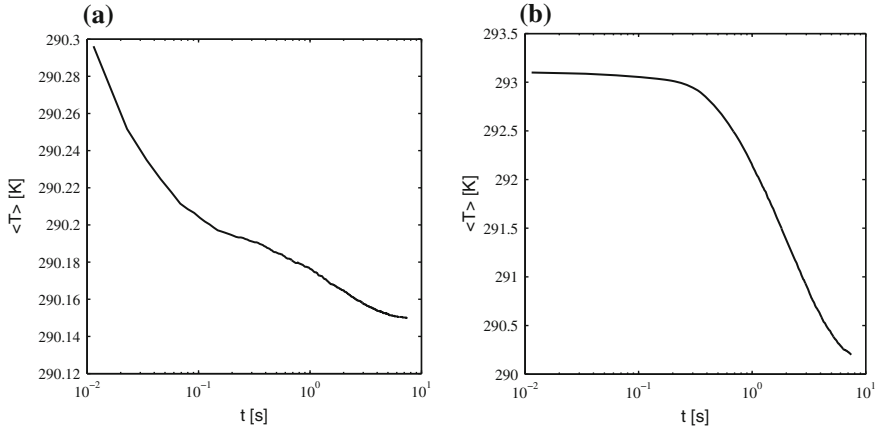

Fig. 2 History of mean gas temperature **a** near the *top* wall and **b** in the *center* of the channel

In Fig. 1 we show the development in time of the mean gas temperature as a function of the wall-normal coordinate. We start from a statistically steady turbulent solution with adiabatic boundary conditions and at $t = 0$ suddenly impose fixed temperatures at both walls, in which the temperature at the top wall is lower than at the bottom wall. This causes the development and propagation of a thermal front from the colder top wall of the channel to the warmer bottom wall. We consider separately the history of the mean gas temperature near the top wall and in the center of the channel, Fig. 2. This figure shows that indeed the temperature near the top wall starts decreasing almost immediately, while it takes some time before the temperature in the center of the channel decreases. The mean gas temperature near the top wall

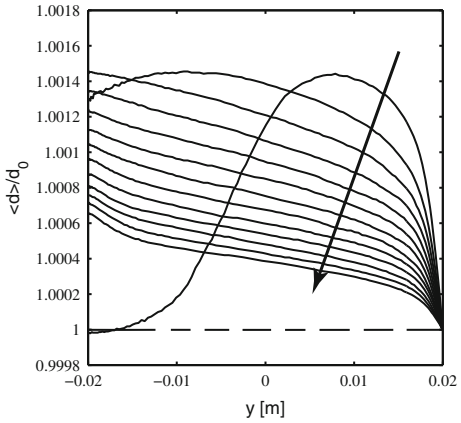

Fig. 3 Mean droplet diameter as a function of the wall-normal coordinate plotted every 0.2 s in the interval [0 s, 3 s]. The *dashed line* indicates the result at $t = 0$

initially decreases significantly because of the imposed lower temperature at the top wall, Fig. 2a, which leads to oversaturation of the gas.

As characteristic for the droplet behavior we consider the evolution of the mean droplet diameter normalized by the initial diameter as a function of the wall-normal coordinate in Fig. 3. A noticeable feature is the presence of a hump in this profile which moves and eventually disappears. It appears because of the intensive initial condensation of water vapor onto the droplet surface which is the result of two mechanisms: first, the positive difference between the gas temperature at the droplet location and the droplet temperature and second, the high relative humidity. Droplets fall towards the bottom wall under the action of gravity and the hump moves with them. The hump disappears in time since the mean droplet growth rate decreases later in time because of the decreasing over-saturation.

5 Conclusions

In this contribution we presented results on a study of turbulent droplet-laden channel flow with phase transition in the presence of gravity in the wall-normal direction and a thin film of water at the bottom wall. We maintain a constant film thickness by draining water from the bottom wall to compensate for (a) the droplets that fall onto the film and (b) evaporation/condensation at the film surface. We also maintain on average the total mass of water in the channel by inserting new droplets at the top wall to compensate for the water that has been drained from the bottom wall. We analyze the behavior of the averaged gas and droplet quantities focusing on the heat and mass transfer properties of the system.

Acknowledgements This work is supported through a PhD grant within the FOM DROP program FOM 08DROP02-2.

References

1. Bukhvostova, A., Russo, E., Kuerten, J.G.M., Geurts, B.J.: Comparison of DNS of compressible and incompressible turbulent droplet-laden heated channel flow with phase transition. Int. J. Multiph. Flow **63**, 68–81 (2014)
2. Russo, E., Kuerten, J.G.M., van der Geld, C.W.M., Geurts, B.J.: Water droplet condensation and evaporation in turbulent channel flow. J. Fluid Mech. **749**, 666–700 (2014)
3. McDonald, C.F., Van Hagan, T., Vepa, K.: Heat exchanger design considerations for gas turbine HTGR power plant. J. Eng. Gas Turbines Power **99**(2), 237–245 (2010)
4. Russo, E., Kuerten, J.G.M., Geurts, B.J.: Delay of biomass pyrolysis by gas-particle interaction. J. Anal. Appl. Pyrol. **110**, 88–99 (2014)
5. Spalart, P.R., Moser, R.D., Rogers, M.M.: Spectral methods for the Navier-Stokes equations with one infinite and two periodic directions. J. Comput. Phys. **96**, 297–324 (1991)

Numerical Predictions of Absolutely Unstable Round Hot Jet

A. Boguslawski, A. Tyliszczak and K. Wawrzak

1 Introduction

Absolute instability of round low-density jets was studied with spatio-temporal linear stability theory by Monkewitz and Sohn [10] and later by Jendoubi and Strykowski [5]. They showed, using Briggs [2] and Bers [1] criterion, that in parallel axi-symmetric low-density jet an absolutely unstable mode growing exponentially at the location of its generation can be triggered. The low density jet behavior predicted with the linear stability theory was confirmed in experimental studies on heated jets by Monkewitz et al. [9] and air-helium jets by Kyle and Sreenivasan [7] and Hallberg and Strykowski [6]. In both experiments strong periodic oscillations of the flow parameters were observed as a result of absolute instability. Self-sustained synchronized oscillations induced by a locally absolutely unstable region, observed experimentally, are called the global mode. Numerical simulations using Large Eddy Simulation (LES) or Direct Numerical Simulation (DNS) could shed a new light on the transition mechanism of globally unstable jets. However, there are surprisingly few numerical works on this flow type available in the literature so far. The LES predictions for variable-density jets were performed recently by Zhou et al. [17], Tyliszczak and Boguslawski [13], Wang et al. [16], Tyliszczak et al. [14]. Still, these LES results did not show clear presence of the absolutely/globally unstable mode which could be compared with the experimental results of Monkewitz et al. [9] and Kyle and Sreenivasan [7]. The DNS predictions of low density jets with a wide range of density ratio and shear layer thickness were recently performed by Lesshafft et al. [8] for the jet at $Re = 7500$. The LES predictions of global mode in round low-density jet at $Re = 7000$ were presented by Foysi et al. [3] for the density ratio S $= 0.14$ and the shear layer thickness $D/\theta = 27$ (D- nozzle diameter, θ - momen-

A. Boguslawski (✉) · A. Tyliszczak · K. Wawrzak
Czestochowa University of Technology, Institute of Thermal Machinery,
al. Armii Krajowej 21, 42-201 Czestochowa, Poland
e-mail: abogus@imc.pcz.pl
URL: http://imc.pcz.pl/pl

D.G.E. Grigoriadis et al. (eds.), *Direct and Large-Eddy Simulation X*,
ERCOFTAC Series 24, https://doi.org/10.1007/978-3-319-63212-4_68

tum thickness). They found excellent agreement with experimental data as far as the oscillations frequency is concerned. They also observed the strong vortex pairing and side jets phenomena confirming presence of global instability in the LES predictions. The present paper is aimed at LES predictions, similar to those presented by Foysi et al. [3], $Re = 7000$, but for a wider range of density ratio. The LES predictions are limited to two different shear layer thicknesses $D/\theta = 27$, as in the work of Foysi et al. [3] and $D/\theta = 40$.

2 Numerical Method

The flow solver used in this work is an academic high-order code based on the low Mach number approximation (SAILOR). For research purposes the SAILOR code includes a variety of sub-grid models used when the code is operated in Large Eddy simulation (LES) mode (Geurts [4]). In the present work we incorporate the sub-grid model as proposed by Vreman [15]. The solution algorithm is based on a projection method with time integration performed by a predictor-corrector (Adams-Bashforth/Adams-Moulton) method. The spatial discretization is based on 6th order compact differencing developed for half-staggered meshes (Tyliszczak [12]). Unlike in the fully staggered approach the velocity nodes are common for all three velocity components whereas the pressure nodes are moved half a grid size from the velocity nodes. This greatly facilitates implementation of the code and is computationally efficient as there is only a small amount of interpolation between the nodes. The inlet density profile is obtained from the Busemann–Crocco [11] relation. The temperature is computed from the equation of state with constant pressure. The inlet velocity profile is assumed as hyperbolic-tangent function. The computational domain is set to $12D \times 20D \times 12D$ which is found large enough to minimize possible errors caused by the numerical treatment of the boundary conditions. Preliminary study were performed in order to assess dependence of the results on the mesh density. It was found that the mesh with $128 \times 192 \times 128$ nodes stretched radially and axially towards the jet region gives nearly grid independent solutions.

3 LES Predictions of Absolutely Unstable Jet

Figure 1 shows the temporal spectrum of the axial velocity fluctuating component in the near jet field for the shear layer thickness characterized by $D/\theta = 27$ and three different density ratios. The density ratio $S = 0.8$ is above the critical one thus only the flow oscillations resulting from the Kelvin–Helmholtz spatial instability are expected. For two lower density ratios absolute instability should be triggered as the critical density ratio for the shear layer thickness considered is $S \approx 0.6$. Indeed, it can be seen from Fig. 1 that for the density ratio $S = 0.8$ some broadband oscillations in the frequency range $St_D = 0.4 - 0.5$ are visible at the distance $x/D = 5$ while

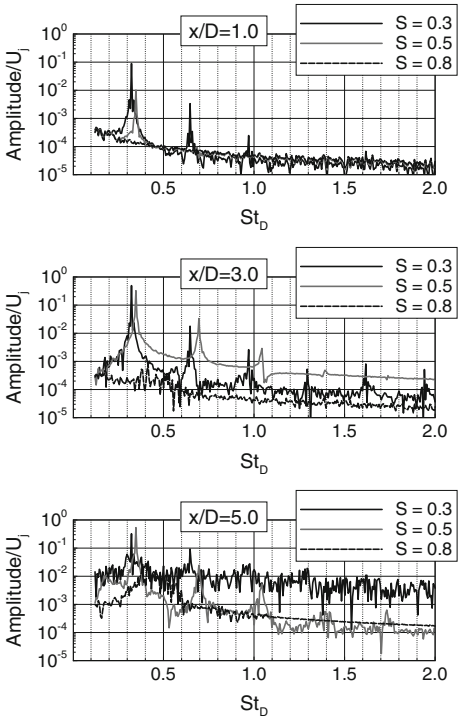

Fig. 1 Evolution of spectra of axial velocity fluctuations, $D/\theta = 27$

closer to the nozzle exit no periodic component is visible. By contrast for the lower density ratios $S = 0.5$ and 0.3 well defined periodic component characterized by the non-dimensional frequency $St_D \approx 0.35$ is present in the whole region $x/D = 1 - 5$. Figure 2 presents the global mode frequency predicted by the current LES compared with the DNS results of Lesschafft et al. [8], LES results of Foysi et al. [3] and the absolute mode frequency predicted by the linear stability theory. The frequency of the global mode predicted with the current LES agreed very well with the linear stability theory for the density ratio close to the critical value while for the lower density ratio it is overpredicted. This frequency is also higher compared to the results of Foysi et al. [3]. Absolute mode frequency is sensitive to the Mach number, as shown by Monkewitz and Sohn [10], and is decreasing with Mach number. In the present simulations the low Mach number expansion of the Navier-Stokes was used that means an incompressible flow is considered, while Foysi et al. [3] used a compressible solver. Unfortunately they do not deliver information on the Mach number in the flow analyzed. The present LES results coincide very well with the DNS calculations of Lesschafft et al. [8], though, their results correspond to slightly thinner shear layer characterized by $D/\theta = 30$. It should be stressed that the tendency of frequency change as a function of the density ratio predicted with LES is very similar to the results of Lesschafft et al. [8] and the linear stability theory.

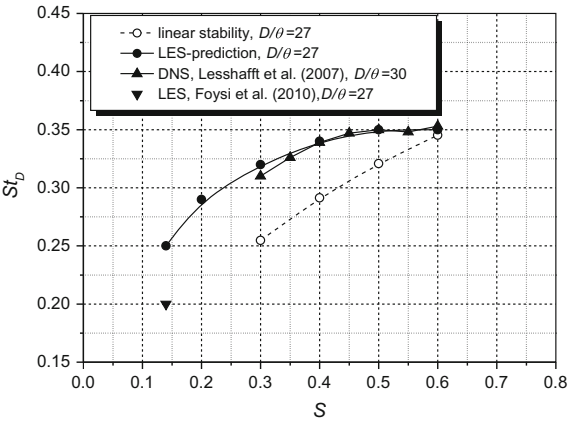

Fig. 2 Global frequency predicted with LES and DNS compared with absolute frequency from linear stability theory

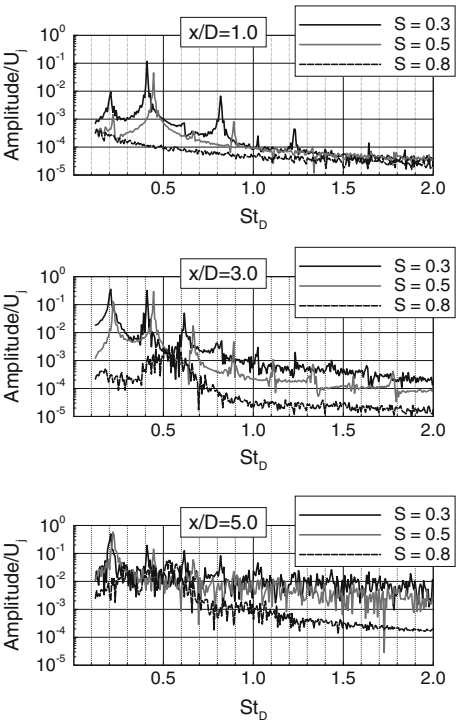

Fig. 3 Evolution of spectra of axial velocity fluctuations, $D/\theta = 40$

Figure 3 shows the spectra of the axial velocity fluctuating component in the near jet field for the shear layer thickness characterized by $D/\theta = 40$ and again for the three different density ratios. In this case the fundamental frequency of the global mode is slightly higher than in the previous case as the periodic oscillations are characterized by the Strouhal number $St_D \approx 0.4 - 0.45$. Moreover, in the case of

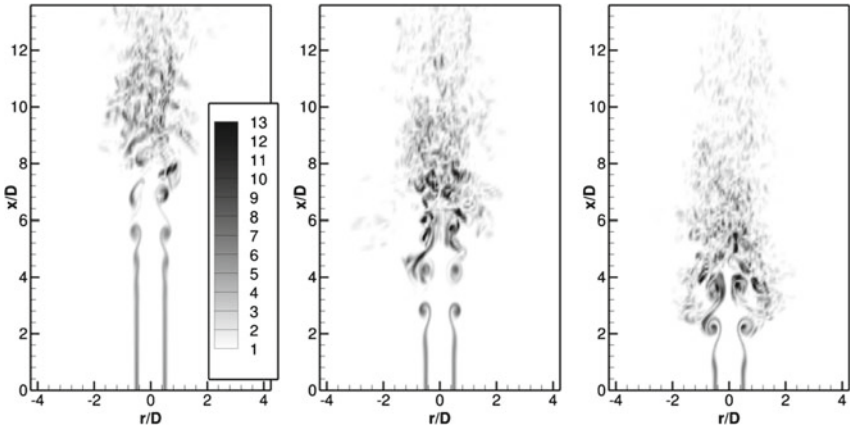

Fig. 4 Iso-contours of vorticity for various density ratios $S = 0.8$ (*left figure*) $S = 0.5$ (*middle figure*) $S = 0.2$ (*right figure*) and shear layer thickness $D/\theta = 27$

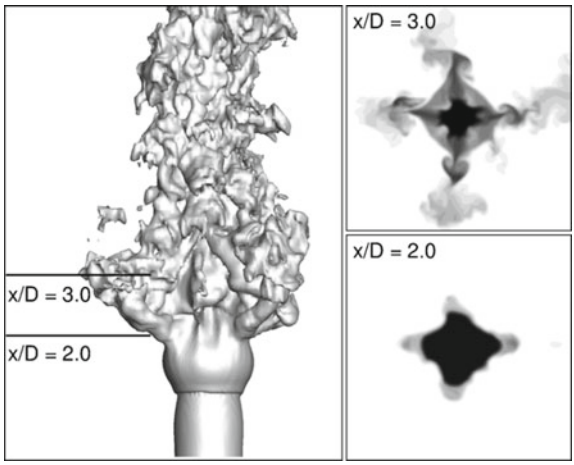

Fig. 5 Iso-surface of temperature with isotherms in two cross-section showing side-jets structure for $S = 0.2$, $D/\theta = 27$

thinner shear layer very well defined subharmonic of the fundamental frequency is observed that denotes the vortex pairing process reported also in the experimental results.

Figure 4 illustrates the flow structure in terms of vorticity iso-contours for three different density ratios $S = 0.8$, 0.5 and 0.2. For the density ratio $S = 0.8$ the jet is convectively unstable and vortices result from Kelvin–Helmholtz instability while for lower density ratios the jet is abolutely unstable with strong vortices formed closer to the nozzle exit. For the density ratio $S = 0.2$ the jet spreads rapidly at the distance $x/D \approx 4$.

It can be seen from Fig. 5 that the jet, for the density ratio $S = 0.2$ breaks up in the form of side jets, observed experimentally in hot [9] and air-helium jets [6]. Small thin jets are visible starting from $x/D = 2$ and they remain until the jet breaks-up. The mechanism of side jets formation is not fully understood so far and needs further studies.

4 Conclusions

The paper presents preliminary results of LES predictions of global mode in hot round free jet. The results show that the global oscillations were reproduced for a wide range of the density ratio below the critical value. The critical density ratio was predicted with reasonable agreement with the results of spatio-temporal linear stability theory. It was shown that the vortex pairing process to be triggered in globally unstable hot jet requires a sufficiently thin shear layer at the nozzle exit.

Acknowledgements The research project was supported by Polish National Science Centre, project no. DEC-2011/03/B/ST8/06401. This research was supported in part by PL-Grid Infrastructure.

References

1. Bers, A.: Linear Waves and Instabilities. Gordon and Breach, Physique des Plasmas (1975)
2. Briggs R.J. Electron-Stream Interaction with Plasmas. Research Monograph vol. 29, The MIT Press, 1964
3. Foysi, H., Mellado, J.P., Sarkar, S.: Large-eddy simulation of variable-density round and plane jets. Int. J. Heat Fluid Flow **31**, 307–314 (2010)
4. Geurts, B.J. Elements of Direct and Large-Eddy Simulation. Edwards Publishing, 2003
5. Jendoubi, S., Strykowski, P.: Absolute and convective instability of axisymmetric jets with external flow. Phys. Fluids **6**, 3000 (1994)
6. Hallberg, M.P., Strykowski, P.: J On the universality of global modes in low-density axisymmetric jets. J. Fluid Mech. **569**, 493–507 (2006)
7. Kyle, D.M., Sreenivasan, K.R.: The instability and breakdown of a round variable density jet. J. Fluid Mech. **249**, 619–664 (1993)
8. Lesshafft, L., Huerre, P., Sagaut, P.: Frequency selection in globally unstable round jets. Phys. Fluids **19**, 054108 (2007)
9. Monkewitz, P.A., Bechert, D.W., Barsikow, B., Lehmann, B.: Self-excited oscillations and mixing in a heated round jet. J. Fluid Mech. **213**, 611–639 (1990)
10. Monkewitz, P.A., Sohn, K.D.: Absolute instability in hot jets. AIAA J. **26**(8), 911–916 (1988)
11. Schlichting, H. Boundary Layer Theory. McGraw-Hill Book Company, 1979
12. Tyliszczak, A.: A high-order compact difference algorithm for half-staggered grids for laminar and turbulent incompressible flows. J. Comput. Phys. **276**, 438–467 (2014)
13. Tyliszczak, A., Boguslawski, A.: LES of variable density bifurcating jets. In: Iacarrino, G., Kassinos, S.C., Langer, C.A., Moin, P. (eds.) Complex Effects in Large Eddy Simulations, number 56 in Lecture Notes in computational science and engineering, pp. 273–288. Springer, Berlin (2007)

14. Tyliszczak A., Boguslawski A., Drobniak S. Quality of LES predictions of isothermal and hot round jet. In: Meyers, J., Geurts, B.J., Sagaut, P. (eds), Quality and Reliability of Large Eddy Simulations, vol. 12 of ERCOFTAC Series, pp. 259–270. Springer, Berlin (2008)
15. Vreman, A.W.: An eddy-viscosity subgrid-scale model for turbulent shear flow: algebraic theory and applications. Phys. Fluids **16**, 3670–3681 (2004)
16. Wang, P., Fröhlich, J., Michelassi, V., Rodi, W.: Large-eddy simulation of variable-density turbulent axisymmetric jets. Int. J. Heat Fluid Flow **29**, 654–664 (2008)
17. Zhou, X., Luo, K.H., Williams, J.J.R.: Study of density effects in turbulent buoyant Jets using large-eddy simulation. Theor. Comput. Fluid Dyn. **15**, 95–120 (2001)

Near Wall Structures in Turbulent Flows with Strong Thermo-Physical Property Variations

J.W.R. Peeters, R. Pecnik, B.J. Boersma, T.H.J.J. van der Hagen and M. Rohde

1 Introduction

In many industrial processes that involve heat transfer and turbulent flows, thermo-physical properties can vary significantly due to pressure and (or) temperature variations. This is especially the case for processes which utilize fluids at supercritical pressures, such as novel power cycles (for instance in innovative nuclear reactors) and refrigeration processes.

During a heating process, a fluid at supercritical pressure transitions from a fluid with liquid-like properties to a fluid with gas-like properties. During this transition, all thermo-physical properties vary significantly around the pseudo-critical temperature T_{pc}; the temperature at which the specific heat capacity c_p has a maximum at constant pressure (see Fig. 1).

The significant thermo-physical property variations of a supercritical fluid can have a profound effect on turbulence statistics, such as the Reynolds stresses and the turbulent heat flux, see for instance [1]. In addition, buoyancy in upward flows can cause laminarization [7]. In this paper, we will show results from Direct Numerical Simulations (DNS) of simultaneously heated and cooled turbulent supercritical fluids flowing upwards in an annular geometry at $Re_b = U_b D_h / \nu(T_{pc}) = 8000$. A schematic of the geometry is shown in Fig. 2.

J.W.R. Peeters (✉) · R. Pecnik (✉) · B.J. Boersma
Energy Technology, Delft University of Technology, Leeghwaterstraat 39,
2628 CB Delft, The Netherlands
e-mail: j.w.r.peeters@tudelft.nl

R. Pecnik
e-mail: r.pecnik@tudelft.nl

T.H.J.J. van der Hagen · M. Rohde
Nuclear Energy and Radiation Applications, Mekelweg 15,
2629 JB Delft, The Netherlands
e-mail: m.rohde@tudelft.nl

D.G.E. Grigoriadis et al. (eds.), *Direct and Large-Eddy Simulation X*,
ERCOFTAC Series 24, https://doi.org/10.1007/978-3-319-63212-4_69

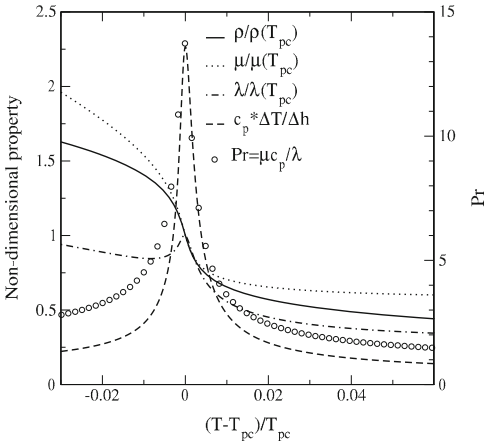

Fig. 1 Non-dimensionalized properties of carbon dioxide at 8 MPa as a function of non-dimensional temperature. $T_{pc} = 307.7$K, see [4] and [5]. The properties have been non-dimensionalized such that all properties vary around unity

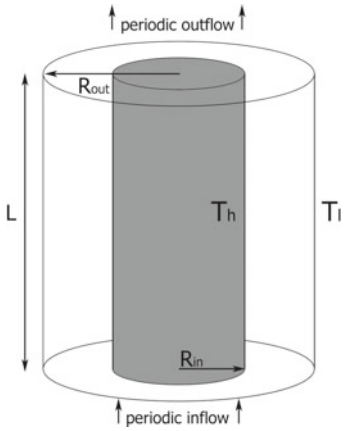

Fig. 2 The annular geometry of the simulations. The inner and outer wall radii (R_{in} & R_{out}), the length L and the inner and outer wall temperatures (T_h & T_l) are shown

In this paper, we observe and discuss the effect of variable thermo-physical properties on near wall structures, like velocity streaks and stream-wise vortices that play an important role in sustaining turbulence.

2 Numerical Details

The low Mach number Navier-Stokes equations are solved to simulate a simultaneously heated and cooled periodic annular flow. In the low Mach number limit of the Navier-Stokes equations the effect of acoustic waves is ignored. The pressure field is decomposed into a thermodynamic part and a hydrodynamic part. Because the hydrodynamic pressure fluctuations are much smaller than the thermodynamic pressure, all thermo-physical properties can be uniquely determined from the enthalpy and the thermodynamic pressure.

Table 1 Summary of direct numerical simulations considered at $Re_b = 8 \cdot 10^3$. In the mixed convection case, $Fr = U_b^2/g\,D_h = 10$. In all simulations, $\Delta y^+ < 1/\sqrt{Pr}$, where Pr is the local Prandtl number

Case	Properties	Flow condition	$N_r \times N_\theta \times N_z$
I	constant	forced	$192 \times 480 \times 512$
II	CO_2 at 8 MPa	forced	$256 \times 768 \times 768$
III	CO_2 at 8 MPa	mixed	$256 \times 768 \times 768$

A 6th order staggered compact finite difference scheme (see [2]) and pseudo-spectral methods are used to calculate the spatial derivatives in the Navier-Stokes equations, while the 2nd order explicit Adams-Bashford scheme is used for time integration.

Three different numerical cases are considered in this paper. A summary of the case specific details can be found in Table 1. In case I, all thermo-physical properties are constant, while in cases II and III, the properties correspond to that of CO_2 at 8 MPa. Upward mixed convection (the combination of both forced- and free convection) effects are considered only in case III. The inner wall of the annulus ($r = R_{in}$) is kept at a constant temperature of 323 K, while the outer wall ($r = R_{out}$) is kept at a lower temperature of 303 K. By simultaneously heating and cooling the fluid, a statistically fully developed turbulent flow can be realized. Note that in the DNS code, the enthalpy and the temperature have been non-dimensionalised such that $0 \leq h \leq 1$ and $0 \leq T \leq 1$, respectively. Therefore, $T_h = 1$ and $T_l = 0$. Similarly, the inner and outer wall wall enthalpies are $h_h = 1$ and $h_l = 0$. $T_{pc} = 0.24$.

3 Results

The inner and outer wall temperatures of the annular geometry have been chosen such that the pseudo-critical temperature (the temperature where the property variations with respect to changes in temperature are the greatest) lies close to the inner hot wall. As a consequence, the largest property variations are also found near the hot inner wall. The normalized root mean square values of the density and the dynamic viscosity fluctuations are shown in Fig. 3. The property fluctuations near the hot wall are slightly larger in the mixed convection case. This difference stems from the fact that the mean enthalpy gradient is steeper in the mixed convection case than in the forced convection case. Because there are large property fluctuations in the region near the hot inner wall, we expect that near wall structures in this region will appreciably be affected.

The variations in thermo-physical properties are found to have a clear effect on the streaks (defined as $\rho w'$) near the hot wall as is shown in Fig. 4. The streaks are smaller with respect to the streamwise direction both in the forced convection case and in the mixed convection case. Furthermore, the magnitude $|\rho w'|$ of the low speed streaks

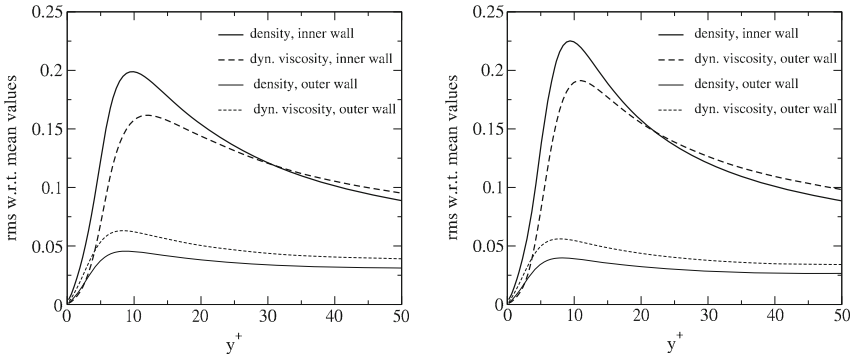

(a) forced convection case **(b)** mixed convection case

Fig. 3 Density and dynamic viscosity rms values w.r.t. to their corresponding ean values

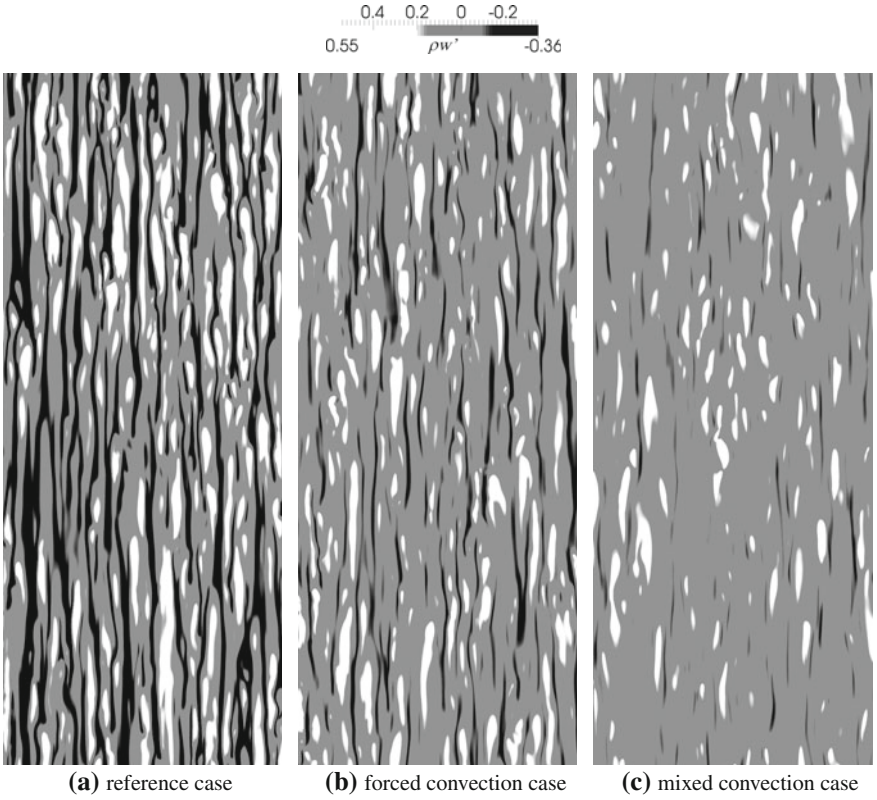

(a) reference case **(b)** forced convection case **(c)** mixed convection case

Fig. 4 Visuatization of streaks (defined as $\rho w'$) in the near hot-wall region ($y^+ = 10$) for all three cases. The legend is shown at the *top*. The direction of the flow is upwards

is reduced in the forced convection case when compared to the reference case. The magnitudes of both the high speed and the low speed streaks are reduced in the mixed convection case. These results show that density and dynamic viscosity fluctuations appreciably affect the streaks near the hot wall.

Near wall streaks are typically created through interactions between stream-wise vortices and mean shear. Such vortices advect low speed fluid away from the wall and advect high speed fluid towards it. Similarly, such vortices advect high temperature fluid away from a hot wall and cold temperature fluid towards it. Therefore, it can be expected that a low speed streak will have a high temperature, while a high speed streak will have a low temperature. By extracting data from low speed regions (in a manner that is similar to [6]) at different time instances, then superimposing the data and subsequently averaging it, average streak velocities and temperatures can be obtained. This is shown in Fig. 5. It is also shown that a low speed streak consists of low viscosity and low density fluid, whereas a high speed streak consists of high viscosity and high density fluid. We expect that the differences in thermo-physical properties between streaks affect the evolution of streaks.

As streaks are typically created by stream-wise vortices, it is also interesting to look at those structures. Contour plots of stream-wise vorticity are shown in Fig. 6. In the forced convection case, the stream-wise vorticity structures near the hot inner wall are less abundant compared to the reference case. There is not much difference in stream-wise vorticity between the forced convection and the mixed convection cases.

As was mentioned above, stream-wise vortices can create streaks, which in turn are unstable, thereby creating motions which may result in the formation of new stream-wise vortices. As such, streaks and vortices are connected to each other in a regenerating cycle [3, 6]. It is possible that the vorticity is modulated either because the streaks are modulated, or because they are directly affected by the thermo-physical property fluctuations or by both.

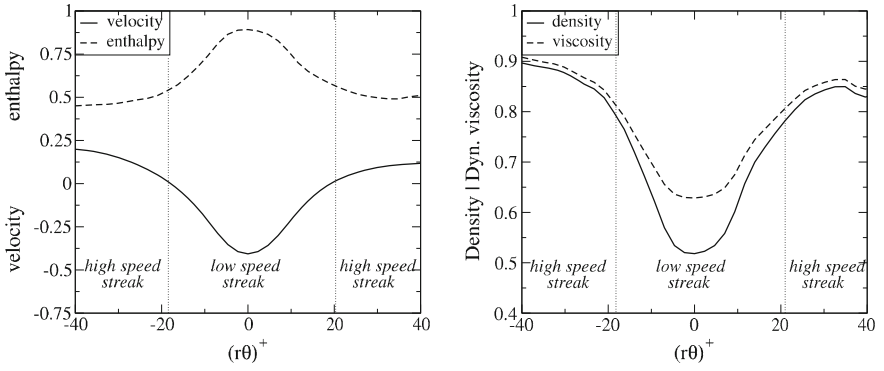

Fig. 5 Conditionally averaged temperature and momentum profiles (*left*) and density and dynamic viscosity profiles (*right*) across a low speed streak and high speed fluid at $y^+ = 10$ in the forced convection case

Fig. 6 Contour levels of streamwise vorticity in the reference case (*top part*), the forced convection case (*lower left part*) and the mixed convection case (*lower right part*). The contour levels are the same for al cases

4 Summary

Strong thermo-physical property variations in heated turbulent flows at supercritical pressure have been found to affect near wall structures such as streaks and streamwise vortices. The streak size near a hot wall is reduced due to variations in density and viscosity as is the magnitude of the streamwise momentum of the low speed streaks. However, it is clear that low speed streaks generally have a high temperature, while high speed regions have a low temperature near a hot wall, which results in low speed streaks having a lower dynamic viscosity and a lower density than the high speed regions. Furthermore, stream-wise vorticity is visibly reduced near a heated wall. Possible mechanisms that describe how variable thermo-physiscal properties physically affect near wall structures will be investigated in the future.

Acknowledgements This research is supported by the Dutch Technology Foundation STW, which is part of the Netherlands Organisation for Scientific Research (NWO), and which is partly funded by the Ministry of Economic Affairs. We also acknowledge PRACE for awarding us access to the Tier-1 supercomputing infrastructure (specifically the Anselm cluster, Ostrava, Czech Republic) through the Distributed European Computing Initiative (DECI-12)

References

1. Bae, J.H., Yoo, J.Y., Choi, H.: Direct numerical simulation of turbulent supercritical flows with heat transfer. Phys. Fluids **17**, 105104 (2005)
2. Boersma, B.J.: A 6th order staggered compact finite difference method for the incompressible Navier-Stokes and scalar transport equations. J. Comp. Phys. **230**, 4940–4954 (2011)
3. Jiménez, J., Pinelli, A.: The autonomous cycle of near-wall turbulence. J. Fluid Mech. **389**, 335–359 (1999)
4. Kunz, O., Klimeck, R., Wagner, W., Jaeschke, M.: The GERG-2004 Wide-Range Equation of State for Natural Gases and Other Mixtures, GERG Technical Monograph 15. VDI-Verlag, Düsseldorf, Fortschritt-Berichte VDI (2007)
5. NIST Standard Reference Database 23, Version 9.0
6. Schoppa, W., Hussain, F.: Coherent strucutre generation in near-wall turbulence. J. Fluid Mech. **453**, 57–108 (2002)
7. Yoo, J.Y.: The turbulent flows of supercritical fluids with heat transfer. Ann. Rev. Fl. Mech. **45**, 495–525 (2013)

The Effects of Thermal Boundary Condition on Flow at Supercritical Pressure

H. Nemati, A. Patel, B.J. Boersma and R. Pecnik

1 Introduction

Fluids at supercritical pressure undergo a continuous phase from a liquid to a gas state if the fluid is heated above the critical pressure. During this phase transition the thermophysical properties of the fluid vary significantly within a narrow temperature range across the pseudo-critical temperature T_{pc} (pseudo-critical temperature is defined as the temperature at which the specific heat at constant pressure (c_p) attains its peak value). Figure 1 shows the variation of thermophysical properties of CO_2 at a thermodynamic supercritical pressure $P_0 = 80$ bar ($P_{critical} = 73.773$ bar) as a function of temperature [1]. These characteristics make supercritical fluids appealing in many industrial applications, such as: desorption, drying and cleaning in extraction processes; pharmaceutical industry; in power cycles as working fluids [2, 3] and biodiesel production [4].

However, the strong property variations also lead to peculiar fluid dynamics that are difficult to model and to predict. For example, large density gradients in supercritical fluids can lead to strong heat transfer deterioration caused by buoyancy and large bulk flow accelerations. Heat transfer to supercritical fluids plays an important role in many of the above mentioned applications and turbulent heat transfer mechanisms have been studied in [5, 6]. In this work we aim to study the effect of thermal effusivity ratios on heat transfer to supercritical fluids. The effusivity ratio is defined

H. Nemati · A. Patel · B.J. Boersma · R. Pecnik (✉)
Delft University of Technology, Leeghwaterstraat 39, 2628 CB Delft, The Netherlands
e-mail: r.pecnik@tudelft.nl

H. Nemati
e-mail: h.nemati@tudelft.nl

A. Patel
e-mail: a.patel@tudelft.nl

B.J. Boersma
e-mail: b.j.boersma@tudelft.nl

D.G.E. Grigoriadis et al. (eds.), *Direct and Large-Eddy Simulation X*,
ERCOFTAC Series 24, https://doi.org/10.1007/978-3-319-63212-4_70

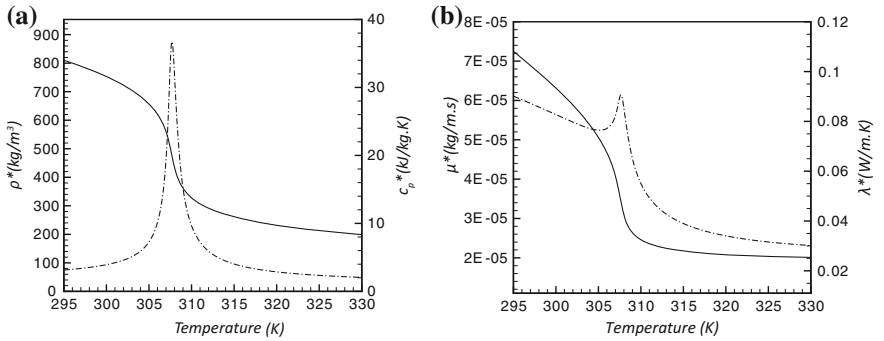

Fig. 1 **a** Density ρ^* (———) and isobaric heat capacity c_p^* (—·—). **b** Dynamic viscosity μ^* (———) and thermal conductivity λ^* (—·—)

as $K = \sqrt{\left(\rho c_p \lambda\right)_f / \left(\rho c_p \lambda\right)_s}$, where ρ, c_p and λ are the density, the isobaric heat capacity and the thermal conductivity for the fluid f and the solid wall s. In general, K defines whether thermal fluctuations at the fluid to solid interface are allowed or suppressed. Previous studies on heat transfer with different thermal effusivity ratios are mostly related to constant property fluids. Kasagi et al. [7] demonstrated that the near–wall thermal statistical quantities, including mean temperature, temperature fluctuations, turbulent heat flux are influenced by the thermal effusivity ratio K. It has also been pointed out that for $K \to \infty$ the wall boundary condition for the scalar can be approximated with an isoflux boundary condition, while in the limit of $K \to 0$ an isothermal boundary condition is appropriate. Later, Tiselj et al. [8] performed a fully developed turbulent DNS with conjugate heat transfer at a Reynolds number of Re_τ=150 and Prandtl numbers of $Pr = 0.7$–7, whereby they confirmed the results of Kasagi et al. [7]. Li et al. [9] investigated the evolution of a passive scalar with both isothermal and isoflux wall boundary conditions and different Prandtl numbers using direct numerical simulation (DNS). Their results showed that the mean temperature profiles and the stream–wise Stanton number distributions are independent of the boundary condition if the Prandtl is above unity.

In the present work we study the effects of different thermal effusivity ratios on heat transfer to supercritical fluids that encompass large variations of thermophysical properties. It is expected that these variations will have a large effect on turbulent heat transfer and skin friction distributions even if the Prandtl number is above unity. Using DNS of a turbulent pipe flow we apply different wall boundary conditions, corresponding to either $K = 0$ and $K = \infty$. The results show that there is a significant dependency on K for turbulent heat transfer rates to supercritical fluids.

2 Governing Equations and Numerical Method

In the present study the anelastic approximation of the Navier–Stokes equations in cylindrical coordinates is solved to simulate a flow in a pipe with CO_2 above its critical pressure. Final set of simplified mass, momentum and enthalpy equations [6], also called low Mach-number equations, are given here

$$\frac{\partial \rho}{\partial t} + \frac{\partial \rho u_i}{\partial x_i} = 0, \tag{1}$$

$$\frac{\partial \rho u_i}{\partial t} + \frac{\partial \rho u_i u_j}{\partial x_j} = -\frac{\partial p}{\partial x_i} + \frac{1}{Re_{\tau 0}} \frac{\partial \tau_{ij}}{\partial x_j}, \tag{2}$$

$$\frac{\partial \rho h}{\partial t} + \frac{\partial \rho u_i h}{\partial x_i} = -\frac{1}{Re_{\tau 0} Pr_0} \frac{\partial q_i}{\partial x_i}, \tag{3}$$

with the stress tensor $\tau_{ij} = \mu \left(\frac{\partial u_i}{\partial x_j} + \frac{\partial u_j}{\partial x_i} - \frac{2}{3} \frac{\partial u_k}{\partial x_k} \delta_{ij} \right)$, the Fourier law for the heat conduction $q_i = -\lambda \frac{\partial T}{\partial x_i} = -\frac{\lambda}{c_p} \frac{\partial h}{\partial x_i}$ and δ_{ij} the Kronecker delta. Symbols t, x_i, ρ, μ, λ, c_p, u_i, T, p, and h are the dimensionless time, coordinates, density, dynamic viscosity, thermal conductivity, isobaric heat capacity, velocity, temperature, hydrodynamic pressure, and enthalpy, respectively. The non-dimensional numbers are inlet Reynolds number $Re_{\tau 0} = 360$ based on the inlet friction velocity and the pipe diameter, and inlet Prandtl number $Pr_0 = 3.19$.

The governing equations are solved using a second order staggered scheme, with the velocity components located at the cell faces and pressure, enthalpy and thermophysical properties at the cell center. Spatial derivatives in circumferential direction for all diffusive terms are treated implicitly, while the other terms are discretized explicitly. The equations are integrated in time using the method developed by Najm et al. [10], with a second-order Crank-Nicolson scheme for the implicit terms and the Adams-Bashforth and Adams-Moulton scheme for all the explicit terms. A detailed description of numerical methodology, grid resolutions and validation cases are given in our previous publication [6].

The boundary conditions with different K values have been implemented as follows. First a simulation with constant wall heat flux $Q = 2.4$ ($K = \infty$) with the length of $L^* = 30D^*$ has been carried out, as depicted in Fig. 2. Then, the obtained averaged wall enthalpy $\overline{h}_w(Q = 2.4)$ of this simulation has been imposed on a successive simulation as a thermal wall boundary condition ($K = 0$). To verify this approach, the same procedure was also performed for the constant property simulations with a shorter pipe of length $L^* = 20D^*$ ($\mathrm{CP}_{K=\infty}$ and $\mathrm{CP}_{K=0}$).

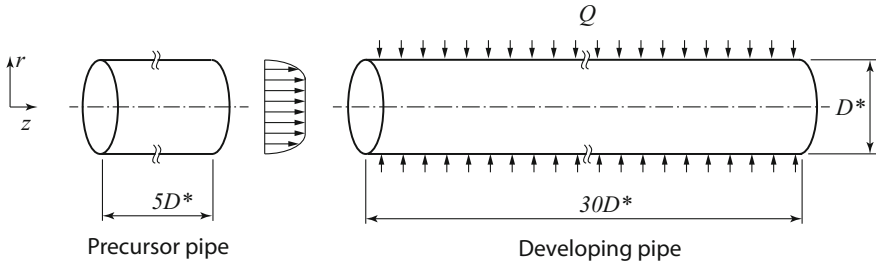

Fig. 2 Simulation setup

3 Results

The effects of thermal effusivity ratios on turbulence can be visually probed by looking at wall–parallel plane ($\theta - z$), depicted in Fig. 3 for instantaneous enthalpy fluctuations. The plane is located at $y^+ = 4.7$ (based on inlet condition) which corresponds to physical radial position of $r = 0.485$. As seen in Fig. 3, streaky patterns are clearly observed in enthalpy fluctuations and differences between $\mathrm{SC}_{K=\infty}$ and $\mathrm{SC}_{K=0}$ can be perceived. The regions of low and high enthalpy fluctuations are weakened for $\mathrm{SC}_{K=0}$. Similar differences in near–wall scalar fluctuations for incompressible boundary layers were also reported in Refs. [9, 11]. Furthermore, Fig. 3 shows a decrease in spanwise gradient and stream–wise coherency for $\mathrm{SC}_{K=0}$, if compared with $\mathrm{SC}_{K=\infty}$.

Figure. 4a shows the distribution of the bulk enthalpy in stream–wise direction for all cases investigated. Based on the overall energy conservation, it follows that for the cases with constant wall heat flux (cases $\mathrm{SC}_{K=\infty}$ and $\mathrm{CP}_{K=\infty}$) the distribution of the bulk enthalpy increases linearly as a function of z, namely $H_b = \frac{4Q}{Re_{b0}Pr_0}z$. The bulk enthalpy is defined as $H_b = \int_0^R \overline{\rho u_z h} / \int_0^R \overline{\rho u}_z$. It can be seen that for the constant property cases, the boundary condition has no influence on the global energy balance (the symbols for cases $\mathrm{CP}_{K=\infty}$ and $\mathrm{CP}_{K=0}$ overlap). This has also been confirmed numerically by Li et al. [9], whereby the Stanton number distributions for flat plate boundary layers with different thermal boundary condition collapse for fluids with $Pr = 2.0$.

For a supercritical fluid with large property fluctuations, however, the bulk enthalpy distributions are affected by the thermal boundary conditions. Based on the bulk enthalpy distribution in Fig. 4a, it can be seen that less energy is transferred to the fluid if the enthalpy at the wall is set to the averaged profile ($\mathrm{SC}_{K=0}$) that has been obtained from the isoflux simulation ($\mathrm{SC}_{K=\infty}$). Figure 4b shows the distribution of Nusselt number $Nu = \overline{\alpha \frac{\partial h}{\partial r}|_w} / \alpha_b (h_w - h_b)$ for all cases. A reduction in Nusselt number is observed in supercritical flow $Nu_{K=\infty}/Nu_{K=0} = 1.07$ while the differences in constant property flow is negligible $Nu_{K=\infty}/Nu_{K=0} = 1$.

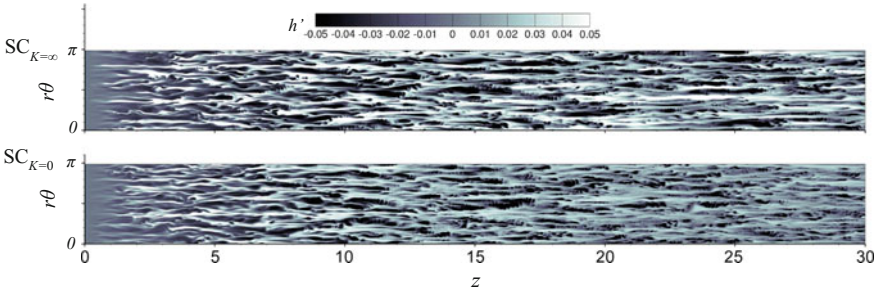

Fig. 3 Instantaneous enthalpy fluctuations h' in $z-\theta$ plane at $y^+ = 4.5$ (base on inlet condition)

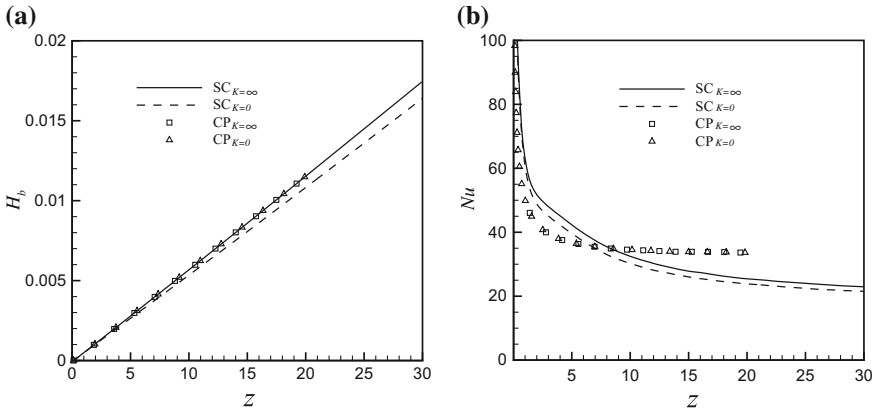

Fig. 4 **a** Bulk enthalpy. **b** Nusselt number

In Fig. 5a the radial turbulent heat fluxes $-\overline{\rho u_r'' h''}$ at $z = 15$ are shown for both $SC_{K=\infty}$ and $SC_{K=0}$ cases. The higher turbulent heat flux for $SC_{K=\infty}$ is obtained, if compared with $SC_{K=0}$. The differences in turbulent heat flux is related to enthalpy fluctuations, which is higher in $SC_{K=\infty}$ (see Fig. 3). In addition to h'', the velocity fluctuations also shows higher values in $SC_{K=\infty}$ case (not shown here). The differences in velocity fluctuations are associated to direct correlation between h' and ρ' ($\rho' \propto h'$). Larger enthalpy fluctuations h' in $SC_{K=\infty}$ results in higher density fluctuations ρ' which causes larger fluctuations in both radial and stream–wise velocity through conservation of mass. Figure 5b shows the evolution of turbulent shear stress $\overline{\rho u_r'' u_z''}$ for $SC_{K=\infty}$ and $SC_{K=0}$ cases at $z = 15$. The reason for the decreasing trend is the flow acceleration due to thermal expansion. As it is expected, it can be clearly seen that, the reduction in turbulent shear stress $\overline{\rho u_r'' u_z''}$ for $SC_{K=0}$ case is higher compared to $SC_{K=\infty}$ in both figures.

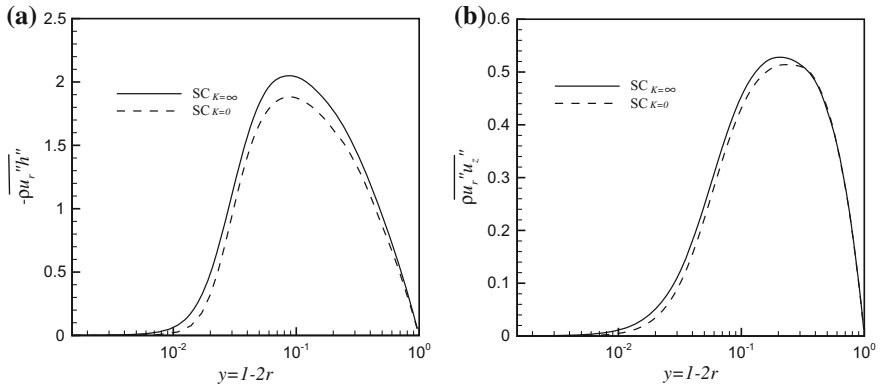

Fig. 5 **a** Radial turbulent heat flux at $z = 15$. **b** Turbulent shear stress at $z = 15$

4 Summary

In this work we used DNS to investigate the effect of thermal wall boundary conditions on developing turbulent pipe flows with CO_2 at a thermodynamic supercritical pressure of $P_0 = 80$ bar. Two different solid–fluid configurations are studied: infinite thermal effusivity ratio $K = \infty$, which is consistent with fluctuating wall enthalpy and zero thermal effusivity ratio $K = 0$, which corresponds to non-fluctuating wall enthalpy. In spite of higher Prandtl numbers in the supercritical case ($1 < Pr < 14$), a significant reduction in Nusselt number and bulk enthalpy is observed ($Nu_{K=\infty}/Nu_{K=0} = 1.07$). The turbulent heat flux $-\overline{\rho u_r'' h''}$ and Reynolds shear stress $\overline{\rho u_r'' u_z''}$ show significant decrease for $\mathrm{SC}_{K=0}$ as compared to $\mathrm{SC}_{K=\infty}$. These variations in turbulent statistics stem form the effects of wall on enthalpy fluctuations. Higher enthalpy fluctuations in the $\mathrm{SC}_{K=\infty}$ case induce higher property fluctuations which results in larger velocity fluctuations due to coupling between enthalpy and momentum.

Acknowledgements We acknowledge that the results of this research have been achieved using the PRACE Research Infrastructure resource Cartesius based in The Netherlands at SURFsara.

References

1. Span, R., Wagner, W.: Equations of state for technical applications. I. Simultaneously optimized functional forms for nonpolar and polar fluids. Int. J. Thermophys. **24**, 1–39 (2003)
2. Chen, H., Goswami, D.Y., Stefanakos, E.K.: A review of thermodynamic cycles and working fluids for the conversion of low-grade heat. Renew. Sustain. Energy Rev. **14**, 3059–3067 (2010)
3. Dostal, V., Hejzlar, P., Driscoll, M.J.: The supercritical carbon dioxide power cycle: comparison to other advanced power cycles. Nucl. Technol. **154**, 283–301 (2006)

4. Saka, S., Kusdiana, D.: Biodiesel fuel from rapeseed oil as prepared in supercritical methanol. Fuel **80**, 225–231 (2001)
5. Bae, J.H., Yoo, J.Y., Choi, H.: Direct numerical simulation of turbulent supercritical flows with heat transfer. Phys. Fluids **17**, 105104 (2005)
6. Nemati, H., Patel, A., Boersma, B.J., Pecnik, R.: Mean statistics of a heated turbulent pipe flow at supercritical pressure. Int. J. Heat Mass Transf. **83**, 741–752 (2015)
7. Kasagi, N., Kuroda, A., Hirata, M.: Numerical investigation of near-wall turbulent heat transfer taking into account the unsteady heat conduction in the solid wall. J. Heat Transf. **111**, 385–392 (1989)
8. Tiselj, I., Bergant, R., Mavko, B., Bajsic, I., Hetsroni, G.: DNS of turbulent heat transfer in channel flow with heat conduction in the solid wall. J. Heat Transf. **123**, 849–857 (2001)
9. Li, Q., Schlatter, P., Brandt, L., Henningson, D.S.: DNS of a spatially developing turbulent boundary layer with passive scalar transport. Int. J. Heat Fluid Flow **30**, 916–929 (2009)
10. Najm, H.N., Wyckoff, P.S., Knio, O.M.: A semi-implicit numerical scheme for reacting flow: I. Stiff chemistry. J. Comput. Phys. **143**, 381–402 (1998)
11. Kong, H., Choi, H., Lee, J.S.: Direct numerical simulation of turbulent thermal boundary layers. Phys. Fluids **12**, 2555–2568 (2000)

Turbulent Kinetic Energy Evolution in the Near Field of a Rotating-Pipe Round Jet

R. Mullyadzhanov, S. Abdurakipov and K. Hanjalić

1 Introduction

Using Large-Eddy Simulations (LES) and Proper Orthogonal Decomposition (POD) we study a turbulent round swirling jet issuing from an axially rotating pipe at Reynolds number $Re_b = 5300$ based on the bulk velocity U_b and diameter D of the pipe flow. The Reynolds number is chosen to match the available Direct numerical simulations (DNS) database for a pipe flow. The rotation rate is defined by the swirl parameter $N = U_w/U_b$ varying from 0 to 0.75 where U_w is the azimuthal velocity of the inner wall of the pipe. The aim is to explore the physics of a swirling flow when the inflow conditions of the problem are well defined. The broad literature on the subject of swirling jets suggests that the incoming velocity profile and the level of turbulence strongly affect the dynamics of the flow. Thus, the most important feature is the way one produces the swirl (e.g. tangential swirlers, rotating honeycombs etc.). The majority of configurations give the case-dependent velocity profiles in experiments which are hard to reproduce in computational studies. Here we study a jet flow issuing from a long rotating pipe. Thus, the incoming velocity profile is well defined. The main emphasis of this work is on coherent structures depending on the swirl intensity. The study in many ways follows the spirit of [1] who studied similar configuration but for low Reynolds numbers (laminar inflow).

R. Mullyadzhanov (✉)
Institute of Thermophysics SB RAS, Novosibirsk, Russia
e-mail: rustammul@gmail.com

S. Abdurakipov
Novosibirsk State University, Novosibirsk, Russia
e-mail: s.s.abdurakipov@gmail.com

S. Abdurakipov · K. Hanjalić
Delft University of Technology, Delft, Netherlands
e-mail: khanjalic@gmail.com

D.G.E. Grigoriadis et al. (eds.), *Direct and Large-Eddy Simulation X*,
ERCOFTAC Series 24, https://doi.org/10.1007/978-3-319-63212-4_71

2 Computational Details and Results

We consider a fully turbulent canonical rotating-pipe jet configuration (see Fig. 1, [2, 3]). The flow from a long clockwise-rotating pipe with the Reynolds number of 5300 is represented with a $1D$ pipe fragment. The total computational domain represents a cylinder of $12D$ in diameter and $16D$ in length. The convective outflow is imposed at the exit boundary, while constant pressure is imposed on the open lateral boundary. A small co-flow of $U_{co} = 0.04U_b$ is imposed at the bottom $x = -1D$. The LES grid has a DNS-like resolution in the near-nozzle area and consists of $252 \times 282 \times 264$ cells ($\sim 16.7 \times 10^6$) in the radial, axial, and azimuthal directions, respectively, with the majority clustered in shear layers and near-wall regions with the stretching factor being less than 5 percent. The minimum axial spacing $x = 0.005D$ is at the nozzle exit. Figure 1 also shows the mean axial and tangential pipe velocity profiles used at the inflow. Axial velocity displays some dependence on N and tendency to laminarization with higher N, while tangential velocity normalized with bulk velocity and N is almost insensitive to the rotation rate in this range.

The LES is performed using the TU Delft unstructured finite-volume computational code T-FlowS. The filtered Navier-Stokes and continuity equations for incompressible fluid are closed by the dynamic Smagorinsky subgrid-scale model. The diffusion and convection terms in the momentum equations are discretised by the second-order central-difference scheme, whereas the time-marching is performed using a fully-implicit three-level time scheme.

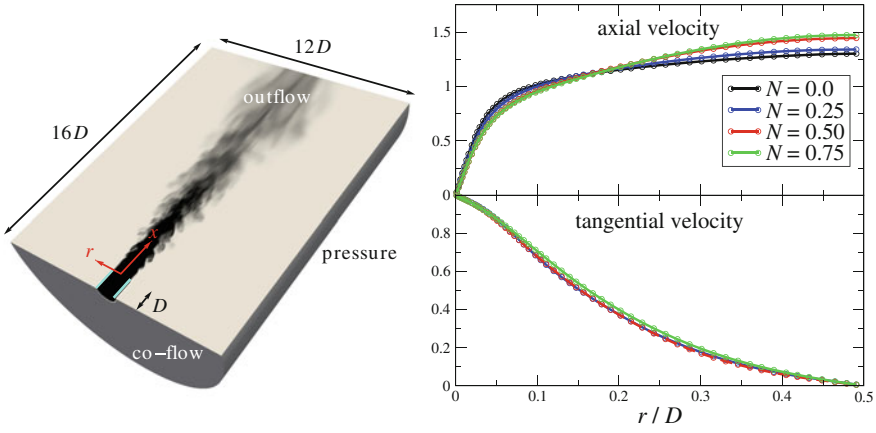

Fig. 1 *Left*: Half of the computational domain, cylindrical coordinate system (r, ϕ, x) and time-averaged axial and tangential velocity profiles from precursor LES of a periodic fully-developed turbulent pipe flow used as boundary conditions. The instanteneous field of a passive scalar is visualised. Cyan lines show the walls of the rotating pipe fragment. *Right*: Mean axial and tangential inflow pipe velocity profiles normalized with bulk velocity (tangential velocity is also normalized with N)

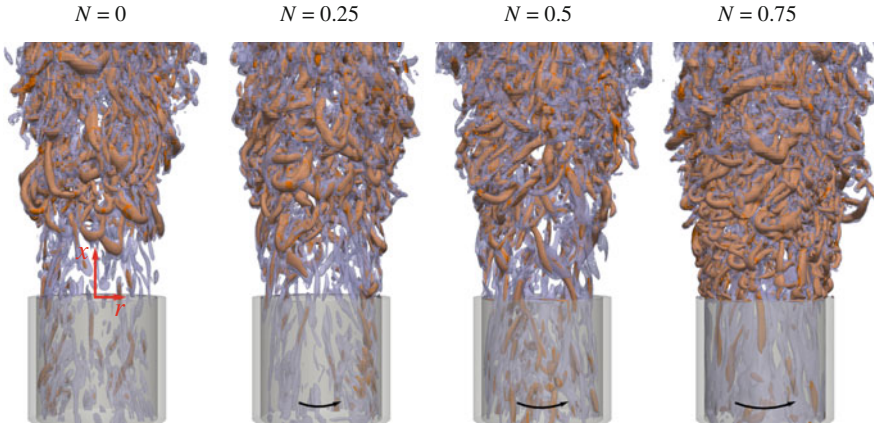

Fig. 2 The visualization of vortical structures near the nozzle of the jet using two isosurfaces of the Q-criterium with $Q = 0.5$ (*transparent violet*) and $Q = 1.5$ (*orange*) for various rotation rates. Black arrows show the clockwise rotation direction of the inner wall of the pipe

Figure 2 shows vortex structures in the near field of the jet. Vortices are visualized by constant levels of the Q-criterium where $Q = (\Omega_{ij}\Omega_{ij} - S_{ij}S_{ij})/2$ with Ω_{ij} and S_{ij} being the rotation rate and the rate-of-strain tensors, respectively. The pipe flow supplies the streamwise streaky structures which can be traced in the range of $0 \leq x/D \leq 1$. For $N = 0$ the interaction of streaky structures and the shear layer of the jet leads to the formation of the large-scale harpin-like structures at $x/D > 0.5$. Harpins are slightly tilted for low rotations $N = 0.25$ and can hardly be recognized for higher swirl. For relatively high rotation rates ($N = 0.75$) structures existing in the pipe are immediately destroyed by a strong azimuthal shear layer in the vicinity of the nozzle edge.

We perform Fourier decomposition with respect to ϕ and POD at various axial stations of the jet flow to get the information on the evolution of the amplitude and spatial distribution of modes corresponding to each azimuthal wavenumber m. We consider 32 stations starting from $x/D = 0$ with the last position at $x/D = 10$. The spatial step close to the nozzle is $\Delta x/D = 0.25$ while in the end it is fixed to $\Delta x/D = 0.5$. While most of low harmonics $|m| \leq 7$ grow with x along all of the distance, high m reach their saturation at $x/D = 1 - 2$ (not shown here). For $N = 0$ the axisymmetric mode $m = 0$ after exponential growth at $x/D < 1$ displays only some mild variations with x having the smallest λ among $|m| \leq 6$. Along $0 \leq x/D \leq 10$, there is a competition between the eigenvalues for different m. We can say that $m = 1, 2, 3$ contain the most of the turbulent kinetic energy, although, probably all low modes $|m| \leq 7$ have to be taken into account to reflect the dynamics correctly. At the same time, each high harmonic contains the more energy, the smaller the value of m. The higher the value of N, the stronger is the separation of $m = 1 - 3$ and other modes.

Further we analyze the motion from separate azimuthal modes m. It is convenient to operate in terms of propagating helical waves appearing as normal modes of the form $e^{i(m\phi+k_x x-\omega t)}$, where k_x is the streamwise wavenumber and ω is the frequency. In [4] they found the presence of single and double helix vortices which were supposed to correspond to $m = 1$ and 2 in the far field of a non-swirling jet. Note that the information obtained from a time sequence of two-dimensional slices of instanteneous velocity contains the mixture of co-rotating and counter-rotating modes with opposite m values (see, for example, the Conclusions in [5]). To be able to separate these helical patterns rotating in opposite directions, one may apply Fourier transform with two variable x and ϕ. However, the Fourier transorm requires periodic direction along the corresponding spatial variable. While possible, for example, for the infinite pipe flow, the Fourier transorm is not applicable to jets due to a significant radial expansion and evolution downstream. Recently, there was a successful attempt to statistically describe the flapping against helical motion of the jet core based on the information about the temporal amplitudes from POD [6].

Following [6], we analyze the temporal behaviour of a corresponding POD mode. We exclusively deal with temporal amplitudes a_q^m, where q is the number of a POD mode. Since they are complex-valued, the following representation is possible:

$$a(t) = \eta(t)e^{2\pi i\gamma(t)}, \tag{1}$$

where η and γ are the time sequences of real numbers. It was previously shown [6] that particular combinations of η and γ correspond to helical and flapping motion. The ideal helical motion represents a rotation of the jet core with constant angular velocity at some distance from the axis. Thus, one expects η to be constant and γ linearly grow in time. In terms of two azimuthal modes with opposite m values it means that one is present while the other cancels out. For the flapping motion both modes are present with the same rotation speed but opposite directions. This results in a more compicated behaviour of η and γ.

Figure 3 shows the behaviour of γ during 150 time units for first four q, m and $N = 0; 0.5$. A striking feature of $\gamma(t)$ is that it contains very long time intervals where it varies linearly. As pointed out above, it means that the corresponding spatial mode rotates around the jet core with some precession frequency. Dashed lines demonstrate the slope for some characteristic regions. This slope is in fact the non-dimensional angular velocity Ω. For example, three typical regions are shown in Fig. 3 (left) for $m = 1$: $\Omega \approx -0.87; -0.21; 0.076$. For $\Omega \approx -0.21$ and $\gamma = \Omega t$ the corresponding POD mode turns around in about 5 time units according to Eq. (1). These curves of $\gamma(t)$ for $m = 1$ demonstrate some intermittency showing changes of rotation direction within short time intervals (say, $t < 25$ with the typical value of $t = 5 - 10$), while in a long run the average rotation is non-zero. For higher m the behaviour is more monotonic, with the maximum absolute values $\Omega \approx -0.167$ for $m = 2$ and $\Omega \approx 0.08$ for $m = 3$. Similar trends can be found for $N = 0.5$.

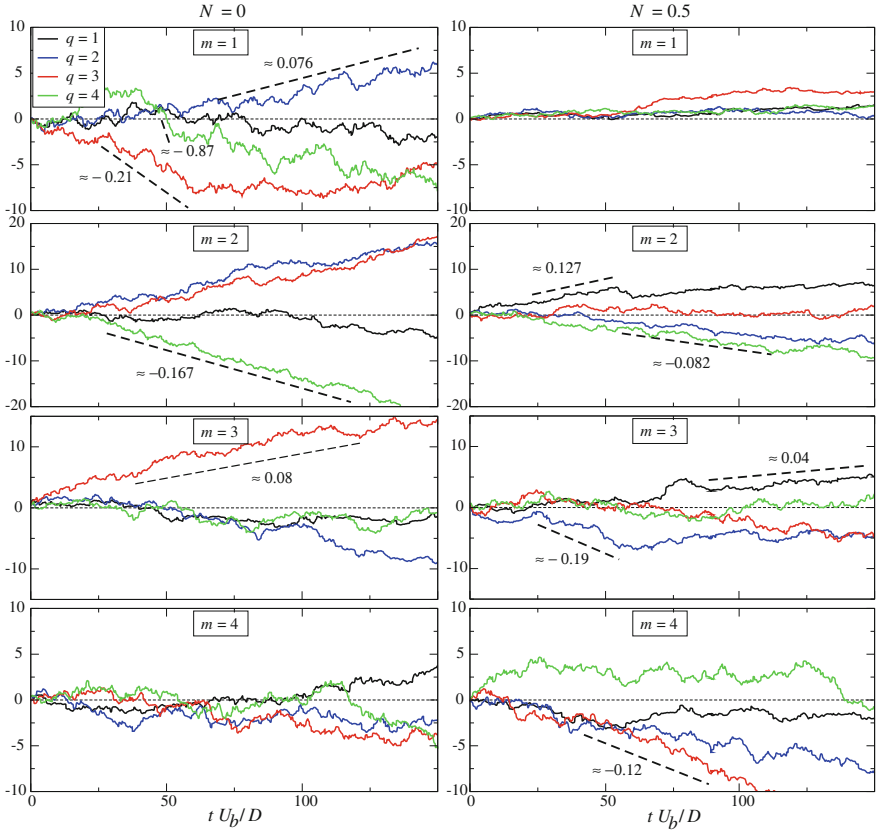

Fig. 3 The time history of the phase γ for different m and q (POD modes) for $x/D = 6$

3 Conclusions

We performed LES and POD analysis to get an insight into the coherent motion of the near nozzle area in a canonical rotating-pipe jet at $Re = 5300$ and $N = 0; 0.25; 0.5; 0.75$. We may conclude the following:

- The near-wall streaky structures identified by POD in a pipe flow can be recognised only along the first diameter of the pipe ($x/D < 1$) for low rotations $N \leq 0.5$. The azimuthal shear layer for a higher swirl ($N = 0.75$) immediately destroys pipe structures. Harpin-like vortices observed for a non-swirling jet as the interation of streaks and the shear layer are tilted at low rotation rates ($N = 0.25$) and cannot be recognized for higher swirl numbers.
- A set of low harmonics with the azimuthal numbers $|m| \leq 7$ are needed to describe the dynamics of the jet; the kinetic energy of high wavenumbers does not grow downstream. The kinetic energy for separate m grows linearly dowstream for first

$x = 5 - 8D$. The higher the rotation rate, the more obvious is the separation of energy between $m = 1 - 3$ modes and others.

- The phase of complex-valued POD temporal amplitudes $a(t)$ informs on the rotation dynamics of the corresponding mode around the axis of the jet. Low wavenumbers show two types of dynamics: "fast" and "slow" rotation. They differ in characteristic time scales of the process with $t < 25$ ($t = 5 - 10$) for the former and with up to $t = 150$ (or more) for the latter.

The described findings imply some important conclusions. As opposed to the periodic pipe flow where Fourier modes in axial and tangential directions are imposed by symmetries and represent basis functions in the form of propagating helical waves, the jet flow is inhomogeneous in axial direction restricting that class of functions. However, it is still possible to show that propagating helices are, indeed, the common form of POD modes for low azimuthal wavenumbers. Finally, it is interesting that the swirl does not ruin the helical structure of the jet. Probably it is due to the fast decay of the azimuthal velocity downstream. Indeed, it is known that the decay rate of the axial velocity in the far field of the jet is mainly governed by the axial momentum conservation law leading to a x^{-1} dependence. At the same time the conservation of angular momentum suggests the x^{-2} decay rate for azimuthal velocity. The same dependence is valid in the far field for the deviations of the axial velocity from the x^{-1} law if the jet nozzle is non-circular (see [7]). Thus, the conclusions made above on the dynamical structure may cover a wide range of free swirling non-circular turbulent jets which is to prove in following studies.

Acknowledgements This work is funded by Russian Science Foundation grant No. 14-19-01685. The computational resources are provided by Siberian Supercomputer Center SB RAS (Novosibirsk) and Joint Supercomputer Center RAS (Moscow).

References

1. Liang, H., Maxworthy, T.: An experimental investigation of swirling jets. J. Fluid Mech. **525**, 115–159 (2005)
2. Mullyadzhanov, R., Abdurakipov, S., Hanjalic, K.: Helical structures in the near field of a turbulent pipe jet. Flow Turbul. Combust. **98**(2), 367–388 (2017)
3. Mullyadzhanov, R., Abdurakipov, S., Hanjalic, K.: On coherent structures and mixing characteristics in the near field of a rotating-pipe jet. Int. J. Heat Fluid Flow **63**, 139–148 (2017)
4. Tso, J., Hussain, F.: Organized motions in a fully developed turbulent axisymmetric jet. J. Fluid Mech. **203**, 425–448 (1989)
5. Yoda, M., Hesselink, L., Mungal, M.G.: Instantaneous three-dimensional concentration measurements in the self-similar region of a round high-Schmidt-number jet. J. Fluid Mech. **279**, 313–350 (1994)
6. Davoust, S., Jacquin, L., Leclaire, B.: Dynamics of $m = 0$ and $m = 1$ modes and of streamwise vortices in a turbulent axisymmetric mixing layer. J. Fluid Mech. **709**, 408–444 (2012)
7. Mullyadzhanov, R.I., Yavorskii, N.I.: Solution of the problem of flow of a non-axisymmetric swirling submerged jet. J. Appl. Mech. Tech. Phys. **54**(2), 207–211 (2013)

Large Eddy Simulation of Turbulent Rayleigh-Bénard Convection in a Cubic Cell

N. Foroozani, J.J. Niemela, Vincenzo Armenio and K.R. Sreenivasan

1 Introduction

Turbulent Rayleigh-Bénard convection (RBC) in a fluid heated from below and cooled from above is a challenging problem in nonlinear physics, with many important applications in natural and engineering systems. Because of the complexity of the governing equations, analytical progress in understanding convection has been slow, and laboratory experiments and numerical simulations have assumed increased importance. The RB system is characterized by three non-dimensional parameters: the Rayleigh number Ra $(= \alpha g \Delta T H^3/\nu\kappa)$, the Prandtl number Pr $(= \nu/\kappa)$, and the aspect ratio Γ $(= L/H)$. Here, α is the thermal expansion coefficient, ΔT is the temperature difference between the horizontal plates of height H, g is the acceleration of gravity, κ and ν are the thermal diffusivity and kinematic viscosity of the fluid, respectively, and L is the horizontal extension of the domain.

The subject of turbulent convection has been studied extensively in the past and mostly focused on the main flow features and heat transfer in a cylinder varying the parameters (Ra, Pr, Γ) but only a few of them focused on 3-dimensional complex

N. Foroozani (✉) · J.J. Niemela (✉)
The Abdus Salam International Centre for Theoretical Physics (ICTP), Strada Costiera 11, 34151 Trieste, Italy
e-mail: nforooza@ictp.it

J.J. Niemela
e-mail: niemela@ictp.it

V. Armenio
Dipartimento di Ingegneria e Architettura, Università di Trieste, 34100 Trieste, Italy
e-mail: armenio@dica.units.it

K.R. Sreenivasan
Departments of Physics and Mechanical Engineering, Courant Institute of Mathematical Sciences, New York University, New York, NY 10012, USA
e-mail: katepalli.sreenivasan@nyu.edu

D.G.E. Grigoriadis et al. (eds.), *Direct and Large-Eddy Simulation X*,
ERCOFTAC Series 24, https://doi.org/10.1007/978-3-319-63212-4_72

geometries. Daya & Ecke [1] –henceforth DE01– investigated the influence of the shape of the container on statistics of the convective flow. They found that global parameters such as the Nusselt number, Nu, are not affected by the *geometrical shape* of the container but significant differences were observed in the local properties of power law scaling with Ra.

The aim of our study is to shed light on previously reported experimental results, DE01, that the scaling of turbulent fluctuations in the geometric center of the convection cell are strongly influenced by the geometrical shape of the convection cell and confirm its validity.

2 Numerical Method

We performed large-eddy simulations (LES) to separate the flow field into a resolved (large) scale and a subgrid-scale (SGS) by a spatial filtering operation whose width is proportional to the cell size, $\bar{\Delta} = (\Delta_x \Delta_y \Delta_z)^{1/3}$. The governing equations under the Boussinesq approximation are;

$$\frac{\partial \overline{u}_j}{\partial x_j} = 0, \tag{1}$$

$$\frac{\partial \overline{u}_i}{\partial t} + \frac{\partial \overline{u}_j \overline{u}_i}{\partial x_j} = -\frac{1}{\rho_0}\frac{\partial \overline{P}}{\partial x_i} + \nu \frac{\partial^2 \overline{u}_i}{\partial x_j \partial x_j} - \frac{\overline{\rho}}{\rho_0} g \delta_{i2} - \frac{\partial \tau_{ij}}{\partial x_j}, \tag{2}$$

$$\frac{\partial \overline{\rho}}{\partial t} + \frac{\partial \overline{u}_j \overline{\rho}}{\partial x_j} = k \frac{\partial^2 \overline{\rho}}{\partial x_j \partial x_j} - \frac{\partial \lambda_j}{\partial x_j}, \tag{3}$$

where the symbol $(^-)$ denotes the filtering operation, $\overline{u}_i$ is the velocity component in $i-$direction, x_i is the spatial coordinate in the $i-$direction with x_2 as the vertical (upward) direction, $\overline{P}$ is the pressure field, t is time, and δ_{ij} is the Kronecker symbol. τ_{ij} and λ_j are SGS stress tensor and the SGS heat flux, respectively. In the model it is assumed that density ρ depends linearly on temperature as $\rho = \rho_0[1 - \alpha(T - T_0)]$, where ρ_0 is the density at the reference temperature T_0. The effect of the unresolved small scales appears through the terms $\tau_{ij} = \overline{u_i u_j} - \overline{u}_i \overline{u}_j$ and $\lambda_j = \overline{u_j \rho} - \overline{u}_j \overline{\rho}$ in the momentum and density equations, respectively. We use a dynamic eddy viscosity model to parametrize the SGS momentum and buoyancy fluxes as described in Armenio & Sarkar [2]. The model is treated according to the Lagrangian technique proposed by Meneveau et al. [3]. It should be noted that our LES methodology has been validated against DNS results of [4] for the case of two infinite and parallel plates, obtaining an excellent agreement for the first-and second-order statistics. We apply the no-slip condition on all six walls. The vertical lateral walls are perfectly adiabatic $\partial \overline{\rho}/\partial \mathbf{n} = 0$, where $\mathbf{n}$ is the normal vector, and the top and bottom walls are isothermal with a fixed temperature difference ΔT giving a density difference

$\Delta\rho/\rho_0 = 1$. The aspect ratio of the container is taken to be one. We confine our study to $Pr = 0.7$, which is a typical Prandtl number for air. The equations are discretized on a non-staggered mesh using a second-order-accurate finite difference method. The Adams-Bashforth technique is used for the time advancement of the convective terms, whereas the diffusive terms are treated with the Crank-Nicolson scheme. The Poisson equation is solved using a multi-grid method. A typical domain size is discretized with $32 \times 64 \times 32$ ($\approx 6.5 \times 10^4$) grid cells in x, y and z directions respectively, for $10^6 \leq Ra \leq 10^8$ with increased resolution to $64 \times 96 \times 64$ ($\approx 4.5 \times 10^6$) for higher Ra. In all simulations, the grid spacing is clustered in the regions close to the walls in order to resolve properly the momentum and thermal boundary layers. It is worth mentioning that for all Ra we verified that the number of grid points (N_{BL}) in the thermal boundary layer was larger than 3–5, exceeding the criterion of Verzicco & Camussi [5]. In our study velocity is normalized by the free-fall-velocity $U_f = \sqrt{(\alpha g \Delta T H)}$, t is normalized by the free-fall time $t_f = H/U_f$, and ρ is the density normalized by $\Delta\rho$. In all the numerical runs, data sampling started once the flow was fully turbulent and had become statistically steady. Moreover, individual runs were performed for over $5000t_f$, which is an order of magnitude larger than that typically used in direct numerical simulation (DNS) (see, e.g., [6]). In order to verify the global properties obtained from our simulations, we compare the Nusselt number, $Nu = \frac{H}{\Delta\rho} \frac{\langle \partial\rho(x,z)\rangle_t}{\partial y} |_{wall}$, with numerical and experimental results from the literature. Here $\langle ... \rangle_t$ denotes a time average of the quantity within the brackets. In terms of its scaling with Ra we obtained $Nu = 0.15Ra^{0.29}$ which is in good agreement with experimental result of Qiu & Xia [7] who obtained $Nu = 0.19Ra^{0.28\pm0.1}$ in their cubic container and using water as a working fluid.

3 Results and Discussions

3.1 Flow Topology

As an example, the instantaneous density iso-surface obtained for two different $Ra = 10^6$ and $Ra = 10^8$ is shown in Fig. 1. Even though the mean flow is similar in both cases (up-flow region on the left and down-flow region on the right) the shape of the iso-surfaces changes dramatically with Ra. Indeed, the size of the structures decreases rapidly with increasing Ra.

3.2 Determination of LSC Orientation

Figure 2 illustrates the time-averaged vertical velocity streamlines over *a finite time-interval* in which the orientation of the large-scale circulation (LSC) is known to be stable along one diagonal plane.

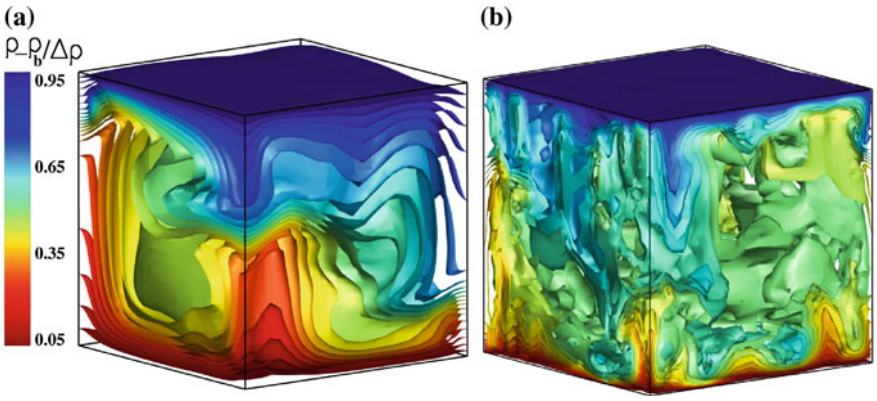

Fig. 1 Instantaneous density iso-surface for **(a)** $Ra = 10^6$ and **(b)** $Ra = 10^8$, $Pr = 0.7$, $\Gamma = 1$ on the $32 \times 64 \times 32$ grids

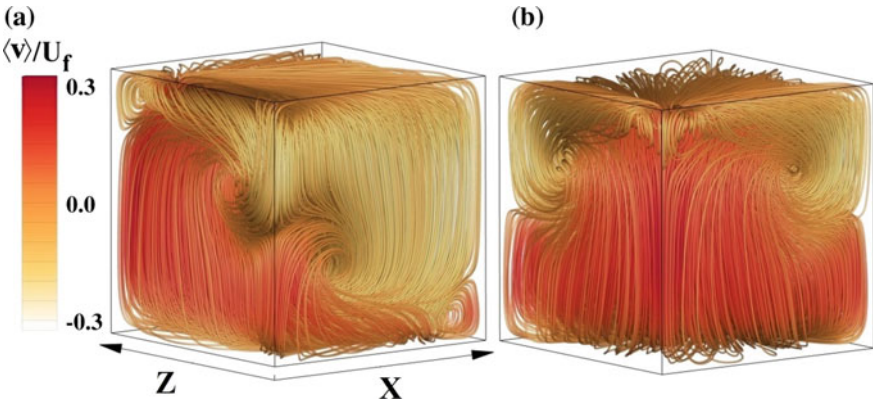

Fig. 2 Streamlines within the full convection cell time averaged for more than $5296t_f$. Colour contour denotes the intensity of the vertical mean velocity, normalized by the free-fall velocity scale $\langle v \rangle / U_f$. Figure **(a)** shows one of the diagonals containing the mean wind and **(b)** shows the opposite diagonal, illustrating strong counter-rotating cells. $Ra = 10^6$, $Pr = 0.7$ and $\Gamma = 1$ on the $32 \times 64 \times 32$ grids

The flow exhibits a *mean wind* (or LSC) [7, 8] moving along one of the diagonal directions (see Fig. 2a) with two small recirculation regions in the corners: one is at the top-left corner of the figure where the mean wind coming from below impinges the upper surface of the cavity and the other is at the lower-right corner where the descending mean wind impinges the bottom surface. In the opposite diagonal (Fig. 2b) two strong counter-rotating vortex structures are shown converging at the mid-plane. Such counter-rotating flows have also been observed in other simulations (see, e.g., [6]). This complex flow structure has significant effects on the resulting turbulent fields.

3.3 Local Fluctuations

We define the root-mean-square (σ) of the resolved density fluctuations as $\sigma_\rho(\mathbf{x}) = [\langle\rho(\mathbf{x})\rho(\mathbf{x})\rangle_t - \langle\rho(\mathbf{x})\rangle_t\langle\rho(\mathbf{x})\rangle_t]^{1/2}$, normalized by $\Delta\rho$, and that of resolved vertical velocity fluctuations as $\sigma_v(\mathbf{x}) = [\langle v(\mathbf{x})v(\mathbf{x})\rangle_t - \langle v(\mathbf{x})\rangle_t\langle v(\mathbf{x})\rangle_t]^{1/2}$ normalized by ν/H. It should be stressed that the SGS contribution to the total *rms* is negligible. The normalized density and velocity fluctuations is shown in Fig. 3 as a function of Ra. The measured fluctuations of density, $\sigma_\rho/\Delta\rho$, are well described at the cell center by the power law $\sigma_\rho/\Delta\rho = 49.03Ra^{-0.46}$ (solid line). The scaling behavior is in excellent agreement with DE01 for a near-cubic cell with $\Gamma = 0.7$ and $Pr = 5.46$.

Indeed, those authors found a power exponent of -0.48 ± 0.03 (the dashed line in Fig. 3a while, for cylindrical cells under the same experimental conditions, they measured the considerably smaller exponent of -0.1 ± 0.02 (the dash-dotted line). In Fig. 3b we show the *rms* velocity fluctuations in our cubic cell and fit it by $\sigma_v H/\nu = 0.31Ra^{0.39}$. This result is also in good agreement with DE01 in which the measured exponent was 0.36 ± 0.05 (dashed line). By way of contrast, their result for the cylindrical cell, shown again by a dashed-dotted line, demonstrates the large difference resulting from the change in cross-sectional geometry. The data in Fig. 3 were taken at the cell center. The time-averaged mapping of density fluctuations is shown in Fig. 4 reveals fixed inhomogeneities in the vertical planes corresponding to the two diagonals. At the mid-height level, the higher levels of *rms* density fluctuations correspond to the diagonal opposite that of the LSC where we observe strong counter-rotating vortex structures (see Fig. 2) which mix hot and cold plumes at their mid-height convergence (Fig. 4b). Thus it is no surprise that the largest gradient in density fluctuations occurs there.

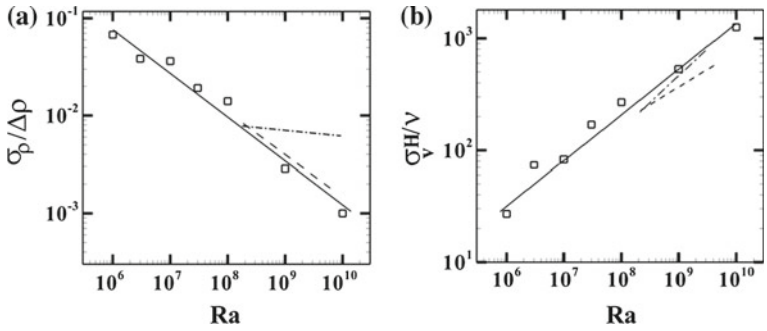

Fig. 3 Normalized fluctuations in **(a)** density given by $\sigma_\rho/\Delta\rho$ and **(b)** the vertical velocity given by $\sigma_v H/\nu$ measured at the cell center. The solid line are the power law fits: $\sigma_\rho/\Delta\rho = 49.03Ra^{-0.46}$ **(a)** and $\sigma_v H/\nu = 0.31Ra^{0.39}$ **(b)** Dashed lines are power law fits for the near-cubic cell and dash-dotted for the cylindrical cell of DE01 for comparison

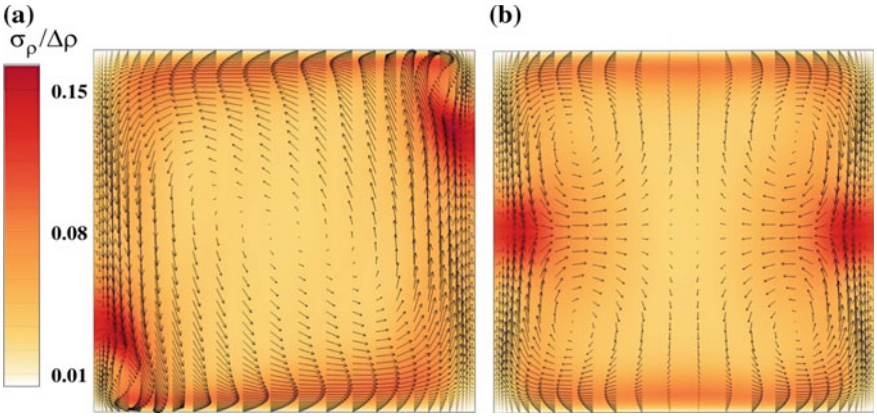

Fig. 4 Time-averaged local *rms* density fluctuation in the units of $\Delta\rho$. $Ra = 10^6$, $Pr = 0.7$, $\Gamma = 1$. Averaging has been performed over $5296\, t_f$. Figure **(a)** shows the vertical diagonal plane containing the large scale circulation and **(b)** shows the other vertical diagonal plane containing the counter-rotating cells. We have included the velocity vectors for clarity

4 Conclusions

To summarize, we investigated numerically the scaling of the local density fluctuations in RBC in a unit aspect ratio cubic confinement. We observed a stable pattern of LSC for all Ra investigated (within a proper time-interval), which has a strong influence on the scaling of fluctuations. Extending the range of Ra accessed by DE01, we have confirmed the scaling seen by those authors for both density (temperature) and velocity fluctuations at the cell center and provide insights on physical mechanisms for the observed scaling properties.

References

1. Daya, Z.A., Ecke, R.E.: Does turbulent convection feel the shape of geometry? Phys. Rev. Lett. **87**, 184501 (2001)
2. Armenio, V., Sarkar, S.: An investigation of stably stratified turbulent channel flow using large eddy simulation. J. Fluid Mech. **459**, 1 (2002)
3. Meneveau, C., Lund, T.S., Cabot, W.H.: A Lagrangian dynamic subgrid-scale model of turbulence. J. Fluid Mech. **319**, 353 (1996)
4. Kimmel, S.J., Domaradzki, J.A.: Large eddy simulations of Rayleigh-Bénard convection using subgrid scale estimation model. Phys. Fluids **12**, 169 (2000)
5. Verzicco, R., Camussi, R.: Numerical experiments on strongly turbulent thermal convection in a slender cylindrical cell. J. Fluid Mech. **477**, 19 (2003)

6. Kaczorowski, M., Xia, K.Q.: Turbulent flow in the bulk of Rayleigh-Bénard convection: small-scale properties in cubic cell. J. Fluid Mech **722**, 596 (2013)
7. Qiu, X.L., Xia, K.Q.: Viscous boundary layers at the side wall of convection cell. Phys. Rev. Lett. **58**, 486 (1998)
8. Niemela, J.J., Skrbek, L., Sreenivasan, K.R., Donnelly, R.J.: The wind in confined thermal convection. J. Fluid Mech. **449**, 169 (2001)